frontiers | Research Topics

Digital revolution in oncology: How digital tools transform the evaluation and management of cancer patients

Edited by
Konstanty Korski, Kee Yuan Ngiam, Mengling Feng and Paolo Ocampo

Published in
Frontiers in Surgery
Frontiers in Digital Health
Frontiers in Oncology

ISSN 1664-8714
ISBN 978-2-8325-4328-3
DOI 10.3389/978-2-8325-4328-3

About Frontiers

Frontiers is more than just an open access publisher of scholarly articles: it is a pioneering approach to the world of academia, radically improving the way scholarly research is managed. The grand vision of Frontiers is a world where all people have an equal opportunity to seek, share and generate knowledge. Frontiers provides immediate and permanent online open access to all its publications, but this alone is not enough to realize our grand goals.

Frontiers journal series

The Frontiers journal series is a multi-tier and interdisciplinary set of open-access, online journals, promising a paradigm shift from the current review, selection and dissemination processes in academic publishing. All Frontiers journals are driven by researchers for researchers; therefore, they constitute a service to the scholarly community. At the same time, the *Frontiers journal series* operates on a revolutionary invention, the tiered publishing system, initially addressing specific communities of scholars, and gradually climbing up to broader public understanding, thus serving the interests of the lay society, too.

Dedication to quality

Each Frontiers article is a landmark of the highest quality, thanks to genuinely collaborative interactions between authors and review editors, who include some of the world's best academicians. Research must be certified by peers before entering a stream of knowledge that may eventually reach the public - and shape society; therefore, Frontiers only applies the most rigorous and unbiased reviews. Frontiers revolutionizes research publishing by freely delivering the most outstanding research, evaluated with no bias from both the academic and social point of view. By applying the most advanced information technologies, Frontiers is catapulting scholarly publishing into a new generation.

What are Frontiers Research Topics?

Frontiers Research Topics are very popular trademarks of the *Frontiers journals series*: they are collections of at least ten articles, all centered on a particular subject. With their unique mix of varied contributions from Original Research to Review Articles, Frontiers Research Topics unify the most influential researchers, the latest key findings and historical advances in a hot research area.

Find out more on how to host your own Frontiers Research Topic or contribute to one as an author by contacting the Frontiers editorial office: frontiersin.org/about/contact

Digital revolution in oncology: How digital tools transform the evaluation and management of cancer patients

Topic editors

Konstanty Korski — Roche, Switzerland
Kee Yuan Ngiam — National University Health System, Singapore
Mengling Feng — National University of Singapore, Singapore
Paolo Ocampo — Genentech Inc., United States

Citation

Korski, K., Ngiam, K. Y., Feng, M., Ocampo, P., eds. (2024). *Digital revolution in oncology: How digital tools transform the evaluation and management of cancer patients*. Lausanne: Frontiers Media SA. doi: 10.3389/978-2-8325-4328-3

Table of contents

frontiers in Digital Health

STUDY PROTOCOL
published: 12 April 2021
doi: 10.3389/fdgth.2021.635524

Personalised, Rational, Efficacy-Driven Cancer Drug Dosing *via* an Artificial Intelligence SystEm (PRECISE): A Protocol for the PRECISE CURATE.AI Pilot Clinical Trial

Benjamin Kye Jyn Tan[1†], *Chong Boon Teo*[1†], *Xavier Tadeo*[2,3,4], *Siyu Peng*[5], *Hazel Pei Lin Soh*[1], *Sherry De Xuan Du*[1], *Vilianty Wen Ya Luo*[6], *Aishwarya Bandla*[2], *Raghav Sundar*[1,2,3,6,7*], *Dean Ho*[2,3,4,8,9*], *Theodore Wonpeum Kee*[2,3,4*] and *Agata Blasiak*[2,3,4*]

[1] Yong Loo Lin School of Medicine, National University of Singapore, Singapore, Singapore, [2] The N.1 Institute for Health (N.1), National University of Singapore, Singapore, Singapore, [3] The Institute for Digital Medicine (WisDM), Yong Loo Lin School of Medicine, National University of Singapore, Singapore, Singapore, [4] Department of Biomedical Engineering, NUS Engineering, National University of Singapore, Singapore, Singapore, [5] Department of Medicine, National University Health System, Singapore, Singapore, [6] Haematology-Oncology Research Group, National University Cancer Institute, Singapore (NCIS), Singapore, Singapore, [7] Department of Haematology-Oncology, National University Health System, Singapore, Singapore, [8] Department of Pharmacology, Yong Loo Lin School of Medicine, National University of Singapore, Singapore, Singapore, [9] Smart Systems Institute, National University of Singapore, Singapore, Singapore

Introduction: Oncologists have traditionally administered the maximum tolerated doses of drugs in chemotherapy. However, these toxicity-guided doses may lead to suboptimal efficacy. CURATE.AI is an indication-agnostic, mechanism-independent and efficacy-driven personalised dosing platform that may offer a more optimal solution. While CURATE.AI has already been applied in a variety of clinical settings, there are no prior randomised controlled trials (RCTs) on CURATE.AI-guided chemotherapy dosing for solid tumours. Therefore, we aim to assess the technical and logistical feasibility of a future RCT for CURATE.AI-guided solid tumour chemotherapy dosing. We will also collect exploratory data on efficacy and toxicity, which will inform RCT power calculations.

Methods and analysis: This is an open-label, single-arm, two-centre, prospective pilot clinical trial, recruiting adults with metastatic solid tumours and raised baseline tumour marker levels who are planned for palliative-intent, capecitabine-based chemotherapy. As CURATE.AI is a small data platform, it will guide drug dosing for each participant based only on their own tumour marker levels and drug doses as input data. The primary outcome is the proportion of participants in whom CURATE.AI is successfully applied to provide efficacy-driven personalised dosing, as judged based on predefined considerations. Secondary outcomes include the timeliness of dose recommendations, participant and physician adherence to CURATE.AI-recommended doses, and the proportion of clinically significant dose changes. We aim to initially enrol 10 participants from two hospitals in Singapore, perform an interim analysis, and consider either

OPEN ACCESS

Edited by:
Konstanty Korski, Roche, Switzerland

Reviewed by:
Paraskevi Papadopoulou, American College of Greece, Greece
Meenakshi Chatterjee, Johnson & Johnson, United States

***Correspondence:**
Agata Blasiak
agata.blasiak@nus.edu.sg
Theodore Wonpeum Kee
bietwk@nus.edu.sg
Dean Ho
biedh@nus.edu.sg
Raghav Sundar
raghav_sundar@nuhs.edu.sg

[†] *These authors have contributed equally to this work*

Specialty section:
This article was submitted to Personalized Medicine, a section of the journal Frontiers in Digital Health

Received: *30 November 2020*
Accepted: *04 February 2021*
Published: *12 April 2021*

Citation:
Tan BKJ, Teo CB, Tadeo X, Peng S, Soh HPL, Du SDX, Luo VWY, Bandla A, Sundar R, Ho D, Kee TW and Blasiak A (2021) Personalised, Rational, Efficacy-Driven Cancer Drug Dosing via an Artificial Intelligence SystEm (PRECISE): A Protocol for the PRECISE CURATE.AI Pilot Clinical Trial. Front. Digit. Health 3:635524. doi: 10.3389/fdgth.2021.635524

cohort expansion or an RCT. Recruitment began in August 2020. This pilot clinical trial will provide key data for a future RCT of CURATE.AI-guided personalised dosing for precision oncology.

Ethics and dissemination: The National Healthcare Group (NHG) Domain Specific Review Board has granted ethical approval for this study (DSRB 2020/00334). We will distribute our findings at scientific conferences and publish them in peer-reviewed journals.

Trial registration number: NCT04522284

Keywords: clinical decision support system, chemotherapy, personalised medicine, clinical trials, artificial intelligence, oncology, precision medicine, PRECISE CURATE.AI pilot clinical trial

INTRODUCTION

Treatment options for oncology patients are increasingly personalised with the onset of precision medicine, which enables drug selection tailored to an individual. To truly optimise the outcome, however, the treatment should also include personalised dosing (1). Faced with a trade-off between efficacy and toxicity, oncologists traditionally administer maximum tolerated dose (MTD)—the highest dose that does not cause unacceptable side effects (2), derived from Phase I trials. If patients experience toxicities, the dose is reduced according to guidelines based on population data. The key underlying assumption is that higher doses will provide greater efficacy, which many now recognize as flawed (3). Large randomised controlled trials (RCTs) show that doubling the dose of some drugs results in more frequent toxicities, which leads to dose reductions and treatment interruptions, despite no improvement in overall survival (4, 5). Conversely, other authors suggest that 30–75% of patients may be underdosed with conventional dosing strategies (6). Given the narrow therapeutic window of oncologic drugs and the 4- to 10-fold interindividual variation in pharmacokinetic clearance (7, 8), these overdosing or underdosing events result in suboptimal results: unnecessary toxicities, low efficacy and potential failure of drug development (9). The complexity of this problem increases exponentially in multi-drug regimens, with unpredictable drug-drug interactions (10, 11).

The challenge of personalised dosing has thus far been practically unsolvable because of its monumental complexity. Pharmacokinetic-based therapeutic drug monitoring and pharmacogenetic testing are promising (12–14), but have thus far not been adopted in chemotherapy drug dosing. In addition, threshold drug exposure does not necessarily correlate with threshold efficacy, particularly due to the individualised nature of patient responses to treatment. With the advent of artificial intelligence (AI), efforts are now focused on big data in pharmacogenomics (15). Though big data modelling is valuable, it is unsuitable for dynamic, multifactorial diseases, as it requires massive volumes of population information, comprehensive prior knowledge and high temporal resolution (16).

The alternative is to use small data, where only the individual's medical profile is used solely for his/her own treatment. Harnessing AI, we previously demonstrated that a quadratic surface can closely describe the relationship between drug doses and a phenotypic response in a human system (17–21). The coefficients of the second-order polynomial are unique to each individual. AI is used to map the extensive dose-response parameter space based on minimal empirical data, thus deterministically predicting the global optimum within a pre-specified safe dose range (22). Uniquely, this process is mechanism-independent and implicitly avoids the complexities stemming from the known or unknown mechanistic components, including pharmacokinetics, pharmacodynamics, pharmacogenomics, and disease biology (23, 24). These personalised profiles, which are visually represented as response surfaces, can also be scaled into higher dimensions to enable predictions for combination drug regimens (25). As such, CURATE.AI—a small data, AI-derived, indication-agnostic and mechanism-independent technology platform—could thus allow for clinically actionable personalised dosing for precision oncology and beyond. Importantly, CURATE.AI implementation is not purely computational, as it pairs prospective calibration of patient-specific responses to treatment at different drug doses with the dose optimisation process.

Predicting the optimal dose at a single point in time is only part of the challenge. The optimal dose evolves throughout the course of treatment, with the participant's response to therapy evolving due to environmental, physiologic and disease changes, including drug resistance (7). Here, CURATE.AI's ability to continually recalibrate personalised profiles allows for dynamic dose optimisation throughout treatment (23, 24). To maximise CURATE.AI's therapeutic potential, it is thus paramount to utilize a phenotypic response biomarker that can be quantified frequently. Though the gold standard for monitoring treatment response in solid tumours is the Response Evaluation Criteria in Solid Tumours (RECIST), these radiological assessments are performed at infrequent intervals after a few chemotherapy cycles, and may not reflect the entire tumour burden in situations such as widespread metastases or central necrosis (26). Blood-based tumour markers, such as carcinoembryonic antigen (CEA) and carbohydrate antigen 19-9 (CA19-9) (27–29), can be measured more frequently. However, these traditional blood biomarkers have limited sensitivity and specificity in reflecting tumour response, especially among patients whose

baseline biomarker levels are in the normal range (30). Recent advances in genomic sequencing have revealed plasma circulating tumour DNA (ctDNA) as a novel biomarker of tumour burden (31). ctDNA are DNA fragments released by tumour cells, *via* apoptosis, necrosis or active secretion. These fragments contain both genetic information (such as point mutation, copy number variation) and epigenetic information (such as DNA methylation). Quantitative changes in ctDNA have been shown to be ultra-sensitive in detecting both macroscopic and microscopic tumour load (32), including in patients without raised traditional tumour markers at baseline. Therefore, serial ctDNA measurements may be more reflective of the evolving tumour response and thus appropriate for CURATE.AI.

Though CURATE.AI has already been applied in a variety of clinical settings (23–25), there are currently no prior RCTs of CURATE.AI in patients with solid tumours. Additionally, the temporal resolution of the change in the selected tumour markers, as required for CURATE.AI, has not been yet characterised. We are thus conducting this pilot clinical trial to assess the technical and logistical feasibility of a future RCT, as well as to collect exploratory data on efficacy and toxicity to enable future sample size calculations.

METHODS AND ANALYSIS

Trial Design

The PRECISE CURATE.AI pilot trial is a single-arm, prospective pilot clinical trial for participants receiving palliative-intent chemotherapy for solid tumours. We anticipate that any feasibility concerns in the future RCT are unlikely to arise from the logistical process or participants acceptability of randomisation. Rather, the more pressing feasibility issues relate to whether CURATE.AI profiles can be created and successfully applied, and whether the recommended doses are different from the standard-of-care. Therefore, to maximise clinical experience in delivering this intervention, we will run this pilot as a single-arm study. This protocol adheres to the Consolidated Standards of Reporting Trials (CONSORT) extension for randomised pilot and feasibility trials (33).

Study Setting and Participant Recruitment

We will recruit participants at two centres: National University Hospital (NUH) and Ng Teng Fong General Hospital (NTFGH), which both belong to the National University Health System (NUHS), Singapore. Clinical investigators will recruit patients from outpatient clinics during routine clinical reviews, weekly trial meetings or multidisciplinary tumour boards. As this is a pilot clinical trial with no precedent data, we intend to first recruit 10 patients and perform an interim analysis, which will include formal power and statistical sample size calculations. Based on these outcomes, we will consider an RCT, or an amendment of this study protocol to expand the current cohort or to include further cohorts of patients with a wider range of chemotherapy regimens or tumour markers. We will consider participants to be evaluable for the primary outcome measures only if participants are able to complete the first two cycles of chemotherapy in an uninterrupted manner. We will replace any unevaluable participants with new participants, though we will continue to monitor and report any adverse events in the unevaluable participants. We will consider replacing participants who withdraw from the study (see **Supplementary Text**) with new participants if we could not collect sufficient data for primary outcome assessment.

Choice of Chemotherapy Regimens

Among the different solid tumour types, gastrointestinal (GI) tumours are one example of an appropriate solid tumour type for an initial trial with CURATE.AI. This is because they are the most prevalent (34), and they also form a significant proportion of tumours with raised levels of serum tumour markers (35), which can serve as an input for CURATE.AI. Therefore, we intend to initially recruit patients with GI tumours for this pilot clinical trial, though the eligibility criteria below permit the recruitment of patients with other solid tumour types.

We chose capecitabine-containing regimens (XELOX, XELIRI and single-agent capecitabine) as capecitabine is one of the most commonly used drugs for a wide range of GI and other solid tumours (36), which facilitates recruitment. In addition, it is generally accepted that the MTD for capecitabine is not well-tolerated in a large proportion of patients (37, 38), with guidelines recommending a starting dose lower than the MTD (39). Furthermore, previous studies have established inter-ethnic differences in tolerability profiles for capecitabine (40). Therefore, patients receiving capecitabine require a personalised approach and may benefit from CURATE.AI dose guidance.

During the trial, participants will receive the treatment in 3-week cycles, according to standard dosing schedules for each regimen (**Figure 2**) (41–43). In this pilot clinical trial, CURATE.AI will only modulate capecitabine doses while the remaining drugs (oxaliplatin in XELOX, and irinotecan in XELIRI regimens) will be held constant or adjusted at the clinical investigator's discretion, as per standard-of-care. Additionally, CURATE.AI will only modulate capecitabine doses between cycles and not within a cycle. The drugs used in these regimens will be subjected to the same storage and accountability conditions as per standard-of-care institutional requirements.

Eligibility Criteria

The key inclusion criteria are as follows: (1) metastatic solid tumours not for curative intent therapy; (2) planned for treatment with the following chemotherapy regimens: XELOX, XELIRI or single-agent capecitabine; (3) presence of raised tumour marker above upper limit of local laboratory normal (e.g., CEA, CA19-9); (4) males and females $\geq$21 years of age (the age of majority in Singapore); (5) Eastern Cooperative Oncology Group (ECOG) Performance Status of 0 to 2; (6) meet the following clinical laboratory criteria within 21 days of starting treatment: (a) Absolute neutrophil count (ANC) $\geq$1,000/mm3 and platelet $\geq$50,000/mm3, (b) total bilirubin $\leq$1.5x the upper limit of the normal range (ULN) and alanine aminotransferase (ALT) and aspartate aminotransferase (AST) $\leq$3x ULN or $\leq$5x ULN in the of the liver involvement, (c) calculated creatinine clearance $\geq$30 mL/min or creatinine $<$1.5x ULN.

The key exclusion criteria as follows: (1) currently lactating or pregnant; (2) major surgery within 28 days prior to start of the treatment; (3) active congestive heart failure (New York Heart Association [NYHA] Class III or IV), symptomatic ischaemia, conduction abnormalities uncontrolled by conventional intervention or myocardial infarction within 4 months prior to date of obtaining informed consent; (4) clinically significant hypersensitivity to one or more of the selected regimen's constituent drug(s); (5) contraindication to any of the required concomitant drugs or supportive treatments; (6) any clinically significant medical disease or psychiatric condition that, in the investigator's opinion, may interfere with protocol adherence or a participant's ability to give informed consent.

Interventions

Definition of CURATE.AI

CURATE.AI in this context refers to the CURATE.AI platform (software), engineering expertise in operating the CURATE.AI platform, drug dose recommendations generated by the CURATE.AI platform and accompanying analyses of clinical data. The Health Sciences Authority in Singapore classifies CURATE.AI as a Class B medical device (low to moderate risk), which is defined as all active therapeutic devices that are software, or which are intended to administer or exchange energy to or with the human body. We have filed the accompanying Clinical Research Materials notification under the National University of Singapore, for the intended purpose of providing dose recommendations within this pilot clinical trial. The CURATE.AI internal workflow is summarised in **Figure 1** and explained in subsequent sections.

CURATE.AI Built-In Safety Mechanisms

All doses recommended by CURATE.AI will always be within the safe dose range pre-specified by the clinical investigator: (1) the predetermined safety range (50–100% of dose used in standard-of-care treatment) and (2) participant-specific dosing range (accounting for the specific participant's personal medical history and clinical context). If CURATE.AI is unable to recommend a dose that fulfils the above requirements, it will not recommend a modulated dose and the clinical investigator will decide the dose according to the standard-of-care. Should the participant experience clinically relevant grade 3 or 4 non-haematological toxicity at a particular dose, we will restrict the next dose recommendation by CURATE.AI to a lower dose. Clinical investigators will have the final say on whether to use the CURATE.AI-recommended dose. Clinical investigators may also adjust the dose beyond CURATE.AI's recommendations as they deem necessary.

CURATE.AI Calibration-Intent Dose Recommendations

For every participant, CURATE.AI will undergo an initial calibration stage (**Figure 1**, Steps 1–4) with the aim of generating a personalised CURATE.AI profile based on that participant data only. CURATE.AI will provide calibration-intent dose recommendations (**Figure 1**, Step 1) to collect data on the participant's phenotypic response (measured by tumour markers e.g., CEA, CA19-9) to a range of drug doses (**Figure 1**, Step 2). Any dose recommended by CURATE.AI to the clinical investigator will always be within the pre-specified safe dose range.

CURATE.AI requires a minimum of three unique data pairs (capecitabine dose and tumour marker), with one data pair collected per cycle, to generate the personalised CURATE.AI profile (**Figure 1**, Step 3) based on a second-order polynomial. After giving participants capecitabine at calibration-intent doses and measuring the corresponding tumour marker levels, we will analyse the data to determine if they fulfil calibration requirements. If not, CURATE.AI will make further calibration-intent dose recommendations and more data pairs will be collected until the CURATE.AI profile can be generated.

CURATE.AI Efficacy-Driven Dose Recommendations

After the CURATE.AI profile is generated, we will check it for actionability, defined as the ability to recommend an optimum dose within the safety requirements pre-specified by the clinical investigator (**Figure 1**, Step 4). For participants with actionable profiles, CURATE.AI will recommend therapeutic-intent, efficacy-driven doses to the clinical investigator (**Figure 1**, Step 5). Any dose recommended by CURATE.AI will always be within the safe dose range pre-specified by the clinical investigator. If the dose-dependent relationship is maintained, CURATE.AI will continue to use the existing profile to provide dynamic dose recommendations before every subsequent cycle (**Figure 1**, Step 6.1). This continues until the end of the participant's involvement in the study (**Figure 1**, Step 7), which is when the clinical investigator decides to cease/change the chemotherapy regimen, or until 12 months, whichever is earlier. If the dose-dependent relationship is not maintained but we do not suspect systemic changes in the participant (**Figure 1**, Step 6.2), CURATE.AI will obtain a new data pair in the next cycle based on the existing profile. If the dose-dependent relationship is not maintained and we suspect systemic changes in the participant at any point during the trial, such as but not limited to the introduction of haemodialysis or drugs with known interactions with the treatment, CURATE.AI may recalibrate the personalised profile (**Figure 1**, Step 6.3) to generate a new profile for the participant. CURATE.AI will select recalibration doses on the basis of previous correlations.

Objectives

Primary Objective

Our primary objective is to assess the technical and logistical feasibility of an RCT for CURATE.AI-guided dosing with the selected chemotherapy regimens and tumour markers. Technical feasibility is defined by the following questions: (1) whether CURATE.AI profiles can be successfully created and applied; (2) whether the specific patient characteristics that predict the successful creation and applicable of CURATE.AI profiles can be identified; (3) whether the CURATE.AI-recommended dose is substantially different from the standard-of-care dose (see **Table 1** footnote e). Logistical feasibility refers to: (1) the timeliness of CURATE.AI dose recommendations

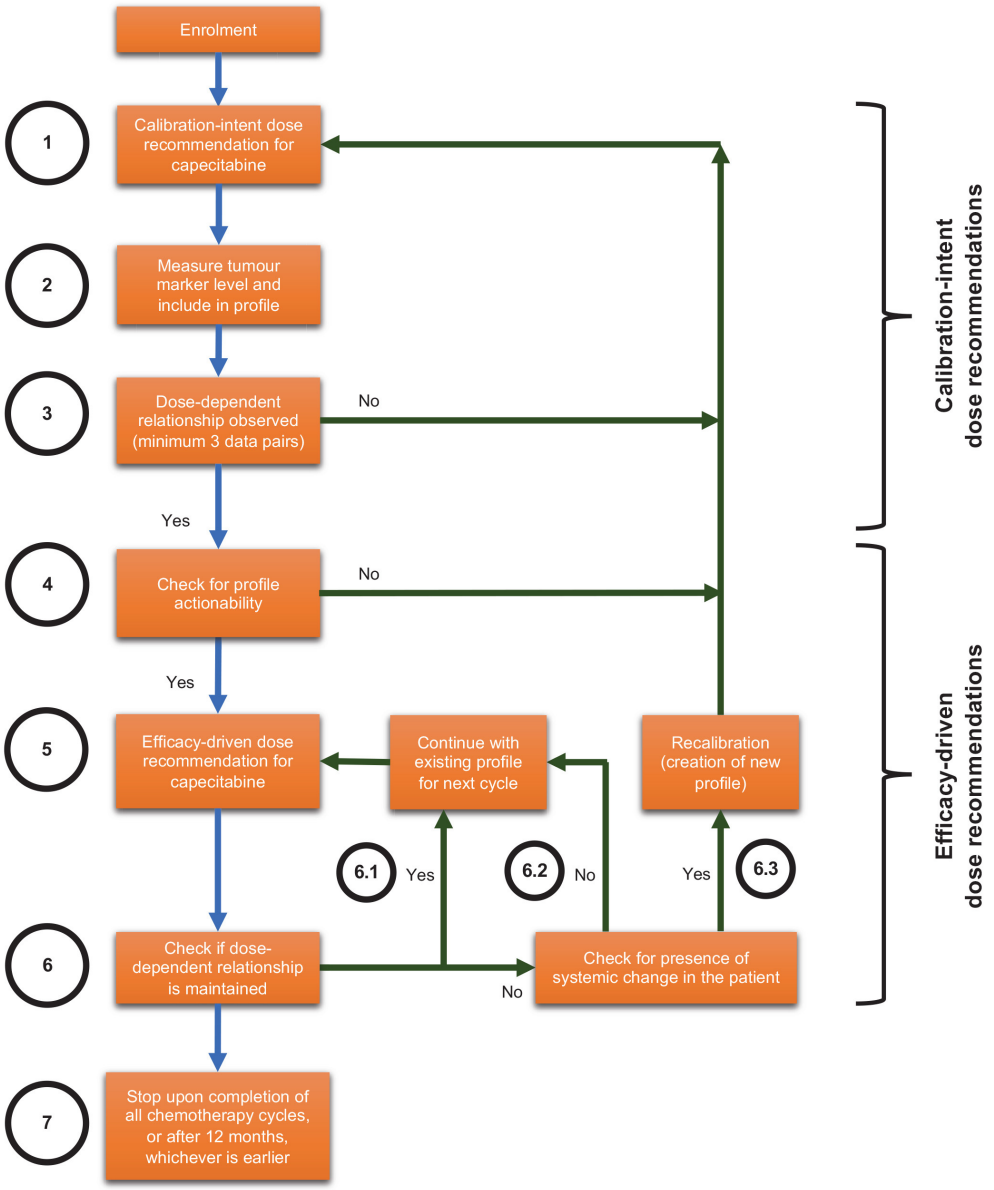

FIGURE 1 | Internal workflow for optimising combination therapy modulation with CURATE.AI for solid tumours, including scenarios that may lead to recalibration.

to the physician; (2) participant adherence to CURATE.AI-recommended doses; (3) physician adherence to CURATE.AI recommended doses. We hypothesize that CURATE.AI will meet these feasibility criteria, as further defined in our outcome measures below, for the selected palliative-intent chemotherapy regimens and respective tumour markers. We will use these data to decide if and how a future RCT should proceed.

Secondary Objective

Our secondary objective is to collect preliminary data on efficacy and toxicity as exploratory outcomes for this pilot. Specifically, we will evaluate the incidence of clinically progressive disease, changes in tumour marker levels, and incidence of clinically relevant toxicities. As an exploratory outcome, we will explore the utility of tumour markers such as CEA, CA19-9 and ctDNA in higher-frequency serial measurements with modulated doses. We will also explore ctDNA as an input for CURATE.AI to generate dose recommendations, however we will not use this analysis to prospectively guide dosing. We provide further details in our outcome measures below.

Study Timeline and Investigations

The study investigations schedule is summarised in **Figure 2**. For each participant, we will perform regular

TABLE 1 | Outcome measures and progression criteria for the PRECISE CURATE.AI pilot clinical trial, based on "the traffic light system" recommended in the CONSORT extension statement for pilot clinical trials (33).

Outcome measures	Green*	Yellow*	Red*
Primary Outcome Measures			
Applicability of CURATE.AI profiles[a]	>70%	10–70%	<10%
Secondary Outcome Measures			
Patient adherence[b]	>90%	10–90%	<10%
Timeliness of CURATE.AI dose recommendations to the physician[c]	100%	10–99%	<10%
Physician adherence[d]	>70%	10–70%	<10%
Clinically significant dose changes[e]	>20%	1–20%	0%
Exploratory Outcome Measures			
Efficacy: (1) Clinical progressive disease[f] (2) Temporal variation in tumour marker level (3) Maximal reduction in tumour marker level	N.A.	N.A.	N.A.
Clinically relevant toxicities[g]	N.A.	N.A.	N.A.
Data collection and exploratory analysis of CEA, CA19-9, and/or other traditional markers in higher frequency serial measurements after modulated dosing in relation to standard frequency readings and other efficacy measures (e.g., RECIST criteria).	N.A.	N.A.	N.A.
Data collection and exploratory analysis of ctDNA as: (1) a tumour marker in serial measurements at given clinical context and after modulated dosing (2) a potential input for CURATE.AI	N.A.	N.A.	N.A.

See section on Data Collection, Management and Analysis.

**Green: a future randomised trial is definitely feasible. Yellow: a future randomised trial is possibly feasible if its design is appropriately modified. Red: a future randomised trial is unfeasible in its current form.*

[a]percentage of participants in whom we successfully apply CURATE.AI profile. A decision on whether we "successfully apply" the CURATE.AI profile requires expert judgement and cannot be made based on a purely numerical process. The expert panel will consider the following factors with careful regard for the individual circumstances of each participant: (1) error/variance (biological/analytical) is allows accurate predictions (see section primary outcome measure); (2) profile can be generated sufficiently early for the participant to potentially benefit; (3) dose-dependent relationship is observed; (4) profile is actionable (i.e., fulfils the clinical investigator's pre-specified safety requirements); (5) systemic changes in the participant which require profile recalibration are rare or readily assimilated into the CURATE.AI algorithm.

[b]percentage of participants who always adhered to the prescribed dose whenever they took their medication, as measured by the standardised pharmacovigilance protocol.

[c]percentage of CURATE.AI recommendations provided in time for the next chemotherapy cycle, across all participants and cycles.

[d]percentage of CURATE.AI recommended doses that were used by the clinical investigator.

[e]percentage of participants in whom the CURATE.AI-guided cumulative dose is substantially (≥10%) different from the projected standard-of-care cumulative dose, which is defined as the maximum dose of capecitabine (1,000 mg/m^2 twice daily for XELOX and XELIRI regimen, 1,250 mg/m^2 twice daily for single agent capecitabine regimen) multiplied by the number of completed chemotherapy cycles.

[f]defined as the clinical investigator deeming that the patient will not benefit any further from the chemotherapy regimen and considering stopping it, at the time of the first radiological assessment performed as per standard-of-care.

[g]of grades 3–4 based on Common Terminology Criteria for Adverse Events (CTCAE) version 4.0.

ctDNA, circulating tumour DNA.

reviews of medical history, physical examination including performance status and vital signs, and documentation of adverse events and concomitant medications as per standard-of-care. We will also perform standard-of-care investigations at regular intervals, such as but not limited to: haematology, serum chemistries, traditional tumour markers (e.g., CEA or CA19-9) and computed tomography (CT) scans. We will conduct these investigations following standard-of-care institutional laboratory techniques and radiographic protocols.

There are two main deviations from standard-of-care in our study investigations. Firstly, we will perform the same blood draws and disease assessments but at more frequent intervals than standard-of-care (weekly compared to 3-weekly), to investigate temporal variations in tumour marker level. However, we will limit this increased frequency to the first two chemotherapy cycles and a maximum of one additional blood test per subsequent cycles. Secondly, we may measure participants' serum ctDNA at a similar or lower frequency as the above blood draws. ctDNA measurements, if performeed, will be regularly spaced, with ∼4 measurements per patient over four cycles. ctDNA is not routinely measured in standard-of-care.

We may perform other blood tests as per the clinical investigator's judgement. The clinical investigator will perform history and physical examination, as well as review of the adverse events prior to the start of every subsequent cycle of chemotherapy, as per local institution standards. We will enrol participants for the entire duration of their treatment with the selected regimens, up to a maximum of 12 months per participant. We will document the above findings for each participant.

Sample Size

Since this is a pilot clinical trial with no precedent data, we did not perform an upfront formal sample size calculation. We

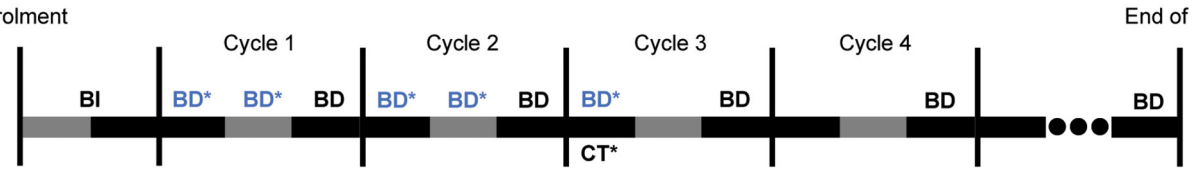

FIGURE 2 | Overall trial schedule for 3 weeks long cycles. BI: Baseline investigations as per standard-of-care, including collection of demographics, medical/treatment history, vital signs, and conducting complete physical examination including performance status evaluation, blood tests [haematology, serum chemistries, tumour marker(s)] and imaging as clinically required. BD: Mandatory blood draws done every 3 weeks for the measurement of tumour marker(s) between Days 17–20 of each cycle, alongside serum chemistries and haematology as per standard-of-care. BD*: Additional blood draws for measurements of tumour markers(s), done once weekly (once between Days 4–7, and another between Days 11–14) performed solely for the purposes of the trial, and are necessary for cycles 1–2 of chemotherapy. Additional blood draws in subsequent cycles will be limited to one draw, if at all. CT*: Computed tomography scans performed approximately every two or three cycles as per standard-of-care. End of study: upon completion of all chemotherapy cycles, or at 12 months, whichever is earlier for each participant.

intend to first recruit 10 patients and perform an interim analysis using the data generated from these participants, which will include formal power and statistical sample size calculations. Based on these outcomes, we will consider cohort expansion or an RCT.

Data Collection, Management, and Analysis

Primary Outcome Measure

The primary outcome measure (**Table 1**) is the percentage of participants in whom we successfully apply a CURATE.AI profile. This is the main outcome which we will use to judge the technical feasibility of a future RCT and corresponds to the first of our primary objectives. A decision on whether we "successfully apply" the CURATE.AI profile requires expert judgement and cannot be made based on a purely numerical process therefore the statistical analyses will be viewed within the broader framework of clinical relevance. An expert panel, comprising physicians and researchers not involved in the trial, will consider the following factors with careful regard for the individual circumstances of each participant: (1) based on clinical experience, judgement and established indicators, the error/variance analyzed with descriptive statistics of numerical performance measures [i.e., mean absolute error, error distribution and bias (the frequency and extent of under- and overpredicting)] is acceptable to guide clinical decisions; (2) profile can be generated sufficiently early for the participant to potentially benefit; (3) dose-dependent relationship is observed; (4) profile is actionable (i.e., fulfils the clinical investigator's pre-specified safety requirements); (5) systemic changes in the participant which require profile recalibration are rare or readily assimilated into the CURATE.AI algorithm. This is the main outcome which we will use to judge the technical feasibility of the RCT. As per the CONSORT extension statement for pilot clinical trials, we are using "the traffic light system" to define progression criteria for the RCT (33).

Secondary and Exploratory Outcome Measures

The secondary outcome measures (**Table 1**) focus on both technical and logistical feasibility, which constitute our primary objectives. Secondary outcomes include: (1) patient adherence to the prescribed dose; (2) timeliness of CURATE.AI recommendations to the physician in time for the next chemotherapy cycle, across all participants and cycles; (3) physician adherence to CURATE.AI recommended doses; (4) clinically significant dose changes where a participant's CURATE.AI-guided cumulative dose is $\geq$10% different from the projected standard-of-care cumulative dose.

Exploratory outcome measures (**Table 1**) mainly relate to efficacy and toxicity, which constitute our secondary objectives. Exploratory outcomes relating to efficacy include: (1) percentage of trial participants with clinical progressive disease defined as the clinical investigator deeming that the patient will not benefit any further from the chemotherapy regimen and considering stopping it, at the time of the first radiological assessment performed as per standard-of-care; as well as (2) temporal variation and (3) maximal reduction in tumour marker level from trial initiation to conclusion. We will also measure clinically relevant toxicities of grades 3–4 as an exploratory outcome, using the Common Terminology Criteria for Adverse Events (CTCAE) version 4.0. Other exploratory outcomes include data collection and exploratory analysis of CEA, CA19-9 and/or other traditional tumour markers in higher frequency serial measurements after modulated dosing in relation to standard frequency readings and other efficacy measures, e.g., RECIST criteria. Finally, we will perform data collection and exploratory analysis of ctDNA as a tumour marker in serial measurements at given clinical context and after modulated dosing, as well as a potential input for CURATE.AI. However, we will not use the analysis of ctDNA to prospectively guide drug dosing in this pilot clinical trial.

Statistical Analysis

We will perform and report descriptive statistics of the outcome measures. We will also perform graphical analyses of the temporal variations in tumour marker level. We will not statistically analyse efficacy and toxicity exploratory outcomes.

Data Availability

The data generated and/or analysed during the current study are available from the corresponding author on reasonable request.

Safety Monitoring and Data Storage

Included in **Supplementary Text**.

Patient and Public Involvement

This pilot trial protocol was designed without patient involvement. We did not involve patients in our study design, protocol writing, development of patient-relevant outcomes, nor dissemination of study results. However, we intend to involve patients and the public in the design of the future RCT.

DISCUSSION

The inclusive recruitment criteria for this pilot clinical trial are enabled by CURATE.AI's personalisation of the treatment and permit substantial variability in the participant population that also reflect the true patient heterogeneity faced in clinical practice. This allows broader applicability of our findings and may also allow us to suggest specific subsets of patients, diseases or chemotherapy regimens where CURATE.AI-guided dosing is particularly beneficial.

Our pilot trial design has several limitations. First, this is a non-randomised pilot clinical trial, which does not simulate an RCT as closely as a randomised pilot. Therefore, it cannot inform us on feasibility issues that may arise from the logistical process or patient acceptability of randomisation, though we view such issues as unlikely in this context. Second, our recruitment criteria intentionally permit substantial variability in the participant population. This is enabled by CURATE.AI's personalisation of the treatment and reflects the true patient population heterogeneity faced in clinical practice and may allow us to identify the factors predicting successful CURATE.AI-guided dosing, for implementation in a future RCT. We nonetheless acknowledge that any identified factors will be based mainly on clinical judgement rather than statistically powered analyses. Third, participants included in this pilot must have raised levels of traditional tumour markers (e.g., CEA or CA19-9). Therefore, our experience with ctDNA in this pilot trial may not be directly generalisable to the intended patient profile in the future RCT if ctDNA were to use as an alternative biomarker for patients who lack elevated levels of traditional tumour markers. Fourth, our primary outcome measure on the successful application of CURATE.AI profiles cannot be measured based only on a numerical process and thus relies on the judgement of an expert panel with consideration for each patient's circumstances. This is inherently subjective. We have nonetheless listed the guiding criteria for the expert panel to reduce any potential bias to the minimum.

CONCLUSIONS

This protocol describes the design of the PRECISE CURATE.AI pilot clinical trial. To date, drug dosing in oncology lacks personalisation. CURATE.AI opens the possibility of personalised dosing for single- and multi-drug regimens, that is dynamically optimized throughout treatment. Furthermore, it is based on a small data set collected only from the treated individual rather than population data. CURATE.AI may thus overcome the challenges that impede the adoption of big data approaches for personalised drug dosing. This pilot will provide technical and logistical feasibility data, as well as exploratory efficacy and toxicity data for sample size calculations, thus laying the clinical foundation for a future RCT of personalised dosing for precision oncology using CURATE.AI.

ETHICS STATEMENT

The studies involving human participants were reviewed and approved by the National Healthcare Group (NHG) Domain Specific Review Board (DSRB), reference: 2020/00334. The patients/participants provided their written informed consent to participate in this study.

AUTHOR CONTRIBUTIONS

RS, DH, TK, and ABl: study conception. BT, CT, ABa, DH, RS, TK, and ABl: study design. BT, CT, XT, SP, and ABl: manuscript drafting (introduction). BT, CT, RS, XT, TK, and ABl: manuscript drafting (interventions). BT, CT, RS, TK, and ABl: manuscript drafting (outcomes). BT, CT, HS, SD, VW, RS, TK, and ABl: manuscript drafting (other methods). RS: principal investigator. All authors: critical revision.

FUNDING

DH gratefully acknowledges the National Research Foundation Singapore under its AI Singapore Programme (Award Number: AISGGC-2019-002), Singapore Ministry of Health's National Medical Research Council under its Open Fund-Large Collaborative Grant (OFLCG) (MOH-OFLCG18May-0003), the Ministry of Education (MOE) Tier 1 FRC grant and Singapore Cancer Society. RS was supported by a National Medical Research Council (NMRC) Fellowship (NMRC/Fellowship/0059/2018). DH and RS acknowledge support from The N.1 Institute for Health under its N.1 Seed Funding Programme.

SUPPLEMENTARY MATERIAL

The Supplementary Material for this article can be found online at: https://www.frontiersin.org/articles/10.3389/fdgth.2021.635524/full#supplementary-material

REFERENCES

1. Peck RW. Precision medicine is not just genomics: the right dose for every patient. *Annu Rev Pharmacol Toxicol.* (2018) 58:105–22. doi: 10.1146/annurev-pharmtox-010617-052446
2. Takimoto CH. Maximum tolerated dose: clinical endpoint for a bygone era? *Target Oncol.* (2009) 4:143–7. doi: 10.1007/s11523-009-0108-y
3. Minasian L, Rosen O, Auclair D, Rahman A, Pazdur R, Schilsky RL. Optimizing dosing of oncology drugs. *Clin Pharmacol Ther.* (2014) 96:572–9. doi: 10.1038/clpt.2014.153
4. Verweij J, Casali PG, Zalcberg J, LeCesne A, Reichardt P, Blay JY, et al. Progression-free survival in gastrointestinal stromal tumours with high-dose imatinib: randomised trial. *Lancet.* (2004) 364:1127–34. doi: 10.1016/S0140-6736(04)17098-0
5. Blanke CD, Rankin C, Demetri GD, Ryan CW, von Mehren M, Benjamin RS, et al. Phase III randomized, intergroup trial assessing imatinib mesylate at two dose levels in patients with unresectable or metastatic gastrointestinal stromal tumors expressing the kit receptor tyrosine kinase: S0033. *J Clin Oncol.* (2008) 26:626–32. doi: 10.1200/JCO.2007.13.4452
6. Gurney H. How to calculate the dose of chemotherapy. *Br J Cancer.* (2002) 86:1297–302. doi: 10.1038/sj.bjc.6600139
7. Mathijssen RH, Sparreboom A, Verweij J. Determining the optimal dose in the development of anticancer agents. *Nat Rev Clin Oncol.* (2014) 11:272–81. doi: 10.1038/nrclinonc.2014.40
8. Gurney H. Dose calculation of anticancer drugs: a review of the current practice and introduction of an alternative. *J Clin Oncol.* (1996) 14:2590–611. doi: 10.1200/JCO.1996.14.9.2590
9. Ji Y, Jin JY, Hyman DM, Kim G, Suri A. Challenges and opportunities in dose finding in oncology and immuno-oncology. *Clin Transl Sci.* (2018) 11:345–51. doi: 10.1111/cts.12540
10. Cascorbi I. Drug interactions–principles, examples and clinical consequences. *Dtsch Arztebl Int.* (2012) 109:546–55. doi: 10.3238/arztebl.2012.0546
11. Palleria C, Di Paolo A, Giofre C, Caglioti C, Leuzzi G, Siniscalchi A, et al. Pharmacokinetic drug-drug interaction and their implication in clinical management. *J Res Med Sci.* (2013) 18:601–10.
12. Gamelin E, Delva R, Jacob J, Merrouche Y, Raoul JL, Pezet D, et al. Individual fluorouracil dose adjustment based on pharmacokinetic follow-up compared with conventional dosage: results of a multicenter randomized trial of patients with metastatic colorectal cancer. *J Clin Oncol.* (2008) 26:2099–105. doi: 10.1200/JCO.2007.13.3934
13. Park JR, Scott JR, Stewart CF, London WB, Naranjo A, Santana VM, et al. Pilot induction regimen incorporating pharmacokinetically guided topotecan for treatment of newly diagnosed high-risk neuroblastoma: a Children's Oncology Group study. *J Clin Oncol.* (2011) 29:4351–7. doi: 10.1200/JCO.2010.34.3293
14. van Schaik RH. CYP450 pharmacogenetics for personalizing cancer therapy. *Drug Resist Updat.* (2008) 11:77–98. doi: 10.1016/j.drup.2008.03.002
15. Barrot CC, Woillard JB, Picard N. Big data in pharmacogenomics: current applications, perspectives and pitfalls. *Pharmacogenomics.* (2019) 20:609–20. doi: 10.2217/pgs-2018-0184
16. Hekler EB, Klasnja P, Chevance G, Golaszewski NM, Lewis D, Sim I. Why we need a small data paradigm. *BMC Med.* (2019) 17:133. doi: 10.1186/s12916-019-1366-x
17. Wong PK, Yu F, Shahangian A, Cheng G, Sun R, Ho CM. Closed-loop control of cellular functions using combinatory drugs guided by a stochastic search algorithm. *Proc Natl Acad Sci USA.* (2008) 105:5105–10. doi: 10.1073/pnas.0800823105
18. Tsutsui H, Valamehr B, Hindoyan A, Qiao R, Ding X, Guo S, et al. An optimized small molecule inhibitor cocktail supports long-term maintenance of human embryonic stem cells. *Nat Commun.* (2011) 2:167. doi: 10.1038/ncomms1165
19. Weiss A, Ding X, van Beijnum JR, Wong I, Wong TJ, Berndsen RH, et al. Rapid optimization of drug combinations for the optimal angiostatic treatment of cancer. *Angiogenesis.* (2015) 18:233–44. doi: 10.1007/s10456-015-9462-9
20. Mohd Abdul Rashid MB, Toh TB, Silva A, Nurrul Abdullah L, Ho CM, Ho D, et al. Identification and optimization of combinatorial glucose metabolism inhibitors in hepatocellular carcinomas. *J Lab Autom.* (2015) 20:423–37. doi: 10.1177/2211068215579612
21. Al-Shyoukh I, Yu F, Feng J, Yan K, Dubinett S, Ho CM, et al. Systematic quantitative characterization of cellular responses induced by multiple signals. *BMC Syst Biol.* (2011) 5:88. doi: 10.1186/1752-0509-5-88
22. Wang H, Lee DK, Chen KY, Chen JY, Zhang K, Silva A, et al. Mechanism-independent optimization of combinatorial nanodiamond and unmodified drug delivery using a phenotypically driven platform technology. *ACS Nano.* (2015) 9:3332–44. doi: 10.1021/acsnano.5b00638
23. Pantuck AJ, Lee D-K, Kee T, Wang P, Lakhotia S, Silverman MH, et al. Modulating BET bromodomain inhibitor ZEN-3694 and enzalutamide combination dosing in a metastatic prostate cancer patient using CURATE.AI, an artificial intelligence platform. *Adv Therapeut.* (2018) 1:1800104. doi: 10.1002/adtp.201800104
24. Zarrinpar A, Lee DK, Silva A, Datta N, Kee T, Eriksen C, et al. Individualizing liver transplant immunosuppression using a phenotypic personalized medicine platform. *Sci Transl Med.* (2016) 8:333ra49. doi: 10.1126/scitranslmed.aac5954
25. Blasiak A, Khong J, Kee T. CURATE.AI: optimizing personalized medicine with artificial intelligence. *SLAS Technol.* (2020) 25:95–105. doi: 10.1177/2472630319890316
26. Schwartz LH, Litiere S, de Vries E, Ford R, Gwyther S, Mandrekar S, et al. RECIST 1.1-update and clarification: from the RECIST committee. *Eur J Cancer.* (2016) 62:132–7. doi: 10.1016/j.ejca.2016.03.081
27. Vukobrat-Bijedic Z, Husic-Selimovic A, Sofic A, Bijedic N, Bjelogrlic I, Gogov B, et al. Cancer antigens (CEA and CA 19-9) as markers of advanced stage of colorectal carcinoma. *Med Arch.* (2013) 67:397–401. doi: 10.5455/medarh.2013.67.397-401
28. Jing JX, Wang Y, Xu XQ, Sun T, Tian BG, Du LL, et al. Tumor markers for diagnosis, monitoring of recurrence and prognosis in patients with upper gastrointestinal tract cancer. *Asian Pac J Cancer Prev.* (2014) 15:10267–72. doi: 10.7314/APJCP.2014.15.23.10267
29. Daamen LA, Groot VP, Heerkens HD, Intven MPW, van Santvoort HC, Molenaar IQ. Systematic review on the role of serum tumor markers in the detection of recurrent pancreatic cancer. *HPB.* (2018) 20:297–304. doi: 10.1016/j.hpb.2017.11.009
30. Kim G, Jung EJ, Ryu CG, Hwang DY. Usefulness of carcinoembryonic antigen for monitoring tumor progression during palliative chemotherapy in metastatic colorectal cancer. *Yonsei Med J.* (2013) 54:116–22. doi: 10.3349/ymj.2013.54.1.116
31. Reece M, Saluja H, Hollington P, Karapetis CS, Vatandoust S, Young GP, et al. The use of circulating tumor DNA to monitor and predict response to treatment in colorectal cancer. *Front Genet.* (2019) 10:1118. doi: 10.3389/fgene.2019.01118
32. Parikh AR, Mojtahed A, Schneider JL, Kanter K, Van Seventer EE, Fetter IJ, et al. Serial ctDNA monitoring to predict response to systemic therapy in metastatic gastrointestinal cancers. *Clin Cancer Res.* (2020) 26:1877–85. doi: 10.1158/1078-0432.CCR-19-3467
33. Eldridge SM, Chan CL, Campbell MJ, Bond CM, Hopewell S, Thabane L, et al. CONSORT 2010 statement: extension to randomised pilot and feasibility trials. *BMJ.* (2016) 355:i5239. doi: 10.1136/bmj.i5239
34. Parkin DM. Global cancer statistics in the year 2000. *Lancet Oncol.* (2001) 2:533–43. doi: 10.1016/S1470-2045(01)00486-7
35. Sharma S. Tumor markers in clinical practice: general principles and guidelines. *Indian J Med Paediatr Oncol.* (2009) 30:1–8. doi: 10.4103/0971-5851.56328
36. Gennatas C, Michalaki V, Gennatas S. The role of capecitabine in the management of tumors of the digestive system. *Rev Recent Clin Trials.* (2009) 4:1–11. doi: 10.2174/157488709787047576
37. Leicher LW, de Graaf JC, Coers W, Tascilar M, de Groot JW. Tolerability of capecitabine monotherapy in metastatic colorectal cancer: a real-world study. *Drugs R D.* (2017) 17:117–24. doi: 10.1007/s40268-016-0154-8
38. Midgley R, Kerr DJ. Capecitabine: have we got the dose right? *Nat Clin Pract Oncol.* (2009) 6:17–24. doi: 10.1038/ncponc1240
39. Hirsch BR, Zafar SY. Capecitabine in the management of colorectal cancer. *Cancer Manag Res.* (2011) 3:79–89. doi: 10.2147/CMAR.S11250
40. Haller DG, Cassidy J, Clarke SJ, Cunningham D, Van Cutsem E, Hoff PM, et al. Potential regional differences for the tolerability profiles of

fluoropyrimidines. *J Clin Oncol.* (2008) 26:2118–23. doi: 10.1200/JCO.2007.15.2090

41. Diaz-Rubio E, Evans TR, Tabemero J, Cassidy J, Sastre J, Eatock M, et al. Capecitabine (Xeloda) in combination with oxaliplatin: a phase I, dose-escalation study in patients with advanced or metastatic solid tumors. *Ann Oncol.* (2002) 13:558–65. doi: 10.1093/annonc/mdf065
42. Patt YZ, Lee FC, Liebmann JE, Diamandidis D, Eckhardt SG, Javle M, et al. Capecitabine plus 3-weekly irinotecan (XELIRI regimen) as first-line chemotherapy for metastatic colorectal cancer: phase II trial results. *Am J Clin Oncol.* (2007) 30:350–7. doi: 10.1097/COC.0b013e31804b40bb
43. He Y, Liu P, Zhang Y, Deng X, Meng W, Wei M, et al. Low-dose capecitabine adjuvant chemotherapy in elderly stage II/III colorectal cancer patients (LC-ACEC): study protocol for a randomized controlled trial. *Trials.* (2015) 16:238. doi: 10.1186/s13063-015-0753-7

Conflict of Interest: DH, ABl, and TK are inventors of pending and issued patents pertaining to artificial intelligence-based drug development and personalised medicine. DH and TK are shareholders of KYAN Therapeutics, which has licensed intellectual property pertaining to AI-based drug development.

The remaining authors declare that the research was conducted in the absence of any commercial or financial relationships that could be construed as a potential conflict of interest.

frontiers in Surgery

HYPOTHESIS AND THEORY
published: 11 October 2021
doi: 10.3389/fsurg.2021.712984

Nomogram for Predicting Risk of Esophagogastric Junction (EGJ) Resection During Laparoscopic Resection of Gastrointestinal Stromal Tumors in EGJ: A Retrospective Multicenter Study

Yuting Xu[1†], Lijie Luo[2†], Xingyu Feng[3†], Yensheng Zheng[2], Tao Chen[4], Rui Zhou[5], Yong Li[3], Guoxin Li[4], Wei Wang[2] and Wenjun Xiong[2*]*

[1] The Affiliated Zhongshan Hospital of Guangzhou University of Chinese Medicine, Zhongshan, China, [2] Guangdong Provincial Hospital of Chinese Medicine, The Second Affiliated Hospital of Guangzhou University of Chinese Medicine, Guangzhou, China, [3] Guangdong General Hospital, Guangdong Academy of Medical Science, Guangzhou, China, [4] Department of General Surgery, Nanfang Hospital, Southern Medical University, Guangzhou, China, [5] The Third Affiliated Hospital of Southern Medical University, Guangzhou, China

OPEN ACCESS

Edited by:
Kee Yuan Ngiam,
National University Health System, Singapore

Reviewed by:
Andrea Botticelli,
Sapienza University of Rome, Italy
Guowei Kim,
National University Hospital, Singapore

***Correspondence:**
Wenjun Xiong
xiongwj1988@163.com
Wei Wang
wangwei16400@163.com

[†]These authors have contributed equally to this work and share first authorship

Specialty section:
This article was submitted to Surgical Oncology, a section of the journal Frontiers in Surgery

Received: 21 May 2021
Accepted: 06 September 2021
Published: 11 October 2021

Citation:
Xu Y, Luo L, Feng X, Zheng Y, Chen T, Zhou R, Li Y, Li G, Wang W and Xiong W (2021) Nomogram for Predicting Risk of Esophagogastric Junction (EGJ) Resection During Laparoscopic Resection of Gastrointestinal Stromal Tumors in EGJ: A Retrospective Multicenter Study. Front. Surg. 8:712984. doi: 10.3389/fsurg.2021.712984

Background: The established criteria for determining whether to excise the cardia during laparoscopic surgery for gastrointestinal stromal tumors in the esophagogastric junction (EGJ-GISTs) remain controversial. This retrospective multicenter study was conducted to develop a nomogram for predicting the risk of the cardia excision during laparoscopic surgery for EGJ-GISTs.

Material and Methods: We reviewed data from 2,127 gastric-GISTs (g-GISTs) patients without distant metastases in four hospital between June 2012 and June 2020. Of those, according to the including criteria, 184 patients [Guangdong Provincial Hospital of Chinese Medicine (n = 81), Nanfang Hospital of Southern Medical University (n = 60), Guangdong General Hospital (n = 34), and The Third Affiliated Hospital of Southern Medical University (n = 9)] with EGJ-GISTs were identified and included in this study. Factors contributing to risk of cardia excision were identified and used to create a nomogram. Nomogram performance was assessed using a bootstrapped concordance index (c-index) and calibration plots.

Results: According to the multivariate analysis, the distance from the margin of the tumor to the esophagogastric line (EG-line) (cm) (OR = 0.001, *95% CI*: 0.00001∼0.056, P = 0.001) and tumor size (cm) (OR = 14.969, *95% CI*: 1.876∼119.410, P = 0.011) were significantly related to likelihood of cardia structure excision in laparoscopic surgery for EGJ-GISTs. These two factors were used to generate a nomogram for predicting risk of cardia excision using a logistic regression model; a bootstrapped *C-index* of 0.988 (calibrated *C-index* = 0.987) indicated strong predictive ability, with broad calibration.

Conclusions: This nomogram based on distance from tumor margin to EG-line and tumor size may serve as a tool for predicting risk of cardia damage during laparoscopic removal of EGJ-GISTs to aid in selection of surgical methods and preoperative neoadjuvant therapy.

Keywords: gastrointestinal stromal tumors in esophagogastric junction, nomogram, resection of cardiac structure, logistic regression, laparoscopic surgery

INTRODUCTION

Gastrointestinal stromal tumors (GISTs) are a common form of mesenchymal tumor, with an estimated incidence of ∼10–15/1,000,000/year, and the most common site of occurrence being the stomach (50–70%) (1, 2). For localized gastric GISTs (gGISTs), the standard treatment is complete surgical excision of the lesion. Laparoscopic surgery has been widely used due to lower patient trauma and shorter recovery time compared to other approaches. Moreover, the National Comprehensive Cancer Network (NCCN) and the European Society for Medical Oncology (ESMO) have both suggested that laparoscopic resection is feasible for GISTs of suitable location and size (3, 4). However, a laparoscopic approach for gGISTs located in the esophagogastric junction (EGJ-GISTs) remains controversial due to the anatomical complexity of this region and the difficulty of preserving function, such as lower esophageal sphincter pressure, which together make this procedure technically challenging.

An EGJ-GIST is defined as a GIST with an upper border <5 cm from the esophagogastric line (5). In 2018, we introduced four methods of laparoscopic resection: "(1) laparoscopic wedge resection using a linear stapler; (2) laparoscopic complete resection by opening the stomach wall and closing with suture or linear stapler; (3) laparoscopic mucosa-preserving resection; and (4) laparoscopic proximal gastrectomy" (citation). All of these methods have acceptable operative indexes and satisfactory postoperative outcomes (6). Local gastrectomy with cardia preservation and proximal gastrectomy without cardia preservation are the current mainstay treatments. Specifically, wedge resection or resection by opening all layers of the stomach wall are typically recommended treatments, since these methods preserve cardia structure. The cardia structure, which consists of an esophageal sphincter, plays an important role in preventing reflux. Cardia resection is accompanied with reflux esophagitis and other concomitant complications, resulting in serious impacts on the patient's quality of life. Since the advent of imatinib, which can increase survival time for patients with GISTs (7, 8), preservation of cardia function will lead to longer lasting positive effects on quality of life in these patients. Moreover, reduction in tumor size due to imatinib treatment should facilitate easier removal of EGJ-GISTs.

In order to better predict whether cardia could be successfully preserved during laparoscopic resection of EJG-GISTs, we performed a retrospective analysis of EGJ-GIST cases spanning 8 years in our clinic in order to develop a nomogram for use in clinic. Nomograms are graphical prediction models that have been widely used in the prognosis of clinical diseases (9–12). However, no nomogram has yet been developed to predict outcomes of laparoscopic cardia excision in EGJ-GISTs. This study therefore aimed to analyze long-term, retrospective, multi-center data to screen for risk factors associated with cardia excision during laparoscopic resection of EGJ-GISTs using Logistic Regression Analysis. Significant risk factors associated with loss of cardia function due to laparoscopic surgery for EGJ-GISTs could then be used to build a nomogram for prediction of cardia resection based on these risks.

MATERIALS AND METHODS

Patients

We retrospectively collected data from 2,127 gGIST patients without distant metastases who underwent laparoscopic surgery with curative intent in Guangdong Provincial Hospital of Chinese Medicine, Nanfang Hospital of Southern Medical University, Guangdong General Hospital, and The Third Affiliated Hospital of Southern Medical University from June 2012 to June 2020. Of these data, we selected the patients who were diagnosed as EGJ-GISTs. All surgical procedure in the study abided by two oncologic surgical principles: protecting the pseudocapsule integrity and achieving microscopically negative margins on final pathology.

The distance from the margin of the tumor to the EG-line, the tumors locations and growth type were identified based on preoperative endoscopy, abdominal computed tomography scan, magnetic resonance imaging and intraoperative measurement. In the light of the NCCN guideline and our experience, the tumors located in the fundus, greater curvature, or anterior wall of the stomach were classified as favorable site while located in the lesser curvature or posterior wall of the stomach were classified as unfavorable site.

In order to minimize errors, we excluded individuals with cancer in other organs regardless of the severity, lack of data, and those who converted to laparotomy (**Figure 1**). Approval was obtained from the Institutional Review Board and the registration number was ZE2020-298-01.

Statistical Analysis

All statistical analyses were carried out using SPSS version 22.0 (SPSS, Chicago, IL, USA) and the R package version 3.6.1 (St. Louis, Missouri, USA). Factors that may affect the success of cardia excision in laparoscopic surgery were evaluated by univariate analyses with a Logistic Regression Model. Risk factors with $P < 0.05$ were included in multivariate analysis. Significant risk factors were used to create a nomogram, which was then

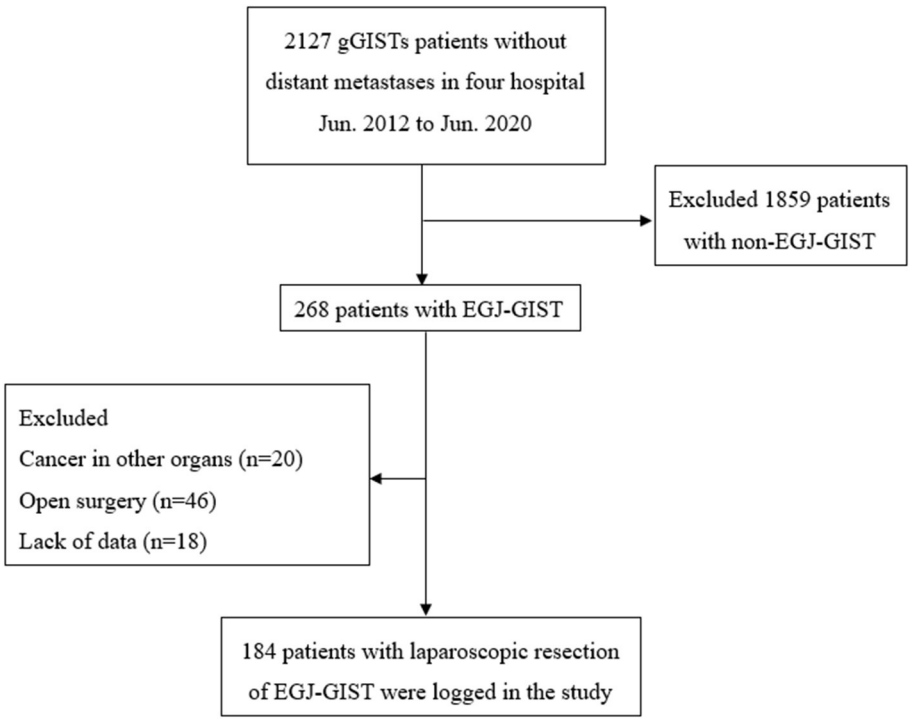

FIGURE 1 | Schematic diagram of patient cohort selection. gGISTs, Gastric gastrointestinal stromal tumors; EGJ-GISTs, Gastrointestinal stromal tumors in esophagogastric junction.

applied to predict the risks associated with laparoscopic cardia excision in EGJ-GIST patients. A concordance index (*C-index*) and calibration curve were then used to assess the nomogram. Differences in categorical data between groups were determined by the chi-square test or Fisher's exact test. Log-Rank (Mantel-Cox) was used for comparing the differences of Relapse-Free Survival (RFS) and Overall Survival (OS) between the groups.

RESULTS

Patient Characteristics

A total of 184 patients admitted to four hospitals were included in the analyses (**Figure 1**). The clinical characteristics of these 184 patients who underwent laparoscopic excision of EGJ-GISTs are summarized in **Table 1**.

TABLE 1 | Clinical characteristics of 184 patients of EGJ-GISTs undergoing laparoscopic surgery.

Factors	Number of patients (%)
Sex	
Male	83 (45.1)
Female	101 (54.9)
Age (years), median (IQR)	58.0 (50.0, 66.0)
BMI (kg/m^2), median (IQR)	22.6 (20.7, 24.3)
The distance from the margin of the tumor to the EG-line(cm), median (IQR)	3.0 (2.0, 4.0)
Tumor size(cm), median (IQR)	3.5 (2.0, 5.0)
Growth type	
Exophytic type	70 (38.0)
Not exophytic type	114 (62.0)
Tumor location	
Favorable site	112 (60.9)
Unfavorable site	72 (39.1)

Risk Factors and Nomogram for Laparoscopic Cardia Excision During Removal of EGJ-GISTs

Laparoscopic cardia excision to remove EGJ-GISTs was reported in 18 patients (9.8%). We evaluated the association between clinical factors and cardia excision during laparoscopic tumor resection in the EGJ by univariate and multivariate analyses. Univariate analyses showed that age, distance from the margin of the tumor to the EG-line, tumor size, and tumor location were significantly related to the incidence of cardia excision during laparoscopic surgery for EGJ-GIST (**Table 2**). Multivariate analysis further showed that distance from the margin of the tumor to the EG-line ($P = 0.001$) and tumor size ($P = 0.011$) were significant factors contributing to the loss of cardia during laparoscopic surgical resection of EGJ-GISTs (**Table 2**). These factors were subsequently combined to create a nomogram to predict the likelihood of cardia excision during laparoscopic gastric tumor removal from the EGJ (**Figure 2**). The nomogram

TABLE 2 | Analyses of the risk of the cardia excision on laparoscopic surgery for EGJ-GISTs.

Factors	Univariate analysis			Multivariate analysis		
	OR	*95%CI*	*P*	*OR*	*95%CI*	*P*
Sex (male vs. female)	0.374	0.134∼1.044	0.060			
Age (years)	0.396	0.198∼0.795	0.009	0.273	0.057∼1.295	0.102
BMI (kg/m^2)	0.720	0.391∼1.325	0.291			
The distance from the margin of the tumor to the EG-line (cm)	0.005	0.001∼0.047	<0.001	0.001	0.00001∼0.056	0.001
Tumor size (cm)	3.316	1.783∼6.165	<0.001	14.969	1.876∼119.410	0.011
Growth type (Exophytic vs. Not exophytic)	0.598	0.204∼1.755	0.349			
Tumor location (Favorable site vs. Unfavorable site)	3.533	1.262∼9.896	0.016	2.777	0.292∼26.393	0.374

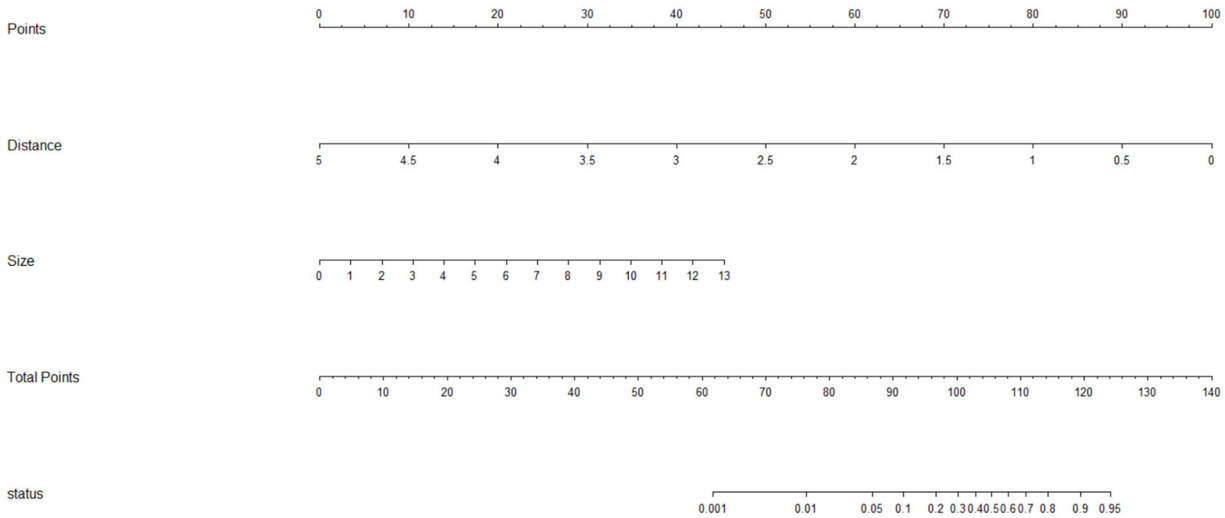

FIGURE 2 | Nomogram for predicting the risk of excising the cardia during laparoscopic surgery for EGJ-GISTs. Distance: Distance from the margin of the tumor to the EG-line (cm); Size: Tumor size (cm); status: probability of EGJ resection.

had a bootstrapped *C-index* of 0.988 (calibrated *C-index* =0.987) with broad calibration (**Figure 3**).

Postoperative and Oncologic Outcomes

The postoperative complication rate was 9.0% in the patients who the EGJ resection was preserved, while 16.7% in the patients who underwent EGJ resection. There was no significant difference between the two groups ($x^2 = 0.381$, $P = 0.537$). The latest follow-up date for the study was in August 1th 2021. Median follow up was 68.1 months (range 13.7–109.0) in the entire cohort. Neither RFS ($P = 0.141$) nor OS ($P = 0.673$) differed between the patients who underwent EGJ resection and those in whom the EGJ was preserved.

DISCUSSION

The main purpose of using a nomogram is to provide a visual tool for assessment of whether cardia excision is avoidable if laparoscopic resection is selected for tumors in the EGJ. Surgery is the primary strategy for effective treatment of GISTs, and laparoscopic surgery is widely performed because it is less invasive than laparotomy, thus facilitating quick recovery with minimal cosmetic impacts. However, for GISTs located in the EGJ, laparoscopy is challenging due to several, complex, anatomical factors as well as the difficulty of preserving cardia function. Moreover, these difficulties associated with laparoscopic surgery make this approach controversial, and therefore it is only recommended by guidelines under certain conditions and tumor locations. Recent advances in laparoscopic technique and the emergence of minimally invasive instruments have increased the safety and effectiveness of laparoscopic surgery for EGJ-GISTs (13–15). The key point of laparoscopic surgery of EGJ-GISTs is to achieve microscopic negative margins on final pathology while also retaining the function of the lower esophageal sphincter (LES) without rupturing the tumor pseudocapsule (3, 4). It is therefore beneficial to know the risk of cardia excision in laparoscopic surgery for EGJ-GISTs that accompanies different surgical methods as well as indications for preoperative neoadjuvant chemotherapy.

As a statistical tool, a nomogram prediction model provides a simple and intuitive graph that can accurately estimate the

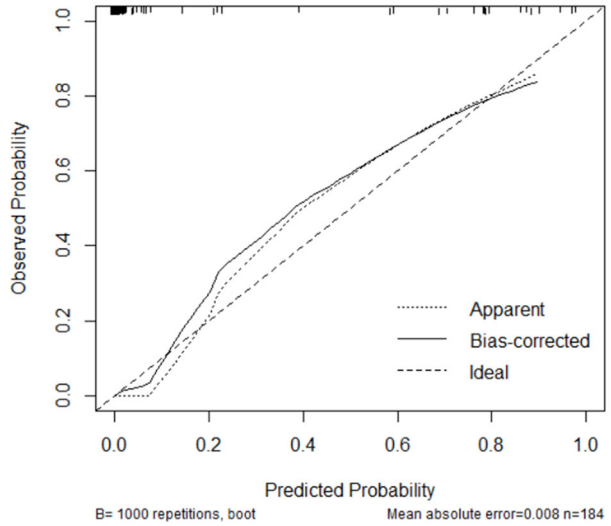

FIGURE 3 | Calibration of the nomogram.

risk of clinical events by integrating the variables that contribute most to these events. Further, nomograms are conducive to individualized treatment, and enable clear and effective communication with patients regarding the risks associated with laparoscopic surgery compared to laparotomy (16–19). In recent years, nomograms have been widely applied to calculate the prognosis of different diseases (9, 10). In this study, we identified the risk factors which may contribute to cardia excision during laparoscopic surgery for EGJ-GISTs through univariate and multivariate logistic regression analyses. Based on our results that the two most significant risk factors were distance from the margin of the tumor to the EG-line and tumor size, we used these measurements to create the first nomographic model, of which we are aware, that forecasts the risk of cardia excision in EGJ-GIST patients.

Han concluded that cardia function could be preserved if the distance between the upper margin of the tumor and the EG-line was at least 1–2 cm and if >50% of the circumference of the EGJ could be reserved after resection (20). In contrast, Kwon proposed that laparoscopic surgery for EGJ-GIST was acceptable if it achieved negative margins (21). In addition, Hiki et al. described Laparoscopic and Endoscopic Cooperative Surgery (LECS) as a treatment for EGJ-GISTs (22), bypassing the difficulty of laparoscopy in order to avoid cardia stenosis and impairment of annular muscle function in the lower esophagus. More recently, the results of a retrospective multicenter study (2017) suggested that laparoscopic and luminal endoscopic cooperative surgery (LECS) was a safe and feasible procedure for the resection of EGJ-GISTs, even in cases when the tumor is located on the EGJ. However, it may be inadvisable if the defect caused by resection is more than one third the circumference of the EGJ (23). In light of previous studies that have sought to minimize the risk of cardia excision, we propose that the nomogram developed in this study can serve as a reliable reference based on tumor size and distance from the upper tumor margin to the EG-line for indication of appropriate surgical methods and neoadjuvant chemotherapy.

In assessing surgical options, it remains controversial whether growth type and tumor location are both important considerations for selection of a treatment strategy and for determining the risk of cardia excision (24, 25). Both NCCN and ESMO recommendations indicate that tumor size, location, growth type, and other factors should be considered in the selection of surgical methods for EGJ-GISTs. Huang et al. enrolled 119 patients with GISTs in the proximity of the EGJ for retrospective review, and concluded that gastric tumors located anywhere but the greater curvature side were more often resected by laparotomy due to the approach angle necessary for linear surgical staplers to access this region of the stomach. However, with advances in technology, since 2016 EGJ-GISTs have been commonly resected laparoscopically (26). Gonzalez et al. reported that LECS for posterior EGJ-GISTs resulted in good efficacy (27). Furthermore, Wang et al. reported performing laparoscopic intragastric surgery for nine cases of cardiac endogenous stromal tumors, all of which resulted in no swallowing disorder or acid reflux symptoms upon follow-up, and therefore concluded that laparoscopic intragastric treatment was safe and feasible for endogenous EGJ-GISTs (28). In addition, techniques such as percutaneous endoscopic intragastric surgery (29) and Single-Incision Laparoscopic Intragastric Surgery (30) have also been reported as safe and feasible for treatment of EGJ-GISTs.

There were several limitations in this study. This was a retrospective study and therefore bias could have been introduced during the analysis; prospective studies are needed to verify our conclusions. In addition, the selection of variables may be incomplete, resulting in limitations for the nomogram prediction model. What's more, we failed to obtain good external verification data for external verification, and only used bootstrap method to verify on the original data set. Despite these limitations, we propose that our nomogram can be informative in the selection of surgical methods and preoperative neoadjuvant therapy.

CONCLUSION

The distance from the upper margin of the tumor to the EG-line and tumor size are independent risk factors associated with excision of cardia structure during laparoscopic surgery for EGJ-GISTs. Our nomogram, based on a logistic regression model, may serve as an informative reference tool for the selection of surgical methods and preoperative neoadjuvant therapy through prediction of the risk of damage to the cardia during laparoscopic removal of EGJ-GISTs.

DATA AVAILABILITY STATEMENT

The original contributions presented in the study are included in the article/supplementary material, further inquiries can be directed to the corresponding author/s.

ETHICS STATEMENT

The studies involving human participants were reviewed and approved by Ethics Committee of Guangdong Provincial Hospital of Chinese Medicine. Written informed consent for participation was not required for this study in accordance with the national legislation and the institutional requirements.

AUTHOR CONTRIBUTIONS

YX: project development, data analysis & collection, and manuscript writing. LL and XF: project development and data collection. YZ, RZ, YL, GL, and TC: data collection. WW: project development and manuscript editing. WX: project development, data collection, and manuscript editing. All authors contributed to the article and approved the submitted version.

FUNDING

The study was supported by Double First-Class and High-level University Discipline Collaborative Innovation Team Project of Guangzhou University of Chinese Medicine(2021xk48), and the Clinical research project of Guangdong Hospital of traditional Chinese medicine (No. YN10101911).

REFERENCES

1. Søreide K, Sandvik OM, Søreide JA, Giljaca V, Jureckova A, Bulusu VR. Global epidemiology of gastrointestinal stromal tumours (GIST): A systematic review of population-based cohort studies. *Cancer Epidemiol.* (2016) 40:39–46. doi: 10.1016/j.canep.2015.10.031
2. Huang Y, Chen G, Lin L, Jin X, Kang M, Zhang Y, et al. Resection of GIST in the duodenum and proximal jejunum: A retrospective analysis of outcomes. *Eur J Surg Oncol.* (2019) 45:1950–6. doi: 10.1016/j.ejso.2019.05.002
3. National Comprehensive Cancer Network(NCCN). *Clinical Practice Guidelines in Oncology. Gastrointestinal stromal tumor (GIST), Version 2* (2019). Available online at: https://www.nccn.org/professionals/physician_gls/f_guidelines.asp
4. Casali PG, Abecassis N, Aro HT, Bauer S, Biagini R, Bielack S, et al. Gastrointestinal stromal tumours: ESMO-EURACAN Clinical Practice Guidelines for diagnosis, treatment and follow-up. *Ann Oncol.* (2018) 29(Suppl. 4):v68–78. doi: 10.1093/annonc/mdy095
5. Siewert JR, Hölscher AH, Becker K, Gössner W. [Cardia cancer: attempt at a therapeutically relevant classification]. *Chirurg.* (1987) 58:25–32.
6. Xiong W, Zhu J, Zheng Y, Luo L, He Y, Li H, et al. Laparoscopic resection for gastrointestinal stromal tumors in esophagogastric junction (EGJ): how to protect the EGJ. *Surg Endosc.* (2018) 32:983–9. doi: 10.1007/s00464-017-5776-6
7. Dematteo RP, Ballman KV, Antonescu CR, Maki RG, Pisters PW, Demetri GD, et al. Adjuvant imatinib mesylate after resection of localised, primary gastrointestinal stromal tumour: a randomised, double-blind, placebo-controlled trial. *Lancet.* (2009) 373:1097–104. doi: 10.1016/S0140-6736(09)60500-6
8. Joensuu H, Eriksson M, Sundby Hall K, Hartmann JT, Pink D, Schütte J, et al. One vs three years of adjuvant imatinib for operable gastrointestinal stromal tumor: a randomized trial. *JAMA.* (2012) 307:1265–72. doi: 10.1001/jama.2012.347
9. Fang C, Wang W, Feng X, Sun J, Zhang Y, Zeng Y, et al. Nomogram individually predicts the overall survival of patients with gastroenteropancreatic neuroendocrine neoplasms. *Br J Cancer.* (2017) 117:1544–50. doi: 10.1038/bjc.2017.315
10. Zhou H, Zhang Y, Qiu Z, Chen G, Hong S, Chen X, et al. Nomogram to predict cause-specific mortality in patients with surgically resected stage i non-small-cell lung cancer: a competing risk analysis. *Clin Lung Cancer.* (2018) 19:e195–203. doi: 10.1016/j.cllc.2017.10.016
11. Weiser MR, Landmann RG, Kattan MW, Gonen M, Shia J, Chou J, et al. Individualized prediction of colon cancer recurrence using a nomogram. *J Clin Oncol.* (2008) 26:380–5. doi: 10.1200/JCO.2007.14.1291
12. Kawai K, Ishihara S, Yamaguchi H, Sunami E, Kitayama J, Miyata H, et al. Nomograms for predicting the prognosis of stage IV colorectal cancer after curative resection: a multicenter retrospective study. *Eur J Surg Oncol.* (2015) 41:457–65. doi: 10.1016/j.ejso.2015.01.026
13. Ye X, Yu J, Kang W, Ma Z, Xue Z. Short- and long-term outcomes of endoscope-assisted laparoscopic wedge resection for gastric submucosal tumors adjacent to esophagogastric junction. *J Gastrointestinal Surg.* (2018) 22:402–13. doi: 10.1007/s11605-017-3628-2
14. Xu X, Chen K, Zhou W, Zhang R, Wang J, Wu D, et al. Laparoscopic transgastric resection of gastric submucosal tumors located near the esophagogastric junction. *J Gastrointest Surg.* (2013) 17:1570–5. doi: 10.1007/s11605-013-2241-2
15. Wang C, Gao Z, Shen Z, Liang B, Jiang K, Shen K, et al. [Efficacy comparison of laparoscopy and open resection for gastrointestinal stromal tumor at the esophagogastric junction]. *Zhonghua Wei Chang Wai Ke Za Zhi.* (2015) 18:881–4. doi: 10.3760/cma.j.issn.1671-0274.2015.09.008
16. Liu J, Geng Q, Liu Z, Chen S, Guo J, Kong P, et al. Development and external validation of a prognostic nomogram for gastric cancer using the national cancer registry. *Oncotarget.* (2016) 7:35853–64. doi: 10.18632/oncotarget.8221
17. Song W, Lv CG, Miao DL, Zhu ZG, Wu Q, Wang YG, et al. Development and validation of a nomogram for predicting survival in patients with gastrointestinal stromal tumours. *Eur J Surg Oncol.* (2018) 44:1657–65. doi: 10.1016/j.ejso.2018.07.004
18. Zhong LP, Li D, Zhu LZ, Fang XF, Xiao Q, Ding KF, et al. [A prognostic nomogram for metastasized colorectal cancer patients treated with cetuximab]. *Zhonghua Wei Chang Wai Ke Za Zhi.* (2020) 23:701–8. doi: 10.3760/cma.j.cn.441530-20190621-00250
19. Iasonos A, Schrag D, Raj GV, Panageas KS. How to build and interpret a nomogram for cancer prognosis. *J Clin Oncol.* (2008) 26:1364–70. doi: 10.1200/JCO.2007.12.9791
20. Han L. Choices and evaluation of digestive tract reconstruction for patients with gastrointestinal stromal tumor of esophagogastric junction. *Chin J Pract Surg.* (2018) 2018:512–4.
21. Kwon SJ. Surgery and prognostic factors for gastric stromal tumor. *World J Surg.* (2001) 25:290–5. doi: 10.1007/s002680020040
22. Hiki N, Yamamoto Y, Fukunaga T, Yamaguchi T, Nunobe S, Tokunaga M, et al. Laparoscopic and endoscopic cooperative surgery for gastrointestinal stromal tumor dissection. *Surg Endosc.* (2008) 22:1729–35. doi: 10.1007/s00464-007-9696-8
23. Matsuda T, Nunobe S, Kosuga T, Kawahira H, Inaki N, Kitashiro S, et al. Laparoscopic and luminal endoscopic cooperative surgery can be a standard treatment for submucosal tumors of the stomach: a retrospective multicenter study. *Endoscopy.* (2017) 49:476–83. doi: 10.1055/s-0043-104526
24. Kim MC, Yook JH, Yang HK, Lee HJ, Sohn TS, Hyung WJ, et al. Long-term surgical outcome of 1057 gastric GISTs according to 7th UICC/AJCC TNM system: multicenter observational study from Korea and Japan. *Medicine (Baltimore).* (2015) 94:e1526. doi: 10.1097/MD.0000000000001526
25. Erko IP, Moloshok AA, Zotov VN. [Surgical treatment of gastrointestinal stromal tumours]. *Klin Khir.* (2013) 2013:18–20.
26. Huang YC, Yeh CN, Chen MY, Wang SY, Liu KH, Tsai CY, et al. Surgical options for submucosal tumors near the esophagogastric junction: does size or location matter?. *BMC Surg.* (2020) 20:179. doi: 10.1186/s12893-020-00840-6

27. Gonzalez JM, Debourdeau A, Philouze G, Beyer L, Berdah S, Barthet M. Laparoscopic and endoscopic cooperative surgery for difficult resection of posterior esophagogastric junction gastrointestinal stromal tumors. *Endoscopy.* (2018) 50:178–9. doi: 10.1055/s-0043-121136
28. Xing-Yu WJ. [Cardiac endogenous gastric intestinal stromal tumors with laparoscopic intragastric surgery: An analysis of 9 cases]. *Chin J Pract Surg.* (2016) 36:797–800. doi: 10.7504/CJPS.ISSN1005-2208.2016.07.21
29. Kanehira E, Kamei A, Umezawa A, Kurita A, Tanida T, Nakagi M. Long-term outcomes of percutaneous endoscopic intragastric surgery in the treatment of gastrointestinal stromal tumors at the esophagogastric junction. *Surg Endosc.* (2016) 30:2036–42. doi: 10.1007/s00464-015-4439-8
30. Katsuyama S, Nakajima K, Kurokawa Y, Takahashi T, Miyazaki Y, Makino T, et al. Single-incision laparoscopic intragastric surgery for gastric submucosal tumor located adjacent to esophagogastric junction: report of four cases. *J Laparoendosc Adv Surg Tech A.* (2018) 28:78–82. doi: 10.1089/lap.2017.0026

Conflict of Interest: The authors declare that the research was conducted in the absence of any commercial or financial relationships that could be construed as a potential conflict of interest.

Publisher's Note: All claims expressed in this article are solely those of the authors and do not necessarily represent those of their affiliated organizations, or those of the publisher, the editors and the reviewers. Any product that may be evaluated in this article, or claim that may be made by its manufacturer, is not guaranteed or endorsed by the publisher.

frontiers in Surgery

ORIGINAL RESEARCH
published: 18 October 2021
doi: 10.3389/fsurg.2021.736737

Pre-operative Prediction of Ki-67 Expression in Various Histological Subtypes of Lung Adenocarcinoma Based on CT Radiomic Features

Zhiwei Huang[1,2†], Mo Lyu[2,3†], Zhu Ai[2†], Yirong Chen[1,2], Yuying Liang[2] and Zhiming Xiang[2]*

[1] Graduate School, Guangzhou University of Chinese Medicine, Guangzhou, China, [2] Department of Radiology, Guangzhou Panyu Central Hospital, Guangzhou, China, [3] School of Life Sciences, South China Normal University, Guangzhou, China

OPEN ACCESS

Edited by:
Kee Yuan Ngiam,
National University Health System, Singapore

Reviewed by:
Zhang Wang,
South China Normal University, China
Jinglei Li,
Guangdong Provincial People's Hospital, China
Kai Wu,
South China University of Technology, China

***Correspondence:**
Zhiming Xiang
xiangzhiming@pyhospital.com.cn

†These authors have contributed equally to this work and share first authorship

Specialty section:
This article was submitted to Surgical Oncology, a section of the journal Frontiers in Surgery

Received: 05 July 2021
Accepted: 09 September 2021
Published: 18 October 2021

Citation:
Huang Z, Lyu M, Ai Z, Chen Y, Liang Y and Xiang Z (2021) Pre-operative Prediction of Ki-67 Expression in Various Histological Subtypes of Lung Adenocarcinoma Based on CT Radiomic Features. Front. Surg. 8:736737. doi: 10.3389/fsurg.2021.736737

Purpose: The aims of this study were to combine CT images with Ki-67 expression to distinguish various subtypes of lung adenocarcinoma and to pre-operatively predict the Ki-67 expression level based on CT radiomic features.

Methods: Data from 215 patients with 237 pathologically proven lung adenocarcinoma lesions who underwent CT and immunohistochemical Ki-67 from January 2019 to April 2021 were retrospectively analyzed. The receiver operating curve (ROC) identified the Ki-67 cut-off value for differentiating subtypes of lung adenocarcinoma. A chi-square test or *t*-test analyzed the differences in the CT images between the negative expression group ($n = 132$) and the positive expression group ($n = 105$), and then the risk factors affecting the expression level of Ki-67 were evaluated. Patients were randomly divided into a training dataset ($n = 165$) and a validation dataset ($n = 72$) in a ratio of 7:3. A total of 1,316 quantitative radiomic features were extracted from the Analysis Kinetics (A.K.) software. Radiomic feature selection and radiomic classifier were generated through a least absolute shrinkage and selection operator (LASSO) regression and logistic regression analysis model. The predictive capacity of the radiomic classifiers for the Ki-67 levels was investigated through the ROC curves in the training and testing groups.

Results: The cut-off value of the Ki-67 to distinguish subtypes of lung adenocarcinoma was 5%. A comparison of clinical data and imaging features between the two groups showed that histopathological subtypes and air bronchograms could be used as risk factors to evaluate the expression of Ki-67 in lung adenocarcinoma ($p = 0.005$, $p = 0.045$, respectively). Through radiomic feature selection, eight top-class features constructed the radiomic model to pre-operatively predict the expression of Ki-67, and the area under the ROC curves of the training group and the testing group were 0.871 and 0.8, respectively.

Conclusion: Ki-67 expression level with a cut-off value of 5% could be used to differentiate non-invasive lung adenocarcinomas from invasive lung adenocarcinomas. It is feasible and reliable to pre-operatively predict the expression level of Ki-67 in lung

adenocarcinomas based on CT radiomic features, as a non-invasive biomarker to predict the degree of malignant invasion of lung adenocarcinoma, and to evaluate the prognosis of the tumor.

Keywords: lung adenocarcinoma, Ki-67, computed tomography, radiomics, pre-operative prediction, non-invasive biomarker

INTRODUCTION

Lung adenocarcinoma is the most commonly diagnosed histological subtype of non-small-cell lung cancer (NSCLC), which is the leading cause of cancer-related deaths worldwide (1). In 2011, a new classification system for lung adenocarcinomas according to the International Association for the study of Lung Cancer (IASLC), American Thoracic Society (ATS), and European Respiratory Society (ERS) has been put forward, wherein the lung adenocarcinomas are mainly classified as atypical adenomatous hyperplasia (AAH), adenocarcinoma *in situ* (AIS), minimally invasive adenocarcinoma (MIA), and invasive adenocarcinoma (IAC). Among them, AAH and AIS were pre-invasive lesions (2). More and more treatment methods can be used for the treatment of lung cancer. However, many patients, even patients with resectable lung cancer, still have poor prognoses (3). For lung adenocarcinoma, studies have found that, even for patients with complete surgical resection and in pathologic stage T1 (pathologic-T1, pT1), the treatment effects and prognoses may be significantly different (4). There is an urgent need to determine reliable prognostic factors that can predict clinical outcomes and more precisely stratify the group of patients susceptible to poorer outcomes.

Currently, Ki-67 is commonly regarded as a prognosis biomarker to predict the cell proliferation and aggressiveness of tumors in clinical practice, which can be used for quantitative analysis of tumor growth fraction and the classification of tumors and for assisting in early diagnosis and therapeutic effect evaluations (5). Ki-67 is expressed at all stages of the cell cycle except G0, with the highest expression levels in the G2/M phase. It has been reported that the overall survival (OS) and disease-free survival (DFS) of patients with high Ki-67 expression are shorter than those with low Ki-67 expression (5–7). Previous studies have identified the Ki-67 labeling index as a strong prognostic biomarker for lung adenocarcinoma (8, 9). Yamashita et al. found that Ki-67 can be used as an indicator of recurrence of lung cancer after resection (10), and the level of its positive expression is closely related to the differentiation degree, lymph node metastasis, and other factors of lung cancer (8, 11). The most commonly used method to quantify Ki-67 expression is immunohistochemistry (IHC), which is not practical for the dynamic monitoring of Ki-67 during lung cancer treatment because of invasion, which is time-consuming (12). Due to the existence of tumor heterogeneity, Ki-67 values varied in different regions of the tumor samples, and traditional invasive immunohistochemical methods only evaluate the biopsy specimens of a small sample of the tissue and cannot reflect the overall heterogeneity of the tumor (13, 14). Therefore, finding a non-invasive, cost-effective, and comprehensive method for clinical Ki-67 expression level assessment is necessary.

Radiomics is a recently emerging technique in computational medical imaging. It involves the extraction and analyses of a large number of quantitative imaging features from medical images (15, 16). It is different from traditional methods because it converts medical images into mineable high-dimensional data. Radiomics can help support patient diagnosis, prognosis, treatment, and prediction in clinical practice. The relationship between Ki-67 expression level and radiomic features has always been a hot topic. Studies have shown that radiomics can be used to pre-operatively predict the expression level of Ki-67 in breast cancer (17) and adrenal cancer (18). In addition, several studies have shown that the quantitative imaging features from CT can predict Ki-67 levels and subtypes in patients with lung cancer (19, 20), but the role of Ki-67 in distinguishing the pathological stages of lung adenocarcinoma remains unclear (12, 21). To our knowledge, there have been no studies on the use of CT-based radiomic features to predict Ki-67 expression levels in subtypes of lung adenocarcinoma.

This study aimed to investigate the correlation between Ki-67 expression level and the subtypes of lung adenocarcinoma and to assess whether CT-based radiomic features could serve as non-invasive predictors of the Ki-67 levels in patients with lung adenocarcinoma.

MATERIALS AND METHODS

Patient Characteristics

We retrospectively collected data from patients who underwent a chest CT scan, Ki-67 expression level detection, and post-operative pathological confirmation of lung adenocarcinoma at our institute from January 2019 to April 2021. The inclusion criteria were: (1) patients confirmed with lung adenocarcinoma by surgical resection, (2) maximum diameter of tumor $\leq$3 cm, (3) complete clinicopathological data, (4) IHC examination of Ki-67 expression levels, and (5) complete CT images. The exclusion criteria were: (1) greatest tumor diameter $>$3 cm, (2) radiotherapy, chemotherapy, or radiotherapy and chemotherapy were performed before surgery, and (3) incomplete or poor-quality CT images. Our institutional review board approved this retrospective study, and the requirement for informed consent was waived.

Computed Tomography Examination

All patients in this study used a 64-slice CT scanner (Discovery CT 750 HD, GE Healthcare, Chicago, IL, USA) for their chest scans. All CT scans were obtained with the patients in the supine position and holding their breath at the end of a full inspiration.

The scan ranged from above the apex of the lungs to below the level of the diaphragm. The scanning parameters were as follows: tube voltage of 120 or 140 kV, tube current of 200–340 mA, beam pitch of 1.2, pixel resolution of 512 × 512, field of view (FOV) of 360 mm, thickness of 5 mm, and reconstructed slice thickness and slice increment of 1 mm. Afterward, the CT scans were reviewed as lung window images (window width = 1,200 HU; window level = −700 HU) and mediastinal window images (window width = 350 HU; window level = 50 HU). All images were exported in a DICOM format for image feature extraction after scanning.

The CT imaging signs included (22): (1) lesion location, (2) maximum diameter of the tumor on axial images, (3) tumor-lung interface: clear or unclear, (4) density: pure ground-glass opacity, mixed ground-glass opacity, and solid nodule, (5) spiculation, (6) lobulation, (7) bubble-like lucency, (8) air bronchogram sign, (9) vascular sign, and (10) pleural traction. Two diagnostic radiologists with 3 and 9 years of experience reviewed the CT images of each patient and identified positive and negative findings by consensus. The entire process was performed without the patient having knowledge of the pathological results.

Immunohistochemical Analysis

Lung tissues were fixed with a 10% buffered formaldehyde solution by transbronchial or transpleural perfusion for ∼48 h and embedded in paraffin wax. Tissue sections were stained with HE. A mouse anti-human Ki-67 monoclonal antibody (Beijing Zhongshan Jinqiao Biotechnology Co., Ltd., Beijing, China) was used to perform the immunohistochemical detection according to the kit instructions. Positive and negative controls were set up, respectively. Ki-67 was positive with brown-yellow granules in the nucleus. The number of Ki-67 positive tumor cells was calculated in five fields of high-power field (×400) under light microscopes. The percentage of Ki-67 expression level positive staining of tumor cells in each field = the number of positive tumor cells in each field/total tumor cells in each field × 100%. The Ki-67 indices in five fields were calculated and averaged. Histological and cytological subtypes were assessed according to the WHO classification system for lung cancer (5th version) (23). The thresholding of the Ki-67 expression level was used to separate the tumor samples into positive and negative groups: The expression level of Ki-67 ≤5% was negative, and >5% was positive (24).

Radiomics Analysis

Image Pre-processing and Image Segmentation

Firstly, the CT scan images of all patients were exported in a DICOM format from the PACS system workstations, and the AK (Analysis Kinetics, V3.2.0, Workbench2014, GE Healthcare) software was used to preprocess the resampled images of 0.5 × 0.5 × 0.5 on the X, Y, and Z axes, respectively. The three-dimensional segmentation of the tumor regions of interest (ROIs) was performed using the ITK-SNAP software (version 3.8, Philadelphia, PA, USA) with the window width and window level as 1,200 HU and −700 HU, respectively. Then, the ROIs were outlined, and the outlined image was saved in the format of "Merge. nii." The scope of the image delineation includes tumor necrosis, cystic, and cavity, excluding burr, thickened pleura, and surrounding signs. The continuous delineation includes the whole lesion. If it is found to be contradictory, other senior radiologists will evaluate the tumor mask again to reach an agreement.

Radiomic Feature Extraction

The data were imported into the AK (V3.2.0, Workbench2014, GE Healthcare) analysis software to extract radiomic features, including features of first order, shape (Shape), gray-level co-occurrence matrix (GLCM), gray-level run-length matrix (GLRLM), gray-level size-zone matrix (GLSZM), gray-level dependence matrix (GLDM), and features of neighborhood gray difference matrix (NGTDM). The selected image transformations were: logarithmic transformation (LoG), parameter Sigma selection 2.0, 3.0; wavelet transformation (Wavelet), Level 1; local binary mode (LBP), Level 2, Radius 1.0, Subdivision select 1. A total of 1,316 features were extracted.

Radiomic Feature Selection and Classifier Construction

The interobserver intraclass correlation coefficient (ICC) selects values >0.75. Stratified sampling was used to divide all the patients into a training cohort ($n = 165$) and a validation cohort ($n = 72$) according to a ratio of 7:3. First, an ANOVA was performed to remove features with $p > 0.05$, and then the rest of the radiomic features were retained to select the most relevant features using recursive feature elimination (RFE). Next, the least absolute shrinkage and selection operator (LASSO) model, which could improve prediction accuracy and interpretation, was used to further select the features. According to Mann–Whitney U test, the top-class features were screened out to build the final logistic regression classifier, which was used to perform radiomic feature selection in the training dataset. Classification performance was evaluated using the area under the receiver operating characteristic curve (AUC). Finally, a radiomic score (Rad score) was developed using the logistic regression model and then used to calculate the training and validation datasets. A simplified flowchart of the study is given in **Figure 1**.

Statistical Analysis

Clinicopathologic Characteristics of Patients

All statistical analyses were performed with SPSS version 21.0 (IBM Corporation, Armonk, NY, USA). Results were given as mean ± SD or median and range values. The chi-square test or Fisher's exact test was adopted to compare the distribution of the categorical variables. Student's t-test or one-way ANOVA was also calculated for the comparison of continuous variables. Manne–Whitney U testing was used for non-parametric data. Binary logistic regression was used to analyze the potential risk factors affecting the Ki-67 expression level. The cut-off value of the labeling index was obtained from the receiver operating curve (ROC) with the Youden index. The statistical analysis was considered significant when the p-value was <0.05.

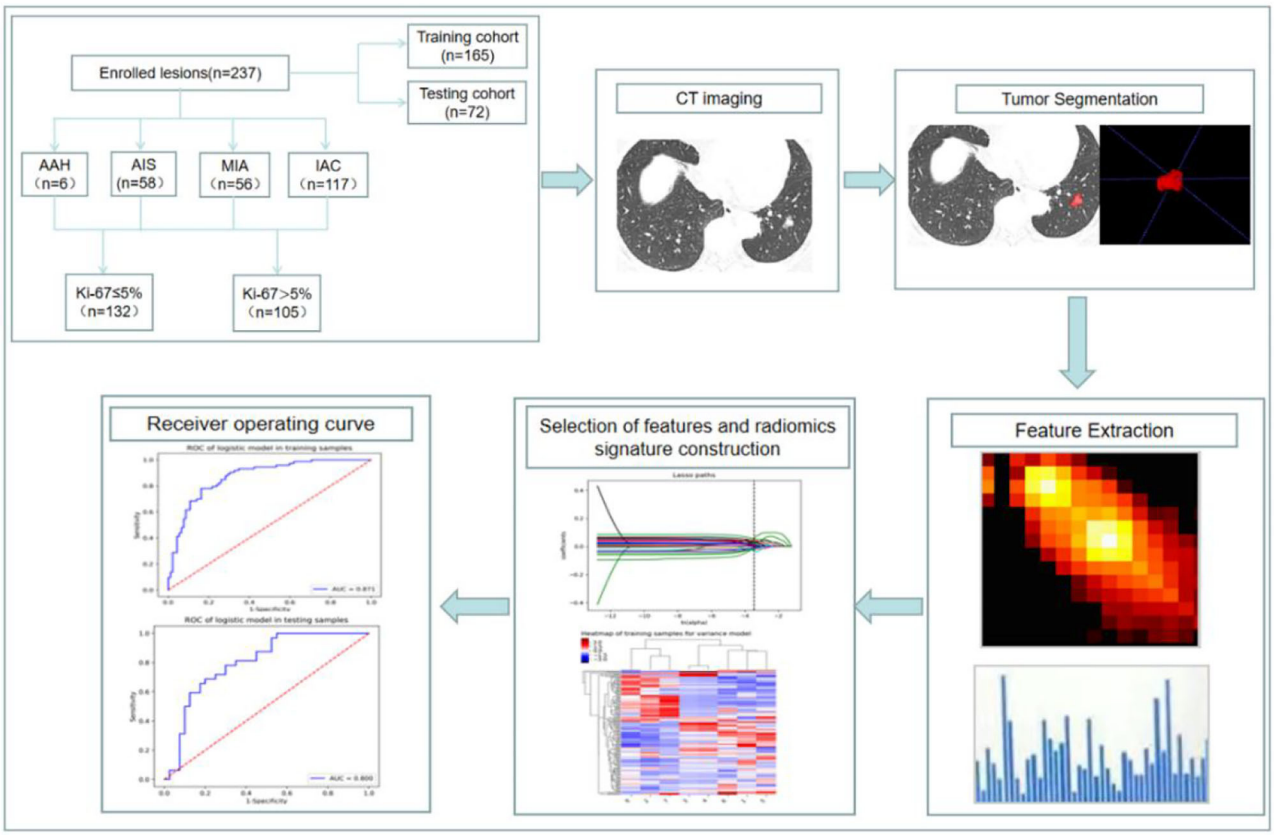

FIGURE 1 | Flowchart of constructing a CT radiomic feature model to predict the Ki-67 expression level in lung adenocarcinoma.

Performance of the Radiomic Prediction Model

To evaluate the performance of the proposed radiomic prediction model, we adopted accuracy, sensitivity, specificity, positive predictive value, and negative predictive value as the evaluation indexes. Furthermore, the ROC curves and the AUCs were calculated to quantitatively assess the predictive capacity of the radiomic classifiers in the training and validation datasets. A p-value of <0.05 was considered statistically significant.

RESULTS

Characteristics of Study Subjects

The clinicopathologic characteristics of the patients with lung adenocarcinoma were summarized in **Table 1**. After screening, a total of 215 patients met the requirements. Among them, 19 patients had multiple lesions. There were 68 males (31.63%) and 147 females (68.37%) with a median age of 56 years old. One hundred ninety-six patients (91.16%) were non-smokers. Seventeen patients (7.91%) had a history of non-pulmonary tumors, 9 had thyroid cancer, 4 had breast cancer, 1 had cervical cancer, 1 had endometrial squamous cell carcinoma, 1 had colon cancer, and 1 had vocal cord squamous cell carcinoma. In the end, 237 lung adenocarcinoma lesions were selected for our study.

TABLE 1 | Patient characteristics on a per patient level.

Variables	*n* (%) or Median (range)
Age (years)	56.00 (22,82)
Gender	
Female	147 (68.37)
Male	68 (31.63)
Smoking history	
Never	196 (91.16)
Ever	19 (8.84)
History of malignancies	17 (7.91)
Breast cancer	4 (1.86)
Cervical cancer	1 (0.47)
Thyroid cancer	9 (4.19)
Colon cancer	1 (0.47)
Endometrial squamous cell carcinoma	1 (0.47)
Vocal cord squamous cell carcinoma	1 (0.47)

Ki-67 Expression Levels and Histological Subtypes

As shown in **Tables 2**, **3**, and **Figures 2A–C**, the pathological diagnoses based on multidisciplinary lung adenocarcinoma

TABLE 2 | The expression level of Ki-67 in various pathological subtypes of lung adenocarcinoma.

Variables	AAH ($n = 6$)	AIS ($n = 58$)	MIA ($n = 56$)	Non-invasive adenocarcinoma (AAH/AIS/MIA) ($n = 120$)	IAC ($n = 117$)	*P*
Ki-67 expression (%)						
mean ± SD	3.00 ± 1.79	3.57 ± 2.63	4.39 ± 3.53	3.93 ± 3.07	17.09 ± 17.12	<0.001
Median (range)	2.5 (1,6)	3 (1,15)	3 (1,20)	3 (1,20)	10 (2,80)	<0.001
Ki-67 Subgroups (%)						<0.001
≤5	5 (83.33)	52 (89.65)	46 (82.14)	103 (85.83)	29 (24.79)	
5–10	1 (16.67)	4 (6.90)	5 (8.93)	10 (8.34)	19 (16.24)	
10–30	0	2 (3.45)	5 (8.93)	7 (5.83)	51 (43.59)	
>30	0	0	0	0	18 (15.38)	

SD, standard deviation.

TABLE 3 | Area under the ROC curve (AUC) of the Ki-67 expression level among different pathological subtypes paired groups.

Pairs	*P*	AUC	Optional cut-off value	Standard deviation	Asymptotic *P*-value	Asymptotic 95% Confidence interval	
						Lower limit	Upper limit
MIA vs. IAC	<0.001	0.851	5.5	0.030	<0.001	0.792	0.909
AAH/AIS vs. MIA/IAC	<0.001	0.787	6.5	0.030	<0.001	0.729	0.846
AAH/AIS/MIA vs. IAC	<0.001	0.872	5.5	0.023	<0.001	0.828	0.916

AAH, atypical adenomatous hyperplasia; AIS, adenocarcinoma in situ; MIA, minimally invasive adenocarcinoma; IAC, invasive adenocarcinoma.

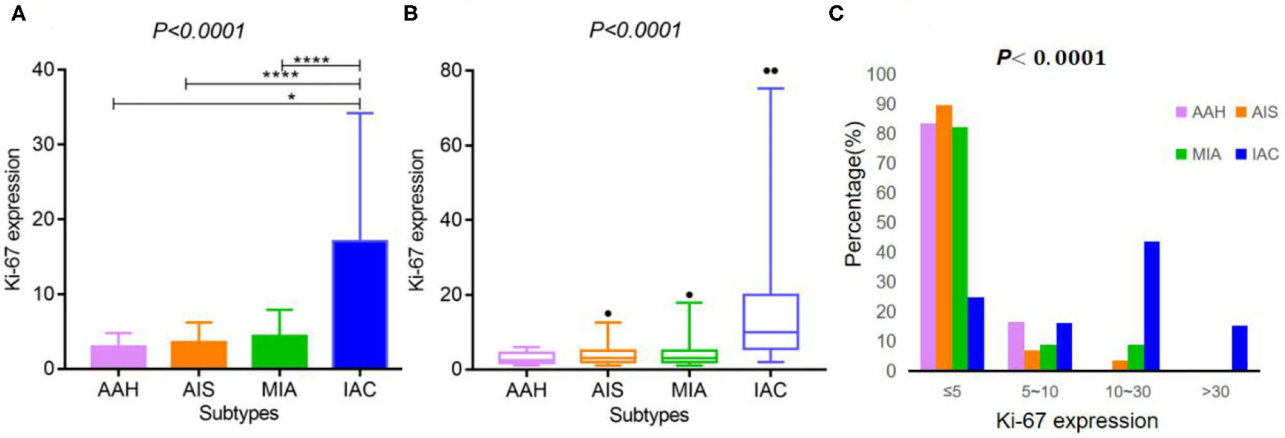

FIGURE 2 | Ki-67 expression according to the histological subtypes of lung adenocarcinoma. **(A,B)** Ki-67 expression differed across various lung adenocarcinoma subtypes [**A**: mean ± SD, **B**: median (2.5–97.5%)]. **(C)** The expression distribution of Ki-67 according to the histological subtypes of lung adenocarcinoma. **** indicates *P*-value <0.01, and * indicates *P*-value <0.05.

criteria were as follows: 6 patients (2.53%) had AAH, 58 patients (24.47%) had AIS, 56 patients (23.63%) had MIA, and 117 (49.37%) had IAC. The AAH subtype had the lowest Ki-67 expression level (3 ± 1.79), followed by AIS (3.57 ± 2.63), MIA (4.39 ± 3.53), and IAC (17.09 ± 17.12). The samples were further divided into four subgroups according to Ki-67 expression: ≤5, 5–10, 10–30, and >30%. In total, the group with Ki-67 expression levels ≤5% was composed of pre-cellular (AAH/AIS) (57/64, 89.06%), minimally invasive (46/56, 82.14%), and invasive adenocarcinomas (29/117, 24.79%). The group with Ki-67 expression levels >5% consisted of pre-cellular (7/64, 10.94%), minimally invasive (10/56, 17.86%), and invasive adenocarcinomas (88/117, 75.21%). By a one-way ANOVA, Tamhane's T2 test (with a Levene test for uneven variance between groups) compared the expression levels of Ki-67, and it was found that there was no significant difference between the

AAH group and AIS group ($p = 0.608$), the AAH group and MIA group ($p = 0.347$), and the AIS group and MIA group ($p = 0.159$), but the AAH group ($p < 0.001$), AIS group ($P < 0.001$), and MIA group ($p < 0.001$) were significantly different from the IAC group.

The Optimal Ki-67 Cut-Off Points Among Different Pathological Subtypes Paired Groups of Lung Adenocarcinoma

As shown in **Table 3** and **Figures 3A–C**, the ROC curve was used to analyze the sensitivity, specificity, and cut-off value of Ki-67 as a discriminant index for different pathological subtypes of lung adenocarcinoma. Non-invasive lung adenocarcinoma (AAH/AIS/MIA) vs. invasive lung adenocarcinoma (AUC = 0.872) had the highest sensitivity and specificity, followed by MIA vs. IAC (AUC = 0.851) and pre-cellular (AAH/AIS) vs. MIA/IAC (AUC = 0.787) ($p < 0.001$). According to the cut-off points of each pairing group, when the expression of Ki-67 was ≤5%, it was more inclined to AAH, AIS, or MIA, while more than 5% corresponded to IAC.

Comparison of CT Imaging Signs and Clinical Data of Lung Adenocarcinoma in Ki-67 Negative and Positive Expression Group

In our study, the median expression of Ki-67 was 5%. In addition, the lung adenocarcinomas were divided into a non-invasive adenocarcinoma group (AAH/AIS/MIA group) and an invasive adenocarcinoma group according to the prognosis of the lesions. Those classified as MIA were grouped with AAH/AIS due to its good prognosis. Therefore, 5% was selected as the cut-off value for grouping different stages of lung adenocarcinoma. Patients were divided into two groups: 132 (55.7%) patients had negative Ki-67 expression, and 105 (44.3%) patients exhibited positive Ki-67 expression. We first explored whether the imaging signs and clinical data could distinguish between the Ki-67 negative expression group and the Ki-67 positive expression group. The results showed that CT imaging signs (maximum diameter, density, shape, lobulation, spiculation, air bronchogram, vascular sign, and pleural traction) could be used to discriminate between the two groups ($p < 0.001$). There was a higher percentage of lymph node metastasis in the Ki-67 positive expression group than in the Ki-67 negative expression group ($p < 0.001$) (**Table 4**). Air bronchogram and histopathological subtype had moderate predictive values, and the AUC values were 0.711 and 0.809, respectively (**Table 5**). The Ki-67 positive expression group was more inclined to have air bronchograms than the Ki-67 negative expression group. The histopathological subtype of the Ki-67 positive expression group was more likely to be IAC, while the Ki-67 negative expression group was more likely to be a pre-invasive lesion (AAH and AIS) or MIA (**Figure 4**).

Feature Selection

Patients were randomly divided into a training dataset ($n = 165$) and a validation dataset ($n = 72$) in a ratio of 7:3. At last, 1,316 radiomic features were extracted from the AK software. After the application of LASSO logistic algorithm, eight radiomic features were finally selected as the optimal radiomic feature subset based on the relationship between the classification accuracy and the number of features for the radiomic classifier. In **Table 6**, eight optimal radiomic features include 1 first order histogram feature, 2 GLCM,3 GLRLM, and 2 GLDM. **Figure 5** shows the correlation between the top eight features, namely, lbp-3D-k_glrlm_LongRunHighGrayLevelEmphasis ($p < 0.001$), lbp-3D-k_glrlm_ShortRunLowGrayLevelEmphasis ($p < 0.001$), log-sigma-3-0-mm-3D_gldm_GrayLevelVariance ($p < 0.001$), original_gldm_LowGrayLevelEmphasis ($p < 0.001$), original_glrlm_LowGrayLevelRunEmphasis ($p < 0.001$), wavelet

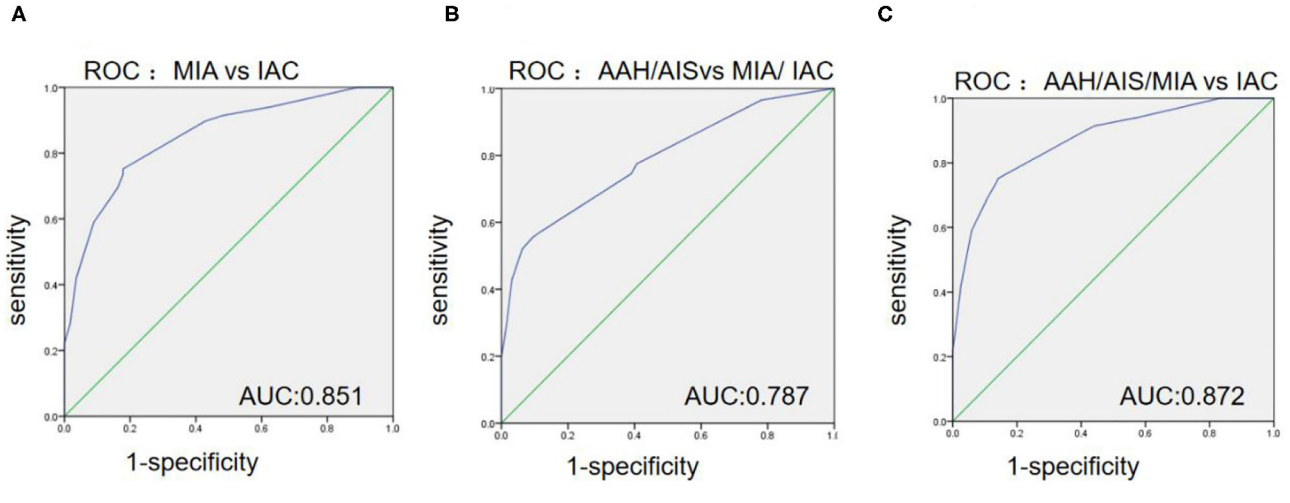

FIGURE 3 | The ROC curves among the different paired groups of pathological subtypes. **(A)** Minimally invasive adenocarcinoma (MIA) vs. invasive adenocarcinoma (IAC); **(B)** Atypical adenomatous hyperplasia (AAH)/adenocarcinoma *in situ* (AIS) vs. MIA/IAC; **(C)** AAH/AIS/MIA vs. IAC.

TABLE 4 | Comparison of imaging features and histopathological subtypes in the Ki-67 negative and positive expression groups of lung adenocarcinoma.

Characteristics	Negative Ki-67 expression group ($n = 132$)		Total	Positive Ki-67 expression group ($n = 105$)		Total	p
	Training cohort ($n = 92$)	Testing cohort ($n = 40$)		Training cohort ($n = 73$)	Testing cohort ($n = 32$)		
Pathological subtype							<0.001
Pre-cellular (AAH/AIS)	38 (28.79)	19 (14.39)	57 (43.18)	4 (3.81)	3 (2.86)	7 (6.67)	
MIA	35 (26.52)	11 (8.33)	46 (34.85)	7 (6.67)	3 (2.86)	10 (9.52)	
IAC	19 (14.39)	10 (7.58)	29 (21.97)	62 (59.05)	26 (24.76)	88 (83.81)	
LPA	1 (0.76)	4 (3.03)	5 (3.79)	11 (10.48)	1 (0.95)	12 (11.43)	
APA	15 (11.36)	4 (3.03)	19 (14.39)	39 (37.14)	19 (18.10)	58 (55.24)	
PPA	2 (1.52)	1 (0.76)	3 (2.27)	7 (6.67)	3 (2.86)	10 (9.52)	
MPA	0	0	0	2 (1.90)	1 (0.95)	3 (2.86)	
SPA	1 (0.76)	1 (0.76)	2 (1.52)	3 (2.86)	2 (1.90)	5 (4.76)	
Lymph node metastasis							<0.001
Yes	0	0	0	10 (9.52)	4 (3.81)	14 (13.33)	
No	92 (69.70)	40 (30.30)	132 (100.00)	63 (60.00)	28 (26.67)	91 (86.67)	
Maximum diameter	7.20 ± 4.30	8.63 ± 5.12	7.63 ± 4.59	14.34 ± 5.82	15.19 ± 6.42	14.60 ± 5.99	<0.001
Lesion location							0.923
Right upper lobe	34 (25.76)	12 (9.09)	46 (34.85)	24 (22.86)	12 (11.43)	36 (34.29)	
Right middle lobe	6 (4.55)	0	6 (4.55)	1 (0.95)	2 (1.90)	3 (2.86)	
Right lower lobe	20 (15.15)	11 (8.33)	31 (23.48)	16 (15.24)	7 (6.67)	23 (21.90)	
Left upper lobe	23 (17.42)	9 (6.82)	32 (24.24)	17 (16.19)	9 (8.57)	26 (24.76)	
Left lower lobe	9 (6.82)	8 (6.06)	17 (12.88)	15 (14.29)	2 (1.90)	17 (16.19)	
Density							<0.001
pGGO	51 (38.64)	21 (15.91)	72 (54.55)	8 (7.62)	1 (0.95)	9 (8.57)	
mGGO	36 (27.27)	15 (11.36)	51 (38.64)	38 (36.19)	20 (19.05)	58 (55.24)	
SN	5 (3.79)	4 (3.03)	9 (6.82)	27 (25.71)	11 (10.48)	38 (36.19)	
Shape							<0.001
Round	70 (53.03)	30 (22.73)	100 (75.76)	30 (28.57)	10 (9.52)	40 (38.10)	
Irregular	22 (16.67)	10 (7.58)	32 (24.24)	43 (40.95)	22 (20.95)	65 (61.90)	
Tumor-lung interface							0.239
Clear	47 (35.61)	19 (14.39)	66 (50.00)	44 (41.90)	17 (16.19)	61 (58.10)	
Unclear	45 (34.09)	21 (15.91)	66 (50.00)	29 (27.62)	15 (14.29)	44 (41.90)	
Lobulation							<0.001
Yes	58 (43.94)	26 (19.70)	84 (63.64)	69 (65.71)	30 (28.57)	99 (94.29)	
No	34 (25.76)	14 (10.61)	48 (36.36)	4 (3.81)	2 (1.90)	6 (5.71)	
Spiculation							<0.001
Yes	35 (26.52)	14 (10.61)	49 (37.12)	56 (53.33)	26 (24.76)	82 (78.10)	
No	57 (43.18)	26 (19.70)	83 (62.88)	17 (16.19)	6 (5.71)	23 (21.90)	
Bubblelike lucency							0.418
Yes	35 (26.52)	16 (12.12)	51 (38.64)	22 (20.95)	13 (12.38)	35 (33.33)	
No	57 (43.18)	24 (18.18)	81 (61.36)	51 (48.57)	19 (18.10)	70 (66.67)	
Air bronchogram							<0.001
Yes	33 (25.00)	13 (9.85)	46 (34.85)	54 (51.43)	23 (21.90)	77 (73.33)	
No	59 (44.70)	27 (20.45)	86 (65.15)	19 (18.10)	9 (8.57)	28 (26.67)	
Vascular sign							<0.001
Yes	72 (54.55)	33 (25.00)	105 (79.55)	72 (68.57)	30 (28.57)	102 (97.14)	
No	20 (15.15)	7 (5.30)	27 (20.45)	1 (0.95)	2 (1.90)	3 (2.86)	
Pleural traction							<0.001
Yes	32 (24.24)	11 (8.33)	43 (32.58)	48 (45.71)	20 (19.05)	68 (64.76)	
No	60 (45.45)	29 (21.97)	89 (67.42)	25 (23.81)	12 (11.43)	37 (35.24)	

pGGO, pure ground-glass opacity; mGGO, mixed ground-glass opacity; SN, solid nodule; AAH, atypical adenomatous hyperplasia; AIS, adenocarcinoma in situ; MIA, minimally invasive adenocarcinoma; IAC, invasive adenocarcinoma; LPA, lepidic-predominant adenocarcinoma; APA, acinar-predominant adenocarcinoma; PPA, papillary-predominant adenocarcinoma; MPA, micropapillary-predominant adenocarcinoma; SPA, solid-predominant adenocarcinoma.

TABLE 5 | ROC curve of the main factors affecting the Ki-67 expression level.

Characteristics	AUC	B	S.E.	Wals	Exp(B)	Exp(B)		*P*
						Low limit	Up limit	
Pathological subtype	0.809	−1.459	0.519	7.90	0.232	0.084	0.643	0.005
Air bronchogram sign	0.711	−0.813	0.406	4.014	0.444	0.200	0.982	0.045

AUC, area under curve; S.E., standard error; Exp, exponential function.

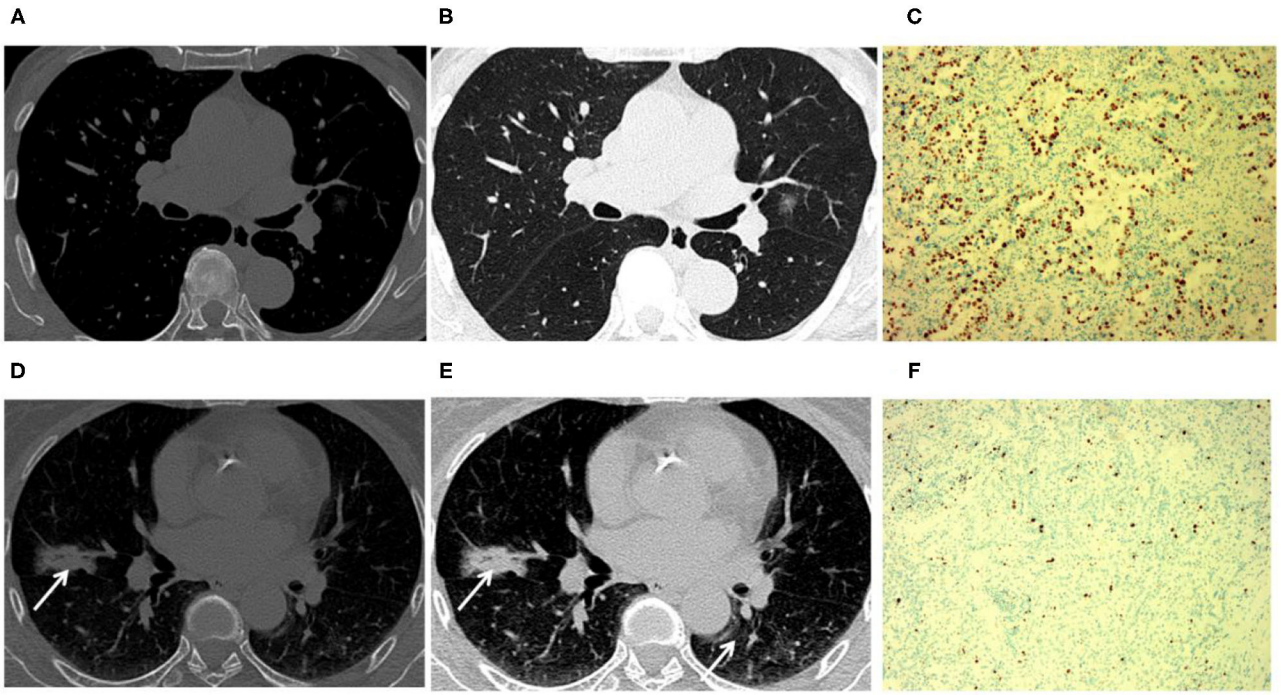

FIGURE 4 | Tumors with positive Ki-67 expression levels were more inclined to have air bronchograms than those with negative Ki-67 expression levels. An 81-year-old male patient with Ki-67 negative expression **(A–C)**. **(A,B)** CT image showed that a tumor had a negative expression of Ki-67 without an air bronchogram. **(C)** The Ki-67 expression was 5% in the glandular epithelium. A 63-year-old female patient with positive Ki-67 expression **(D–F)**. **(D,E)** CT image showed that a tumor had positive Ki-67 expression with an air bronchogram. **(F)** The Ki-67 expression was 55% in the glandular epithelium (arrow).

-HHL_glcm_MCC ($p < 0.001$), wavelet-LHH_glcm_MCC ($p < 0.001$), and wavelet-LLL_firstorder_Median ($p < 0.001$).

Development and Validation of the Radiomic Prediction Model

In the training set, the expression level of Ki-67 was taken as the dependent variable, and the CT radiomic features of lung adenocarcinoma were used as the independent variable to establish a pre-operative prediction model of Ki-67 expression level. The AUC value was 0.871 in the training dataset, the sensitivity was 76.7%, and the specificity was 83.7%, with a positive predictive value of 0.789. For the testing set, the classifier had an AUC value of 0.8, the sensitivity was 68.8%, and the specificity was 80%, with a positive predictive value of 0.733 (**Table 7**, **Figures 6A,B**). The calibration curve of the radiomic features also showed that the predicted probability was in good agreement with the actual probability in the training cohort (**Figures 6C,D**).

DISCUSSION

Ki-67 is considered to represent the proliferative state of tumors and is a prognostic biomarker in multiple malignant tumors, such as breast, prostate, and lung cancer (14). Ki-67 has a broad prospect in the study of lung cancer, especially the occurrence, development, early diagnosis, and prognosis of ground-glass opacity (GGO) in early lung cancer under low-dose CT scans (25, 26). Ki-67 has been widely introduced into clinical practice to differentiate lung cancer subtypes and predict oncology outcomes (26–28). In our study, we systematically evaluated the expression level of Ki-67 according to the histological subtypes of lung adenocarcinoma and revealed the prognostic role of

TABLE 6 | Analysis of the radiomic features between negative and positive Ki-67 levels in the training set.

Radiomic features	Ki-67 negative expression group ($n = 92$)	Ki-67 positive expression group ($n = 73$)	p
	Mean (range)	Mean (range)	
lbp-3D-k_glrlm_LongRunHighGrayLevelEmphasis	−0.3747 (−2.55, 1.88)	0.4722 (−0.89, 5.79)	<0.001
lbp-3D-k_glrlm_ShortRunLowGrayLevelEmphasis	0.3820 (−1.68, 6.27)	−0.4814 (−0.3279, −2.36)	<0.001
log-sigma-3-0-mm-3D_gldm_GrayLevelVariance	−5.124 (−1.27, 1.40)	0.6458 (−1.17, 2.80)	<0.001
original_gldm_LowGrayLevelEmphasis	0.1915 (−0.70, 7.08)	−0.2414 (−0.71, 3.68)	0.004
original_glrlm_LowGrayLevelRunEmphasis	0.2163 (−0.78, 4.82)	−0.2726 (−0.80, 3.80)	0.001
wavelet-HHL_glcm_MCC	0.2603 (−2.16, 3.68)	−0.3280 (−1.70, 1.57)	<0.001
wavelet-LHH_glcm_MCC	0.2364 (−1.52, 4.38)	−0.2980 (−2.01, 3.53)	0.001
wavelet-LLL_firstorder_Median	−0.4528 (−1.13, 2.01)	0.5707 (−1.11, 2.30)	<0.001

MCC, Maximal Correlation Coefficient.

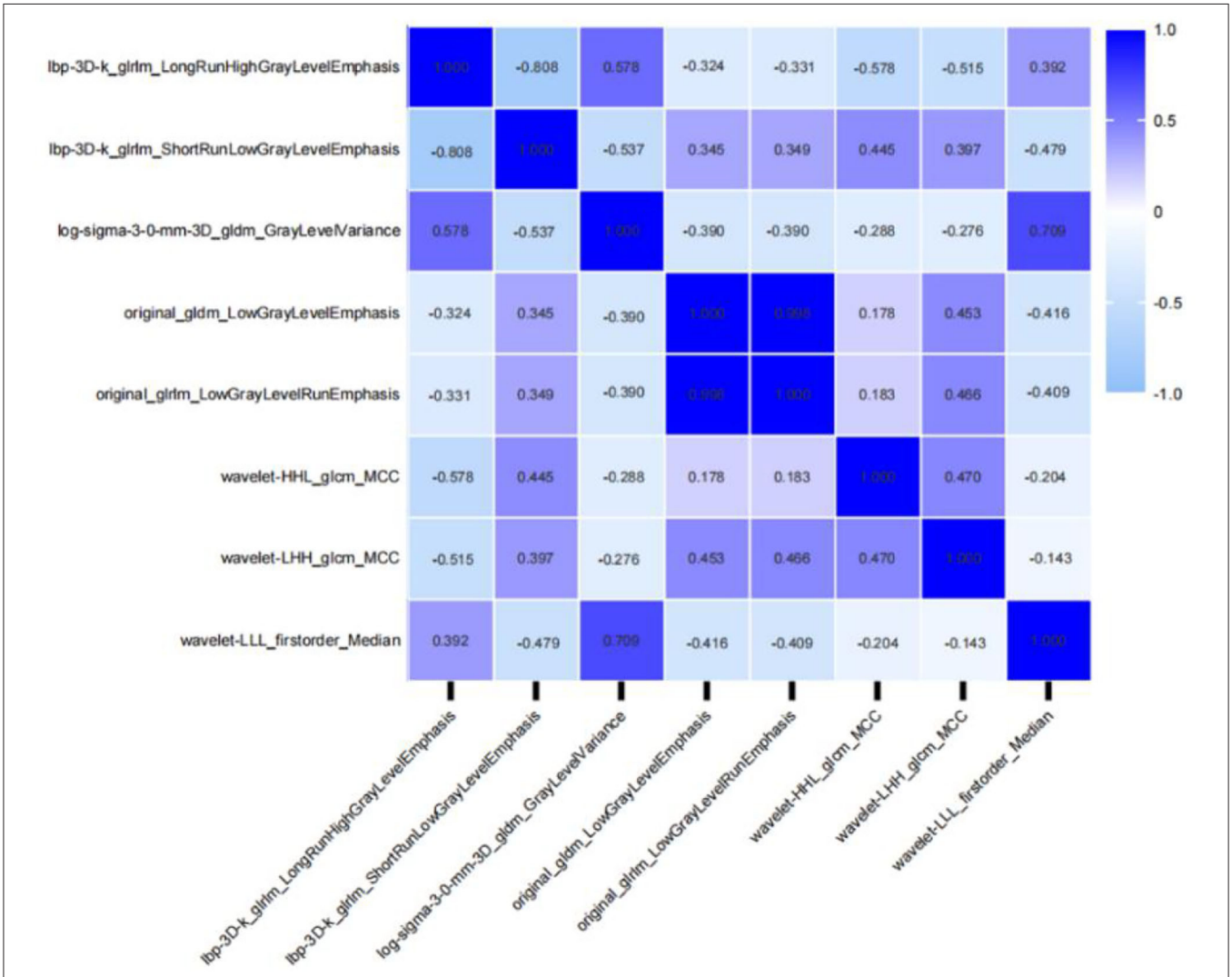

FIGURE 5 | Correlative heatmap between eight top-class radiomic features and Ki-67 levels. The values in the square lattices represent the magnitude of the R-value of a correlation analysis displayed by color difference.

TABLE 7 | The predictive performance of radiomic classifier in training and validation sets.

Datasets	AUC	SEN	SPE	Accuracy	PPV	NPV
Training (n = 165)	0.871	0.767	0.837	0.806	0.789	0.819
Testing (n = 72)	0.800	0.688	0.800	0.750	0.733	0.762

AUC, area under curve; SEN, sensitivity; SPE, specificity; PPV, positive predictive value; NPV, negative predictive value.

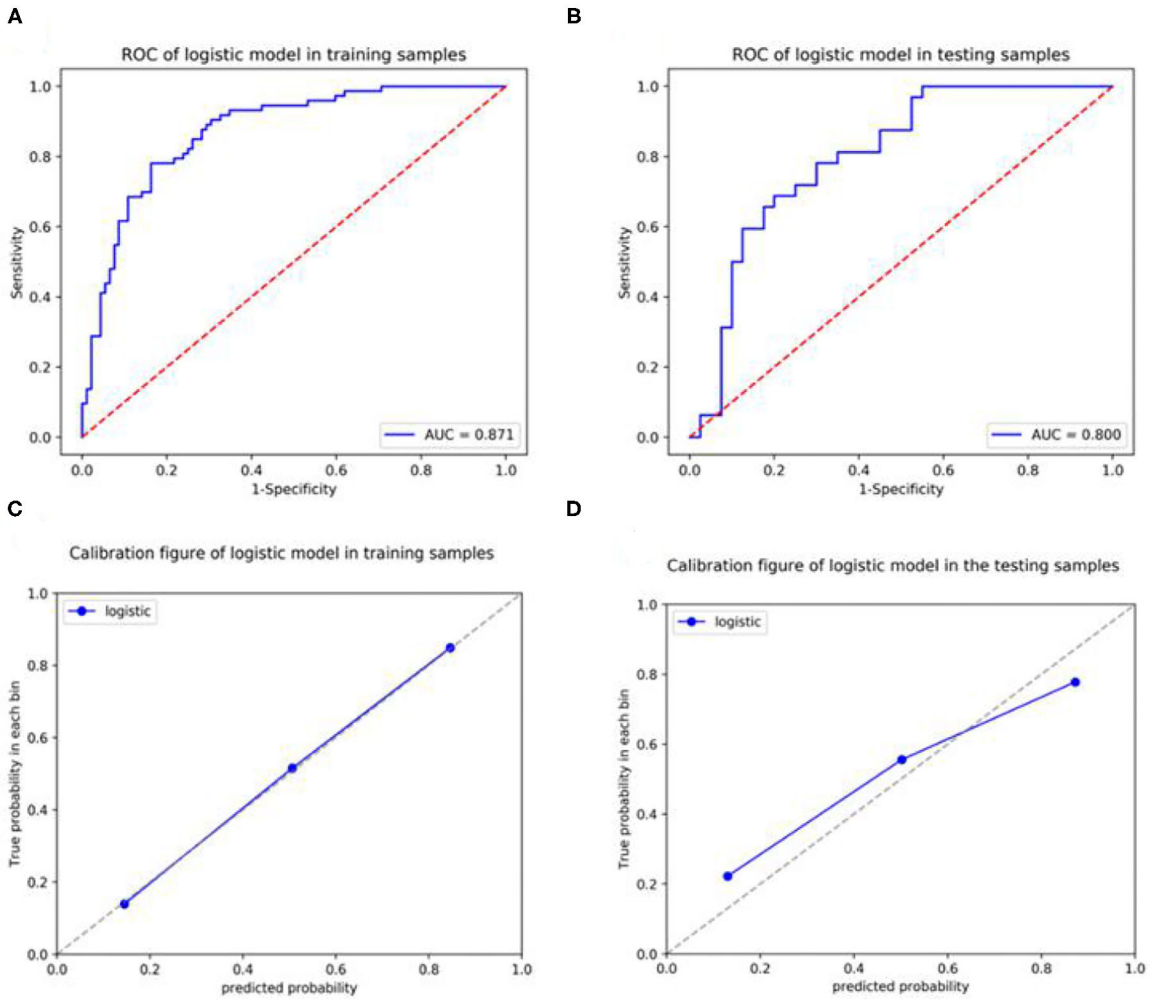

FIGURE 6 | Receiver operating curves **(**ROCs) and a calibration curve analysis for the radiomic signature for predicting the expression level of Ki-67 in the training set and testing set. [**(A,C)** training dataset, **(B,D)** testing dataset]. Calibration curves depict the calibration of each model in terms of the agreement between the predicted and actual probability of the positive Ki-67 expression level rate. The Y-axis represents the actual rate. The X-axis represents the predicted probability. The diagonal dotted line represents perfect prediction by an ideal model. The blue line represents the performance of the radiomic prediction model, of which a closer fit to the diagonal blue dotted line represents a better prediction.

Ki-67 in lung adenocarcinoma. Strikingly, we found that Ki-67 expression differed across lung adenocarcinoma histological subtypes, with IAC harboring the highest expression level, followed by the MIA, AIS, and AAH subtypes, which was consistent with the finding by Ishida et al. and Yan et al. (29, 30). Ki-67 expression levels demonstrated good performance in our study, with AUCs of 0.851, 0.787, and 0.872 for differentiating between MIA and IAC, AAH/AIS and MIA/IAC, and AAH/AIS/MIA and IAC, respectively. The Youden index of the paired groups of pathological subtypes were 5.5, 6.5, and 5.5, respectively. It showed that the Ki-67 values were below 5% for non-invasive adenocarcinomas (AAH/AIS/MIA) and more than 5% for invasive adenocarcinomas. Notably, it means that Ki-67 expression could be identified as an independent prognostic factor of lung adenocarcinoma (28). The overexpression of Ki-67 infers poor differentiation and prognosis. Hence, the accurate pre-operative evaluation of the Ki-67 level may be helpful in distinguishing the different subtypes of patients with

lung adenocarcinoma (31). For some suspicious patients with follow-up observations and no indication of surgery or needle biopsy, Ki-67 could serve as a useful predictive biomarker to select suspicious lesions with high proliferation. The early detection of this cancer could enhance the cure of the disease and even prolong overall survival.

Several previous studies demonstrated that conventional CT images could be a non-invasive measurement to predict the Ki-67 index in lung adenocarcinoma. Our results showed that the degree of Ki-67 expression was related to nodule diameter, density, spiculation, lobulation, and air bronchogram sign. Moreover, an air bronchogram was the independent factor influencing the Ki-67 expression level, and the AUC in the ROC analysis for distinguishing different Ki-67 expression levels was 0.711. It inferred that the CT images of lung adenocarcinoma were related to the expression of Ki-67 (30). Our results were consistent with previous findings (32–36). Thus, the conventional CT examination might indirectly reflect the proliferative activity of lung adenocarcinoma, which was of high value to the early identification of the positive Ki-67 expression from negative Ki-67 expression and the facilitation of early diagnoses and individualized treatments, improving the survival rate. However, the ability of CT images to predict the Ki-67 index is controversial. Conventional CT provides limited information regarding lung adenocarcinoma grading and cannot replace the biopsy and surgery in obtaining specimens for a definitive diagnosis (37).

Radiomics can extract information-rich imaging functions with high throughput, which is different from traditional subjective imaging, and can quantify imaging information that the human eye cannot detect (15, 38, 39). In mathematics, radiomic features have different functions and definitions. Thus, it has a very good advantage in measuring the heterogeneity of tumor texture features (40). Several studies have shown that radiomics have been effective in predicting the Ki-67 index in multiple tumors (41). In this study, we established a pre-operative Ki-67 classification model in patients with lung adenocarcinoma using CT-based radiomic features. The result shows that eight radiomic features were significantly different between the negative Ki-67 group and the positive Ki-67 group ($p < 0.001$) (42). The CT-based radiomic predictive model demonstrated a stable and reliable performance, reaching an AUC of 0.871 and 0.8 and an accuracy of 80.6 and 75% in the training and testing cohorts, respectively. Therefore, the analysis revealed that CT-based radiomic features could pre-operatively predict Ki-67 levels in patients with lung adenocarcinoma, especially for suspicious patients under conservative treatment or patients who have lost the opportunity of a biopsy. The preliminary judgment of tumor proliferative activity through radiomic features can improve the accuracy and effectiveness of treatment, and could avoid the delay of disease and economic loss caused by ineffective treatment, which could have potential implications for future patient management and aid in the implementation of precision medicine.

Choosing an appropriate Ki-67 cut-off value is convenient for clinicians to treat and manage patients. However, no consensus on the prognostic value of the Ki-67 expression level was found among the published studies, neither according to disease stage nor histological subtype. In previous studies on lung cancer, the cutoff values for Ki-67 prediction of prognosis were mostly used at 25, 30, 40, and 50% (43–45). For stage I lung adenocarcinoma, a cut-off value of 0.1 was commonly used. Ishida suggested that the Ki-67 index of 2.8% might be used as a marker to distinguish between MIA and AIS (29). Determining a cut-off value is often based on the median value. In this study, 5% was selected as the classification threshold based on our data characteristics and previous similar studies, and relatively good results were obtained, which indicated that proliferative activity with a Ki-67 expression level of 5% may be a crucial turning point for progression from non-invasive adenocarcinomas (AAH/AIS/MIA) to invasive adenocarcinomas.

Our study had some limitations. First, this study had a small sample size, which may increase concerns regarding selection bias. Moreover, this study was a single-centered retrospective study. Further studies involving multiple centers and a large number of patients are necessary. Second, the manual outline of ROIs is time and labor-consuming, and there is no standardized outline process and rules, which may lead to poor consistency among different radiologists. The automatic recognition of tumor lesions and the characterization of ROIs for feature extraction are some of the future research directions. Third, the largest diameter of the lung adenocarcinoma lesions included in this study was <3 cm, and there is a bias in the selection of study subjects, which may affect the results of the study. In the future, how to better mine information to assist clinical decision-making so that patients can get more accurate individualized treatments is also an opportunity and challenge in the development of radiomics.

In conclusion, Ki-67 expression levels with a cut-off value of 5% could be used to differentiate non-invasive lung adenocarcinomas (AAH/AIS/MIA) from invasive lung adenocarcinomas. The radiomic characteristics of CT have potential as non-invasive biomarkers for predicting Ki-67 levels in patients with lung adenocarcinoma, which might allow for a precise evaluation of tumor biological behavior, aid in clinical treatment decision making for the precise management of patients with lung adenocarcinoma, as well as provide supplemental information for depicting the heterogeneity of lung adenocarcinoma in different histological subtypes.

DATA AVAILABILITY STATEMENT

The original contributions presented in the study are included in the article/supplementary material, further inquiries can be directed to the corresponding author/s.

ETHICS STATEMENT

Written informed consent was obtained from the individual(s) for the publication of any potentially identifiable images or data included in this article.

AUTHOR CONTRIBUTIONS

ZH and ZX: conception and designation. ML and ZH: data collection. ML and ZA: data analysis and drafting the manuscript. ML and ZX: statistical analysis. YC and YL: technical support. All authors contributed to the article and approved the submitted version.

FUNDING

This research was supported by grants from the National Natural Science Foundation of China (No. 82171931), Natural Science Foundation of Guangdong (No. 2015A030313753), the Science and Technology Program of Guangzhou (Nos. 201903010032 and 202102080572), and the Panyu Science and Technology Program of Guangzhou (Nos. 2017-Z04-12, 2019-Z04-01, and 2019-Z04-23).

REFERENCES

1. Allemani C, Matsuda T, Di Carlo V, Harewood R, Matz M, Nikšić M, et al. Global surveillance of trends in cancer survival 2000-14 (CONCORD-3): analysis of individual records for 37 513 025 patients diagnosed with one of 18 cancers from 322 population-based registries in 71 countries. *Lancet.* (2018) 391:1023–75. doi: 10.1016/S0140-6736(17)33326-3
2. Travis WD, Brambilla E, Noguchi M, Nicholson AG, Geisinger KR, Yatabe Y, et al. International association for the study of lung cancer/american thoracic society/european respiratory society international multidisciplinary classification of lung adenocarcinoma. *J Thorac Oncol.* (2011) 6:244–85. doi: 10.1097/JTO.0b013e318206a221
3. Jamal-Hanjani M, Quezada SA, Larkin J, Swanton C. Translational implications of tumor heterogeneity. *Clin Cancer Res.* (2015) 21:1258–66. doi: 10.1158/1078-0432.CCR-14-1429
4. Weissferdt A, Kalhor N, Marom EM, Benveniste MF, Godoy MC, Correa AM, et al. Early-stage pulmonary adenocarcinoma (T1N0M0): a clinical, radiological, surgical, and pathological correlation of 104 cases. The MD Anderson Cancer Center Experience. *Mod Pathol.* (2013) 26:1065–75. doi: 10.1038/modpathol.2013.33
5. Zhou Y, Hu W, Chen P, Abe M, Shi L, Tan SY, et al. Ki67 is a biological marker of malignant risk of gastrointestinal stromal tumors: a systematic review and meta-analysis. *Medicine.* (2017) 96:e7911. doi: 10.1097/MD.0000000000007911
6. Pyo JS, Kim NY. Meta-analysis of prognostic role of Ki-67 labeling index in gastric carcinoma. *Int J Biol Markers.* (2017) 32:e447–53. doi: 10.5301/ijbm.5000277
7. Chen M, Li X, Wei Y, Qi L, Sun YS. Spectral CT imaging parameters and Ki-67 labeling index in lung adenocarcinoma. *Chin J Cancer Res.* (2020) 32:96–104. doi: 10.21147/j.issn.1000-9604.2020.01.11
8. Wei DM, Chen WJ, Meng RM, Zhao N, Zhang XY, Liao DY, et al. Augmented expression of Ki-67 is correlated with clinicopathological characteristics and prognosis for lung cancer patients: an up-dated systematic review and meta-analysis with 108 studies and 14,732 patients. *Respir Res.* (2018) 19:150. doi: 10.1186/s12931-018-0843-7
9. Okudela K, Woo T, Saigusa Y, Arai H, Matsumura M, Mitsui H, et al. A method to obtain reproducible Ki-67 indices in lung adenocarcinoma. *Histopathology.* (2021) 78:414–23. doi: 10.1111/his.14234
10. Yamashita S, Moroga T, Tokuishi K, Miyawaki M, Chujo M, Yamamoto S, et al. Ki-67 labeling index is associated with recurrence after segmentectomy under video-assisted thoracoscopic surgery in stage I non-small cell lung cancer. *Ann Thorac Cardiovasc Surg.* (2011) 17:341–6. doi: 10.5761/atcs.oa.10.01573
11. Sterlacci W, Stockinger R, Schmid T, Bodner J, Hilbe W, Waldthaler C, et al. The elderly patient with surgically resected non-small cell lung cancer–a distinct situation? *Exp Gerontol.* (2012) 47:237–42. doi: 10.1016/j.exger.2011.12.008
12. Gu Q, Feng Z, Liang Q, Li M, Deng J, Ma M, et al. Machine learning-based radiomics strategy for prediction of cell proliferation in non-small cell lung cancer. *Eur J Radiol.* (2019) 118:32–7. doi: 10.1016/j.ejrad.2019.06.025
13. Polk SL, Choi JW, McGettigan MJ, Rose T, Ahmed A, Kim J, et al. Multiphase computed tomography radiomics of pancreatic intraductal papillary mucinous neoplasms to predict malignancy. *World J Gastroenterol.* (2020) 26:3458–71. doi: 10.3748/wjg.v26.i24.3458
14. Boros M, Moncea D, Moldovan C, Podoleanu C, Georgescu R, Stolnicu S. Intratumoral heterogeneity for Ki-67 index in invasive breast carcinoma: a study on 131 consecutive cases. *Appl Immunohistochem Mol Morphol.* (2017) 25:338–40. doi: 10.1097/PAI.0000000000000315
15. Gillies RJ, Kinahan PE, Hricak H. Radiomics: images are more than pictures, they are data. *Radiology.* (2016) 278:563–77. doi: 10.1148/radiol.2015151169
16. Limkin EJ, Sun R, Dercle L, Zacharaki EI, Robert C, Reuzé S, et al. Promises and challenges for the implementation of computational medical imaging (radiomics) in oncology. *Ann Oncol.* (2017) 28:1191–206. doi: 10.1093/annonc/mdx034
17. Yu H, Meng X, Chen H, Liu J, Gao W, Du L, et al. Predicting the level of tumor-infiltrating lymphocytes in patients with breast cancer: usefulness of mammographic radiomics features. *Front Oncol.* (2021) 11:628577. doi: 10.3389/fonc.2021.628577
18. Avanzo M, Stancanello J, El Naqa I. Beyond imaging: the promise of radiomics. *Phys Med.* (2017) 38:122–39. doi: 10.1016/j.ejmp.2017.05.071
19. Lee G, Lee HY, Park H, Schiebler ML, van Beek EJR, Ohno Y, et al. Radiomics and its emerging role in lung cancer research, imaging biomarkers and clinical management: state of the art. *Eur J Radiol.* (2017) 86:297–307. doi: 10.1016/j.ejrad.2016.09.005
20. Wilson R, Devaraj A. Radiomics of pulmonary nodules and lung cancer. *Transl Lung Cancer Res.* (2017) 6:86–91. doi: 10.21037/tlcr.2017.01.04
21. Zhou B, Xu J, Tian Y, Yuan S, Li X. Correlation between radiomic features based on contrast-enhanced computed tomography images and Ki-67 proliferation index in lung cancer: a preliminary study. *Thorac Cancer.* (2018) 9:1235–40. doi: 10.1111/1759-7714.12821
22. Hyun-Ju Lee, Young Tae Kim, Chang Hyun Kang, Zhao B, Tan Y, Lawrence H. Schwartz, et al. Epidermal growth factor receptor mutation in lung adenocarcinomas: relationship with CT characteristics and histologic subtypes. *Radiology.* (2013) 268:254–64. doi: 10.1148/radiol.13112553
23. Travis WD, Brambilla E, Nicholson AG, Yatabe Y, Austin JHM, Beasley MB, et al. The 2015 World Health Organization classification of lung tumors: impact of genetic, clinical and radiologic advances since the 2004 classification. *J Thorac Oncol.* (2015) 10:1243–60. doi: 10.1097/JTO.0000000000000630
24. K.T.Dermawan J, Farver CF. The role of histologic grading and Ki-67 index in predicting outcomes in pulmonary carcinoid tumors. *Am J Surg Pathol.* (2019) 44:224–31. doi: 10.1097/PAS.0000000000001358
25. van Bree SH, Nemethova A, Cailotto C, Gomez-Pinilla PJ, Matteoli G, Boeckxstaens GE. New therapeutic strategies for postoperative ileus. *Nat Rev Gastroenterol Hepatol.* (2012) 9:675–83. doi: 10.1038/nrgastro.2012.134
26. Wen S, Zhou W, Li CM, Hu J, Hu XM, Chen P, et al. Ki-67 as a prognostic marker in early-stage non-small cell lung cancer in Asian patients: a meta-analysis of published studies involving 32 studies. *BMC Cancer.* (2015) 15:520. doi: 10.1186/s12885-015-1524-2

27. Borghaei H, Paz-Ares L, Horn L, Spigel DR, Steins M, Ready NE, et al. Nivolumab vs. docetaxel in advanced nonsquamous non-small-cell lung cancer. *N Engl J Med.* (2015) 373:1627–39. doi: 10.1056/NEJMoa1507643
28. Li Z, Li F, Pan C, He Z, Pan X, Zhu Q, et al. Tumor cell proliferation (Ki-67) expression and its prognostic significance in histological subtypes of lung adenocarcinoma. *Lung Cancer.* (2021) 154:69–75. doi: 10.1016/j.lungcan.2021.02.009
29. Ishida H, Shimizu Y, Sakaguchi H, Nitanda H, Kaneko K, Yamazaki N, et al. Distinctive clinicopathological features of adenocarcinoma *in situ* and minimally invasive adenocarcinoma of the lung: a retrospective study. *Lung Cancer.* (2019) 129:16–21. doi: 10.1016/j.lungcan.2018.12.020
30. Yan J, Wang H, Zhou H, He H, Qiu L, Wang Z. Correlation between expression of Ki-67 and MSCT signs in different types of lung adenocarcinoma. *Medicine.* (2020) 99:e18678. doi: 10.1097/MD.0000000000018678
31. Warth A, Cortis J, Soltermann A, Meister M, Budczies J, Stenzinger A, et al. Tumour cell proliferation (Ki-67) in non-small cell lung cancer: a critical reappraisal of its prognostic role. *Br J Cancer.* (2014) 111:1222–9. doi: 10.1038/bjc.2014.402
32. Si MJ, Tao XF, Du GY, Cai LL, Han HX, Liang XZ, et al. Thin-section computed tomography-histopathologic comparisons of pulmonary focal interstitial fibrosis, atypical adenomatous hyperplasia, adenocarcinoma *in situ*, and minimally invasive adenocarcinoma with pure ground-glass opacity. *Eur J Radiol.* (2016) 85:1708–15. doi: 10.1016/j.ejrad.2016.07.012
33. Moon Y, Sung SW, Lee KY, Sim SB, Park JK. Pure ground-glass opacity on chest computed tomography: predictive factors for invasive adenocarcinoma. *J Thorac Dis.* (2016) 8:1561–70. doi: 10.21037/jtd.2016.06.34
34. Jin X, Zhao SH, Gao J, Wang DJ, Wu J, Wu CC, et al. CT characteristics and pathological implications of early stage (T1N0M0) lung adenocarcinoma with pure ground-glass opacity. *Eur Radiol.* (2015) 25:2532–40. doi: 10.1007/s00330-015-3637-z
35. Takahashi M, Shigematsu Y, Ohta M, Tokumasu H, Matsukura T, Hirai T. Tumor invasiveness as defined by the newly proposed IASLC/ATS/ERS classification has prognostic significance for pathologic stage IA lung adenocarcinoma and can be predicted by radiologic parameters. *J Thorac Cardiovasc Surg.* (2014) 147:54–9. doi: 10.1016/j.jtcvs.2013.08.058
36. Lim HJ, Ahn S, Lee KS, Han J, Shim YM, Woo S, et al. Persistent pure ground-glass opacity lung nodules >/= 10 mm in diameter at CT scan: histopathologic comparisons and prognostic implications. *Chest.* (2013) 144:1291–9. doi: 10.1378/chest.12-2987
37. Tamrazi B, Pekmezci M, Aboian M, Tihan T, Glastonbury CM. Apparent diffusion coefficient and pituitary macroadenomas: pre-operative assessment of tumor atypia. *Pituitary.* (2017) 20:195–200. doi: 10.1007/s11102-016-0759-5
38. Zhang N, Zeng Q, Chen C, Yu J, Zhang X. Distribution, diagnosis, and treatment of pulmonary sequestration: report of 208 cases. *J Pediatr Surg.* (2019) 54:1286–92. doi: 10.1016/j.jpedsurg.2018.08.054
39. Ahmed AA, Elmohr MM, Fuentes D, Habra MA, Fisher SB, Perrier ND, et al. Radiomic mapping model for prediction of Ki-67 expression in adrenocortical carcinoma. *Clin Radiol.* (2020) 75:479.e17–22. doi: 10.1016/j.crad.2020.01.012
40. Davnall F, Yip CS, Ljungqvist G, Selmi M, Ng F, Sanghera B, et al. Assessment of tumor heterogeneity: an emerging imaging tool for clinical practice? *Insights Imaging.* (2012) 3:573–89. doi: 10.1007/s13244-012-0196-6
41. Fan Y, Chai Y, Li K, Fang H, Mou A, Feng S, et al. Non-invasive and real-time proliferative activity estimation based on a quantitative radiomics approach for patients with acromegaly: a multicenter study. *J Endocrinol Invest.* (2020) 43:755–65. doi: 10.1007/s40618-019-01159-7
42. Guo J, Ren J, Shen J, Cheng R, He Y. Do the combination of multiparametric MRI-based radiomics and selected blood inflammatory markers predict the grade and proliferation in glioma patients? *Diagn Interv Radiol.* (2021) 27:440–9. doi: 10.5152/dir.2021.20154
43. Jakobsen JN, Sørensen JB. Clinical impact of ki-67 labeling index in non-small cell lung cancer. *Lung Cancer.* (2013) 79:1–7. doi: 10.1016/j.lungcan.2012.10.008
44. Lin L, Cheng J, Tang D, Zhang Y, Zhang F, Xu J, et al. The associations among quantitative spectral CT parameters, Ki-67 expression levels and EGFR mutation status in NSCLC. *Sci Rep.* (2020) 10:3436. doi: 10.1038/s41598-020-60445-0
45. Ahn HK, Jung M, Ha SY, Lee JI, Park I, Kim YS, et al. Clinical significance of Ki-67 and p53 expression in curatively resected non-small cell lung cancer. *Tumour Biol.* (2014) 35:5735–40. doi: 10.1007/s13277-014-1760-0

Conflict of Interest: The authors declare that the research was conducted in the absence of any commercial or financial relationships that could be construed as a potential conflict of interest.

The reviewer ZW declared a shared affiliation with one of the authors, ML, to the handling editor at the time of the review.

frontiers | Frontiers in Surgery

CASE REPORT
published: 07 April 2022
doi: 10.3389/fsurg.2022.874006

Benign Pancreatic Neurofibroma with Malignant Imaging Features: A Case Report and Literature Review

*Ling Song, Zhenpeng Jiang, Jian Cui, BinYang Gao and Yan Luo**

West China Hospital, Sichuan University, Chengdu, China

Pancreatic neurofibroma is a very rare benign neurogenic tumor unrelated to neurofibromatosis type 1 (NF-1). As the volume increases, it has the risk of malignant transformation. The surgical prognosis of pancreatic neurofibroma is good, but its preoperative imaging features are very similar to those of malignant tumors, which may affect the formulation of treatment plans. This article reports a case of giant neurofibroma of the pancreas with contrast-enhanced ultrasound (CEUS) as one of the diagnostic methods and discusses the tumor's preoperative clinical features, laboratory examinations, and imaging features.

Keywords: pancreas, neurofibroma, ultrasound diagnosis, general surgery, case report

OPEN ACCESS

Edited by:
Mengling Feng,
National University of Singapore, Singapore

Reviewed by:
José Manuel Lopes,
Faculdade de Medicina, Universidade do Porto, Portugal
Jaques Waisberg,
Faculdade de Medicina do ABC, Brazil

***Correspondence:**
Yan Luo
slguangyu@163.com

Speciality section:
This article was submitted to Surgical Oncology, a section of the journal Frontiers in Surgery

Received: *18 February 2022*
Accepted: *28 March 2022*
Published: *07 April 2022*

Citation:
Song L, Jiang Z, Cui J, Gao B and Luo Y (2022) Benign Pancreatic Neurofibroma with Malignant Imaging Features: A Case Report and Literature Review. Front. Surg. 9:874006. doi: 10.3389/fsurg.2022.874006

INTRODUCTION

Pancreatic neurofibroma is a benign tumor derived from nerve cells. In the absence of neurofibromatosis type 1 (NF-I), its malignant potential is very low. Isolated neurofibroma unrelated to NF-I is very rare and is not found until they grow too large to cause serious complications (1). This study focuses on analyzing the imaging data of pancreatic neurofibroma and discussing its imaging features to improve the understanding of the disease. Previously reported cases of neurofibromas were all diagnosed using CT or MRI before surgery (2–5). Here, we report a case of pancreatic neurofibroma with contrast-enhanced ultrasound as one of the diagnostic methods.

CASE PRESENTATION

A 35-year-old male patient had dull pain in his right abdomen for 2 months without obvious cause or medical history. At the local hospital, computed tomography (CT) of the upper abdomen revealed a large mass on the neck of the pancreas. Five days later, he came to the biliary surgery department of our hospital for further treatment. On physical examination after admission, the abdomen was soft, and a slight mass was palpable in the upper abdominal area, with poor mobility and mild tenderness. Laboratory examination results showed that CA19-9 was slightly increased, and the values of other tumor markers were normal. White blood cell count, alanine aminotransferase (ALT) and aspartate aminotransferase (AST) were significantly increased, while other laboratory data, such as amylase, lipase and total bilirubin, were not abnormal.

Contrast-enhanced magnetic resonance (MR) revealed an 8.2 × 5.7 cm circular confounding signal mass on the pancreatic neck (**Figure 1**). It had a slightly higher T1 signal and equal T2 signal with a small patch of high T2 signal inside. Contrast enhancement was heterogeneous high enhancement. The adjacent common hepatic artery and splenic artery were pushed, causing their lumens to narrow slightly, and their local boundaries with the tumor were not clear. The fat space between the splenic vein and the tumor is not clear. The main pancreatic duct and bile duct were not dilated. MR finally considered pancreatic malignant cystadenoma or solid pseudopapillary tumor (SPT). Two-dimensional ultrasonography revealed a slightly weaker echogenic mass of approximately 8.6 × 6.4 cm in the pancreatic neck body area, with clear boundaries, clear capsules, heterogeneous internal echoes, and small hypoechoic areas (**Figure 2A**). CEUS showed rapid and high enhancement at the margin and equal enhancement at the interior of the mass in the arterial phase. In the parenchymal phase, the overall enhancement was low. CEUS considered mostly SPT (**Figures 2B,C**).

Due to the large size of the mass, the clinician decided to perform an exploratory laparotomy. During the operation, a hard mass of approximately 10 × 8 × 9 cm with a capsule was found above the neck of the pancreas and the portal vein. The tumor surrounds surrounding tissues and organs, including the proper hepatic artery, splenic artery, portal vein and left adrenal gland. Based on the intraoperative findings, the surgeon decided to perform total tumor resection.

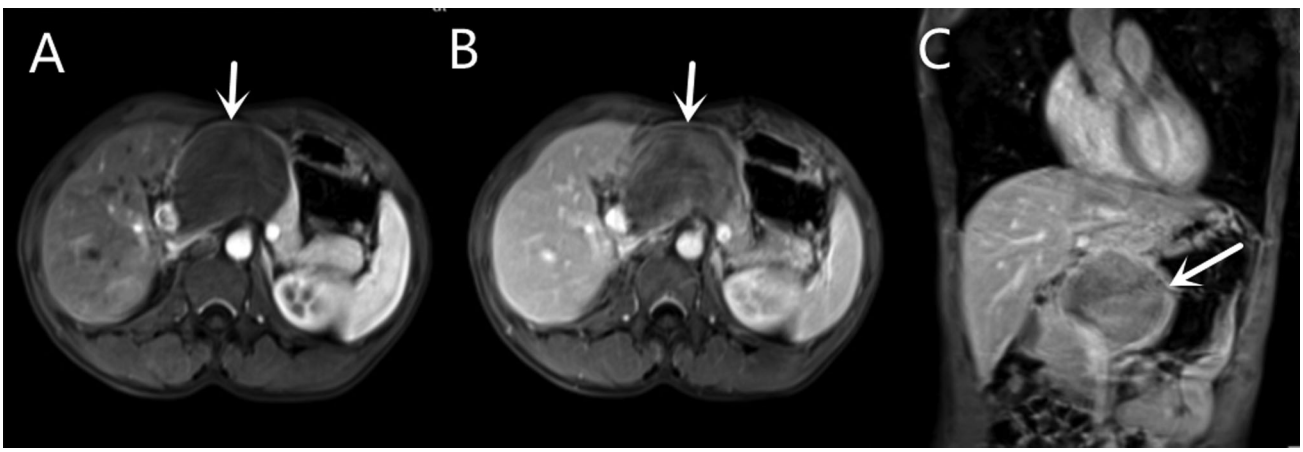

FIGURE 1 | Contrast-enhanced magnetic resonance (MR) of a mass on the pancreatic neck-body. (**A**) T1W Cross-sections MR in arterial phase. (**B**) T1W Cross-sections MR in portal phase. (**C**) T2W Axial MR in arterial phase.

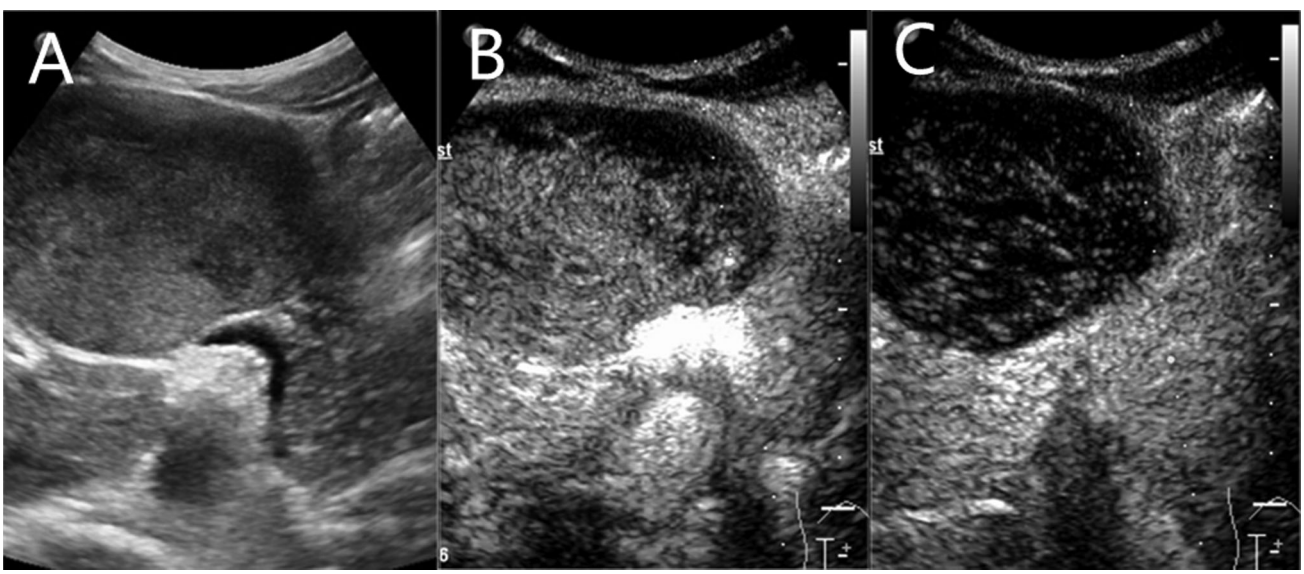

FIGURE 2 | A slightly weaker echogenic mass on ultrasound. (**A**) Two-dimensional ultrasonography. (**B**) contrast-enhanced ultrasound (CEUS) in arterial phase. (**C**) CEUS in parenchymal phase.

Histopathology found that the tumor was mainly composed of spindle cells with cytologically bland wavy nuclei in a collagenous matrix (**Figure 3**). Immunohistochemical staining was S100 (+), CD34 (+), and Ki67 (+2%) (**Figures 4A,B**). Combined with histological morphology and immunohistochemical results, it was considered a peripheral nerve tumor, and its subtype was consistent with solitary neurofibroma. After two years of follow-up, CT, MRI and CEUS were used alternately for examination, and there was no sign of tumor recurrence **Supplementary Materials**.

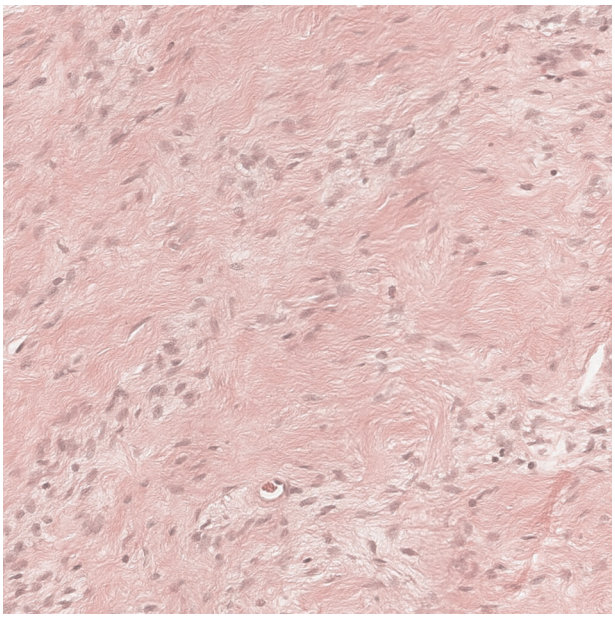

FIGURE 3 | Photomicrograph of pancreatic neurofibroma. Collagen fibers contain a large number of spindle cells (H&E stain, ×100).

DISCUSSION

Neurofibroma is a benign neurogenic tumor that can be divided into solitary neurofibroma and neurofibromatosis. Neurofibroma generally originates from peripheral or central nerve cells and is composed of Schwann cells and fibroblasts. Most of them are isolated masses in the dermis or subcutaneous tissue. Neurofibroma occurring locally in the body is the most common, accounting for approximately 90%. It is rare that it appears in the pancreas, and solitary neurofibroma of the pancreas not related to NF-I is even rarer (6).

The solitary neurofibromas that have been reported now mostly appear under the skin, in the bones and in the gastrointestinal tract (3, 5, 7–13). The number of reports of solitary neurofibromas that appeared in the pancreas is very limited (**Table 1**). Moletta et al. reported that pancreatic neurofibroma combined the cerebral neurofibroma (14). NF-1 was suspected but the patient refused genetic tests. The other three cases were not related to NF-1 (2, 15, 16).

Unlike superficial neurofibromas, which can be easily palpated, abdominal neurofibromas are most often found because of abdominal pain (2, 17). By this time, the large tumor has already produced a space-occupying effect. Tsai et al. reported that patients with pancreatic neurofibroma had a history of acute pancreatitis, so they believed that the occurrence of solitary

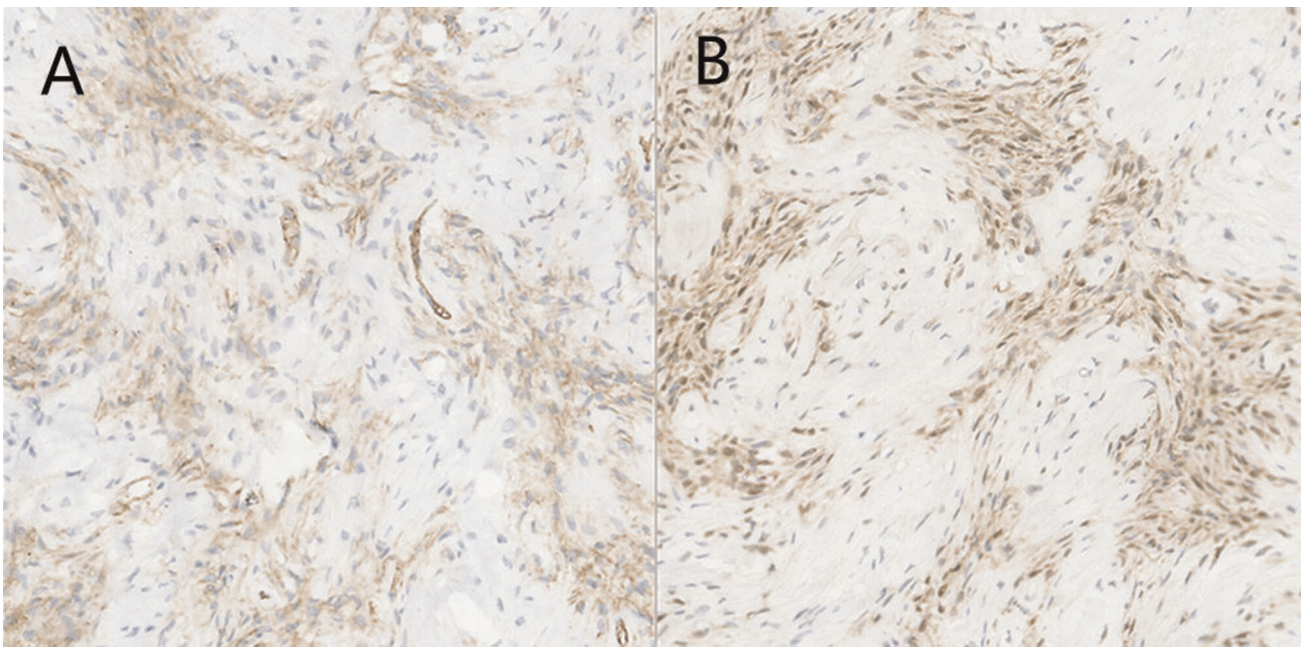

FIGURE 4 | Photomicrograph of pancreatic neurofibroma. (**A**) Immunohistochemical staining [CD34(+)]. (**B**) Immunohistochemical staining [S100(+)].

TABLE 1 | Clinical characteristics of neurofibromas in the pancreas.

Authors	Year	Age (y)	Gender	Location in the pancreas	Surgical treatment	Association with neurofibromatosis type 1
Moletta et al. (14)	2015	25	Male	Head	Pancreaticoduode-nectomy	Suspicious
Tsai et al. (2)	2012	44	Female	Body	Distal pancreatectomy	No
Imai et al. (15)	1989	57	Male	Uncinate process	Pancreaticoduode-nectomy	No
Kato et al. (16)	1982	51	Male	Head	Total pancreatectomy	No

neurofibroma might be related to chronic inflammation, ischemia, trauma and other long-term chronic stimulation (2). In this case, the tumor capsule was intact, and the boundary with surrounding tissues was clear. In contrast, the pancreatic neurofibroma we reported was infiltrative growth invading surrounding organs and tissues. Both imaging features and intraoperative findings were very similar to malignant tumors (17).

After the literature review, this study should be the first to report the use of CEUS to participate in the diagnosis and observation of pancreatic neurofibroma. CEUS showed that neurofibroma was a solid masse with signs of fast in and out, which led to the final diagnosis of low-grade SPT. MRI findings of tumor invasion of surrounding tissue made the diagnosis result more inclined to malignant pancreatic cystadenoma. Because the results of the two imaging results were inconsistent and the patient requested surgery, the clinician finally decided to open the abdominal exploration. Because pancreatic neurofibroma is very rare and there is a lack of large-scale research to statistically analyze its imaging characteristics and because the growth pattern of this tumor is very similar to that of malignant tumors, there is indeed a great possibility of misdiagnosis in clinical practice. Histopathology showed that the tumor was mainly composed of spindle cells, and the immunohistochemical results showed that the tumor expressed S-100 protein and CD34 protein, which was consistent with other reports (6, 18).

In the diagnosis process, pancreatic neurofibroma needs to be differentiated from pancreatic mucinous cystic neoplasms and SPT. Unlike pancreatic cystic tumors, pancreatic neurofibroma has little or no cystic components and is not connected to the main pancreatic duct, so there is no dilation of the main pancreatic duct (19). Moreover, although giant pancreatic neurofibroma infiltrates other organs, rarely causes to cause lymph node metastasis or other organ metastasis, such as pancreatic mucinous cystadenocarcinoma (20).

At present, the preoperative differential diagnosis of pancreatic neurofibroma and other pancreatic tumors is still difficult. In clinical practice, various imaging methods should be combined to fully understand the relationship between the tumor and surrounding tissues, and pathological biopsy should be taken to confirm the diagnosis if necessary. Radical resection is often used to treat pancreatic neurofibroma. Most patients have no recurrence or metastasis after surgery, which confirms the effectiveness of surgical resection. It should be noted that the clinician must confirm that it is not related to NF-1 after the diagnosis of neurofibroma (21). The patient had no family history of NF-1 and no symptoms such as café-au-lait spots and subcutaneous nodules, so he was ruled out.

We described the appearance of pancreatic neurofibroma under contrast-enhanced ultrasound, which accumulated experience for the diagnosis of this rare case in the future.

CONCLUSION

Pancreatic neurofibroma is a very rare benign tumor of the pancreas. It is very important to fully analyze the imaging data and adopt an individualized surgical approach for patients to preserve the function of the pancreas to the greatest extent and minimize postoperative complications while ensuring complete tumor resection.

DATA AVALIABILITY STATEMENT

The original contributions presented in the study are included in the article/**supplementary material**, further inquiries can be directed to the corresponding author/s.

ETHICS SATATEMENT

The studies involving human participants were reviewed and approved by West China Hospital of Sichuan University Biomedical Research Ethics Committee, and West China Hospital of Sichuan University. The patients/participants provided their written informed consent to participate in this study.

AUTHOR CONTRIBUTIONS

LS and YL designed this study and drafted the report. JC provided the histological results. ZJ and BG reviewed the report critically and gived revisions. All authors issued final approval for the version to be submitted. All authors contributed to the article and approved the submitted version.

ACKNOWLEDGMENTS

We express our thanks to Yan Luo and Jiawu Li for their help in finding this case and revising our article several times.

SUPPLEMENTARY MATERIAL

The Supplementary Material for this article can be found online at: https://www.frontiersin.org/articles/10.3389/fsurg.2022.874006/full#supplementary-material.

REFERENCES

1. Louis DN, Perry A, Wesseling P, Brat DJ, Cree IA, Figarella-Branger D, et al. The 2021 WHO Classification of Tumors of the Central Nervous System: a summary. *Neuro-Oncology*. (2021) 23(8):1231–51. doi: 10.1093/neuonc/noab106
2. Tsai PJ, Liu KY, Wang SE, Shyr YM, Su CH, Chen TH. Solitary neurofibroma of the pancreas body not associated with type 1 neurofibromatosis. *J Chin Med Assoc*. (2012) 75(3):132–5. doi: 10.1016/j.jcma.2011.12.016
3. Chen N, Hsu Y-H, Lee Y-C. Solitary neurofibroma of eyelid masquerading as chalazion. *Int Med Case Rep J*. (2017) 10:177–9. doi: 10.2147/imcrj.S136255
4. Iqbal A, Tamgadge S, Tamgadge A, Chande M. Intraosseous neurofibroma in a 13-year-old male patient: A case report with review of literature. *J Cancer Res Ther*. (2018) 14(3):712–5. doi: 10.4103/0973-1482.176173
5. Sleiman Z, Abboud L, Mehanna E, Mahmoud R, Yaacoub E, Ghanime G. Mandibular neurofibroma: Case report of a rare tumor. *Clin Pract*. (2019) 9(4):111–3. doi: 10.4081/cp.2019.1143
6. Wang XY, Cai JP, Song LL, Huang CS, Chen W, Huang XT, et al. Identification of genomic alterations in sporadic pancreatic neurogenic tumors. *Pancreas*. (2020) 49(10):1393–7. doi: 10.1097/mpa.0000000000001680
7. Shah AM, Dash SP, Das SP, Rangan VS, Bhartiya SC. An unusual presentation of neurofibroma masquerading as a vascular hamartoma, post-iatrogenic intervention. *J Clin Diagn Res*. (2015) 9(1):PD18–9. doi: 10.7860/jcdr/2015/9852.5442
8. Tall A, N'Diaye C, Diom ES, Thiam I. Solitary neurofibroma originating from the posterior nasal septum: Transnasal endoscopic resection. *Eur Ann Otorhinolaryngol Head Neck Dis*. (2015) 132(4):223–5. doi: 10.1016/j.anorl.2015.03.001
9. da Silva LP, Goes Gonzaga AK, Santana T, Cobe Sena DA, de Souza LB. Solitary intraosseous neurofibroma: Report of a rare entity. *J Oral Maxillofac Surg Med Pathol*. (2018) 30(6):566–8. doi: 10.1016/j.ajoms.2018.06.001
10. Rotili A, De Maria F, Di Venosa B, Ghioni M, Pizzamiglio M, Cassano E, et al. Solitary breast neurofibroma: imaging aspects. *Ecancermedicalscience*. (2018) 12:800. doi: 10.3332/ecancer.2018.800
11. Sekhar P, Nandhini G, Kumar KR, Kumar AR. Solitary neurofibroma of the palate mimicking mucocele: A rare case report. *J Oral Maxillofac Pathol*. (2019) 23(Suppl 1):23–6. doi: 10.4103/jomfp.JOMFP_196_18
12. Behrad S, Sohanian S, Ghanbarzadegan A. Solitary intraosseous neurofibroma of the mandible: Report of an extremely rare histopathologic feature. *Indian J Pathol Microbiol*. (2020) 63(2):276–8. doi: 10.4103/ijpm.Ijpm_28_19
13. Gupta A, Jajoo SN. Intrascrotal solitary neurofibroma. *J Clin Diagn Res*. (2020) 14(6):PD06–8. doi: 10.7860/jcdr/2020/43656.13790
14. Moletta L, Milanetto AC, Lico V, Farinati F, Alaggio R, Pedrazzoli S, et al. Neuroendocrine pancreatic tumor associated with a cerebral neurofibroma. A case report. *Neuroendocrinology*. (2015) 102(1–2):152. doi: 10.1016/j.pan.2014.05.651
15. Imai H, Kobayashi J, Manabe R, Namio H, Ichinona T. A case of neurofibroma located in the retroperitoneum involving the uncinate process of the pancreas. *Gastroenterol Jpn*. (1989) 24(4):421–4. doi: 10.1007/bf02774351
16. Kato O, Hattori K, Matsuyama M, Yoshizaki S. Neurofibroma of the pancreas - differentiation from carcinoma. *Am J Gastroenterol*. (1982) 77(9):630–2.
17. Gupta P, Aggarwal R, Sarangi R. Solitary neurofibroma of the adrenal gland not associated with type-1 neurofibromatosis. *Urol Ann*. (2015) 7(1):124–6. doi: 10.4103/0974-7796.148661
18. Abdullah, Xing J-p. A case report of solitary neurofibroma of the Vas deferens. *Urol Case Rep*. (2020) 28:101057. doi: 10.1016/j.eucr.2019.101057
19. Burk KS, Knipp D, Sahani DV. Cystic pancreatic tumors. *Magn Reson Imaging Clin N Am*. (2018) 26(3):405–20. doi: 10.1016/j.mric.2018.03.006
20. Doulamis IP, Mylonas KS, Kalfountzos CE, Mou D, Haj-Ibrahim H, Nasioudis D. T Pancreatic mucinous cystadenocarcinoma: Epidemiology and outcomes. *Int J Surg*. (2016) 35:76–82. doi: 10.1016/j.ijsu.2016.09.017
21. Wen PY, Packer RJ. The 2021 WHO Classification of Tumors of the Central Nervous System: clinical implications. *Neuro-Oncology*. (2021) 23(8):1215–7. doi: 10.1093/neuonc/noab120

Conflict of Interest: The authors declare that the research was conducted in the absence of any commercial or financial relationships that could be construed as a potential conflict of interest.

frontiers | Frontiers in Surgery

ORIGINAL RESEARCH
published: 25 April 2022
doi: 10.3389/fsurg.2022.797377

Application of the Machine-Learning Model to Improve Prediction of Non-Sentinel Lymph Node Metastasis Status Among Breast Cancer Patients

Qian Wu[1†], *Li Deng*[1†], *Ying Jiang*[2] *and Hongwei Zhang*[2*]

[1] Department of General Surgery, Shanghai Public Health Center, Shanghai, China, [2] Department of General Surgery, Zhongshan Hospital, Fudan University, Shanghai, China

Background: Performing axillary lymph node dissection (ALND) is the current standard option after a positive sentinel lymph node (SLN). However, whether 1–2 metastatic SLNs require ALND is debatable. The probability of metastasis in non-sentinel lymph nodes (NSLNs) can be calculated using nomograms. In this study, we developed an individualized model using machine-learning (ML) methods to select potential variables, which influence NSLN metastasis.

Materials and methods: Cohorts of patients with early breast cancer who underwent SLN biopsy and ALND between 2012 and 2021 were created (training cohort, N 157 and validation cohort, N 58) for the development of the nomogram. Three ML methods were trained in the training set to create a strong predictive model. Finally, the multiple iterations of the least absolute shrinkage and selection operator regression method were used to determine the variables associated with NSLN status.

Results: Four independent variables (positive SLN number, absence of lymph node hilum, lymphovascular invasion (LVI), and total number of SLNs harvested) were combined to generate the nomogram. The area under the receiver operating characteristic curve (AUC) value of 0.759 was obtained in the entire set. The AUC values for the training set and the test set were 0.782 and 0.705, respectively. The Hosmer-Lemeshow test of the model fit accuracy was identified with $p = 0.759$.

Conclusion: This study developed a nomogram that incorporates ultrasound (US)-related variables using the ML method and serves to clinically predict the non-metastatic status of NSLN and help in the selection of the appropriate treatment option.

Keywords: breast neoplasms, sentinel lymph node, nomogram, ultrasound, machine learning

OPEN ACCESS

Edited by:
Kee Yuan Ngiam,
National University Health System, Singapore

Reviewed by:
Noemi Eiro,
Jove Hospital Foundation, Spain
Anurag Srivastava,
Balco Medical Centre, India

***Correspondence:**
Hongwei Zhang
zhang.hongwei@zs-hospital.sh.cn

[†]These authors have contributed equally to this work and share first authorship

Specialty section:
This article was submitted to Surgical Oncology, a section of the journal Frontiers in Surgery

Received: *18 October 2021*
Accepted: *18 March 2022*
Published: *25 April 2022*

Citation:
Wu Q, Deng L, Jiang Y and Zhang H (2022) Application of the Machine-Learning Model to Improve Prediction of Non-Sentinel Lymph Node Metastasis Status Among Breast Cancer Patients. Front. Surg. 9:797377. doi: 10.3389/fsurg.2022.797377

INTRODUCTION

In 2020, breast cancer was surpassed lung cancer as the world's most commonly diagnosed cancer. This is despite being arguably negligible in men (1). The most common route of breast cancer metastasis is lymphatic spread within the axilla. Axillary lymph node dissection (ALND) and sentinel lymph node biopsy (SLNB) are the main axillary surgeries for breast cancer (2). ALND

could completely remove the metastatic lymph nodes, clarify the TNM stage of the cancer, and inform the prognosis (3). However, ALND can cause many complications, such as lymphedema, hematoma, sensory abnormalities, and limitation of upper limb movement (4, 5). Furthermore, approximately 50% of patients with positive sentinel lymph nodes (SLNs) are found to have no additional nodal metastases (6).

The possibility of exempting ALND in early breast cancer (cT1-2N0) has been widely explored in several clinical trials (7–10). This suggestion has essentially achieved good follow-up data reports. According to St. Gallen guidelines of 2017, women with 1 or 2 positive SLNs who have had breast conservation can avoid ALND and receive whole breast radiation and adjuvant systemic therapies only (11). However, with the limited randomized, multicenter clinical trials and strict inclusion criteria, proper selection of axillary surgeries for patients who fail to meet the criteria has become a priority of many clinicians.

The prediction of the risk of non-sentinel lymph nodes (NSLNs) metastasis determines the selection of axillary surgery. Previous reports show that nomograms have been developed and are validated as the commonly used method of predicting cancer prognosis. The Memorial Sloan-Kettering Cancer Center (MSKCC) nomogram (12) is undoubtedly the most authoritative nomogram. Different cancer centers have validated and confirmed MSKCC nomogram as a robust method of predicting NSLNs metastasis (13, 14).

Multivariate logistic regression is the most common method of incorporating variables into cancer prognostication. Machine learning (ML) is an emerging tool for predicting cancer prognosis that is making significant contributions in different cancer fields (15, 16). It is a learning process, which utilized techniques, such as decision trees (DTs), artificial neural networks (ANNs), and support vector machines (SVMs). Ayer et al. applied the ANN technique in the prediction of breast cancer susceptibility (17) while Zeng et al. predicted the breast cancer recurrence through SVMs (18). Further, Madekivi et al. filtered the variables by a gradient-boosted trees model to develop a final model for predicting NSLNs (19). All these studies show ML as a feasible and superior cancer prediction method. The aim of our study was to employ ML-based statistical methods to select variables with potential influence on NSLN metastasis status. The study ultimately developed an individualized prediction model that could guide clinicians for a better choice of cancer treatment options for different patients.

METHOD

Patients and Data Collection

The clinical data of patients who underwent surgery between January 2012 and May 2021 at Zhongshan Hospital (an affiliate of Fudan University) and Shanghai Public Health Center (Zhongshan Hospital South Branch) were collected and retrospectively analyzed. A total of 532 patients were screened ($n = 532$). The inclusion criteria were postoperative pathologically confirmed diagnosis of primary breast cancer, no history of other tumors, and that the patient has received both SLNB and ALND.

The exclusion criteria were lack of preoperative breast ultrasound (US) or pathological information, patients were not preoperatively staging as clinical T1-2N0 or had received neoadjuvant therapy, only axillary surgery without breast tumor resection in our hospital, and a negative pathological result of SLNs. Only 215 patients were retained by the exclusion criteria. The working protocol of our study is as shown in **Figure 1**. The ethical approval of this study was granted by the ethics committee of Zhongshan Hospital and Shanghai Public Health Center. There was no additional informed consent required from the patients because this was a retrospective study.

The SLNs were identified before surgery using Methylene blue dye, and blue-stained nodes were removed and sent for frozen pathology to the Pathology Department. It was stained with H&E and microscopically examined by an experienced pathologist. Routine H&E analysis was performed for all additional nodes identified by ALND.

The collected clinical and medical information of patients included the patient age, breast tumor location, postoperative pathological features [histology, estrogen receptor (ER) status, proliferation index (Ki-67), progesterone receptor (PR) status, human epidermal growth factor receptor 2 (HER-2) overexpression, lymphovascular invasion (LVI), Scarff-Bloom-Richardson (SBR) grade, total number of SLNs harvested, T stage, number of positive SLNs, and number of NSLNs metastasis] and ultrasonic parameters of tumor and axillary lymph nodes [sizes, mass echogenicity, regular or irregular tumor margin, presence or absence of lymph node hilum, and color Doppler flow imaging (CDFI)].

Statistical Analysis

Clinical and pathological variables associated with the risk of lymph node metastasis were assessed on the basis of their clinical importance and predictors identified in previously published articles (20, 21). Categorical variables were reported as integers and proportions. The continuous variables were described as means [±standard deviation (SD)]. Collinearity for all explanatory variables was assessed using a correlation matrix and plausible interaction terms were also tested. Therefore, interaction terms were excluded in the multivariate analysis. To relax the assumption of a linear relationship between continuous predictors and the risk of NSLN metastasis status, continuous predictors that include the patient age, tumor size, and number of SLNs, etc., were categorized after evaluation using restricted cubic splines (22). Regarding the strong U- or S-shaped relation between continuous predictors and NSLNs metastasis results, the value of the turning in the graph was used as the dividing point (**Supplementary Figure S1**).

Patients were randomly sampled into the training and validation sets in the ratio of 7:3. To select the strongest predictive model, three ML methods were trained in the training set. These ML methods were random forest (RF) (23), SVMs (24), multiple iterations of the least absolute shrinkage, and least absolute shrinkage and selection operator (LASSO) regression (25). The best hyper-parameter for ML models was 10-fold cross-validation to avoid overfitting. The best classification model was selected to compare the performance of the ML methods.

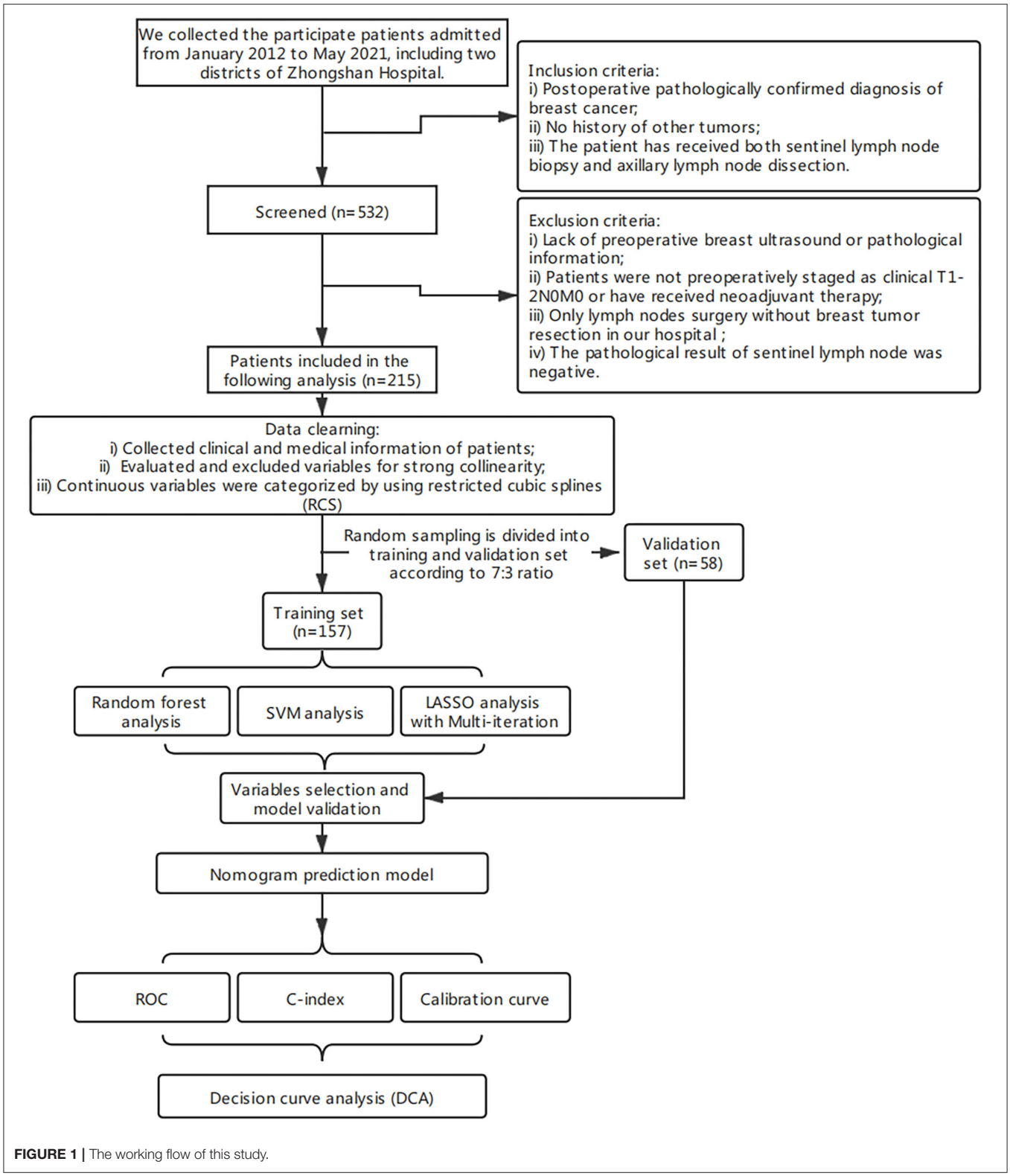

FIGURE 1 | The working flow of this study.

We created a nomogram that could make a linear predictor in patients who were easily accessible to clinicians on the basis of the best-performing model. Further, we assessed the discriminating ability and predictive accuracy in both the validation and entire sets using the ROC curves (C-index and calibration curves) (26, 27). Finally, the decision curve analysis (DCA) was used

to support the clinical decisions of the prepared prediction model (28). All the statistical analyses were carried out using the R software (version 3.6.3, http://www.r-project.org). The R-software packages used for statistical data analysis were "caret," "rms," "glmnet," "randomForest," "e1071," "kernlab," "pROC," "rmda," and "ResourceSelection." A two-sided $p < 0.05$ was considered statistically significant.

RESULTS

Demographic and Clinical Characteristics

Clinicopathological information of 215 patients with breast cancer after surgical operation was assessed between January 2012 and May 2021. Patients who participated were grouped into two groups based on the presence or absence of NSLNs metastasis. The observed clinicopathological characteristics of both metastasis and non-metastasis patients are presented in **Table 1**. All patients are Asian. The median age of patient was 56 years. The patients with tumors located in the upper-outer quadrant were 51.2%. Largely, all participating patients (97.6%) were at the T1-T2 stages and showed no difference in histology, ER, PR, and ki-67 or HER-2 status. A small proportion of patients in stage T3 were included as the preoperative assessment was T1-T2 but the postoperative pathology confirmed stage T3. However, the ultrasonic features (longitudinal diameter of lymph node, lymphatic echogenicity, and absence of lymph node hilum) and pathological features (LVI, number of positive SLNs, and proportion of positive SLNs) in the two groups were statistically different ($p < 0.05$).

Predictive Model and Factors Selection

All participants were randomly divided into two groups (training and validation cohorts) in the ratio of 7:3. The explanatory variables were transformed into categorical forms. The US transverse and longitudinal diameter of tumor or lymph were highly correlated, so only the largest diameter was retained. No other significant interaction was found. There were no statistical differences between the variables in both the training and validation sets ($p > 0.05$; **Supplementary Table S1**). Three ML algorithms were performed in the training set. The best SVM model was obtained when nine candidate variables were selected, as shown in **Figure 2A**. RF was effective in feature selection and the removal of redundant features. The RF model obtained the highest accuracy (0.689) with five predictive features (**Figure 2B**). The LASSO could select significantly predictive features but the results may not be identical each time. In this study, we conducted 500 times iterations and selected the features with more than 300 repeated occurrences. Then, these features were sequentially introduced into the logistic regression model to calculate the AUC values. The results showed that the final model with four predictive factors had the highest AUC of 0.705 in the validation set (**Figure 2C**). Comparisons of the predictive performance of validation sets among the three algorithms models (with each optimal variable and tuning parameter) are shown in **Figure 2D** and **Supplementary Table S2**. It turned out that the LASSO regression model demonstrated the highest performance. In detail, the relative weights of the final variables in the LASSO-based logistic regression model are displayed in **Figure 2E**.

Nomograms and Model Performance

The four independent factors used to create a predictive nomogram were the number of positive SLNs (1–2, 3–4, or ≥5), the total number of SLNs harvested (≤2, 3–5, or ≥6), absence of lymph node hilum (no/not described or yes), and LVI (no or yes). According to the sum of the assigned points for each factor in the nomogram, a higher total score was associated with the absence of NSLN metastasis (**Figure 3**). The c-index in the logistic regression was equal to the area under the ROC curve. In **Figure 4A**, an AUC value of 0.759 is achieved in the entire set, while AUC values of 0.782 and 0.705 are obtained in the training and validation sets, respectively. The Hosmer-Lemeshow test was used to assess the accuracy of model fit and no departure from perfect fit was identified ($p = 0.759$). The sample bootstrapped calibration plot for the prediction is also presented in **Figure 4B**.

Clinical Application Evaluation

Decision curve analysis showed that using this nomogram provides an additional benefit when the threshold probability of the entire set is between 0 and 87% (**Figure 5**). A similar observation was also reported in entire and test cohorts. Therefore, the nomogram model can predict the probability of NSLN metastasis in patients with breast cancer to facilitate early clinical intervention and support personalized postoperative cancer rehabilitation.

DISCUSSION

The axillary surgery has been de-escalating since the awareness grows in breast cancer (29). Systemic treatments, such as chemotherapy therapies, are recognized as important control measures of cancer recurrence rather than the local therapy, such as the extent of surgical excision. The National Surgical Adjuvant Breast and Bowel Project (NSABP) b-32 trial (7) first investigated the necessity of ALND in patients with negative SLN. This trial found that SLNB alone without further axillary dissection is an appropriate therapy for the targeted patients. This report has been widely accepted in clinical practice to the point where it has become a surgical routine. Nevertheless, breast surgeons still explore the surgical indications. The After Mapping of the Axilla, Radiotherapy or Surgery (AMAROS) trial (8) revealed that ALND and axillary radiotherapy after a positive SLN provide comparable axillary control for patients with early breast cancer. The American College of Surgeons Oncology Group (ACOSOG) Z0011 (9) suggested that early breast cancer patients with 1 or 2 SLN metastases, breast-conserving lumpectomy, and whole-breast irradiation can be exempted from ALND. Furthermore, International Breast Cancer Study Group (IBCSG) 23-01 (10) trial argued the necessity of ALND in patients with micrometastatic SLN (metastases <2 mm). The discussion for sparing ALND is rooted in resultant series of complications that include range of motion, lymphoedema, pain, and sensory defects (4, 5, 30). In contrast, SLNB can significantly lower the morbidity of such complications (31). Furthermore, clinical data indicated

TABLE 1 | Differences in clinicopathological characteristics between the patients with and without NSLNs metastasis.

	Metastasis ($n = 96$)	Non-Metastasis ($n = 119$)	all ($n = 215$)	*P*-value
Age	56.3 (12.2)	55.7 (11.7)	56 (11.9)	0.703
Tumor location				
UOQ	51 (53.1%)	59 (49.6%)	110 (51.2%)	
LOQ	18 (18.8%)	25 (21.0%)	43 (20.0%)	
UIQ	15 (15.6%)	25 (21.0%)	40 (18.6%)	
LIQ	12 (12.5%)	10 (8.4%)	22 (10.2%)	0.58
Ultrasonic features				
Transverse diameter of tumor (mm)	23.5 (10.3)	21.5 (9.1)	22.4 (9.7)	0.115
Longitudinal diameter of tumor (mm)	14.6 (5.8)	14.4 (5.9)	14.5 (5.9)	0.672
longitudinal/transverse axis ratio of tumor	1.7 (0.5)	1.5 (0.5)	1.6 (0.5)	0.052
Tumor margin				
regular	8 (8.3%)	7 (5.9%)	15 (7.0%)	
irregular	88 (91.7%)	112 (94.1%)	200 (93.0%)	0.666
Tumor CDFI	0.8 (0.1)	0.8 (0.1)	0.8 (0.1)	0.593
Transverse diameter of lymph nodes (mm)	11 (7.1)	9.5 (7.1)	10.2 (7.1)	0.16
Longitudinal diameter of lymph nodes (mm)	6.1 (4)	4.9 (3.8)	5.5 (4)	0.024
Longitudinal/transverse axis ratio of lymph nodes	1.6 (0.9)	1.5 (1)	1.5 (1)	0.923
Lymphatic echogenicity				
None	17 (17.7%)	32 (26.9%)	49 (22.8%)	
High	18 (18.8%)	37 (31.1%)	55 (25.6%)	
Low	59 (61.5%)	49 (41.2%)	108 (50.2%)	
Moderate	2 (2.1%)	1 (0.8%)	3 (1.4%)	0.018
Absence of lymph node hilum				
No or not described	82 (85.4%)	113 (95.0%)	195 (90.7%)	
Yes	14 (14.6%)	6 (5.0%)	20 (9.3%)	0.031
Pathological features				
Histology				
Ductal	92 (95.8%)	116 (97.5%)	208 (96.7%)	
Lobular	3 (3.1%)	3 (2.5%)	6 (2.8%)	
Others	1 (1.1%)	0 (0%)	1 (0.5%)	0.516
Estrogen receptor status				
Negative	16 (16.7%)	21 (17.6%)	37 (17.2%)	
Positive	80 (83.3%)	98 (82.4%)	178 (82.8%)	0.994
Progesterone receptor status				
Negative	31 (32.3%)	32 (26.9%)	63 (29.3%)	
Positive	65 (67.7%)	87 (73.1%)	152 (70.7%)	0.475
Proliferation index (Ki-67)				
$<$14%	19 (19.8%)	24 (20.2%)	43 (20.0%)	
$\geq$14%	77 (80.2%)	95 (79.8%)	172 (80.0%)	1
Her-2 overexpression				
Negative	71 (74.0%)	90 (75.6%)	161 (74.9%)	
Positive	25 (26.0%)	29 (24.4%)	54 (25.1%)	0.902
Lymphovascular invasion				
No	61 (63.5%)	100 (84.0%)	161 (74.9%)	
Yes	35 (36.5%)	19 (16.0%)	54 (25.1%)	0.001
SBR stage				
I	2 (2.1%)	1 (0.8%)	3 (1.4%)	
II	48 (50.0%)	72 (60.5%)	120 (55.8%)	
III	46 (47.9%)	46 (38.7%)	92 (42.8%)	0.259
T stage				
$\leq$2 cm	39 (40.6%)	63 (52.9%)	102 (47.4%)	
2–5 cm	54 (56.2%)	54 (45.4%)	108 (50.2%)	
$\geq$5 cm	3 (3.1%)	2 (1.7%)	5 (2.3%)	0.18
Number of SLNs harvested	5 (2.8)	5.4 (3.6)	5.2 (3.3)	0.728
Number of positive SLNs	2.7 (1.8)	1.7 (1.1)	2.1 (1.5)	0
Proportion of positive SLNs	0.6 (0.3)	0.4 (0.3)	0.5 (0.3)	0

UOQ, Upper-outer quadrant; LOQ, Lower-outer quadrant; UIQ, Upper-inner quadrant; LIQ, Lower-inner quadrant; CDFI, color Doppler flow imaging; SBR grade, Scarff-Bloom-Richardson grade; SLNs, sentinel lymph nodes.

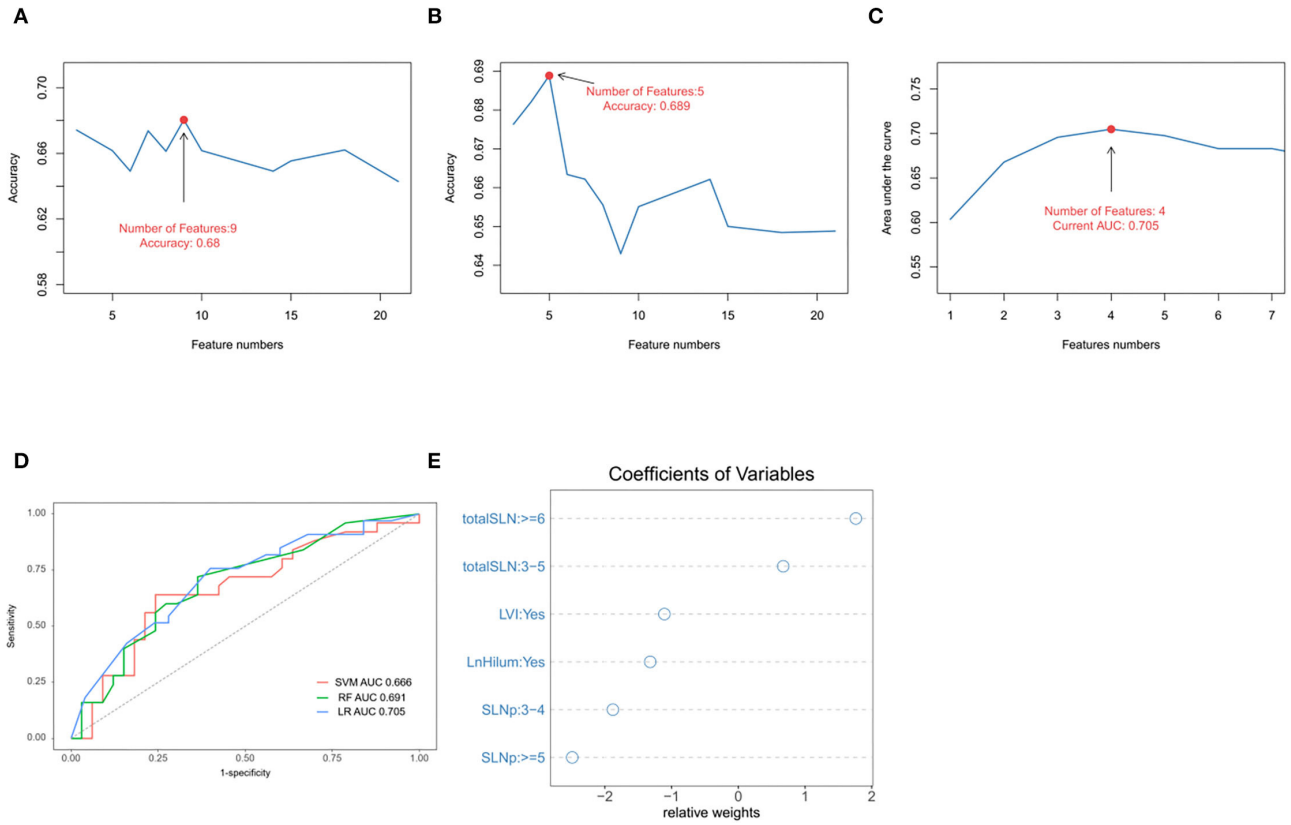

FIGURE 2 | Predictive model and factors selection. **(A)** The line graph shows the relationship between the number of candidate features and the accuracy in support vector machines (SVMs) model. **(B)** The line graph shows the relationship between the number of selected features and the accuracy in random forest (RF) model. **(C)** The line graph shows the relationship between the number of features and the area under the curve (AUC) values in the least absolute shrinkage and selection operator (LASSO)-based logistical model. **(D)** ROC curve analysis of machine-learning algorithms for prediction of non-sentinel lymph nodes (NSLN) without metastasis in the validation set. **(E)** The dot plot shows the coefficients of variables in the final model. LVI: lymphovascular invasion; totalSLN: total number of SLNs harvested; LnHilum: absence of lymph node hilum; SLNp: number of positive SLNs.

that the majority of patients with positive SLNs had no additional nodes metastasis (6), which is consistent with our finding that roughly 55% of all patients had no metastasis. Despite the various clinical trials that explored the necessity of ALND, it is still apparent that the inclusion of patients is relatively stringent and the precise individualization of the choice is still pondering.

Previous studies have been conducted to predict NSLN metastasis (12, 20, 32–36). The MSKCC model is a widely acknowledged tool that incorporates eight variables (12). The variables combined in the MSKCC model were pathological size, ER status, multifocality, tumor type, tumor nuclear grade, LVI, method of detection, and the number of positive and negative SLNs with an AUC of 0.77 for the validation cohort. That the number of positive SLNs in the MSKCC model had the highest weight that is consistent with the findings of our study. The MSKCC model has been validated in various countries, for instance, in Australia where an AUC of 0.66 was obtained from the inclusion of 526 patients (14). The model of MD Anderson Cancer Center (33) is another frequently mentioned model. This model added two variables of SLN metastasis size and extracapsular extension, which are tied with the emphasis on SLN micrometastasis status. These variables were excluded in this study because some patients did not have SLN metastatic size as a result of the limitations of our pathology department. In contrast, the Helsinki University model (20) included a prediction variable of HER-2 status instead of PR status. Despite the fact that HER-2 positive is generally associated with NSLN positivity, the relationship between HER-2 status and NSLN positivity remains controversial (37), and the current study yielded no statistically significant differences.

Preoperative assessment of axillary lymph burden in breast cancer is routinely performed using different imaging techniques. US is considered to be the most recommended imaging technique owing to its inexpensive, convenience, and absence of radiation exposure. The Sentinel Node vs. Observation after Axillary Ultrasound (SOUND) trial (38) is exploring the potential possibility of US as a replacement for SLNB. Previous studies have also suggested that the inclusion of US parameters in the model could improve its predictive capacity (39, 40). Zhu (40) suggested that the Doppler resistance index and the extent of extension of the enhancing lesion were correlated with lymph node metastasis. Qiu et al. (39), on the other hand, incorporated three US-based

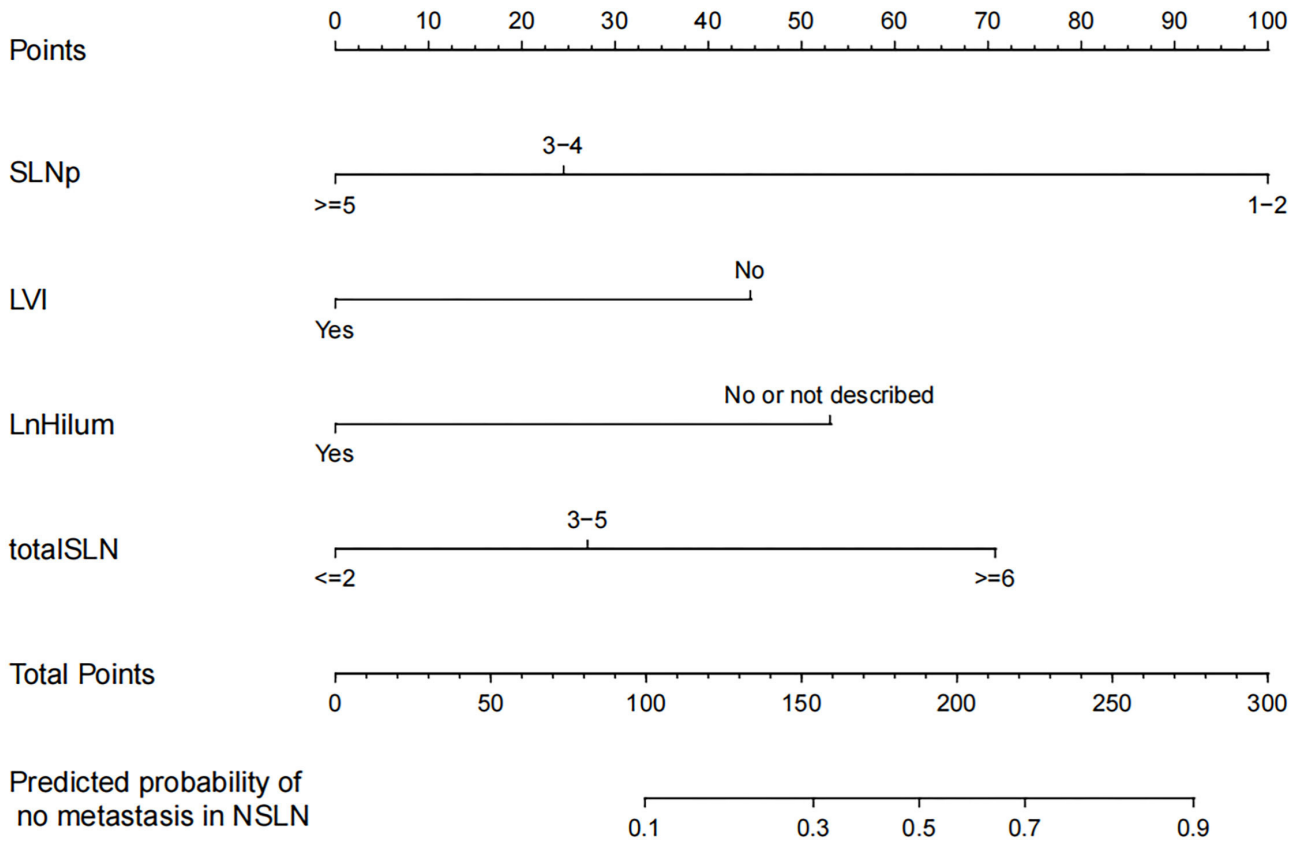

FIGURE 3 | Nomogram for prediction of the absence of non-sentinel lymph nodes (NSLN) metastasis. SLNp: number of positive SLNs; LVI: lymphovascular invasion; LnHilum: absence of lymph node hilum; totalSLN: total number of SLNs harvested.

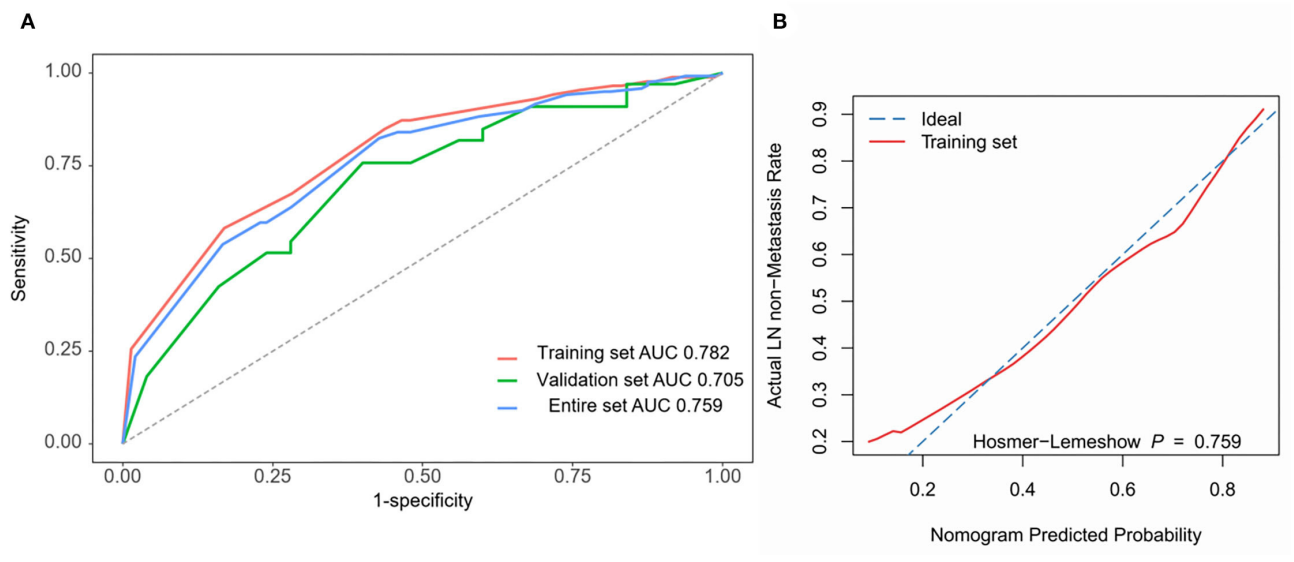

FIGURE 4 | Nomogram prediction model validation. **(A)** ROC curves are used for all sets. AUC values for training set (red), validation set (green), and entire set (blue) are 0.782, 0.705, and 0.759. **(B)** The bootstrapped calibration plot and Hosmer-Lemeshow test for the training set.

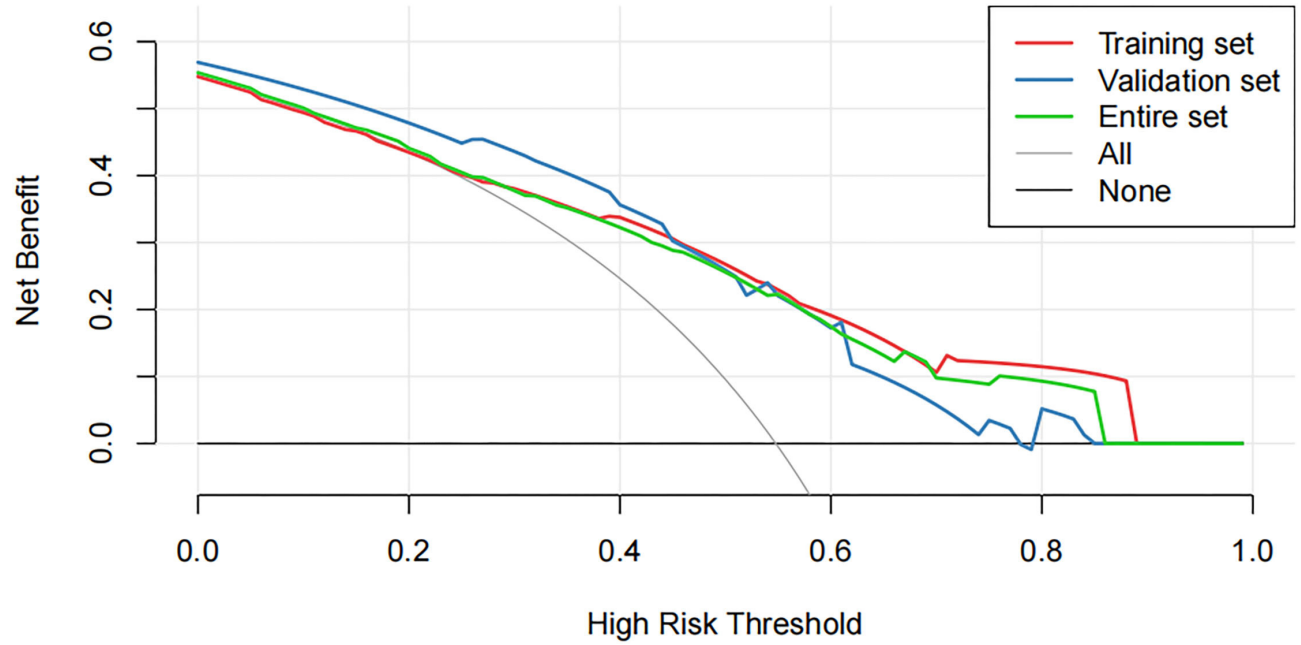

FIGURE 5 | The decision curve analysis (DCA) curve shows the decision analysis for the entire set, the training set, and the validation set.

variables of cortical thickness of SLN, transverse diameter of SLN, and lymph node hilum status in their nomogram, with an AUC of 0.864. This is consistent with the findings obtained in this study. However, the validity of the model is challenged by its dependence on adjustable parameters by the operator.

Apart from predicting NSLN status based on imaging features, such as ultrasound or clinical features, the role of molecular markers has also been explored. Metalloprotease-1 (41) and cytokeratin 19 mRNA copy (42, 43) have been suggested to be highly correlated with NSNL metastasis. Prediction models based on molecular markers usually showed a high specificity and sensitivity, but the time taken for intraoperative measurements and the high cost may be the reasons why they are difficult to extend.

Our nomogram provides an individual prediction of the probability of having negative NSLNs for patients with positive SLNs. A woman with 2 positive SLNs, out of 5 SLNs harvested, the preoperative US showed the presence of lymph node hilum and pathology revealed tumor LVI, might be considered to have a 20% risk of having negative NSLNs, which implies that the patient is at high risk of additional nodes metastasis and ALND should be recommended clinically. However, the study result is limited and requires much more validation before it can be applied to clinical reasoning.

Machine learning has been applied to different tumors as an innovative method for cancer prediction and prognosis (15, 16). It provides excellent accuracy through a continuous ML approach. According to Ayer et al. (17), a prediction model that enrolled 48,774 patients yielded an AUC of 0.965 and could distinguish malignant from benign mammographic findings. Such precision is unfathomable in alternative models. Typically, an AUC above 0.7 is regarded as reasonable. Madekivi et al. (19) narrowed down to seven variables by utilizing XG-Boost's capabilities for self-learning and eventually developed a nomogram with an AUC of 0.80. This study compared the performance of three ML methods, and the best classification model was selected. To reduce the number of variables, LASSO conducted 500 times iterations and selected the features with more than 300 repeated occurrences. This showed a well predictive effectiveness in the validation cohort.

The inclusion of US-related variables and the application of the ML approach are the two aspects of innovation in our prediction model. Eventually, the four variables included in the development of the nomogram were the number of positive SLNs, total number of SLNs harvested, LVI, and lymph node hilum status. The AUC values of 0.759 and 0.705 were used for the training and validation cohorts, respectively. Therefore, in comparison with other previous studies, the validation cohort in this study had a higher AUC value for the fewer variables. The continuous predictors were categorized using restricted cubic splines, which are better suited for the daily practice of clinicians. However, some limitations of the study were noted. First, the number of patients enrolled in this study is far from satisfaction. The inclusion criteria entailed only the patient who received both SLNB and ALND and this dramatically reduced the number. The nomogram lacked external validation due to the limitation in numbers, which meant that patients had to be studied as a single center although we included patients in multicenter. This study was short of a large sample that is technically required for ML to support a more convincing result. On the other hand, our pathology department was failed to accurately depict the size of SLN metastases at the beginning, owing to the inclusion of

patients over a long time interval. This was significantly regretted because the existing literature already supports a relationship between SLN metastasis size and NSLN status.

Overall, the trend of de-escalation of axillary surgery is inevitable. However, the selection of appropriate patients remains a crucial issue to be addressed. It is essential to have some multicenter, prospective trials, such as Z0011, to upgrade the guidelines. This study revealed more areas that need future research to validate our findings.

DATA AVAILABILITY STATEMENT

The raw data supporting the conclusions of this article will be made available by the authors, without undue reservation.

AUTHOR CONTRIBUTIONS

QW collected the data and was a major contributor to writing the manuscript. LD analyzed and interpreted the patient data. YJ made substantial contributions to the conception. HZ designed the work and revised it. All authors contributed to the article and approved the submitted version.

SUPPLEMENTARY MATERIAL

The Supplementary Material for this article can be found online at: https://www.frontiersin.org/articles/10.3389/fsurg.2022.797377/full#supplementary-material

Supplementary Figure S1 | The line graph shows the relationship between the continuous variables and the risk of non-sentinel lymph nodes (NSLNs) metastasis status by using restricted cubic splines analysis. Y-axis means risk ratio and the X-axis means values of variables. **(A)** age; **(B)** tumor color Doppler flow imaging (CDFI); **(C)** total number of SLNs harvested; **(D)** number of positive SLNs; **(E)** longitudinal/transverse axis ratio of tumor; **(F)** longitudinal/transverse axis ratio of lymph nodes; **(G)** proportion of positive SLNs; **(H)** transverse axis of tumor; **(I)** transverse axis of lymph nodes.

Supplementary Table S1 | Differences in clinicopathological characteristics between the training and validation sets.

Supplementary Table S2 | Comparisons of the predictive performance of validation sets among the three algorithms models.

REFERENCES

1. Sung H, Ferlay J, Siegel RL. Global cancer statistics 2020: GLOBOCAN estimates of incidence and mortality worldwide for 36 cancers in 185 countries. *CA Cancer J Clin.* (2021) 71:209–49. doi: 10.3322/caac.21660
2. Veronesi U, Paganelli G, Viale G. A randomized comparison of sentinel-node biopsy with routine axillary dissection in breast cancer. *N Engl J Med.* (2003) 349:546–53. doi: 10.1056/NEJMoa012782
3. Magnoni F, Galimberti V, Corso G. Axillary surgery in breast cancer: an updated historical perspective. *Semin Oncol.* (2020) 47:341–52. doi: 10.1053/j.seminoncol.2020.09.001
4. Soares EW, Nagai HM, Bredt LC. Morbidity after conventional dissection of axillary lymph nodes in breast cancer patients. *World J Surg Oncol.* (2014) 12:67. doi: 10.1186/1477-7819-12-67
5. Dinas K, Kalder M, Zepiridis L. Axillary web syndrome: incidence, pathogenesis, and management. *Curr Probl Cancer.* (2019) 43:100470. doi: 10.1016/j.currproblcancer.2019.02.002
6. Abdessalam SF, Zervos EE, Prasad M. Predictors of positive axillary lymph nodes after sentinel lymph node biopsy in breast cancer. *Am J Surg.* (2001) 182:316–20. doi: 10.1016/S0002-9610(01)00719-X
7. Krag DN, Anderson SJ, Julian TB. Sentinel-lymph-node resection compared with conventional axillary-lymph-node dissection in clinically node-negative patients with breast cancer: overall survival findings from the NSABP B-32 randomised phase 3 trial. *Lancet Oncol.* (2010) 11:927–33. doi: 10.1016/S1470-2045(10)70207-2
8. Donker M, van Tienhoven G, Straver ME. Radiotherapy or surgery of the axilla after a positive sentinel node in breast cancer (EORTC 10981-22023 AMAROS): a randomised, multicentre, open-label, phase 3 non-inferiority trial. *Lancet Oncol.* (2014) 15:1303–10. doi: 10.1016/S1470-2045(14)70460-7
9. Giuliano AE, Ballman KV, McCall L. Effect of axillary dissection vs no axillary dissection on 10-year overall survival among women with invasive breast cancer and sentinel node metastasis: the ACOSOG Z0011 (Alliance) randomized clinical trial. *JAMA.* (2017) 318:918–26. doi: 10.1001/jama.2017.11470
10. Galimberti V, Cole BF, Viale G. Axillary dissection versus no axillary dissection in patients with breast cancer and sentinel-node micrometastases (IBCSG 23-01): 10-year follow-up of a randomised, controlled phase 3 trial. *Lancet Oncol.* (2018) 19:1385–93.
11. Curigliano G, Burstein HJ, Winer EP. De-escalating and escalating treatments for early-stage breast cancer: the St. Gallen International Expert Consensus Conference on the Primary Therapy of Early Breast Cancer 2017. *Ann Oncol.* (2017) 28:1700–12. doi: 10.1093/annonc/mdx308
12. Van Zee KJ, Manasseh DM, Bevilacqua JL. A nomogram for predicting the likelihood of additional nodal metastases in breast cancer patients with a positive sentinel node biopsy. *Ann Surg Oncol.* (2003) 10:1140–51. doi: 10.1245/ASO.2003.03.015
13. Nadeem RM, Gudur LD, Saidan ZA. An independent assessment of the 7 nomograms for predicting the probability of additional axillary nodal metastases after positive sentinel lymph node biopsy in a cohort of British patients with breast cancer. *Clin Breast Cancer.* (2014) 14:272–9. doi: 10.1016/j.clbc.2014.02.006
14. Tapia G, Ying V, Di Re A. Predicting non-sentinel lymph node metastasis in Australian breast cancer patients: are the nomograms still useful in the post-Z0011 era? *Anz J Surg.* (2019) 89:712–7. doi: 10.1111/ans.15173
15. Stojadinovic A, Nissan A, Eberhardt J. Development of a bayesian belief network model for personalized prognostic risk assessment in colon carcinomatosis. *Am Surg.* (2011) 77:221–30. doi: 10.1177/000313481107700225
16. Lee JH, Ha EJ, Kim D. Application of deep learning to the diagnosis of cervical lymph node metastasis from thyroid cancer with CT: external validation and clinical utility for resident training. *Eur Radiol.* (2020) 30:3066–72. doi: 10.1007/s00330-019-06652-4
17. Ayer T, Alagoz O, Chhatwal J. Breast cancer risk estimation with artificial neural networks revisited: discrimination and calibration. *Cancer-Am Cancer Soc.* (2010) 116:3310–21. doi: 10.1002/cncr.25081
18. Zeng Z, Espino S, Roy A. Using natural language processing and machine learning to identify breast cancer local recurrence. *BMC Bioinformatics.* (2018) 19:498. doi: 10.1186/s12859-018-2466-x
19. Madekivi V, Boström P, Karlsson A. Can a machine-learning model improve the prediction of nodal stage after a positive sentinel lymph node biopsy in breast cancer? *Acta Oncol.* (2020) 59:689–95. doi: 10.1080/0284186X.2020.1736332
20. Meretoja TJ, Leidenius MH, Heikkilä PS. International multicenter tool to predict the risk of nonsentinel node metastases in breast cancer. *J Natl Cancer Inst.* (2012) 104:1888–96. doi: 10.1093/jnci/djs455
21. Al-Hilli Z, Hieken TJ, Boughey JC. Axillary ultrasound in the management of the newly diagnosed breast cancer patient. *Breast J.* (2015) 21:634–41. doi: 10.1111/tbj.12497
22. Harrell FJ, Lee KL, Mark DB. Multivariable prognostic models: issues in developing models, evaluating assumptions and adequacy,

and measuring and reducing errors. Stat Med. (1996) 15:361–87. doi: 10.1002/(SICI)1097-0258(19960229)15:4<361::AID-SIM168>3.0.CO;2-4
23. Buxton RT, McKenna MF, Clapp M. Efficacy of extracting indices from large-scale acoustic recordings to monitor biodiversity. *Conserv Biol.* (2018) 32:1174–84. doi: 10.1111/cobi.13119
24. Huang ML, Hung YH, Lee WM. SVM-RFE based feature selection and Taguchi parameters optimization for multiclass SVM classifier. *Sci World J.* (2014) 2014:795624. doi: 10.1155/2014/795624
25. Sveen A, Ågesen TH, Nesbakken A. ColoGuidePro: a prognostic 7-gene expression signature for stage III colorectal cancer patients. *Clin Cancer Res.* (2012) 18:6001–10. doi: 10.1158/1078-0432.CCR-11-3302
26. Harrell FJ, Califf RM, Pryor DB. Evaluating the yield of medical tests. *JAMA*. (1982) 247:2543–6. doi: 10.1001/jama.247.18.2543
27. Kramer AA, Zimmerman JE. Assessing the calibration of mortality benchmarks in critical care: the hosmer-lemeshow test revisited. *Crit Care Med.* (2007) 35:2052–6. doi: 10.1097/01.CCM.0000275267.64078.B0
28. Van Calster B, Wynants L, Verbeek J. Reporting and interpreting decision curve analysis: a guide for investigators. *Eur Urol.* (2018) 74:796–804. doi: 10.1016/j.eururo.2018.08.038
29. Yan M, Abdi MA, Falkson C. Axillary management in breast cancer patients: a comprehensive review of the key trials. *Clin Breast Cancer.* (2018) 18:e1251–9. doi: 10.1016/j.clbc.2018.08.002
30. Roses DF, Brooks AD, Harris MN. Complications of level I and II axillary dissection in the treatment of carcinoma of the breast. *Ann Surg.* (1999) 230:194–201. doi: 10.1097/00000658-199908000-00009
31. Killelea BK, Long JB, Dang W. Associations between sentinel lymph node biopsy and complications for patients with ductal carcinoma in situ. *Ann Surg Oncol.* (2018) 25:1521–9. doi: 10.1245/s10434-018-6410-0
32. Degnim AC, Reynolds C, Pantvaidya G. Nonsentinel node metastasis in breast cancer patients: assessment of an existing and a new predictive nomogram. *Am J Surg.* (2005) 190:543–50. doi: 10.1016/j.amjsurg.2005.06.008
33. Mittendorf EA, Hunt KK, Boughey JC. Incorporation of sentinel lymph node metastasis size into a nomogram predicting nonsentinel lymph node involvement in breast cancer patients with a positive sentinel lymph node. *Ann Surg.* (2012) 255:109–15. doi: 10.1097/SLA.0b013e318238f461
34. Pal A, Provenzano E, Duffy SW. A model for predicting non-sentinel lymph node metastatic disease when the sentinel lymph node is positive. *Br J Surg.* (2008) 95:302–9. doi: 10.1002/bjs.5943
35. Kohrt HE, Olshen RA, Bermas HR. New models and online calculator for predicting non-sentinel lymph node status in sentinel lymph node positive breast cancer patients. *BMC Cancer.* (2008) 8:66. doi: 10.1186/1471-2407-8-66
36. Wang XY, Wang JT, Guo T. Risk factors and a predictive nomogram for non-sentinel lymph node metastases in Chinese breast cancer patients with one or two sentinel lymph node macrometastases and mastectomy. *Curr Oncol.* (2019) 26:e210–5. doi: 10.3747/co.26.4295
37. Lale A, Yur M, Özgül H. Predictors of non-sentinel lymph node metastasis in clinical early stage (cT1-2N0) breast cancer patients with 1-2 metastatic sentinel lymph nodes. *Asian J Surg.* (2020) 43:538–49. doi: 10.1016/j.asjsur.2019.07.019
38. Gentilini O, Veronesi U. Abandoning sentinel lymph node biopsy in early breast cancer? A new trial in progress at the European Institute of Oncology of Milan (SOUND: Sentinel node vs Observation after axillary UltraSouND). *Breast.* (2012) 21:678–81. doi: 10.1016/j.breast.2012.06.013
39. Qiu SQ, Zeng HC, Zhang F. A nomogram to predict the probability of axillary lymph node metastasis in early breast cancer patients with positive axillary ultrasound. *Sci Rep.* (2016) 6:21196. doi: 10.1038/srep21196
40. Zhu Y, Lv W, Wu H. A preoperative nomogram for predicting the risk of sentinel lymph node metastasis in patients with T1-2N0 breast cancer. *Jpn J Radiol.* (2022). doi: 10.1007/s11604-021-01236-z. [Epub ahead of print].
41. Eiró N, González LO, Atienza S. Prediction of metastatic breast cancer in non-sentinel lymph nodes based on metalloprotease-1 expression by the sentinel lymph node. *Eur J Cancer.* (2013) 49:1009–17. doi: 10.1016/j.ejca.2012.09.019
42. Pina H, Salleron J, Gilson P. Intraoperative prediction of non-sentinel lymph node metastases in breast cancer using cytokeratin 19 mRNA copy number: a retrospective analysis. *Mol Clin Oncol.* (2022) 16:58. doi: 10.3892/mco.2022.2491
43. Shimazu K, Miyake T, Okuno J. One-step nucleic acid amplification can identify sentinel node-negative breast cancer patients with excellent prognosis. *Anticancer Res.* (2019) 39:1447–54. doi: 10.21873/anticanres.13261

Conflict of Interest: The authors declare that the research was conducted in the absence of any commercial or financial relationships that could be construed as a potential conflict of interest.

frontiers | Frontiers in Oncology

ORIGINAL RESEARCH
published: 13 May 2022
doi: 10.3389/fonc.2022.875990

Anatomical Computerized Exploration to Excise Malignancies in Deep Facial Compartments: An Advanced Virtual Reality Protocol for a Tailored Surgical Approach

Alessandro Tel[1], *Daniele Bagatto*[2], *Fabio Costa*[1], *Salvatore Sembronio*[1] *and Massimo Robiony*[1]*

[1] Department of Maxillofacial Surgery, University Hospital of Udine, Udine, Italy, [2] Department of Neuroradiology, University Hospital of Udine, Udine, Italy

Objective/Hypothesis: This study describes the design and application of a novel advanced protocol for virtual three-dimensional anatomical reconstruction of the deep facial compartments, aiming to improve the preoperative understanding and the intraoperative assistance in complex resective surgeries performed for malignant diseases which extend in complex spaces, including the pterygomaxillopalatine fossa, the masticator space, and the infratemporal fossa.

Methods: This study is a non-profit, retrospective, and single-institution case series. The authors clearly describe in detail imaging acquisition protocols which are suitable to segment each target, and a multilayer reconstruction technique is presented to simulate anatomical structures, with particular focus on vascular networks. Virtual surgical planning techniques are individually designed for each case to provide the most effective access to the deep facial compartments. Intraoperative guidance systems, including navigation and virtual endoscopy, are presented, and their role is analyzed.

Results: The study included seven patients with malignant disease located in the deep facial compartments requiring radical resection, and all patients underwent successful application of the protocol. All lesions, except one, were subject to macroscopically radical resection. Vascular structures were identified with overall reconstruction rates superior to 90% for major caliber vessels. Prominent landmarks for virtual endoscopy were identified for each case.

Conclusions: Virtual surgical planning and multilayer anatomical reconstruction are valuable methods to implement for surgeries in deep facial compartments, providing the surgeon with improved understanding of the preoperative condition and intraoperative guidance in critical phases for both open and endoscopic phases. Such techniques allow to tailor each surgical access, limiting morbidity to strictly necessary approaches to reach the disease target.

Keywords: virtual surgical planning, 3D vessels, deep facial compartments, navigation, virtual endoscopy

OPEN ACCESS

Edited by:
Konstanty Korski, Roche, Switzerland

Reviewed by:
Fabio Ferreli, Humanitas University, Italy
Kamil Krystkiewicz, 10th Military Research Hospital and Polyclinic, Poland

***Correspondence:**
Massimo Robiony
massimo.robiony@uniud.it

Specialty section:
This article was submitted to Surgical Oncology, a section of the journal Frontiers in Oncology

Received: *14 February 2022*
Accepted: *14 April 2022*
Published: *13 May 2022*

Citation:
Tel A, Bagatto D, Costa F, Sembronio S and Robiony M (2022) Anatomical Computerized Exploration to Excise Malignancies in Deep Facial Compartments: An Advanced Virtual Reality Protocol for a Tailored Surgical Approach. Front. Oncol. 12:875990. doi: 10.3389/fonc.2022.875990

1 INTRODUCTION

The pterygo-maxillo-palatine fossa (PMPF), the infratemporal fossa (ITF), and the deep masticatory space (DMS) are deep facial compartments (DFC) of difficult access, due to their location, enclosed in a narrow, rigid space between the posterior wall of the maxilla and the skull base, and to the presence of densely packed vascular and nervous structures. Malignant lesions arising in such spaces can show variable infiltration of critical structures, which have to be preliminarily identified. In particular, such lesions frequently develop in critical points in which multiple vessels and nerves reciprocally cross in complex networks which are difficult to visualize using a standard two-dimensional imaging.

It is well known that in malignant tumors, the major role of surgery is to minimize the entity of a macroscopic residual disease; therefore, a wide, margin-free resection still represents the gold standard to achieve surgical radicality, allowing adjuvant therapies to maximize their effect, but at the cost of sacrificing nearby crucial structures, posing surgery at high risk of complications (1). As such, anatomical regions offer very narrow spaces for surgical maneuvers, often impairing vision; each case demands designing specific accesses. Moreover, patients presenting with diseases in DFC often present at late stages, due to a silent growing process which might cause mild disturbances, mimicking symptoms attributable to more common diseases. The result is an advanced disease, which often grows across major caliber vessels, where surgery necessarily involves a meticulous dissection of tumor tissue from arteries and veins, which in several cases have to be anticipately identified for sacrifice.

Such considerations translate in the importance to perform a preoperative, patient-specific, anatomical study as an essential step when approaching DFC, but so far, despite advances in computerized 3D reconstruction, only few incomplete reports on the virtual representation of such regions are available, which often adopt an excessively simplified approach to represent a very complex anatomy. Moreover, masses developing DFC often project within paranasal sinuses, requiring endoscopy both as a visualization improvement and as a precise tool to accomplish specific phases of surgery. Endoscopy provides a small field vision within such spaces, often in the presence of a distorted anatomy or in the presence of a major vessel concealed beneath mucosal surfaces; thus, the simulation of endoscopic approaches as part of the virtual planning is equally important, especially to ascertain the vicinity of nearby critical structures. In computerized simulation, a virtual reality animation allows to merge open surgery with endoscopic vision, replicating any endoscopic view exactly as it would appear using an optical device as the camera proceeds in depth, providing an animated sequence (2, 3).

Alongside the lack of examples for a virtual reconstruction of DFC, literature provides limited evidence on the most suitable imaging protocols that should be implemented to study diseases arising in such spaces. To address such issues, our Department has developed a novel workflow based on optimized image acquisition protocols and tailored segmentation techniques. The purpose of this study is to provide a replicable methodology to perform multilayered anatomical reconstruction of DFC, to sequentially represent structures from the skeletal backbone to finest details of vasculature and soft tissues. Moreover, the Authors show how this protocol translates into clinical applicability through intraoperative navigation and simulated endoscopy, resulting in tailored approaches optimized for each disease.

2 MATERIALS AND METHODS

2.1 Patient Population/Study Design

This is an institutional review board-approved, single-institution, retrospective case series concerning the clinical application of an innovative protocol to study lesions arising in the DFC. We recruited seven patients with a malignant disease requiring radical resection located in the DFC, defined medially by the parapharyngeal space, posteriorly by a plane intersecting the clivus, anteriorly by the maxillary tuberosity, and laterally by the TMJ, including at least one between the deep lobe of the parotid gland and the lateral pterygoid muscle (**Table 1**).

2.2 Multilayer Imaging and Segmentation Protocol

Dedicated imaging acquisition protocols are needed to reproduce all anatomical structures for virtual planning according to a layer-by-layer model, including the skeletal framework, mucosal lining, muscles, vasculature, and lesions:

- Skeletal framework and mucosal lining: an ultrathin CT was performed with the following parameters: slice thickness = 0.625 mm, matrix = 512 × 512 px. The bony anatomy is simply segmented by using a thresholding algorithm within the bone tissue Hounsfield unit (HU) range. The resulting segmentation mask is then split into a mandible and skull-base subunit using semiautomatic techniques. The mucosal lining defined the spatial boundaries to simulate virtual endoscopy and was reconstructed from CT scan as well by applying thresholding on the density interval of the internal surface of paranasal sinuses.
- Tumor and other soft tissue: patients underwent MR with a 1.5-Tesla system (Aera; Siemens; Erlangen, Germany). After contrast medium administration, a 3D-VIBE T1-w sequence was acquired with a slice thickness of 1 mm and a matrix of 512 × 512 px.
- Arteries: to better delineate the anatomical relationships between the lesion and both extracranial portions of the internal carotid artery and external carotid artery, patients underwent 3D time-of-flight (TOF) MR with the following parameters: TR = 25.0 ms; TE = 7.15 ms; slice thickness = 0.5 mm; in-plane resolution: 0.4 × 0.4 mm; slice GAP = -25%; matrix 256 × 256 px.
- Veins: to detail venous vasculature, phase-contrast MR venography was also performed using a 2D-TOF sequence adapted for the study of posterior cranial fossa, paying particular attention to the positioning of saturation slabs and carefully avoiding any possible inflow artifacts.

TABLE 1 | Characteristics of patients in relation to disease process, surgery, and protocol applicability.

ID	Sex	Age	Localization	Pathology	Surgical approach	Imaging protocol (with MR sequences)	Virtually segmented structures	Simulated procedures	Major surgical pitfalls
1	F	38	Pterygo-maxillo-palatine fossa	Adenoid cystic carcinoma	Transnasal endoscopic, transoral endoscopic, transmandibular open	CT MR 3D-VIBE T1 MR 3D-TOF MR venography	Skeletal and mucosal layer Arteries Veins Mucosal lining Tumor Masticatory muscles Parotid gland	Virtual endoscopy Mandibular swing Zygomatic flap Maxillary antrostomy	Loss of V3 and V2 (involved in radical resection) Postoperative severe limitation of mouth opening
2	M	43	Middle cranial fossa and infratemporal fossa	Anaplastic meningioma	Transcranial (neurosurgical), transzygomatic, transmandibular	CT MR 3D-VIBE T1 MR 3D-TOF MR venography	Skeletal and mucosal layer Arteries Veins Mucosal lining Tumor Masticatory muscles	Zygomatic flap Mandibular swing Craniotomy	CSF leak Meningitis Macroscopic residual neoplasm
3	M	69	Left maxilla with nasal floor erosion and extension to the DFC	Adenoid cystic carcinoma	Transoral with Jager's jugal extended incision, endoscopic exploration	CT MR 3D-VIBE T1 MR 3D-TOF MR venography	Skeletal and mucosal layer Arteries Veins Mucosal lining Tumor Masticatory muscles	Virtual endoscopy Maxillectomy	Visible scar over the cheek
4	F	65	Deep lobe of the parotid with extension to the deep masticatory space	Mucoepidermoid carcinoma	Deep parotidectomy	CT MR 3D-VIBE T1 MR 3D-TOF MR facial nerve sequences	Skeletal and mucosal layer Arteries Parotid gland Main trunk of facial nerve	Parotid gland removal	Facial nerve resection
5	F	63	Pterygo-maxillo-palatine fossa, masticatory space	Adenocarcinoma	Transnasal endoscopic, Transmandibular open	CT MR 3D-VIBE T1 MR 3D-TOF MR venography	Skeletal and mucosal layer Arteries Mucosal lining Tumor Masticatory muscles	Virtual endoscopy Mandibular swing	Loss of V2 and V3
6	M	70	Retromandibular trigone invading the masticatory space	Squamocellular carcinoma	Transmandibular open, endoscopic exploration	CT MR 3D-VIBE T1 MR 3D-TOF MR venography	Skeletal and mucosal layer Arteries Veins Mucosal lining Tumor Masticatory muscles	Virtual endoscopy Mandibular swing	Postoperative severe limitation of mouth opening
7	M	45	Right posterior maxilla with extension to the deep masticatory space	Squamocellular carcinoma	Maxillectomy (Weber-Ferguson approach), transnasal endoscopic	CT MR 3D-VIBE T1 MR 3D-TOF	Skeletal and mucosal layer Arteries Mucosal lining Tumor Masticatory muscles	Transfacial swing, virtual endoscopy	None

Using Materialise Mimics v24.0 (Materialise, Leuven, Belgium), CT and MR sequences were coregistered with univocal coordinates to achieve superimposition. Vessels were segmented using dynamic thresholding algorithms, which implement criteria of spatial vicinity and HU similarity to capture potentially related voxels, such as those that compose the course of a vessel. All segmentation masks were reviewed and carefully inspected for optimal correspondence with each set of DICOM images and were then re-tessellated into STL files (**Figure 1**). The result was a hierarchical tree of anatomical structures, which could be selectively inspected or hidden.

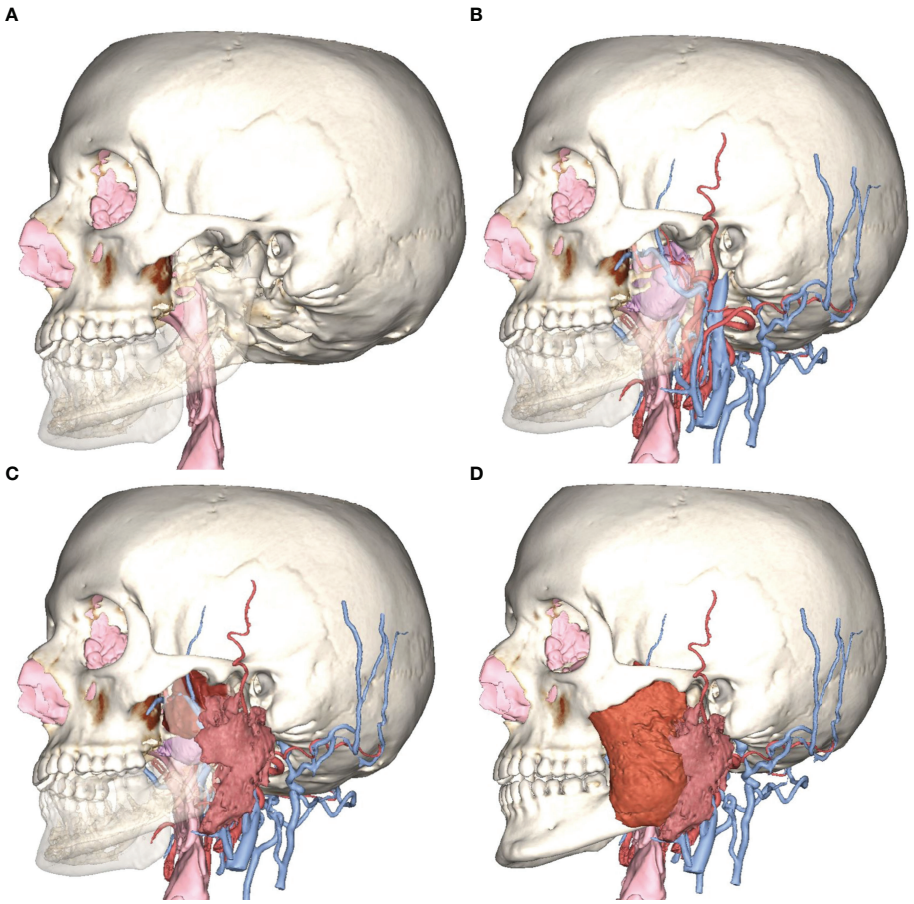

FIGURE 1 | Example of multilayer anatomical reconstruction. **(A)** Skeletal and mucosal framework; **(B)** reconstruction of tumor (purple), arteries, and veins; **(C)** reconstruction of the parotid gland; and **(D)** reconstruction of masticatory muscles.

2.3 Virtual Surgical Planning

2.3.1 Virtual Vasculature Study

Vessels were virtually reconstructed according to the multilayer segmentation protocol. Vessels were mapped and named by two operators (AT and DB). In particular, operators identified the contributors to arterial flow and venous drainage located around the tumor and at least each of the major vessels: internal carotid, external carotid, internal maxillary artery, maxillary vein, retromandibular vein, and internal jugular vein (**Figure 2**). For major vessels, labels were added to the surgical planning and transferred in the navigation plan.

2.3.2 Planning of Surgical Accesses in Virtual Reality

The Mimics project was imported in 3-Matic v16.0 (Materialise, Leuven, Belgium), where osteotomies were designed to simulate accesses to the deep structures. Each patient underwent individualized approach simulation depending on the location of the disease, although three common threads in virtual surgical planning were identified according to our case series:

- PMPF was exposed by simulating a mandibular swing approach, by an outward rotation of the mandibular segment across the Z-axis with a fulcrum positioned over the condyle area. The rotational movement of the mandible allowed to uncover a straightforward corridor exposing the oropharynx and the skull base.
- To access the IF, a superior-lateral transzygomatic approach yielded optimal exposure, especially if associated with a coronoidectomy and temporalis muscle disinsertion, paving the way to the lateral skull base.
- For more cranially located malignancies, especially with concomitant involvement of the paranasal sinuses, the transmaxillary portal configured a corridor for the forward exploration of the PMPF as well as the anterior skull base. The transmaxillary portal is particularly suitable for endoscopic exploration (**Figure 3**), as it develops within an empty cavity (the maxillary sinus) that offers space for surgical maneuvers without involving injuries to critical structures and reduced bleeding.

2.3.3 Virtual Endoscopic Setup

STL files of segmented anatomy were imported into Autodesk Maya (Autodesk Inc, San Jose, CA), a comprehensive software

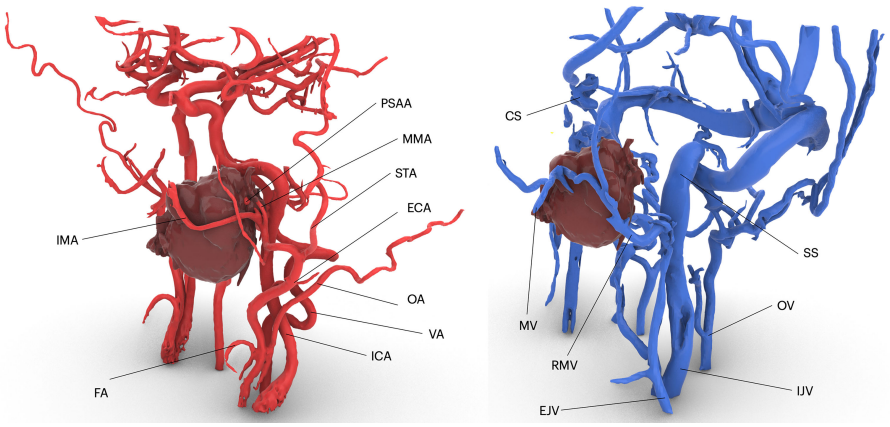

FIGURE 2 | Virtual vascularization study conducted on three-dimensional models of arterial and venous vasculature, respectively derived from 3D TOF MR sequences and phase-contrast venography. IMA, internal maxillary artery; FA, facial artery; ICA, internal carotid artery; VA, vertebral artery; OA, occipital artery; ECA, external carotid artery; STA, superficial temporal artery; MMA, middle meningeal artery; PSAA, posterior superior alveolar artery; CS, cavernous sinus; M, maxillary vein; SS, sigmoid sinus; OV, occipital vein; RMV, retromandibular vein.

package designed for 3D animation. A digital replica of the endoscopic optical system was simulated, and a see-through camera with defined lens parameters (focal distance: 18 mm, image refreshing rate: 50 fps) was parented to the tip of the virtual optics, allowing to scope the endonasal space with the same vision provided by the real endoscope. Surgeons virtually moved the camera within anatomical spaces and set specific key frames corresponding to prominent landmarks for each phase, which the software interpolated to yield a smooth animation sequence. Landmarks identified in nasal endoscopy were the following: head of inferior and middle turbinate, bulla, antral foramen, vidian canal, choanal opening, ethmoidal roof, pterygoid plates, Eustachian tube opening, sphenoid sinus opening, paraclival tract of ICA. Endoscopic animation was scoped for both superficial and deep layers, allowing to virtually remove mucosae to reveal underlying vasculature in critical areas around the tumor (**Figure 4**). The simulation was brought inside the operating room to be used as reference during real endoscopy.

2.4 Computer-Guided Surgery

2.4.1 Navigation

In this protocol, navigational assistance was implemented to evaluate the position of each maneuver in relation with the virtual plan. Using Brainlab Elements (Brainlab, Munich, Germany), STLs from the virtual plan were imported into the navigation project matching their position over the DICOM data, and the exported file was uploaded into the navigator. An optical stereoscopic camera was installed in the operating room, and a receiver was mounted on the patient's head, allowing to track the probe independent of head movements required by the operators. A point-based, anatomical-landmark, recognition method was used to perform patient-to-image registration.

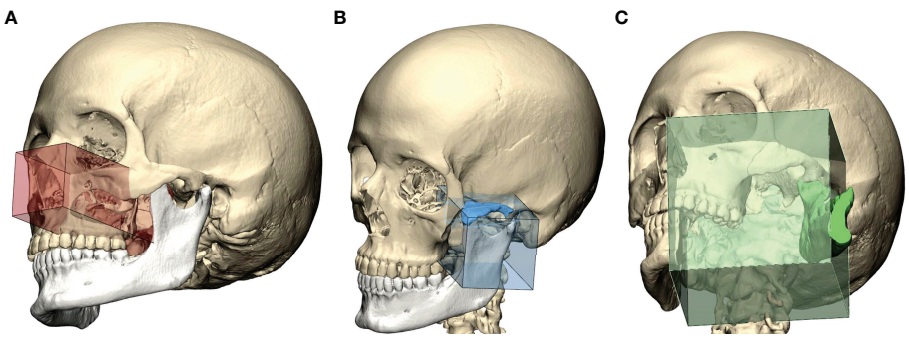

FIGURE 3 | Preoperative definition of access portals for the PMPF: **(A)** anterior maxillectomy exposes the PMPF from a frontal sight, just behind the maxillary tuberosity; **(B)** transzygomatic approach raising a bone flap of zygomatic arch exposes the infratemporal fossa; **(C)** the transmandibular corridor achieved using a mandibular swing approach widens the corridor to the inferior aspect of the PMPF.

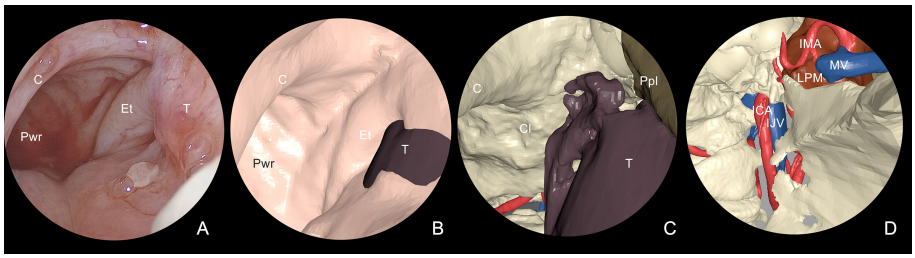

FIGURE 4 | Multilayer anatomical reconstruction applied to endoscopic view. **(A)** Overview of real endoscopic scenario; **(B)** virtual endoscopy shows the mucosal lining and the tumor bulging around the tubaric orifice area; **(C)** selective hiding of the mucosa reveals the underlying tumor in relation with skeletal structures and underlying vessels; **(D)** tumor hiding reveals the proximity with dangerous structures, including IMA and ICA. T, tumor; Et, eustachian tube; C, choana; Pwr, posterior wall of the rhinopharynx; Cl, clivus; Ppl, pterygoid plate; LPM, lateral pterygoid muscle; IMA, internal maxillary artery; ICA, internal carotid artery; MV, maxillary vein; IJV, internal jugular vein.

Both phases of endoscopic and open surgery were navigated according to the virtual surgical plan (**Figure 5**).

2.4.2 Surgery

Lesions arising in DFC were approached with both open and endoscopic approaches.

During transnasal endoscopy, the initial phase consisted of an inferior turbinectomy to increase space for surgical maneuvers, widening the corridor to the choanal opening. Subsequently, a medial maxillectomy was conducted extending from the antral foramen to the pterygomaxillary junction to trace the medial osteotomy line. In case of sphenoid sinus involvement, an additional phase in endoscopy was represented by widening the sinus overture using a high-speed rotating bur, scoping the intrasinusal space to reveal the underlying internal carotid artery (ICA) in its paraclival trait. Inferiorly, the emergence of the maxillary nerve and the vidian canal were systematically localized. Endoscopic osteotomies were then traced to yield mobilization of the tumor along inner bone walls; for instance, to mobilize tumors involving the PMPF, pterygoid plates were sectioned at their insertion onto the basisphenoid. As surgery progressed forward, all anatomical landmarks encountered during the virtual endoscopy were localized and related with the virtual plan (**Figure 6**).

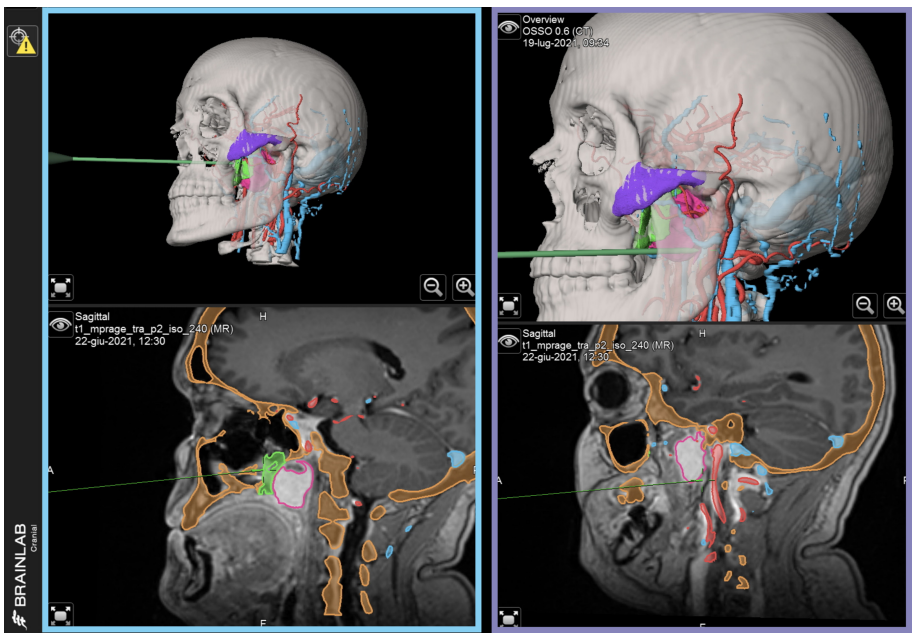

FIGURE 5 | Intraoperatively navigated sequences. STL files of virtual surgical planning are navigated during surgery, providing reference for each phase. Left, blue panel: navigation of transnasal endoscopy. Right, purple panel: navigation of transoral endoscopy.

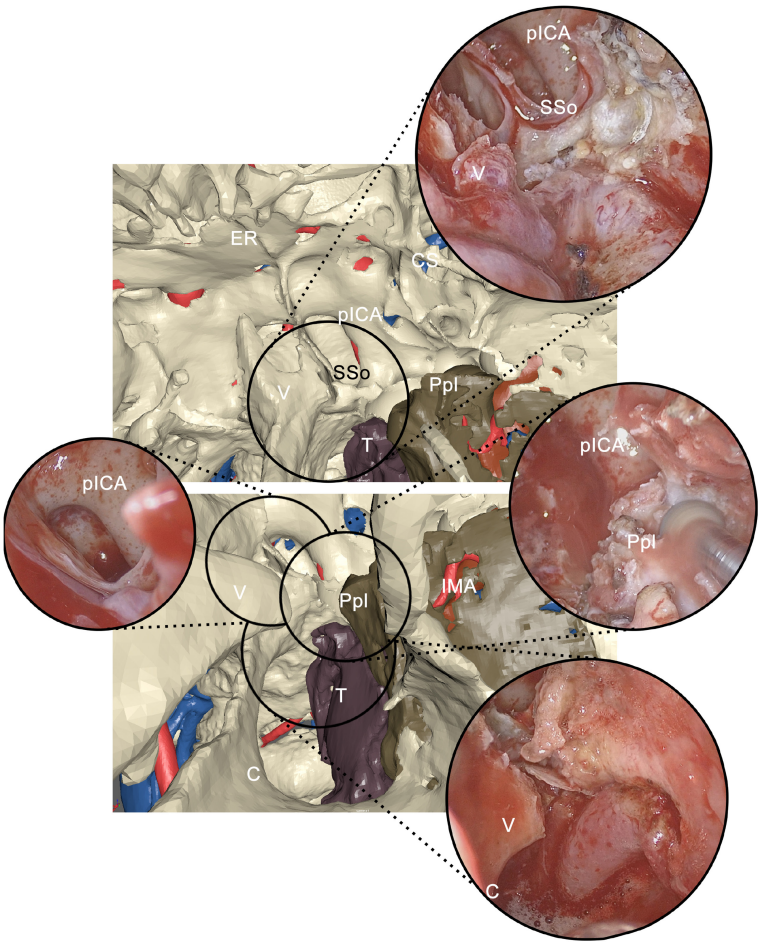

FIGURE 6 | Correlation between virtual endoscopy and real endoscopy using anatomical landmarks. Virtual endoscopy allows to anticipately examine the endoscopic view. pICA, paraclival internal carotid artery; SSo, sphenoid sinus opening; CS, cavernous sinus; ER, ethmoidal roof; V, vomer; Ppl, pterygoid plate; T, tumor; C, choana; IMA, internal maxillary artery.

Open surgery was necessary for en-bloc resection of malignant tumors, by connecting resection margins with osteotomies traced using endoscopic approaches. PMPF was exposed by creating a transmandibular open corridor through a mandibular swing approach and a parasymphyseal osteotomy using a lip-split incision continuing with a submandibular incision. To access IF, a transzygomatic approach through zygomatic arch osteotomies was used, based on a preauricular approach and subperiosteal elevation, paying attention not to injure the frontal branch of the facial nerve crossing the zygomatic arch. Moreover, an adjunctive corridor to the PMPF was achieved through the transmaxillary route, creating a straightforward path to the retromaxillary spaces. Endoscopy was also used to check in-depth anatomy in open approaches as well, especially in the transmaxillary portal, magnifying detail and facilitating exploration of narrow spaces (**Figure 7**).

3 RESULTS

All patients underwent successful application of the protocol. In three patients, it was not possible to simulate venous vessels due to the lack of MR venography.

In all patients, detailed virtual models for skeleton and mucosal lining were reconstructed from CT. Concerning the effectiveness of the protocol in detailing three-dimensional vasculature, a score of 0 was applied when it was impossible to reconstruct the vessel, 1 when reconstruction was inferior to 30% of its course, 2 when between 30% and 70%, and 3 when above 70%. In addition, an average quality score for reconstruction of each vessel was achieved by correlating individual scores with the maximum score. Major caliber vessels, including ICA, IJV, and ECA, were constantly identified and easily reconstructed in all patients, whereas inferior caliber vessels, including FA, IMA, STA, MMA, EJV, FV, RMV, and MV, were more subject to

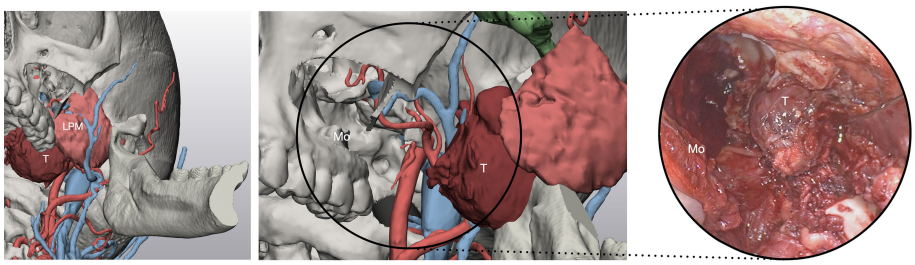

FIGURE 7 | Virtual surgical planning through the transmaxillary and transmandibular portal predicts the exposure of the tumor afforded by such approaches. T, tumor; LPM, lateral pterygoid muscle; Mo, maxillary opening.

variability depending on the quality of the MR. It was possible to reconstruct at least two masticatory muscles between the masseter, internal and external pterygoid, and parotid gland in 100% of cases using 3D-VIBE T1-w sequences. The quality of reconstruction for anatomical structures is reported for each case in **Table 2**.

All surgeries were conducted using virtual endoscopy as guidance, which included the following stable, always identifiable, landmarks: the head of inferior turbinate, head of middle turbinate, choanal opening, ethmoid roof, pterygoid plates, Eustachian tube opening, and sphenoid sinus opening were successfully represented in virtual models in all cases. Other structures showed more variability in virtual reconstruction, including bulla (57%), antral foramen (85%), vidian canal (14%), and parasellar imprint of ICA (71%).

Surgeries were successful in all cases, and lesions were subject to macroscopic radical resection, confirmed by clean margins at histology examination, except for one patient. Postoperative MR confirmed complete extirpation of PMPF and ITF in six cases (**Figure 8**), except for two patients, one case of anaplastic meningioma, whose extension in both the intracranial and extracranial space represented a limit for complete excision, and a case of adenoid cystic carcinoma, in which a residual disease was present in the posterior wall of PMPF at postoperative MR and was excised with a subsequent endoscopic procedure.

Patients undergoing surgery in the PMPF had trigeminal branches sacrificed owing to radical resection. Severe limitation of mouth opening developed in almost the totality of patients undergoing surgery in the PMPF/DMS owing to extensive muscle resection in the masticator space with subsequent scarring and radiotherapy.

The adoption of the advanced virtual reality protocol made possible to perform surgeries that in the past years were not feasible, due to the complexity of anatomical relationships with the tumor. Surgeons retrospectively reviewed the same number of cases operated for malignancies in DFC before the implementation of this protocol in a time span ranging from 2015 to 2018, as virtual-reality technologies were introduced in routine practice since 2019 at our institution. Compared with the group studied by applying the advanced computerized reconstruction, patients operated in the past showed a mean surgical time increase of 85 min (SD ± 47 min), due to phases related to tumor exposure and strategy-making, whereas in the group studied and operated using the computer-guided protocol, navigation helped to target the disease from the beginning of surgery in both endoscopic and open phases; therefore, the major

TABLE 2 | Quality scores defining the computerized reconstruction for vascular and muscular structures.

	1	2	3	4	5	6	7	Overall quality of virtual reconstruction (%)
Arteries								
ICA	3	3	3	3	3	3	3	100
ECA	3	3	2	3	3	2	3	90.5
IMA	2	3	2	1	1	2	3	66.7
STA	1	2	0	0	1	0	1	23.8
MMA	0	2	1	0	2	1	2	33.3
FA	1	2	0	1	1	1	2	38.1
Veins								
IJV	3	3	2	3	3	2	3	90.5
EJV	2	2	1	0	2	1	0	38.1
RMV	2	3	1	0	1	2	0	42.8
MV	2	2	2	0	2	2	0	47.6
FV	1	1	0	1	0	0	1	19.1
Masticatory muscles	3	3	3	2	3	3	2	90.5

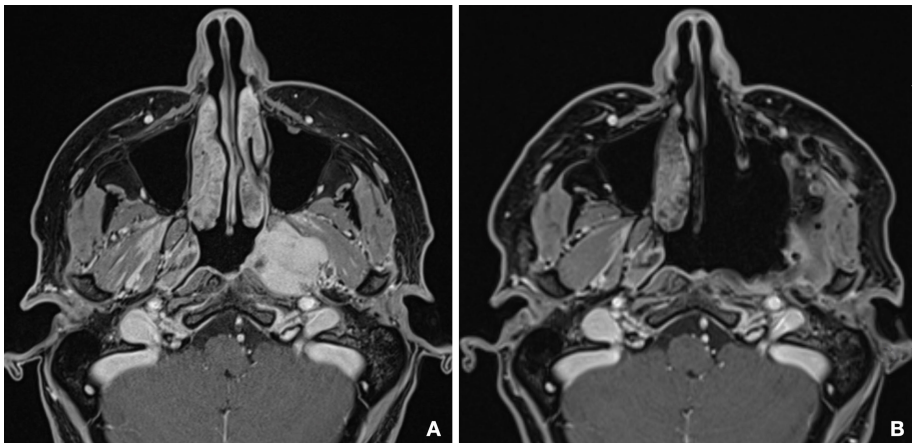

FIGURE 8 | Comparison between preoperative **(A)** and postoperative **(B)** MR shows the complete emptying of the PMPF and macroscopically radical excision of the tumor.

benefit in terms of surgical time reduction using the computerized workflow occurred in the approach phase. Additionally, in the group operated between 2015 and 2018, four patients had macroscopic disease residual, as localization of the tumor was only performed on raw imaging data and it was not possible to interactively check the intraoperative field in relation to a virtual project using navigation. Surgeons were asked to define their approach toward surgery both before and after the introduction of the advanced virtual anatomical reconstruction, and they unanimously reported a change in mindset, with an increase in their preoperative understanding of the patient's anatomy and diminished frequency of intraoperative imaging consultation, due to deeper understanding of the case and availability of navigation.

4 DISCUSSION

Approaches to the DFC, including the PMPF, the DMS, and the ITF, represent a major challenge even for the expert surgeon, due to narrow spaces in which vulnerable vascular and nervous structures are enclosed within complex-shaped bone walls. Malignancies primarily involving these spaces or invading them as a consequence of nearby disease require difficult, multistage surgeries, in which the risk of injuring critical structures is considerable; therefore, conceptualizing in detail the patient's anatomy before surgery is a fundamental prerequisite.

Conventional imaging techniques can define the localization of disease but fail to provide a three-dimensional representation of anatomy, especially for vascular structures, which have a tortuous course that intersects multiple spatial planes. Volume rendering, today available for many medical image software, provides accurate volumetric visualization based on DICOM data by placing specific thresholds, which succeeds in characterizing bone but does not represent soft tissues. Most of all, volume rendering-based approaches do not allow to selectively separate a specific anatomical structure and fail to provide a geometry file, which can undergo surgical planning procedures, including osteotomies and virtual endoscopy. As a consequence, unsegmented structures from raw DICOM data cannot be selectively shown or hidden, making it impossible to differentiate between venous and arterial vessels. Literature on this topic is limited, reporting only few examples of virtual anatomical reconstruction of structures through segmentation and 3D model creation. For instance, in 2021, Yang et al. interestingly described a CT-MRI image fusion-based technique to characterize tumors arising between middle cranial and infratemporal fossa: yet they managed to isolate different anatomical structures, and their reconstruction was limited to the IJV and ICA axes, with an exceedingly approximated representation of the tumor (4). A more detailed, although simplified, anatomical model to study the PPF is described by Javan and colleagues (5): the Authors designed an interactively explorable model of the PPF with attention on the limits of this space and the presence of neurovascular bundles; however, this model failed to provide a trustful representation of the actual anatomy, as it is based on simplified visualization and isolated PPF inspection, regardless of contiguous structures. Another considerable limitation of this study is that both vessels and nerves were modeled independent of their conformation on the medical images, and this step might cause inaccuracies and omissions of anatomical variations. In this study, we have shown how a very detailed vasculature study can be performed by segmenting both arterial and venous vessels directly from the patient's imaging, enabling the virtual models to reproduce as faithfully as possible the real anatomy of a patient. Compared to the traditional two-dimensional slice-by-slice identification of vessels, three-dimensional evaluation is more immediate, allowing to inspect vessels along their spatial course, including the relationship with nearby structures and resection margins.

Three-dimensional vasculature reconstruction is also important for decision making, as it can clearly represent situations in which major caliber vessels, including ECA and IJV, lie within the tumor and have to be sacrificed, allowing surgeons to anticipately know that vessel ligation can be performed, decreasing the risk of significant bleeding.

Actually, our protocol is not able to solve the issue related to cranial nerve segmentation, as nerve tracking for calibers like cranial nerves is very limited with current imaging technology. Some attempts have been made to develop imaging acquisition protocols allowing to identify tiny nervous structures in these anatomical regions: Bratbak et al. (6) described the successful identification of the pterygopalatine ganglion and the vidian canal on MR using a 3T magnet; however, not all centers own a 3T MR machine, and the sequence is not specific for nerve tracing, as for instance TOF sequences are for arteries, with the result of a very difficult and possibly inaccurate segmentation. Therefore, current imaging technology fails to provide nerve images suitable for segmentation. As a consequence, the spatial course of small caliber nerves, like the facial nerve, is still mostly deductive, according to the position of their emergence foramina, which nevertheless require a high-resolution CT scan. In particular, while the foramen rotundum and foramen ovale can be readily visualizable in almost all studies, the vidian canal, which was shown to be an important landmark to identify the anterior genu of the petrous ICA (7), should be carefully reconstructed, as shown by Fu et al. (8). Other studies focused on the utility of the infraorbital nerve as a landmark for the PMPF, hence the importance to find a reliable method to trace the nerve course (9).

As mentioned, the importance of virtual models is also related to the possibility to inspect them, simulating the same views during surgery. Concerning open surgery of the PMPF and DMS, this represents a consistent advantage, allowing to define the most adequate accesses directly on the virtual models, thus bringing the patient to surgery with a clear project in mind. By testing accesses on virtual models, the surgeon is able to define which surgical exposure is optimal for each patient, allowing to individualize surgical approaches and maximizing their effectiveness. For instance, Fahmy and colleagues conducted a study on surgical approaches by comparing exposure obtained through both open and endoscopic approaches and measured the volume of visualization yielded for each case (10). Their study was performed on two-dimensional CT data and not on virtually reconstructed segmented structures, significantly limiting the possibility to selectively manipulate objects, visualize vascularization, and perform osteotomies. Exploration of patient-specific virtual models plays a crucial role especially for endoscopic approaches, allowing to preoperatively define complex trajectories and to highlight anatomical landmarks by providing a vision totally superimposable to the real endoscopic field. The same Authors previously described a protocol to perform virtual endoscopy in orbital surgery, but this workflow is applicable to any region of the craniofacial skeleton (11). Actually, a simplified version of this protocol and suitable for the sphenoid sinus was described by Wang and colleagues (12), although the representation of critical adjacent structures, such as the ICA and the sphenopalatine artery, was roughly drafted over a volume-rendered version of the CT; conversely, our multilayer segmentation protocol allows to separately reconstruct bone, mucosa, muscles, vasculature, and tumor and to navigate between them. Virtual reality allows to identify and simulate portals which would not be visible without performing osteotomies: for instance, the incremental maxillectomy directed over the anterior maxillary wall creates an adjunctive corridor to frontally approach the PMPF (13), while a retromaxillary approach raising a zygomatic arch flap favorably exposes the infratemporal fossa (14). The possibility to simulate an outward rotation of the hemimandible with a fulcrum over the condyle allows to anticipately visualize the exposure of PMPF from an inferior sight (15). Specific transcutaneous approaches, including the Weber-Ferguson and jugal incision described by Jager (16), can be designed directly on virtual soft tissue models to aid in the choice of the most appropriate incision line to yield an exposure of the skeletal plane. Therefore, virtual planning allows to entirely customize surgical accesses, tailoring the most suitable corridor to each individual localization of disease, and it is not limited to the possibilities described in our series, but it may include in addition several transfacial swing approaches, which can be combined with endoscopy at any stage (17). Therefore, our experience is that surgeons enter the operating room having already performed a number of simulations, with a well-defined idea in mind on which accesses they should create and which sequences demolition should follow.

In this regard, especially when midface osteotomies are planned, navigational guidance allows to check the optimal tracing of bone cuts. In addition, navigation performed over virtual 3D models allows to carefully check resection margins around the tumor borders and to trace osteotomies exactly as planned (18), a consistent advantage especially for endoscopic procedures, which are not blindly performed but follow the correct path suggested by the navigator. Therefore, although navigation has been scarcely studied in the PMPF/DMS, it represents a valuable aid for surgery in the deep spaces of the face (19), especially when implemented in the setting of a reliable three-dimensional anatomical reconstruction, where it allows to interactively move within the simulated anatomy.

Virtual endoscopy can be simulated at any stage of the surgical planning, even in open surgery allowing to represent multiple scenarios which replicate the endoscopic vision encountered by the surgeon. In this respect, virtual endoscopy might also be useful to anticipately visualize the results of endoscopic exploration, establishing its correct timing within the surgical sequence and which vision correlates with a specific phase, overall improving the orientation of the surgeon.

Additionally, the whole animated sequence provides an immediate vision that, beyond the surgical purpose, is useful to convey the operative workflow to students and residents, which can start to hypothesize treatment plans in a safe environment, which takes into account the underlying anatomical complexity.

5 CONCLUSIONS

Despite sampling a limited number of patients, our experience suggests that the modern surgeon approaching such areas should rely upon all available instrumentation to accurately study anatomy and define a personalized treatment strategy. Virtual examination of such anatomical regions not just aids the preoperative study of patients but also provides guidance also during surgery thanks to surgical navigation and virtual endoscopy. Especially for malignancies, in which resection extends to remove the macroscopic residual of disease, the prompt identification of structures contributes to operate more safely and with an increased awareness.

DATA AVAILABILITY STATEMENT

The raw data supporting the conclusions of this article will be made available by the authors, without undue reservation.

ETHICS STATEMENT

The studies involving human participants were reviewed and approved by the Institutional Review Board, University of Udine, # IRB_45_2020. The patients/participants provided their written informed consent to participate in this study.

AUTHOR CONTRIBUTIONS

AT designed the study, performed the virtual endoscopy, created the virtual models and 3D-printed models, and wrote the full paper. DB acquired the radiologic images with required protocols and wrote the imaging part of this paper. FC made the endoscopic surgery. SS read the manuscript. MR coordinated the research team and approved the final manuscript before submission. All authors contributed to the article and approved the submitted version.

REFERENCES

1. Xie L, Huang W, Wang J, Zhou Y, Chen J, Chen X. Modified Maxillary-Swing Approach for Resection of Primary Malignancies in the Pterygopalatine Fossa. *Front Oncol* (2020) 10:530381. doi: 10.3389/fonc.2020.530381
2. Anand SM, Frenkiel S, Le BQH, Glikstein R. Virtual Endoscopy: Our Next Major Investigative Modality? *J Otolaryngol - Head Neck Surg = Le J D'oto Rhino Laryngologie Et Chirurgie Cervico Faciale* (2009) 38:642–5. doi: 10.2310/7070.2009.080227
3. Karkas A, Zimmer LA, Theodosopoulos PV, Keller JT, Prades J-M. Endonasal Endoscopic Approach to the Pterygopalatine and Infratemporal Fossae. *Eur Ann Otorhinolaryngol Head Neck Dis* (2020) 138(5):391–5. doi: 10.1016/j.anorl.2020.12.009
4. Yang R, Lu H, Wang Y, Peng X, Mao C, Yi Z, et al. CT-MRI Image Fusion-Based Computer-Assisted Navigation Management of Communicative Tumors Involved the Infratemporal-Middle Cranial Fossa. *J Neurol Surg B Skull Base* (2021) 82:e321–9. doi: 10.1055/s-0040-1701603
5. Javan R, Rao A, Jeun BS, Herur-Raman A, Singh N, Heidari P. From CT to 3D Printed Models, Serious Gaming, and Virtual Reality: Framework for Educational 3d Visualization of Complex Anatomical Spaces From Within—the Pterygopalatine Fossa. *J Digit Imaging* (2020) 33:776–91. doi: 10.1007/s10278-019-00315-y
6. Bratbak DF, Folvik M, Nordgård S, Stovner LJ, Dodick DW, Matharu M, et al. Depicting the Pterygopalatine Ganglion on 3 Tesla Magnetic Resonance Images. *Surg Radiol Anat* (2018) 40:689–95. doi: 10.1007/s00276-017-1960-6
7. Kassam AB, Vescan AD, Carrau RL, Prevedello DM, Gardner P, Mintz AH, et al. Expanded Endonasal Approach: Vidian Canal as a Landmark to the Petrous Internal Carotid Artery: Technical Note. *J Neurosurg* (2008) 108:177–83. doi: 10.3171/JNS/2008/108/01/0177
8. Fu Z, Chen Y, Jiang W, Yang S, Zhang J, Zhang W, et al. The Anatomical and Clinical Details of the Pterygoid Canal: A Three-Dimensional Reconstructive Virtual Anatomic Evaluation Based on CT. *Surg Radiol Anat* (2014) 36:181–8. doi: 10.1007/s00276-013-1161-x
9. Elhadi AM, Zaidi HA, Yagmurlu K, Ahmed S, Rhoton AL, Nakaji P, et al. Infraorbital Nerve: A Surgically Relevant Landmark for the Pterygopalatine Fossa, Cavernous Sinus, and Anterolateral Skull Base in Endoscopic Transmaxillary Approaches. *JNS* (2016) 125:1460–8. doi: 10.3171/2015.9.JNS151099
10. Fahmy CE, Carrau R, Kirsch C, Meeks D, de Lara D, Solares CA, et al. Volumetric Analysis of Endoscopic and Traditional Surgical Approaches to the Infratemporal Fossa: Volumetric Analysis of Infratemporal Fossa. *Laryngoscope* (2014) 124:1090–6. doi: 10.1002/lary.24428
11. Tel A, Arboit L, Sembronio S, Costa F, Nocini R, Robiony M. The Transantral Endoscopic Approach: A Portal for Masses of the Inferior Orbit—Improving Surgeons' Experience Through Virtual Endoscopy and Augmented Reality. *Front Surg* (2021) 8:715262. doi: 10.3389/fsurg.2021.715262
12. Wang S-S, Xue L, Jing J-J, Wang R-M. Virtual Reality Surgical Anatomy of the Sphenoid Sinus and Adjacent Structures by the Transnasal Approach. *J Cranio Maxillofacial Surg* (2012) 40:494–9. doi: 10.1016/j.jcms.2011.08.008
13. Upadhyay S, Dolci R, Buohliqah L, Fiore M, Filho L, Prevedello D, et al. Effect of Incremental Endoscopic Maxillectomy on Surgical Exposure of the Pterygopalatine and Infratemporal Fossae. *J Neurol Surg B* (2015) 77:066–74. doi: 10.1055/s-0035-1564057
14. Woodford R, Chaudhary N, Wolf A, Lownie S, Armstrong JE. A Modified Retromaxillary Approach to the Infratemporal Fossa: Three Case Studies. *J Oral Maxillofacial Surg* (2015) 73:769–80. doi: 10.1016/j.joms.2014.10.025
15. Anehosur V, Bindal M, Kumar N, Shetty C. Mandibulotomy Approach for Resection of Maxillary Tumours: A Clinical Review. *J Maxillofacial Oral Surg* (2019) 18:360–5. doi: 10.1007/s12663-018-1164-6
16. Brusati R, Raffaini M, Bozzetti A. Jaeger's Jugal Extended Incision to Approach the Pterygomaxillary Region. *Int J Oral Maxillofacial Surg* (1989) 18:298–301. doi: 10.1016/S0901-5027(89)80099-2
17. Moreira-Gonzalez A, Pieper DR, Cambra JB, Simman R, Jackson IT. Skull Base Tumors: A Comprehensive Review of Transfacial Swing Osteotomy Approaches. *Plast Reconstructive Surg* (2005) 115:711–20. doi: 10.1097/01.PRS.0000152437.71574.4F
18. Tel A, Bagatto D, Tuniz F, Sembronio S, Costa F, D'Agostini S, et al. The Evolution of Craniofacial Resection: A New Workflow for Virtual Planning in Complex Craniofacial Procedures. *J Cranio Maxillofacial Surg* (2019) 47:1475–83. doi: 10.1016/j.jcms.2019.06.016
19. Liu T, Sun Y, Li J, Bai W. Navigation-Assisted Treatment of Giant Cysts in the Pterygopalatine Fossa With Endoscopy Method. *J Craniofacial Surg* (2020) 31:e137–9. doi: 10.1097/SCS.0000000000006073

Conflict of Interest: The authors declare that the research was conducted in the absence of any commercial or financial relationships that could be construed as a potential conflict of interest.

this article, or claim that may be made by its manufacturer, is not guaranteed or endorsed by the publisher.

frontiers | Frontiers in Oncology

SYSTEMATIC REVIEW
published: 16 June 2022
doi: 10.3389/fonc.2022.918580

Technical and Diagnostic Issues in Whole Slide Imaging Published Validation Studies

Paola Chiara Rizzo[1], Ilaria Girolami[2], Stefano Marletta[1,3], Liron Pantanowitz[4], Pietro Antonini[1], Matteo Brunelli[1], Nicola Santonicco[1], Paola Vacca[5], Nicola Tumino[5], Lorenzo Moretta[5], Anil Parwani[6], Swati Satturwar[6], Albino Eccher[7] and Enrico Munari[8]*

[1] Department of Pathology and Diagnostics and Public Health, Section of Pathology, University Hospital of Verona, Verona, Italy, [2] Division of Pathology, Central Hospital, Bolzano, Italy, [3] Department of Pathology, Pederzoli Hospital, Peschiera del Garda, Italy, [4] Department of Pathology & Clinical Labs, University of Michigan, Ann Arbor, MI, United States, [5] Bambino Gesù Children's Hospital, Istituto di Ricovero e Cura a Carattere Scientifico (IRCCS), Rome, Italy, [6] Department of Pathology, Ohio State University Medical Center, Columbus, OH, United States, [7] Department of Pathology and Diagnostics, University and Hospital Trust of Verona, Verona, Italy, [8] Department of Molecular and Translational Medicine, University of Brescia, Brescia, Italy

OPEN ACCESS

Edited by:
Konstanty Korski, Roche, Switzerland

Reviewed by:
Danielle Maracaja, Wake Forest University, United States
Aidan D. Meade, Technological University Dublin, Ireland

***Correspondence:**
Albino Eccher
albino.eccher@aovr.veneto.it

Specialty section:
This article was submitted to Surgical Oncology, a section of the journal Frontiers in Oncology

Received: *12 April 2022*
Accepted: *24 May 2022*
Published: *16 June 2022*

Citation:
Rizzo PC, Girolami I, Marletta S, Pantanowitz L, Antonini P, Brunelli M, Santonicco N, Vacca P, Tumino N, Moretta L, Parwani A, Satturwar S, Eccher A and Munari E (2022) Technical and Diagnostic Issues in Whole Slide Imaging Published Validation Studies. Front. Oncol. 12:918580. doi: 10.3389/fonc.2022.918580

Objective: Digital pathology with whole-slide imaging (WSI) has many potential clinical and non-clinical applications. In the past two decades, despite significant advances in WSI technology adoption remains slow for primary diagnosis. The aim of this study was to identify common pitfalls of WSI reported in validation studies and offer measures to overcome these challenges.

Methods: A systematic search was conducted in the electronic databases Pubmed-MEDLINE and Embase. Inclusion criteria were all validation studies designed to evaluate the feasibility of WSI for diagnostic clinical use in pathology. Technical and diagnostic problems encountered with WSI in these studies were recorded.

Results: A total of 45 studies were identified in which technical issues were reported in 15 (33%), diagnostic issues in 8 (18%), and 22 (49%) reported both. Key technical problems encompassed slide scan failure, prolonged time for pathologists to review cases, and a need for higher image resolution. Diagnostic challenges encountered were concerned with grading dysplasia, reliable assessment of mitoses, identification of microorganisms, and clearly defining the invasive front of tumors.

Conclusion: Despite technical advances with WSI technology, some critical concerns remain that need to be addressed to ensure trustworthy clinical diagnostic use. More focus on the quality of the pre-scanning phase and training of pathologists could help reduce the negative impact of WSI technical difficulties. WSI also seems to exacerbate specific diagnostic tasks that are already challenging among pathologists even when examining glass slides with conventional light microscopy.

Keywords: whole slide imaging, digital pathology, validation study, systematic (literature) reviews, artificial intelligence

INTRODUCTION

Virtual microscopy (VM) using digital whole slide imaging (WSI) is a technology by which glass slides in pathology are digitally scanned at high-resolution for viewing on a computer screen. Ever since WSI scanners first became commercially available around two decades ago, progress in the technology of these devices has continually improved their image resolution, image quality, slide throughput, end-user software tools, and integration with laboratory information systems (1). Applications of WSI for clinical (e.g. telepathology, quantitative image analysis) and non-clinical (e.g. education and research) have markedly increased (2–6). Ample literature has been published demonstrating excellent concordance between utilizing WSI versus glass slides with traditional light microscopy (LM) to render diagnoses (7, 8). Nevertheless prior to implementing WSI for diagnostic use in clinical practice, several associations have recommended that such technology be validated by pathology laboratories for their intended use (9). Recently, the College of American Pathologists (CAP) updated their guideline providing recommendations for validating WSI for primary diagnosis (10). The validation process should "stress test" the WSI system in the appropriate clinical environment in order to assess that it allows pathologists to accurately diagnose cases, at least at the same level of accuracy as LM, and to identify and control for potential interfering artifacts or technological risks that could impair patient safety (10, 11).

Whilst published validation studies have largely focused on the success of WSI for specific clinical use cases, some of the "negative issues" that were encountered including technical failures or particular diagnostic difficulties were often under-reported. Furthermore, only few systematic analyses on this topic devoted to the tribulations of employing WSI in clinical practice have been performed. In the literature review undertaken by Goacher et al. from 2017, for example, the authors reported that there was in fact a slower time to diagnosis when using WSI compared with LM (7). The aim of this study was to systematically review the literature of published validation studies that evaluated the feasibility of WSI for diagnostic clinical use in pathology, recording and subsequently analyzing any technical and/or diagnostic problems encountered.

MATERIAL AND METHODS

A systematic review of the literature was conducted according to the guideline for Preferred Reporting Items for a Systematic Review and Meta-Analysis (12).

Electronic searches were carried out in the databases PubMed-MEDLINE and Embase until the 5th of December, 2021. No study type filters were used nor language restriction applied. References listed in all identified studies were also hand-searched to retrieve potential additional studies. Initial screening of articles by title/abstract was performed with the aid of the online systematic review web-app QRCI (13). Eligibility of published studies was determined independently by two reviewers with disagreement resolved through consensus. Inclusion criteria included the details of a validation study with a series of surgical pathology cases assessed with WSI and with LM, not only reporting concordance data but also noting any negative issues encountered during the validation process. Studies represented only by abstracts were excluded, as were reviews and published letters to the editor with no original data. Data extracted included: authors, year published, country of study, number and type of cases selected, critical issues reported divided ac-cording to issues pertaining to diagnostic and technical problems. Specific technical problems searched for included slide scan failures, delayed scan time, and difficulties related to viewing and navigating digital slides.

RESULTS

The search strategy identified a total of 1560 records, with only 45 suitable articles finally included in our analysis (**Figure 1**). Publication dates ranged from 2007 to 2021. Twenty (45%) of the included studies were from North American countries, nineteen (42%) were from European countries and six (13%) were from non-European and non-North American countries. In more than half of the included studies (n=24, 57%) the participating pathologists were experienced in digital pathology. The length of the washout period between LM and WSI diagnosis ranged from 7 days to 2 years, but 13 studies did not report any washout time. The number of cases in the included studies varied from 23 to 3222. Twenty-two studies included cases from various pathology subspecialties, while 23 selected a specific diagnostic field. The majority of Authors used Aperio scanners (n=18, 40%), followed by Ventana scanners (n=6, 13%), NanoZoomer (n=5, 11%), MIRAMAX (n=3, 7%), Philips (n=3, 7%), Pannoramic (n=2, 4%), DHistech (n=2, 4%), NAVIGO (n=1, 3%), Grandium Ocus (n=1, 1%), and OMYX (n=1, 3%). Twelve of the viewer systems used in these studies were APERIO (26%), 5 Ventana (11%), 3 Leica (7%), 3 DHistech (7%), 3 Philips (7%), 2 PathXL (4%), 2 Pannoramic (4%), 1 OMYX (3%), 1 Grandium Ocus (3%), and 1 CaloPix (3%). Only one study tested the use of tablets, specifically the iPad (14). Only one study tested the use of tablets, specifically the iPad (14).

In order to summarize the pitfalls documented in the various validation studies, we categorized all the discordances into two main groups: technical issues and diagnostic issues (**Table 1**).

Technical Issues

Sixteen (36%) studies reported about technical issues only, eight (18%) reported on diagnostic issues only, and 21 (46%) reported both on technical and diagnostic issue. Among the technical issues described, nine studies (20%) reported failures in scanning glass slides, 19 studies (42%) considered WSI more time consuming than LM, and nine studies (20%) reported specifically the need for higher magnification (better image resolution) with WSI to more easily view and navigate cases. Other technical issues reported were: lack of focus (n=8, 18%), suboptimal navigation tools (n=2, 4%), need for polarization

TABLE 1 | Characteristics of technical and diagnostic issues of the included studies.

Technical issue	n (%)	Diagnostic issue	n (%)
Timing (scanning, viewing)	19 (42%)	Grade of dysplasia	8 (18%)
Scanning failure	9 (20%)	Mitotic count	6 (13%)
Need for higher magnification	9 (20%)	Misinterpretation of diagnosis	4 (9%)
Storage	7 (15%)	Lack of confidence	3 (6%)
Lack of multiple focus planes	8 (18%)	Identification of microorganisms	3 (6%)
Color inaccuracy	3 (6%)	Legal issues	2 (4%)
Difficulty using mouse	2 (4%)	Misinterpretation of inflammatory cells	2 (4%)
Need for polarization	2 (4%)	Identification of tumor invasion	2 (4%)
Underexposure of images	1 (2%)	Misinterpretation of fibrosis	1 (2%)
Server	1 (2%)	Misinterpretation of intraepithelial lymphocytes	1 (2%)
Workstation ergonomics	1 (2%)	Misinterpretation of calcification and focal atypia	1 (2%)
Presence of artifacts	1 (2%)	Overestimation of blasts' count	1 (2%)

(n=2, 4%), and lack of adequate color fidelity for special stain or immunohistochemical staining (n=3, 7%). In addition, some validation studies (n=7, 15%) reported difficulty related to image storage.

Diagnostic Issues

Concerning diagnostic issues when using WSI, in eight studies (18%) grading of dysplasia represented the most common problem encountered. Furthermore, six (13%) studies reported challenges in assessing mitotic count, four (9%) studies reported general misdiagnosis, while three (7%) studies reported discordant diagnoses related to the identification of microorganisms. In three (7%) studies the authors mentioned there was lack of diagnostic confidence, and in two (4%) that pathologists experienced difficulty interpreting the invasive component of tumors.

The characteristics of each of the included studies are extensively detailed in **Supplementary Table S1**.

DISCUSSION

Digital pathology has been increasingly deployed in many institutions (15, 16). Nevertheless, problems encountered when using WSI for routine pathology diagnosis still remain. A critical appraisal of such issues is important to understand and hopefully re-solve. Our systematic review identified 45 articles that specifically reported problems experienced with WSI usage for primary diagnosis during a validation process.

As expected, technical issues when validating WSI were the most frequently reported. The most commonly mentioned technical issue involved scan failures with the need for re-scan slides and the consequent prolonging of turn-around-time (TAT). When combined with the reported experience by participating pathologists that it took them longer to evaluate digital slides in order to establish a diagnosis, switching to WSI for primary diagnosis has the potential to delay TAT. This drawback would need to be offset by some of the other workflow benefits of digital pathology such as decreased time for slide distribution, quicker archival image retrieval, in addition to ensuring faster network connections, better workstations and improved viewing software.

Newer scanners with higher throughput capacity and reduced image acquisition time have further helped overcome TAT issues. The quality of pre-imaging factors can also help re-duce the aforementioned limitation of delayed TAT. For example, striving to produce uniform histological sections without folds and clean, dry slides without artifacts such as air bubbles are important to reduce the probability of scan failures. Such pre-imaging measures are especially important for the digitization of cytology slides (17, 18), where thick smears, three dimensional cell groups and obscuring material make it harder for scanners without z-stacking capability to achieve optimal focus. For some studies, the technical difficulty noted when viewing digital slides was related to the monitor and input device (specifically, computer mouse) used. Hanna et al. (19) suggested trying different input devices instead of a conventional mouse to circumvent problems with digital slide navigation. Similarly, Brunelli et al. (14) tested the use of a tablet to improve WSI navigation. Although a validation study should not suffice for official training of end-users, spending more time training pathologists to better use WSI and allowing them to become more familiar with this technology can certainly improve their ease with utilizing WSI. Alassiri et al. (20) showed that at the beginning of their validation study participating pathologists were slow-er in assessing cases with WSI, but by the end of their validation process they experienced no notable time difference when reading cases with either WSI or LM modalities.

The other important category of shortcomings with WSI that emerged in published validation studies was concerned with performing certain challenging diagnostic tasks. The most frequently reported were misinterpretation regarding grading of dysplasia, in a variety of settings including gastrointestinal biopsies (21–23) and melanocytes atypia (24). Such errors were related to both downgrading or upgrading lesions (25–30). Apart from the cited discordance related to interpreting gastrointestinal dysplasia, other challenging diagnostic areas that were reported in validation studies included urothelial dysplasia, cervical dysplasia, grading of ovarian and endometrial cancers, *in situ* lesions of the breast, and brain pathology. However, in most studies, especially the most recent publications, overall diagnostic concordance was above the cutoff of 95% recommended in the CAP guidelines for WSI vali-dation, and discordances with a potential impact on clinical management were often lower than 3% (8, 10, 21, 29–31).

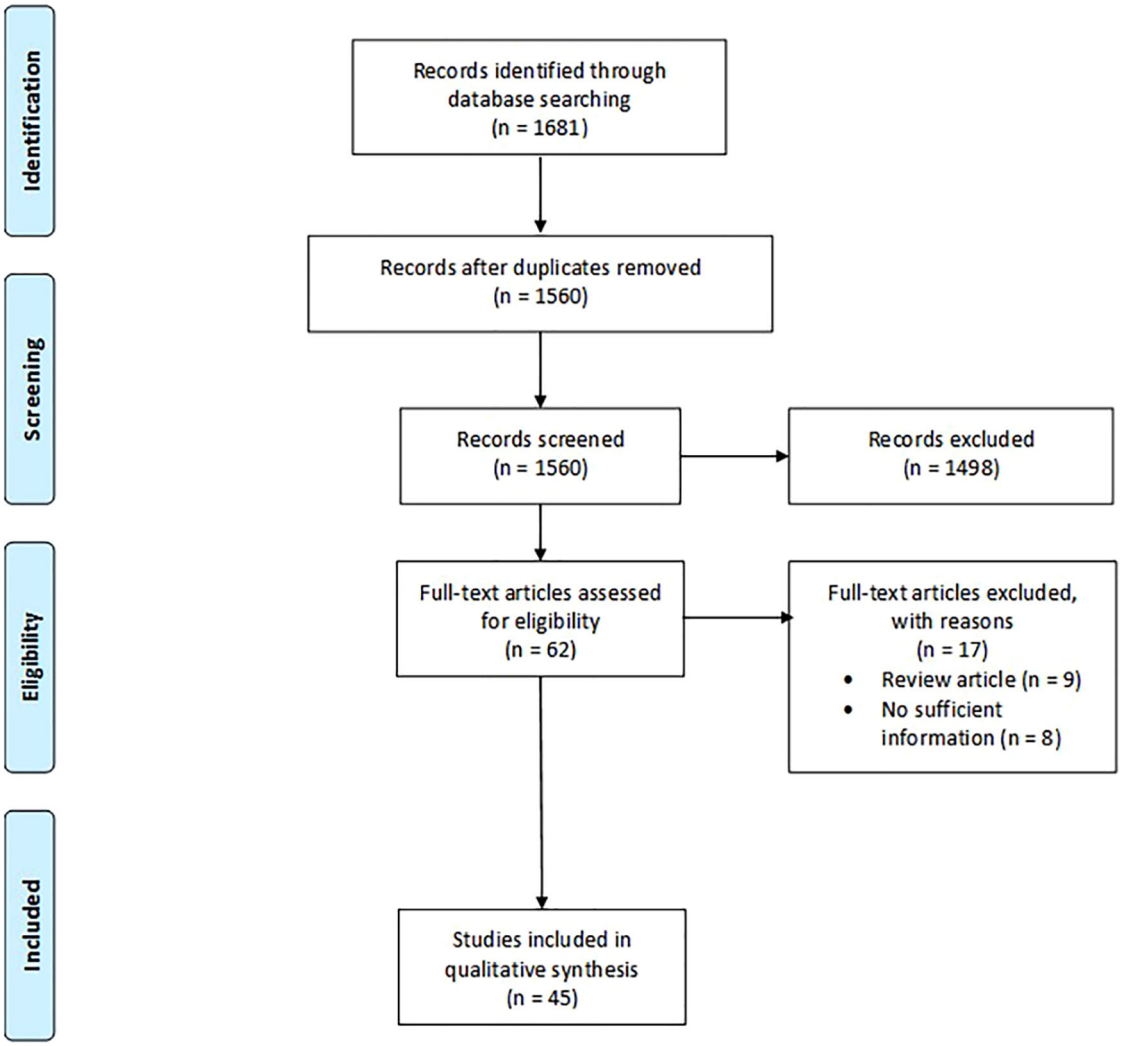

FIGURE 1 | Search flow diagram. The diagram was designed according to the template of the PRISMA flow diagram from Page et al. (12) available at the PRISMA website (www.prismastatement.org).

Another frequently reported area of discordance, as well source of dissatisfaction among pathologists, when using WSI relates to counting mitoses, such as is required in grading meningiomas (32) or breast carcinoma (33, 34) or when diagnosing malignancy in a melanocytic lesion (35). Other less frequently reported. but still relevant, reported diagnostic difficulties with WSI were the detection of microorganisms (19), discriminating single inflammatory cell types in dermatopathology and hematopathology (24, 36–38), assessment of tumor budding and tumor pattern of invasion in colon cancer (39), and overestimation of steatosis and fibrosis in liver cases (40). In general, pathologists reported lower diagnostic confidence when signing out with WSI. Similar considerations have also been observed in the setting of pediatric pathology (41), where WSI showed to be at least as reliable as LM, fully satisfying the CAP guidelines. Even in this setting the few reported discrepancies concerned subtle morphological features, such as identification of Candida spores and hypha, likely linked to the difficult of the case rather than to the classic or digital method of evaluation of the slides. Many of these diagnostic concerns are being addressed with improvements in WSI technology (e.g. incorporating higher resolution cameras and objectives into scanners) and leveraging artificial intelligence (AI) to apply algorithms for specific (narrow) tasks such as counting mitoses, screening slides for microorganisms, and standardizing the grading of dysplasia or cancer. Development and deployment of these technologies are foreseeably going to increase in the near future, further allowing pathologists to benefit from digital supports to proficiently reach proper histological diagnoses for both adults and pediatric patients.

Additional collateral problems were also reported in published validation studies, which were mainly of a technical

and institution's organizational nature. Some authors reported problems related to the storage of WSI cases, given the huge size of WSI files and consequent high demand this has on information technology (IT) infra-structure for image management (31, 37, 42, 43). Lastly, Ordi et al. (44) and Al-Janabi et al. (43) reported about the cultural barrier of pathologists, including their concerns about legal is-sues and resistant mindset to accept WSI over more familiar LM for routine primary diagnosis. However, since then we have witnessed increased regulatory approval of WSI solutions, such as clearances issued by the Food and Drug Administration (FDA) in the USA (45, 46) for primary diagnosis which has helped increase overall confidence in the adoption of WSI. Moreover, with the rapid shift experienced towards using digital pathology to permit re-mote signing-out during the Coronavirus Disease 2019 (COVID-19) pandemic many pre-pandemic skeptics have since been convinced about the value of digital pathology (47).

CONCLUSIONS

Digital pathology with WSI is nowadays a reality in many laboratories, but there are still some negative aspects that may restrain an even wider spread adoption of WSI. When reviewing the literature for validation studies highlighting these conflicting aspects, we found both some technical and diagnostic critical issues still remain of concern. The majority of technical points could be reasonably overcome by further improvement of technology and dedicated training of pathologists. Likewise, the diagnostic issues are mainly represented by subtle tasks which yield per se an unsatisfactory reproducibility among pathologists with conventional glass slides as well. In the near future, the development of dedicated and more objective AI tools could be of aid to further support pathologists in reducing the gap between LM and WSI in order to increase the efficiency of the diagnostic process and ultimately improve patients' management and care.

DATA AVAILABILITY STATEMENT

The original contributions presented in the study are included in the article/**Supplementary Material**. Further inquiries can be directed to the corresponding author.

AUTHOR CONTRIBUTIONS

Conceptualization, IG, SM, LP and AE. Data curation, PR, IG, SM and AE. Formal analysis, PR, IG and SM. Methodology, IG, LP and AE. Project administration, AE and EM. Supervision, AE and EM. Validation, PA, MB, NS, PV, NT, LM, and EM. Writing – original draft, PRC, IG and SM. Writing – review & editing, PA, MB, NS, PV, NT, LM, AP, SS, AE and EM. All authors contributed to the article and approved the submitted version.

FUNDING

This work was supported by grants from Associazione Italiana Ricerca sul Cancro (AIRC) Investigator Grant ID 19920 (LM); Special Program Metastatic disease: the key unmet need in oncology 5 per mille 2018, ID 21147 (LM).

SUPPLEMENTARY MATERIAL

The Supplementary Material for this article can be found online at: https://www.frontiersin.org/articles/10.3389/fonc.2022.918580/full#supplementary-material

REFERENCES

1. Hanna MG, Reuter VE, Samboy J, England C, Corsale L, Fine SW, et al. Implementation of Digital Pathology Offers Clinical and Operational Increase in Efficiency and Cost Savings. *Arch Pathol Lab Med* (2019) 143:1545–55. doi: 10.5858/arpa.2018-0514-OA
2. Santonicco N, Marletta S, Pantanowitz L, Fadda G, Troncone G, Brunelli M, et al. Impact of Mobile Devices on Cancer Diagnosis in Cytology. *Diagn Cytopathol* (2022) 50:34–45. doi: 10.1002/dc.24890
3. Eccher A, Fontanini G, Fusco N, Girolami I, Graziano P, Rocco EG, et al. Digital Slides as an Effective Tool for Programmed Death Ligand 1 Combined Positive Score Assessment and Training: Lessons Learned From the "Programmed Death Ligand 1 Key Learning Program in Head-And-Neck Squamous Cell Carcinoma. *J Pathol Inform* (2021) 12:1. doi: 10.4103/jpi.jpi_63_20
4. Eccher A, Neil D, Ciangherotti A, Cima L, Boschiero L, Martignoni G, et al. Digital Reporting of Whole-Slide Images is Safe and Suitable for Assessing Organ Quality in Preimplantation Renal Biopsies. *Hum Pathol* (2016) 47:115–20. doi: 10.1016/j.humpath.2015.09.012
5. Pantanowitz L, Wiley CA, Demetris A, Lesniak A, Ahmed I, Cable W, et al. Experience With Multimodality Telepathology at the University of Pittsburgh Medical Center. *J Pathol Inform* (2012) 3:45. doi: 10.4103/2153-3539.104907
6. Fraggetta F, Garozzo S, Zannoni GF, Pantanowitz L, Rossi ED. Routine Digital Pathology Workflow: The Catania Experience. *J Pathol Inform* (2017) 8:51. doi: 10.4103/jpi.jpi_58_17
7. Goacher E, Randell R, Williams B, Treanor D. The Diagnostic Concordance of Whole Slide Imaging and Light Microscopy: A Systematic Review. *Arch Pathol Lab Med* (2017) 141:151–61. doi: 10.5858/arpa.2016-0025-RA
8. Williams BJ, DaCosta P, Goacher E, Treanor D. A Systematic Analysis of Discordant Diagnoses in Digital Pathology Compared With Light Microscopy. *Arch Pathol Lab Med* (2017) 141:1712–8. doi: 10.5858/arpa.2016-0494-OA
9. Hanna MG, Pantanowitz L, Evans AJ. Overview of Contemporary Guidelines in Digital Pathology: What is Available in 2015 and What Still Needs to be Addressed? *J Clin Pathol* (2015) 68:499–505. doi: 10.1136/jclinpath-2015-202914
10. Evans AJ, Brown RW, Bui MM, Chlipala EA, Lacchetti C, Milner DA, et al. Validating Whole Slide Imaging Systems for Diagnostic Purposes in Pathology. *Arch Pathol Lab Med* (2022) 146:440–50. doi: 10.5858/arpa.2020-0723-CP
11. Pantanowitz L, Sinard JH, Henricks WH, Fatheree LA, Carter AB, Contis L, et al. Validating Whole Slide Imaging for Diagnostic Purposes in Pathology: Guideline From The College of American Pathologists Pathology and Laboratory Quality Center. *Arch Pathol Lab Med* (2013) 137:1710–22. doi: 10.5858/arpa.2013-0093-CP

12. Page MJ, McKenzie JE, Bossuyt PM, Boutron I, Hoffmann TC, Mulrow CD, et al. The PRISMA 2020 Statement: An Updated Guideline for Reporting Systematic Reviews. *BMJ* (2021) 372:n71. doi: 10.1136/bmj.n71
13. Ouzzani M, Hammady H, Fedorowicz Z, Elmagarmid A. Rayyan-A Web and Mobile App for Systematic Reviews. *Syst Rev* (2016) 5:210. doi: 10.1186/s13643-016-0384-4
14. Brunelli M, Beccari S, Colombari R, Gobbo S, Giobelli L, Pellegrini A, et al. Ipathology Cockpit Diagnostic Station: Validation According to College of American Pathologists Pathology and Laboratory Quality Center Recommendation at the Hospital Trust and University of Verona. *Diagn Pathol* (2014) 9 Suppl 1:S12. doi: 10.1186/1746-1596-9-S1-S12
15. Fraggetta F, Caputo A, Guglielmino R, Pellegrino MG, Runza G, L'Imperio V. A Survival Guide for the Rapid Transition to a Fully Digital Workflow: The "Caltagirone Example. *Diagnostics (Basel Switzerland)* (2021) 11(10):1916. doi: 10.3390/diagnostics11101916
16. Retamero JA, Aneiros-Fernandez J, Del Moral RG. Complete Digital Pathology for Routine Histopathology Diagnosis in a Multicenter Hospital Network. *Arch Pathol Lab Med* (2020) 144:221–8. doi: 10.5858/arpa.2018-0541-OA
17. Eccher A, Girolami I. Current State of Whole Slide Imaging Use in Cytopathology: Pros and Pitfalls. *Cytopathology* (2020) 31:372–8. doi: 10.1111/cyt.12806
18. Girolami I, Pantanowitz L, Marletta S, Brunelli M, Mescoli C, Parisi A, et al. Diagnostic Concordance Between Whole Slide Imaging and Conventional Light Microscopy In Cytopathology: A Systematic Review. *Cancer Cytopathol* (2020) 128:17–28. doi: 10.1002/cncy.22195
19. Hanna MG, Reuter VE, Hameed MR, Tan LK, Chiang S, Sigel C, et al. Whole Slide Imaging Equivalency and Efficiency Study: Experience at a Large Academic Center. *Mod Pathol an Off J United States Can Acad Pathol Inc* (2019) 32:916–28. doi: 10.1038/s41379-019-0205-0
20. Alassiri A, Almutrafi A, Alsufiani F, Al Nehkilan A, Al Salim A, Musleh H, et al. Whole Slide Imaging Compared With Light Microscopy for Primary Diagnosis in Surgical Neuropathology: A Validation Study. *Ann Saudi Med* (2020) 40:36–41. doi: 10.5144/0256-4947.2020.36
21. Snead DRJ, Tsang Y-W, Meskiri A, Kimani PK, Crossman R, Rajpoot NM, et al. Validation of Digital Pathology Imaging for Primary Histopathological Diagnosis. *Histopathology* (2016) 68:1063–72. doi: 10.1111/his.12879
22. Gui D, Cortina G, Naini B, Hart S, Gerney G, Dawson D, et al. Diagnosis of Dysplasia in Upper Gastro-Intestinal Tract Biopsies Through Digital Microscopy. *J Pathol Inform* (2012) 3:27. doi: 10.4103/2153-3539.100149
23. Loughrey MB, Kelly PJ, Houghton OP, Coleman HG, Houghton JP, Carson A, et al. Digital Slide Viewing for Primary Reporting in Gastrointestinal Pathology: A Validation Study. *Virchows Arch* (2015) 467:137–44. doi: 10.1007/s00428-015-1780-1
24. Velez N, Jukic D, Ho J. Evaluation of 2 Whole-Slide Imaging Applications in Dermatopathology. *Hum Pathol* (2008) 39:1341–9. doi: 10.1016/j.humpath.2008.01.006
25. Campbell WS, Hinrichs SH, Lele SM, Baker JJ, Lazenby AJ, Talmon GA, et al. Whole Slide Imaging Diagnostic Concordance With Light Microscopy for Breast Needle Biopsies. *Hum Pathol* (2014) 45:1713–21. doi: 10.1016/j.humpath.2014.04.007
26. Bauer TW, Slaw RJ. Validating Whole-Slide Imaging for Consultation Diagnoses in Surgical Pathology. *Arch Pathol Lab Med* (2014) 138:1459–65. doi: 10.5858/arpa.2013-0541-OA
27. Bauer TW, Slaw RJ, McKenney JK, Patil DT. Validation of Whole Slide Imaging for Frozen Section Diagnosis in Surgical Pathology. *J Pathol Inform* (2015) 6:49. doi: 10.4103/2153-3539.163988
28. Thrall MJ, Wimmer JL, Schwartz MR. Validation of Multiple Whole Slide Imaging Scanners Based on the Guideline From the College of American Pathologists Pathology and Laboratory Quality Center. *Arch Pathol Lab Med* (2015) 139:656–64. doi: 10.5858/arpa.2014-0073-OA
29. Mukhopadhyay S, Feldman MD, Abels E, Ashfaq R, Beltaifa S, Cacciabeve NG, et al. Whole Slide Imaging Versus Microscopy for Primary Diagnosis in Surgical Pathology: A Multicenter Blinded Randomized Noninferiority Study of 1992 Cases (Pivotal Study). *Am J Surg Pathol* (2018) 42:39–52. doi: 10.1097/PAS.0000000000000948
30. Villa I, Mathieu M-C, Bosq J, Auperin A, Pomerol J-F, Lacroix-Triki M, et al. Daily Biopsy Diagnosis in Surgical Pathology: Concordance Between Light Microscopy and Whole-Slide Imaging in Real-Life Conditions. *Am J Clin Pathol* (2018) 149:344–51. doi: 10.1093/ajcp/aqx161
31. Tabata K, Mori I, Sasaki T, Itoh T, Shiraishi T, Yoshimi N, et al. Whole-Slide Imaging at Primary Pathological Diagnosis: Validation of Whole-Slide Imaging-Based Primary Pathological Diagnosis at Twelve Japanese Academic Institutes. *Pathol Int* (2017) 67:547–54. doi: 10.1111/pin.12590
32. Ammendola S, Bariani E, Eccher A, Capitanio A, Ghimenton C, Pantanowitz L, et al. The Histopathological Diagnosis of Atypical Meningioma: Glass Slide Versus Whole Slide Imaging for Grading Assessment. *Virchows Arch* (2021) 478:747–56. doi: 10.1007/s00428-020-02988-1
33. Williams BJ, Hanby A, Millican-Slater R, Nijhawan A, Verghese E, Treanor D. Digital Pathology for the Primary Diagnosis of Breast Histopathological Specimens: An Innovative Validation and Concordance Study on Digital Pathology Validation and Training. *Histopathology* (2018) 72:662–71. doi: 10.1111/his.13403
34. Davidson TM, Rendi MH, Frederick PD, Onega T, Allison KH, Mercan E, et al. Breast Cancer Prognostic Factors in the Digital Era: Comparison of Nottingham Grade Using Whole Slide Images and Glass Slides. *J Pathol Inform* (2019) 10:11. doi: 10.4103/jpi.jpi_29_18
35. Sturm B, Creytens D, Cook MG, Smits J, van Dijk MCRF, Eijken E, et al. Validation of Whole-Slide Digitally Imaged Melanocytic Lesions: Does Z-Stack Scanning Improve Diagnostic Accuracy? *J Pathol Inform* (2019) 10:6. doi: 10.4103/jpi.jpi_46_18
36. Bauer TW, Schoenfield L, Slaw RJ, Yerian L, Sun Z, Henricks WH. Validation of Whole Slide Imaging for Primary Diagnosis in Surgical Pathology. *Arch Pathol Lab Med* (2013) 137:518–24. doi: 10.5858/arpa.2011-0678-OA
37. van den Brand M, Nooijen PTGA, van der Laan KD, de Bruin PC, van Leeuwen AMG, Leeuwis JW, et al. Discrepancies in Digital Hematopathology Diagnoses for Consultation and Expert Panel Analysis. *Virchows Arch* (2021) 478:535–40. doi: 10.1007/s00428-020-02907-4
38. Fertig RM, Gaudi S, Cervantes J, Maddy A, Sangueza O, Vu J, et al. Feasibility Study in Teledermatopathology: An Examination of the Histopathologic Features of Mycosis Fungoides and Spongiotic Dermatitis. *J Cutan Pathol* (2017) 44:919–24. doi: 10.1111/cup.13018
39. Hacking S, Nasim R, Lee L, Vitkovski T, Thomas R, Shaffer E, et al. Whole Slide Imaging and Colorectal Carcinoma: A Validation Study for Tumor Budding and Stromal Differentiation. *Pathol Res Pract* (2020) 216:153233. doi: 10.1016/j.prp.2020.153233
40. Cima L, Brunelli M, Parwani A, Girolami I, Ciangherotti A, Riva G, et al. Validation of Remote Digital Frozen Sections for Cancer and Transplant Intraoperative Services. *J Pathol Inform* (2018) 9:34. doi: 10.4103/jpi.jpi_52_18
41. Al-Janabi S, Huisman A, Nikkels PGJ, ten Kate FJW, van Diest PJ. Whole Slide Images for Primary Diagnostics of Paediatric Pathology Specimens: A Feasibility Study. *J Clin Pathol* (2013) 66:218–23. doi: 10.1136/jclinpath-2012-201104
42. Al-Janabi S, Huisman A, Nap M, Clarijs R, van Diest PJ. Whole Slide Images as a Platform for Initial Diagnostics in Histopathology in a Medium-Sized Routine Laboratory. *J Clin Pathol* (2012) 65:1107–11. doi: 10.1136/jclinpath-2012-200878
43. Al-Janabi S, Huisman A, Vink A, Leguit RJ, Offerhaus GJA, Ten Kate FJW, et al. Whole Slide Images for Primary Diagnostics in Dermatopathology: A Feasibility Study. *J Clin Pathol* (2012) 65:152–8. doi: 10.1136/jclinpath-2011-200277
44. Ordi J, Castillo P, Saco A, Del Pino M, Ordi O, Rodríguez-Carunchio L, et al. Validation of Whole Slide Imaging in the Primary Diagnosis of Gynaecological Pathology in a University Hospital. *J Clin Pathol* (2015) 68:33–9. doi: 10.1136/jclinpath-2014-202524
45. US Food & Drug Administration, in: *FDA News Release: FDA Allows Marketing of First Whole Slide Imaging System for Digital Pathology* (2017). Available at: https://www.fda.gov/news-events/press-announcements/fda-allows-marketing-first-whole-slide-imaging-system-digital-pathology (Accessed April 10, 2022).
46. Image Technology News, in: *Leica Biosystems Receives FDA Clearance for Aperio AT2 DX Digital Pathology System* (2019). Available at: https://www.itnonline.com/content/leica-biosystems-receives-fda-clearance-aperio-at2-dx-digital-pathology-system (Accessed April 10, 2022).

47. Williams BJ, Fraggetta F, Hanna MG, Huang R, Lennerz J, Salgado R, et al. The Future of Pathology: What can We Learn From the COVID-19 Pandemic? *J Pathol Inform* (2020) 11:15. doi: 10.4103/jpi.jpi_29_20

Conflict of Interest: The authors declare that the research was conducted in the absence of any commercial or financial relationships that could be construed as a potential conflict of interest.

Publisher's Note: All claims expressed in this article are solely those of the authors and do not necessarily represent those of their affiliated organizations, or those of the publisher, the editors and the reviewers. Any product that may be evaluated in this article, or claim that may be made by its manufacturer, is not guaranteed or endorsed by the publisher.

frontiers | Frontiers in Oncology

TYPE Original Research
PUBLISHED 23 August 2022
DOI 10.3389/fonc.2022.946800

OPEN ACCESS

EDITED BY
Mengling Feng,
National University of Singapore,
Singapore

REVIEWED BY
Gianluca Perroni,
San Raffaele Hospital (IRCCS), Italy
Claudia Bardoni,
University of Milan, Italy
Mehmet Ali Bedirhan,
Yedikule Teaching Hospital, Turkey

*CORRESPONDENCE
Yuhong Liu
qdlyuhong@sohu.com

SPECIALTY SECTION
This article was submitted to
Surgical Oncology,
a section of the journal
Frontiers in Oncology

RECEIVED 18 May 2022
ACCEPTED 27 July 2022
PUBLISHED 23 August 2022

CITATION
Shao S, Song G, Wang Y, Yi T, Li S, Chen F, Li Y, Liu X, Han B and Liu Y (2022) Selection of the surgical approach for patients with cStage IA lung squamous cell carcinoma: A population-based propensity score matching analysis.
Front. Oncol. 12:946800.
doi: 10.3389/fonc.2022.946800

Selection of the surgical approach for patients with cStage IA lung squamous cell carcinoma: A population-based propensity score matching analysis

Shengteng Shao, Guisong Song, Yuanyong Wang, Tengfei Yi, Shuo Li, Fuhui Chen, Yang Li, Xiaotong Liu, Bin Han and Yuhong Liu*

Department of Thoracic Surgery, The Affiliated Hospital of Qingdao University, Qingdao, China

Background: This study aimed to conduct a comparative analysis of the survival rates after segmentectomy, wedge resection, or lobectomy in patients with cStage IA lung squamous cell carcinoma (SCC).

Methods: We enrolled 4,316 patients who had cStage IA lung SCC from the Surveillance, Epidemiology, and End Results (SEER) database. The Cox proportional hazards model was conducted to recognize the potential risk factors for overall survival (OS) and lung cancer-specific survival (LCSS). To eliminate potential biases of included patients, the propensity score matching (PSM) method was used. OS and LCSS rates were compared among three groups stratified according to tumor size.

Results: Kaplan–Meier analyses revealed no statistical differences in the rates of OS and LCSS between wedge resection (WR) and segmentectomy (SG) groups for patients who had cStage IA cancers. In patients with tumors ≤ 1 cm, LCSS favored lobectomy (Lob) compared to segmentectomy (SG), but a similar survival rate was obtained for wedge resection (WR) and lobectomy (Lob). For patients with tumors sized 1.1 to 2 cm, lobectomy had improved OS and LCSS rates compared to the segmentectomy or wedge resection groups, with the exception of a similar OS rate for lobectomy and segmentectomy. For tumors sized 2.1 to 3 cm, lobectomy had a higher rate of OS or LCSS than wedge resection or segmentectomy, except that lobectomy conferred a similar LCSS rate compared to segmentectomy. Multivariable analyses showed that patients aged ≥75 and tumor sizes of >2 to ≤3 cm were potential risk factors for OS and LCSS, while lobectomy and first malignant primary indicator were considered protective factors. The Cox proportional analysis also confirmed that male patients aged ≥65 to <75 were independent prognostic factors that are indicative of a worse OS rate.

Conclusions: The tumor size can influence the surgical procedure recommended for individuals with cStage IA lung SCC. For patients with tumors ≤1 cm, lobectomy is the recommended approach, and wedge resection or segmentectomy might be an alternative for those who cannot tolerate lobectomy if adequate surgical margin is achievable and enough nodes are sampled. For tumors >1 to ≤3 cm, lobectomy showed better survival outcomes than sublobar resection. Our findings require further validation by randomized controlled trial (RCT) or other evidence.

KEYWORDS

cStage IA lung squamous cell carcinoma, survival, segmentectomy, wedge resection, lobectomy, propensity score matching, SEER

Introduction

Lung cancer is the leading cause of cancer-related mortality worldwide, with non-small cell lung cancer (NSCLC) accounting for over 85% of cases (1). As one of the major pathological types of NSCLC, squamous cell carcinoma (SCC) accounts for about 30% (2). With the increasing use of low-dose helical computed tomography (CT) and high-resolution CT (HRCT) for lung cancer screening and diagnosis, a growing number of patients are diagnosed earlier (3, 4), the majority of whom are non-smokers with small-sized peripheral lung adenocarcinomas (ADCs). Meanwhile, the number of patients with early-stage SCC is also increasing gradually (5).

For early-stage NSCLC, stereotactic ablative radiotherapy (SBRT) does not achieve surgically equivalent oncological outcomes (6) and is recommended for patients who are medically inappropriate for surgery (7). Surgery is still regarded to be the mainstay treatment for patients with early-stage NSCLCs (8, 9). Lobectomy plus lymph node removal has been acknowledged as standard treatment for stage I NSCLC since the randomized controlled trials (RCTs) conducted by the Lung Cancer Study Group in 1995 (10). Additionally, lobectomy not only has lower regional and distant recurrence rates, but also has better survival outcomes compared with wedge resection or segmentectomy in stage I NSCLC (11). However, patients who cannot undergo lobectomy due to old age, poor lung function, or other preoperative comorbidities often need to undergo a limited resection instead (12–14). Currently, wedge resection (WR) and segmentectomy (SG) have become important treatment strategies for patients with stage IA NSCLCs (14, 15). Moreover, segmentectomy is widely used in small-sized NSCLC tumors (16, 17) and has been reported to achieve similar long-term survival benefits as patients that received lobectomy (15, 18).

Several studies have investigated the appropriate surgical procedures for early-stage lung ADC (19) and NSCLC. However, no specific research comparing the survival outcomes of segmentectomy, wedge resection, and lobectomy in patients with cStage IA SCCs is currently available. To that end, we utilized the SEER database to analyze and compare the survival rates of patients with cStage IA SCC receiving different treatment approaches to provide more insight into the optimal surgical strategy for cStage IA SCC based on tumor size.

Methods

Patient population

The patients in this research were extracted from the Surveillance, Epidemiology, and End Results (SEER) database, a population-based cancer database that provides information on cancer incidence in 18 registries of the United States and covers about 30% of the population. We identified all individuals with cStage IA (T1N0M0) lung SCC (SEER codes 8052, 8070–8075, 8083, 8084, and 8123) who were verified by pathology and had undergone wedge resection, segmentectomy, or lobectomy (SEER codes were 21, 22, and 30 to 33, respectively) from January 2010 to December 2015. Patients were not eligible if they had received chemotherapy or radiation prior to, during, or after the surgical treatment or if the baseline characteristics were unknown.

In this retrospective study, the information of demography (age, gender, marital status, and race), characteristics of the tumor (primary site, laterality, differentiation, and size), treatment (surgical procedure, chemotherapy, and radiotherapy), the cause of death, and first malignant primary indicator were collected from the SEER database. Based on the surgical approach received, patients were separated into three groups: wedge resection (WR), segmentectomy (SG), and lobectomy (Lob).

Outcomes

We defined overall survival (OS) and lung cancer-specific survival (LCSS) using the codes provided by the SEER database. The OS rate was the primary endpoint in our research. This was calculated from the surgery date to the date of the patient's death from any cause or last follow-up. The secondary endpoint was the LCSS rate, which was calculated from the surgery date to the date of death due to lung cancer. The last follow-up date was 31 December 2018 (time range from 1 to 107 months).

Statistical analysis

The categorical variables were compared using Pearson's χ^2 test for baseline characteristics. Cox proportional hazards regressions model were performed to identify the potential and independent risk factors affecting the rates of OS and LCSS for cStage IA SCC patients. We divided the eligible patients into three groups according to the surgical approach, namely, lobectomy (Lob), segmentectomy (SG), and wedge resection (WR). According to different outcome events (patient death or loss to follow-up and patient death due to lung cancer) of patients, we performed univariate and multivariate Cox regression analysis to screen out the independent risk factors influencing the OS and LCSS. Significant variables in multivariate analysis were independent risk factors affecting the prognosis of patients. The variables affecting the OS of patients were age, gender, tumor size, surgical method, and first malignant primary indicator, and the variables affecting LCSS of patients were age, tumor size, surgical method, and first malignant primary indicator. Combining the differences in patients' baseline characteristics and clinical practice, we defined age, gender, the laterality of the tumor, the lobe of the tumor, and first malignant primary indicator as variables used in propensity score matching (PSM).

PSM methods were applied to minimize the potential biases in the basic features between the cases and controls. The patients were separated into three strata according to tumor size (≤1.0 cm, 1.1 to 2.0 cm, and 2.1 to 3.0 cm), and in each stratum, three groups of patients who underwent different surgeries were separately matched in a ratio of 1:1. For example, for individuals with tumors smaller than 1 cm and the outcome event of death or loss to follow-up, 1:1 PSM was performed for segmentectomy versus wedge resection, segmentectomy versus lobectomy, and wedge resection versus lobectomy group, respectively.

The Kaplan–Meier method was used to analyze and compare the rates of OS and LCSS among patients with cStage IA lung SCC of 1 cm or smaller, 1.1 to 2.0 cm, and 2.1 to 3.0 cm receiving segmentectomy, wedge resection, or lobectomy in both the entire cohort and the cohort after PSM.

For statistical results, IBM SPSS 26.0 (SPSS, Inc, Chicago, IL) was used for all analyses, and GraphPad Prism 9.0 (GraphPad Software, San Diego, CA) was used to draw the survival curve. The reported significance levels were two-sided, and statistical significance was defined as the value of $p \leq 0.05$.

Results

Patient characteristics

A total of 4,316 eligible patients with cStage IA lung SCC (≤3 cm) were identified, namely, 254 (5.9%) who received segmentectomy, 1,085 (25.1%) who underwent wedge resection, and 2,977 (69.0%) who had a lobectomy. The median follow-up time was 50.5 months for the entire cohort, 47 months for segmentectomy, 45 months for wedge resection, and 53 months for lobectomy. A total of 2,052 patients died [141 (6.9%) from segmentectomy, 619 (30.1%) from the wedge resection, and 1,292 (63.0%) from the lobectomy groups] and 927 patients suffered from lung cancer-specific deaths [65 (7.0%) from the segmentectomy, 300 (32.4%) from the wedge resection, and 562 (60.6%) from the lobectomy groups].

Our research revealed that sublobar resection (wedge resection or segmentectomy) was operated in patients who were more elderly or had a smaller tumor size, especially if the tumor is ≤2.0 cm. When a patient had only one primary malignant neoplasm, lobectomy or segmentectomy was more likely to be performed. Table 1 demonstrates the baseline characteristics of the primary cohort.

Tumors ≤ 1.0 cm

We identified 497 patients with cStage IA lung SCC with a tumor size of 1.0 cm or smaller. Thirty-six (7.2%) of them underwent segmentectomy, 216 (43.5%) received wedge resection, and 245 (49.3%) had their lobe removed. The median follow-up time was 52 months. OS analysis revealed that the unmatched and propensity-matched results showed no statistical differences in the OS rates among the three treatment groups (Figure 1). On the other hand, LCSS analysis revealed that lobectomy achieved a better LCSS than segmentectomy or wedge resection in the unmatched cohort. Interestingly, lobectomy still showed a better LCSS rate when compared with segmentectomy in the matched cohort. However, there was no statistical difference between lobectomy and wedge resection (Figure 2).

TABLE 1 Baseline characteristics of patients with stage IA squamous cell lung cancer.

Variables	Segmentectomy (*N* = 254)	Wedge resection (*N* = 1,085)	Lobectomy (*N* = 2,977)	*p*-value
Marital status				0.114
Married	122 (48.0%)	582 (53.6%)	1,641 (55.1%)	
Unmarried	113 (44.5%)	453 (41.8%)	1,193 (40.1%)	
Unknown	19 (7.5%)	50 (4.6%)	143 (4.8%)	
Age (years)				<0.001
<55	2 (0.8%)	23 (2.1%)	119 (4.0%)	
≥55, <65	36 (14.2%)	166 (15.3%)	614 (20.6%)	
≥65, <75	116 (45.7%)	481 (44.3%)	1,385 (46.5%)	
≥75	100 (39.4%)	415 (38.2%)	859 (28.9%)	
Sex				<0.001
Male	107 (42.1%)	578 (53.3%)	1,642 (55.2%)	
Female	147 (57.9%)	507 (46.7%)	1,335 (44.8%)	
Race				0.074
White	219 (86.2%)	972 (89.6%)	2,648 (8.9%)	
Black	30 (11.8%)	74 (6.8%)	233 (7.8%)	
Others	5 (2.0%)	39 (3.6%)	96 (3.2%)	
Primary site				0.016
Upper lobe	148 (58.3%)	694 (64.0%)	1,082 (60.5%)	
Middle lobe	5 (2.0%)	38 (3.5%)	145 (4.9%)	
Lower lobe	101 (39.8%)	353 (32.5%)	1,030 (34.6%)	
Laterality				0.005
Left	134 (52.8%)	488 (45.0%)	1,267 (42.6%)	
Right	120 (47.2%)	597 (55.0%)	1,710 (57.4%)	
Differentiation				0.191
Well	8 (3.1%)	37 (3.4%)	110 (3.7%)	
Moderately	153 (60.2%)	604 (55.7%)	1,614 (54.2%)	
Poorly	93 (36.6%)	436 (40.2%)	1,244 (41.8%)	
No	0 (0%)	8 (0.7%)	9 (0.3%)	
Tumor size (mm)				<0.001
≤10	36 (14.2%)	216 (19.9%)	245 (8.2%)	
>10, ≤20	139 (54.7%)	615 (56.7%)	1,429 (48.0%)	
>20, ≤30	79 (31.1%)	254 (23.4%)	1,303 (43.8%)	
T1 verified by pathology				0.481
Yes	249 (98.0%)	1,073 (98.9%)	2,932 (98.5%)	
No	5 (2.0%)	12 (1.1%)	45 (1.5%)	
N0 verified by pathology				<0.001
Yes	186 (73.2%)	544 (50.1%)	2,797 (94.0%)	
No	68 (26.8%)	541 (49.9%)	180 (6.0%)	
Cause of dead				0.093
Lung cancer	65 (25.6%)	300 (27.6%)	562 (18.9%)	
Chronic pulmonary disease	24 (9.4%)	69 (6.4%)	141 (4.7%)	
Diseases of heart	16 (6.3%)	70 (6.5%)	173 (5.8%)	
Others	36 (14.2%)	180 (16.6%)	416 (14.0%)	
First malignant primary indicator				<0.001
Yes	153 (60.2%)	581 (53.5%)	2,052 (68.9%)	
No	101 (39.8%)	504 (46.5%)	925 (31.1%)	

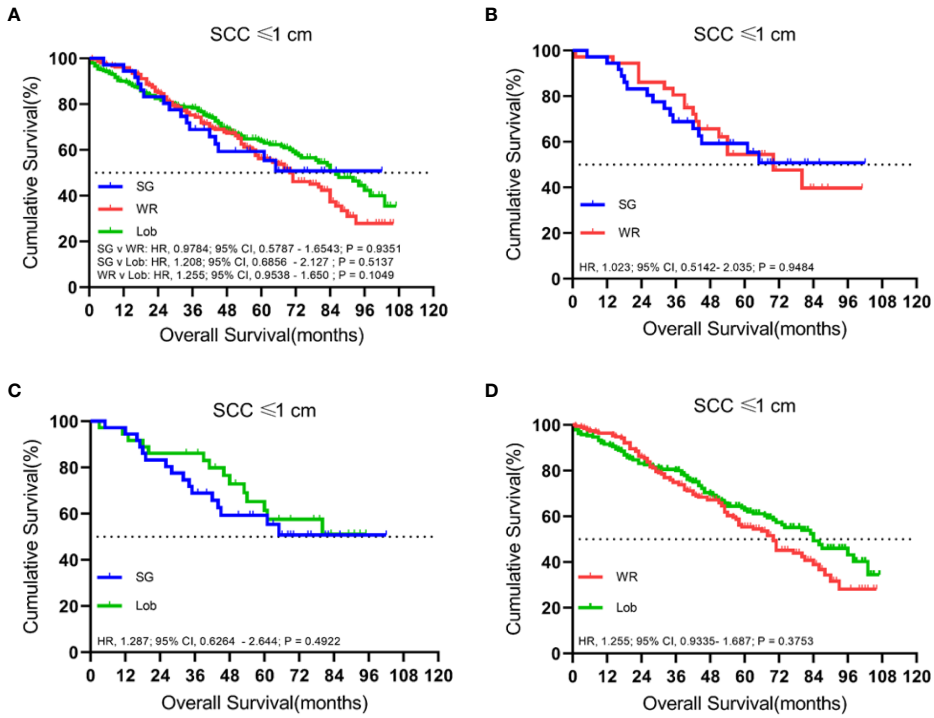

FIGURE 1
Kaplan–Meier survival curves of overall survival for tumors of ≤1.0 cm in the primary cohort **(A)** and the propensity score-matched cohort: **(B)** SG versus WR (*n* = 36 pairs), **(C)** SG versus Lob (*n* = 36 pairs), and **(D)** WR versus Lob (*n* = 193 pairs).

Tumors sized 1.1 to 2.0 cm

There were 2,183 patients with cStage IA lung SCC with tumor sizes ranging from 1.1 to 2.0 cm. A total of 1,429 (65.5%) patients received lobectomy, 615 (28.2%) underwent wedge resection, and 139 (6.4%) had a segmentectomy. The median follow-up time was 52 months.

In both unmatched and matched cohorts, lobectomy was found to be superior to segmentectomy or wedge resection in terms of OS (Figure 3). Meanwhile, LCSS analysis showed that lobectomy was better than segmentectomy or wedge resection in the unmatched cohort. In contrast, lobectomy and segmentectomy displayed no significant difference in the matched cohort (Figure 4).

Tumors sized 2.1 to 3.0 cm

A total of 1,636 patients were identified with cStage IA lung SCC with a tumor size of 2.1 to 3.0 cm who underwent segmentectomy (79; 4.8%), wedge resection (254; 15.5%), or lobectomy (1,303; 79.6%). The median follow-up time was 48.5 months. OS analysis revealed that segmentectomy was associated with a superior OS compared to wedge resection but had an inferior OS rate in comparison to lobectomy in the unmatched cohort. Similarly, a better OS rate was observed for those patients who had undergone a lobectomy rather than a wedge resection in the matched cohorts (Figure 5). Importantly, lobectomy had a better LCSS rate than wedge resection in both unmatched and matched cohorts. In addition, lobectomy achieved a better LCSS than segmentectomy in the matched cohorts (Figure 6).

Cox regression analysis

We used the Cox proportional hazards regressions model to identify the potential risk factors correlating with OS and LCSS in cStage IA SCC patients (Table 2). Univariate Cox regression analysis showed that age, surgical procedure, tumor size, and first malignant primary indicator were significantly correlated with OS and LCSS. Moreover, OS was also found to be associated with gender.

Furthermore, all variables with a *p*-value less than 0.05 were included in the multivariate analysis. We found that patients aged ≥ 75 with a tumor size of >2.0 to ≤3.0 cm were negatively correlated to OS and LCSS, while the lobectomy and first malignant primary indicator were considered to be protective

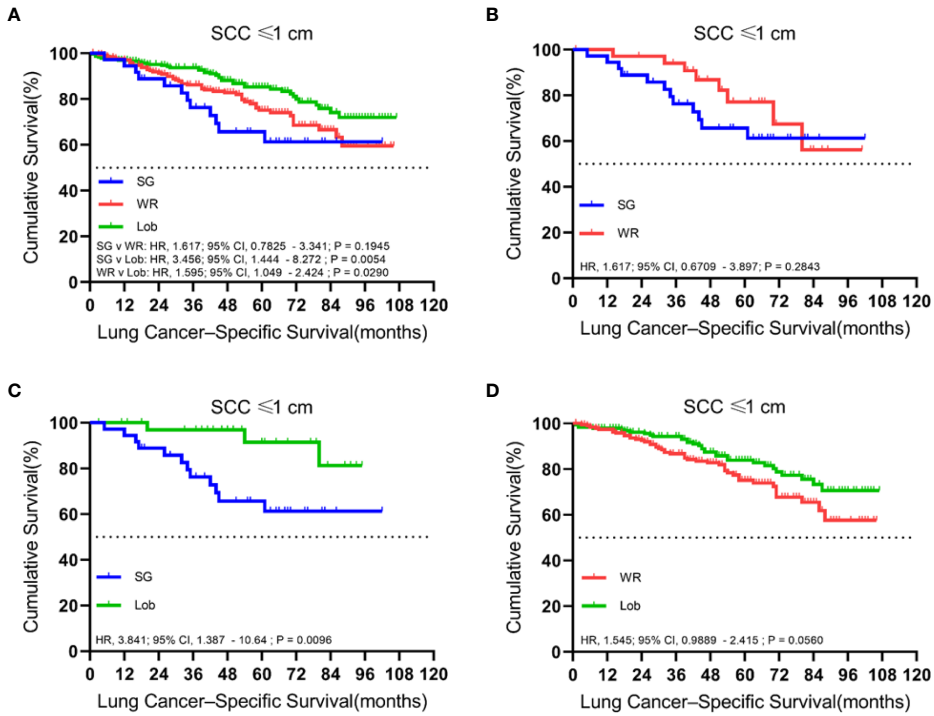

FIGURE 2
Kaplan–Meier survival curves of lung cancer-specific survival for tumors of ≤1.0 cm in the primary cohort **(A)** and the propensity score-matched cohort: **(B)** SG versus WR (*n* = 36 pairs), **(C)** SG versus Lob (*n* = 36 pairs), and **(D)** WR versus Lob (*n* = 193 pairs).

factors. Additionally, we found that the male gender and those aged ≥65 to <75 were independent factors for poor OS while there was no statistical significance for cancer-specific survival.

Discussion

The Lung Cancer Study Group reported that lobectomy could achieve a better OS and lower local recurrence rate than sublobar resection in the treatment of stage I NSCLC after a randomized prospective multi-institutional controlled trial in 1995 (10). Since then, lobectomy with lymph node dissection has been implemented as the standard for resectable early-stage NSCLC (8, 20). However, with the recent improvements in screening methods and surgical techniques, there is a growing body of evidence showing that sublobar resection is comparable to lobectomy in terms of surgical outcomes.

Dai et al. and Cao et al. previously corroborated on the use of the recommended surgical option for early-stage NSCLC based on tumor size (15, 18). However, they found that the SCC subtype showed significant differences in terms of clinicopathological and genetic features compared to the ADC subtype, showing a worse clinical outcome for early-stage lung cancer patients (21). Moreover, Li et al. found that segmentectomy was superior to wedge resection in patients with stage IA SCC, but the prognosis of wedge resection and segmentectomy were roughly equivalent in stage IA ADC patients (22). Several studies have been carried out to determine the appropriate surgical approach for small-sized SCC. For instance, Chen et al. compared the survival rate after patients with stage I lung SCC with a tumor size ≤ 3 cm received sublobar resection or lobectomy (23). Herein, we attempted to investigate the effectiveness of three surgical approaches (segmentectomy, wedge resection, and lobectomy) in cStage IA SCC. Importantly, we included a larger number of patients compared to Chen et al.'s study.

Previous studies have shown that patients with NSCLC benefit more from segmentectomy than wedge resection. For instance, Dai et al. concluded that segmentectomy is supposed to be suggested for NSCLC patients who are not candidates for lobectomy (15). Hou et al. found that segmentectomy achieved a better survival rate than wedge resection in stage I NSCLC (24). Additionally, Reveliotis et al. identified that segmentectomy is better than wedge resection on the aspects of the rates of regional recurrence and cancer-related mortality (25). However, there are also conflicting reports. Several retrospective studies reported that wedge resection might be ontologically equivalent to segmentectomy in patients with tumors ≤ 1 cm (18, 26). Moreover, a meta-analysis has identified that WR and SG might be comparable in select patients with early-stage lung cancer, especially for tumors sized 2 cm or smaller (27). In addition, a

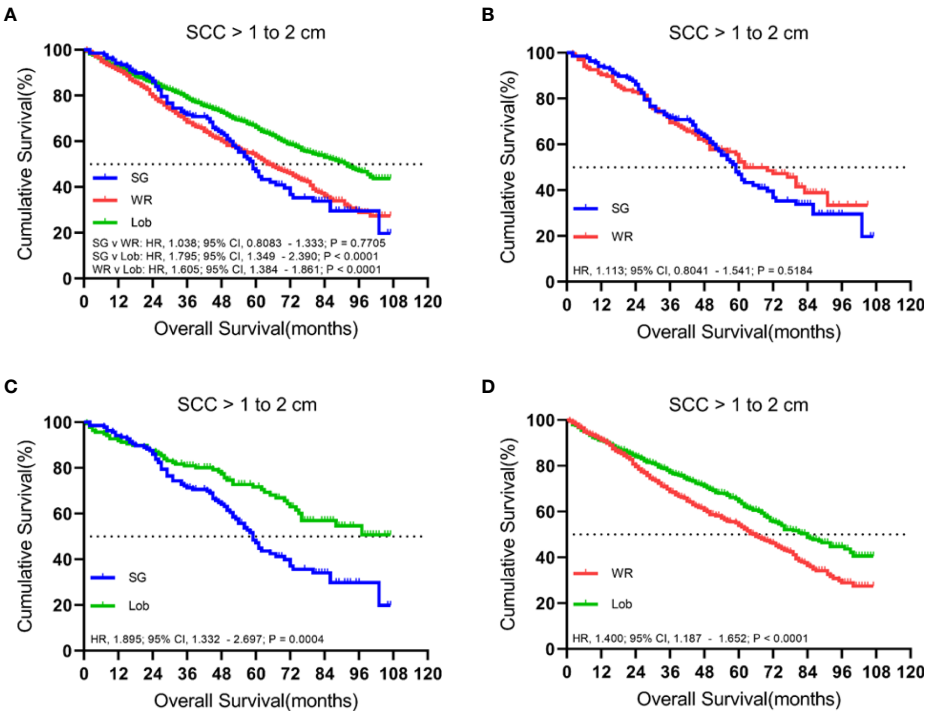

FIGURE 3
Kaplan–Meier survival curves of overall survival for tumors from 1.1 to 2.0 cm in the primary cohort **(A)** and propensity score-matched cohort: **(B)** SG versus WR (*n* = 139 pairs), **(C)** SG versus Lob (*n* = 138 pairs), and **(D)** WR versus Lob (*n* = 598 pairs).

prospective randomized trial (ACOSOG Z4032) by Sybron Harrison et al. supported the view that wedge resection is comparable to segmentectomy (28). Our study analyzed the prognosis of segmentectomy versus wedge resection in cStage IA SCC patients on the basis of the eighth TNM classification. We found that the survival difference was not significant between segmentectomy and wedge resection for tumors of T1a (≤1 cm), T1b (>1 to 2 cm), and T1c (>2 to 3 cm) (29). In contrast, Li et al. discovered that segmentectomy outperformed wedge resection in terms of survival for patients with stage IA SCC (22), but their study sample was considerably smaller than ours, and no subgroup analysis of SCC stratified by tumor size was performed.

Lobectomy is commonly accepted as being better than wedge resection for patients with stage I NSCLC (30). In clinical practice, wedge resection is usually performed in patients with poor lung function or those with other comorbidities that might not be suitable for lobectomy (14). A study using the SEER database also reported that Lob showed better survival rates than WR for NSCLC of ≤ 2 cm (15). However, several studies suggested that no significant difference was found in survival outcome among patients with stage IA NSCLC sized ≤ 1 cm who underwent lobectomy and wedge resection (31, 32). Our study obtained the same result for cStage IA SCC ≤ 1 cm and identified that lobectomy was superior to wedge resection for cStage IA SCC > 1 to 3 cm.

As for segmentectomy versus lobectomy in cStage IA SCC ≤ 1 cm, patients showed similar OS, but lobectomy was superior to segmentectomy in terms of LCSS rate. This may be attributed to the intraoperative assessment of lymph node metastasis and adequate surgical margin (33). SG has adequate surgical margin to achieve a successful resection of peripheral small-sized SCC. However, for some nodules, standard segmentectomy cannot achieve a safe margin distance, which could result in a worse clinical outcome (34). Therefore, we recommend lobectomy as the surgical procedure for patients with cStage IA SCC ≤ 1 cm. For those who cannot tolerate lobectomy (advanced age, poor lung function, previous lung surgery, or other serious comorbidities), WR or SG might be the proper treatment under the premise of sufficient surgical margin and lymph node sampling.

The appropriate surgical procedures for stage IA NSCLC have been discussed in several papers. They discovered that for tumors measuring ≤ 1.0 cm and between 1.1 and 2.0 cm, lobectomy and segmentectomy have identical survival outcomes (18, 27). A meta-analysis has also suggested that segmentectomy was potentially feasible for NSCLC ≤ 2 cm (35). Results from a recently released Phase 3 clinical trial (JCOG0802/WJOG4607L) confirm the above conclusions (36). However, most of the patients included in JCOG0802 were peripheral ADCs. Whether this conclusion is suitable for small lung SCC remains to be investigated. Also, lobectomy is considered superior to segmentectomy for tumors

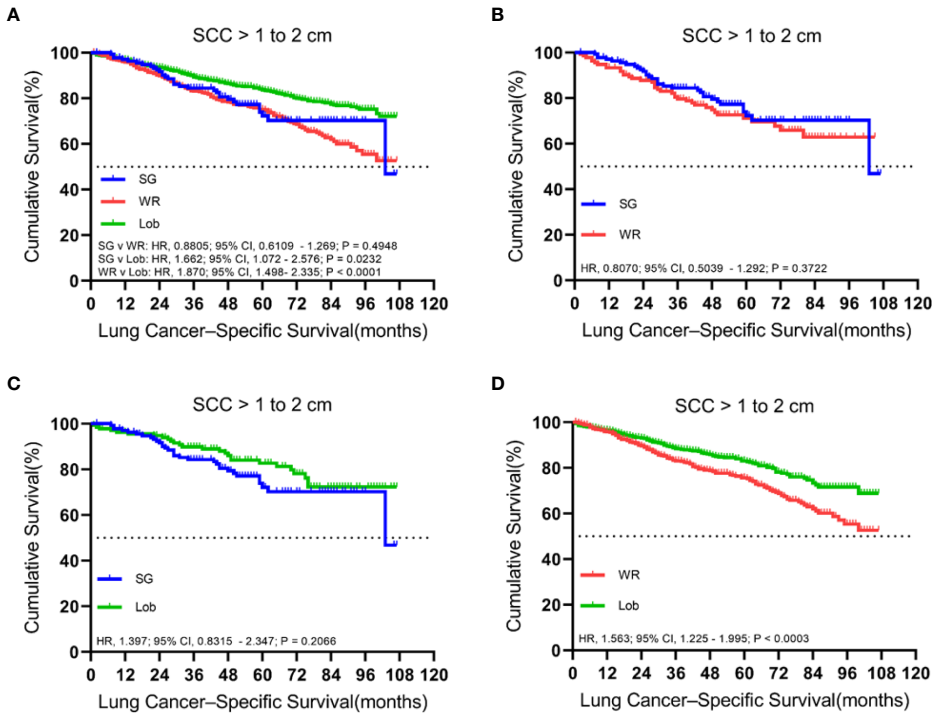

FIGURE 4
Kaplan–Meier survival curves of lung cancer-specific survival for tumors from 1.1 to 2.0 cm in the primary cohort **(A)** and the propensity score-matched cohort: **(B)** SG versus WR (*n* = 139 pairs), **(C)** SG versus Lob (*n* = 138 pairs), and **(D)** WR versus Lob (*n* = 598 pairs).

sized between 2.1 and 3.0 cm (15, 18, 27). In our study, we found that lobectomy showed a better OS rate than segmentectomy for cStage IA SCC >1 to ≤2 cm, but not for those >2 to ≤3 cm. As for LCSS rate, there was no statistical difference for tumors >1 to ≤2 cm between lobectomy and segmentectomy. Patients with cStage IA SCC >2 to 3 cm may benefit from lobectomy with a lower risk of cancer-related death. In addition, lobectomy was superior to WR for cStage IA SCC >1 to 2 cm and >2 to 3 cm. Therefore, we conclude that for patients with cStage IA SCC sized >1 to 2 cm or >2 to ≤3 cm, the conventional surgical approach may still be lobectomy, while segmentectomy could be an alternative approach for those not suitable for lobectomy.

In the Cox proportional analysis, apart from surgical procedures, we also verified other independent prognostic factors in node-negative SCC. Our retrospective study showed that patients aged ≥65 and ≥75 are at higher risk for worse OS and LCSS, respectively. The male gender was revealed to be a risk factor correlated to the OS rate, while the LCSS rate was not significantly influenced by gender. Several studies also confirmed that age and gender were validated factors for predicting personal survival rate (37). Tumor size may correspond with the appropriate surgical procedure on those patients with early-stage SCC (18, 23). The results of our study revealed that a tumor size of >2 to ≤3 cm may pose a risk for OS and LCSS in comparison to those smaller than 2 cm, and that a lobectomy procedure was considered to be a protective factor for patients with cStage IA SCC sized >2 to ≤3 cm. In addition, one stage IA SCC individual with two or more histologically distinct malignancies had a worse OS and LCSS, while the first malignant primary indicator was found to be an independent factor synonymous with a good survival outcome.

Nevertheless, there are several limitations to our study. Firstly, this is a retrospective study, and all the data were collected from the SEER database. Although we attempted to balance the baseline characteristics of the patients using the propensity score-matched method, there are some inevitable inherent biases. Secondly, in some cases, where a total lobectomy is not feasible, wedge resection or segmentectomy may be an effective treatment, especially for elderly patients, those with severe impairments in lung function, or others (12–14). However, the comorbidities and pulmonary function data were not included in the SEER database. Thirdly, the SEER database did not provide tumor location data (central or peripheral). Sung Ye et al. previously uncovered that peripheral SCC has different clinicopathological and genetic features compared to the central type (38), showing a significantly better disease-free survival (DFS) and OS (39). Lastly, the SEER database did not provide other important information, such as detailed surgical records (open or minimally invasive, intentional segmentectomy or not, lymph node sampling or mediastinal lymph node dissection) and imaging appearance of tumor (the imaging size of the tumor, solid component proportion), to name a few.

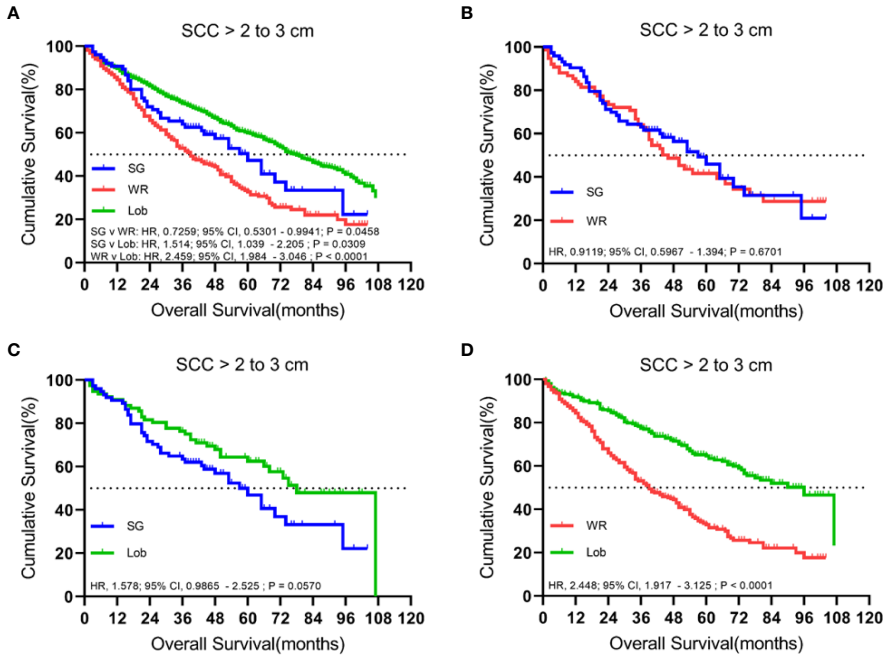

FIGURE 5
Kaplan–Meier survival curves of overall survival for tumors from 2.1 to 3.0 cm in the primary cohort **(A)** and the propensity score-matched cohort: **(B)** SG versus WR (*n* = 77 pairs), **(C)** SG versus Lob (*n* = 78 pairs), and **(D)** WR versus Lob (*n* = 253 pairs).

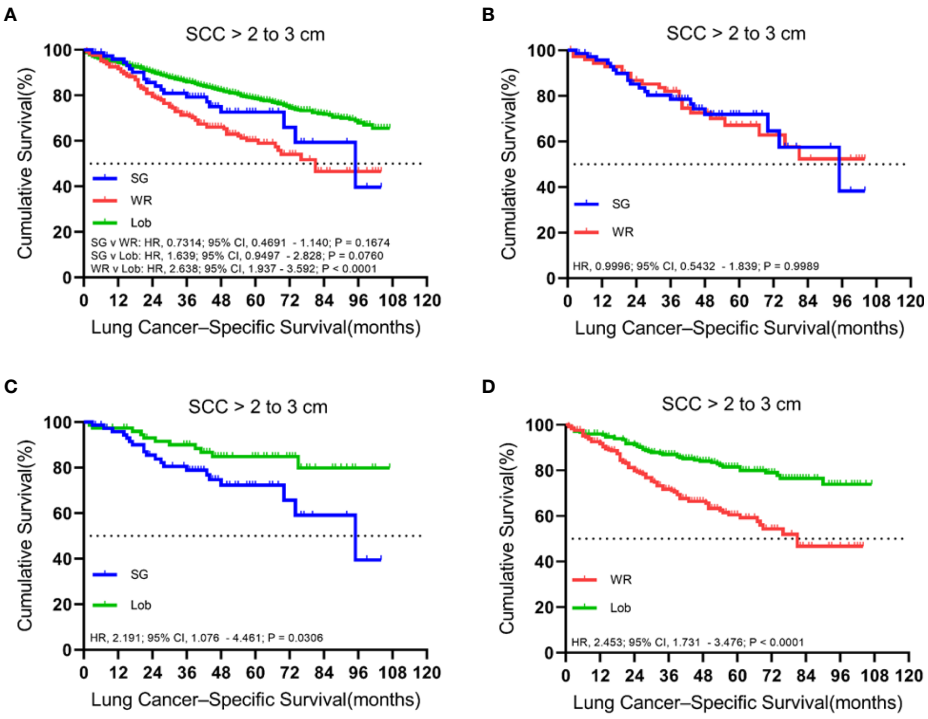

FIGURE 6
Kaplan–Meier survival curves of lung cancer-specific survival for tumors from 2.1 to 3.0 cm in the primary cohort **(A)** and the propensity score-matched cohort: **(B)** SG versus WR (*n* = 77 pairs), **(C)** SG versus Lob (*n* = 78 pairs), and **(D)** WR versus Lob (*n* = 253 pairs).

TABLE 2 Cox proportional hazards regression model for overall survival and lung cancer-specific survival in patients with stage IA squamous cell lung cancer.

Variables	OS				LCSS			
	Univariable analysis	Multivariable analysis			Univariable analysis	Multivariable analysis		
	p	HR	95% CI	*p*	*p*	HR	95% CI	*p*
Marital status	0.171				0.245			
Married								
Unmarried								
Unknown								
Age (years)	<0.001				<0.001			
<55		1	(Reference)			1	(Reference)	
≥55, <65		1.258	0.923–1.716	0.146		0.973	0.644–1.469	0.896
≥65, <75		1.546	1.149–2.080	0.004		1.195	0.810–1.765	0.369
≥75		2.146	1.593–2.891	<0.001		1.508	1.018–2.234	0.041
Sex	<0.001				0.052			
Male		1	(Reference)					
Female		0.773	0.707–0.844	<0.001				
Race	0.823				0.630			
White								
Black								
Others								
Primary site	0.242				0.103			
Upper lobe								
Middle lobe								
Lower lobe								
Laterality	0.385				0.927			
Left								
Right								
Differentiation	0.505				0.233			
Well								
Moderately								
Poorly								
No								
Surgical approach	<0.001				<0.001			
Segmentectomy		1	(Reference)			1	(Reference)	
Wedge resection		1.011	0.841–1.214	0.909		1.098	0.839–1.437	0.496
Lobectomy		0.674	0.565–0.803	<0.001		0.651	0.503–0.844	0.001
Tumor size (mm)	0.001				0.002			
≤10		1	(Reference)			1	(Reference)	
>10, ≤20		1.035	0.896–1.195	0.642		1.064	0.857–1.320	0.577
>20, ≤30		1.344	1.148–1.550	<0.001		1.509	1.206–1.888	<0.001
First malignant primary indicator	<0.001				<0.001			
Yes		1	(Reference)			1	(Reference)	
No		1.263	1.154–1.381	<0.001		1.312	1.149–1.499	<0.001

Conclusion

In conclusion, for patients with cStage IA SCC sized ≤ 1 cm, lobectomy is more advantageous in improving their cancer-specific survival and may be the standard procedure. WR and SG are found to be comparable in terms of OS and recommended for those who cannot tolerate lobectomy. For tumors >1 to ≤2 cm or >2 to ≤3 cm, our study revealed that lobectomy showed better survival outcomes compared to sublobar resection. Therefore, lobectomy is supposed to be performed for those

patients, while segmentectomy may be an adequate alternative. The conclusions in this article still need more evidence to be further confirmed. For example, RCTs on cStage IA SCC, or PSM with more treatment details may lead to more convincing conclusions.

Data availability statement

The data from the SEER database is free and publicly available. Further inquiries can be directed to the corresponding author.

Ethics statement

Ethical review and approval was not required for the study on human participants in accordance with the local legislation and institutional requirements. Written informed consent for participation was not required for this study in accordance with the national legislation and the institutional requirements.

Author contributions

YHL and SS conceived and designed the study. YL, XL, and BH collected the data. SS and GS analyzed the data. SS, YW, TY, SL, and FC wrote this manuscript. All authors contributed to the article and approved the submitted version.

Acknowledgments

The authors are grateful for the invaluable support and useful discussions with other members of the Department of Thoracic Surgery, and thank Home for Researchers (www.home-for-researchers.com) for language enhancement of this paper.

Conflict of interest

The authors declare that the research was conducted in the absence of any commercial or financial relationships that could be construed as a potential conflict of interest.

Publisher's note

References

1. Siegel RL, Miller KD, Fuchs HE, Jemal A. Cancer statistics, 2021. *CA Cancer J Clin* (2021) 71(1):7–33. doi: 10.3322/caac.21654

2. Wahbah M, Boroumand N, Castro C, El-Zeky F, Eltorky M. Changing trends in the distribution of the histologic types of lung cancer: A review of 4,439 cases. *Ann Diagn Pathol* (2007) 11(2):89–96. doi: 10.1016/j.anndiagpath.2006.04.006

3. Patz EFJr, Greco E, Gatsonis C, Pinsky P, Kramer BS, Aberle DR. Lung cancer incidence and mortality in national lung screening trial participants who underwent low-dose CT prevalence screening: a retrospective cohort analysis of a randomised, multicentre, diagnostic screening trial. *Lancet Oncol* (2016) 17 (5):590–9. doi: 10.1016/S1470-2045(15)00621-X

4. de Koning HJ, van der Aalst CM, de Jong PA, Scholten ET, Nackaerts K, Heuvelmans MA, et al. Reduced lung-cancer mortality with volume CT screening in a randomized trial. *N Engl J Med* (2020) 382(6):503–13. doi: 10.1056/NEJMoa1911793

5. Kinoshita T, Ohtsuka T, Yotsukura M, Asakura K, Goto T, Kamiyama I, et al. Prognostic impact of preoperative tumor marker levels and lymphovascular invasion in pathological stage I adenocarcinoma and squamous cell carcinoma of the lung. *J Thorac Oncol* (2015) 10(4):619–28. doi: 10.1097/JTO.0000000000000480

6. Ijsseldijk MA, Shoni M, Siegert C, Wiering B, van Engelenburg AKC, Tsai TC, et al. Oncologic outcomes of surgery versus SBRT for non-Small-Cell lung carcinoma: A systematic review and meta-analysis. *Clin Lung Cancer* (2021) 22(3): e235–92. doi: 10.1016/j.cllc.2020.04.017

7. Tandberg DJ, Tong BC, Ackerson BG, Kelsey CR. Surgery versus stereotactic body radiation therapy for stage I non-small cell lung cancer: A comprehensive review. *Cancer* (2018) 124(4):667–78. doi: 10.1002/cncr.31196

8. Rice D, Sepesi B, Heymach J, Swisher S, Vaporciyan A. SABR vs surgery for NSCLC in the media. *Lancet Oncol* (2015) 16(9):e422. doi: 10.1016/S1470-2045(15)00230-2

9. Mangiameli G, Cioffi U, Testori A. Lung cancer treatment: From tradition to innovation. *Front Oncol* (2022) 12:858242. doi: 10.3389/fonc.2022.858242

10. Ginsberg RJ, Rubinstein LV. Randomized trial of lobectomy versus limited resection for T1 N0 non-small cell lung cancer. Lung cancer study group. *Ann Thorac Surg* (1995) 60(3):615–22. doi: 10.1016/0003-4975(95)00537-U

11. Veluswamy RR, Ezer N, Mhango G, Goodman E, Bonomi M, Neugut AI, et al. Limited resection versus lobectomy for older patients with early-stage lung cancer: Impact of histology. *J Clin Oncol* (2015) 33(30):3447–53. doi: 10.1200/JCO.2014.60.6624

12. Zhang B, Liu R, Ren D, Li X, Wang Y, Huo H, et al. Comparison of lobectomy and sublobar resection for stage IA elderly NSCLC patients (≥70 years): A population-based propensity score matching's study. *Front Oncol* (2021) 11:610638. doi: 10.3389/fonc.2021.610638

13. Wisnivesky JP, Henschke CI, Swanson S, Yankelevitz DF, Zulueta J, Marcus S, et al. Limited resection for the treatment of patients with stage IA lung cancer. *Ann Surg* (2010) 251(3):550–4. doi: 10.1097/SLA.0b013e3181c0e5f3

14. Sihoe AD, Van Schil P. Non-small cell lung cancer: When to offer sublobar resection. *Lung Cancer* (2014) 86(2):115–20. doi: 10.1016/j.lungcan.2014.09.004

15. Dai C, Shen J, Ren Y, Zhong S, Zheng H, He J, et al. Choice of surgical procedure for patients with non-small-cell lung cancer ≤ 1 cm or > 1 to 2 cm among lobectomy, segmentectomy, and wedge resection: A population-based study. *J Clin Oncol* (2016) 34(26):3175–82. doi: 10.1200/JCO.2015.64.6729

16. Hwang Y, Kang CH, Kim HS, Jeon JH, Park IK, Kim YT. Comparison of thoracoscopic segmentectomy and thoracoscopic lobectomy on the patients with non-small cell lung cancer: a propensity score matching study. *Eur J Cardiothorac Surg* (2015) 48(2):273–8. doi: 10.1093/ejcts/ezu422

17. Landreneau RJ, Normolle DP, Christie NA, Awais O, Wizorek JJ, Abbas G, et al. Recurrence and survival outcomes after anatomic segmentectomy versus

lobectomy for clinical stage I non-small-cell lung cancer: A propensity-matched analysis. *J Clin Oncol* (2014) 32(23):2449–55. doi: 10.1200/JCO.2013.50.8762

18. Cao J, Yuan P, Wang Y, Xu J, Yuan X, Wang Z, et al. Survival rates after lobectomy, segmentectomy, and wedge resection for non-small cell lung cancer. *Ann Thorac Surg* (2018) 105(5):1483–91. doi: 10.1016/j.athoracsur.2018.01.032

19. Tsutani Y, Miyata Y, Nakayama H, Okumura S, Adachi S, Yoshimura M, et al. Oncologic outcomes of segmentectomy compared with lobectomy for clinical stage IA lung adenocarcinoma: Propensity score-matched analysis in a multicenter study. *J Thorac Cardiovasc Surg* (2013) 146(2):358–64. doi: 10.1016/j.jtcvs.2013.02.008

20. Whitson BA, Groth SS, Andrade RS, Maddaus MA, Habermann EB, D'Cunha J. Survival after lobectomy versus segmentectomy for stage I non-small cell lung cancer: A population-based analysis. *Ann Thorac Surg* (2011) 92(6):1943–50. doi: 10.1016/j.athoracsur.2011.05.091

21. Fukui T, Taniguchi T, Kawaguchi K, Fukumoto K, Nakamura S, Sakao Y, et al. Comparisons of the clinicopathological features and survival outcomes between lung cancer patients with adenocarcinoma and squamous cell carcinoma. *Gen Thorac Cardiovasc Surg* (2015) 63(9):507–13. doi: 10.1007/s11748-015-0564-5

22. Li G, Xie S, Hu F, Tan M, Fan L, Wang C. Segmentectomy or wedge resection in stage IA lung squamous cell carcinoma and adenocarcinoma? *J Cancer* (2021) 12(6):1708–14. doi: 10.7150/jca.49683

23. Chen C, Wang Y, Pan X, Fu S, Shi Y, Yang J, et al. Choice of the surgical approach for patients with stage I lung squamous cell carcinoma ≤3 cm. *J Thorac Dis* (2018) 10(12):6771–82. doi: 10.21037/jtd.2018.11.51

24. Hou B, Deng XF, Zhou D, Liu QX, Dai JG. Segmentectomy versus wedge resection for the treatment of high-risk operable patients with stage I non-small cell lung cancer: A meta-analysis. *Ther Adv Respir Dis* (2016) 10(5):435–43. doi: 10.1177/1753465816667121

25. Reveliotis K, Kalavrouziotis G, Skevis K, Charpidou A, Trigidou R, Syrigos K. Wedge resection and segmentectomy in patients with stage I non-small cell lung carcinoma. *Oncol Rev* (2014) 8(2):234. doi: 10.4081/oncol.2014.234

26. Altorki NK, Kamel MK, Narula N, Ghaly G, Nasar A, Rahouma M, et al. Anatomical segmentectomy and wedge resections are associated with comparable outcomes for patients with small cT1N0 non-small cell lung cancer. *J Thorac Oncol* (2016) 11(11):1984–92. doi: 10.1016/j.jtho.2016.06.031

27. Bao F, Ye P, Yang Y, Wang L, Zhang C, Lv X, et al. Segmentectomy or lobectomy for early stage lung cancer: a meta-analysis. *Eur J Cardiothorac Surg* (2014) 46(1):1–7. doi: 10.1093/ejcts/ezt554

28. Harrison S, Stiles B, Altorki N. What is the role of wedge resection for T1a lung cancer? *J Thorac Dis* (2018) 10(Suppl 10):S1157–62. doi: 10.21037/jtd.2018.03.188

29. Rami-Porta R, Bolejack V, Crowley J, Ball D, Kim J, Lyons G, et al. IASLC staging and prognostic factors committee, advisory boards and participating institutions. The IASLC lung cancer staging project: Proposals for the revisions of the T descriptors in the forthcoming eighth edition of the TNM classification for lung cancer. *J Thorac Oncol* (2015) 10(7):990–1003. doi: 10.1097/JTO.0000000000000559

30. Liu Q, Wang H, Zhou D, Deng X, Min J, Dai J. Comparison of clinical outcomes after thoracoscopic sublobectomy versus lobectomy for stage I nonsmall cell lung cancer: A meta-analysis. *J Cancer Res Ther* (2016) 12(2):926–31. doi: 10.4103/0973-1482.174181

31. Widder J, Van De Wauwer C, Langendijk JA. Lobectomy or sublobectomy for small non-small-cell lung cancer: The question remains. *J Clin Oncol* (2017) 35(5):572–3. doi: 10.1200/JCO.2016.70.0872

32. Kates M, Swanson S, Wisnivesky JP. Survival following lobectomy and limited resection for the treatment of stage I non-small cell lung cancer<=1 cm in size: a review of SEER data. *Chest* (2011) 139(3):491–6. doi: 10.1378/chest.09-2547

33. Tsubokawa N, Tsutani Y, Miyata Y, Handa Y, Misumi K, Hanaki H, et al. Segmentectomy versus lobectomy for radiologically pure solid clinical T1a-bN0M0 lung cancer. *World J Surg* (2018) 42(8):2493–501. doi: 10.1007/s00268-018-4514-0

34. Qiu B, Ji Y, Zhang F, Bai G, Xue Q, Polaczek M, et al. Outcomes and experience of anatomical partial lobectomy. *J Thorac Cardiovasc Surg* (2021) S0022-5223(21)01662–7. doi: 10.1016/j.jtcvs.2021.11.044

35. Cao C, Chandrakumar D, Gupta S, Yan TD, Tian DH. Could less be more?-a systematic review and meta-analysis of sublobar resections versus lobectomy for non-small cell lung cancer according to patient selection. *Lung Cancer* (2015) 89(2):121–32. doi: 10.1016/j.lungcan.2015.05.010

36. Saji H, Okada M, Tsuboi M, Nakajima R, Suzuki K, Aokage K, et al. Segmentectomy versus lobectomy in small-sized peripheral non-small-cell lung cancer (JCOG0802/WJOG4607L): A multicentre, open-label, phase 3, randomised, controlled, non-inferiority trial. *Lancet* (2022) 399(10335):1607–17. doi: 10.1016/S0140-6736(21)02333-3

37. Agarwal M, Brahmanday G, Chmielewski GW, Welsh RJ, Ravikrishnan KP. Age, tumor size, type of surgery, and gender predict survival in early stage (stage I and II) non-small cell lung cancer after surgical resection. *Lung Cancer* (2010) 68(3):398–402. doi: 10.1016/j.lungcan.2009.08.008

38. Saijo T, Ishii G, Nagai K, Funai K, Nitadori J, Tsuta K, et al. Differences in clinicopathological and biological features between central-type and peripheral-type squamous cell carcinoma of the lung. *Lung Cancer* (2006) 52(1):37–45. doi: 10.1016/j.lungcan.2005.12.006

39. Sung YE, Cho U, Lee KY. Peripheral type squamous cell carcinoma of the lung: clinicopathologic characteristics in comparison to the central type. *J Pathol Transl Med* (2020) 54(4):290–9. doi: 10.4132/jptm.2020.05.04

frontiers | Frontiers in Surgery

TYPE Original Research
PUBLISHED 25 August 2022
DOI 10.3389/fsurg.2022.913967

OPEN ACCESS

EDITED BY
Kee Yuan Ngiam,
National University Health System (Singapore), Singapore

REVIEWED BY
Anurag Srivastava,
National Institute of Cancer Prevention and Research (ICMR), India
Jun Cao,
Affiliated Hospital of Yangzhou University, China
Mingwei Gao,
Second Affiliated Hospital of Dalian Medical University, China

*CORRESPONDENCE
Tao Hong
ht710812@sohu.com

†These authors have contributed equally to this work and share first authorship

SPECIALTY SECTION
This article was submitted to Surgical Oncology, a section of the journal Frontiers in Surgery

RECEIVED 06 April 2022
ACCEPTED 18 July 2022
PUBLISHED 25 August 2022

CITATION
Zhuang F, Bai X, Shi Y, Chang L, Ai W, Du J, Liu W, Liu H, Zhou X, Wang Z and Hong T (2022) Metabolomic profiling identifies biomarkers and metabolic impacts of surgery for colorectal cancer.
Front. Surg. 9:913967.
doi: 10.3389/fsurg.2022.913967

Metabolomic profiling identifies biomarkers and metabolic impacts of surgery for colorectal cancer

Feng Zhuang[1†], Xuesong Bai[2†], Yang Shi[1], Le Chang[1], Wanchao Ai[1], Juan Du[1], Wei Liu[2], Humin Liu[1], Xukun Zhou[1], Zhong Wang[1] and Tao Hong[2*]

[1]General Surgery Department, Hospital of Xinjiang Production and Construction Corps, Urumchi, China, [2]General Surgery Department, Peking Union Medical College Hospital, China Academy of Medical Science & Peking Union Medical College, Beijing, China

Background: Colorectal cancer (CRC) is one of the most common malignant tumors with recurrence and metastasis after surgical resection. This study aimed to identify the physiological changes after surgery and explore metabolites and metabolic pathways with potential prognostic value for CRC.
Methods: An ultra-high-performance liquid chromatography Q-exactive mass spectrometry was used to profile serum metabolites from 67 CRC patients and 50 healthy volunteers. Principal component analysis (PCA) and orthogonal projections to latent structures-discriminant analysis were used to distinguish the internal characteristics of data in different groups. Multivariate statistics were compiled to screen the significant metabolites and metabolic pathways.
Result: A total of 180 metabolites were detected. Under the conditions of variable importance in projection >1 and p-value <0.05, 46 differentially expressed metabolites were screened for further pathway enrichment analysis. Based on the Kyoto Encyclopedia of Genes and Genomes database and Small Molecule Pathway Database, three metabolic pathways—arginine and proline metabolism, ascorbate and aldarate metabolism, and phenylalanine metabolism—were significantly altered after surgical resection and identified as associated with the removal of CRC. Notably, gamma-linolenic acid was upregulated in the CRC preoperative patients compared with those in healthy volunteers but returned to healthy levels after surgery.
Conclusion: Through serum-based metabolomics, our study demonstrated the differential metabolic characteristics in CRC patients after surgery compared with those before surgery. Our results suggested that metabonomic analysis may be a powerful method for exploring physiological alterations in CRC patients after surgery as well as a useful tool for identifying candidate biomarkers and monitoring disease recurrence.

Abbreviations
CRC, colorectal cancer; UHPLC, ultra-high-performance liquid chromatography; CEA, carcinoma embryonic antigen; BMI, body mass index; PCA, principal component analysis; OPLS-DA, orthogonal projections to latent structures-discriminant analysis; KEGG, Kyoto Encyclopedia of Genes and Genomes; SMPDB, Small Molecule Pathway Database; VIP, variable importance in projection; GLA, gamma-linolenic acid; P5C/GSA, pyrroline-5-carboxylate/glutamate-γ-semialdehyde; PYCRs, P5C reductases; PRODH/POX, proline dehydrogenase/proline oxidase; AMPK, AMP-activated protein kinase.

KEYWORDS

colorectal cancer, metabolomic profiling, tumorectomy, gamma-linolenic acid (GLA), proline, ascorbate, phenylalanine

Introduction

Colorectal cancer (CRC) ranks third among malignant tumors and second among the leading causes of cancer-related deaths worldwide (1). Despite the great advances in early detection and multimodality therapy for CRC (2), the outcome of patients with advanced tumors is still not satisfactory. Distant metastasis and recurrence are the major causes of death in patients with CRC (3). Therefore, there is an urgent need to better understand the underlying mechanisms of CRC occurrence and progression and to explore more effective interventions to prevent CRC recurrence.

Previous studies have shown that metabolic disorders contribute to the formation of a protumorigenic environment and are associated with the risk of CRC (4). Metabolomics, as a branch of systems biology following genomics, transcriptomics, and proteomics, was established to detect and analyze the profiling of metabolites in biofluids, cells, and tissues (5). Metabolomics is a technology used for identifying endogenous compounds as biomarkers in diseases and for unveiling potential mechanisms associated with disease processes (6). A variety of analytical platforms, including high-performance liquid chromatography/mass spectrometry (HPLC/MS), UPLC time-of-flight MS (UPLC-TOF-MS), and ultra-performance LC–MS (LC–MS), have been used to profile metabolites in various tumors by using tissue, urine, and serum samples (7, 8). A variety of metabolites, including tyrosine and glutamine–leucine, have been identified as biomarkers for the early diagnosis of CRC (9, 10). Our previous study also showed the important predictive role of hexadecanedioic acid, 4-dodecylbenzenesulfonic acid, 2-pyrocatechuic acid, and formylanthranilic acid in CRC patients by comparing serum differential metabolites between CRC patients and healthy controls (11).

Currently, surgical resection, including sufficient adjacent large intestine, mesentery, nearby lymph nodes, and blood vessels, is still the mainstay treatment for CRC patients (12). However, there are few studies exploring the changes in the serum metabolite profiles before and after surgery for patients with CRC. The metabolic impact of radical tumor resection on CRC patients remains unknown. In addition, there is still a lack of effective biomarkers for monitoring tumor recurrence after surgery. In our study, metabolomic technology based on ultra-high-performance liquid chromatography (UHPLC) was used to analyze the metabolic differences in the serum of CRC patients before and after radical surgical resection. The identification of affected metabolites and metabolic pathways may reveal the metabolic alterations associated with radical resection of colorectal tumors, providing insights into the comprehensive physiological changes associated with radical resection for CRC and improving guidelines for postoperative care, which may offer new methods for predicting the prognosis of surgical resection in CRC patients.

Materials and methods

Participants

The inclusion criteria for the healthy control group were healthy adults aged 18–80 years without any forms of cancer. Patients were included in the CRC group of this research if they met the following inclusion criteria: those who were 18–80 years old, had a definite diagnosis of carcinoma by biopsy pathology through colonoscopy or proctoscopy, successfully underwent radical resection of CRC, and had provided informed consent to participate in the study.

Patients who met the following conditions were excluded: those who had any other malignancy; had chronic renal failure; had human immunodeficiency virus infection or metabolic diseases, such as diabetes, fatty liver and obesity; or declined to participate.

A total of 50 healthy volunteers and 67 CRC patients were recruited for this study at the Peking Union Medical College Hospital between 2019 and 2021. All 67 CRC patients underwent radical resection of CRC by the same experienced surgical team. Information on the clinical characteristics of the patients, namely, sex, age, body mass index (BMI), level of serum carcinoma embryonic antigen (CEA), and histopathology classification, was collected and analyzed retrospectively. The research conformed to the Declaration of Helsinki and the guidelines of ethical standards. The research was reviewed and approved by the Ethics Committee of Peking Union Medical College Hospital. Signed informed consent was provided by all participants in this research.

Collection and preparation of samples

All blood samples were collected in the morning after fasting for 12 h, centrifuged at 3,000 rpm for 15 min at 4°C to separate the serum within 2 h, and preserved at −80°C for subsequent analysis. Blood samples of CRC patients were collected just before surgery and 1 week after the operation.

All serum samples were thawed at 4°C for approximately 1 h. Then, a 150 µl of serum was added to a 100 µl of freshly prepared internal standard solution and a 450 µl of precooled formaldehyde. The thoroughly mixed samples in a 2.0-ml Eppendorf tube were then centrifuged at 14,000 × *g* for 15 min at room temperature. The resulting supernatants were collected and dried in a centrifugal vacuum evaporator for 18 h.

Metabolomic analysis

The identification and quantitation of metabolites were performed by LC–MS/MS analyses using UHPLC on a Thermo Scientific UltiMate Dionex 3000 RSLC HPF system (Thermo Fisher Scientific, U.S.) with a UPLC BEH Amide column (2.1 mm × 100 mm, 1.7 µm) coupled to Q-Exactive Orbitrap (Thermo Fisher Scientific, USA). The instrument operated at a 60,000 resolution with a full mass scan ranging from 67 to 1,000 *m/z*. The mobile phase consisted of 25 mmol/L ammonium acetate plus an aqueous solution of 25 ammonia hydroxide (pH = 9.75) (A), and acetonitrile (B) was used to conduct chromatographic separation at 3 µl/min at 4°C.

Under the control of acquisition software (Xcalibur, Thermo Fisher Scientific), a QE HFX mass spectrometer was used to acquire MS/MS spectra in information-dependent acquisition (IDA) mode. The parameters are detailed as follows: sheath gas flow rate=30 Arb, aux gas flow rate=25 Arb, capillary temperature=350°C, full MS resolution=60,000, MS/MS resolution=7,500, and collision energy=10/30/60 in NCE mode. All the serum samples were complementarily analyzed in positive ion mode (+3.6 kV) and negative ion mode (−3.2 kV) in metabolic profiling studies. The metabolites were identified on the basis of a detected chromatographic peak with an associated retention time and a unique accurate *m/z* for UHPLC. MetaboScape 3.0 software was used for UHPLC data analyses including peak extraction, denoising, and normalization.

Statistical analysis

SIMCA software (V16.0.2, Sartorius Stedim Data Analytics AB, Umea, Sweden) was employed to perform logarithmic (LOG) and centralization (CTR) conversions on the data. Then, principal component analysis (PCA) and orthogonal projections to latent structures-discriminant analysis (OPLS-DA) were conducted to estimate the classification and validate grouping trends in different groups. A 200-iter permutation test for the OPLS-DA model was implemented to prevent overfitting. The intercept of R2 on the *Y*-axis was less than 0.4 and that of Q2 on the *Y*-axis was less than 0, indicating that the model was not overfitting with good robustness.

A paired *t*-test was conducted to compare the differences in metabolites between the pre- and postoperation groups. Differences in metabolites between CRC patients and healthy volunteers were compared with the unpaired Student's *t*-test. The VIP value represents the overall contribution and importance of each *X*-variable. A VIP value of <1 was considered significant. A *p*-value of <0.05 was considered statistically significant. MetaboAnalyst 4.0 (http://www.metaboanalyst.ca/MetaboAnalyst/) was used for pathway analysis and enrichment analysis based on the Kyoto Encyclopedia of Genes and Genomes (KEGG, http://www.genome.jp/kegg/) database and Small Molecule Pathway Database (SMPDB, http://smpdb.ca/) to further explore the metabolic pathways involved in the change in metabolites. iPath 3.0 (http://pathways.embl.de/) was used for the visualization of the crucial metabolites and significant metabolic pathways.

Results

Characteristics of participants

The population demographics and clinical characteristics of our study subjects are presented in **Table 1**, and these are sex, age, BMI value, level of serum CEA, and cancer location. The mean age was 60.79 years for patients with CRC and 61.52 years for controls ($p = 0.648$). There was also no difference in BMI or sex between CRC patients and healthy controls ($p = 0.214$, 0.88). In all 67 patients, the diagnosis of colon carcinoma was confirmed by a histopathological examination in 32 patients, and rectal carcinoma was confirmed in 35 patients. The mean value of CEA was 5.91 mmol/L for CRC patients.

Metabolic profiling of colorectal cancer patients

A total of 180 metabolites were detected by UHPLC. PCA and OPLS-DA were used to perform discriminative pattern recognition

TABLE 1 Clinical characteristics of the study population.

Parameters	CRC group (*N* = 67)	Control group (*N* = 50)	*p*-Value
Gender			
Male, *n* (%)	42 (62.7%)	32 (64.0%)	
Female, *n* (%)	25 (37.3%)	18 (36.0%)	0.88
Age, mean (range)	60.79 (40–87)	61.52 (50–82)	0.648
BMI (kg/m^2), mean ± SD	24.39 ± 3.31	25.13 ± 3.01	0.214
CEA (ng/ml), mean ± SD	5.91 ± 10.63	—	
Cancer location			
Colon, *n* (%)	32	—	
Rectum, *n* (%)	35	—	

A value of $p < 0.05$ was considered significant. BMI, body mass index; CEA, carcinoembryonic antigen; SD, standard deviation.

analysis for the metabolite data. PCA is an unsupervised projection method that converts a set of observed potentially correlated variables into linearly unrelated variables by orthogonal transformation. In our research, PCA revealed that the metabolomic characteristics between the pre- and postoperation groups were significantly different (Figure 1A). OPLS-DA score plots also displayed a well-distinguished and clustered pattern between pre- and postoperative patients (Figure 1B). The permutation test verified the validity of the OPLS-DA model with all permuted Q^2 and R^2 values lower than the original values, and the Q^2 (cum) intercepted the Y-axis at −1.23 (Figure 1C).

Identification of different metabolites

Based on the variable importance of the projection (VIP) threshold and p values in the paired-samples t-test for metabolites identified through the OPLS-DA model that we established, 46 differentially expressed metabolites were screened between pre- and postoperation groups with the criteria of VIP > 1 and p values <0.05. The log fold change values represent the difference between the two groups. Thirty-two metabolites with log fold change values <0 were downregulated, while 14 metabolites with log fold change values >0 were upregulated in postoperative patients compared with those in preoperative patients. The expression levels of these metabolites are presented in the heat map (Figure 2A). In addition, the correlations of these differentiated metabolites are declared by chord analysis in Figure 2B.

Metabolic pathway analysis

Next, pathway analysis was conducted on the basis of the KEGG database for the differentially expressed metabolites. The metabolic pathways potentially associated with these 46 differential metabolites were screened and are presented in Table 2 and Figure 3A, including arginine and proline metabolism, ascorbate and aldarate metabolism, and phenylalanine metabolism ($p = 0.0149$, 0.0165, and 0.0256). In addition, the enrichment analysis module of MetaboAnalyst 4.0 based on the metabolite sets from SMPDB was used to strengthen the understanding of the altered metabolic pathways and validate the correlation of arginine and proline metabolism with radical resection of CRC (Figure 3B, Supplementary Table S1, $p = 0.0272$). The metabolic network of the differential metabolites and altered metabolic pathways in the KEGG general metabolic pathway map is shown in Figure 3C.

Identification of the significant metabolites in colorectal cancer

By combining the serum metabolites in the control group, we identified significantly altered metabolites for both the preoperative group vs. the postoperative group and the preoperative group vs. the control group. Interestingly, there was one metabolite, gamma-linolenic acid (GLA), which was evidently decreased in the preoperative CRC patients compared with that in healthy volunteers, and then returned to the healthy group level after the operation (Figure 4). Ultimately, we selectively compared the expression levels of metabolites involved in the metabolic pathways associated with radical resection of CRC. In the process of arginine and proline metabolism, L-arginine in the postoperation group was increased, while L-proline, *cis*-4-hydroxy-D-proline, and phosphocreatine in the postoperation group were decreased compared with those in the healthy control group. The serum levels of *cis*-4-hydroxy-D-proline and phosphocreatine in CRC patients before hydroxy were significantly lower than those in

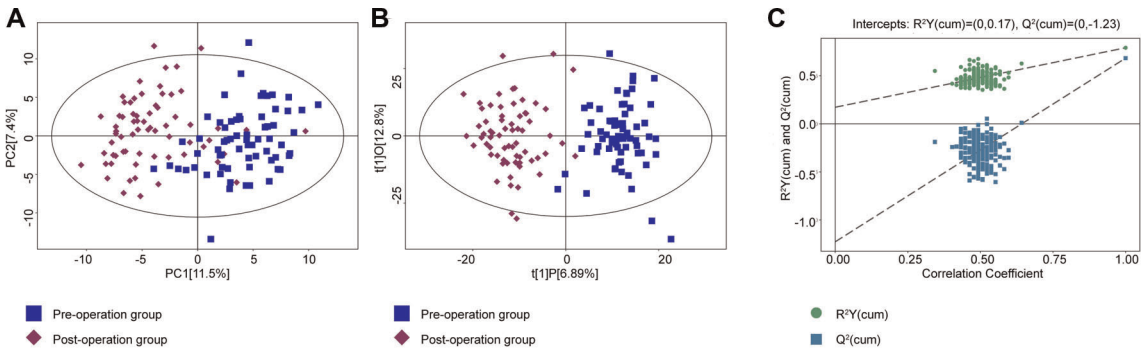

FIGURE 1
(A) PCA was conducted between the preoperation group (blue dots) and postoperation group (purple dots). (B) The OPLS-DA model was constructed using data from 67 CRC patients' serum metabonomics before (blue) and after (purple) surgery. (C) The permutation test plot of OPLS-DA (green, the value of R^2Y; blue, the value of Q^2; permutation test with 200 times, a p value of CV-ANOVA < 0.01). PCA, principal component analysis; OPLS-DA, orthogonal projections to latent structures-discriminant analysis; CRC, colorectal cancer.

FIGURE 2
(A) The heat map for the 46 critical metabolites between the pre- and postoperation groups, including 32 downregulated metabolites and 14 upregulated metabolites. (B) The correlation network of the 46 differentially expressed metabolites.

TABLE 2 Pathway analysis for the 46 critical metabolites based on KEGG.

Pathway name	Total	Hits	*p*	−log (*p*)	Impact
Arginine and proline metabolism	38	4	0.015	1.8266	0.13566
Ascorbate and aldarate metabolism	8	2	0.016	1.7829	0
Phenylalanine metabolism	10	2	0.026	1.591	0.2619
Aminoacyl-tRNA biosynthesis	48	4	0.033	1.4862	0
Arginine biosynthesis	14	2	0.049	1.3134	0.30457
Glycine, serine, and threonine metabolism	33	3	0.051	1.2935	0.3387
Butanoate metabolism	15	2	0.055	1.2583	0.03175
Pentose and glucuronate interconversions	18	2	0.077	1.1158	0.29688
Pyrimidine metabolism	39	3	0.077	1.1154	0.09694
Phenylalanine, tyrosine, and tryptophan biosynthesis	4	1	0.099	1.0027	0
Pentose phosphate pathway	22	2	0.108	0.96468	0.04712

healthy volunteers. In the metabolic pathways of ascorbate and aldarate, the preoperative myo-orthosito was significantly lower than that of healthy volunteers and higher than that of postoperative patients, while the postoperative L-gulono-1,4-lactone was significantly higher than that of healthy volunteers without any difference between the preoperative and healthy groups. Among the phenylalanine metabolism pathways, the postoperative phenylpyruvate was increased, while postoperative hippurate was prominently decreased compared with that of healthy volunteers.

Discussion

In this study, we used UHPLC to conduct serum untargeted metabolomic analysis for CRC patients and revealed the characteristic differences in the metabolomic profiles in CRC patients before and after surgery. Furthermore, the significant metabolic pathways related to CRC were also identified.

Our results showed that the metabolic profiles of arginine and proline were significantly altered in the serum of patients before and after surgery, among which, L-proline, *cis*-4-hydroxy-D-proline, and *cis*-4-hydroxy-D-proline were significantly downregulated after surgery. However, L-arginine was upregulated after surgery. As a nonessential amino acid, proline is the only proteinogenic secondary amino acid with an α amino group within the pyrrolidine ring (13). Proline is an important product of glutamine, which can be converted to proline *via* pyrroline-5-carboxylate/glutamate-γ-semialdehyde (P5C/GSA) (14). Proline and P5C are interconvertibly catalyzed by proline dehydrogenase/proline oxidase (PRODH/POX) and PYCRs, which play a role in maintaining redox homeostasis between the cytosol and the mitochondria, and contribute to the recycling of cellular NAD(P)H to NAD(P). Recently, studies have focused on the conducive role of proline for metabolic reprogramming of cancer and its clinical significance (14–16). Two well-recognized oncogenes, namely, c-MYC and phosphoinositide 3-kinase (PI3K), robustly upregulate the proline biosynthetic pathway by increasing its enzymes (P5CS, PYCR1/2/L) (13). Meanwhile, proline catabolism involving PRODH/POX, which is regulated by P53, peroxisome proliferator-activated receptor γ (PPARγ), and AMP-activated protein kinase (AMPK), can also initiate ROS-mediated senescence, apoptosis, and autophagy in tumors. The process of proline synthesis has been demonstrated to be necessary for tumor cell growth, and an increased level of proline synthesis has been observed in breast metastatic cancer cells, melanoma cells, and ovarian cancer stem cells (14). In addition, in lung cancer cell lines expressing high levels of endogenous MYC and proline synthetic enzymes, a knockdown of proline enzymes or MYC could significantly inhibit tumor growth. Supplementation with proline or P5C partly rescued the decrease in proliferation induced by a knockdown of P5CS or PYCR1/2. A high expression of PYCR1 was also significantly associated with poor prognostic molecular subtypes of breast cancer, which is consistent with our results of downregulated proline levels post operation compared with that of the preoperative period. However, its underlying mechanisms remain unclear. Here, it deserves mention that, not necessarily due to the disruption of protein synthesis, the proline metabolic pathway also functions to regulate redox-dependent signaling through parametabolic mechanisms. In tumors, proline for protein synthesis is lower than that in adjacent normal tissues. On the other hand, proline is also indispensable for tumors to help manage stress during tumorigenic growth (13). This might explain why there were no differences in proline levels in our results between samples from preoperative patients and healthy people.

It is generally accepted that ascorbate has a potential therapeutic effect on tumors by generating sustainable ascorbate radical and H_2O_2 in extracellular fluid (17). However, the underlying mechanisms for the selective cytotoxicity to cancer cells but not to normal ascorbate cells are not well understood. Recent research showed that high-dose intravenous ascorbate as an adjuvant could improve chemosensitivity and relieve the toxicity of chemotherapy for ovarian cancer, which was related to an activation of the ATM/AMPK pathway and inhibition of mTOR signaling due to DNA damage and ATP depletion triggered by ascorbate-generated ROS (18). In addition, another study reported that some genes involved in ascorbate and aldarate metabolism were overexpressed in adenocarcinoma compared with those in normal tissues (19). It has also been reported that ascorbate and aldarate metabolism are significantly disordered in renal cell carcinoma (20). In CRC, intravenous ascorbate is

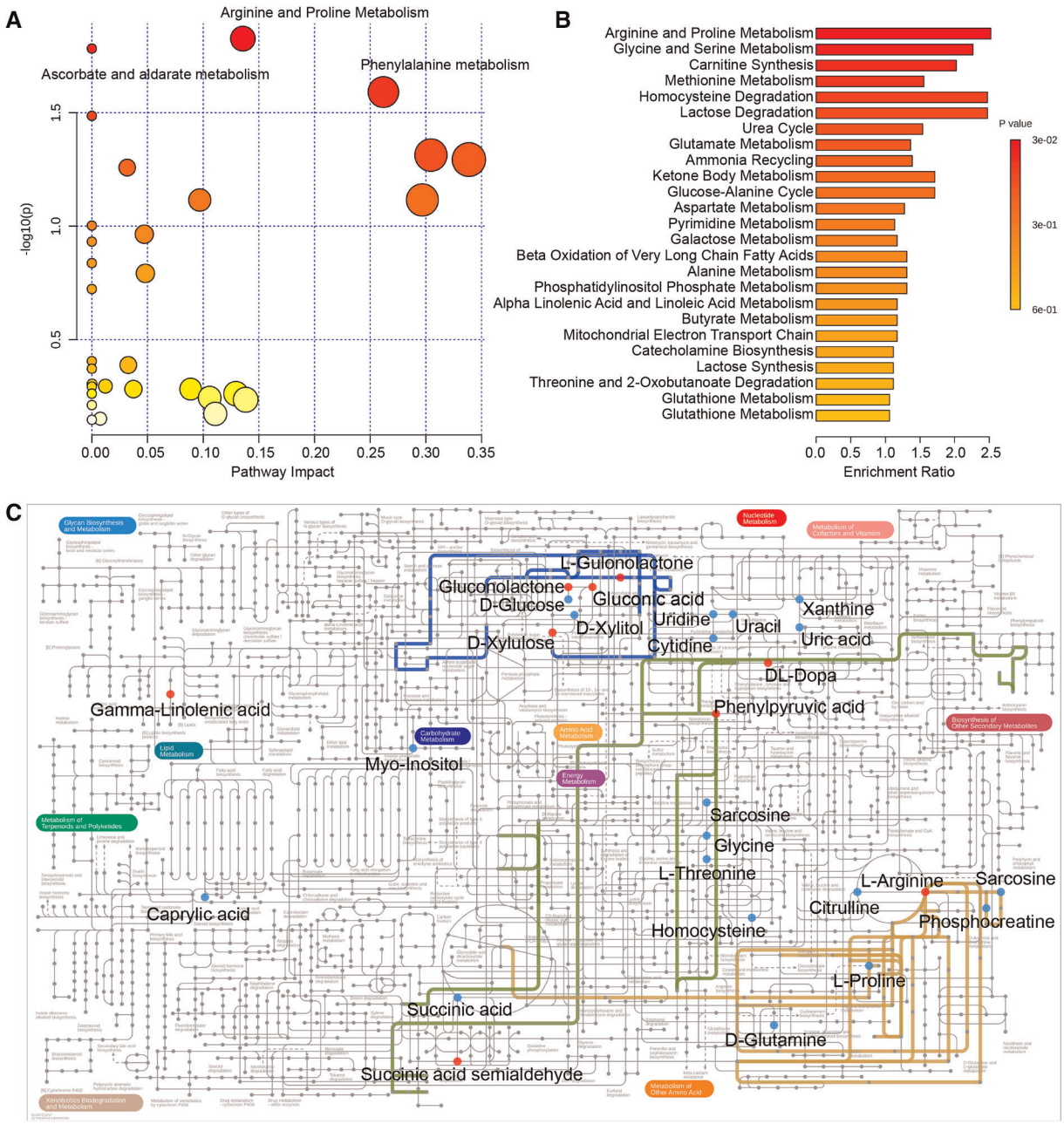

FIGURE 3
(A) Pathway analysis based on the KEGG database. (B) Enrichment analysis based on SMPDB. (C) Metabolic network of the crucial metabolites and significant metabolic pathways in the KEGG general metabolic pathway map. The following colored dots and lines denote the following: red dots, increased metabolites after surgery; blue dots, decreased metabolites after surgery; blue line, ascorbate and aldarate metabolism; yellow line, arginine and proline metabolism; green line, phenylalanine metabolism. KEGG, Kyoto Encyclopedia of Genes and Genomes; SMPDB, Small Molecule Pathway Database.

associated with the inhibition of tumor glycolysis, thus advancing tumor regression and improving the tolerance and side effects of chemotherapy (21, 22). However, the impact of surgical resection of CRC tumors on ascorbate and aldarate metabolism has not been studied. We found that the levels of compounds involved in ascorbate and aldarate metabolism increased following surgery, which may play a potential role in inhibiting tumor recurrence and may be a potential factor that improves the prognosis of CRC.

We also noticed that phenylalanine metabolism changed after the operation. Previous studies have shown the significant differences in serum phenylalanine levels

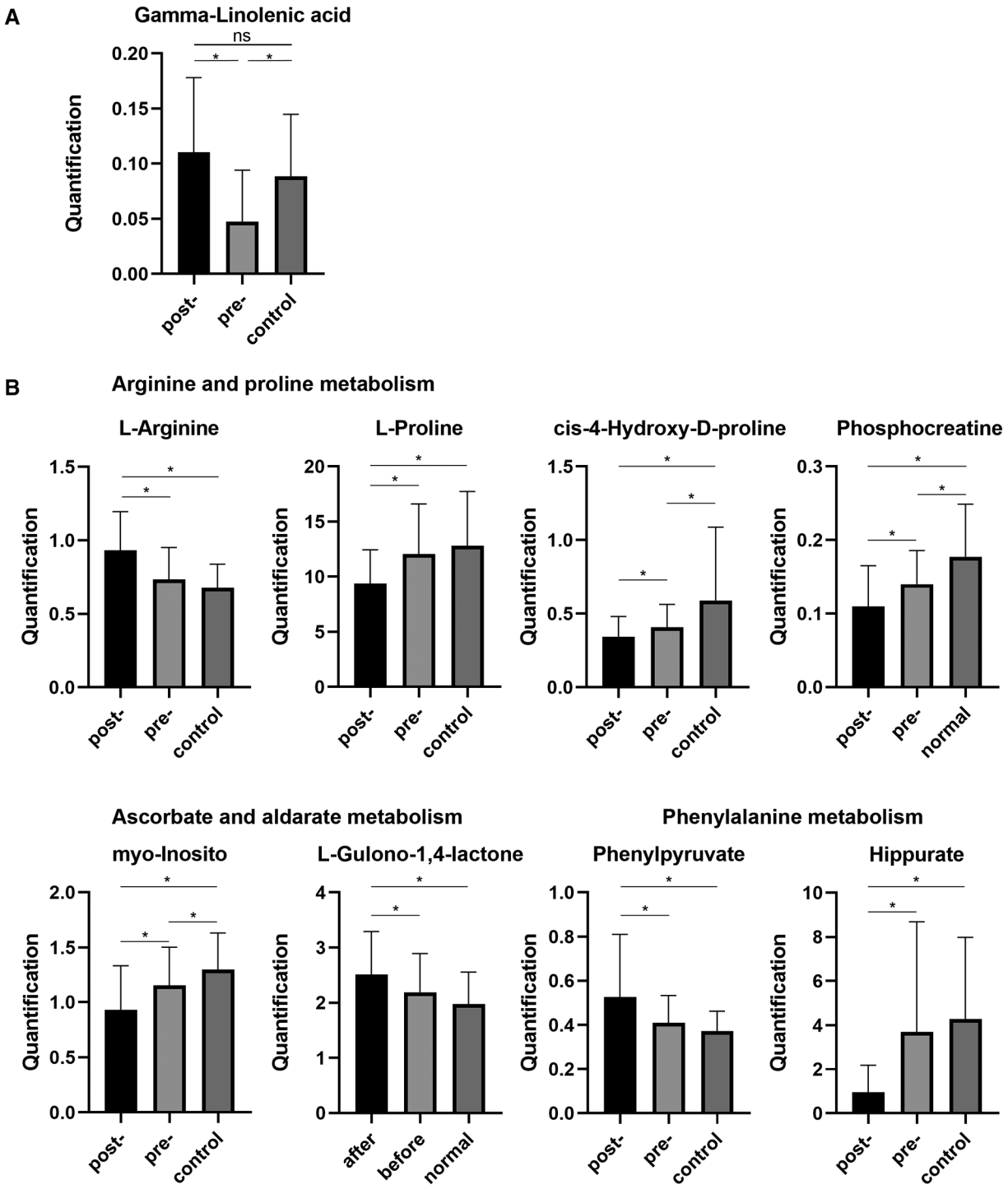

FIGURE 4
(A) Serum levels of GLA in healthy samples and preoperative and postoperative samples. (B) The expression levels of metabolites involved in the metabolic pathways associated with radical resection of CRC. GLA, gamma-linolenic acid. CRC, colorectal cancer. *$p < 0.05$. ns, not significant.

between gastroesophageal cancer patients and healthy volunteers, which may be accounted for by the dysfunction of phenylalanine hydroxylase activity in inflammatory or malignant disease states (23–25). In some tumors such as melanoma, hepatocarcinoma, leukemia, and breast cancer, lowering the serum levels of tyrosine and phenylalanine could inhibit the growth and metastases of tumors and improve the response to

chemotherapy. A low tyrosine and phenylalanine diet might be correlated with the stabilization and regression of cancer (26). However, the underlying mechanism remains unclear. In our research, instead of serum levels of phenylalanine or tyrosine, significant changes in phenethylamine and hippurate levels were observed compared with those before surgery. Even so, we think the elevated phenylpyruvate levels can also indicate the reduced activity of phenylalanine hydroxylase in patients with CRC, which may suggest that it is necessary to control and monitor serum phenylalanine levels after surgery.

GLA, as a polyunsaturated fatty acid (PUFA), is an intermediate product in the process of linoleic acid (all *cis*-6,9-octadecadienoic acid) metabolism (27). Recently, GLA has gained importance due to its antifibrotic, anti-inflammatory, and tumoricidal properties with little or no side effects. Previous studies have reported that low GLA levels are associated with the progression of inflammatory breast cancer (28). In mammary gland carcinoma induced by 7,12-dimethylbenz (*a*) anthracene (DMBA), GLA has been proven to activate the mitochondrial-mediated death apoptosis pathway, regulate hypoxia-induced cell signaling, and decrease the synthesis of *de novo* fatty acids fatty acid to execute its antitumor effect by mediating the cholinergic anti-inflammatory pathway (29). In addition, GLA has been reported to decrease the expression of the metastasis-associated protein osteonectin (or SPARC) and increase the expression of metastasis suppressor genes to inhibit tumor metastasis. GLA could also decrease the β-catenin expression of Wnt/b-catenin signaling pathway to inhibit gastric cancer cell growth and EMT induced by hypoxia (30). Additionally, polyunsaturated fatty acids, including GLA, could induce an apoptosis of colon cancer cells (31). However, further research is needed to determine the impact of GLA on CRC and its underlying mechanism. In our results, the preoperative serum GLA levels of CRC patients were significantly lower than those of the normal control group, which is consistent with the tendency described in previous studies. Interestingly, we observed that postoperative serum GLA levels in CRC patients were significantly elevated and approached the preoperative level, highlighting the potential role of GLA as an effective biomarker for CRC to help predict prognosis following surgery and detect postoperative recurrence.

Although we found that CRC surgery resection could bring about changes in some metabolic pathways, including arginine and proline metabolism, phenylalanine metabolism, and ascorbate and aldarate metabolism, there is no evidence in serum metabolomics that surgery can reverse the metabolic reprogramming caused by CRC. In addition, limited by the sample size, we could not group tumors according to their clinical stage, which might have effects on serum metabolites. In future studies, larger sample sizes and longer follow-up periods are necessary to explore the metabolomic profile associated with CRC and confirm its prognostic value. Furthermore, metabolomic information from CRC patients with adjuvant chemotherapy is needed to analyze differences in the sensitivity of different metabolomic characteristics to chemotherapy and the target metabolites for adjuvant treatments.

Conclusion

In summary, our study established a serum metabolomic signature associated with CRC surgery resection and explored the physiological alterations in CRC patients after surgery. The results suggested that removal of the tumor may affect the metabolic profiling of organisms caused by CRC, which provides insights into the scheme for postoperative nutritional support and postoperative adjuvant therapy. In addition, we identified the diagnostic and prognostic value of GLA as a novel CRC effective biomarker that can monitor treatment efficacy and tumor recurrence.

Data availability statement

The raw data supporting the conclusions of this article will be made available by the authors without undue reservation.

Ethics statement

The studies involving human participants were reviewed and approved by the Ethics Committee of Peking Union Medical College Hospital. The patients/participants provided their written informed consent to participate in this study. Written informed consent was obtained from the individuals for the publication of any potentially identifiable images or data included in this article.

Author contributions

FZ and XB contributed to the design of this study and data analysis, drafted the article, and revised the article. All authors contributed to the acquisition of the data and to the draft and revised versions of the article. All authors agreed on the journal to which the article will be submitted and gave final approval of the version to be published. All authors contributed to the article and approved the submitted version.

Funding

This study was funded by the Technology Cooperation Programme of Xinjiang Production and Construction Corps (2020BC010).

Acknowledgments

We gratefully thank all the subjects who participated in this study and acknowledge the support of Biotree Biomedical Technology Co.

Conflict of interest

The authors declare that the research was conducted in the absence of any commercial or financial relationships that could be construed as a potential conflict of interest.

Publisher's note

Supplementary material

The Supplementary Material for this article can be found online at: https://www.frontiersin.org/articles/10.3389/fsurg.2022.913967/full#supplementary-material.

References

1. Sung H, Ferlay J, Siegel RL, Laversanne M, Soerjomataram I, Jemal A, et al. Global cancer statistics 2020: GLOBOCAN estimates of incidence and mortality worldwide for 36 cancers in 185 countries. *CA Cancer J Clin*. (2021) 71 (3):209–49. doi: 10.3322/caac.21660

2. Punt CJ, Koopman M, Vermeulen L. From tumour heterogeneity to advances in precision treatment of colorectal cancer. *Nat Rev Clin Oncol*. (2017) 14 (4):235–46. doi: 10.1038/nrclinonc.2016.171

3. Choi JH, Jang TY, Jeon SE, Kim JH, Lee CJ, Yun HJ, et al. The small-molecule Wnt inhibitor ICG-001 efficiently inhibits colorectal cancer stemness and metastasis by suppressing MEIS1 expression. *Int J Mol Sci*. (2021) 22(24):13413. doi: 10.3390/ijms222413413

4. Esposito K, Chiodini P, Colao A, Lenzi A, Giugliano D. Metabolic syndrome and risk of cancer: a systematic review and meta-analysis. *Diabetes Care*. (2012) 35 (11):2402–11. doi: 10.2337/dc12-0336

5. Johnson CH, Ivanisevic J, Siuzdak G. Metabolomics: beyond biomarkers and towards mechanisms. *Nat Rev Mol Cell Biol*. (2016) 17(7):451–9. doi: 10.1038/nrm.2016.25

6. Rinschen MM, Ivanisevic J, Giera M, Siuzdak G. Identification of bioactive metabolites using activity metabolomics. *Nat Rev Mol Cell Biol*. (2019) 20 (6):353–67. doi: 10.1038/s41580-019-0108-4

7. Yang QJ, Zhao JR, Hao J, Li B, Huo Y, Han YL, et al. Serum and urine metabolomics study reveals a distinct diagnostic model for cancer cachexia. *J Cachexia Sarcopenia Muscle*. (2018) 9(1):71–85. doi: 10.1002/jcsm.12246

8. Jang C, Chen L, Rabinowitz JD. Metabolomics and isotope tracing. *Cell*. (2018) 173(4):822–37. doi: 10.1016/j.cell.2018.03.055

9. Li J, Li J, Wang H, Qi LW, Zhu Y, Lai M. Tyrosine and glutamine–leucine are metabolic markers of early-stage colorectal cancers. *Gastroenterology*. (2019) 157 (1):257–259.e5. doi: 10.1053/j.gastro.2019.03.020

10. Zhang A, Sun H, Yan G, Wang P, Han Y, Wang X. Metabolomics in diagnosis and biomarker discovery of colorectal cancer. *Cancer Lett*. (2014) 345 (1):17–20. doi: 10.1016/j.canlet.2013.11.011

11. Zhang C, Zhou S, Chang H, Zhuang F, Shi Y, Chang L, et al. Metabolomic profiling identified serum metabolite biomarkers and related metabolic pathways of colorectal cancer. *Dis Markers*. (2021) 2021:6858809. doi: 10.1155/2021

12. Hashiguchi Y, Muro K, Saito Y, Ito Y, Ajioka Y, Hamaguchi T, et al. Japanese society for Cancer of the Colon and rectum. Japanese Society for Cancer of the Colon and Rectum (JSCCR) guidelines 2019 for the treatment of colorectal cancer. *Int J Clin Oncol*. (2020) 25(1):1–42. doi: 10.1007/s10147-019-01485-z

13. Phang JM. Proline metabolism in cell regulation and cancer biology: recent advances and hypotheses. *Antioxid Redox Signal*. (2019) 30(4):635–49. doi: 10.1089/ars.2017.7350

14. Liu W, Hancock CN, Fischer JW, Harman M, Phang JM. Proline biosynthesis augments tumor cell growth and aerobic glycolysis: involvement of pyridine nucleotides. *Sci Rep*. (2015) 5:17206. doi: 10.1038/srep17206

15. Elia I, Broekaert D, Christen S, Boon R, Radaelli E, Orth MF, et al. Proline metabolism supports metastasis formation and could be inhibited to selectively target metastasizing cancer cells. *Nat Commun*. (2017) 8:15267. doi: 10.1038/ncomms15267

16. Sahu N, Dela Cruz D, Gao M, Sandoval W, Haverty PM, Liu J, et al. Proline starvation induces unresolved ER stress and hinders mTORC1-dependent tumorigenesis. *Cell Metab*. (2016) 24(5):753–61. doi: 10.1016/j.cmet.2016.08.008

17. Kouakanou L, Peters C, Brown CE, Kabelitz D, Wang LD. Vitamin C, from supplement to treatment: a re-emerging adjunct for cancer immunotherapy? *Front Immunol*. (2021) 12:765906. doi: 10.3389/fimmu.2021.765906

18. Ma Y, Chapman J, Levine M, Polireddy K, Drisko J, Chen Q. High-dose parenteral ascorbate enhanced chemosensitivity of ovarian cancer and reduced toxicity of chemotherapy. *Sci Transl Med*. (2014) 6(222):222ra18. doi: 10.1126/scitranslmed.3007154

19. Liu CC, Chen WS, Lin CC, Liu HC, Chen HY, Yang PC, et al. Topology-based cancer classification and related pathway mining using microarray data. *Nucleic Acids Res*. (2006) 34(14):4069–80. doi: 10.1093/nar/gkl583

20. Atrih A, Mudaliar MA, Zakikhani P, Lamont DJ, Huang JT, Bray SE, et al. Quantitative proteomics in resected renal cancer tissue for biomarker discovery and profiling. *Br J Cancer*. (2014) 110(6):1622–33. doi: 10.1038/bjc.2014.24

21. Tian W, Wang Z, Tang NN, Li JT, Liu Y, Chu WF, et al. Ascorbic acid sensitizes colorectal carcinoma to the cytotoxicity of arsenic trioxide via promoting reactive oxygen species-dependent apoptosis and pyroptosis. *Front Pharmacol*. (2020) 11:123. doi: 10.3389/fphar.2020.00123

22. El Halabi I, Bejjany R, Nasr R, Mukherji D, Temraz S, Nassar FJ, et al. Ascorbic acid in colon cancer: from the basic to the clinical applications. *Int J Mol Sci*. (2018) 19(9):2752. doi: 10.3390/ijms19092752

23. Neurauter G, Grahmann AV, Klieber M, Zeimet A, Ledochowski M, Sperner-Unterweger B, et al. Serum phenylalanine concentrations in patients with ovarian carcinoma correlate with concentrations of immune activation markers and of isoprostane-8. *Cancer Lett*. (2008) 272(1):141–7. doi: 10.1016/j.canlet.2008.07.002

24. Ploder M, Neurauter G, Spittler A, Schroecksnadel K, Roth E, Fuchs D. Serum phenylalanine in patients post trauma and with sepsis correlate to neopterin concentrations. *Amino Acids*. (2008) 35(2):303–7. doi: 10.1007/s00726-007-0625-x

25. Wiggins T, Kumar S, Markar SR, Antonowicz S, Hanna GB. Tyrosine, phenylalanine, and tryptophan in gastroesophageal malignancy: a systematic review. *Cancer Epidemiol Biomarkers Prev*. (2015) 24(1):32–8. doi: 10.1158/1055-9965.EPI-14-0980

26. Harvie MN, Campbell IT, Howell A, Thatcher N. Acceptability and tolerance of a low tyrosine and phenylalanine diet in patients with advanced cancer—a pilot study. *J Hum Nutr Diet*. (2002) 15(3):193–202. doi: 10.1046/j.1365-277X.2002.00365.x

27. Kapoor R, Huang YS. Gamma linolenic acid: an antiinflammatory omega-6 fatty acid. *Curr Pharm Biotechnol*. (2006) 7(6):531–4. doi: 10.2174/138920106779116874

28. Chas M, Goupille C, Arbion F, Bougnoux P, Pinault M, Jourdan ML, et al. Low eicosapentaenoic acid and gamma-linolenic acid levels in breast adipose tissue are associated with inflammatory breast cancer. *Breast*. (2019) 45:113–7. doi: 10.1016/j.breast.2019.04.001

29. Roy S, Singh M, Rawat A, Devi U, Gautam S, Yadav RK, et al. GLA supplementation regulates PHD2 mediated hypoxia and mitochondrial apoptosis in DMBA induced mammary gland carcinoma. *Int J Biochem Cell Biol*. (2018) 96:51–62. doi: 10.1016/j.biocel.2018.01.011

30. Wang Y, Shi J, Gong L. Gamma linolenic acid suppresses hypoxia-induced gastric cancer cell growth and epithelial-mesenchymal transition by inhibiting the Wnt/b-catenin signaling pathway. *Folia Histochem Cytobiol*. (2020) 58(2):117–26. doi: 10.5603/FHC.a2020.0012

31. Zhang C, Yu H, Shen Y, Ni X, Shen S, Das UN. Polyunsaturated fatty acids trigger apoptosis of colon cancer cells through a mitochondrial pathway. *Arch Med Sci*. (2015) 11(5):1081–94. doi: 10.5114/aoms.2015.54865

frontiers | Frontiers in Surgery

TYPE Original Research
PUBLISHED 09 September 2022
DOI 10.3389/fsurg.2022.917061

OPEN ACCESS

EDITED BY
Mengling Feng,
National University of Singapore, Singapore

REVIEWED BY
Linqiang Ma,
First Affiliated Hospital of Chongqing Medical University, China
Christos K. Kontos,
National and Kapodistrian University of Athens, Greece
Qianli Ma,
Yunnan Cancer Hospital, China

*CORRESPONDENCE
Dongsheng Pan
pands312@126.com
Peng Liang
1021091883@qq.com

†These authors have contributed equally to this work

SPECIALTY SECTION
This article was submitted to Surgical Oncology, a section of the journal Frontiers in Surgery

RECEIVED 10 April 2022
ACCEPTED 17 August 2022
PUBLISHED 09 September 2022

CITATION
Gan Y, Yang Y, Wu Y, Li T, Liu L, Liang F, Qi J, Liang P and Pan D (2022) Comprehensive transcriptomic analysis of immune-related eRNAs associated with prognosis and immune microenvironment in melanoma.
Front. Surg. 9:917061.
doi: 10.3389/fsurg.2022.917061

Comprehensive transcriptomic analysis of immune-related eRNAs associated with prognosis and immune microenvironment in melanoma

Yuling Gan[1†], Yuan Yang[2†], Yajiao Wu[3†], Tingdong Li[1], Libing Liu[1], Fudong Liang[1], Jianghua Qi[1], Peng Liang[1*] and Dongsheng Pan[1*]

[1]The 1st Department of Bone and Soft Tissue Oncology, Gansu Provincial Cancer Hospital, Lanzhou, China, [2]Department of Gastroenterology, The First Hospital of Lanzhou University, Lanzhou, China, [3]Department of Ophthalmology, The First Hospital of Lanzhou University, Lanzhou, China

Background: Recent evidence suggests that enhancer RNAs (eRNAs) play key roles in cancers. Identification of immune-related eRNAs (ireRNAs) in melanoma can provide novel insights into the mechanisms underlying its genesis and progression, along with potential therapeutic targets.
Aim: To establish an ireRNA-related prognostic signature for melanoma and identify potential drug candidates.
Methods: The ireRNAs associated with the overall survival (OS-ireRNAs) of melanoma patients were screened using data from The Cancer Genome Atlas (TCGA) *via* WGCNA and univariate Cox analysis. A prognostic signature based on these OS-ireRNAs was then constructed by performing the least absolute shrinkage and selection operator (LASSO) Cox regression analysis. The immune landscape associated with the prognostic model was evaluated by the ESTIMATE algorithm and CIBERSORT method. Finally, the potential drug candidates for melanoma were screened through the cMap database.
Results: A total of 24 OS-ireRNAs were obtained, of which 7 ireRNAs were used to construct a prognostic signature. The ireRNAs-related signature performed well in predicting the overall survival (OS) of melanoma patients. The risk score of the established signature was further verified as an independent risk factor, and was associated with the unique tumor microenvironment in melanoma. We also identified several potential anti-cancer drugs for melanoma, of which corticosterone ranked first.
Conclusions: The ireRNA-related signature is an effective prognostic predictor and provides reliable information to better understand the mechanism of ireRNAs in the progression of melanoma.

KEYWORDS

eRNA, tumor immune, prognosis, melanoma, corticosterone

Introduction

Melanoma is the most aggressive form of skin cancer, responsible for 90% of skin cancer-related death (1). While complete surgical resection is curative for early melanoma, it is largely ineffective against the metastatic cancer (2). In addition, targeted therapies have also not been able to improve survival outcomes of patients with metastatic melanoma (3). Accurate assessment of melanoma prognosis is crucial to guide clinical decision-making. To date, there are no highly sensitive and accurate prognostic biomarkers for melanoma. Given this, identification of novel biomarkers with prognostic and therapeutic significance is urgently needed.

Currently, melanoma staging is based on the American Joint Committee on Cancer (AJCC) melanoma TNM staging system, and is used by clinicians to assess prognosis and establish a treatment regimen (4). However, this system has its shortcomings and cannot meet the need for precision medicine. To improve the accuracy in assessing the melanoma prognosis, we need more objective methods. Recent evidence is accumulating on promising biomarkers, including enhancer RNAs (eRNAs) (5, 6).

Enhancers are principal gene regulatory elements that control transcription of linked genes (7). Studies increasingly show that enhancers also transcribe long noncoding RNAs (lncRNAs), known as the enhancer RNAs or eRNAs (8, 9), that were initially considered as transcriptional by-products. However, emerging evidence supports that most eRNAs are not transcriptional byproducts and play crucial roles in transcriptional activation and regulation of chromatin modeling (10). Previous studies have shown their direct involvement in tumorigenesis of cancers (11). Bal et al. found that mutations located in transcribed sequences encoding eRNAs impaired enhancer activity and ACTRT1 expression, which was instrumental in the initiation of basal cell carcinoma (12). Furthermore, the eRNA AP001056.1 was reported to be associated with overall survival (OS) in patients with head and neck carcinoma (13). Together these findings reveal that eRNAs play crucial roles in cancers and could serve as potential therapeutic targets. Identifying eRNAs from active enhancers enabled us to understand deeper complexity of the transcription program in cancers. However, eRNAs with functional significance in melanoma remain largely elusive.

Compared to non-cutaneous melanoma, cutaneous melanoma has the highest genomic mutational load, which translates to increased immunogenicity (14) and potentially greater responsiveness to immunotherapies. In fact, antagonists of immune checkpoint molecules such as cytotoxic T-lymphocyte-associated protein 4 (CTLA-4) and programmed cell death protein 1 (PD-1) have been used for the treatment of unresectable or metastatic melanoma (15). However, a significant subset of melanoma patients are either unresponsive to these drugs or eventually develop resistance (16). Therefore, it is essential to explore the molecular mechanisms associated with melanoma genesis and immune evasion in order to identify more effective targets for immunotherapies. A recent study showed that eRNAs are involved in the activation of immune responses (17). Additionally, most causal variants in autoimmune diseases located in immune cell enhancers that produced eRNAs under immune stimulation (18). Zhang et al. found that the expression levels of immune checkpoints in cancer cells correlate with eRNAs (19). Although these findings strongly indicate a functional interaction between eRNAs and tumor immune, it remains to be ascertained whether it influences the genesis and progression of melanomas.

In the present study, we identified immune-related eRNAs (ireRNAs) with prognostic significance using The Cancer Genome Atlas (TCGA) database. Subsequently, a prognostic signature based on these ireRNAs was established and validated in two separate subsets, which showed a good performance in predicting the OS of patients with melanoma. We also explored the underlying mechanisms by performing functional enrichment analyses and assessing the characteristics of tumor immune in the high- and low-risk groups. Finally, we identified 1,309 potential drug candidates for melanoma using the Connectivity Map (cMap) database, of which corticosterone was ranked first (**Supplementary Table S1**).

Methods

Identification of survival-related immune genes

The RNA-Seq transcriptome data and corresponding clinical information regarding cutaneous melanoma were downloaded from the TCGA data portal (https://tcga-data.nci.nih.gov/tcga/). After excluding samples from patients lacking complete survival information, a total of 447 samples were included in this analysis. These samples were randomly divided into a training data set ($n = 224$) and testing set ($n = 223$) as 1:1 rate using "caret" R package. Meanwhile, 1,811 immune-related genes were acquired from the ImmPort database (http://www.immport.org). Weighted gene co-expression network analysis (WGCNA) was performed to identify the prognosis-related modules in cutaneous melanoma using the "WGCNA" R package. These genes in the module were identified as survival-related immune genes and incorporated in subsequent analyses. The flow diagram of the study is shown in **Figure 1**.

Construction of the prognostic signature based on survival-related ireRNAs

A total of 1,580 eRNAs were identified in cutaneous melanoma using the PreSTIGE algorithm as previously described (20), and the

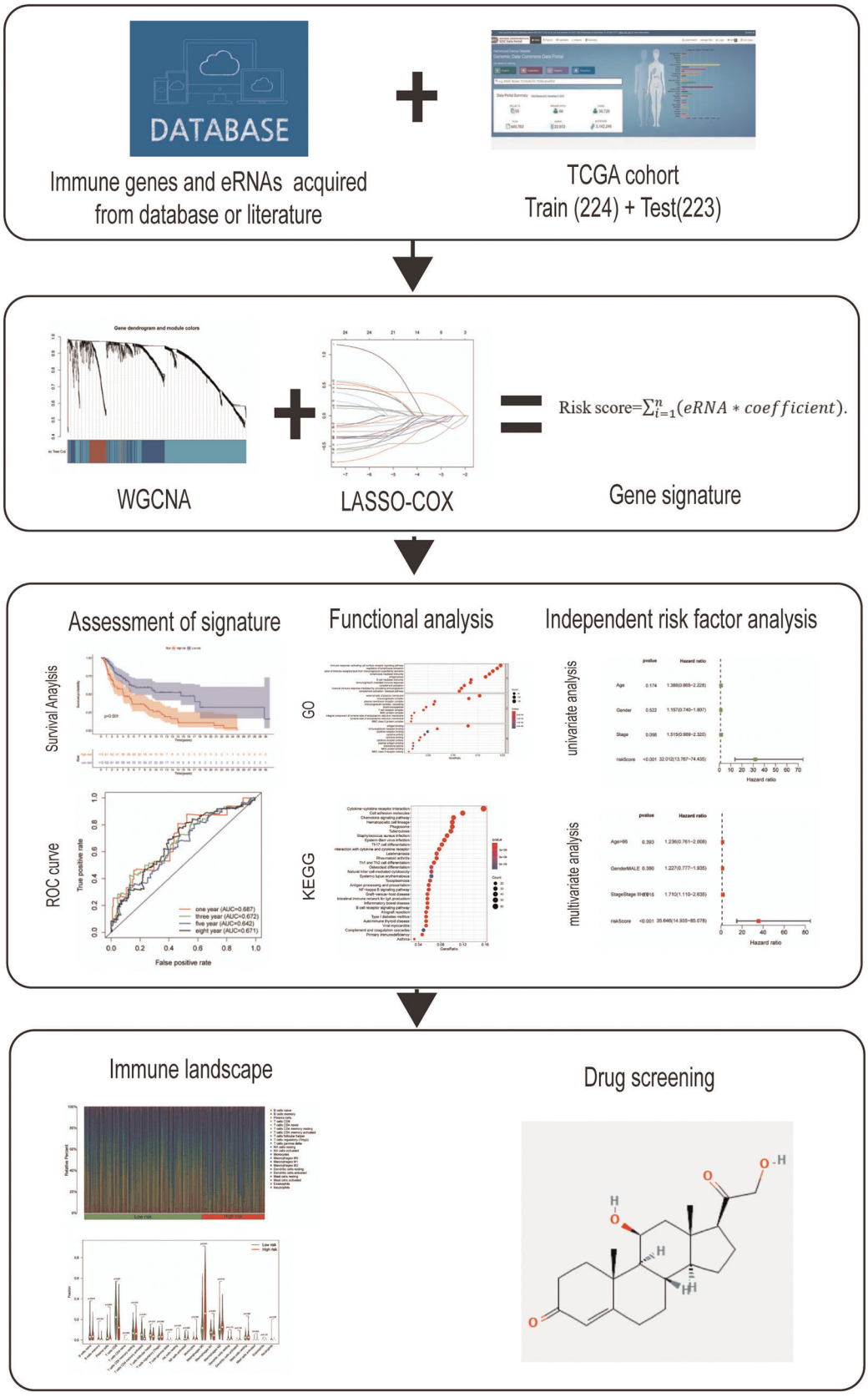

FIGURE 1
Flow diagram of the study.

ireRNAs were further screened using correlation analysis with correlation coefficient >0.4 and *P*-value <0.05 as the thresholds (21). After performing univariate Cox regression analysis, those ireRNAs with *P*-value of <0.05 were identified as OS-associated ireRNAs (OS-ireRNAs) and included subsequent analysis. The ireRNAs with the highest correlation to OS were then screened by least absolute shrinkage and selection operator (LASSO) analysis according to the optimal penalty parameter (λ) value determined by 10-round cross-validation. These filtered OS-ireRNAs were incorporated into the multivariate Cox regression model to establish the prognostic signature. The following formula to calculate the risk score of each patient is: Risk score $= \sum_{i=1}^{n}$ (expression level of eRNA $*$ LASSO regression coefficient). The median risk score among these patients in train cohort was used as the cut-off value. According to the median risk score, patients with cutaneous melanoma were divided into the high- and low-risk groups. To assess the prognostic value of the ireRNA-related signature, Kaplan–Meier survival curves were constructed to compare OS between the high- and low-risk groups using the "survival" and "survminer" R packages. And the log-rank test was used to assess whether they are statistically different. the prognostic performance of the model was determined by measuring the area under the receiver operating characteristic curve (AUC-ROC) with the "timeROC" R package. Univariate and multivariate Cox regression analyses were used to evaluate the relationship between OS and risk score and clinical characteristics. *P*-values <0.05 were regarded as statistically significant.

Analyses of the immune landscape

The "estimate" R package was used to calculate the ratio of immune-stromal components in the tumor microenvironment for each melanoma sample, and to compared the differences in ESTIMATE score, stromal score, and immune score between the high- and low-risk groups. The relative proportions of 22 infiltrating immune cell populations in the two risk groups were evaluated according to the gene expression profile using the CIBERSORT computational method.

Functional enrichment analyses

The differentially expressed genes (DEGs) between the high-risk and low-risk groups were screened according to absolute fold change (log2) >1.5 and FDR <0.05 as the thresholds. The DEGs were functionally annotated by Gene Ontology (GO) and Kyoto Encyclopedia of Genes and Genomes (KEGG) analyses using the "clusterProfiler" R package.

Exploration of potential drugs for melanoma

To select potential drugs for cutaneous melanoma, the filtered list of DEGs between the high-risk and low-risk groups were utilized to query the cMap database (http://cmap-online.org/).

Results

Construction and validation of an ireRNA-related signature for melanoma

As previously mentioned, the entire cohort was divided into a training cohort ($n = 224$) and a testing cohort ($n = 223$). The detailed clinical characteristics of training cohort, testing cohort and entire cohort are summarized in **Table 1**. The training cohort was utilized to construct the model. A total of 353 immune-related genes involved in the MEblue module were characterized as survival-related immune genes and rolled into subsequent analyses (**Supplementary Figure S1**). We identified 33 ireRNAs, of which 24 were significantly correlated to the OS (**Figure 2A**). Subsequently, the LASSO regression analysis was performed to select the key OS-ireRNAs as candidates (**Figures 2B,C**). Finally, we built the

TABLE 1 Clinical characteristics of the melanoma patients used in the present study.

Clinical characteristics	Entire cohort	Train cohort	Test cohort
No. of patients	447	224	223
Age			
≤65	294 (65.77%)	146 (65.18%)	148 (66.37%)
>65	153 (34.23%)	78 (34.82%)	75 (33.63%)
Gender			
Female	168 (37.58%)	92 (41.07%)	76 (34.08%)
Male	279 (62.42%)	132 (58.93%)	147 (65.92%)
T			
T0–2	140 (31.32%)	61 (27.23%)	79 (35.43%)
T3–4	233 (52.13%)	126 (56.25%)	107 (47.98%)
Tis	7 (1.57%)	5 (2.23%)	2 (0.9%)
Tx	67 (14.99%)	32 (14.29%)	35 (15.7%)
N			
N0	222 (49.66%)	112 (50%)	110 (49.33%)
N1–3	176 (39.37%)	87 (38.84%)	89 (39.91%)
NX	49 (10.96%)	25 (11.16%)	24 (10.76%)
M			
M0	402 (89.93%)	205 (91.52%)	197 (88.34%)
M1	21 (4.7%)	11 (4.91%)	10 (4.48%)
Mx	24 (5.37%)	8 (3.57%)	16 (7.17%)

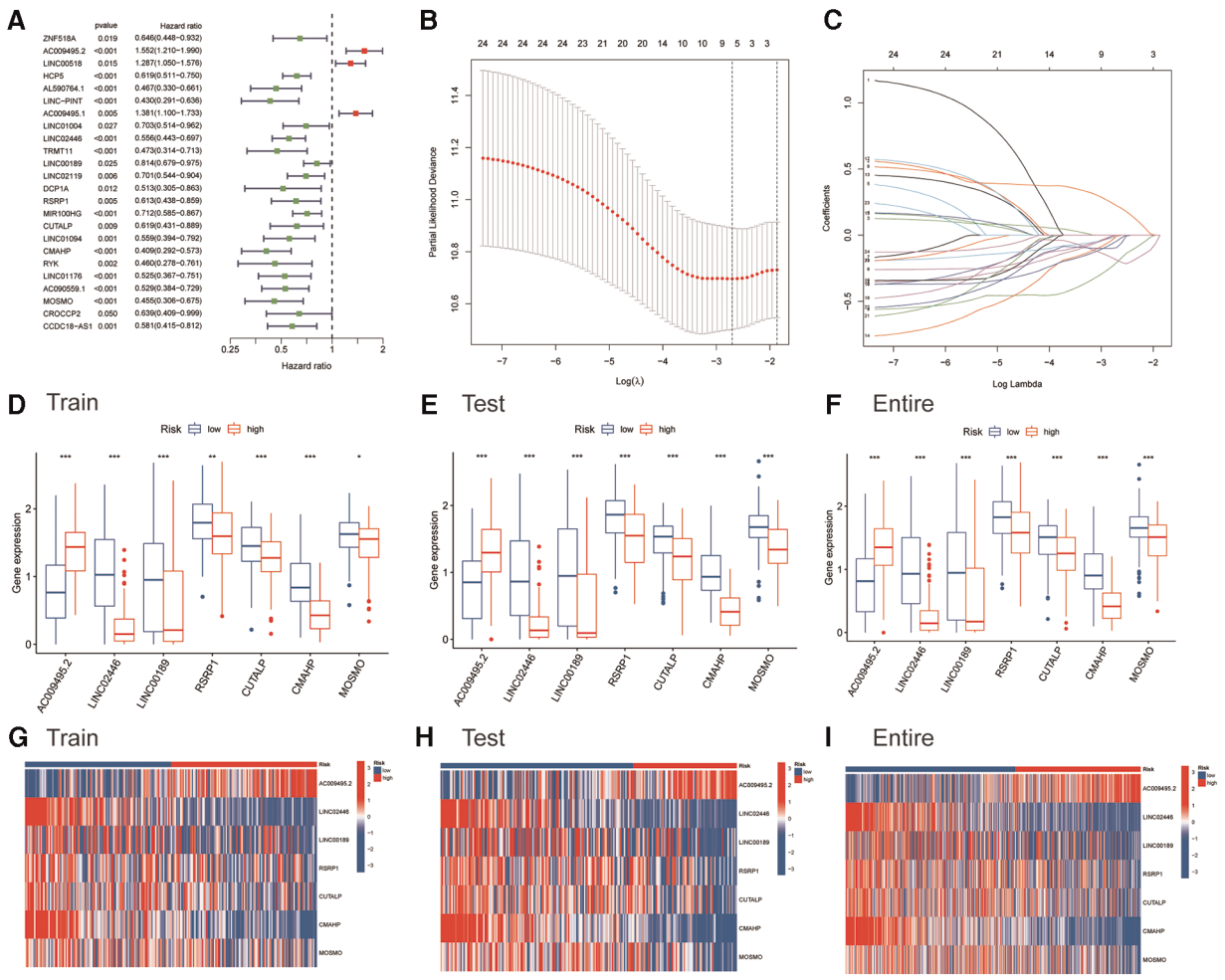

FIGURE 2
Identifying immune-related eRNAs (ireRNAs) associated with melanoma prognosis for construction of a signature. (A) Forest plots for hazard ratios of overall survival-related ireRNAs. (B) LASSO Cox analysis revealed 7 ireRNAs strongly correlated with the prognosis of melanoma. (C) The model's penalty parameter (λ) was determined by 10-round cross-validation. (D–F) Differentially expressed analyses for ireRNAs between high- and low-risk groups in the training, testing, and entire cohorts, respectively. (G–I) Heatmap for ireRNAs involved in the signatures of the training, testing, and entire cohorts, respectively.

prognostic signature with 7 OS-ireRNAs. The risk score of every patient was computed based on the following formula: risk score = AC009495.2 × 0.2300 + LINC02446 × (−0.2078) + LINC00189 × (−0.0083) + RSRP1 × (−0.0088) + CUTALP × (−0.0454) + CMAHP × (−0.1873) + MOSMO × (−0.0942). The median risk score was calculated as 0.817. According to the median risk score, patients with cutaneous melanoma in three cohorts (training cohort, testing cohort and entire cohort) were divided into the high- and low-risk groups, respectively. As shown in Figures 2D–F, there were significant differences in the expression of 7 OS-ireRNAs between the high-risk and low-risk groups in each cohort. Moreover, the heatmaps of these OS-ireRNAs expression profiles are shown in Figures 2G–I.

We generated the figures to show the risk score and survival status of each cutaneous melanoma sample (Figures 3A–C). The results indicated that the outcomes of patients in the high-risk group were worse compared to those in the low-risk group. Furthermore, the high-risk group had significantly shorter OS compared to the low-risk group in the training cohort (Figure 3D). Consistent results were observed in the testing cohort as well as the entire cohort (Figures 3E,F). The AUC-ROC values of the prognostic signature for 1-, 3-, 5- and 8-year OS in the training cohort were 0.687, 0.672, 0.642 and 0.671 respectively (Figure 3G). The corresponding values were 0.676, 0.621, 0.768 and 0.778 in the test cohort, and 0.686, 0.651, 0.705 and 0.716 in the entire cohort (Figure 3H,I). Therefore, the above results showed that the established signature expressed a good performance in monitoring survival and was robust when validated in another cohort.

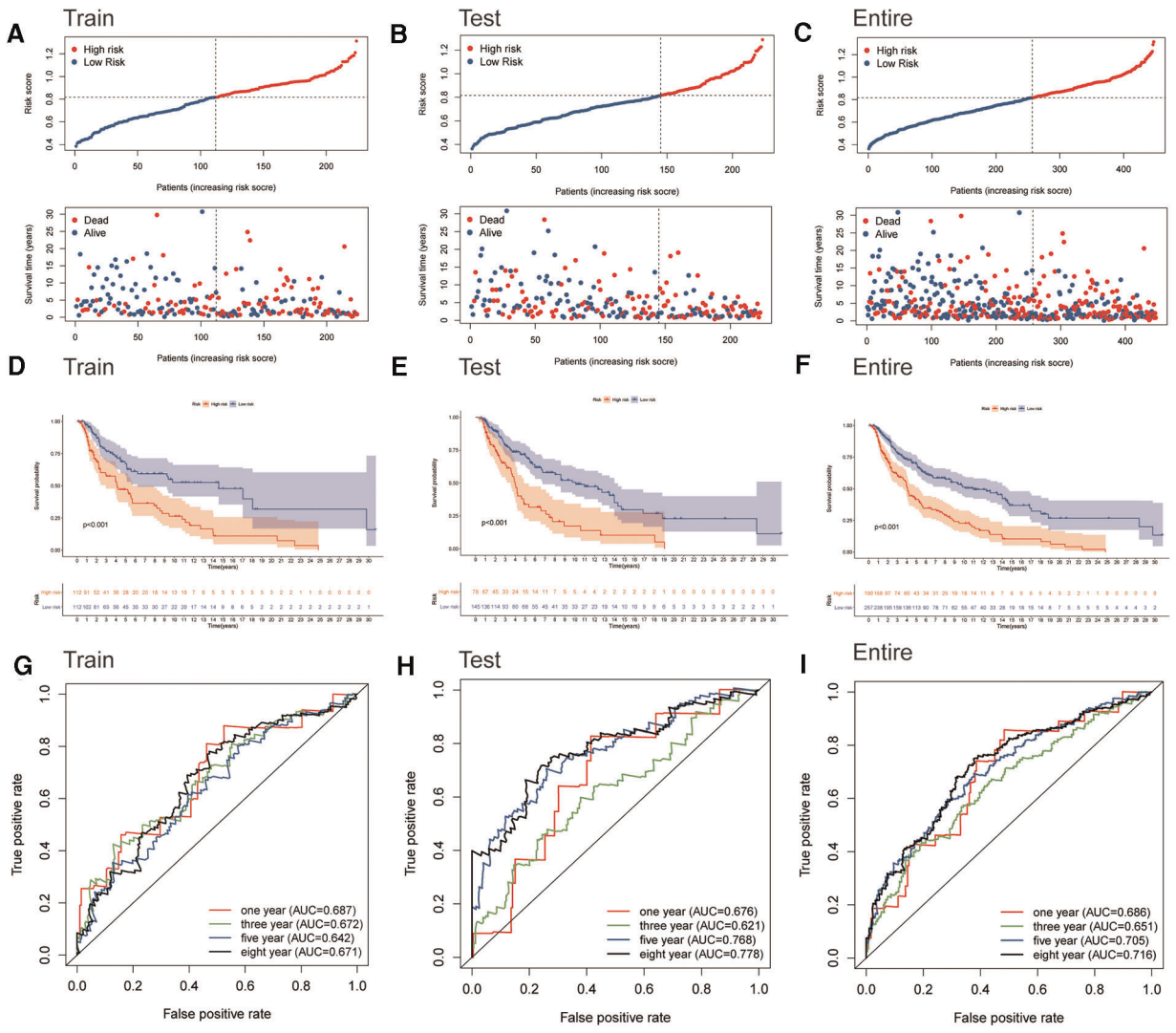

FIGURE 3
Assessment of the prognostic signature for melanoma. (A–C) Distributions of risk scores and OS status in the training, testing, and entire cohorts, respectively. (D–F) Kaplan-Meier survival analyses of the signature for the training, testing, and entire cohorts, respectively. (G–I) ROC curve of the prognostic signature in the training, testing, and entire cohorts, respectively.

The ireRNA-related signature independently predicts OS

We next subjected the ireRNA signature risk score and other clinicopathological parameters, including age, gender and TNM stage, to Cox regression analyses to further identify the independent risk factors of cutaneous melanoma. According to the univariate analysis, the risk score was significantly correlated with the OS in the training cohort (Figure 4A). The multivariate analysis further identified the risk score, T stage and N stage as independent risk factors for cutaneous melanoma (Figure 4B). These findings were verified in the test cohort and the entire cohort (Figures 4C–F).

Immune landscape of the ireRNA-related signature

To evaluate the immune landscape associated with the ireRNA-based signature, we calculated the stromal score, immune score and ESTIMATE score in both risk groups. As shown in Figures 5A–C, all immune-related scores were lower in the high-risk group compared to the low-risk group. The median scores were used to further stratify the patients into the respective high-score and low-score groups. As shown in Figures 5D–F, patients with high immune/ESTIMATE scores had significantly longer OS compared to those in the low-score group. In addition, we also compared

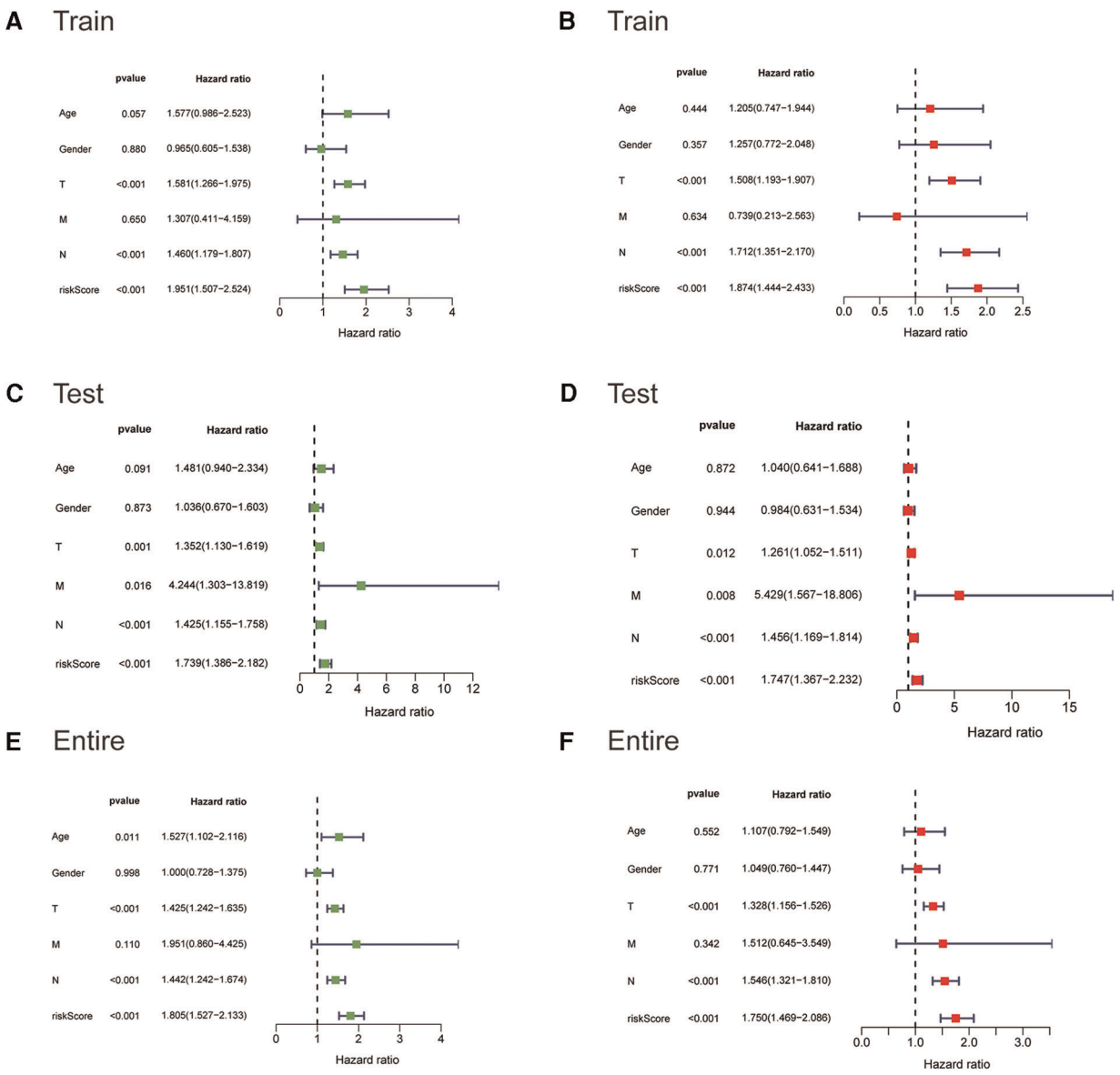

FIGURE 4
The Cox regression analyses for evaluating the independent prognostic value of the risk score. (A,C,E) Univariate Cox regression analyses of the association between survival and clinicopathological parameters and risk score for the training, testing, and entire cohorts, respectively. (B,D,F) Multivariate Cox regression analyses of the association between survival and clinicopathological parameters and risk score for the training, testing, and entire cohorts, respectively.

the immune infiltration status in the high-risk and low-risk-groups using CIBERSORT. As shown in Figure 5G, the high-risk group had significantly lower proportions of infiltrating plasma cells, T cells CD8, T cells CD4 memory activated, T cells follicular helper and macrophages M1, and significantly higher proportions of NK cells resting, macrophages M0 and macrophages M2 compared to the low-risk group. The association between each immune cell population and the risk score is shown in Figures 5H,I.

Functional analysis of the ireRNA-related signatures

To elucidate the potential biological processes and signaling pathways involving the ireRNA signature in cutaneous melanoma, we functionally annotated the 1,013 DEGs between the high-risk and low-risk groups (Supplementary Table S2) through GO and KEGG analyses. The genes in the high-risk group were mainly enriched in

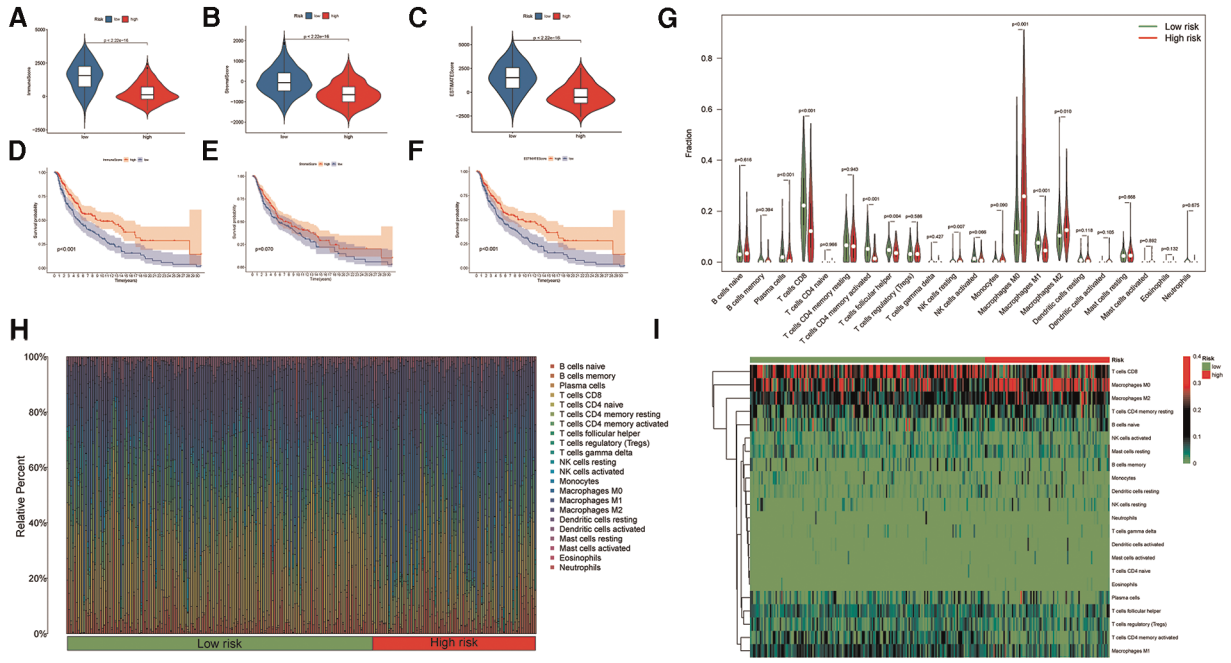

FIGURE 5
Association between the signature and immune landscape in melanoma. (A–C) The difference in immune, stromal, and ESTIMATE scores between the high- and low-risk groups. (D–F) Kaplan-Meier survival analyses of the risk scores based on the immune, stromal, and ESTIMATE scores, respectively. (G) Comparison of the infiltrating immune cells between the low- and high-risk groups. (H) Barplot showing the proportions of infiltrating immune cells in the low- and high-risk groups. (I) Heatmap for differences in the scores of immune cells between low- and high-risk groups.

immune-related processes and pathways, including cytokine–cytokine receptor interaction, immune response–activating cell surface receptor signaling pathway, regulation of lymphocyte activation, adaptive immune response, etc. (**Figures 6A,B**). These results suggested that the prognostically relevant ireRNAs identified for cutaneous melanoma may influence tumor progression by regulating the immune microenvironment.

Identifying the potential anti-cancer drug using cMap database

A total of 1,309 anti-cancer drug candidates were identified for cutaneous melanoma, of which corticosterone was ranked first and therefore may have the highest therapeutic potential.

Discussion

Melanoma is the most lethal form of skin cancer and has the potential for metastasis at the early stage. Until recently, metastatic melanoma could evade nearly all attempts at therapy. Accurate biomarkers are essential for improving the design of therapies to increase survival. However, the currently used AJCC staging system cannot predict the prognosis of melanoma patients accurately or consistently due to the variability between pathologists, and the inability to identify tumors with high risk of metastasis at the early stage (3, 22). Thus, these problems warrant the development of novel prognostic markers. There is ample evidence suggesting that eRNAs regulate the transcriptional activation of target genes in human diseases, including cancer, which is indicative of their potential as therapeutic targets (23). The identification of eRNAs is a breakthrough in the field, enabling us to in-depth characterize the landscape of transcriptional circuitry in cancers. Moreover, eRNAs are increasingly realized to be involved in the immune response. Interestingly, cutaneous melanoma is one of the most immunogenic tumors. In this study, therefore, we focused on identifying ireRNAs with prognostic significance to construct a signature for cutaneous melanoma. Compared with single eRNA-analysis, this method combined eRNAs and immune had higher information content and could reflect the complex interaction of eRNAs and tumor immune that mediated melanoma development and progression.

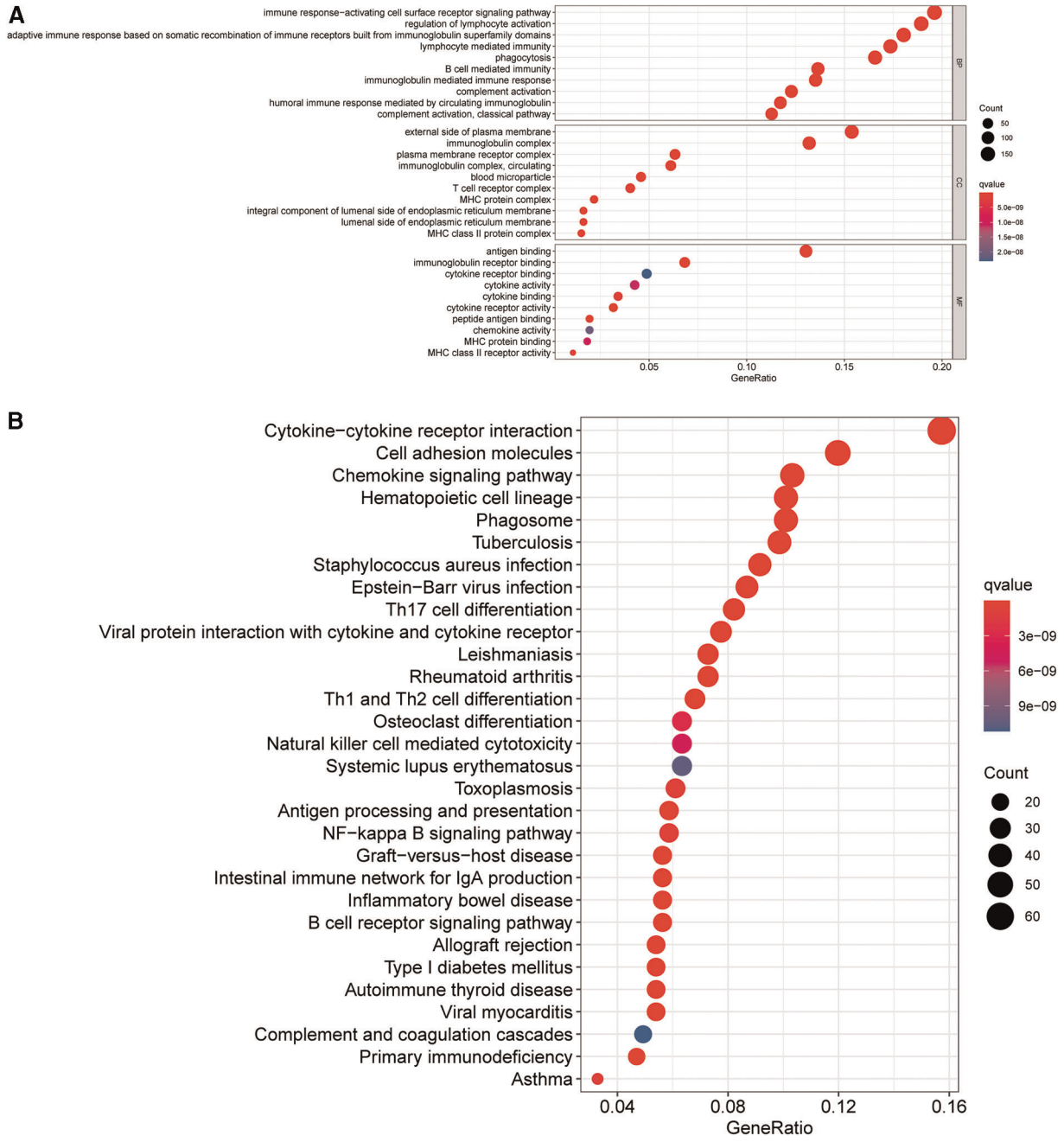

FIGURE 6
Functional analysis for the signature. (A) Significantly enriched biological processes in GO analysis. (B) Significantly enriched pathways in KEGG analysis.

We identified 33 ireRNAs, of which some are associated with immune functions and cancer progression. For example, HCP5 is aberrantly expressed in several different cancers and correlates with poor prognosis in patients with lung adenocarcinoma (24). In our study as well, HCP5 was identified as a survival-relevant eRNA in cutaneous melanoma. Furthermore, recent findings suggested that HCP5 was involved in adaptive and innate immune responses (25). Besides, Xu et al. found that LINC-PINT suppressed the tumorigenicity of melanoma by recruiting EZH2 to the promoter of target genes (26). Importantly, LINC-PINT has been proved to be a positive regulator of host innate immune responses, especially IFN signaling (27). LINC01094 expression predicted poor prognosis in patients

with gastric cancer and was correlated with the macrophage infiltration (28). Moreover, one study showed that MIR100HG participated in the immune escape of gastric cancer cells (29). Taken together, these results demonstrated a significant relationship between identified eRNAs and immune. In this regard, these findings also verified the accuracy of the results of this present study. However, the molecular mechanisms of ireRNAs in melanoma remain largely unstudied.

The prognostic signature based on the OS-ireRNAs included AC009495.2, LINC02446, LINC00189, RSRP1, CUTALP, CMAHP and MOSMO, and accurately predicted the prognosis of melanoma patients, especially for those who survived for more than 3 years. Additionally, the ireRNA-related signature proved robust when validated in another cohort. More importantly, multivariate analysis verified the risk score as an independent prognostic factor. Thus, our study provided an additional accurate predictive tool to clinical practice, in order to provide support in treatment decision-making.

The enhancer elements are frequently dysregulated during cancer initiation and progression. The eRNAs are the most reliable predictor of enhancer activity, and may alter the expression of several key genes during cancer progression (30). Therefore, we explored the biological function of the established risk score in melanoma, and found significant enrichment of immune-related processes and pathways in the GO and KEGG analyses. This was not surprising given the fact that eRNAs are ubiquitously produced in response to immunological and other stimuli (18, 31, 32). Furthermore, since the eRNAs are associated with coding genes involved in immune-regulatory pathways (33), we characterized the immune landscape in melanoma based on the risk score. In this study, the high-risk patients had lower proportions of Macrophages M1 and higher proportions of Macrophages M2. Tumor-associated macrophages (TAMs) are the major immune components of the tumor microenvironment, oscillating between an M1, anti-cancer phenotype and an M2, tumor-promoting phenotype (34). An increased proportion of infiltrating TAMs is found in the melanoma microenvironment, specifically in the M2 phenotype, which favors neoplastic growth and dissemination (35, 36). Studies have confirmed that the enrichment of M2 was a poor indicator for the outcome of patients with melanoma (35, 37). Our results are in agreement with previous findings. CD8+ T cells are the primary effectors of the anti-tumor adaptive immune response, which not only inhibit tumor growth but also mediate responses to cancer immunotherapies (38). Furthermore, increased infiltration of CD8+ T cells has been linked to prolonged survival of cutaneous melanoma patients (39). Consistent with this, the high-risk patients in our cohorts had lower infiltration of CD8+ cells. In this regard, these results suggested that the identified signature was closely associated with the tumor immune in melanoma.

Increasing evidence points to the potential of eRNAs as therapeutic targets for cancers. In addition, eRNAs have been proved to have an essential role in mediating cancer cell drug response (40). Zhang et al. found that *NET1e* overexpression increased IC50 of Obatoclax and BEZ235 in breast cancer cells, indicating a direct role of eRNAs in drug response (19, 40). Therefore, we also screened for the drug candidates of melanoma, and identified corticosterone as a novel therapeutic drug. A recent study showed that stress-induced increase in corticosterone levels suppressed tumor growth in a model of malignant melanoma (41). It was worth mentioning that the antitumor effect is mainly through reducing recruitment of TAMs (41). As mentioned above, the infiltration of TAMs is an adverse prognostic factor for melanoma. Thus, there might be a crosstalk between tumor immune and the antitumor effects of corticosterone in melanoma. It will be an important future direction to illustrate the molecular mechanism of corticosterone suppressing melanoma growth and the influences on tumor immunity.

Notwithstanding the salient points of the present study, there were some limitations that ought to be considered. Firstly, due to the lack of datasets containing all the information needed for this analysis, we just analyzed the data from the TCGA cohort. Although we verified the signature in two separate subsets, the data was relatively insufficient. Furthermore, datasets for the analysis were all retrospective, and these results were not validated prospectively.

Conclusion

In this present study, we constructed a prognostic signature for melanoma by integrating eRNAs and immune-related genes, which provided reliable information to better understand the mechanism of ireRNAs in the progression of melanoma. Moreover, we identified corticosterone as a potential antitumor-drug for melanoma, which warrants further research.

Data availability statement

The datasets presented in this study can be found in online repositories. The names of the repository/repositories and accession number(s) can be found in the article/ Supplementary Material.

Author contributions

YG, YY and YW conceptualized the idea, prepared the design, and wrote the manuscript. TL, LL, and FL developed the methodology. YG, YY, YW and JQ involved in analysis and interpretation of data. All authors reviewed and approved the manuscript. DP and PL supervised the study. All authors contributed to the article and approved the submitted version.

Conflict of interest

The authors declare that the research was conducted in the absence of any commercial or financial relationships that could be construed as a potential conflict of interest.

Publisher's note

Supplementary material

The Supplementary Material for this article can be found online at: https://www.frontiersin.org/articles/10.3389/fsurg.2022.917061/full#supplementary-material.

References

1. Siegel RL, Miller KD, Jemal A. Cancer statistics, 2020. *CA Cancer J Clin*. (2022) 70(1):7–30. doi: 10.3322/caac.21590

2. Patel H, Yacoub N, Mishra R, White A, Long Y, Alanazi S, et al. Current advances in the treatment of BRAF-mutant melanoma. *Cancers*. (2020) 12(2):482. doi: 10.3390/cancers12020482

3. Davis LE, Shalin SC, Tackett AJ. Current state of melanoma diagnosis and treatment. *Cancer Biol Ther*. (2019) 20(11):1366–79. doi: 10.1080/15384047.2019.1640032

4. Gershenwald JE, Scolyer RA, Hess KR, Sondak VK, Long GV, Ross MI, et al. Melanoma staging: evidence-based changes in the American Joint Committee on Cancer eighth edition cancer staging manual. *CA Cancer J Clin*. (2017) 67(6):472–92. doi: 10.3322/caac.21409

5. Yang S, Zou X, Yang H, Li J, Zhang A, Zhang L, et al. Identification of enhancer RNA CDK6-AS1 as a potential novel prognostic biomarker in gastric cancer. *Front Genet*. (2022) 13:854211. doi: 10.3389/fgene.2022.854211

6. Cheng L, Han T, Chen B, Nie K, Peng W. TBX5-AS1, An enhancer RNA, is a potential novel prognostic biomarker for lung adenocarcinoma. *BMC Cancer*. (2021) 21(1):794. doi: 10.1186/s12885-021-08517-w

7. Shlyueva D, Stampfel G, Stark A. Transcriptional enhancers: from properties to genome-wide predictions. *Nat Rev Genet*. (2014) 15(4):272–86. doi: 10.1038/nrg3682

8. Kim TK, Hemberg M, Gray JM, Costa AM, Bear DM, Wu J, et al. Widespread transcription at neuronal activity-regulated enhancers. *Nature*. (2010) 465(7295):182–7. doi: 10.1038/nature09033

9. Natoli G, Andrau JC. Noncoding transcription at enhancers: general principles and functional models. *Annu Rev Genet*. (2012) 46:1–19. doi: 10.1146/annurev-genet-110711-155459

10. Ye R, Cao C, Xue Y. Enhancer RNA: biogenesis, function, and regulation. *Essays Biochem*. (2020) 64(6):883–94. doi: 10.1042/EBC20200014

11. Adhikary S, Roy S, Chacon J, Gadad SS, Das C. Implications of enhancer transcription and eRNAs in cancer. *Cancer Res*. (2021) 81(16):4174–82. doi: 10.1158/0008-5472

12. Bal E, Park HS, Belaid-Choucair Z, Kayserili H, Naville M, Madrange M, et al. Mutations in ACTRT1 and its enhancer RNA elements lead to aberrant activation of Hedgehog signaling in inherited and sporadic basal cell carcinomas. *Nat Med*. (2017) 23(10):1226–33. doi: 10.1038/nm.4368

13. Gu X, Wang L, Boldrup L, Coates PJ, Fahraeus R, Sgaramella N, et al. AP001056.1, A prognosis-related enhancer RNA in squamous cell carcinoma of the head and neck. *Cancers (Basel)*. (2019) 11(3):347. doi: 10.3390/cancers11030347

14. Hayward NK, Wilmott JS, Waddell N, Johansson PA, Field MA, Nones K, et al. Whole-genome landscapes of major melanoma subtypes. *Nature*. (2017) 545(7653):175–80. doi: 10.1038/nature22071

15. Luke JJ, Flaherty KT, Ribas A, Long GV. Targeted agents and immunotherapies: optimizing outcomes in melanoma. *Nat Rev Clin Oncol*. (2017) 14(8):463–82. doi: 10.1038/nrclinonc.2017.43

16. Gide TN, Wilmott JS, Scolyer RA, Long GV. Primary and acquired resistance to immune checkpoint inhibitors in metastatic melanoma. *Clin Cancer Res*. (2018) 24(6):1260–70. doi: 10.1158/1078-0432

17. Huang Z, Du G, Huang X, Han L, Han X, Xu B, et al. The enhancer RNA lnc-SLC4A1-1 epigenetically regulates unexplained recurrent pregnancy loss (URPL) by activating CXCL8 and NF-kB pathway. *EBioMedicine*. (2018) 38:162–70. doi: 10.1016/j.ebiom

18. Farh KK, Marson A, Zhu J, Kleinewietfeld M, Housley WJ, Beik S, et al. Genetic and epigenetic fine mapping of causal autoimmune disease variants. *Nature*. (2015) 518(7539):337–43. doi: 10.1038/nature13835

19. Zhang Z, Lee JH, Ruan H, Ye Y, Krakowiak J, Hu Q, et al. Transcriptional landscape and clinical utility of enhancer RNAs for eRNA-targeted therapy in cancer. *Nat Commun*. (2019) 10(1):4562. doi: 10.1038/s41467-019-12543-5

20. Vučićević D, Corradin O, Ntini E, Scacheri PC, Ørom UA. Long ncRNA expression associates with tissue-specific enhancers. *Cell Cycle*. (2015) 14(2):253–60. doi: 10.4161/15384101

21. Yang Y, Shi L, Zhang J, Zheng Y, Wu G, Sun J, et al. A novel matrisomal-related LncRNA signature associated with survival outcome and immune evasion in patients with gastric cancer. *Front Oncol*. (2022) 12:926404. doi: 10.3389/fonc.2022.926404

22. Abbas O, Miller DD, Bhawan J. Cutaneous malignant melanoma: update on diagnostic and prognostic biomarkers. *Am J Dermatopathol*. (2014) 36(5):363–79. doi: 10.1097/DAD.0b013e31828a2ec5

23. Li W, Notani D, Rosenfeld MG. Enhancers as non-coding RNA transcription units: recent insights and future perspectives. *Nat Rev Genet*. (2016) 17(4):207–23. doi: 10.1038/nrg.2016.4

24. Jiang L, Wang R, Fang L, Ge X, Chen L, Zhou M, et al. HCP5 Is a SMAD3-responsive long non-coding RNA that promotes lung adenocarcinoma metastasis via miR-203/SNAI axis. *Theranostics*. (2019) 9(9):2460–74. doi: 10.7150/thno.31097

25. Kulski JK. Long noncoding RNA HCP5, a hybrid HLA class I endogenous retroviral gene: structure, expression, and disease associations. *Cells*. (2019) 8(5):480. doi: 10.3390/cells8050480

26. Xu Y, Wang H, Li F, Heindl LM, He X, Yu J, et al. Long non-coding RNA LINC-PINT suppresses cell proliferation and migration of melanoma via recruiting EZH2. *Front Cell Dev Biol*. (2019) 7:350. doi: 10.3389/fcell.2019.00350

27. Khatun M, Zhang J, Ray R, Ray RB. Hepatitis C virus evades interferon signaling by suppressing long noncoding RNA linc-pint involving C/EBP-β. *J Virol*. (2021) 95(17):e0095221. doi: 10.1128/JVI.00952-21

28. Ye Y, Ge O, Zang C, Yu L, Eucker J, Chen Y. LINC01094 predicts poor prognosis in patients with gastric cancer and is correlated with EMT and

macrophage infiltration. *Technol Cancer Res Treat*. (2022) 21:15330338221080977. doi: 10.1177/15330338221080977

29. Li P, Ge D, Li P, Hu F, Chu J, Chen X, et al. CXXC Finger protein 4 inhibits the CDK18-ERK1/2 axis to suppress the immune escape of gastric cancer cells with involvement of ELK1/MIR100HG pathway. *J Cell Mol Med*. (2020) 24 (17):10151–65. doi: 10.1111/jcmm.15625

30. Sartorelli V, Lauberth SM. Enhancer RNAs are an important regulatory layer of the epigenome. *Nat Struct Mol Biol*. (2020) 27(6):521–8. doi: 10.1038/s41594-020-0446-0

31. Li W, Notani D, Ma Q, Tanasa B, Nunez E, Chen AY, et al. Functional roles of enhancer RNAs for oestrogen-dependent transcriptional activation. *Nature*. (2013) 498(7455):516–20. doi: 10.1038/nature12210

32. Rahnamoun H, Lee J, Sun Z, Lu H, Ramsey KM, Komives EA, et al. RNAs interact with BRD4 to promote enhanced chromatin engagement and transcription activation. *Nat Struct Mol Biol*. (2018) 25(8):687–97. doi: 10.1038/s41594-018-0102-0

33. Agirre X, Meydan C, Jiang Y, Garate L, Doane AS, Li Z, et al. Long non-coding RNAs discriminate the stages and gene regulatory states of human humoral immune response. *Nat Commun*. (2019) 10(1):821. doi: 10.1038/s41467-019-08679-z

34. Jayasingam SD, Citartan M, Thang TH, Mat Zin AA, Ang KC, Ch'ng ES. Evaluating the polarization of tumor-associated macrophages into M1 and M2 phenotypes in human cancer tissue: technicalities and challenges in routine clinical practice. *Front Oncol*. (2020) 9:1512. doi: 10.3389/fonc.2019.01512

35. Falleni M, Savi F, Tosi D, Agape E, Cerri A, Moneghini L, et al. M1 and M2 macrophages' clinicopathological significance in cutaneous melanoma. *Melanoma Res*. (2017) 27(3):200–10. doi: 10.1097/CMR.0000000000000352

36. Salmi S, Siiskonen H, Sironen R, Tyynelä-Korhonen K, Hirschovits-Gerz B, Valkonen M, et al. The number and localization of CD68+ and CD163+ macrophages in different stages of cutaneous melanoma. *Melanoma Res*. (2019) 29(3):237–47. doi: 10.1097/CMR.0000000000000522

37. Buscher K, Ehinger E, Gupta P, Pramod AB, Wolf D, Tweet G, et al. Natural variation of macrophage activation as disease-relevant phenotype predictive of inflammation and cancer survival. *Nat Commun*. (2017) 8:16041. doi: 10.1038/ncomms16041

38. Gonzalez H, Hagerling C, Werb Z. Roles of the immune system in cancer: from tumor initiation to metastatic progression. *Genes Dev*. (2018) 32(19-20) :1267–84. doi: 10.1101/gad.314617.118

39. Piras F, Colombari R, Minerba L, Murtas D, Floris C, Maxia C, et al. The predictive value of CD8, CD4, CD68, and human leukocyte antigen-D-related cells in the prognosis of cutaneous malignant melanoma with vertical growth phase. *Cancer*. (2005) 104(6):1246–54. doi: 10.1002/cncr.21283

40. Lee JH, Xiong F, Li W. Enhancer RNAs in cancer: regulation, mechanisms and therapeutic potential. *RNA Biol*. (2020) 17(11):1550–9. doi: 10.1080/15476286.2020.1712895

41. Steinberger KJ, Bailey MT, Gross AC, Sumner LA, Voorhees JL, Crouser N, et al. Stress-induced norepinephrine downregulates CCL2 in macrophages to suppress tumor growth in a model of malignant melanoma. *Cancer Prev Res*. (2020) 13(9):747–60. doi: 10.1158/1940-6207.CAPR-19-0370

frontiers | Frontiers in Oncology

TYPE Original Research
PUBLISHED 04 October 2022
DOI 10.3389/fonc.2022.942425

OPEN ACCESS

EDITED BY
Mengling Feng,
National University of Singapore, Singapore

REVIEWED BY
Yuming Jiang,
Stanford University, United States
Huan Zhang,
Shanghai Jiao Tong University, China

*CORRESPONDENCE
Jin-rong Qu,
qjryq@126.com

SPECIALTY SECTION
This article was submitted to Surgical Oncology, a section of the journal Frontiers in Oncology

RECEIVED 20 June 2022
ACCEPTED 16 September 2022
PUBLISHED 04 October 2022

CITATION
Li J, Wang Y, Wang R, Gao J-b and Qu J-r (2022) Spectral CT for preoperative prediction of lymphovascular invasion in resectable gastric cancer: With external prospective validation.
Front. Oncol. 12:942425.
doi: 10.3389/fonc.2022.942425

Spectral CT for preoperative prediction of lymphovascular invasion in resectable gastric cancer: With external prospective validation

Jing Li[1], Yi Wang[2], Rui Wang[3], Jian-bo Gao[3] and Jin-rong Qu[1]*

[1]Department of Radiology, The Affiliated Cancer Hospital of Zhengzhou University (Henan Cancer Hospital), Zhengzhou, China, [2]Department of Pathology, The Affiliated Cancer Hospital of Zhengzhou University (Henan Cancer Hospital), Zhengzhou, China, [3]Department of Radiology, The first Affiliated Hospital of Zhengzhou University, Zhengzhou, China

Objectives: To develop and externally validate a spectral CT based nomogram for the preoperative prediction of LVI in patients with resectable GC.

Methods: The two centered study contained a retrospective primary dataset of 224 pathologically confirmed gastric adenocarcinomas (161 males, 63 females; mean age: 60.57 ± 10.81 years, range: 20-86 years) and an external prospective validation dataset from the second hospital (77 males and 35 females; mean age, 61.05 ± 10.51 years, range, 31 to 86 years). Triple-phase enhanced CT scans with gemstone spectral imaging mode were performed within one week before surgery. The clinicopathological characteristics were collected, the iodine concentration (IC) of the primary tumours at arterial phase (AP), venous phase (VP), and delayed phase (DP) were measured and then normalized to aorta (nICs). Univariable analysis was used to compare the differences of clinicopathological and IC values between LVI positive and negative groups. Independent predictors for LVI were screened by multivariable logistic regression analysis in primary dataset and used to develop a nomogram, and its performance was evaluated by using ROC analysis and tested in validation dataset. Its clinical use was evaluated by decision curve analysis (DCA).

Results: Tumor thickness, Borrmann classification, CT reported lymph node (LN) status and nICDP were independent predictors for LVI, and the nomogram based on these indicators was significantly associated with LVI (P<0.001). It yielded an AUC of 0.825 (95% confidence interval [95% CI], 0.769-0.872) and 0.802 (95% CI, 0.716-0.871) in primary and validation datasets (all P<0.05), with promising clinical utility by DCA.

Conclusion: This study presented a dual energy CT quantification based nomogram, which enables preferable preoperative individualized prediction of LVI in patients with GC.

KEYWORDS

spectral CT, iodine concentration, lymphovascular invasion, gastric cancer, nomogram

Highlights

- This study firstly developed and externally validated a dual-energy CT based nomogram to predict lymphovascular invasion in patients with resectable gastric cancer.
- The nomogram incorporated risk factors of tumor thickness, Borrmann classification, CT reported LN status and normalized iodine concentration at delay phase, which enable superior preoperative individualized prediction of lymphovascular invasion in gastric cancer.
- Normalized iodine concentration at delayed phase was an independent predictor for lymphovascular invasion, which indicates the importance of delayed enhanced scan in quantitative description of aggressiveness in gastric cancer.

Introduction

Gastric cancer (GC) is the fifth most common cancer and the third leading cause of cancer related deaths worldwide, despite declining morbidity and mortality in the past five years (1). Curative surgery is the best treatment option for patients with resectable advanced GC, but with local recurrence up to 30% of patients (2). Although the American Joint Committee on Cancer (AJCC) was considered the gold standard to predict outcome generally, it failed to predict heterogeneous survival rates individually in GC patients with the same stage (3, 4). Recently, studies have revealed that lymphovascular invasion (LVI) was associated with recurrence and prognosis in GC patients (5, 6), patients in LVI positive status after surgery presented with higher possibility of recurrence and poorer 5 years' survival. Thus, some researchers (7, 8) recommended combining LVI in risk stratification of prognosis and selection criteria for the need of adjuvant therapies to improve overall survival in GC patients.

LVI refers to tumor cells invading into lymphatic and/or blood vessel near tumor, and serves as an important path of locoregional tumor dissemination (9, 10), and is a predictor of lymph node metastasis (LNM) and biological aggressiveness in GC (11). Despite the significant prognostic importance of LVI, it only can be acquired on surgical specimen, this hysteretic nature limits its use in preoperative practice stage. Therefore, finding a preoperative maker to predict LVI status is clinically desirable. Meng Y et al. (12) have developed a nomogram based on preoperative features to predict LVI, but without involving quantitative indicators on enhanced CT. Ma Z et al. (13) found correlation of LVI with CT attenuation values on multiphasic enhanced CT, but without external validation of the results. To date, some researchers have focus on the prediction of LVI using the emerging radiomics and deep learning algorithm (14, 15), but these single center based radiomics have limitations for being accepted as broad consensus classifier due to the lack of simplicity, reproducibility, repeatability, and availability in real practice.

Spectral CT is the milestone in the development of CT technique, has greatly improved the diagnostic ability in tumor staging and therapeutic efficacy evaluation for GC (16, 17). Previous study have revealed ICs derived from spectral CT are associated with angiogenesis in GC (18), tumor angiogenesis is highly related to LVI in patients with GC (19, 20), and a groundwork have proved IC in venous phase is a promising predictor for LNM in GC (21). Thus, we hypothesis that the incorporation of quantitative dual energy data could further improve the preoperative prediction of LVI in GC. To our knowledge, there is no research on the relationship between spectral CT and LVI is GC. Therefore, the aim of the study is to investigate the predictive value of spectral CT quantification for LVI in GC, by primarily developing an IC based nomogram in a retrospective cohort, then validating its efficacy in a prospective cohort externally.

Material and methods

Patients

The institutional review board approved this study. The requirement for informed consent was waived in the primary

dataset because the retrospective nature, and was obtained from each patient in the prospective validation dataset (NCT04028375). The primary dataset comprised an evaluation of imaging data and medical records between Jan 2018 and Dec 2020 to identify patients with histologically confirmed gastric adenocarcinomas who underwent surgical resection with curative intent. The validation dataset consisted of patients with histologically confirmed GC who underwent surgical resection and gemstone spectral imaging (GSI) enhanced scans before surgery between Dec 2020 and Dec 2021. The inclusion criteria, exclusion criteria and recruitment pathway of patients were presented in Figure 1. In total, 224 consecutive patients were identified and comprised the primary dataset: 161 males and 63 females, mean age, 60.33 ± 11.19 years, range20-85 years. An independent external validation dataset of 112 consecutive patients (77 males and 35 females; mean age, 61.05 ± 10.51 years, range, 31 to 86 years) was selected from 246 consecutive patients according to the inclusion criteria and exclusion criteria presented in Figure 1. Clinical data, including age and gender, tumor location was obtained from medical records.

CT imaging study

CT data in the primary dataset were collected on two spectral CT scanner with GSI mode (Discovery CT scanner and Revolution CT scanner, both from GE Medical System). Prospective CT data in the external validation dataset were acquired on Revolution CT scanner. All patients were overnight fasted, 20 mg of scopolamine (Hangzhou Minsheng Pharmaceutical Group Co., Ltd. Specifications: 10 mg/mL) were administered intramuscularly to reduce gastrointestinal peristalsis 20 min before CT examination. Patients drank 600-1000 ml warm water to distend the stomach prior to CT examination. The CT scans, covering the entire stomach region, were acquired with breath-hold with the patient supine in all of the phases. For enhanced CT scans, patients were infused 1.5 ml/kg of ionic contrast agent (Ultravist 370, Bayer Schering Pharma) with a pump injector (Urich REF XD 2060-Touch, Ulrich Medical) at a rate of 3.0 ml/s into the antecubital vein. Arterial phase (AP), venous phase (VP) and delayed phase (DP) contrast enhanced CT images were established at 30s, 60 s and 90s after contrast agent injection. The other acquisition parameters were as follows: (1) tube voltage of spectral imaging mode switching between 80 kVp and 140 kVp; (2) tube current 375 mA on Discovery CT scanner (selected optimization), and 400 mA on Revolution CT; (3) rotation time of 0.8s; (4) detector collimation of 64×0.625mm; (5) image matrix of 512×512; (6) FOV (field of view) of 380 mm×380 mm, 400 mm×380 mm; (8) reconstruction section thickness of 1.25 mm; (9) pitch of 1.375:1 for Discovery CT scanner, 0.992:1 for Revolution CT. An

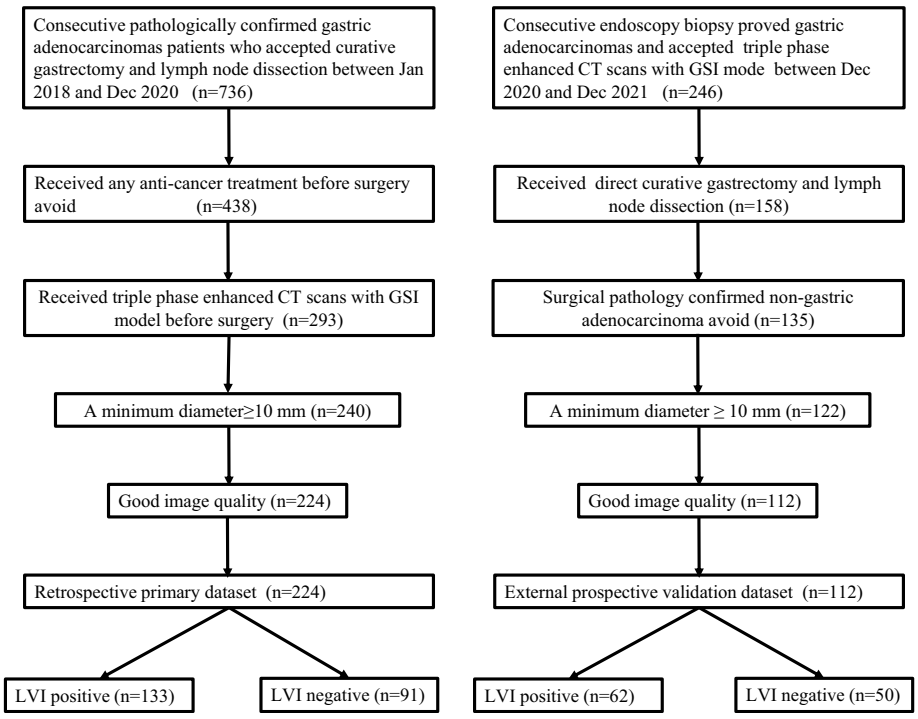

FIGURE 1
Flowchart of patient's enrollment in the primary and validation dataset.

adaptive statistical iterative reconstruction (ASIR, index ¼ 30%) and adaptive statistical iterative reconstruction veo (ASIR-V, index ¼ 50%) algorithm was used on Discovery CT and Revolution CT platform respectively to reduce image noise and the radiation dose on spectral CT.

Image interpretation

The CT images were transferred to GE ADW 4.7 workstation (GE Healthcare, Milwaukee, WI, USA) and interpreted by two radiologists (6 and 10 years of experience in gastrointestinal radiology) on GSI Viewer software with a standard soft-tissue window (Window Level 40 and Window Width 400). Before analysis, the two radiologists were informed of tumor location. Because tumor thickness was proved to be a risk factor for LNM in a prior study (21), it was included in this present study continuously, defined as the maximal diameter perpendicular to the longest axis on the maximal cross-section. Borrmann classification on CT was evaluated according to tumor morphology, infiltration scale and presence of ulceration (21, 22). Circumscribed mass as classification I, circumscribed mass presented with ulcers as II, infiltrative mass with ulcers as III, and diffuse infiltrative mass as IV (16). Clinical T staging (cT) was evaluated by the invasion depth of tumor; CT reported LN status, the presence of either regional LN of >10 mm with or without heterogeneous enhancement and/or clusters of ≥3 lymph nodes was scored as CT reported LN positive, and vice versa (17). All the imaging features was evaluated by reaching two readers' consistency, if there was divergence between the two readers for classification of any features, a third senior reader was included for reaching a consensus or obeying the majoritarian.

ICs in the arterial phase (ICAP), venous phase (ICVP) and delayed phase (ICDP) were measured separately. A free hand, phase-based individualized ROI outlining the whole tumor profile was manually drawn on material deposition (MD) images in the largest cross-sectional area by the two radiologists independently, and then the IC value was automatically generated. ICs of the aorta were obtained by placing circular ROIs at the same slice, avoiding calcified plaque. Then IC in the tumor was normalized by dividing IC of tumor to that of aorta to derive a normalized iodine concentration (nIC=IClesion/ICaorta) (21). All measurements were repeated three times, and the average values were calculated.

Histopathology

Samples were obtained from each surgical specimen, and pathologic indicators was analyzed using hematoxylin and eosin stained 4um thick sections. Each slide was independently analyzed by two experienced pathologists who were masked to imaging findings. Consensus was reached by discussion or introduction of a third pathologist for uncertain cases. LVI was defined as the presence of tumor emboli within either the lymphatic or vascular channels (9, 10). The other pathologic parameters included: T staging, N staging, perineural invasion, histodifferentiation, ulceration, Lauren subtype, positive node numbers (PN), total dissected node numbers (TN), and positive lymph node ratios (PNR) was also recorded. TN was defined as the total number of dissected nodes, PN was defined as number of pathologically diagnosed metastatic nodes, PNR is the ratio of PN to TN (PNR=PN/TN).

Statistical analyses

Statistical analyses were performed using SPSS software (version 23.0), MedCalc software (version 18.0) and R software (version 3.6.1). Interobserver agreements were assessed by intraclass correlation coefficient (ICC). Kolmogorov-Smirnov test was used to check the normality assumption. Enumeration data were compared *via* Student's *t* test or Mann-Whitney U test. Categorical data were compared through chi-square test or Fisher' exact test. Beginning with the significant variables in the unviable analysis, multivariable logistic regression with backward step wise selection was applied to identify independent predictors based on the primary cohort. Using the regression coefficients, an easy-to-use nomogram was built to predict the individual probability of LVI. The predictive value of nomogram was assessed with the area under curve (AUC) of the receiver operating characteristic (ROC) curve with 95% confidence intervals (95% CIs). The differences of AUCs among nomogram and ICs in each dataset, as well as AUCs yielded by the nomogram between the primary and validation datasets were compared by Delong test. The calibration curve and decision curve were plotted using the "rms" package (version 6.2) and the "rmda" package (version 1.6), respectively. A two-sided p value less than 0.05 was considered statistically significant.

Results

Interobserver agreement

The interobserver agreement between two readers was excellent, and the ICC value was 0.955, 0.976, 0.934, 0.912, 0.943, 0.925 respectively, for ICAP, ICVP, ICDP, nICAP, nICVP and ICDP measurements.

Demographic and pathological characteristics

A total of 336 GC patients (238 males, 98 females; mean age: 60.57 ± 10.96 years, range: 20-86 years) were included. Tumor thickness range from 5.3 to 38.2 mm, (mean: 14.90 ± 5.89 mm). Patient characteristics in the primary and validation cohorts

were listed in Table 1. There were no significant differences between the two cohorts in LVI positive prevalence (59.38% in primary cohort and 55.46% in validation cohort (χ^2 =0.495, P=0.278) and other background clinicopathological characteristics. There were no significant differences in clinical characteristics between the primary and the validation dataset neither within the LVI positive cohort (t=1.686, P = 0.684 for age; χ^2 =2.347, P=0.556 for sex; χ^2 =4.403, P=0.221 for location) nor the LVI negative cohort (t=1.125, P= 0.263 for age, χ^2 =2.693, P=0.117 for sex; χ^2 =2.657, P=0.448 for location). Table 2 illustrated the comparison of clinicopathological characteristics between LVI (+) and LVI (-) groups in both primary dataset and validation dataset. Except tumor location, age and gender, the other clinicopathologic characteristics were statistically different between LVI positive and negative groups in both primary and validation dataset, justifying their use as training and validation datasets. LVI positive group contained more patients with T3-4a, LNM, poor differentiated, positive LVI, greater TN, PN, PNR, but less patients in intestinal Lauren subtype in both primary and validation datasets.

CT imaging features

The ICVP, ICDP, nICVP, nICDP in LVI positive cohort (Figure 2) were significantly higher than those in LVI negative cohort (Figure 3) in both primary and validation dataset (all P<0.05). Tumor thickness, clinical T staging, CT reported LN status, Borrmann classification in LVI positive group were statistically different from those in LVI negative group in the two cohorts (all P<0.05). The prevalence of Borrmann III-IV, cT3-4a, CT reported LN positive status of LVI positive group

TABLE 1 Patients background characteristics between primary dataset and validation datasets.

Characteristics		Primary dataset	Validation dataset	$t/Z/\chi^2$	P
Age	Range: 24-85	60.33 ± 11.19	61.05 ± 10.51	-0.573	0.567
Sex	Male	161	77	0.353	0.532
	Female	63	35		
LVI	Positive	133	62	0.495	0.278
	Negative	91	50		
Tumor location	Cardia/Fundus	78	51	6.656	0.084
	Body	68	36		
	Antrum	76	25		
	≥2/3 stomach	2	0		
pT	1	56	22	3.912	0.271
	2	46	27		
	3	77	46		
	4a	45	16		
pN	0	100	49	1.622	0.805
	1	37	21		
	2	48	26		
	3a	30	10		
	3b	9	6		
PN*	Range:0-28	1 (0-5)	1 (0-4)	0.545	0.586
TN*	Range:0-93.33	25 (19.25-31)	25 (19-33)	0.835	0.404
PNR*(%)	Range:0-78	5.26 (0-20)	2.54 (0-17.21)	0.567	0.572
Differentiation	Good	128	54	5.271	0.072
	Moderate	83	55		
	Poor	13	3		
Ulceration	Present	162	83	0.137	0.795
	Absent	62	29		
Lauren subtype	Intestinal	62	29	2.100	0.552
	Mixed	79	34		
	Diffused	83	49		
Perineural invasion	Negative	113	56	0.006	0.939
	Positive	111	56		

*PN, positive node numbers; TN, total dissected nodes numbers; PNR, positive node ratio=PN/TN (%). Comparison of PN, TN, PNR between two datasets using Mann-Whitney U or Wilcoxon W test. The median value (25%quanter, 75%quanter) of PN, TN, PNR in primary dataset was 1(0-5), 25 (19.25-31), 5.26(0-20) with range of 0-28, 0-78, 0-90.91%, respectively; and was 1 (0-4), 25 (19-33), 2.54(0-17.21) in validation dataset, with range of 0-25, 0-70, 0-86.21%, respectively.

TABLE 2 Comparison of clinicopathological characteristics between LVI positive and LVI negative groups in the primary and validation datasets.

Characteristics		Primary dataset				Validation dataset			
		LVI (-) (n = 91)	LVI (+) (n = 133)	$t/Z/\chi^2$	*P*	LVI (-) (n = 50)	LVI (+) (n = 62)	$t/Z/\chi^2$	*P*
Age mean± SD, years	Range: 24-85	61.18 ± 10.46	59.74 ± 11.68	0.940	0.348	59.08 ± 10.82	62.65 ± 10.06	1.803	0.052
Sex				1.932	0.177			0.949	0.413
	Male	70	91			32	45		
	Female	21	42			18	17		
Tumor location				0.255	0.968			10.710	0.004
	Cardia/Fundus	31	47			19	10		
	Body	29	39			27	35		
	Antrum	30	46			4	17		
	≥2/3 stomach	1	1			0	0		
pT	1	50	6	87.073	<0.001	18	4	34.259	<0.001
	2	22	24			19	8		
	3	12	65			10	37		
	4a	7	38			3	13		
pN	0	85	15	147.899	<0.001	43	6	68.080	<0.001
	1	1	36			3	18		
	2	4	44			2	24		
	3a	1	29			1	9		
	3b	0	9			0	5		
PN*	Range:0-28	0 (0, 0)	4 (1.5, 8)	11.243	<0.001	0 (0,0)	4 (1, 6)	8.010	<0.001
TN*	Range:0-93.33%	22 (19, 30)	25 (20, 31)	1.627	0.052	25 (19.75,30.25)	26 (19,37.25)	6.712	0.479
PNR*(%)	Range:0-78	0 (0, 0)	15.00 (5.72,33.60)	10.854	<0.001	0 (0, 0)	13.9 (5.80,28.36)	7.984	<0.001
Differentiation	Good	10	3	10.640	0.005	3	0	4.597	0.100
	Moderate	38	45			26	29		
	Poor	43	85			21	33		
Ulceration	Present	46	116	37.041	<0.001	31	52	6.900	0.010
	Absent	45	17			19	10		
Lauren subtype	Intestinal	33	29	9.043	0.024	17	12	3.141	0.208
	Mixed	31	49			14	20		
	Diffused	27	55			19	30		
Perineural invasion	Negative	73	38	57.657	<0.001	35	21	14.452	<0.001
	Positive	18	95			15	41		

LVI, perineural invasion; (-), negative; (+), positive. *PN, positive node numbers; TN, total dissected nodes numbers; PNR, positive node ratio=PN/TN (%). Comparison of PN, TN, PNR between two groups using Mann-Whitney U or Wilcoxon W test. The median value (25%quanter, 75%quanter) of PN, TN, PNR in primary dataset was 1(0-5), 25 (19.25-31), 5.26(0-20) with range of 0-28, 0-78, 0-90.91%, respectively; and was 1 (0-4), 25 (19-33), 2.54(0-17.21) in validation dataset, with range of 0-25, 0-70, 0-86.21%, respectively. The mean value here is the mean rank calculated by statistical analysis.

was 22/133(16.54%), 49/133(36.84%), 70/133(52.63%) in primary cohort, and was 17/62(27.42%), 49/62(79.03%), 43/62 (69.35%) in validation cohort, respectively (Table 3), all were higher than LVI negative group.

Development and validation of individualized predictive nomogram

When including significant preoperative parameters (tumour thickness, Borrmann classification, cT, CT reported LN status, ICVP, ICDP, nICVP, nICDP) in primary cohort into multivariable analysis, results revealed tumor thickness, Borrmann classification, CT reported LN status and nICDP were independent predictors for LVI (Table 4). Incorporating the above indicators, a nomogram was built to predict LVI probability individually (Figure 4). The nomogram had good performance for discrimination between LVI positive and negative with AUCs of 0.825(95% CI, 0.769-0.872) in the primary cohort and 0.802 (95%CI, 0.716-0.871)in the validation cohort (Z=11.295, 7.146, all P<0.001) (Figure 5; Table 5). Delong test showed the nomogram exhibited statistically higher AUC than ICVP, ICDP, ICVP, ICDP, respectively (Z=4.394, 4.594, 4.104, 3.713, P<0.001) in primary

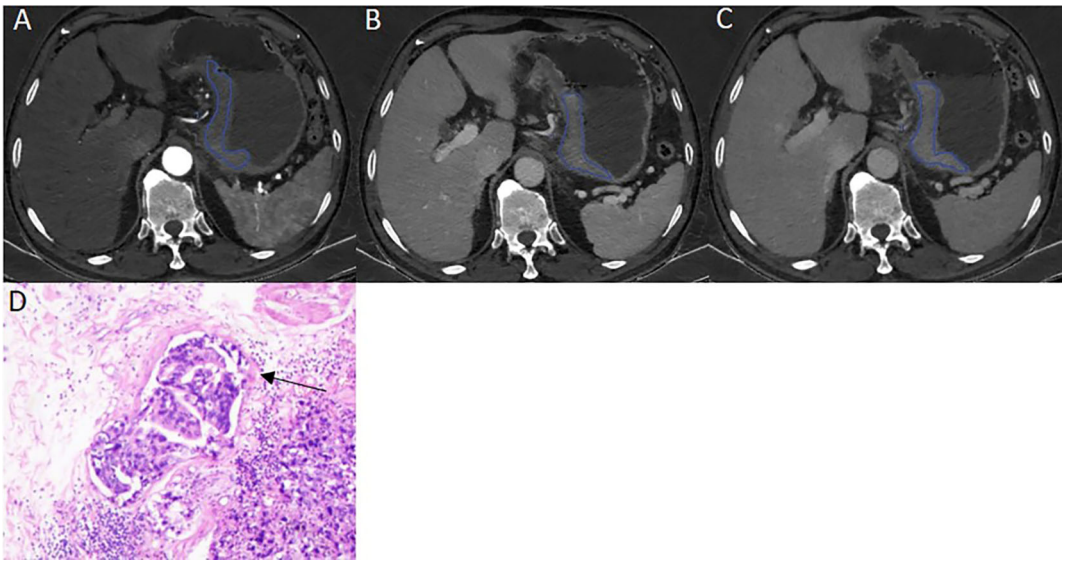

FIGURE 2
A 57 years old male patient with pathologically confirmed gastric adenocarcinoma, staging of pT4aN3aM0, LVI positive. The tumor thickness was 21.72mm, Borrmann classification of III. **(A)** Iodine map at arterial phase, tumor was hyperintense, IC value was 23.11 (100μg/ml); **(B)** Iodine map at venous phase, IC value was 37.65(100μg/ml); **(C)** Iodine map at delay phase, IC value was 38.94 (100μg/ml); **(D)** The histopathology (HE, magnification: ×200) showed adenocarcinomas cells infiltrate into lymphovascular structure (arrow).

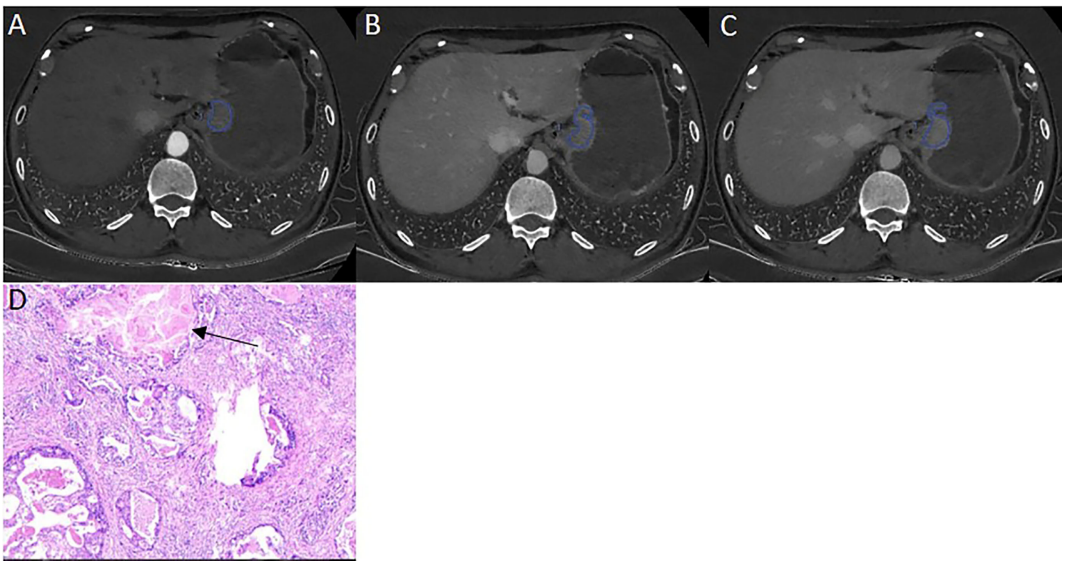

FIGURE 3
A 46 years old male patient with pathologically confirmed gastric adenocarcinoma, staging of pT3N0M0, LVI negative. The tumor thickness was 18.23 mm, Borrmann classification of III. **(A)** Iodine map at arterial phase, tumor was hyperintense, IC value was 21.34(100μg/ml); **(B)** Iodine map at venous phase, IC value was 37.65(100μg/ml); **(C)** Iodine map at delay phase, IC value was 33.40 (100μg/ml); **(D)** The histopathology (HE, magnification: ×200) showed normal lymphovascular structure (arrow).

TABLE 3 Comparison of CT parameters between LVI positive and negative group in the primary and validation datasets.

Parameters		Primary dataset				Validation dataset			
		LVI (-) (n = 91)	LVI (+) (n = 133)	*t*	*P*	LVI (-) (n = 50)	LVI (+) (n = 62)	*t*	*P*
Borrmann classification	I	59	15	6.462	<0.001*	19	10	10.710	0.004*
	II	37	45			27	35		
	III	2	19			4	17		
	IV	0	3			0	0		
Tumor thickness (mm)	Range: 5.3-38.2	13.48 ± 5.65	16.77 ± 6.01	5.345	<0.001*	15.49 ± 6.04	18.26 ± 5.12	2.627	0.010*
cT	1	44	7	6.014	<0.001*	7	1	19.971	<0.001*
	2	34	26			23	12		
	3	17	42			18	39		
	4a	3	7			2	10		
CT reported LN status	Negative	74	63	2.910	0.002*	35	19	17.169	<0.001*
	Positive	17	70			15	43		
ICAP (100μg/ml)		20.36 ± 6.90	17.83 ± 4.90	1.692	0.093	21.52 ± 7.76	21.07 ± .28	0.339	0.736
nICAP		0.18 ± 0.07	0.18 ± 0.06	1.833	0.068	0.20 ± 0.08	0.19 ± 0.05	0.818	0.415
ICVP(100μg/ml)		25.54 ± 7.19	25.35 ± 6.17	4.262	<0.001*	28.97 ± 7.43	30.62 ± 6.52	1.251	0.214
nICVP		0.44 ± 0.11	0.52 ± 0.13	4.240	<0.001*	0.49 ± 0.10	0.54 ± 0.10	2.552	0.012*
ICDP(100μg/ml)		21.10 ± 5.14	25.60 ± 6.67	4.993	<0.001*	26.89 ± 6.53	29.78 ± 6.49	2.343	0.021*
nICDP		0.52 ± 0.09	0.64 ± 0.15	6.332	<0.001*	0.56 ± 0.11	0.66 ± 0.12	4.326	<0.001*

AP, arterial phase; VP, venous phase; DP, delayed phase; HU, Hounsfield unit; IC, iodine concentration; nIC, normalized iodine concentration; LVI, perineural invasion; (-), negative; (+), positive; *P < 0.05.

cohort, and in validation cohort (*Z*=4.031, 3.322, 3.134, 2.066, *P*=0.0001, 0.0009, 0.0027, 0.0389). There was no statistical difference of AUC yielded by the nomogram between primary and validation cohort (*Z*=0.891, *P*=0.173).

Calibration and clinical use of the nomogram

The Hosmer & Lemeshow test and calibration curve (Figure 6) showed good agreement between observed probability and the predicted probability by nomogram in the primary and validation dataset (χ^2 =8.337, 8.695, *P*=0.401, 0.369). The DCA of the nomogram in the validation cohort was demonstrated in Figure 7. The nomogram exhibited higher net benefit in differentiating LVI positive status from LVI negative status across the range of threshold probabilities from 0.22 to 0.90 than the treat-none and treat-all strategy.

Discussion

This study presented a spectral CT quantification based nomogram for the preoperative individualized prediction of LVI with acceptable predictive performance. The nomogram incorporated three preoperatively available items of tumor thickness, CT reported LN status, Borrmann classification and nICDP. The nomogram was easy-to-use, quantitative and non-invasive, which could successfully stratify patients according to their risk of LVI.

Meng Y et al. (12) found clinical TNM stage was associated with LVI in GC. Chen X et al. (15) reported radiomics features related to

TABLE 4 Risk Factors for lymphovascular invasion in gastric cancer.

Variable	Nomogram			
	β	Wald	OR (95% CI)	*P*
Borrmann classification	0. 823	9.420	2.278 (1.347-3.854)	0.002
nICDP	4.561	9.937	95.640 (5.612-1629.828)	0.002
CT reported LN status	0.853	5.360	2.347 (1.140-4.832)	0.021
Thickness	0.091	8.630	1.095 (1.031-1.164)	0.003

IC, iodine concentration; DP, delayed phase; OR, odds ratio; CI, confident interval.

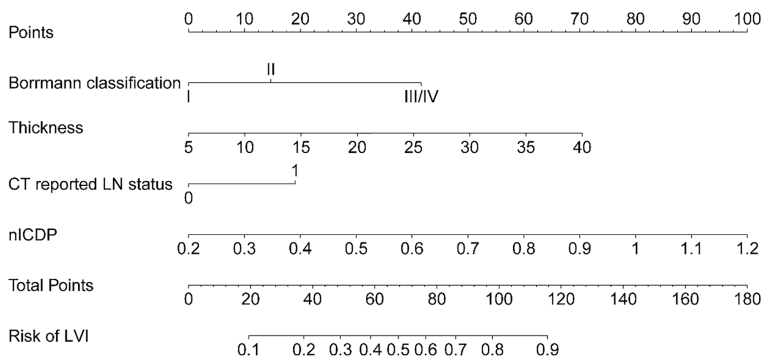

FIGURE 4
The developed nomogram, incorporating Borrmann classification, tumor thickness, CT reported LN status, and nICDP.

tumor size and heterogeneity were top ranked indicators for predicting LVI, clinical T and N stage were independent risk factors for LVI. Our results of tumor size and CT reported LN status was predictive for LVI were consistent with the above studies. Besides, we found CT based Borrmann classification was significant in multivariable analysis and contained in model construction. Borrmann classification descripts tumor aggressiveness by tumor size, infiltration scale and the presence of ulceration, which represents distinct biological entities and reflect tumor aggressiveness (22). A preliminary work (21) proved Borrmann classification was an independent risk factor for LNM in GC, thus, we continued to analyze Borrmann classification in this study and found it is an independent predictor for LVI. Based on these findings, tumor thickness, CT reported LN status, and Borrmann classification were considered as easy-to-obtain risk factors of LVI in GC. To our knowledge, this is the first investigation on the relationship of spectral CT and LVI in GC. In terms of ICs, nICDP was screened as an independent risk factor for LVI in the present study, which added a quantitative imaging marker for operative prediction of LVI. Tumor thickness, CT reported LN status, Borrmann classification and nICDP were selected to build a predictive model for LVI in the primary datasets and validated in an independent external prospective dataset. Compared with Meng Y et al's model, our model appears simple, quantitative and easy to use, it is superior to any other ICs with relatively high AUCs of 0.825 and 0.802 in primary and validation dataset. These findings support the selection of variables for model development is reasonable and feasible.

Several researchers have explored the association of multi-enhanced CT with LVI in GC, but with inconsistent results (24,

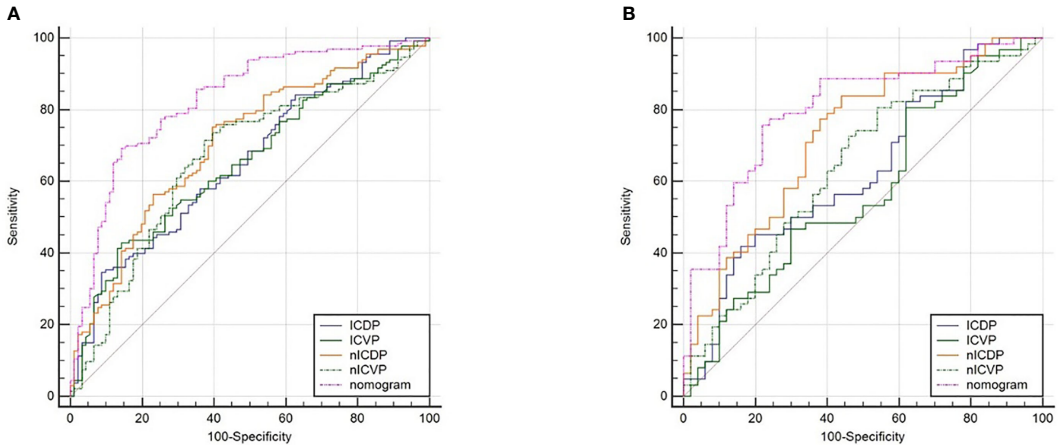

FIGURE 5
ROC analyses of IC parameters and the nomogram for the prediction of lymphovascular invasion in the primary dataset **(A)** and validation dataset **(B)**. The nomogram yielded the highest area under the curve of 0.825 (95%CI, 0.769-0.872) in the primary dataset and 0.802 (95%CI, 0.716-0.871) in the validation dataset.

TABLE 5 ROC analyses of ICs and the developed nomogram.

Variable	Primary dataset						Validation dataset					
	AUC (95%CI)	Sensitivity	Specificity	Accuracy	*Z*	*P*	AUC (95%CI)	Sensitivity	Specificity	Accuracy	*Z*	*P*
ICVP (100μg/ml)	0.651(0.584-0.713)	0.429	0.857	0.643	4.102	<0.001	0.572 (0.475-0.665)	0.806	0.380	0.593	1.301	0.193
ICDP (100μg/ml)	0.653(0.586-0.715)	0.768	0.346	0.557	4.146	<0.001	0.627 (0.530-0.716)	0.419	0.840	0.623	2.373	0.018
nICVP	0.663(0.597-0.725)	0.737	0.604	0.671	4.353	<0.001	0.641 (0.545-0.730)	0.806	0.460	0.633	2.662	0.008
nICDP	0.705(0.641-0.764)	0.692	0.604	0.648	5.820	<0.001	0.7254 (0.632-0.805)	0.839	0.560	0.700	4.632	<0.001
Nomogram	0.825(0.769-0.872)	0.692	0.857	0.775	11.295	<0.001	0.802 (0.716-0.871)	0.758	0.780	0.769	7.146	<0.001

AP, arterial phase; VP, venous phase; DP, delayed phase; IC, iodine concentration; nIC, normalized iodine concentration.

25). For example, Yin et al. (24) showed that CERAP (contrasted enhanced ratio at arterial phase) was significant for LVI, but Ma Z et al. (13) stated that Δpp (=CT attenuation at VP minus that at non-enhanced phase) was an independent predictor. It is noticeable that these studies were retrospective one centered study, the efficacy of enhanced CT for preoperative LVI assessment is far from clinical satisfactory. Vascular endothelial growth factor (VEGF) family can induce both angiogenesis and lymphangiogenesis (25), and tumor angiogenesis was highly related to LVI in GC. ICs showed perfect consistency with true iodine deposition in tube experiment (17). ICVP and nICVP were proved to be positive correlation with microvascular density (MVD) and VEGF on gross specimen of GC after surgery (18), which means that ICs can reflect tumor angiogenesis quantitatively and non-invasively. Our results showed ICVP, ICDP, nICVP and nICDP in LVI positive group was statistically higher than those in LVI negative group in both datasets, a significant finding suggested that IC values enable effective discrimination between different LVI status in GC. Gastric adenocarcinoma is well-known tumor with abundant fibrosis and featured by persistent enhancement after contrast agent administration (16, 17). We prospectively applied bolus tracking technique to set individualized acquisition timing, and the DP was obtained around 90s delay. We observed that although CT attenuation at DP decreased mildly, primary tumor still presented relatively high enhancement. Theoretically, DP enhancement at 90s reflects the fibrosis abundance nature of GC, ICDP represents the late-phase retention of contrast agent in interstitial spaces. LVI is refer to destruction of lymphovascular structures by

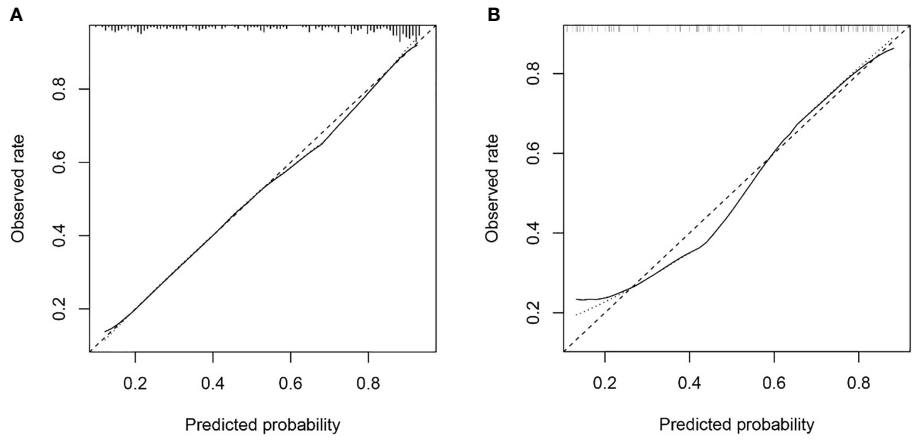

FIGURE 6
The calibration curve of nomogram in the primary dataset **(A)** and validation dataset **(B)** showed good agreement between the predicted probability of lymphovascular invasion (LVI) by the nomogram and actual probability of LVI after surgery. Calibration curves depict the calibration of each model in terms of the agreement between the predicted risks of LVI and observed rate of LVI. The y-axis represents the actual. The x-axis represents the predicted LVI prevalence. The diagonal dotted line represents a perfect prediction by an ideal model. The solid line represents the performance of the nomogram, of which a closer fit to the diagonal dotted line represents a better prediction.

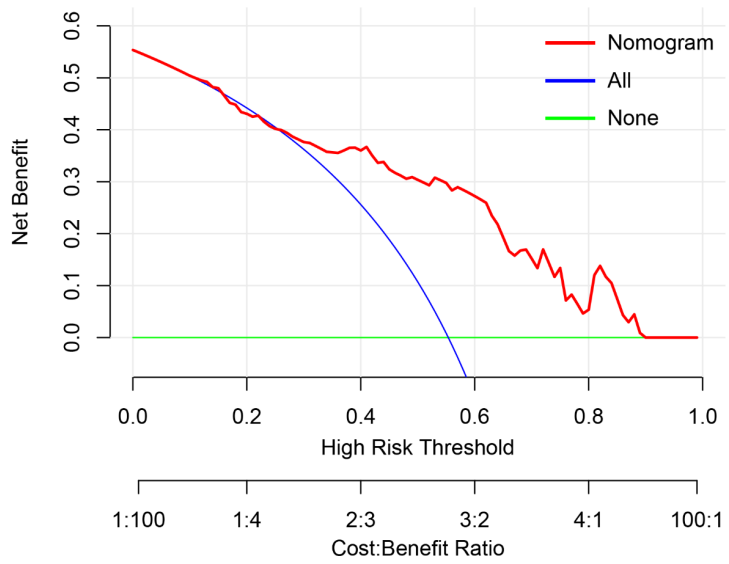

FIGURE 7
The decision curve analysis of nomogram in validation cohort. The y-axis measures the net benefit. The red line represents the developed nomogram. The blue line represents the assumption that all patients are presented with lymphovascular invasion (LVI). The green line represents the assumption that no patients are presented with LVI. The net benefit was calculated by subtracting the proportion of all patients who are false positive from the proportion who are true positive, weighting by the relative harm of forgoing treatment compared with the negative consequences of an unnecessary treatment. Here, the relative harm was calculated by. ($\frac{pt}{1-pt}$), "pt" (threshold probability) is where the expected benefit of treatment is equal to the expected benefit of avoiding treatment; at which time a patient will opt for treatment informs us of how a patient weighs the relative harms of false-positive results and false-negative results. $\frac{a-c}{b-d}$) $=\frac{1-pt}{pt}$); a–c is the harm from a false-negative result; b–d is the harm from a false positive result. a, b, c and d give, respectively, the value of true positive, false positive, false negative, and true negative (23) The nomogram exhibited higher net benefit in predicting LVI positive status across the range of threshold probabilities from 0.22 to 0.90 than the treat-none and treat-all strategy.

tumor cell infiltration (9, 10), may increase the microvascular permeability and locoregional tumor cell density, and account for higher ICs and nICs at venous phase and delay phase.

In previous studies, nICs was introduced to minimize or eliminate circulation varies among individuals and exhibited comparable performance in tumor characteristic description, staging and treatment response evaluation (15–17), especially nICVP. We found that nICDP was significant in multivariable analysis and predictive for LVI, rather than nICVP. Differences may mainly due to different protocol and timing, the previous studies used dual phase enhanced protocol, the VP was acquired at 60~70s after contrast agent administration, whereas we applied triple phase enhanced method, DP was obtained around 90s delay, when primary GC still present with persistent enhancement, nICDP at this time point represent the balance of blood supply and the late-phase retention of contrast agent in interstitial spaces, which is in accordance to the abundant fibrosis nature of GC. Despite nICs were useful and relatively reliable, the usage of nICs has not achieved worldwide consensus and generalization. More studies are needed to verify the predictive value of nICs in GC.

Several researchers developed nomograms for LVI prediction with acceptable AUCs. Meng Y et al. (12) proposed a nomogram consisted of clinical indicators with AUC of 0.774 in the testing datasets. Chen X et al. (15) and Li Q et al. (14) proposed radiomics models from enhanced CT images and yielded AUC of 0.792 and 0.725 in testing dataset respectively. Different from the existing nomograms, our nomogram firstly contained quantitative imaging marker (nICDP) and clinically meaningful and available features (CT reported LN status, tumor thickness and Borrmann classification) from one stop scan on spectral CT with comparable or better AUC of 0.802 in the validation dataset, but without complicated radiomics algorithm. The predictive efficacy of the nomoram was externally validated in a prospective cohort, suggestive of its good generalization.

Study limitations include that data acquired on fast kV DECT platform, which may not be applicable to other DECT platforms. Besides, laboratory and genetic markers have not yet been incorporated in the nomogram. Therefore, multiscale studies are expectable to establish a more comprehensive method to predict LVI in patients with GC.

In conclusion, this study presents and externally validates a spectral CT based and clinically available predictive tool that combined quantitative parameter of nICDP and significant risk factors for preoperative LVI in GC with favorable accuracy.

Data availability statement

The raw data supporting the conclusions of this article will be made available by the authors, without undue reservation.

Ethics statement

The studies involving human participants were reviewed and approved by the Affiliated Cancer Hospital of Zhengzhou University (Henan Cancer Hospital) and the first Affiliated Hospital of Zhengzhou University. The written informed consent was obtained from each patients in the Affiliated Cancer Hospital of Zhengzhou University (Henan Cancer Hospital) and waived in the first Affiliated Hospital of Zhengzhou University.

Author contributions

Guarantor of integrity of the entire study: JL and J-rQ. Study conception and design: J-rQ and J-bG. Data acquisition: JL and RW. Pathologic diagnoses: YW. Imaging analysis: JL and RW. Statistical analyses: JL and J-rQ. Manuscript writing: JL. Manuscript editing: J-rQ and J-bG. All authors contributed to the article and approved the submitted version.

Funding

Science and Technology Development Foundation of Henan Province (202102310736), Henan Provincial Medical Science and Technology Project (SBGJ202003011), Projects of the General Programs of the National Natural Science Foundation of China (No.81972802, 82202146), Special funding of Henan Health Science and Technology Innovation Talent Project (No.YXKC2020011, No. YXKC2021054).

Conflict of interest

The authors declare that the research was conducted in the absence of any commercial or financial relationships that could be construed as a potential conflict of interest.

Publisher's note

References

1. Sung H, Ferlay J, Siegel RL, Laversanne M, Soerjomataram I, Jemal A, et al. Global cancer statistics 2020: GLOBOCAN estimates of incidence and mortality worldwide for 36 cancers in 185 countries. *CA Cancer J Clin* (2021) 71:209–49. doi: 10.3322/caac.21660

2. Smyth EC, Nilsson M, Grabsch HI, van Grieken NC, Lordick F. Gastric cancer. *Lancet* (2020) 396:635–48. doi: 10.1016/S0140-6736(20)31288-5

3. Zhu Z, Gong Y, Xu H. Clinical and pathological staging of gastric cancer: Current perspectives and implications. *Eur J Surg Oncol* (2020) 46(10 Pt B):e14–9. doi: 10.1016/j.ejso.2020.06.006

4. Li P, He HQ, Zhu CM, Ling YH, Hu WM, Zhang XK, et al. The prognostic significance of lymphovascular invasion in patients with resectable gastric cancer: A large retrospective study from southern China. *BMC Cancer* (2015) 15:370. doi: 10.1186/s12885-015-1370-2

5. Fujita K, Kanda M, Ito S, Mochizuki Y, Teramoto H, Ishigure K, et al. Association between lymphovascular invasion and recurrence in patients with pT1N+ or pT2-3N0 gastric cancer: A multi-institutional dataset analysis. *J Gastric Cancer* (2020) 20:41–9. doi: 10.5230/jgc.2020.20.e3

6. Choi S, Song JH, Lee S, Cho M, Kim YM, Kim HI, et al. Lymphovascular invasion: Traditional but vital and sensible prognostic factor in early gastric cancer. *Ann Surg Oncol* (2021) 28:8928–35. doi: 10.1245/s10434-021-10224-6

7. Lu J, Dai Y, Xie JW, Wang JB, Lin JX, Chen QY, et al. Combination of lymphovascular invasion and the AJCC TNM staging system improves prediction of prognosis in N0 stage gastric cancer: Results from a high-volume institution. *BMC Cancer* (2019) 19:216. doi: 10.1186/s12885-019-5416-8

8. Hirabayashi S, Kosugi S, Isobe Y, Nashimoto A, Oda I, Hayashi K, et al. Development and external validation of a nomogram for overall survival after curative resection in serosa-negative, locally advanced gastric cancer. *Ann Oncol* (2014) 25:1179–84. doi: 10.1093/annonc/mdu125

9. Padera TP, Kadambi A, di Tomaso E, Carreira CM, Brown EB, Boucher Y, et al. Lymphatic metastasis in the absence of functional intratumor lymphatics. *Science* (2002) 296:1883–6. doi: 10.1126/science.1071420

10. Kikuchi E, Margulis V, Karakiewicz PI, Roscigno M, Mikami S, Lotan Y, et al. Lymphovascular invasion predicts clinical outcomes in patients with node-negative upper tract urothelial carcinoma. *J Clin Oncol* (2009) 27:612–8. doi: 10.1200/JCO.2008.17.2361

11. Liu J, Li H, Zhou P, Cai T, Tang Z, Wang Y, et al. Reevaluation of lymphovascular invasion in gastric cancer using endothelial markers D2-40 and EVG: Enhanced detection, better predictor of lymph node metastasis and biological aggressiveness. *J Surg Oncol* (2021) 123:1736–41. doi: 10.1002/jso.26468

12. Meng Y, Huang X, Liu J, Chen J, Bu Z, Wu G, et al. A novel nomogram for individually predicting of vascular invasion in gastric cancer. *Technol Cancer Res Treat* (2021) 20:15330338211004924. doi: 10.1177/15330338211004924

13. Ma Z, Liang C, Huang Y, He L, Liang C, Chen X, et al. Can lymphovascular invasion be predicted by preoperative multiphasic dynamic CT in patients with advanced gastric cancer? *Eur Radiol* (2017) 27:3383–91. doi: 10.1007/s00330-016-4695-6

14. Li Q, Feng QX, Qi L, Liu C, Zhang J, Yang G, et al. Prognostic aspects of lymphovascular invasion in localized gastric cancer: New insights into the radiomics and deep transfer learning from contrast-enhanced CT imaging. *Abdom Radiol (NY).* (2022) 47:496–507. doi: 10.1007/s00261-021-03309-z

15. Chen X, Yang Z, Yang J, Liao Y, Pang P, Fan W, et al. Radiomics analysis of contrast-enhanced CT predicts lymphovascular invasion and disease outcome in gastric cancer: A preliminary study. *Cancer Imaging* (2020) 20(1):24. doi: 10.1186/s40644-020-00302-5

16. Pan Z, Pang L, Ding B, Yan C, Zhang H, Du L, et al. Gastric cancer staging with dual energy spectral CT imaging. *PloS One* (2013) 8:e53651. doi: 10.1371/journal.pone.0053651

17. Tang L, Li ZY, Li ZW, Zhang XP, Li YL, Li XT, et al. Evaluating the response of gastric carcinomas to neoadjuvan chemotherapy using iodine concentration on spectral CT: A comparison with pathological regression. *Clin Radiol* (2015) 70:1198–204. doi: 10.1016/j.crad.2015.06.083

18. Chen XH, Ken K, Liang P, Chai YR, Chen KS, Gao JB, et al. Spectral computed tomography in advanced gastric cancer: Can iodine concentration non-

invasively assess angiogenesis? *World J Gastroenterol* (2017) 23:1666–75. doi: 10.3748/wjg.v23.i9.1666

19. Maehara Y, Kabashima A, Koga T, Tokunaga E, Takeuchi H, Kakeji Y, et al. Vascular invasion and potential for tumor angiogenesis and metastasis in gastric carcinoma. *Surgery* (2000) 128:408–16. doi: 10.1067/msy.2000.107265

20. Komori M, Asayama Y, Fujita N, Hiraka K, Tsurumaru D, Kakeji Y, et al. Extent of arterial tumor enhancement measured with preoperative MDCT gastrography is a prognostic factor in advanced gastric cancer after curative resection. *AJR Am J Roentgenol* (2013) 201:W253–61. doi: 10.2214/AJR.12.9206

21. Li J, Fang M, Wang R, Dong D, Tian J, Liang P, et al. Diagnostic accuracy of dual-energy CT-based nomograms to predict lymph node metastasis in gastric cancer. *Eur Radiol* (2018) 28(12):5241–9. doi: 10.1007/s00330-018-5483-2

22. Díaz Del Arco C, Ortega Medina L, Estrada Muñoz L, Molina Roldán E, Cerón Nieto MÁ, García Gómez de Las Heras S, et al. Are borrmann's types of advanced gastric cancer distinct clinicopathological and molecular entities? a Western study. *Cancers (Basel)* (2021) 13(12):3081. doi: 10.3390/cancers13123081

23. Vickers AJ, Cronin AM, Elkin EB, Gonen M. Extensions to decision curve analysis, a novel method for evaluating diagnostic tests, prediction models and molecular markers. *BMC Med Inform Decis Mak* (2008) 8:53. doi: 10.1186/1472-6947-8-53

24. Yin XD, Huang WB, Lu CY, Zhang L, Wang LW, Xie GH, et al. A preliminary study on correlations of triple-phase multi-slice CT scan with histological differentiation and intratumoral microvascular/lymphatic invasion in gastric cancer. *Chin Med J* (2011) 124:347–51. doi: 10.3760/cma.j.issn.0366-6999.2011.03.005

25. Holopainen T, Bry M, Alitalo K, Saaristo A. Perspectives on lymphangiogenesis and angiogenesis in cancer. *J Surg Oncol* (2011) 103:484–8. doi: 10.1002/jso.21808

frontiers | Frontiers in Surgery

TYPE Original Research
PUBLISHED 04 January 2023
DOI 10.3389/fsurg.2022.1003525

OPEN ACCESS

EDITED BY
Mengling Feng,
National University of Singapore, Singapore

REVIEWED BY
Qing He Zhou,
Jiaxing University, China
Dmitry Frank,
Soroka Medical Center, Israel

*CORRESPONDENCE
Lixin Jiang
✉ jianglixin1969@hotmail.com
Xixun Wang
✉ w70063@sina.com

†These authors share first authorship

SPECIALTY SECTION
This article was submitted to Surgical Oncology, a section of the journal Frontiers in Surgery

RECEIVED 26 July 2022
ACCEPTED 08 December 2022
PUBLISHED 04 January 2023

CITATION
Cui H, Zhao D, Jian J, Zhang Y, Jian M, Yu B, Hu J, Li Y, Han X, Jiang L and Wang X (2023) Risk factor analysis and construction of prediction models for short-term postoperative complications in patients undergoing gastrointestinal tract surgery.
Front. Surg. 9:1003525.
doi: 10.3389/fsurg.2022.1003525

Risk factor analysis and construction of prediction models for short-term postoperative complications in patients undergoing gastrointestinal tract surgery

Hongming Cui[1†], Dawei Zhao[1†], Jingren Jian[2†], Yifei Zhang[1], Mi Jian[1], Bin Yu[1], Jinchen Hu[1], Yanbao Li[3], Xiaoli Han[3], Lixin Jiang[1,3]* and Xixun Wang[1]*

[1]Department of Gastrointestinal Surgery, Yantai Yuhuangding Hospital, Qingdao University, Yantai, China, [2]Department of Surgical Department, Jinxiang Hongda Hospital Affiliated to Jining Medical University, Jining, China, [3]Department of Surgical Department, Yantai Yeda Hospital, Yantai, China

Purpose: To identify risk factors associated with short-term postoperative complications in patients with gastrointestinal cancer and develop and validate prediction models to predict the probability of complications.
Methods: A total of 335 patients enrolled in the primary cohort of this study were divided into training and validation sets in a chronological order. Using univariate and multivariate logistic regression analyses, the risk factors for postoperative complications were determined, and nomogram prediction models were constructed. The performance of the nomogram was assessed with respect to the receiver operator characteristic and calibration curves.
Results: Patients with complications had a stronger postoperative stress response and a longer duration of daily fluid intake/output ratio >1 after surgery. Logistic analysis revealed that body mass index (BMI), body temperature on POD4 (T.POD4), neutrophil percentage on POD4 (N.POD4), fasting blood glucose on POD4 (FBG.POD4), and the presence of fluid intake/output ratio <1 within POD4 were risk factors for POD7 complications, and that BMI, T.POD7, N.POD7, FBG.POD4, FBG.POD7, and the duration of daily fluid intake/output ratio >1 were risk factors for POD30 complications. The areas under the curve of Nomogram-A for POD7 complications were 0.867 and 0.833 and those of Nomogram-B for POD30 complications were 0.920 and 0.918 in the primary and validation cohorts, respectively. The calibration curves showed good consistency in both cohorts.
Conclusion: This study presented two nomogram models to predict short-term postoperative complications in patients with gastrointestinal cancer. The results could help clinicians identify patients at high risk of complications within POD7 or POD30.

KEYWORDS

gastrointestinal tumor, postoperative complications, stress response, fluid intake and output, clinicopathological characteristics, nomogram

Introduction

Gastric and colorectal cancers are among the top five causes of morbidity and mortality among all cancer patients in China (1, 2). Surgical treatment of gastrointestinal cancers remains an essential but aggressive treatment option (3). Meanwhile, postoperative complications represent the greatest obstacle that hinders recovery (4). When complications are treated inappropriately, they may lead to a rapid decline in the quality of life of the patient as well as an increase in medical expenses and mortality (5, 6). Therefore, early detection of and intervention for complications can effectively reduce the duration of hospitalization and medical expenditure.

Most gastrointestinal surgical complications are not obvious and are difficult to detect in the early stages (7). Therefore, early recognition and intervention are critical for postoperative treatment. Physical symptoms or laboratory tests can reveal early signs of postoperative complications; however, only a handful of studies have efficiently integrated these clinical data to assist in clinical decision-making (8).

The occurrence of complications is intimately linked to the stress response after surgery, and their occurrence usually indicates a high level of stress in the body. The high stress response in the early postoperative period also indicates that postoperative complications are likely to occur, which provides a reference point for predicting postoperative complications (9, 10).

Minimally invasive surgery combined with enhanced recovery after surgery is an important aspect of standardized gastrointestinal tumor management. Clinical trials have shown that they can improve short-term outcomes and long-term survival. However, postoperative complications remain an important clinical problem (11–13). The aim of the current study was to develop and validate a nomogram to estimate the possibility of postoperative complications in patients undergoing gastrointestinal tract surgery by incorporating routine indicators monitored in the postoperative setting.

Materials and methods

Patient selection

This study included patients with gastrointestinal tumors who underwent standard surgical treatment between June 2020 and July 2021 in the Gastrointestinal Unit of Yantai Yuhuangding Hospital, Qingdao University. The inclusion criteria were as follows: (i) age ≥18 years; (ii) no obvious contraindications in preoperative examination; (iii) preoperative pathology determined to be gastric or colorectal cancer; (iv) Eastern Cooperative Oncology Group performance status of ≤3; and (v) life expectancy of ≥6 months. The exclusion criteria were as follows: (i) without complete baseline examination; (ii) with the presence of secondary tumor or comorbidities on the preoperative examination that required emergency surgery; (iii) current or a history of malignancy in addition to gastrointestinal tumors; (iv) with other diseases that could either affect the study results or were uncontrollable.

This retrospective study was approved by the ethics committee of Yantai Yuhuangding Hospital, Qingdao University, and the requirement for informed consent was waived due to the retrospective nature of the study.

Selection of research variables

Perioperative clinical data, such as baseline characteristics and laboratory results, were collected from each patient. The baseline characteristics included sex, age, body mass index (BMI), history of smoking and alcohol consumption, neoadjuvant chemoradiotherapy (nCR, and previous cardiovascular disease and diabetes. Laboratory data included preoperative white blood cell count, neutrophil percentage (N), fasting blood glucose (FBG), alanine aminotransferase, and aspartate aminotransferase levels on postoperative days 1 (POD1), 4 (POD4), and 7 (POD7). We also recorded the daily fluid intake and output per patient, including perioperative infusion, bleeding, drainage, and urine volume. We further calculated the daily fluid output and fluid difference using the following formula:

$$\textbf{Fluid output}\,(\textbf{ml}) = VOL_{urine} + VOL_{drainage} + VOL_{invisible\,water\,loss}$$
$$\textbf{Fluid difference}\,(\textbf{ml}) = VOL_{intake} - \textbf{Fluid output}\,(\textbf{ml})$$

Note that *VOL* is short for the letter "volume". Invisible water loss was set at 900 ml and increased with increasing body temperature; by 200 ml when body temperature was between 37.3 °C and 37.7 °C, 500 ml between 37.8 °C and 38.3 °C, and 800 ml above 38.3 °C. Then, we assessed whether each patient had a fluid intake/output ratio <1 within POD4 (It means two consecutive days of daily fluid intake/output ratio <1 within POD4) and the final duration of daily fluid intake/output ratio >1. The first day of the first two consecutive days with a ratio <1 was estimated as the final duration of fluid intake/output ratio >1 from POD1. If there were two consecutive days without a ratio <1 within POD7, the duration was estimated as 7 days when there was a ratio <1 on POD7 and 8 days when there was still a ratio >1 on POD7. To explore the stress status of the patients, we measured levels of stress indicators, including perioperative C-reactive protein (CRP), interleukin-6 (IL-6), and cortisol.

In addition, according to each of their postoperative monitored vital signs, laboratory test results, and postoperative treatment measures, the presence of postoperative complications was assessed and recorded within POD7 or POD30 based on

TABLE 1 Patient characteristics and short-term outcomes in the training and validation set.

Characteristics		Training set ($N = 223$)	Validation set ($N = 112$)	*P* value
Age (years, Mean ± SD)		65.83 ± 10.20	63.94 ± 11.11	0.121
Sex (%)	Male	146 (65.5)	78 (69.6)	0.444
	Female	77 (34.5)	34 (30.4)	
BMI (kg/m^2, Mean ± SD)		24.45 ± 3.12	24.69 ± 3.16	0.500
Smoking, *n* (%)		75 (33.6)	45 (40.2)	0.238
Alcohol, *n* (%)		58 (26.0)	26 (23.2)	0.578
Cardiovascular disease, *n* (%)		78 (35.0)	35 (31.3)	0.496
Diabetes, *n* (%)		38 (17.0)	11 (9.8)	0.078
Surgical spot (%)	Stomach	94 (42.2)	52 (46.4)	0.457
	Intestines	129 (57.8)	60 (53.6)	
nCRT, *n* (%)		38 (17.0)	22 (19.6)	0.558
Fasting time (days, Mean ± SD)		5.3 ± 3.0	5.2 ± 2.1	0.685
First time of exhaust (days, Mean ± SD)		4.63 ± 2.40	4.62 ± 1.47	0.971
Time of urinary catheter withdrawal (days, Mean ± SD)		3.28 ± 2.69	3.26 ± 1.95	0.941
the duration of operation (minutes, Mean ± SD)		200.49 ± 56.73	208.30 ± 62.52	0.252
the duration of anesthesia (minutes, Mean ± SD)		243.81 ± 59.16	253.35 ± 65.34	0.180
Postoperative hospital stay (days, Mean ± SD)		8.7 ± 5.1	8.6 ± 4.2	0.825
Intraoperative blood transfusion		5	1	0.352
Maximum length of primary tumor				
(cm, Mean ± SD)		4.09 ± 2.24	4.15 ± 2.38	0.819
Lymph node metastasis, *n* (%)		92 (41.3)	47 (42.0)	0.901
Vascular invasion, *n* (%)		52 (23.3)	18 (16.1)	0.124
Nerve infiltration, *n* (%)		62 (27.8)	29 (25.9)	0.711

BMI, body mass index; *nCRT*, neoadjuvant chemoradiotherapy.

the first day of its appearance. Each postoperative complication was graded according to the Clavien–Dindo classification (14).

Surgical treatment and postoperative management

Preoperative laboratory tests and examinations were performed in all patients to exclude clear contraindications to surgery. All surgeries were performed by five gastrointestinal specialists who performed more than 80 similar surgeries annually at Yantai Yuhuangding Hospital. At the end of the surgery, one or two drains were placed at the anastomosis and closed stump subcutaneously in all patients. All patients were routinely treated with prophylactic antibiotics, nutritional support, pain relief, and other symptomatic treatments after surgery. Postoperative routine blood tests and biochemistry were performed every 3 days. Gastrointestinal tract images was reviewed before discharge, and drains were removed if there were no signs of leakage. Simultaneously, patients were closely monitored for postoperative complications during the treatment process. Once they occurred, early intervention was provided.

Development and validation of nomogram

We identified independent risk factors associated with postoperative complications by univariate and multifactorial logistic regression analyses, and the nomogram was built based on the independent risk factors in the multivariate analysis. First, we identified the independent risk factors associated with POD7 complications by using research variables and the presence or absence of a fluid intake/output ratio <1 within POD4 and then developed Nomogram A (Nomogram-A). Secondly, we identified the

TABLE 2 Display of postoperative complications in the training and validation set.

		Training set ($N = 223$)	Validation set ($N = 112$)	P value
Complication	Total patients	68	34	0.960
	Anastomotic leakage	11	4	
	Abdominal hemorrhage	2	2	
	Gastrointestinal dysfunction[a]	7	3	
	Wound infection	4	4	
	Chylous leakage	3	/	
	Pleural effusion	6	3	
	Pneumonia	7	5	
	Respiratory and circulatory dysfunction[b]	9	2	
	Severe thrombosis[c]	3	/	
	Urinary abnormalities[d]	1	3	
	Metabolite or electrolyte imbalance[e]	8	3	
	Fever[f]	15	8	
Major complication[g]		13	7	0.818

We repeated the count if the patient had two or more comorbidities.
[a]Postoperative gastroparesis, residual gastritis, intestinal obstruction, intestinal adhesions and recurrent diarrhea, etc.
[b]Postoperative ventricular fibrillation, recurrent atrial fibrillation, heart failure, respiratory failure and unexplained severe chest tightness, etc.
[c]Thrombotic pulmonary embolism and cerebral infarction, severe venous thrombosis, etc.
[d]Urinary tract infection, hematuria, urethral fistula, etc.
[e]Persistent hypokalemia or hyperglycemia, abnormal liver and kidney function, etc.
[f]Transient temperature above 38.5 °Cor temperature above 37.5 °C for 2 or more days.
[g]Clavien-dindo Grade III/IV/V.

independent risk factors associated with POD30 complications by using research variables and the final duration of fluid intake/output ratio >1 within POD7 and then developed Nomogram B (Nomogram-B).

The recognition performance of Nomograms-A and -B were evaluated using receiver operator characteristic (ROC) curves in the training and validation sets (15). Comparisons between ROC curves were performed using the Delong test (16). The prediction accuracy of the nomogram was evaluated using calibration curves and the Hosmer–Lemeshow test (17).

Statistical analysis

Statistical analyses were performed using SPSS (version 26.0) and R (version 3.6.2) software. Exact variables were analyzed using Student's t-test, and categorical variables were analyzed using the χ^2 test or Fisher's exact test in the baseline table. Correlation analysis was performed using Spearman's correlation test. The independent risk factors were determined using univariate and multifactorial logistic regression analyses. Nomograms and calibration curves were plotted using the "RMS" software package. The ROC curves were plotted using the "pROC" software package. For all tests, a two-sided $P < 0.05$ was considered statistically significant.

Results

Patient characteristics

A total of 335 patients (225 men and 110 women) were included in this study and were divided chronologically into training ($n = 223$) and validation ($n = 112$) sets. The patients were also divided into a group with ($n = 233$) and without ($n = 102$) complications. Baseline patient characteristics and outcomes of the training and validation sets are shown in **Table 1**. There were no significant differences in the baseline patient characteristics between the training and validation sets, indicating good consistency between the two cohorts.

Among all patients, 146 had gastric cancer and 189 had colorectal cancer. Additionally, 60 patients had defined borderline resectable tumors, and 60 patients received 2–4 cycles of nCRT. The median and average postoperative hospital stay were 7 and 8.7 days, respectively.

TABLE 3 Perioperative fluid volume in patients with or without complications.

		With complications ($N = 102$)	Without complications ($N = 233$)	P value
Fluid difference (mL, Mean ± SD)	POD1	402.09 ± 626.50	350.36 ± 754.66	0.100
	POD2	304.39 ± 617.95	98.29 ± 630.61	0.006
	POD3	301.04 ± 626.51	124.17 ± 649.42	0.021
	POD4	72.90 ± 670.03	−339.15 ± 731.84	<0.001
	POD5	−68.50 ± 769.37	−553.18 ± 752.41	<0.001
	POD6	−205.14 ± 879.00	−735.72 ± 741.77	<0.001
	POD7	−530.46 ± 608.57	−685.11 ± 732.79	0.035
Intraoperative fluid intake (mL, Mean ± SD)		1827.27 ± 702.56	1736.08 ± 600.45	0.303
Intraoperative bleeding volume (mL, Mean ± SD)		70.29 ± 201.33	47.52 ± 78.88	0.271
Presence of ratio <1 (%)		9 (10.5)	91 (36.5)	<0.001
Duration of ratio >1 (days, Mean ± SD)		6.12 ± 1.59	3.86 ± 1.76	<0.001

Fluid difference = daily fluid intake—output; *Presence of ratio <1*, The presence of fluid intake/output ratio < 1 within POD4 was analyzed with the occurrence of POD7 complications; *Duration of ratio > 1*, the final duration of fluid intake/output >1.

In the group with complications, 86 and 102 patients developed postoperative complications within POD7 and POD30 (including those within POD7), respectively (Table 2). According to the Clavien–Dindo classification, 20 patients had major complications (Clavien–Dindo grades III/IV/V). One patient with Clavien–Dindo grade V was a man who suffered respiratory failure after radical gastric cancer surgery and died after ineffective treatment in the ICU. The complications in the remaining patients were effectively controlled or cured after standard treatment.

Study of the correlation between stress and postoperative complications

We monitored the preoperative CRP, IL-6, and cortisol levels on POD1, POD4, and POD7 in partial patients from the training set ($n = 168$). Comparing the stress indicators between the groups with and without complications, the CRP, IL-6, and cortisol levels were significantly higher in the group with complications than in those without complications on POD1, POD4, and POD7 ($P < 0.05$); however, there was no significant difference between the groups before surgery ($P > 0.05$) (Table 3).

The results of this study further confirm that patients with postoperative complications generally have a stronger postoperative stress response than those without postoperative complications, and the presence of a strong stress response in the early postoperative period may reflect the occurrence of postoperative complications.

Study of the correlation between fluid volume and postoperative complications

This study also analyzed perioperative fluid volumes between the groups of patients with and without postoperative complications. Intraoperative bleeding and infusion volumes in the group with complications were not significantly different from those in the group without complications ($P > 0.05$) (Table 4). In contrast, during postoperative fluid therapy, the daily fluid difference from POD2 in the group with complications was lower than that in the group without complications ($P < 0.05$), and the fluid gap increased significantly from POD4. This gap between the two groups persisted until the last day of statistical analysis. Short-term postoperative complications tended to occur 3–5 days after surgery; therefore, we considered this increase in variance to be related to the timing of postoperative complications. We also compared the presence or absence of fluid intake/output ratio <1 within POD4 and the final duration of fluid intake/output ratio >1 between both groups. Patients with complications were less likely to have a fluid intake/output ratio <1 within POD4 (10.5% vs. 36.5%, $P < 0.05$) and had a significantly longer duration of fluid intake/output ratio >1 postoperatively than those without complications (6.18 days vs. 3.86 days, $P < 0.05$).

Through our study, we considered that changes in postoperative fluid difference may be associated with the development of postoperative complications and further discuss whether they could be risk factors for the development of postoperative complications.

TABLE 4 Perioperative stress index in patients with or without complications.

	With complications	Without complications	*P* value
CRP.pre (mg/L, Mean ± SD)	5.98 ± 8.85	3.80 ± 5.94	0.488
CRP.POD1 (mg/L, Mean ± SD)	63.22 ± 30.72	38.88 ± 23.89	0.002
CRP.POD4 (mg/L, Mean ± SD)	106.35 ± 53.65	31.37 ± 15.64	<0.001
CRP.POD7 (mg/L, Mean ± SD)	81.86 ± 60.15	29.36 ± 30.89	<0.001
IL-6.pre (U/ml, Mean ± SD)	3.11 ± 3.29	11.92 ± 31.40	0.412
IL-6.POD1 (U/ml, Mean ± SD)	160.86 ± 115.78	92.16 ± 95.99	0.023
IL-6.POD4 (U/ml, Mean ± SD)	114.65 ± 52.72	26.04 ± 22.68	<0.001
IL-6.POD7 (U/ml, Mean ± SD)	79.11 ± 78.25	19.00 ± 14.76	0.013
Cortisol.pre (nmol/L, Mean ± SD)	325.14 ± 88.16	344.23 ± 93.43	0.598
Cortisol.POD1 (nmol/L, Mean ± SD)	582.17 ± 137.51	413.83 ± 151.13	<0.001
Cortisol.POD4 (nmol/L, Mean ± SD)	663.18 ± 110.77	390.39 ± 136.35	<0.001
Cortisol.POD7 (nmol/L, Mean ± SD)	576.66 ± 156.07	365.34 ± 115.12	<0.001

CRP.pre, preoperative C-reactive protein; *CRP.POD1*, CRP on the postoperative day 1; *CRP.POD4*, CRP on the postoperative day 4; *CRP.POD7*, CRP on the postoperative day 7; *IL-6*, interleukin-6; IL-6 and Cortisol in the same way.

TABLE 5 Univariate and multivariate analysis for POD7 complication in the training set.

Characteristics	Univariate analysis		Multivariate analysis	
	OR (95%CI)	*P* value	OR (95%CI)	*P* value
Cardiovascular disease	3.52 (1.89–6.56)	<0.001		
Diabetes	5.69 (2.72–11.93)	<0.001		
Age ≥ 65	2.89 (1.45–5.75)	0.003		
BMI ≤ 25	2.96 (1.51–5.81)	0.002	2.60 (1.02–6.62)	0.045
T.POD4 ≥ 37	9.24 (3.13–27.31)	<0.001	6.30 (1.43–27.73)	0.015
WBC.POD4 ≥ 9.5	3.89 (1.92–7.87)	<0.001		
N.POD4 ≥ 75	6.83 (3.44–13.55)	<0.001	3.60 (1.46–8.87)	0.005
FBG.POD4 ≥ 6.2	12.92 (6.13–27.23)	<0.001	8.28 (3.20–21.42)	<0.001
Absence of ratio <1	5.62 (2.29–13.89)	<0.001	5.56 (1.63–18.87)	0.006

BMI, body mass index, kg/m^2; *T.POD4*, the temperature on the postoperative day 4, °C; *WBC.POD4*, white cell count on the postoperative day 4, ×10^9/l; *N.POD4*, neutrophil percentage on the postoperative day 4, %; *FBG.POD4*, fasting blood glucose on the postoperative day 4, mmol/l; *Absence of ratio <1*, the absence of fluid intake/output <1 within POD4.

Development and validation of nomogram

First, we used clinical data within POD4 and identified five risk factors associated with the occurrence of complications within POD7 by univariate and multifactorial logistic regression analyses (Table 5): BMI, body temperature on POD4 (T.POD4), neutrophil percentage on POD4 (N.POD4), FBG on POD4 (FBG.POD4), and fluid intake/output ratio <1 within POD4. Subsequently, we developed Nomogram-A (Figure 1A). In the training set, the nomogram yielded an area under the curve (AUC) of 0.867 (95% CI, 0.814–0.920) with a sensitivity of 0.764 and a specificity of 0.845 (Figure 1B). In the validation set, the nomogram exhibited an AUC of 0.833 (95% CI, 0.744–0.923) with a sensitivity of 0.821 and a specificity of 0.762 (Figure 1C).

Similarly, we identified six independent risk factors associated with the occurrence of complications within POD30 in Table 6, including BMI, body temperature on POD7 (T.POD7), neutrophil percentage on POD7 (N.POD7), FBG on POD4 and POD7 (FBG.POD4 and FBG.POD7), and duration of fluid intake/output ratio >1. To avoid data redundancy, we compared FBG.POD4 and FBG.POD7 and

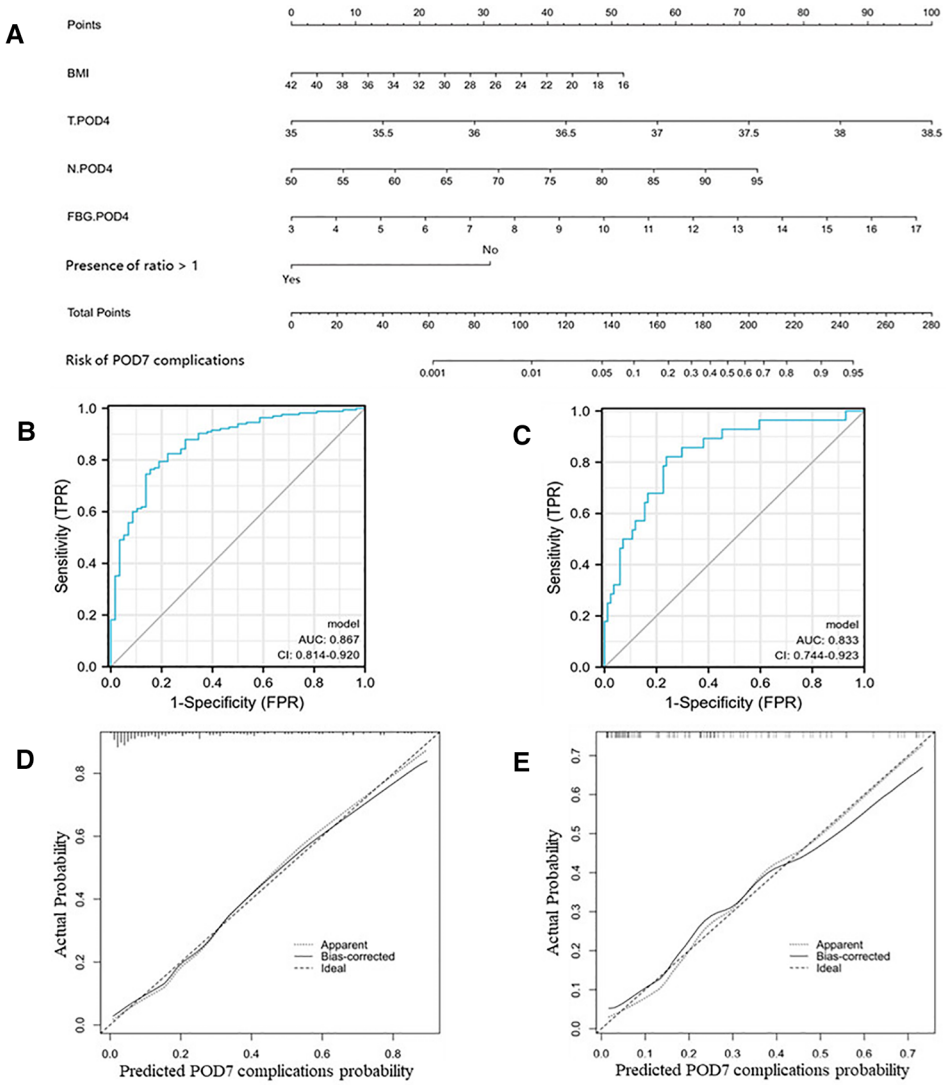

FIGURE 1
Nomogram-A and performance of the nomogram. (A) The possibility of POD7 complication was estimated by summing the scores corresponding to each risk factor. ROC and calibration curves of the nomogram for the probability of POD7 complication in the training set (B,D) and the validation set (C,E). In the calibration curve, the *y*-axis represents the probability of actual POD7 complication occurring and the *x*-axis represents the predicted probability. The wide dashed line represented a perfect prediction of the ideal model, and the solid line represented the actual performance of the Nomogram-A. The closer they were, the better the prediction performed.

further defined the higher values as the maximum FBG (FBG.MAX). Further, we used BMI, T.POD7, N.POD7, FBG.MAX, and a fluid intake/output ratio of >1 to develop Nomogram-B (Figure 2A). In the training set, the nomogram yielded an AUC of 0.920 (95% CI, 0.884–0.955) with a sensitivity of 0.813 and specificity of 0.882 (Figure 2B). In the validation set, the nomogram exhibited an AUC of 0.918 (95% CI, 0.855–0.980) with a sensitivity of 0.971 and a specificity of 0.833 (Figure 2C).

The calibration curves and Hosmer–Lemeshow test showed good agreement between the predicted and actual probabilities of the two nomograms in the training and validation sets ($P_A = 0.755$ vs. 0.738 (Figures 1D,E), $P_B = 0.768$ vs. 0.125 (Figures 2D,E)).

Discussion

In the present study, we successfully developed and validated nomograms for predicting postoperative complications within POD7 and POD30 in patients with gastrointestinal tumors. Both nomogram models were developed based on routine clinical indicators, including body temperature, neutrophil percentage, fasting glucose, and fluid

TABLE 6 Univariate and multivariate analysis for POD30 complication in the training set.

Characteristics	Univariate analysis		Multivariate analysis	
	OR (95%CI)	*P* value	OR (95%CI)	*P* value
Cardiovascular disease	3.03 (1.67–5.48)	<0.001		
Diabetes	5.49 (2.62–11.53)	<0.001		
Age ≥ 65	2.54 (1.35–4.78)	0.004		
BMI ≤ 25	3.29 (1.73–6.26)	<0.001	3.62 (1.12–11.64)	0.031
T.POD4 ≥ 37	14.34 (3.99–51.49)	<0.001		
T.POD7 ≥ 37	7.73 (2.02–29.54)	0.003	7.87 (1.05–59.20)	0.045
WBC.POD4 ≥ 9.5	5.38 (2.64–10.96)	<0.001		
WBC.POD7 ≥ 9.5	7.25 (3.11–16.91)	<0.001		
N.POD4 ≥ 75	7.33 (3.83–14.04)	<0.001		
N.POD7 ≥ 75	12.55 (6.13–25.72)	<0.001	6.08 (1.82–20.27)	0.003
FBG.POD4 ≥ 6.2	12.11 (6.10–24.05)	<0.001	6.62 (1.86–23.53)	0.003
FBG.POD7 ≥ 6.2	12.48 (6.32–24.67)	<0.001	5.02 (1.43–17.68)	0.012
(Duration of ratio >1) ≥ 6	10.87 (5.60–21.13)	<0.001	8.19 (2.83–23.70)	<0.001

BMI, body mass index, kg/m^2; *T.POD4*, the temperature on the postoperative day 4, °C; T.POD7, the temperature on the postoperative day 7, °C; *WBC.POD4*, white cell count on the postoperative day 4, ×10^9/l; *WBC.POD7*, white cell count on the postoperative day 7, ×10^9/l; *N.POD4*, neutrophil percentage on the postoperative day 4, %; *N.POD7*, neutrophil percentage on the postoperative day 7, %; *FBG.POD4*, fasting blood glucose on the postoperative day 4, mmol/l; *FBG.POD7*, fasting blood glucose on the postoperative day 7, mmol/l; *Duration of ratio > 1*, the final duration of fluid intake/output > 1.

volume within POD7. The AUCs of Nomogram-A and Nomogram-B were both greater than 0.8 in the training and validation sets, which may achieve the best performance in predicting the likelihood of postoperative complications. Comprehensively, this model is used to identify people at high risk of postoperative complications, thereby reducing its impact on postoperative recovery. The goal of both models is to improve short-term outcomes and quality of life after surgery and to reduce healthcare costs.

It has been documented that the occurrence of postoperative complications is closely associated with stress, and their occurrence usually indicates a strong stress response in the patient that induces hypermetabolism (9, 18). The main reparative cells and leukocytes increase in activity and number to satisfy the glucose supply for body recovery during this period (19). Meanwhile, with the upregulation of pro-inflammatory cytokines and acute-phase proteins and activation of the hypothalamic-pituitary-adrenal axis, there is an increase or decrease in the levels of some hormones, including cortisol, catecholamines, insulin, and glucagon, which promote glycogen catabolism and gluconeogenesis in muscle tissue that induces hyperglycemia to compensate for the "concentration gradient" needed for tissue repair (20). In addition, with the influence of hormones, capillary permeability and urine concentration increase (21). A large amount of fluid is stored in the interstitial space, resulting in tissue edema and is known as "water and sodium retention" When the stress response is reduced due to intervention and self-healing, excessive fluid is reabsorbed into the blood and excreted in the urine (22).

In our study, we also found a higher level of the stress response in patients with postoperative complications. In line with the study by Espiner EA, the alteration of stress results in increased water and sodium retention and further leads to more liquid intake than output, ultimately resulting in a higher daily fluid intake/output ratio (23). And we further observed that the presence of fluid intake/output ratio <1 within POD4 was related to the occurrence of complications within POD7, and that patients who developed complications within POD30 had a longer duration of fluid intake/output ratio >1. Under theoretical frameworks of perioperative stress response, we investigated the relationship between postoperative complications and fluid intake and output. The results demonstrated that the fluid intake/output ratio could be a convincing risk factor and predictor for the occurrence of complications.

Our study also validated the correlation between postoperative complications and routine monitoring indicators, such as body temperature, neutrophil percentage, and FBG (24). Slight changes in one or more these indicators were often overlooked by clinicians, leading to a failure of early identification of complications. Numerous studies have shown that changes in routine monitoring indicators may be affected by the regulation of inflammatory cytokines and hormones during the hypermetabolic period of the stress response (25, 26). In our analysis, stress level was positively correlated with

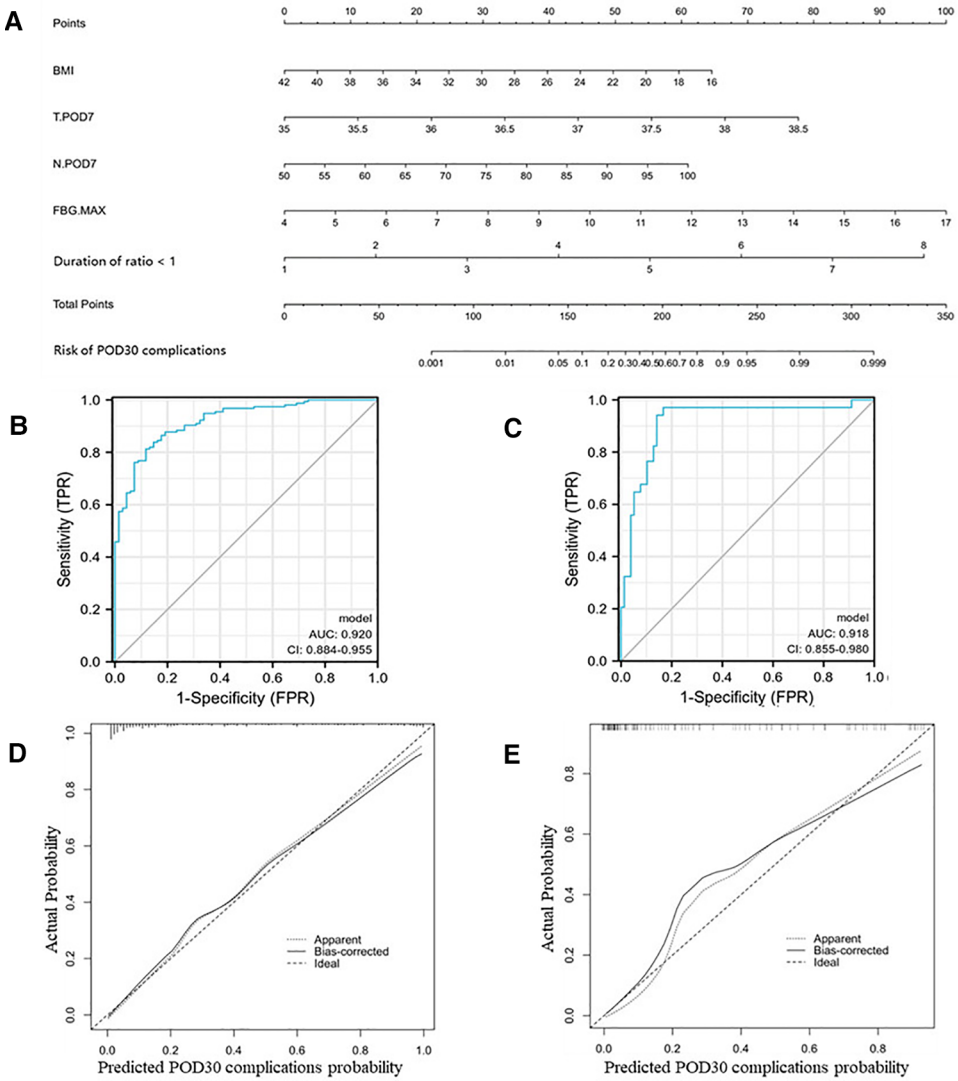

FIGURE 2
Nomogram-B and performance of the nomogram. (A) The possibility of POD30 complication was estimated by summing the scores corresponding to each risk factor. ROC and calibration curves of the nomogram for the probability of POD30 complication in the training set (B,D) and the validation set (C,E). In the calibration curve, the *y*-axis represents the probability of actual POD30 complication occurring and the *x*-axis represents the predicted probability. The wide dashed line represented a perfect prediction of the ideal model, and the solid line represented the actual performance of the Nomogram-B. The closer they were, the better the prediction performed.

certain routine monitoring indicators, such as body temperature, neutrophil percentage and FBG levels. Considering the correlation between acute stress pathophysiological and postoperative complications, these routine monitoring indicators may be potential risk factors and candidate predictors for postoperative complications (27–30). In addition, it is generally believed that perioperative routine monitoring indicators also reflect inflammation level. Elevated level of these indicators indicated a higher inflammatory level in patients with complications (31). In this study, we use acute stress-associated indicators to reflect inflammation level, thereby provide an early warning tool for complications. For patients with gastrointestinal tumor undergoing radical surgery, surgery- and tumor-associated factors, such as loss of blood, tissue injury, infection, impaired nutritional status and immunocompromised status, may place the patients in a high risk of complications (10, 32, 33). Timely identification of postoperative complication will urge us to recognize the problems in patient management, and timely intervention may reduce likelihood of severe advent events (33, 34). Mechanically, timely intervention for complication will reduce overconsumption of protein and duration of immune dysregulation, and further decrease the possibility of malnutrition, infection, thrombosis, etc. The final objective is to

improve outcomes for patients and save medical resources (35, 36). Similarly, evidence by previous researches showed that preoperative glucocorticoid therapy combined with fast-track surgery can attenuate the inflammatory response, avoid organ dysfunction, and prevent the occurrence of complications, resulting in improved short-term outcome (37–39).

Our study had some limitations. First, this study was a retrospective study that might have led to bias. Further prospective data are needed to validate the accuracy of our model. Second, a small number of patients were not included in this study owing to missing data, which resulted in a higher population of the group with complications. This may also lead to selection bias. Third, because of the high cost of measuring stress indicators, we only collected partial data from training set. And we will further consider ending the limitations by future prospective studies needed.

Conclusion

This study presents two nomogram models for predicting short-term postoperative complications in patients with gastrointestinal tumors. Our results can help clinicians identify patients at high risk of complications within POD7 or POD30. In addition, we explored the correlation between postoperative complications and fluid intake and output under the framework of pathophysiology and stress response and successfully identified new risk factors for complications. This study also provides a novel idea for predicting postoperative complications.

Data availability statement

The raw data supporting the conclusions of this article will be made available by the authors, without undue reservation.

Ethics statement

The studies involving human participants were reviewed and approved by the Ethics Committee at Yantai Yuhuangding Hospital Affiliated to Medical College of Qingdao University. The patients/participants provided their written informed consent to participate in this study.

Author contributions

HC, DZ, and JJ: contributed equally to this study, performed the experiments, analyzed the data, and wrote the manuscript. YZ, MJ and JH: designed the experiments. BY and YL: collected the data. XH: checked and revised the manuscript. LJ: confirmed all the data in the manuscript. XW and LJ: firstly modified the language of the manuscript. All authors contributed to the article and approved the submitted version.

Funding

This study was supported by grants from the National Natural Science Foundation of China (No. 82102785), the Natural Science Foundation of Shandong Province (ZR2021QH314) and the Natural Science Foundation of Yantai Yuhuangding Hospital (No. 2020-14, No. 2021-24, No. 2021-36). The funding bodies did not have any role in the design of the study, data collection, and analysis, nor on the interpretation and dissemination of the results.

Conflict of interest

The authors declare that the research was conducted in the absence of any commercial or financial relationships that could be construed as a potential conflict of interest.

Publisher's note

References

1. Qiu H, Cao S, Xu R. Cancer incidence, mortality, and burden in China: a time-trend analysis and comparison with the United States and United Kingdom based on the global epidemiological data released in 2020. *Cancer Commun.* (2021) 41:1037–48. doi: 10.1002/cac2.12197

2. Wei W, Zeng H, Zheng R, Zhang S, An L, Chen R, et al. Cancer registration in China and its role in cancer prevention and control. *Lancet Oncol.* (2020) 21: e342–9. doi: 10.1016/S1470-2045(20)30073-5

3. Wang FH, Zhang XT, Li YF, Tang L, Qu XJ, Ying JE, et al. The Chinese society of clinical oncology (CSCO): clinical guidelines for the diagnosis and treatment of gastric cancer, 2021. *Cancer Commun.* (2021) 41:747–95. doi: 10.1002/cac2.12193

4. Slankamenac K, Slankamenac M, Schlegel A, Nocito A, Rickenbacher A, Clavien P, et al. Impact of postoperative complications on readmission and long-term survival in patients following surgery for colorectal cancer. *Int J Colorectal Dis.* (2017) 32:805–11. doi: 10.1007/s00384-017-2811-y

5. van Kooten RT, Bahadoer RR, Peeters KCMJ, Hoeksema JHL, Steyerberg EW, Hartgrink HH, et al. Preoperative risk factors for major postoperative

complications after complex gastrointestinal cancer surgery: a systematic review. *Eur J Surg Oncol*. (2021) 47:3049–58. doi: 10.1016/j.ejso.2021.07.021

6. Selby LV, Gennarelli RL, Schnorr GC, Solomon SB, Schattner MA, Elkin EB, et al. Association of hospital costs with complications following total gastrectomy for gastric adenocarcinoma. *JAMA Surg*. (2017) 152:953. doi: 10.1001/jamasurg.2017.1718

7. Ghaferi AA, Birkmeyer JD, Dimick JB. Variation in hospital mortality associated with inpatient surgery. *N Engl J Med*. (2009) 361:1368–75. doi: 10.1056/NEJMsa0903048

8. Watt DG, McSorley ST, Park JH, Horgan PG, McMillan DC. A postoperative systemic inflammation score predicts short- and long-term outcomes in patients undergoing surgery for colorectal cancer. *Ann Surg Oncol*. (2017) 24:1100–9. doi: 10.1245/s10434-016-5659-4

9. Crippa J, Mari GM, Miranda A, Costanzi ATM, Maggioni D. Surgical stress response and enhanced recovery after laparoscopic surgery—a systematic review. *Chirurgia*. (2018) 113:455. doi: 10.21614/chirurgia.113.4.455

10. Wilmore DW. From cuthbertson to fast-track surgery: 70 years of progress in reducing stress in surgical patients. *Ann Surg*. (2002) 236:643–8. doi: 10.1097/00000658-200211000-00015

11. Liu K, Wang Y, Wang J, Luo N, Gong J, Wang J, et al. Application of accelerated rehabilitation surgery in gastrointestinal surgery. *Comput Math Method M*. (2021) 2021:1–9. doi: 10.1155/2021/2968347

12. Pędziwiatr M, Mavrikis J, Witowski J, Adamos A, Major P, Nowakowski M, et al. Current status of enhanced recovery after surgery (ERAS) protocol in gastrointestinal surgery. *Med Oncol*. (2018) 35(6):95. doi: 10.1007/s12032-018-1153-0

13. Ramshaw BJ. Laparoscopic surgery for cancer patients. *CA Cancer J Clin*. (1997) 47:327–50. doi: 10.3322/canjclin.47.6.327

14. Clavien PA, Barkun J, de Oliveira ML, Vauthey JN, Dindo D, Schulick RD, et al. The clavien-dindo classification of surgical complications. *Ann Surg*. (2009) 250:187–96. doi: 10.1097/SLA.0b013e3181b13ca2

15. Halabi S, Small EJ, Kantoff PW, Kattan MW, Kaplan EB, Dawson NA, et al. Prognostic model for predicting survival in men with hormone-refractory metastatic prostate cancer. *J Clin Oncol*. (2003) 21:1232–7. doi: 10.1200/JCO.2003.06.100

16. Delong ER, Delong DM, Clarke-Pearson DL. Comparing the areas under two or more correlated receiver operating characteristic curves: a nonparametric approach. *Biometrics*. (1988) 44:837–45. doi: 10.2307/2531595

17. Kramer AA, Zimmerman JE. Assessing the calibration of mortality benchmarks in critical care: the hosmer-lemeshow test revisited*. *Crit Care Med*. (2007) 35:2052–6. doi: 10.1097/01.CCM.0000275267.64078.B0

18. Oka Y, Nishijima J, Oku K, Azuma T, Inada K, Miyazaki S, et al. Usefulness of an estimation of physiologic ability and surgical stress (E-PASS) scoring system to predict the incidence of postoperative complications in gastrointestinal surgery. *World J Surg*. (2005) 29:1029–33. doi: 10.1007/s00268-005-7719-y

19. Monk DN, Plank LD, Franch-Arcas G, Finn PJ, Streat SJ, Hill GL. Sequential changes in the metabolic response in critically injured patients during the first 25 days after blunt trauma. *Ann Surg*. (1996) 223:395–405. doi: 10.1097/00000658-199604000-00008

20. Carli F. Physiologic considerations of enhanced recovery after surgery (ERAS) programs: implications of the stress response. *Can J Anesth*. (2015) 62:110–9. doi: 10.1007/s12630-014-0264-0

21. Scott MJ, Miller TE. Pathophysiology of Major surgery and the role of enhanced recovery pathways and the anesthesiologist to improve outcomes. *Anesthesiol Clin*. (2015) 33:79–91. doi: 10.1016/j.anclin.2014.11.006

22. Feldheiser A, Aziz O, Baldini G, Cox BPBW, Fearon KCH, Feldman LS, et al. Enhanced recovery after surgery (ERAS) for gastrointestinal surgery, part 2: consensus statement for anaesthesia practice. *Acta Anaesth Scand*. (2016) 60:289–334. doi: 10.1111/aas.12651

23. Espiner EA. 7—the Effects of stress on salt and water balance. *Baillière's Clin Endocrinol Metab*. (1987) 1:375–90. doi: 10.1016/S0950-351X(87)80068-X

24. Watt DG, Horgan PG, McMillan DC. Routine clinical markers of the magnitude of the systemic inflammatory response after elective operation: a systematic review. *Surgery*. (2015) 157:362–80. doi: 10.1016/j.surg.2014.09.009

25. Romain B, Chemaly R, Meyer N, Chilintseva N, Triki E, Brigand C, et al. Diagnostic markers of postoperative morbidity after laparoscopic roux-en-Y gastric bypass for obesity. *Langenbeck's Arch Surg*. (2014) 399:503–8. doi: 10.1007/s00423-014-1180-z

26. Albanopoulos K, Alevizos L, Natoudi M, Dardamanis D, Menenakos E, Stamou K, et al. C-reactive protein, white blood cells, and neutrophils as early predictors of postoperative complications in patients undergoing laparoscopic sleeve gastrectomy. *Surg Endosc*. (2013) 27:864–71. doi: 10.1007/s00464-012-2526-7

27. Margraf A, Ludwig N, Zarbock A, Rossaint J. Systemic inflammatory response syndrome after surgery: mechanisms and protection. *Anesth Analg*. (2020) 131:1693–707. doi: 10.1213/ANE.0000000000005175

28. McSorley ST, Watt DG, Horgan PG, McMillan DC. Postoperative systemic inflammatory response, complication severity, and survival following surgery for colorectal cancer. *Ann Surg Oncol*. (2016) 23:2832–40. doi: 10.1245/s10434-016-5204-5

29. Podgoreanu MV, Michelotti GA, Sato Y, Smith MP, Lin S, Morris RW, et al. Differential cardiac gene expression during cardiopulmonary bypass: ischemia-independent upregulation of proinflammatory genes. *J Thorac Cardiovasc Surg*. (2005) 130:330–9. doi: 10.1016/j.jtcvs.2004.11.052

30. Bauer AJ, Boeckxstaens GE. Mechanisms of postoperative ileus. *Neurogastroenterol Motil*. (2004) 16(Suppl 2):54–60. doi: 10.1111/j.1743-3150.2004.00558.x

31. Cuthbertson D, Tilstone WJ. Metabolism during the postinjury period. *Adv Clin Chem*. (1969) 12:1–55. doi: 10.1016/S0065-2423(08)60257-7

32. Finnerty CC, Mabvuure NT, Ali A, Kozar RA, Herndon DN. The surgically induced stress response. *JPEN J Parenter Enteral Nutr*. (2013) 37:21S–9S. doi: 10.1177/0148607113496117

33. Kohl BA, Deutschman CS. The inflammatory response to surgery and trauma. *Curr Opin Crit Care*. (2006) 12:325–32. doi: 10.1097/01.ccx.0000235210.85073.fc

34. Van den Berghe GH. Acute and prolonged critical illness are two distinct neuroendocrine paradigms. *Verh K Acad Geneeskd Belg*. (1998) 60:487–518, 518–520.

35. Shirakawa Y, Noma K, Maeda N, Tanabe S, Sakurama K, Sonoyama-Hanaoka A, et al. Early intervention of the perioperative multidisciplinary team approach decreases the adverse events during neoadjuvant chemotherapy for esophageal cancer patients. *Esophagus*. (2021) 18:797–805. doi: 10.1007/s10388-021-00844-y

36. Jhanji S, Pearse RM. The use of early intervention to prevent postoperative complications. *Curr Opin Crit Care*. (2009) 15:349–54. doi: 10.1097/MCC.0b013e32832c4a7e

37. Prete A, Yan Q, Al-Tarrah K, Akturk HK, Prokop LJ, Alahdab F, et al. The cortisol stress response induced by surgery: a systematic review and meta-analysis. *Clin Endocrinol*. (2018) 89:554–67. doi: 10.1111/cen.13820

38. Hall K, Shahrokhi S, Jeschke M. Enteral nutrition support in burn care: a review of current recommendations as instituted in the ross tilley burn centre. *Nutrients*. (2012) 4:1554–65. doi: 10.3390/nu4111554

39. Kehlet H, Dahl JB. Anaesthesia, surgery, and challenges in postoperative recovery. *Lancet*. (2003) 362:1921–8. doi: 10.1016/S0140-6736(03)14966-5

frontiers | Frontiers in Surgery

TYPE Original Research
PUBLISHED 06 January 2023
DOI 10.3389/fsurg.2022.1046713

OPEN ACCESS

EDITED BY
Mengling Feng,
National University of Singapore, Singapore

REVIEWED BY
Michael Kueht,
University of Texas Medical Branch at Galveston, United States
Nguyen Minh Duc,
Pham Ngoc Thach University of Medicine, Vietnam

*CORRESPONDENCE
Chuandong Sun
✉ sunchuandong@hotmail.com
Hao Zou
✉ zh37759@qdu.edu.cn

SPECIALTY SECTION
This article was submitted to Surgical Oncology, a section of the journal Frontiers in Surgery

RECEIVED 17 September 2022
ACCEPTED 14 December 2022
PUBLISHED 06 January 2023

CITATION
Wang X, Fu Y, Zhu C, Hu X, Zou H and Sun C (2023) New insights into a microvascular invasion prediction model in hepatocellular carcinoma: A retrospective study from the SEER database and China.
Front. Surg. 9:1046713.
doi: 10.3389/fsurg.2022.1046713

New insights into a microvascular invasion prediction model in hepatocellular carcinoma: A retrospective study from the SEER database and China

Xingchang Wang[1], Yiling Fu[2], Chengzhan Zhu[1], Xiao Hu[1], Hao Zou[1]* and Chuandong Sun[1]*

[1]Department of Hepatobiliary and Pancreatic Surgery, The Affiliated Hospital of Qingdao University, Qingdao, China, [2]Department of Rehabilitation Medicine, Qilu Hospital of Shandong University (Qingdao), Qingdao, China

Background and Aims: The prognosis of liver cancer is strongly influenced by microvascular infiltration (MVI). Accurate preoperative MVI prediction can aid clinicians in the selection of suitable treatment options. In this study, we constructed a novel, reliable, and adaptable nomogram for predicting MVI.
Methods: Using the Surveillance, Epidemiology, and End Results (SEER) database, we extracted the clinical data of 1,063 patients diagnosed with hepatocellular carcinoma (HCC) and divided it into either a training ($n = 739$) or an internal validation cohort ($n = 326$). Based on multivariate analysis, the training cohort data were analyzed and a nomogram was generated for MVI prediction. This was further verified using an internal validation cohort and an external validation cohort involving 293 Chinese patients. Furthermore, to evaluate the efficacy, accuracy, and clinical use of the nomogram, we used concordance index (C-index), calibration curve, and decision curve analysis (DCA) techniques.
Results: In accordance with the multivariate analysis, tumor size, tumor number, alpha-fetoprotein (AFP), and histological grade were independently associated with MVI. The established model exhibited satisfactory performance in predicting MVI. The C-indices were 0.719, 0.704, and 0.718 in the training, internal validation, and external validation cohorts, respectively. The calibration curves showed an excellent consistency between the predictions and actual observations. Finally, DCA demonstrated that the newly developed nomogram had favorable clinical utility.
Conclusions: We established and verified a novel preoperative MVI prediction model in HCC patients. This model can be a beneficial tool for clinicians in selecting an optimal treatment plan for HCC patients.

KEYWORDS

hepatocellular carcinoma, microvascular invasion, predicting model, nomogram, SEER, external validation

Introduction

Primary liver cancer is one of the most prevalent cancers and is a major contributor to the global cancer mortality rate. Its morbidity and mortality rates are among the highest worldwide (1). Mortality from primary liver cancer is the second highest among malignant tumors and the fourth most common type of cancer in China (2). Annually, the number of new cases and deaths of primary liver cancer is about 466,100 and 422,000, respectively (3). Hepatocellular carcinoma (HCC) is the most prevalent pathological type of primary liver cancer and respects about 80% of all primary liver cancer worldwide (4).. To date, the most effective interventions for HCC are hepatectomy and liver transplantation. However, patient prognosis following these treatments remains relatively poor (5). Moreover, it has a recurrence rate of 70% 5 years after surgery (6, 7). Thus, despite the rapid development of HCC diagnosis and treatment, its high recurrence rate remains a considerable challenge (8).

Vascular invasion is strongly linked with tumor malignancy, disease recurrence, and poor patient prognosis. In individuals with HCC, this invasion may be divided into two subtypes: macrovascular and microvascular. Macrovascular invasion is typically identified by imaging, and patients experiencing this form of invasion often do not have the chance to undergo radical resection or liver transplantation. Alternatively, microvascular infiltrations (MVI) status is only available by pathological examination of surgical specimens. It is a nest of cancer cells in endothelium-lined vessels, which may be observed under a microscope and are usually present at the small branches of the portal vein in the surrounding liver tissues (9). MVI can result in the dissemination and metastasis of tumor cells within the liver, or even lead to metastasis to other parts of the body (10). Therefore, MVI is thought to be one of the main risk factor influencing tumor recurrence and survival (11), and it is often employed as a prognostic indicator to guide the choice of an appropriate treatment regimen in patients with both primary and recurrent HCC (12, 13). Meanwhile, emerging evidence has revealed that MVI assists in clinical decision-making. For instance, it was suggested that the precise preoperative prediction of MVI status can assist in identifying surgical resection margins to enhance patient outcomes (14, 15). Furthermore, individuals with MVI-positive HCC whose surgeries were accompanied by adjuvant intervention or targeted treatment had better overall survival (OS) than those who underwent surgery alone (16, 17). Hence, accurate prediction of MVI status is crucial for providing an efficient and successful intervention for HCC patients.

Unfortunately, MVI diagnosis is established only by histopathological assessment of surgical specimens following HCC resection or liver transplantation. At present, there is no effective or precise prediction method prior to surgery, which greatly limits the effect of preoperative assessment on surgical planning and patient outcome. Hence, finding a method to accurately and efficiently predict MVI is an urgent problem to be solved at present (18). A nomogram is a feasible and efficient tool that integrates and quantifies marked risk factors to predict patient outcome (19). Numerous studies have generated and verified different nomograms for MVI predictions. However, most of these nomograms were based on single-center studies that lack external verification, which puts into question the reliability and applicability of these models (20, 21). In addition, there are limited studies available on the risk assessment of MVI.

Hence, the purpose of the present study was to generate a novel, reliable, and adaptable nomogram to predict the incidence of MVI in HCC patients. This can aid clinicians in selecting suitable therapeutic measures for patients with MVI-positive HCC.

Methods

Data sources and patient population

Patient records were retrospectively obtained from the Surveillance, Epidemiology, and End Results (SEER) database, maintained by the US National Cancer Institute. Co-created by 18 registries throughout the United States, this database includes information on the prevalence of illness and outcomes for patients with tumors across approximately 28% of the country. Patient data included the following demographics: age, sex, ethnicity, country of birth, and specifics of the patient's tumor (including its histology and grade) and treatment (including details about any surgeries, radiation, or other interventions). Recently added data include AJCC stage, surgical parameters, tumor size, and lymph node involvement. In addition to a large patient pool and improved data accuracy, this database contains tumor profiling specimens.

Using the SEER stat program (SEER*Stat 8.4.0.1), we were able to access the SEER database and obtain records of HCC patients diagnosed between 2007 and 2017. The inclusion criteria were shown below: (I) patients with HCC (ICD-0–3:8170–8175), and the primary tumor site was liver; (II) age at diagnosis ≥18 years; (III) those who undergo liver resection or liver transplantation with postoperative histopathological confirmation. The following patients were excluded from the analysis: (I) pathologically confirmed other than HCC; (II) those with MVI status not determined *via* histopathological evaluation; (III) patients with HCC with macrovascular or extrahepatic infiltration; and (IV) those with missing clinical information. The selection process is illustrated in **Figure 1**. Ultimately, we acquired information on 1,063 patients. Subsequently, we randomly spilt all cases into either a training cohort and an internal validation cohort in a 7:3 ratio.

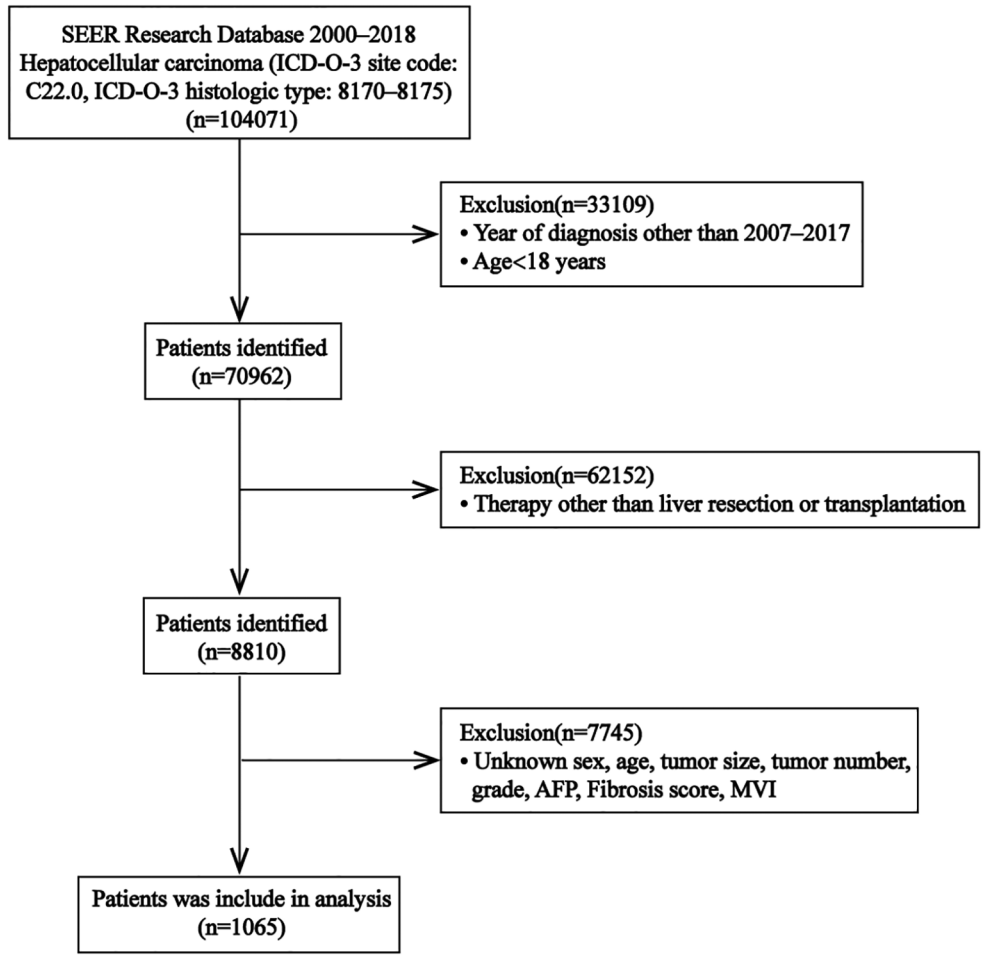

FIGURE 1
Flow chart for selection of the study population from SEER database. Abbreviations: SEER, Surveillance, Epidemiology, and End Results; ICD-O-3, International Classification of Diseases for Oncology, 3rd edition; MVI, microvascular invasion; AFP, alpha fetal protein.

Next, we assessed the general applicability of the proposed model. We employed an external validation cohort composed of 293 Chinese patients with HCC who received treatment at the Affiliated Hospital of Qingdao University from January 2017 to December 2019 using the same patient selection criteria as mentioned above. Our study was reviewed and approved by the Ethics Committee of the Affiliated Hospital of Qingdao University (approval no: QYFY WZLL 27357) and was performed according to the latest version of the Declaration of Helsinki. Written informed consent was waived due to the retrospective nature of the study.

Clinical variables and pathological characteristics

Clinicopathological features, such as patient age, sex, tumor size, tumor number, MVI status, histological grade, alpha-fetoprotein (AFP), and fibrosis score, were acquired from the SEER database and the Affiliated Hospital of Qingdao University. Fibrotic stage was divided into F0–4 (no fibrosis to moderate fibrosis) and F5–6 (severe fibrosis) based on the Ishak score from the SEER database.

Statistical analysis

Categorical data, analyzed using the chi-square or Fisher's exact tests, are presented statistically as numbers of cases with percentages. The Wilcoxon rank sum test was used to analyze continuous data, which were provided as means with interquartile ranges (IQRs). To assess the MVI risk factors, we conducted univariate analyses on the training cohort information. All data ($P < 0.05$) in the univariate analyses were subjected to multivariate analysis to identify independent MVI risk factors, and an MVI prediction nomogram was generated according to the multivariate analysis results.

TABLE 1 Baseline demographics and clinical characteristics of the training, internal validation, and external validation cohort.

Baseline Characteristics	Number (%)/Median (IQR)*			*P* value
	Training Cohort (*n* = 739)	Internal Validation Cohort (*n* = 326)	External Validation Cohort (*n* = 293)	
Sex				0.792
Male	243 (74.5)	536 (72.5)	214 (73.0)	
Female	83 (25.5)	203 (27.5)	79 (27.0)	
Age(years)				0.802
<60	131 (40.2)	289 (39.1)	121 (41.3)	
≥60	195 (59.8)	450 (60.9)	172 (58.7)	
Tumor size (cm)	3.50 (2.30, 5.20)	3.60 (2.40, 5.50)	3.50 (2.50, 5.50)	0.655
Tumor number				<0.001
Multiple	71 (21.8)	155 (21.0)	30 (10.2)	
Single	255 (78.2)	584 (79.0)	263 (89.8)	
MVI				<0.001
Negative	258 (79.1)	598 (80.9)	135 (46.1)	
Positive	68 (20.9)	141 (19.1)	158 (53.9)	
Grade				<0.001
I	90 (27.6)	170 (23.0)	10 (3.4)	
II	180 (55.2)	444 (60.1)	148 (50.5)	
III	54 (16.6)	116 (15.7)	125 (42.7)	
IV	2 (0.6)	9 (1.2)	10 (3.4)	
AFP				0.001
Negative	137 (42.0)	286 (38.7)	150 (51.2)	
Positive	189 (58.0)	453 (61.3)	143 (48.8)	
Fibrosis score				0.452
F0–4	131 (40.2)	298 (40.3)	130 (44.4)	
F5–6	195 (59.8)	441 (59.7)	163 (55.6)	

Abbreviations: MVI, microvascular invasion; AFP, a-fetoprotein.
*Median with interquartile range are shown for quantitative variables, whereas counts with proportions are shown for categorical variables.

We calculated the concordance index (C-index) using 1,000 bootstrap samples for measurement discrimination to evaluate the predictive performance of the nomogram. Using calibration plots, we checked how well our predictions matched the real-world data. Using decision curve analysis (DCA), we were able to assess the nomogram's clinical efficacy by quantifying their net benefit at different cutoff probabilities. Statistical significance was set at $P < 0.05$. All analyses were performed using R v3.6.3.

Results

Clinicopathological profiles

The SEER database was mined for 1,065 patients with HCC. To develop and verify the nomogram, the patients' data were randomized into a training cohort ($n = 739$) and an internal validation cohort ($n = 326$). The external validation cohort consisted of 293 Chinese patients with HCC. The training cohort included 536 males and 203 females, the internal validation cohort consisted of 243 males and 83 females, and the external validation cohort consisted of 214 males and 79 females. The median tumor sizes were 3.6 cm (range 2.4–5.5), 3.5 cm (range 2.3–5.5), and 3.5 cm (range 2.5–5.5) in the training, internal validation, and external validation cohort, respectively. Histopathological MVI detection was positive in 141 of 739 patients (19.1%) in the training cohort; 68 of 326 patients (20.9%) in the internal validation cohort; and 158 of 293 patients (53.9%) in the external validation cohort. Patient demographics and clinicopathological profiles of the three patient populations are summarized in Table 1.

TABLE 2 Univariate ordinal logistic analysis for MVI status in the training cohort ($N = 739$).

Factor	Number (%)/Median (IQR) *		*P* value
	Negative ($n = 598$)	Positive ($n = 141$)	
Sex			0.79
Male	435 (72.74%)	101 (71.63%)	
Female	163 (27.26%)	40 (28.37%)	
Age (years)			0.869
<60	233 (38.96%)	56 (39.72%)	
≥60	365 (61.04%)	85 (60.28%)	
Tumor size (cm)	3.3 (2.3, 5.0)	4.8 (3.2, 7.0)	<0.001
Tumor number			0.015
Multiple	136 (22.74%)	19 (13.48%)	
Single	462 (77.26%)	122 (86.52%)	
Grade			<0.001
I	159 (26.59%)	11 (7.8%)	
II	355 (59.36%)	89 (63.12%)	
III	77 (12.88%)	39 (27.66%)	
IV	7 (1.17%)	2 (1.42%)	
AFP			<0.001
Negative	255 (42.64%)	31 (21.99%)	
Positive	343 (57.36%)	110 (78.01%)	
Fibrosis score			0.081
F0–4	232 (38.8%)	66 (46.81%)	
F5–6	366 (61.2%)	75 (53.19%)	

P value: categorical variables-χ^2test or Fisher's exact test; continuous variables-Wilcoxon rank sum test.
Abbreviations: HCC, hepatocellular carcinoma; MVI, microvascular invasion; AFP, a-fetoprotein.
*Median with interquartile range are shown for quantitative variables, whereas counts with proportions are shown for categorical variables.

Independent risk factors associated with MVI Status

Tumor size, tumor number, histological grade, and AFP were all shown to have significant correlations with MVI based on the univariate analyses of clinicopathological characteristics between the MVI-positive and negative patient groups (Table 2). Furthermore, using the multivariate analysis, all the aforementioned variables were shown to be independent risk factors of MVI (Table 3).

TABLE 3 Multivariable analysis of predictors associated with MVI in the training cohort ($N = 739$).

Factor	OR	95% CI	*P* value
Tumor size (cm)	1.005	1–1.009	0.04
Tumor number			
Multiple			1 (reference)
Single	1.101	1.029–1.178	0.005
Grade			
I			1 (reference)
II	1.123	1.049–1.202	0.001
III	1.262	1.152–1.383	<0.001
IV	1.075	0.832–1.39	0.58
AFP			
Negative			1 (reference)
Positive	1.117	1.054–1.183	<0.001

Abbreviations: AFP, a-fetoprotein; OR, (odds ratio) = $e^{Estimate}$; CI, confidence interval.

Construction and verification of an MVI prediction nomogram

Using prognostic indicators, including tumor size, tumor number, histological grade, and AFP, we built a nomogram to predict MVI (Figure 2). We can predict the incidence of MVI by employing this nomogram to compute the total points for individual patients. In the training cohort, the C-index was 0.719 (95% CI: 0.674–0.764), in the internal validation cohort, it was 0.704 (95% CI: 0.639–0.77), and in the external validation cohort, it was 0.718 (95% CI: 0.659–0.777) Figure 3). Based on these data, nomogram exhibited excellent performance in delineating between negative and positive MVI incidence.

Furthermore, we constructed calibration plots to assess the calibration of our prediction model. Based on our analysis, there was excellent agreement between the actual and predicted likelihood of MVI among HCC patients in the training, internal validation, and external validation cohorts, respectively (Figures 4A–C). DCA was employed for the evaluation of total benefit under varying clinical decisions at different threshold likelihood. According to the DCA results of training and internal validation cohort (Figures 5A,B), it is useful to employ this nomogram to predict MVI between threshold probabilities of 0 and 0.4; and the DCA results of external validation cohort (Figure 5C) revealed that it is useful to employ this nomogram to predict MVI between threshold probabilities of 0 and 0.8, thus, indicating a

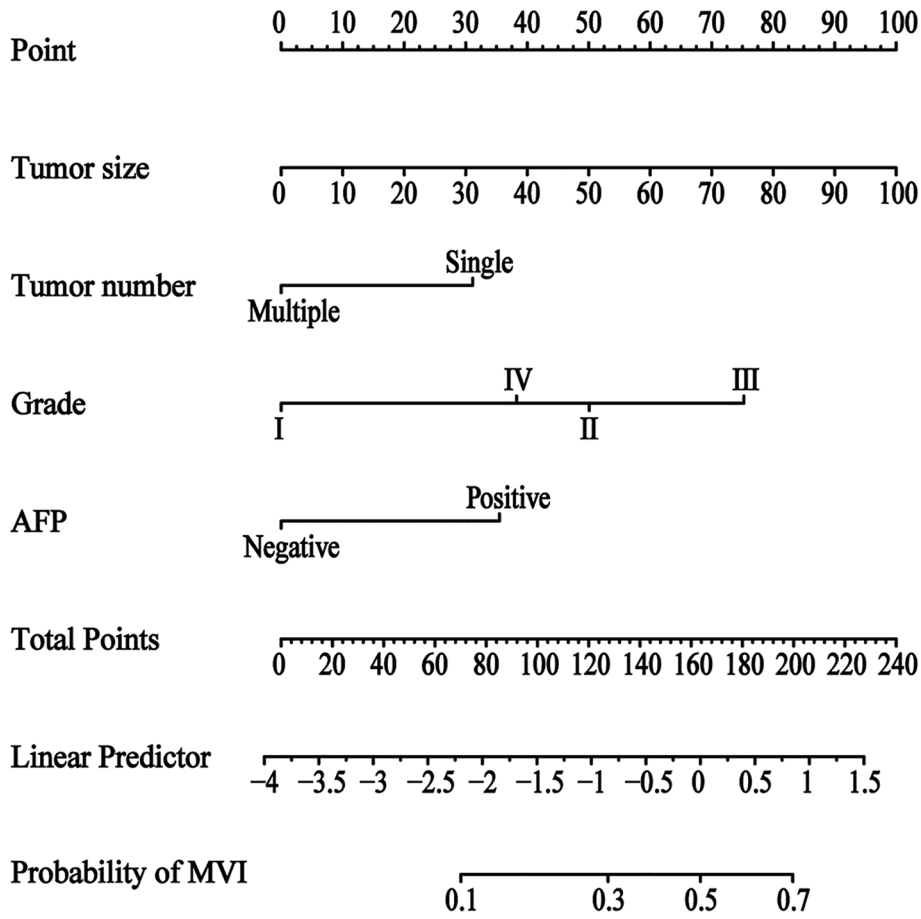

FIGURE 2
Nomogram for predicting the status of microvascular invasion preoperatively in patients with hepatocellular carcinoma. The MVI nomogram was built by incorporating tumor size, tumor number, histological grade and AFP. Locate the patient's characteristic on a variable row and draw a vertical line straight up to the points' row (top) to assign a point value for the variable. Adding up the total number of points and drop a vertical line from the total points' row to obtain the probability of predictive outcomes. Abbreviations: MVI, microvascular invasion; AFP, a-fetoprotein.

satisfactory clinical application of the developed nomogram. To better understand their significance, nomogram clinical impact curves for MVI prediction were plotted (**Supplementary Figures S1A–C**). Based on our results, the model exhibited a substantial predictive value.

Discussion

The major factor behind the poor outcome of HCC patients is the high relapse rate of this disease (9, 22). As one of the major contributor to HCC recurrence, MVI can strongly influence tumor cell intrahepatic metastasis *via* the portal circulation (23) and induce tumor recurrence following operation (24). Hence, MVI is typically considered an essential prognostic indicator for HCC following surgery. Additionally, MVI also impacts preoperative decision-making. In 2017, Zhao et al. demonstrated that anatomical hepatectomy enhances recurrence-free survival in MVI-positive patients (25). Mazzaferro et al. revealed no obvious variability in the 5-year OS rate following liver transplantation between the Milan and MVI-negative Up-to-seven criteria usage (26). However, MVI can only be detected *via* histopathological evaluation following surgical resection (27), which limits its clinical application. Therefore, it is crucial to preoperatively predict MVI for guiding clinical decision-making and improving patient prognosis.

Using a retrospective investigation of the SEER and Affiliated Hospital of Qingdao University databases, we established and verified a novel preoperative prediction model for MVI in HCC patients. The nomogram accurately identified patients with negative and positive preoperative MVI. Furthermore, the estimated likelihood was comparable with the true incidence of MVI. Herein, we demonstrated that tumor size, tumor number, histological grade, and AFP were markedly related to MVI occurrence. In the multivariate

analysis, the amplitude of the odds ratios statistically significant. But no value had an independent predictive contribution over 26%, they had worthwhile predictive power together. The relationship between some of these factors and the MVI has also been verified in other studies. A prior report suggested that MVI incidence increased with tumor size in HCC patients (≤3 cm, 25%; 3.1–5 cm, 40%; 5.1–6.5 cm, 55%; >6.5 cm, 63%) (28). Kim et al. (29) and Siegel et al. (30) revealed that tumor sizes over 2 or 3 cm are risk indicators of MVI, respectively. Our investigation corroborates the aforementioned reports. Multiple studies have suggested that an elevated AFP level is independently associated with MVI incidence (31, 32), which is in accordance with our results. Histological grade represents the HCC differentiation status. Preoperative HCC diagnosis usually requires liver biopsy. Once HCC is confirmed, further information on HCC differentiation can be obtained at the same time. Yao et al. revealed that tumor size and histological grade are independent factors related to MVI (33), which is in accordance with our data. Notably, to date, there is no consensus on the relationship between tumor quantity and MVI. Wang et al. reported that multiple tumors strongly indicate MVI (10). Alternatively, Yan et al. revealed that solitary nodules were distinctly related to MVI (34). Based on our multivariate analysis, patients with HCC with a single tumor were more vulnerable to MVI formation. However, this finding requires further validation.

Numerous investigations have explored the risk factors for predicting MVI. For instance, Mao et al. reported that preoperative large tumor diameter, AFP over 20 ng/ml, and total bilirubin level > 23 umol/L were strongly related to MVI. Moreover, they constructed an MVI prediction nomogram using these factors (21). Deng et al. established a nomogram that combined tumor size, preoperative AFP level, and neutrophil-to-lymphocyte ratio to predict MVI (35). Lin et al. generated a nomogram that included the intratumoral artery, tumor type, tumor diameter, and AFP level, and it exhibited satisfactory performance in predicting MVI occurrence in patients with HCC (36). However, the majority of previous studies were single-center investigations and employed relatively small sample populations. It is possible that such study characteristics may have impeded the reliability, limited generalizability, and external applicability of their models.

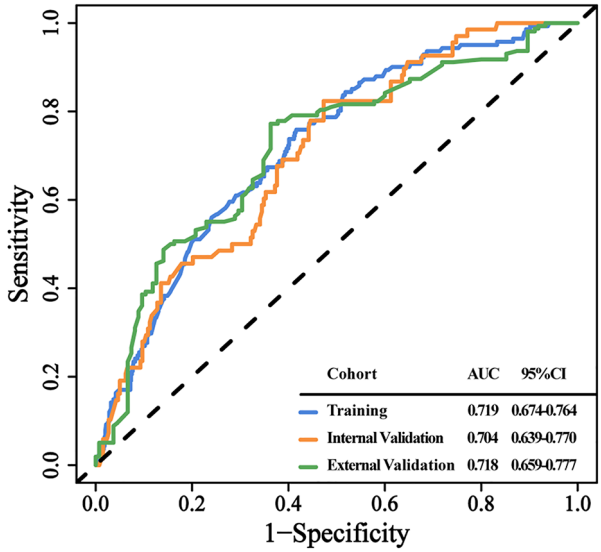

FIGURE 3
The discrimination of the clinical prediction model in the 3 data cohorts. ROC curves for MVI probability in the training (A), internal validation (B), and external validation cohort (C), respectively. Abbreviations: ROC, receiver operating characteristic curve. AUC, area under curve.

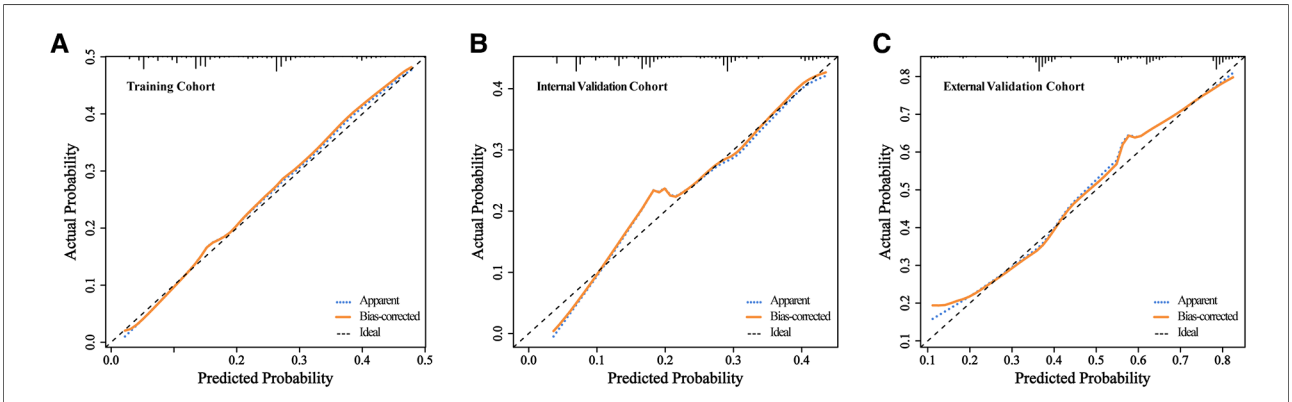

FIGURE 4
The calibration of the clinical prediction model in the 3 data cohorts. Calibration curves for predicting patient MVI at each time point in the training (A), internal validation (B), and external validation cohort (C), respectively. Model-predicted MVI is plotted on the x-axis, and actual MVI is plotted on the y-axis. The calibration curves of the nomogram based on internal validation with a bootstrap resampling frequency of 1,000. A plot along the 45-degree line (dotted black line) would indicate a perfect calibration model in which the predicted probabilities are identical to the actual outcomes.

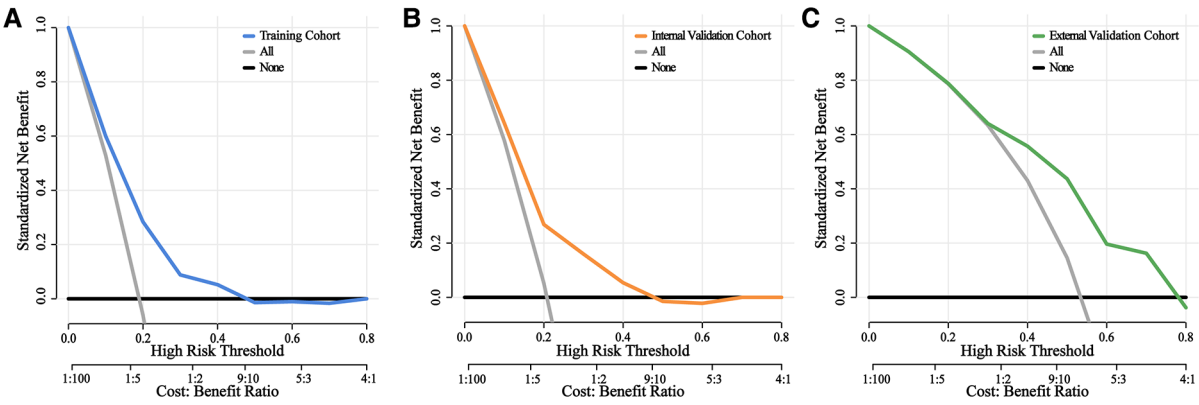

FIGURE 5
Decision curves of the nomograms for predicting status of MVI. DCA curves of the nomogram at each time point in the training (A), internal validation (B), and external validation cohort (C), respectively. The horizontal solid black line represents the hypothesis that no patients experienced the status of MVI, and the solid gray line represents the hypothesis that all patients met the endpoint. The blue, orange, and green line, represents the net benefit of the nomogram at different threshold probabilities. The net clinical benefit was calculated as the true-positive rate minus the weighted false-positive rate.

Relative to those studies, our MVI prediction model was established and validated using a multicenter platform, which included a relatively large sample population, and it demonstrated strong predictability among different populations (American and hospitalized Chinese populations). Hence, our model is more reliable and applicable.

Currently, there is much interest in MVI prediction models based on radiomics. To predict MVI, Xu et al. developed a novel computational method that integrates extensive clinico-radiologic and radiomic data, including AST, AFP, tumor margin, growth pattern, capsule, peritumoral enhancement, radio-genomic venous invasion, and radiomic score, with promising results (37). To predict MVI status in HCC, Hyun et al. constructed a nomogram that includes the tumor-to-normal liver standardized uptake value ratio on FDG PET/CT, clinical tumor size, and AFP (38). Zhang et al. used some Gd-EOB-DTPA MRI features and biochemical indicators to develop a new diagnostic scoring system to predict MVI, consisting of maximum tumor diameter, peritumoral hepatobiliary phase reduced intensity, incomplete capsule, apparent diffusion coefficient, and [alkaline phosphatase (U/L) + gamma-glutamyl transpeptidase (U/L)]/lymphocyte count (×109/L) ratio (39). However, the accuracy and practicality of these models are doubtful because of the lack of uniformity in radiomics and overreliance on the judgment of diagnostic radiologists (40). Additionally, certain specialized radiological parameters are often not understood or used by clinicians. In contrast, we built our model using data from regular laboratory tests, which are easily accessible, standardized, and manageable. It is also simple and straightforward to compare and contrast the data from different sources. Thus, it is clear that our model is not only better in terms of standardization and popularization but also facilitates clinical use.

Although our study has many advantages, it also has certain limitations. First, owing to its retrospective nature, this study may suffer from potential bias. Hence, further studies using prospective patient data are required. Second, owing to the limited clinical information acquired from the SEER database, many reported clinical risk factors known to be associated with MVI, such as platelet count (32), neutrophils (10) and total bilirubin level (21), were not included in this research. This may have negative effect on the prediction ability of the model, to a certain extent. Third, at present, radiographic diagnosis with LIRADs criteria in appropriate risk groups gradually replaced biopsy as the standard diagnostic method for HCC. However, the SEER database lacks relevant imaging information, so it is necessary to collect relevant imaging information in the following research to further improve the nomogram. Fourth, this model was established and verified using the SEER database, and external validation was done in a single-center in China. However, the applicability of this model to individuals of other ethnicities or racial is uncertain. Thus, external verification using other centers is required prior to the widespread use of this model in clinics.

In summary, we established and verified a novel, reliable, and adaptable preoperative prediction model for MVI in HCC patients. Our model was composed of four routine laboratory parameters (tumor size, tumor number, histological grade, and AFP), and it demonstrated superior delineation properties in terms of MVI diagnosis. This model can potentially aid clinicians in establishing the individualized risk of patients with MVI development, which in turn, can assist in proper treatment application.

Data availability statement

The datasets presented in this study can be found in online repositories. The names of the repository/repositories and accession number(s) can be found in the article/ **Supplementary Material**.

Ethics statement

The studies involving human participants were reviewed and approved by the Ethics Committee of the Affiliated Hospital of Qingdao University. Written informed consent for participation was not required for this study in accordance with the national legislation and the institutional requirements.

Author contributions

XW and CS: conceived the study. YF and XW: collected and analyzed the data. HZ, CZ and XW: generated the tables and figures. XW: drafted the manuscript. XH and HZ: revised the manuscript. CS: supervised the study. All authors contributed to the article and approved the submitted version.

Funding

This study was supported by grants from the National Natural Science Foundation of P.R. China (Grant Nos. 5207051760).

Acknowledgments

We would like to thank the researchers and study participants for their contributions. Meanwhile, We would like to thank Editage (www.editage.cn) for English language editing.

Conflict of interest

The authors declare that the research was conducted in the absence of any commercial or financial relationships that could be construed as a potential conflict of interest.

Publisher's note

All claims expressed in this article are solely those of the authors and do not necessarily represent those of their affiliated organizations, or those of the publisher, the editors and the reviewers. Any product that may be evaluated in this article, or claim that may be made by its manufacturer, is not guaranteed or endorsed by the publisher.

Supplementary material

The Supplementary Material for this article can be found online at: https://www.frontiersin.org/articles/10.3389/fsurg.2022.1046713/full#supplementary-material.

References

1. Sung H, Ferlay J, Siegel RL, Laversanne M, Soerjomataram I, Jemal A, et al. Global cancer statistics 2020: gLOBOCAN estimates of incidence and mortality worldwide for 36 cancers in 185 countries. *CA Cancer J Clin*. (2021) 71 (3):209–49. doi: 10.3322/caac.21660

2. Zhou M, Wang H, Zeng X, Yin P, Zhu J, Chen W, et al. Mortality, morbidity, and risk factors in China and its provinces, 1990–2017: a systematic analysis for the global burden of disease study 2017. *Lancet*. (2019) 394(10204):1145–58. doi: 10.1016/S0140-6736(19)30427-1

3. Chen W, Zheng R, Baade PD, Zhang S, Zeng H, Bray F, et al. Cancer statistics in China, 2015. *CA Cancer J Clin*. (2016) 66(2):115–32. doi: 10.3322/caac.21338

4. Hilmi M, Vienot A, Rousseau B, Neuzillet C. Immune therapy for liver cancers. *Cancers*. (2019) 12(1):77. doi: 10.3390/cancers12010077

5. Erstad DJ, Tanabe KK. Prognostic and therapeutic implications of microvascular invasion in hepatocellular carcinoma. *Ann Surg Oncol*. (2019) 26 (5):1474–93. doi: 10.1245/s10434-019-07227-9

6. Sherman M. Recurrence of hepatocellular carcinoma. *N Engl J Med*. (2008) 359(19):2045–7. doi: 10.1056/NEJMe0807581

7. Islami F, Miller KD, Siegel RL, Fedewa SA, Ward EM, Jemal A. Disparities in liver cancer occurrence in the United States by race/ethnicity and state. *CA Cancer J Clin*. (2017) 67(4):273–89. doi: 10.3322/caac.21402

8. Tabrizian P, Jibara G, Shrager B, Schwartz M, Roayaie S. Recurrence of hepatocellular cancer after resection: patterns, treatments, and prognosis. *Ann Surg*. (2015) 261(5):947–55. doi: 10.1097/SLA.0000000000000710

9. Zhou J, Sun H-C, Wang Z, Cong W-M, Wang J-H, Zeng M-S, et al. Guidelines for diagnosis and treatment of primary liver cancer in China (2017 edition). *Liver Cancer*. (2018) 7(3):235–60. doi: 10.1159/000488035

10. Wang L, Jin Y-X, Ji Y-Z, Mu Y, Zhang S-C, Pan S-Y. Development and validation of a prediction model for microvascular invasion in hepatocellular carcinoma. *World J Gastroenterol*. (2020) 26(14):1647–59. doi: 10.3748/wjg.v26.i14.1647

11. Lim K-C, Chow PK-H, Allen JC, Chia G-S, Lim M, Cheow P-C, et al. Microvascular invasion is a better predictor of tumor recurrence and overall survival following surgical resection for hepatocellular carcinoma compared to the milan criteria. *Ann Surg*. (2011) 254(1):108–13. doi: 10.1097/SLA.0b013e31821ad884

12. Xiao H, Chen Z-B, Jin H-L, Li B, Xu L-X, Guo Y, et al. Treatment selection of recurrent hepatocellular carcinoma with microvascular invasion at the initial hepatectomy. *Am J Transl Res*. (2019) 11(3):1864–75. PMID: 30972210; PMCID: PMC6456518

13. Imai K, Yamashita Y-I, Yusa T, Nakao Y, Itoyama R, Nakagawa S, et al. Microvascular invasion in small-sized hepatocellular carcinoma: significance for outcomes following hepatectomy and radiofrequency ablation. *Anticancer Res*. (2018) 38(2):1053–60. doi: 10.21873/anticanres.12322

14. Han J, Li Z-L, Xing H, Wu H, Zhu P, Lau WY, et al. The impact of resection margin and microvascular invasion on long-term prognosis after curative resection of hepatocellular carcinoma: a multi-institutional study. *HPB*. (2019) 21(8):962–71. doi: 10.1016/j.hpb.2018.11.005

15. Shindoh J, Hasegawa K, Inoue Y, Ishizawa T, Nagata R, Aoki T, et al. Risk factors of post-operative recurrence and adequate surgical approach to improve long-term outcomes of hepatocellular carcinoma. *HPB*. (2013) 15(1):31–9. doi: 10.1111/j.1477-2574.2012.00552.x

16. Sun JJ, Wang K, Zhang CZ, Guo WX, Shi J, Cong WM, et al. Postoperative adjuvant transcatheter arterial chemoembolization after R0 hepatectomy improves outcomes of patients who have hepatocellular carcinoma with microvascular invasion. *Ann Surg Oncol*. (2016) 23(4):1344–51. doi: 10.1245/s10434-015-5008-z

17. Zhang X-P, Chai Z-T, Gao Y-Z, Chen Z-H, Wang K, Shi J, et al. Postoperative adjuvant sorafenib improves survival outcomes in hepatocellular carcinoma patients with microvascular invasion after R0 liver resection: a propensity score matching analysis. *HPB*. (2019) 21(12):1687–96. doi: 10.1016/j.hpb.2019.04.014

18. Wang W, Guo Y, Zhong J, Wang Q, Wang X, Wei H, et al. The clinical significance of microvascular invasion in the surgical planning and postoperative sequential treatment in hepatocellular carcinoma. *Sci Rep*. (2021) 11(1):2415. doi: 10.1038/s41598-021-82058-x

19. Iasonos A, Schrag D, Raj GV, Panageas KS. How to build and interpret a nomogram for cancer prognosis. *J Clin Oncol*. (2008) 26(8):1364–70. doi: 10.1200/JCO.2007.12.9791

20. Zhang C, Zhao R, Chen F, Zhu Y, Chen L. Preoperative prediction of microvascular invasion in non-metastatic hepatocellular carcinoma based on nomogram analysis. *Transl Oncol*. (2021) 14(1):100875. doi: 10.1016/j.tranon.2020.100875

21. Mao S, Yu X, Yang Y, Shan Y, Mugaanyi J, Wu S, et al. Preoperative nomogram for microvascular invasion prediction based on clinical database in hepatocellular carcinoma. *Sci Rep*. (2021) 11(1):13999. doi: 10.1038/s41598-021-93528-7

22. Forner A, Llovet JM, Bruix J. Hepatocellular carcinoma. *Lancet*. (2012) 379 (9822):1245–55. doi: 10.1016/S0140-6736(11)61347-0

23. Roayaie S, Blume IN, Thung SN, Guido M, Fiel M-I, Hiotis S, et al. A system of classifying microvascular invasion to predict outcome after resection in patients with hepatocellular carcinoma. *Gastroenterology*. (2009) 137(3):850–5. doi: 10.1053/j.gastro.2009.06.003

24. Sumie S, Nakashima O, Okuda K, Kuromatsu R, Kawaguchi A, Nakano M, et al. The significance of classifying microvascular invasion in patients with hepatocellular carcinoma. *Ann Surg Oncol*. (2014) 21(3):1002–9. doi: 10.1245/s10434-013-3376-9

25. Zhao H, Chen C, Gu S, Yan X, Jia W, Mao L, et al. Anatomical versus non-anatomical resection for solitary hepatocellular carcinoma without macroscopic vascular invasion: a propensity score matching analysis. *J Gastroenterol Hepatol*. (2017) 32(4):870–8. doi: 10.1111/jgh.13603

26. Mazzaferro V, Llovet JM, Miceli R, Bhoori S, Schiavo M, Mariani L, et al. Predicting survival after liver transplantation in patients with hepatocellular carcinoma beyond the milan criteria: a retrospective, exploratory analysis. *Lancet Oncol*. (2009) 10(1):35–43. doi: 10.1016/S1470-2045(08)70284-5

27. Cong W-M, Bu H, Chen J, Dong H, Zhu Y-Y, Feng L-H, et al. Practice guidelines for the pathological diagnosis of primary liver cancer: 2015 update. *World J Gastroenterol*. (2016) 22(42):9279–87. doi: 10.3748/wjg.v22.i42.9279

28. Kim BK, Han KH, Park YN, Park MS, Kim KS, Choi JS, et al. Prediction of microvascular invasion before curative resection of hepatocellular carcinoma. *J Surg Oncol*. (2008) 97(3):246–52. doi: 10.1002/jso.20953

29. Pawlik TM, Delman KA, Vauthey J-N, Nagorney DM, Ng IO-L, Ikai I, et al. Tumor size predicts vascular invasion and histologic grade: implications for selection of surgical treatment for hepatocellular carcinoma. *Liver Transpl*. (2005) 11(9):1086–92. doi: 10.1002/lt.20472

30. Siegel AB, Wang S, Jacobson JS, Hershman DL, Lim EA, Yu J, et al. Obesity and microvascular invasion in hepatocellular carcinoma. *Cancer Invest*. (2010) 28 (10):1063–9. doi: 10.3109/07357907.2010.483500

31. Yang L, Gu D, Wei J, Yang C, Rao S, Wang W, et al. A radiomics nomogram for preoperative prediction of microvascular invasion in hepatocellular carcinoma. *Liver Cancer*. (2019) 8(5):373–86. doi: 10.1159/000494099

32. Lei Z, Li J, Wu D, Xia Y, Wang Q, Si A, et al. Nomogram for preoperative estimation of microvascular invasion risk in hepatitis B virus-related hepatocellular carcinoma within the milan criteria. *JAMA Surg*. (2016) 151 (4):356–63. doi: 10.1001/jamasurg.2015.4257

33. Yao W, Yang S, Ge Y, Fan W, Xiang L, Wan Y, et al. Computed tomography radiomics-based prediction of microvascular invasion in hepatocellular carcinoma. *Front Med*. (2022) 9:819670. doi: 10.3389/fmed.2022.819670

34. Yan Y, Zhou Q, Zhang M, Liu H, Lin J, Liu Q, et al. Integrated nomograms for preoperative prediction of microvascular invasion and lymph node metastasis risk in hepatocellular carcinoma patients. *Ann Surg Oncol*. (2020) 27(5):1361–71. doi: 10.1245/s10434-019-08071-7

35. Deng G, Yao L, Zeng F, Xiao L, Wang Z. Nomogram for preoperative prediction of microvascular invasion risk in hepatocellular carcinoma. *Cancer Manag Res*. (2019) 11:9037–45. doi: 10.2147/CMAR.S216178

36. Lin S, Ye F, Rong W, Song Y, Wu F, Liu Y, et al. Nomogram to assist in surgical plan for hepatocellular carcinoma: a prediction model for microvascular invasion. *J Gastrointest Surg*. (2019) 23(12):2372–82. doi: 10.1007/s11605-019-04140-0

37. Xu X, Zhang H-L, Liu Q-P, Sun S-W, Zhang J, Zhu F-P, et al. Radiomic analysis of contrast-enhanced CT predicts microvascular invasion and outcome in hepatocellular carcinoma. *J Hepatol*. (2019) 70(6):1133–44. doi: 10.1016/j.jhep.2019.02.023

38. Hyun SH, Eo JS, Song B-I, Lee JW, Na SJ, Hong IK, et al. Preoperative prediction of microvascular invasion of hepatocellular carcinoma using F-FDG PET/CT: a multicenter retrospective cohort study. *Eur J Nucl Med Mol Imaging*. (2018) 45(5):720–6. doi: 10.1007/s00259-017-3880-4

39. Zhang K, Xie S-S, Li W-C, Ye Z-X, Shen Z-W, Shen W. Prediction of microvascular invasion in HCC by a scoring model combining gd-EOB-DTPA MRI and biochemical indicators. *Eur Radiol*. (2022) 32(6):4186–97. doi: 10.1007/s00330-021-08502-8

40. Ni M, Zhou X, Lv Q, Li Z, Gao Y, Tan Y, et al. Radiomics models for diagnosing microvascular invasion in hepatocellular carcinoma: which model is the best model? *Cancer Imaging*. (2019) 19(1):60. doi: 10.1186/s40644-019-0249-x

frontiers | Frontiers in Surgery

TYPE Original Research
PUBLISHED 06 January 2023
DOI 10.3389/fsurg.2022.1055338

Construction of a mortality risk prediction model for elderly people at risk of lobectomy for NSCLC

Hongzhen Zhang[1†], Dingfei Ren[2†], Danqing Cheng[3], Wenping Wang[3], Yongtian Li[4], Yisong Wang[4], Dekun Lu[5] and Feng Zhao[5*]

[1]Shanghai Fengxian District Central Hospital, Affiliated to Anhui University of Science and Technology, Fengxian, China, [2]Occupational Control Hospital of Huai He Energy Group, Huainan, China, [3]Graduate School of Bengbu Medical College, Bengbu, China, [4]Anhui University of Science and Technology College of Medicine, Huainan, China, [5]The First Hospital of Anhui University of Science & Technology (Huai nan First People's Hospital), Huainan, China

OPEN ACCESS

EDITED BY
Mengling Feng,
National University of Singapore, Singapore

REVIEWED BY
Duilio Divisi,
University of L'Aquila, Italy
Mingran XIE,
USTC Life Sciences and Medicine, China

*CORRESPONDENCE
Feng Zhao
✉ doctorzhaofeng@163.com

†These authors have contributed equally to this work

SPECIALTY SECTION
This article was submitted to Surgical Oncology, a section of the journal Frontiers in Surgery

RECEIVED 27 September 2022
ACCEPTED 13 December 2022
PUBLISHED 06 January 2023

CITATION
Zhang H, Ren D, Cheng D, Wang W, Li Y, Wang Y, Lu D and Zhao F (2023) Construction of a mortality risk prediction model for elderly people at risk of lobectomy for NSCLC. Front. Surg. 9:1055338. doi: 10.3389/fsurg.2022.1055338

Background: An increasing number of lung cancer patients are opting for lobectomy for oncological treatment. However, due to the unique organismal condition of elderly patients, their short-term postoperative mortality is significantly higher than that of non-elderly patients. Therefore, there is a need to develop a personalised predictive tool to assess the risk of postoperative mortality in elderly patients.

Methods: Information on the diagnosis and survival of 35,411 older patients with confirmed lobectomy NSCLC from 2009 to 2019 was screened from the SEER database. The surgical group was divided into a high-risk mortality population group (≤90 days) and a non-high-risk mortality population group using a 90-day criterion. Survival curves were plotted using the Kaplan-Meier method to compare the differences in overall survival (OS) and lung cancer-specific survival (LCSS) between the two groups. The data set was split into modelling and validation groups in a ratio of 7.5:2.5, and model risk predictors of postoperative death in elderly patients with NSCLC were screened using univariate and multifactorial logistic regression. Columnar plots were constructed for model visualisation, and the area under the subject operating characteristic curve (AUC), DCA decision curve and clinical impact curve were used to assess model predictiveness and clinical utility.

Results: Multi-factor logistic regression results showed that sex, age, race, histology and grade were independent predictors of the risk of postoperative death in elderly patients with NSCLC. The above factors were imported into R software to construct a line graph model for predicting the risk of postoperative death in elderly patients with NSCLC. The AUCs of the modelling and validation groups were 0.711 and 0.713 respectively, indicating that the model performed well in terms of predictive performance. The DCA decision curve and clinical impact curve showed that the model had a high net clinical benefit and was of clinical application.

Conclusion: The construction and validation of a predictive model for death within 90 days of lobectomy in elderly patients with lung cancer will help the clinic to identify high-risk groups and give timely intervention or adjust treatment decisions.

KEYWORDS

SEER, NSCLC, lobectomy, propensity matching, columnar maps

Introduction

Lung cancer is one of the most common malignancies in the world, killing nearly 2 million people each year, mainly in the older age group of 65 years and above (1, 2). Non-small cell lung cancer (NSCLC) accounts for approximately 85% of lung cancers. With the accelerated ageing of the population and widespread screening by low-dose CT, the number of confirmed cases of NSCLC in the elderly has increased significantly (3, 4), posing a serious threat to human health and life.

Surgical resection is the treatment of choice for early-stage lung cancer, but there are many factors that affect post-operative survival due to the high mortality rate, multiple comorbidities and complex post-operative non-cancer related conditions that characterise the elderly lung cancer population (5–7). In 2021, Jiao et al. (8) constructed a prediction model combining radiological features and mortality risk parameters with a c-index as high as 0.734, which helped clinical identification of patients with early-stage NSCLC and was not an effective predictor of survival in NSCLC patients after surgery. A recent study (9) combined clinical and genomic features to construct a columnar graph model for risk stratification of early-stage NSCLC to assess the prognostic value of postoperative prognosis in NSCLC patients. These recent studies have used diverse approaches to construct postoperative predictive models for NSCLC, giving the models greater clinical predictive value, but these models are generally applicable to postoperative NSCLC patients without specific age differentiation.

Few current studies have investigated predictive models for monitoring risk factors for death and survival at 90 days after lobectomy in elderly (age ≥75 years) NSCLC. Based on the (SEER) database, this study retrospectively analysed the consultation and survival information of elderly patients with confirmed lobectomy NSCLC from 2009 to 2019 to develop a clinical line chart for predicting mortality after lobectomy in elderly NSCLC patients to facilitate clinical assessment of postoperative survival and development of individualised treatment strategies for elderly NSCLC patients.

Materials and methods

Data sources and study population

The data used in this study were all obtained from the National Cancer Institute's SEER database (SEER.cancer.gov) registry, a publicly available cancer database covering approximately 34.6% of the US population. Data from older patients with confirmed NSCLC from (2009 to 2019) were downloaded using SEER*Stat version 8.3.6 for analysis of the study. Screening inclusion criteria: (1) age ≥75 years; (2) meeting diagnostic criteria for NSCLC, confirmed clinically and pathologically; (3) Patients who underwent lobectomy for NSCLC; (4) Those with complete clinical data, including age, race, gender, tumour histological grade, molecular typing, postoperative survival time, and survival outcome. Exclusion criteria: (1) age <75 years; (2) previous history of lung tumors and other malignancies; (3) patients with non-NSCLC lobectomy; (4) those with incomplete clinical information. A total of 35,411 patients were eventually included as study subjects.

PSM analysis

In this study, patients aged >75 years in the NSCLC surgery group were classified as non-high-risk for survival >90 days after surgery, and those with survival ≤90 days were classified as high-risk for death. To eliminate the influence of confounding factors on the study results, the 1:1 propensity score matching (PSM) was used to eliminate differences in baseline information between the two groups of data, and survival curves were plotted using the Kaplane-Meier method and log-rank tests were used to compare the differences in survival curves between the groups.

Variable filtering

All enrolled CSCLC patients were further randomly split into a modelling and validation group in a ratio of 7.5:2.5. For the modelling group, univariate and multifactorial logistic regression were used to screen independent risk predictors for elderly patients undergoing lobectomy for NSCLC as the construct variables for the line graph model.

Model construction and evaluation

Screened independent risk predictors for elderly patients undergoing lobectomy for NSCLC were incorporated into the prediction model, and the risk factors were presented visually using R software version 3.6.3 (http://www.r-project.org/). The predictive efficacy and clinical utility of the line graph prediction model was evaluated by analysing the receiver operating characteristic curve (ROC curve) and Decision Curve Analysis (DCA).

Statistical analysis

All statistical analyses were performed using EmpowerStats (version 2.2) and R software (version 4.0.5). Count data were

TABLE 1 Patient information based on their baseline features before and after 1:1 PSM in surgery and non surgery groups.

Variable	Beofre PSM		*P*-value	After PSM		*P*-value
	Surgery *n* = 21,658	Non-sugery *n* = 13,753		Surgery *n* = 9,058	Non-sugery *n* = 9,058	
Age	80.99 ± 4.44	79.32 ± 3.55	<0.001	81.41 ± 4.53	79.35 ± 3.56	<0.001
Gender (%)			<0.001			0.656
Female	10,202 (47.10%)	7,120 (51.77%)		4,563 (50.38%)	4,593 (50.71%)	
Male	11,456 (52.90%)	6,633 (48.23%)		4,495 (49.62%)	4,465 (49.29%)	
Marital Status			<0.001			<0.001
Married	10,156 (46.89%)	7,320 (53.22%)		4,340 (47.91%)	4,656 (51.40%)	
Signal	10,621 (49.04%)	5,855 (42.57%)		4,376 (48.31%)	4,040 (44.60%)	
Other	881 (4.07%)	578 (4.20%)		342 (3.78%)	362 (4.00%)	
Race			<0.001			0.008
White	18,057 (83.37%)	12,073 (87.78%)		7,906 (87.28%)	7,835 (86.50%)	
Black	1,988 (9.18%)	772 (5.61%)		577 (6.37%)	545 (6.02%)	
Other	1,613 (7.45%)	908 (6.60%)		575 (6.35%)	678 (7.49%)	
Involved lung lobes			<0.001			0.056
Lung segments	640 (2.96%)	33 (0.24%)		26 (0.29%)	33 (0.36%)	
Lobe	19,476 (89.93%)	13,386 (97.33%)		8,773 (96.85%)	8,724 (96.31%)	
Overlapping	172 (0.79%)	104 (0.76%)		57 (0.63%)	87 (0.96%)	
Lung	1,370 (6.33%)	230 (1.67%)		202 (2.23%)	214 (2.36%)	
Lung lobectomy			<0.001			<0.001
Left	9,153 (42.26%)	5,653 (41.10%)		3,955 (43.66%)	3,661 (40.42%)	
Right	12,182 (56.25%)	8,089 (58.82%)		5,094 (56.24%)	5,387 (59.47%)	
Bialateral	195 (0.90%)	6 (0.04%)		5 (0.06%)	6 (0.07%)	
Unknow	128 (0.59%)	5 (0.04%)		4 (0.04%)	4 (0.04%)	
Histologic Type			<0.001			<0.001
SQC	8,484 (39.17%)	3,802 (27.64%)		3,194 (35.26%)	2,967 (32.76%)	
ADC	10,120 (46.73%)	7,896 (57.41%)		4,736 (52.29%)	4,853 (53.58%)	
OC	3,054 (14.10%)	2,055 (14.94%)		1,128 (12.45%)	1,238 (13.67%)	
Grade			<0.001			<0.001
I–II	9,426 (43.52%)	9,107 (66.22%)		4,959 (54.75%)	4,737 (52.30%)	
III–IV	12,232 (56.48%)	4,646 (33.78%)		4,099 (45.25%)	4,321 (47.70%)	
AJCC-T			<0.001			0.527
T1–2	11,648 (53.78%)	11,595 (84.31%)		7,128 (78.69%)	7,093 (78.31%)	
T3–4	10,010 (46.22%)	2,158 (15.69%)		1,930 (21.31%)	1,965 (21.69%)	
AJCC-N			<0.001			0.022
N0	10,048 (46.39%)	11,320 (82.31%)		6,763 (74.66%)	6,628 (73.17%)	
N1–3	11,610 (53.61%)	2,433 (17.69%)		2,295 (25.34%)	2,430 (26.83%)	
AJCC-M			<0.001			0.948
M0	12,418 (57.34%)	13,251 (96.35%)		8,558 (94.48%)	8,556 (94.46%)	
M1	9,240 (42.66%)	502 (3.65%)		500 (5.52%)	502 (5.54%)	

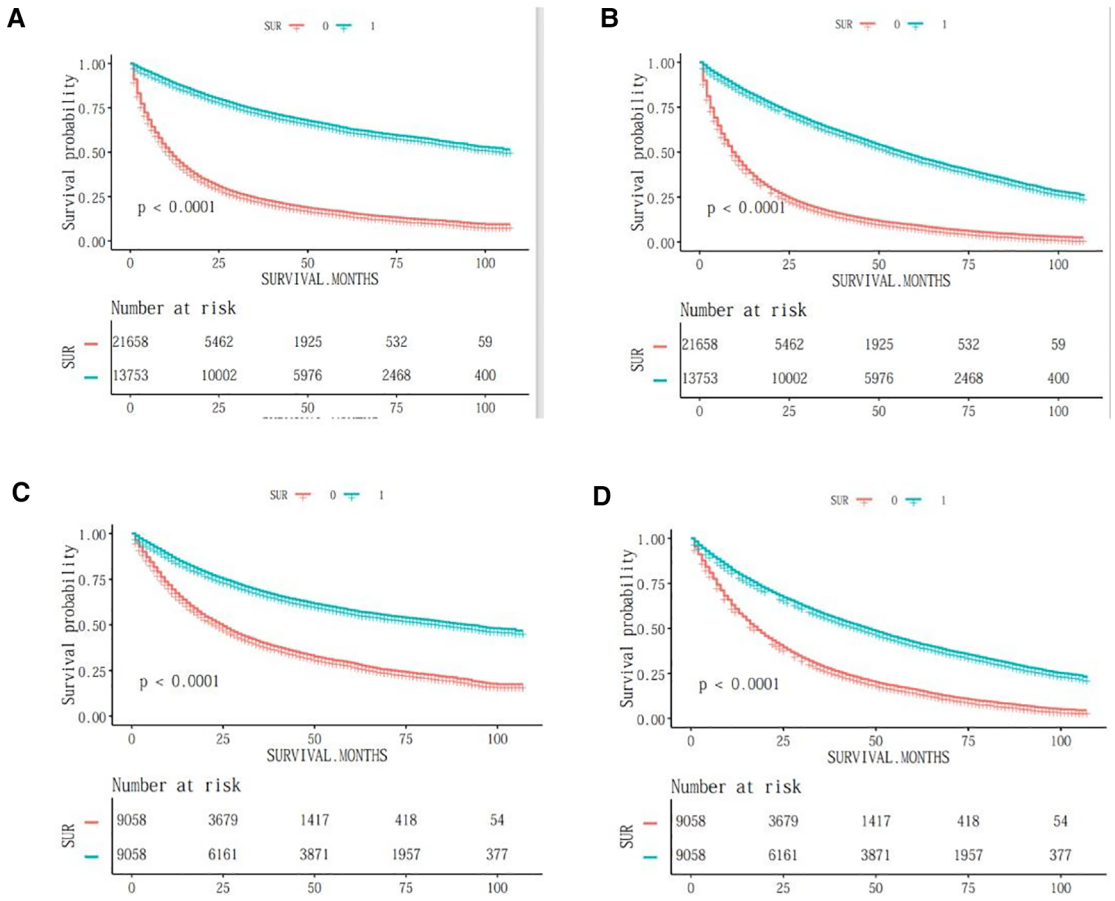

FIGURE 1
OS survival curves before and after PSM in elderly patients with NSCLC. (A) css-tumour-specific mortality before PSM; (B) os-tumour overall survival before PSM; (C) css-tumour-specific mortality after PSM; (D) os-tumour overall survival after PSM.

expressed as relative numbers and comparisons were made using the χ^2 test; measurement data conforming to a normal distribution were expressed as ($\bar{x} \pm s$) and measurement data not conforming to a normal distribution were expressed as M (P_{25}, P_{75}); one-way and multi-way logistic regression analyses were used to screen risk factors in CSCLC patients, and $P < 0.05$ was considered a statistically significant difference.

Results

Comparison of baseline information of elderly NSCLC cases

A total of 35,411 elderly patients with NSCLC aged ≥75 years in the SEER database were included in this study. To eliminate the influence of confounding factors on this study, we used a 1:1 propensity score matching (PSM) method for analysis. 21,658 patients in the NSCLC surgical group and 13,753 patients in the NSCLC non-surgical group before PSM were analyzed in both groups in terms of Age, Gender Marrital ststus, Race, Tuomor Position, Lung lobectomy, Histologic Type, Grade, AJCC-T, AJCC-N, AJCC-M were statistically significant ($P < 0.05$); after PSM, 9,058 patients in the NSCLC surgery group were compared with 9,058 patients in the NSCLC non-surgical group were successfully matched, with statistically significant differences in all variables except for the four confounding variables Gender, Involved lung lobes, AJCC-T, and AJCC-M, which were not statistically significant between groups ($P > 0.05$) (Table 1).

Analysis of OS survival in the modelling and validation groups of elderly patients with NSCLC

Kaplan-Meier plots visualise the differences in survival time after lobectomy in older patients with NSCLC. Overall, before

TABLE 2 Univariable and multivariable logistic regression analysis in development group.

Variable	Statistics	Univariable		Multivariable	
		HR (95% CI)	*P*-value	HR (95% CI)	*P*-value
Sex					
Female	5,325 (51.86%)	ref		ref	
Male	4,944 (48.14%)	1.50 (1.19, 1.88)	0.0005	1.37 (1.08, 1.74)	0.0086
Age	79.28 ± 3.55	1.04 (1.00, 1.07)	0.0237	1.04 (1.01, 1.08)	0.0091
Marital status					
Married	5,472 (53.29%)	ref			
Signal	4,377 (42.62%)	0.86 (0.68, 1.08)	0.1935		
Other	420 (4.09%)	0.50 (0.23, 1.07)	0.073		
Race					
White	9,031 (87.94%)	ref		ref	
Black	563 (5.48%)	0.38 (0.18, 0.81)	0.0118	0.36 (0.17, 0.78)	0.0094
Other	675 (6.57%)	0.64 (0.37, 1.10)	0.1047	0.71 (0.41, 1.23)	0.2259
Involved lung lobes					
Lung segments	21 (0.20%)	ref			
Lobe	9,989 (97.27%)	0.28 (0.06, 1.20)	0.0861		
Overlapping	79 (0.77%)	1.38 (0.28, 6.83)	0.6954		
Lung. Nos	180 (1.75%)	0.86 (0.18, 4.07)	0.8529		
Lung lobectomy					
Left	4,216 (41.06%)	ref			
Right	6,044 (58.86%)	1.11 (0.88, 1.40)	0.3869		
Bialateral	6 (0.06%)	6.83 (0.79, 58.88)	0.0806		
Unknow	3 (0.03%)	0.00 (0.00, inf.)	0.9741		
Histologic type					
SQC	2,833 (27.59%)	ref		ref	
ADC	5,874 (57.20%)	0.62 (0.48, 0.79)	0.0001	0.66 (0.51, 0.86)	0.002
OC	1,562 (15.21%)	0.77 (0.55, 1.09)	0.1374	0.70 (0.49, 1.00)	0.0473
Grade					
I–II	6,774 (65.97%)	ref		ref	
III–IV	3,495 (34.03%)	2.10 (1.68, 2.64)	<0.0001	1.54 (1.21, 1.96)	0.0004
AJCC-T					
T1–2	8,659 (84.32%)	ref		ref	
T3–4	1,610 (15.68%)	2.78 (2.18, 3.54)	<0.0001	1.83 (1.41, 2.39)	<0.0001
AJCC-N					
N0	8,463 (82.41%)	ref		ref	
N1–3	1,806 (17.59%)	2.26 (1.77, 2.88)	<0.0001	1.71 (1.32, 2.22	<0.0001
AJCC-M					
M0	9,892 (96.33%)	ref		ref	

(*continued*)

TABLE 2 Continued

Variable	Statistics	Univariable		Multivariable	
		HR (95% CI)	*P*-value	HR (95% CI)	*P*-value
M1	377 (3.67%)	8.36 (6.23, 11.22)	<0.0001	6.00 (4.36, 8.25)	<0.0001
Preoperative RT					
Yes	71 (0.69%)	ref			
No	10,198 (99.31%)	1.08 (0.26, 4.42)	0.9169		

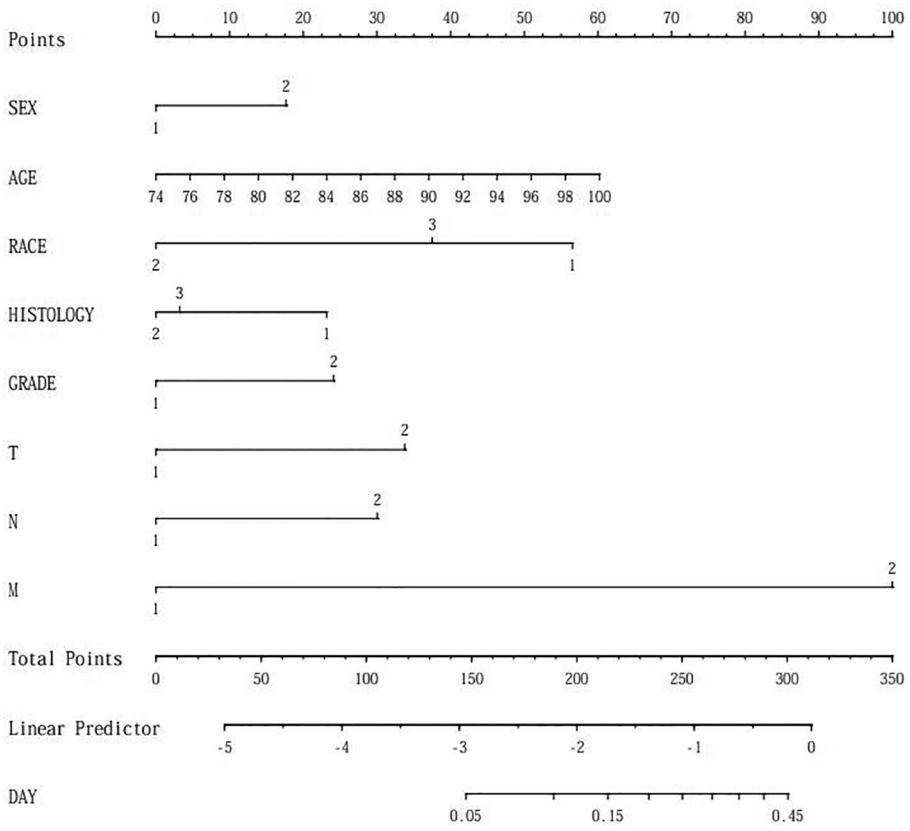

FIGURE 2
Predicted survival line graph for elderly patients undergoing lobectomy for NSCLC.

and after propensity score matching (PSM), OS was shorter in the NSCLC high-risk mortality group than in the NSCLC non-high-risk group ($P < 0.001$). When comparing survival data between the two groups, survival rates were higher in the NSCLC non-high-risk group than in the NSCLC high-risk death group before and after matching, with survival rates of 73%, 43% and 18% at 25, 50 and 75 months in the NSCLC non-high-risk group and 25%, 8% and 2% at 25, 50 and 75 months in the NSCLC high-risk death group, respectively. Post-matching survival rates at 25, 50 and 75 months were 68%, 22% and 4% for the NSCLC non-high-risk group and 41%, 16% and 5% for the NSCLC high-risk mortality group, respectively. As shown in **Figure 1**.

Screening for independent risk factors for survival in older patients with CSCLC

In the modeled group, the results of the one-way logistic regression analysis showed that the risk factors affecting the survival of elderly patients with confirmed lobectomy NSCLC were Sex, Age, Race, Histologic Type, and Grade (T, N, M),

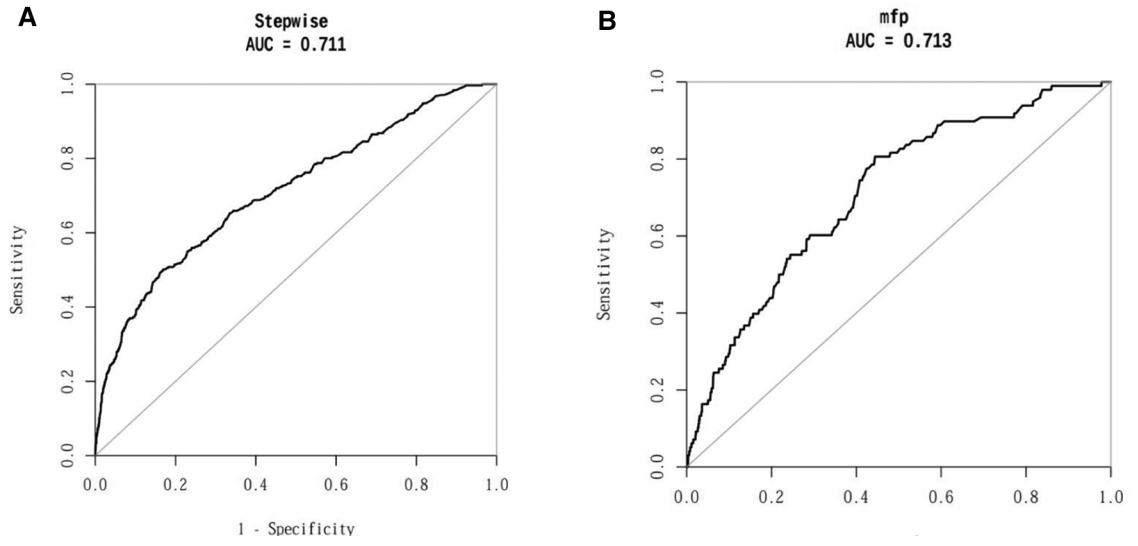

FIGURE 3
ROC curves of the prediction model for the column line graph of elderly patients with NSCLC. (A) AUC of the modelling group; (B) AUC of the validation group.

and the differences were all statistically significant at $P < 0.05$. These five risk factors were included again in the further multifactorial logistic regression analysis, and the results proved that these five risk factors were independent risk factors for survival in elderly patients with confirmed lobectomy NSCLC (Table 2).

Development of a line graph prediction model for elderly patients with NSCLC

Based on the results of multi-factor logistic regression analysis, the survival of elderly patients diagnosed with lobectomy NSCLC was visualized and analyzed by including 5 factors affecting survival prognosis, sex, age, race, histology and grade, and a Nomogram prediction model was constructed based on the above 5 risk factors, as shown in Figure 2.

Validation of the column line graph prediction model for elderly patients with NSCLC

The Nomogram prediction model was validated by applying ROC curves, and the results showed that the area under the ROC curve for the modelling group prediction model was 0.711 AUC, and the area under the ROC curve for the validation group prediction model was 0.713 AUC, indicating that the Nomogram model has good prediction accuracy; as shown in Figures 3A,B. DCA decision curves and clinical impact curves are method to assess the value of the prediction model for clinical application. When the threshold probability of the DCA decision curve was shown to be between 1% and 90%, it indicated that the column line graph prediction model developed in this study had a high net clinical benefit, as shown in Figure 4.

Discussion

Non-small cell lung cancer (NSCLC), is the leading cause of cancer deaths worldwide (10–12). Surgery is currently the main treatment for non-small cell lung cancer (NSCLC), with anatomical lobectomy being the main surgical treatment modality for NSCLC (13–15). With the development of lung cancer epidemiology and an ageing population, elderly patients with non-small cell lung cancer (NSCLC) have become an important patient group in lung cancer surgery. In this study, we analyzed the risk factors for postoperative mortality and the incidence of postoperative mortality in a special population of elderly patients undergoing lobectomy for NSCLC, and developed a practical prediction model to predict survival after lobectomy in elderly patients with NSCLC. The results of the study showed that the model has good predictive performance and has good clinical utility, providing guidance and decision making for the clinical survival of elderly patients undergoing lobectomy for NSCLC.

A prediction model (16) for NSCLC after radiotherapy has been proposed and predicts patient survival at 6 months, 1 year,

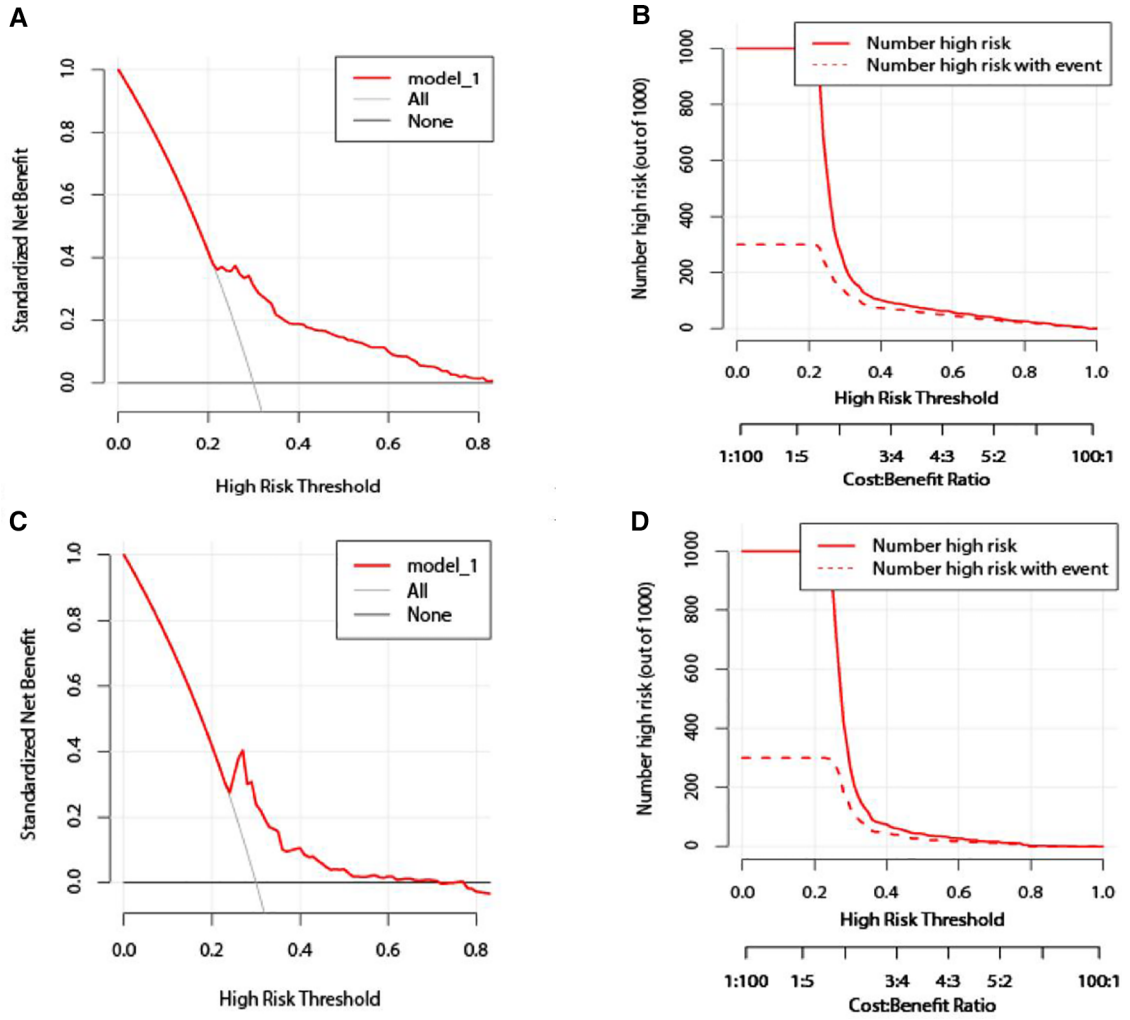

FIGURE 4
Validation of the column line graph prediction model. (A,C) Modeling group/validation group DCA decision curve; (B,D) modeling group/validation group clinical impact curve.

2 years and 3 years, but the model is only predictive of survival for patients treated with radiation for NSCLC. In the latest study on columnar graph prediction models for NSCLC, Chen (17) constructed a columnar graph model to predict prognosis of lymph node metastasis in NSCLC patients by four factors: age, SIRI, PNI and CEA. Zhang et al. (18) developed a line graph model to predict the development of advanced non-small cell lung cancer by combining clinical and molecular features. Xiaoping (19) developed a personalised line graph model based on CT-based sarcopenic to predict survival of patients with non-small cell lung cancer after receiving chemotherapy, which has some similarities to the present study. This study explored postoperative prognosis and survival model construction in NSCLC patients, but its study population was broad, none of which had predictive model construction regarding survival within 90 days after lobectomy in older (age ≥75 years) NSCLC patients.

As people continue to age, changes in the physiology and pathology of the elderly patient's organism are influenced by a number of factors, particularly physiological changes in the cardiovascular and respiratory systems (20, 21). This is mainly reflected in the reduced catecholamine response to stress, significantly reduced cardiac output, reduced lung tissue compliance, reduced expiratory effort and reduced pulmonary ventilation-perfusion capacity in elderly patients (22–24). In elderly patients with a long history of smoking, their vulnerability to hypoxaemia and hypercapnia presents a significant challenge for the surgical management of elderly patients with NSCLC (25–27). At the same time, the fact that patients older than 75 years of age often have many other underlying conditions (e.g., diabetes, hypertension, chronic

bronchitis and emphysema) increases the risk of surgery and seriously affects the post-operative recovery of elderly patients.

We found that age, race, gender, degree of differentiation, histological type, and grade (T, N stage) were independent factors for OS in studies related to lung cancer, and these factors were consistent with findings on risk factors for non-small cell lung cancer (28–30). However, many previous studies have not clarified the multi-prognostic analysis of survival at 90 days postoperatively in elderly patients undergoing lobectomy for NSCLC (31–33). In this study, as many variables related to postoperative survival information for elderly patients undergoing lobectomy for NSCLC as possible will be included in the clinical prediction model to improve its accuracy. In this study, age and tumour infiltration grade were found to have a considerable impact on the survival of NSCLC patients. Guo et al. (34) showed that plasma-related pulmonary artery embolism levels in NSCLC patients increased significantly with increasing age, and that the prognostic hypercoagulable status of NSCLC patients was related to patients' age, tumour infiltration grade and metastasis, and their postoperative treatment needed to take these factors into account. In addition, gender and ethnicity are important prognostic factors for patients with NSCLC, and gender is a strong prognostic factor when assessing the survival of patients with non-small cell lung cancer (35–37). Prognostic studies related to NSCLC (38–42) have also shown that the histologic subtype of NSCLC is associated with the risk of postoperative death in NSCLC patients, and that the overall postoperative survival OS of patients with different non-small cell lung cancer (NSCLC) histologic subtypes varies. Therefore, we identified Sex, Age, Race, Histologic Type, and Grade (T, N, M) as variables used in the column line graph, and the column line graph model constructed by these variables is of great importance in predicting the survival rate of elderly patients after lobectomy for NSCLC and guiding their treatment.

In this study, we constructed a survival prediction line graph model for elderly patients after lobectomy for NSCLC, which was based on a large database population to predict OS in patients undergoing lobectomy for NSCLC. in the model testing and validation, we found that the area under the ROC curve AUC of the model was 0.711 and 0.713 in the testing and validation groups, respectively, which were both much greater than 0.5, indicating that the model was predictive of survival of elderly patients after lobectomy for NSCLC is predictive efficacy and the model has good predictive performance. The clinical utility of the model was assessed by DCA decision curves and clinical impact curves, and the results of the validation group showed that the column line graph prediction model developed in our study has a high net clinical benefit and can be used as a tool for clinical decision making. Physicians and patients can use the column line graph model prediction scoring system to understand the individualised survival expectations of elderly patients after lobectomy for NSCLC, and based on the results of the column line graph prediction, effective interventions can be made to improve the survival of elderly patients after lobectomy for NSCLC with low survival rates.

This study was enrolled in the National Cancer Institute's SEER database, and although the sample size was large, there were some limitations. (1) This study is a retrospective study with a low level of evidence compared to prospective cohort studies. (2) In order to eliminate the influence of confounding factors on the study results, the data were processed using propensity score matching (PSM), but there was still an unavoidable selective bias in the two data sets. (3) This study is a single-centre study, with both the test and validation sets from the same database, and lacks external datasets to validate the prediction model of this study. Our next research direction is to conduct a multicentre, large sample size prospective study of elderly patients after lobectomy for NSCLC. (4) The SEER database does not provide more information on elderly patients undergoing lobectomy for NSCLC, such as cause of death, surgical approach, and postoperative adjuvant treatment options, which may also be important factors influencing the information on postoperative survival of elderly patients with NSCLC. Despite some limitations, the Nomogram was constructed based on a large population and provides a practical and effective clinical tool for predicting survival in elderly patients undergoing lobectomy for NSCLC.

Conclusion

In this study, sex, age, race, histology and grade were important factors influencing postoperative survival in elderly patients after lobectomy for NSCLC. For elderly patients after lobectomy for NSCLC, timely and effective postoperative survival assessment and enhanced clinical supervision are beneficial to improve the survival rate of elderly patients after lobectomy for NSCLC.

Data availability statement

The original contributions presented in the study are included in the article/Supplementary Material, further inquiries can be directed to the corresponding author.

Ethics statement

This is a retrospective clinical study with a dataset from the SEER public database in the USA, conducted in accordance with

the ethical standards of the World Medical Association Declaration of Helsinki.

Author contributions

FZ and HZ contributed to the writing of the manuscript, DC and WW design of the study and statistical analysis. DR and DC contributed to data retrieval and manuscript review. WW, YL and DL contributed to data collection and data collation. All authors contributed to the article and approved the submitted version.

Funding

The authors carried out all the work in this study with the support of the Organization Department of the Huainan Municipal Committee of Anhui Province and the Huainan Science and Technology Bureau. This study was funded by the Key Research Project of Anhui Provincial Education Department (No. KJ2019A0094), the Key Research Project of Anhui Provincial Education Department (No. KJ2019A0095), and the Research Project Plan of Bengbu Medical College (No. BYKY2019318ZD).

Acknowledgments

This work was supported by the Huainan City Occupational Disease Control Institute, Anhui Province, China; the School of Medicine of Anhui University of Technology; and the First People's Hospital affiliated to Anhui University of Technology (Huainan First People's Hospital).

Conflict of interest

The authors declare that the research was conducted in the absence of any commercial or financial relationships that could be construed as a potential conflict of interest.

Publisher's note

References

1. Bray F, Ferlay J, Soerjomataram I, Siegel RL, Torre LA, Jemal A. Global cancer statistics 2018: GLOBOCAN estimates of incidence and mortality worldwide for 36 cancers in 185 countries. *CA Cancer J Clin*. (2018) 68:394–424. doi: 10.3322/caac.21492

2. Siegel RL, Miller KD, Fuchs HE, Jemal A. Cancer statistics, 2022. *CA Cancer J Clin*. (2022) 72:7–33. doi: 10.3322/caac.21708

3. Aberle DR, Adams AM, Berg CD, Black WC, Clapp JD, Fagerstrom RM, et al. Reduced lung-cancer mortality with low-dose computed tomographic screening. *N Engl J Med*. (2011) 365:395–409. doi: 10.1056/NEJMoa1102873

4. Kwan TY, Chowdhury EH. Clinical outcomes of chemotherapeutic molecules as single and multiple agents in advanced non-small-cell lung carcinoma (NSCLC) patients. *Medicina*. (2021) 57(11), 1252. doi: 10.3390/medicina57111252

5. Blanco R, Maestu I, de la Torre MG, Cassinello A, Nuñez I. A review of the management of elderly patients with non-small-cell lung cancer. *Ann Oncol*. (2015) 26:451–63. doi: 10.1093/annonc/mdu268

6. Rocco G, Weder W. Lung surgery in the elderly today. *Lung Cancer*. (2013) 80:115–9. doi: 10.1016/j.lungcan.2013.01.004

7. Zhang B, Liu R, Ren D, Li X, Wang Y, Huo H, et al. Comparison of lobectomy and sublobar resection for stage IA elderly NSCLC patients (≥70 years): a population-based propensity score matching's study. *Front Oncol*. (2021) 11:610638. doi: 10.3389/fonc.2021.610638

8. Jiao Z, Li H, Xiao Y, Aggarwal C, Galperin-Aizenberg M, Pryma D, et al. Integration of risk survival measures estimated from pre- and posttreatment computed tomography scans improves stratification of patients with early-stage non-small cell lung cancer treated with stereotactic body radiation therapy. *Int J Radiat Oncol Biol Phys*. (2021) 109:1647–56. doi: 10.1016/j.ijrobp.2020.12.014

9. Hu C, Shu L, Chen C, Fan S, Liang Q, Zheng H, et al. A prediction model integrated genomic alterations and immune signatures of tumor immune microenvironment for early recurrence of stage I NSCLC after curative resection. *Transl Lung Cancer Res*. (2022) 11:24–42. doi: 10.21037/tlcr-21-751

10. Miller KD, Nogueira L, Mariotto AB, Rowland JH, Yabroff KR, Alfano CM, et al. Cancer treatment and survivorship statistics, 2019. *CA Cancer J Clin*. (2019) 69:363–85. doi: 10.3322/caac.21565

11. Siegel RL, Miller KD, Jemal A. Cancer statistics, 2019. *CA Cancer J Clin*. (2019) 69:7–34. doi: 10.3322/caac.21551

12. Xia L, Wang Z, Wu X, Zeng T, Luo W, Hu X, et al. Multiplatform discovery and regulatory function analysis of structural variations in non-small cell lung carcinoma. *Cell Rep*. (2021) 36:109660. doi: 10.1016/j.celrep.2021.109660

13. Ginsberg RJ, Rubinstein LV. Randomized trial of lobectomy versus limited resection for T1 N0 non-small cell lung cancer. Lung cancer study group. *Ann Thorac Surg*. (1995) 60:615–22; discussion 622–3. doi: 10.1016/0003-4975(95)00537-u

14. Veluswamy RR, Ezer N, Mhango G, Goodman E, Bonomi M, Neugut AI, et al. Limited resection versus lobectomy for older patients with early-stage lung cancer: impact of histology. *J Clin Oncol*. (2015) 33:3447–53. doi: 10.1200/JCO.2014.60.6624

15. Song C, Lu Z, Li D, Pan S, Li N, Geng Q. Survival after wedge resection versus lobectomy for stage IA second primary NSCLC with previous lung cancer-directed surgery. *Front Oncol*. (2022) 12:890033. doi: 10.3389/fonc.2022.890033

16. Duijm M, Oomen-de Hoop E, van Voort van der Zyp N, van de Vaart P, Tekatli H, Hoogeman M, et al. The development and external validation of an overall survival nomogram in medically inoperable centrally located early-stage non-small cell lung carcinoma. *Radiother Oncol*. (2021) 156:223–30. doi: 10.1016/j.radonc.2020.12.038

17. Chen M, Yang Y, He C, Chen L, Cheng J. Nomogram based on prognostic nutrition index and chest CT imaging signs predicts lymph node metastasis in NSCLC patients. *J Xray Sci Technol*. (2022) 30:599–612. doi: 10.3233/XST-211080

18. Zhang Y, Zeng L, Zhang X, Li Y, Liu L, Xu Q, et al. Clinical and molecular feature-based nomogram model for predicting benefit from bevacizumab combined with first-generation EGFR-tyrosine kinase inhibitor (TKI) in EGFR-

mutant advanced NSCLC. *BMC Med*. (2021) 19:245. doi: 10.1186/s12916-021-02118-x

19. Yi X, Chen Q, Yang J, Jiang D, Zhu L, Liu H, et al. CT-based sarcopenic nomogram for predicting progressive disease in advanced non-small-cell lung cancer. *Front Oncol*. (2021) 11:643941. doi: 10.3389/fonc.2021.643941

20. Zhang X, Lin G, Li J. Comparative effectiveness of lobectomy, segmentectomy, and wedge resection for pathological stage I non-small cell lung cancer in elderly patients: a population-based study. *Front Surg*. (2021) 8:652770. doi: 10.3389/fsurg.2021.652770

21. Adachi T, Tsunekawa Y, Tanimura D. Association among mild cognitive impairment, social frailty, and clinical events in elderly patients with cardiovascular disease. *Heart Lung*. (2022) 55:82–8. doi: 10.1016/j.hrtlng.2022.04.011

22. Gök G, Kılıç S, Sinan ÜY, Turkoglu E, Kemal H, Zoghi M. Epidemiology and clinical characteristics of hospitalized elderly patients for heart failure with reduced, mid-range and preserved ejection fraction. *Heart Lung*. (2020) 49:495–500. doi: 10.1016/j.hrtlng.2020.03.023

23. Shi X, Shen Y, Yang J, Du W, Yang J. The relationship of the geriatric nutritional risk index to mortality and length of stay in elderly patients with acute respiratory failure: a retrospective cohort study. *Heart Lung*. (2021) 50:898–905. doi: 10.1016/j.hrtlng.2021.07.012

24. Lee H, Kim HK, Kang D, Kong S, Lee JK, Lee G, et al. Prognostic value of 6-min walk test to predict postoperative cardiopulmonary complications in patients with non-small cell lung cancer. *Chest*. (2020) 157:1665–73. doi: 10.1016/j.chest.2019.12.039

25. Fu D, Wu C, Li X, Chen J. Elevated preoperative heart rate associated with increased risk of cardiopulmonary complications after resection for lung cancer. *BMC Anesthesiol*. (2018) 18:94. doi: 10.1186/s12871-018-0558-9

26. Yang H, Yun Y, Mao Y. Clinical analysis of the impact of sublobectomy on pulmonary function. *Medicine*. (2017) 96:e8662. doi: 10.1097/MD.0000000000008662

27. Arrieta O, Campos-Parra AD, Zuloaga C, Avilés A, Sánchez-Reyes R, Manríquez ME, et al. Clinical and pathological characteristics, outcome and mutational profiles regarding non-small-cell lung cancer related to wood-smoke exposure. *J Thorac Oncol*. (2012) 7:1228–34. doi: 10.1097/JTO.0b013e3182582a93

28. Zeng Y, Mayne N, Yang CJ, D'Amico TA, Ng C, Liu CC, et al. A nomogram for predicting cancer-specific survival of TNM 8th edition stage I non-small-cell lung cancer. *Ann Surg Oncol*. (2019) 26:2053–62. doi: 10.1245/s10434-019-07318-7

29. Liang W, Zhang L, Jiang G, Wang Q, Liu L, Liu D, et al. Development and validation of a nomogram for predicting survival in patients with resected non-small-cell lung cancer. *J Clin Oncol*. (2015) 33:861–9. doi: 10.1200/JCO.2014.56.6661

30. Agarwal M, Brahmanday G, Chmielewski GW, Welsh RJ, Ravikrishnan KP. Age, tumor size, type of surgery, and gender predict survival in early stage (stage I and II) non-small cell lung cancer after surgical resection. *Lung Cancer*. (2010) 68:398–402. doi: 10.1016/j.lungcan.2009.08.008

31. Douillard JY, Rosell R, De Lena M, Carpagnano F, Ramlau R, Gonzáles-Larriba JL, et al. Adjuvant vinorelbine plus cisplatin versus observation in patients with completely resected stage IB-IIIA non-small-cell lung cancer (adjuvant navelbine international trialist association [ANITA]): a randomised controlled trial. *Lancet Oncol*. (2006) 7:719–27. doi: 10.1016/S1470-2045(06)70804-X

32. Arriagada R, Dunant A, Pignon JP, Bergman B, Chabowski M, Grunenwald D, et al. Long-term results of the international adjuvant lung cancer trial evaluating adjuvant cisplatin-based chemotherapy in resected lung cancer. *J Clin Oncol*. (2010) 28:35–42. doi: 10.1200/JCO.2009.23.2272

33. Shang S, Wang R, Wang F, Wu M, Chen D, Yu J. Treatment patterns for patients with unresected stage III NSCLC: analysis of the surveillance, epidemiology, and End results (SEER) database. *Front Oncol*. (2022) 12:874022. doi: 10.3389/fonc.2022.874022

34. Guo J, Gao Y, Gong Z, Dong P, Mao Y, Li F, et al. Plasma D-dimer level correlates with age, metastasis, recurrence, tumor-node-metastasis classification (TNM), and treatment of non-small-cell lung cancer (NSCLC) patients. *Biomed Res Int*. (2021) 2021:9623571. doi: 10.1155/2021/9623571

35. Upadhyay VA, Shah KA, Makwana DP, Raval AP, Shah FD, Rawal RM. Putative stemness markers octamer-binding transcription factor 4, sex-determining region Y-box 2, and NANOG in non-small cell lung carcinoma: a clinicopathological association. *J Cancer Res Ther*. (2020) 16:804–10. doi: 10.4103/jcrt.JCRT_213_18

36. Gardner LD, Loffredo PhD CA, Langenberg P, George D, Deepak J, Harris CC, et al. Associations between history of chronic lung disease and non-small cell lung carcinoma in Maryland: variations by sex and race. *Ann Epidemiol*. (2018) 28:543–8. doi: 10.1016/j.annepidem.2018.04.012

37. Barquín M, Calvo V, García-García F, Nuñez B, Sánchez-Herrero E, Serna-Blasco R, et al. Sex is a strong prognostic factor in stage IV non-small-cell lung cancer patients and should be considered in survival rate estimation. *Cancer Epidemiol*. (2020) 67:101737. doi: 10.1016/j.canep.2020.101737

38. Jia B, Zheng Q, Wang J, Sun H, Zhao J, Wu M, et al. A nomogram model to predict death rate among non-small cell lung cancer (NSCLC) patients with surgery in surveillance, epidemiology, and end results (SEER) database. *BMC Cancer*. (2020) 20:666. doi: 10.1186/s12885-020-07147-y

39. Pastuszak-Lewandoska D, Domańska-Senderowska D, Antczak A, Kordiak J, Górski P, Czarnecka KH, et al. The expression levels of IL-4/IL-13/STAT6 signaling pathway genes and SOCS3 could help to differentiate the histopathological subtypes of non-small cell lung carcinoma. *Mol Diagn Ther*. (2018) 22:621–9. doi: 10.1007/s40291-018-0355-7

40. Nagasaka M, Pansare RS, Abdulfatah E, Guan H, Tranchida P, Gadgeel SM. Histologic transformation in NSCLC with PD-1 therapy. *J Thorac Oncol*. (2017) 12:e133–134. doi: 10.1016/j.jtho.2017.04.026

41. Patel MI, Cheng I, Gomez SL. US lung cancer trends by histologic type. *Cancer*. (2015) 121:1150–2. doi: 10.1002/cncr.29180

42. Ji M, Zhang Y, Shi B, Hou P. Association of promoter methylation with histologic type and pleural indentation in non-small cell lung cancer (NSCLC). *Diagn Pathol*. (2011) 6:48. doi: 10.1186/1746-1596-6-48

frontiers | Frontiers in Surgery

TYPE Original Research
PUBLISHED 06 January 2023
DOI 10.3389/fsurg.2022.1008448

OPEN ACCESS

EDITED BY
Kee Yuan Ngiam,
National University Health System (Singapore), Singapore

REVIEWED BY
Shuai Xiao,
University of South China, China
Marius Kryzauskas,
Vilnius University, Lithuania

*CORRESPONDENCE
Weihua Fu
tjmughgs_fwh@163.com

†These authors have contributed equally to this work and share first authorship

SPECIALTY SECTION
This article was submitted to Surgical Oncology, a section of the journal Frontiers in Surgery

RECEIVED 31 July 2022
ACCEPTED 24 October 2022
PUBLISHED 06 January 2023

CITATION
Zhang Z, Sun W, Wang J, Deng Y, Yan Y, Li D and Fu W (2023) A nomogram to predict the risk of colorectal anastomotic leakage combining inflammatory-nutritional and abdominal aorta calcium index.
Front. Surg. 9:1008448.
doi: 10.3389/fsurg.2022.1008448

A nomogram to predict the risk of colorectal anastomotic leakage combining inflammatory-nutritional and abdominal aorta calcium index

Zhaoxiong Zhang[1†], Weilin Sun[1†], Jun Wang[1,2], Yuanlin Deng[3], Yongjia Yan[1], Dong Li[3] and Weihua Fu[1*]

[1]Department of General Surgery, Tianjin Medical University General Hospital, Tianjin, China, [2]Department of Gastrointestinal Surgery, The People's Hospital of Qiannan, Duyun, China, [3]Department of Radiology, Tianjin Medical University General Hospital, Tianjin, China

Background: Anastomotic leakage is a serious complication after colorectal cancer surgery, which affects the quality of life and the prognosis. This study aims to create a novel nomogram to predict the risk of anastomotic leakage for patients with colorectal cancer based on the preoperative inflammatory-nutritional index and abdominal aorta calcium index.

Methods: 292 patients at Tianjin Medical University General Hospital (Tianjin, China) from January 2018 to October 2021 who underwent colorectal cancer surgery with a primary anastomosis were retrospectively reviewed. A nomogram was constructed based on the results of multivariate logistic regression model. The calibration curves and receiver operating characteristic curves were used to verify the efficacy of the nomogram.

Results: Univariate and multivariate analyses showed that tumor location (P = 0.002), preoperative albumin (P = 0.006), preoperative lymphocyte (P = 0.035), preoperative neutrophil to lymphocyte ratio (P = 0.024), and superior mesenteric artery calcium volumes score (P = 0.004) were identified as the independent risk factors for postoperative anastomotic leakage in patients with colorectal carcinoma. A nomogram was constructed based on the results of the multivariate analysis, and the C-index of the calibration curves was 0.913 (95%CI: 0.870–0.957) in the training cohort and 0.840 (95%CI: 0.753–0.927) in the validation cohort.

Conclusion: The nomogram, combining basic variables, inflammatory-nutritional index and abdominal aorta calcium index, could effectively predict the possibility of postoperative anastomotic leakage for patients with colorectal cancer, which could guide surgeons to carry out the appropriate treatment for the prevention of anastomotic leakage.

KEYWORDS

arterial calcification, anastomotic fistula, colorectal cancer, inflammation, nutrition

Introduction

With the progress of surgical technology and oncology surgery, surgical treatment has become the principal treatment for the patients with resectable colorectal cancer, which greatly improves their survival prognosis (1, 2). However, postoperative complications, which affect the recovery of patients after surgery, and even threaten the survival of patients, have always been an urgent problem that plagues surgeons. Among postoperative complications, anastomotic leakage (AL) is one of the most common and serious postoperative complications, with an incidence of 4%–29% (3) AL not only prolongs the patient's hospital stay, reduces the patient's quality of life, but even affects the patient's survival after surgery (4–6). Surgeons have made much effort to avoid AL in clinical practice, such as prophylactic ileostomy, and intraoperative evaluation of blood flow with indocyanine green (7–9) However, there is still no objective method for helping surgeons to predict the occurrence of AL in patients with colorectal cancer before surgery.

At present, while the recognized factors related to AL after colorectal cancer surgery were not clear, we could confirm that AL is the result of multiple factors (10, 11). Some studies showed that the tumor located in the rectum, preoperative malnutrition, excessive inflammatory response and other factors could be related to postoperative AL (10, 12–14). Patients with gastrointestinal cancer usually had a higher risk of preoperative malnutrition, which might be associated with poor postoperative outcomes (14, 15). Several studies showed that adequate nutritional support might improve this situation for patients with high nutritional risk (16). The nutritional status of the patients seemed to be an important factor for clinicians to predict the early prognosis. In recent years, numerous studies confirmed that cancer-associated inflammation was an important factor to produce tumor-promoting effects (17). Preoperative systemic inflammation of colorectal cancer patients was an important factor associated with the poor prognosis and high morbidity of AL (10, 18). The results of hematological tests were great indicators of preoperative systemic inflammation in patients with colorectal cancer, and the relevant data was readily available in almost all patients. Moreover, abdominal aorta calcification, which could damage the vascular function and might reduce anastomotic blood flow, might increase the risk of colorectal AL (19, 20). Therefore, accurate preoperative assessment of the above risk factors was essential to prevent AL.

This study aimed to establish a model that could predict the probability of postoperative AL by assessing the preoperative status of patients with colorectal cancer. In this study, the index of nutrition, the index of inflammation and the artery calcium volumes score were considered as the risk factors for AL, and a better nomogram was prepared to guide clinicians in decision-making.

Patients and methods

Patients

Between January 2018 and October 2021, a total of 327 patients underwent colorectal cancer resection at Tianjin Medical University General Hospital. The clinicopathologic data of these patients were retrospectively reviewed from the hospital information system after receiving Institutional Review Board approval. The data included basic variables (gender, age, alcohol, smoke, diabetes, BMI, tumor location, Obstruction, ASA score and pTNM stage), preoperative nutritional variables (hemoglobin, albumin, and prognostic nutritional index), inflammatory variables (WBC, neutrophil, lymphocyte, platelet, neutrophil-lymphocyte ratio; and platelet-lymphocyte ratio), and vascular condition variables (superior mesenteric artery calcium volumes score, inferior mesenteric artery calcium volumes score, and abdominal aorta calcium volumes score). Eligibility criteria included: (I) proven histologically primary colorectal carcinoma; (II) R0 colorectal cancer surgery with D3 lymph node dissection and a primary anastomosis; (III) complete and available clinicopathological data. The exclusion criteria were: (I) less than 18 years old; (II) history of neoadjuvant chemotherapy or radiotherapy; (III) the patients who had surgery for other cancers or bowel resection for any reason.

The authors are accountable for all aspects of the work in ensuring that questions related to the accuracy or integrity of any part of the work are appropriately investigated and resolved.

Surgical procedure

All patients underwent open or laparoscopic radical surgery for colorectal cancer. The linear stapler device was applied in the intestinal anastomosis of colon cancer patients, and the circular stapler device was applied in the anastomosis of rectal cancer patients. Then we performed the seromuscular suturing with a 3–0 absorbable suture to reduce the intestinal tension and ensure the mechanical integrity of the anastomosis for colon cancer surgery. And the air-leak test was used to confirm mechanical integrity after intestinal anastomosis in rectal cancer surgery.

Evaluation of Al

AL was diagnosed by the presence of gas or intestinal contents drained from the wound or drainage tube, the evidence of the intraperitoneal infection, or the positive signs of CT or endoscopy. Digital rectal examination was also used to identify AL in patients with rectal cancer.

Preoperative variables and vascular evaluation

We recorded the results of the preoperative laboratory examination 7 days before the operation. The pathological TNM staging was assessed according to the 8th editions of the American Joint Committee on Cancer (AJCC) staging system. Prognostic nutritional index (PNI) values were calculated with the formula: $10 \times$ albumin (g/L) $+ 0.005 \times$ total lymphocyte count. Neutrophil-lymphocyte ratio (NLR) value was calculated as neutrophils count divided by absolute lymphocyte count. Platelet-lymphocyte ratio (PLR) value was calculated as platelet count divided by absolute lymphocyte count. The vascular condition was evaluated through a preoperative multi-detector computed tomography (MDCT) image. The MDCT images of aortic between the origin of the superior mesenteric artery (SMA) and inferior mesenteric artery (IMA) were analyzed on the software (Syngo Calcium Scoring, Siemens). The plaque area in the aortic lumen, which was more hyperdense than the vascular lumen and adjacent parenchyma (density more than 130 HU), was considered as vascular calcification (21). The artery calcium volume score was measured by calculating the plaque area multiplied by the slice spacing. The SMA and IMA calcium volume score was determined by calcium volume scores at the origin of SMA and IMA on the aorta, respectively. In this study, the abdominal aorta calcium volume score was calculated as the total score of SMA and IMA calcium volume (**Figure 1**).

Patients were divided into a low or high group according to the cut-off value of albumin, WBC, neutrophil, lymphocyte, platelet, NLR, PLR, PNI, SMA calcium volume score, IMA calcium volume score and abdominal aorta calcium volume score, which was calculated through receiver operating characteristic (ROC) curve analysis.

Nomogram model

First, the univariate and multivariate analyses were performed to identify the independent risk factors for AL after colorectal cancer surgery. Then, the nomogram was created based on the results of the multivariate logistic regression analysis. The nomogram was subjected to 1,000 bootstrap resamples to calculate the concordance index (c-index) which could be used to estimate the predictive accuracy of the model (22). And the calibration curves were created to graphically present the relationship between the observed results and the predicted probabilities.

Statistical analysis

The χ^2 or Fisher's exact test was used for categorical variables, and the *t*-test was used for continuous variables. Factors that showed significant differences in the univariate analysis ($P < 0.05$) were included in the multivariate analysis. Multivariate analysis was performed using a logistic regression model for the evaluation of the predictive risk factors, in which, the odds ratios (ORs) and 95% confidence interval (CI) were calculated. In all the other statistical analyses, significance was defined as $P < 0.05$ (two-sided). ROC analysis was performed to compare the accuracy of the nomogram and five independent risk factors and area under the curve (AUC) were

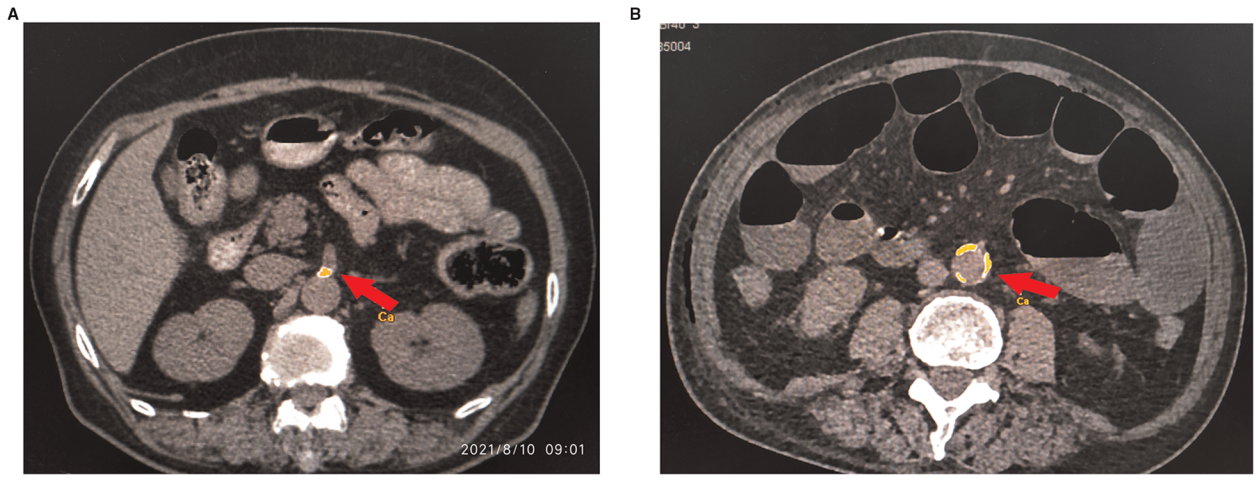

FIGURE 1
The MDCT images of abdominal aorta, SMA and IMA calcification. The arrow in the images indicates the site of arterial calcification. The plaque was outlined, and then its area was obtained by the software (Syngo Calcium Scoring, Siemens). (**A**) The calcification at the origin of SMA on the aorta. (**B**) The calcification of the abdominal aorta.

also calculated. All statistical analyses were performed using the statistical analysis program package IBM SPSS Statistics (Version 24.0; IBM Corp., New York, USA, RRID: SCR_019096). And R 4.0.1 software (RMS, riskRegression and pROC packages; Institute for Statistics and Mathematics, Vienna, Austria; http://www.r-project.org/, RRID: SCR_001905).

Results

Clinical characteristics of patients

According to the above eligibility and exclusion criteria, 292 patients in total were included in this study. These patients were classified into training cohort (date of surgery: 2018–2019, $n = 177$) and validation cohort (date of surgery: 2020–2021, $n = 115$) according to the date of surgery (**Figure 2**). The clinical and pathologic characteristics of 292 patients in this retrospective study were listed in **Table 1**. These patients included 168 males and 124 females. The median age was 67 (range 26–90). A total of 87 (29.79%) patients had a history of alcohol, and 94 (32.19%) had a history of smoking. 66 (22.60%) patients were diagnosed of diabetes. The median BMI was 23.73 (range 14.61–34.19). Tumors were distributed on right colon ($n = 121$, 41.44%), transverse colon ($n = 12$, 4.11%), left colon ($n = 25$, 8.56%), sigmoid colon ($n = 58$, 19.86%) and rectum ($n = 76$, 26.03%). A total of 37 (12.67%) patients had AL, and the number of patients with AL was 6 in the right-sided colon, 3 in the transverse colon, 3 in the left-sided colon, 9 in the sigmoid colon and 16 in the rectum. 49 (16.78%) patients had preoperative obstruction and the ASA score of 135 (46.23%) patients is 3. The pT stage of tumor for most patients was pT4a (203, 69.52%), and most patients had no lymph node metastasis (N0: 178, 60.96%). The results of hematological tests were presented in the form of the median (range) and mean (SD). Then, the Clinical characteristics between the training and validation cohort were estimated and no significant differences were shown, which was presented in **Table 2**.

We chose the cutoff value of the albumin, WBC, neutrophil, lymphocyte, platelet, NLR, PLR, PNI, SMA calcium volumes score, IMA calcium volumes score and abdominal aorta calcium volumes score to divide the patients into low and high groups, according to ROC curves.

Correlation analysis of risk factors for postoperative AI

We investigated the potential risk factors for AL by univariate analysis in the training cohort (**Table 3**). The univariate analysis showed the tumor located in the sigmoid colon and rectum ($P = 0.007$), low preoperative albumin ($P = 0.011$), high preoperative lymphocyte ($P = 0.021$), high preoperative NLR ($P = 0.016$), high SMA calcium volumes score ($P = 0.001$), high IMA calcium volumes score ($P = 0.001$)

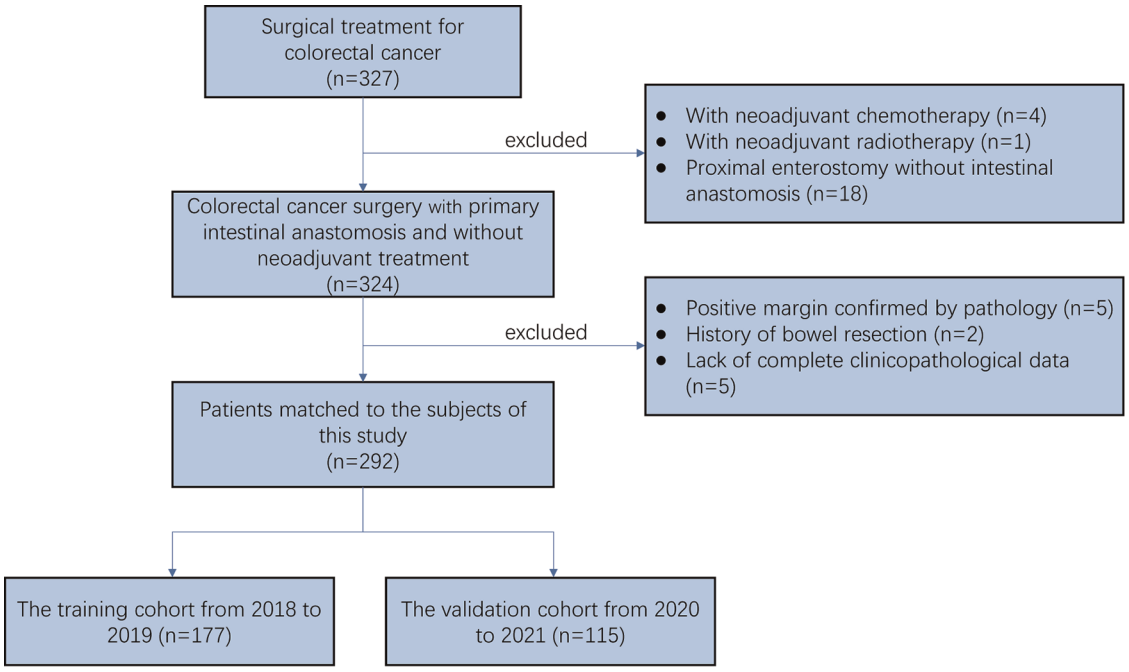

FIGURE 2
The flow chart of the selection process for the colorectal cancer patients from from January 2018 to October 2021.

TABLE 1 Clinicopathologic characteristics of all patients.

Characteristics	All patients ($n = 292$)	
Gender [No. (%)]		
Male	168	(57.53%)
Female	124	(42.47%)
Age [No. (%)]		
<60 years	57	(19.52%)
≥60 years	235	(80.48%)
Alcohol [No. (%)]		
No	205	(70.21%)
Yes	87	(29.79%)
Smoke [No. (%)]		
No	198	(67.81%)
Yes	94	(32.19%)
Diabetes [No. (%)]		
No	226	(77.40%)
Yes	66	(22.60%)
BMI [No. (%)]		
<18.5 kg/m^2	23	(7.88%)
18.5–24 kg/m^2	138	(47.26%)
≥24 kg/m^2	131	(44.86%)
Tumor location [No. (%)]		
Right-sided colon	121	(41.44%)
Transverse colon	12	(4.11%)
Left-sided colon	25	(8.56%)
Sigmoid colon	58	(19.86%)
Rectum	76	(26.03%)
Obstruction [No. (%)]		
No	243	(83.22%)
Yes	49	(16.78%)
ASA score [No. (%)]		
≤2	157	(53.77%)
3	135	(46.23%)
pT stage [No. (%)]		
pTis	12	(4.11%)
pTI	16	(5.48%)
pTII	32	(10.96%)
pT4a	203	(69.52%)
pT4b	29	(9.93%)
pN stage [No. (%)]		
pN0	178	(60.96%)
pN1a	32	(10.96%)
pN1b	42	(14.38%)
pN2a	22	(7.53%)
pN2b	18	(6.16%)
pM stage [No. (%)]		
pM0	279	(95.55%)
pM1	13	(4.45%)
Preoperative hemoglobin [No. (%)]		
<110 g/L	114	(39.04%)
≥110 g/L	178	(60.96%)
Preoperative albumin (g/L)		
Median (range)	37	(27–51)
Mean (SD)	37.15	(3.80)
Preoperative WBC (×10^9/L)		
Median (range)	6.24	(2.55–16.47)
Mean (SD)	6.55	(2.04)
Preoperative neutrophil (×10^9/L)		
Median (range)	3.66	(1.09–12.88)
Mean (SD)	4.03	(1.87)
Preoperative lymphocyte (×10^9/L)		
Median (range)	1.64	(0.3–4.15)
Mean (SD)	1.71	(0.64)
Preoperative platelet (×10^9/L)		
Median (range)	268.00	(106–717)
Mean (SD)	282.87	(100.42)
Preoperative NLR		
Median (range)	2.17	(0.47–24.30)
Mean (SD)	2.95	(2.98)
Preoperative PLR		
Median (range)	162.43	(53.58–750.00)
Mean (SD)	190.77	(115.05)
Preoperative PNI		
Median (range)	45.25	(30.35–62.05)
Mean (SD)	45.72	(5.19)
SMA calcium volumes core (mm^3)		
Median (range)	0.00	(0–1514.50)
Mean (SD)	51.62	(164.72)
IMA calcium volumes core (mm^3)		
Median (range)	25.95	(0–3145.40)
Mean (SD)	174.78	(390.63)
abdominal aorta calcium volumes core (mm^3)		
Median (range)	39.75	(0–4659.90)
Mean (SD)	226.40	(539.13)
Anastomotic leakage [No. (%)]		
No	255	(87.33%)
Yes	37	(12.67%)

Note: WBC, white blood cell; NLR, neutrophil-lymphocyte ratio; PLR, platelet-lymphocyte ratio; PNI, prognostic nutritional index; SMA, superior mesenteric artery; IMA, inferior mesenteric artery; SD, standard deviation.

and high abdominal aorta calcium volumes score ($P = 0.001$) were significantly correlated with the occurrence of postoperative AL. Then, these significant variables were performed in the forward step procedures by the multivariate

TABLE 2 Comparison of patients in the training and validation cohorts.

Characteristics	Training cohort ($n = 177$)	Validation cohort ($n = 115$)	*P*
Gender (No.)			
Male	105	63	0.443
Female	72	52	
Age (No.)			
<60 years	35	22	0.892
≥60 years	142	93	
Alcohol (No.)			
No	125	80	0.847
Yes	52	35	
Smoke (No.)			
No	118	80	0.604
Yes	59	35	
Diabetes (No.)			
No	135	91	0.568
Yes	42	24	
BMI (No.)			
<18.5 kg/m^2	12	11	0.554
18.5–24 kg/m^2	82	56	
≥24 kg/m^2	83	48	
Tumor location (No.)			
Right-sided colon	84	37	0.067
Transverse colon	8	4	
Left-sided colon	11	14	
Sigmoid colon	31	27	
Rectum	43	33	
Obstruction (No.)			
No	148	95	0.822
Yes	29	20	
ASA score (No.)			
≤2	97	60	0.660
3	80	55	
pT stage (No.)			
pTis	8	4	0.114
pTI	8	8	
pTII	19	13	
pT4a	118	85	
pT4b	24	5	
pN stage (No.)			
pN0	103	75	0.431
pN1a	20	12	
pN1b	28	14	
pN2a	12	10	
pN2b	14	4	
pM stage (No.)			
pM0	168	111	0.515
pM1	9	4	
Preoperative hemoglobin (No.)			
<110 g/L	72	42	0.477
≥110 g/L	105	73	
Preoperative albumin (No.)			
<37.5 g/L	89	65	0.297
≥37.5 g/L	88	50	
Preoperative WBC (No.)			
<6.5 × 10^9/L	94	67	0.387
≥6.5 × 10^9/L	83	48	
Preoperative neutrophil (No.)			
<2.6 × 10^9/L	34	20	0.696
≥2.6 × 10^9/L	143	95	
Preoperative lymphocyte (No.)			
<1.35 × 10^9/L	45	41	0.061
≥1.35 × 10^9/L	132	74	
Preoperative platelet (No.)			
<270.5 × 10^9/L	92	64	0.539
≥270.5 × 10^9/L	85	51	
Preoperative NLR (No.)			
<1.465	47	22	0.145
≥1.465	130	93	
Preoperative PLR (No.)			
<195.715	121	73	0.388
≥195.715	56	42	
Preoperative PNI (No.)			
<41.825	35	25	0.685
≥41.825	142	90	
SMA calcium volumes core (No.)			
<3.2 mm^3	111	74	0.777
≥3.2 mm^3	66	41	
IMA calcium volumes core (No.)			
<19.7 mm^3	85	50	0.447
≥19.7 mm^3	92	65	
Abdominal aorta calcium volumes core (No.)			
<19.6 mm^3	84	50	0.505
≥19.6 mm^3	93	65	
Anastomotic leakage (No.)			
No	156	99	0.607
Yes	21	16	

Note: WBC, white blood cell; NLR, neutrophil-lymphocyte ratio; PLR, platelet-lymphocyte ratio; PNI, prognostic nutritional index; SMA, superior mesenteric artery; IMA, inferior mesenteric artery.

logistics regression model. We observed tumor location (transverse colon, OR: 2.891, 95% CI: 0.194–43.017, $P = 0.441$; left colon, OR: 10.417, 95% CI: 0.668–162.511, $P = 0.095$; sigmoid colon, OR: 12.162, 95% CI: 2.213–66.836, $P = 0.004$;

TABLE 3 Univariate analysis of risk factors for anastomotic leakage in training cohort.

Characteristics	Anastomotic leakage		*P*
	No (*n* = 156)	Yes (*n* = 21)	
Gender (No.)			
Male	95	10	0.245
Female	61	11	
Age (No.)			
<60 years	29	6	0.432†
≥60 years	127	15	
Sake index	46.1 ± 132.9	38.6 ± 74.9	0.067
Brinkman index	183.1 ± 394.5	178.1 ± 286.9	0.329
Diabetes (No.)			
No	122	13	0.169†
Yes	34	8	
BMI (No.)			
<18.5 kg/m^2	11	1	0.599
18.5–24 kg/m^2	74	8	
≥24 kg/m^2	71	12	
Tumor location (No.)			
Right-sided colon	80	3	0.007*‡
Transverse colon	7	1	
Left-sided colon	10	1	
Sigmoid colon	25	7	
Rectum	34	9	
Obstruction (No.)			
No	132	16	0.506†
Yes	24	5	
ASA score (No.)			
≤2	87	10	0.481
3	69	11	
pT stage (No.)			
pTis	8	0	0.509‡
pTI	6	2	
pTII	17	2	
pT4a	105	13	
pT4b	20	4	
pN stage (No.)			
pN0	91	12	0.734‡
pN1a	17	3	
pN1b	24	4	
pN2a	12	0	
pN2b	12	2	
pM stage (No.)			
pM0	149	19	0.647†
pM1	7	2	
Preoperative hemoglobin (No.)			
<110 g/L	63	9	0.829
≥110 g/L	93	12	
Preoperative albumin (No.)			
<37.5 g/L	73	16	0.011*
≥37.5 g/L	83	5	
Preoperative WBC (No.)			
<6.5 × 10^9/L	87	7	0.053
≥6.5 × 10^9/L	69	14	
Preoperative neutrophil (No.)			
<2.6 × 10^9/L	34	1	0.122†
≥2.6 × 10^9/L	122	20	
Preoperative lymphocyte (No.)			
<1.35 × 10^9/L	44	1	0.021*
≥1.35 × 10^9/L	112	20	
Preoperative platelet (No.)			
<270.5 × 10^9/L	86	10	0.517
≥270.5 × 10^9/L	70	11	
Preoperative NLR (No.)			
<1.465	46	1	0.016*
≥1.465	110	20	
Preoperative PLR (No.)			
<195.715	103	18	0.069
≥195.715	53	3	
Preoperative PNI (No.)			
<41.825	28	7	0.171†
≥41.825	128	14	
SMA calcium volumes core (No.)			
<3.2 mm^3	105	6	0.001*
≥3.2 mm^3	51	15	
IMA calcium volumes core (No.)			
<19.7 mm^3	82	3	0.001*
≥19.7 mm^3	74	18	
Abdominal aorta calcium volumes core (No.)			
<19.6 mm^3	81	3	0.001*
≥19.6 mm^3	75	18	

Note: WBC, white blood cell; Brinkman index: Number of cigarettes per day multiplied by years of smoking; Sake index: weight (g)/22 of ethanol consumed per day multiplied by years of drinking; NLR, neutrophil-lymphocyte ratio; PLR, platelet-lymphocyte ratio; PNI, prognostic nutritional index; SMA, superior mesenteric artery; IMA, inferior mesenteric artery.
*$P < 0.05$.
†Continuity correction.
‡Fisher's exact test.

rectum, OR: 13.568, 95% CI: 2.590–71.082, $P = 0.002$), preoperative albumin (OR: 0.157, 95% CI: 0.042–0.593, $P = 0.006$), preoperative lymphocyte (OR: 10.623, 95% CI: 1.175–96.071, $P = 0.035$), preoperative NLR (OR:13.004, 95% CI: 1.406–120.226, $P = 0.024$), SMA calcium volumes score (OR: 6.810, 95% CI: 1.870–24.801, $P = 0.004$) were identified as the

independent risk factors for postoperative AL in patients with colorectal carcinoma (Figure 3).

Creation and confirmation of the nomogram

Based on the above results of univariate and multivariate analysis, we chose the tumor location, preoperative albumin, preoperative lymphocyte, preoperative NLR, and SMA calcium volumes score as factors to create a nomogram for predicting postoperative AL in patients with colorectal carcinoma. The occurrence probability of postoperative AL can be predicted by calculating the points of each variate and projecting the total points to the bottom scale (Figure 4).

Then, in order to evaluate the predictive ability of the nomogram model, we performed 1,000 resampling bootstrap analyses in both the training cohort and validation cohort. And the calibration curves were illustrated to verify the relationship between the predicted risk and observed frequency (Figure 5). The C-index of the training cohort and validation cohort was 0.913 (95%CI: 0.870–0.957), and 0.840 (95%CI: 0.753–0.927), respectively. And the brier score was 0.077 (95%CI: 0.051–0.103), and 0.106 (95%CI: 0.066–0.146) respectively. These results demonstrated the nomogram model had a good accuracy in predicting postoperative AL in patients with colorectal carcinoma.

Receiver operating characteristic analysis

We then used ROC analysis to compare the accuracy of the nomogram and five independent risk factors. The AUC for postoperative AL in training cohort and validation cohort were calculated: the nomogram, 0.913 (95%CI: 0.869–0.957) and 0.840 (95%CI: 0.751–0.929); tumor location, 0.711 (95%CI: 0.607–0.815) and 0.573 (95%CI: 0.449–0.698); preoperative lymphocyte, 0.617 (95%CI: 0.559–0.676) and 0.598 (95%CI: 0.448–0.708); preoperative NLR, 0.624 (95%CI: 0.565–0.682) and 0.611 (95%CI: 0.570–0.652); preoperative albumin, 0.647 (95%CI: 0.546–0.748) and 0.644 (95%CI: 0.533–0.754); SMA calcium volumes score, 0.694 (95%CI: 0.588–0.799) and 0.692 (95%CI: 0.566–0.818), respectively (Figure 6).

Discussion

AL is a serious complication that can affect the short-term quality of life and long-term prognosis after colorectal cancer surgery (5). Surgeons usually judge whether the anastomotic bowel is ischemic by observing the color of the bowel in surgery, but this method is too subjective. Recent studies showed that intraoperative application of indocyanine green, selective ileostomy and other methods could also reduce the morbidity of postoperative AL (7, 9, 23). However, these methods were easily biased by some factors and new evaluation methods were needed. Preoperative malnutrition, serious inflammatory response and abdominal artery calcification might have an adverse effect on postoperative tissue healing (10, 12, 19, 20), and these risk factors were included in this study to construct the nomogram.

The baseline data of 292 patients were retrospectively collected in this study and multivariate analysis showed that tumor location, preoperative albumin, preoperative lymphocyte, preoperative NLR, and SMA calcium volumes score were the risk factors for AL after colorectal cancer surgery. It was worth noting that BMI, brinkman index and sake index were not significantly correlated with the occurrence of AL, which may be attributed to the small sample size and single-center study. Many studies showed that the morbidity of AL was the greatest in the patients after low anterior resection for rectal cancer (12, 24). The patients had higher morbidity of AL when the tumor was closer to the anal margin. This study demonstrated that tumor location was the strongest risk factor for colorectal cancer surgery, and surgeons should pay special attention to the prevention of AL in these patients. The preoperative nutrition of the patients could affect the occurrence of postoperative complications. A multicenter prospective study of 3,193 patients conducted by Matteo et al. showed that low preoperative albumin was an independent risk factor for AL after colon resection for cancer (25). The low albumin usually represented severe malnutrition in cancer patients, and the patients were generally in poor condition with serious symptoms and more malignant tumors. Adequate preoperative nutritional support for such patients was necessary to improve postoperative recovery. The preoperative systemic inflammatory response was significantly associated with postoperative AL, but the mechanism of inflammation in AL was still unclear (10). The preoperative NLR was a better indicator to reflect the basic level of the inflammatory response (18, 26). The preoperative NLR was associated with the occurrence of major postoperative surgical complications (27), and one study showed that the high perioperative lymphocyte and NLR were related to the occurrence of AL in patients with colorectal cancer surgery (28). Another study showed that preoperative NLR was an independent risk factor for postoperative AL of rectal cancer, but its specificity was not high (29). This study concluded that high preoperative lymphocytes and NLR may lead to AL, which might be due to the local continuous infiltration of numerous inflammatory cells, which inhibited angiogenesis and fibroblast growth (17).

The abdominal aorta and its branches are important blood vessels that surgeons should pay special attention to protecting. Some studies have shown that some factors related to vascular

	OR	95%CI		P
		Up	Down	
Tumor location				
Right-sided colon	ref	-	-	0.026
Transverse colon	2.891	0.194	43.017	0.441
Left-sided colon	10.417	0.668	162.511	0.095
Sigmoid colon	12.162	2.213	66.836	0.004
Rectum	13.568	2.590	71.082	0.002
Peroperative albumin				
<37.5	Ref			-
≥37.5	0.157	0.042	0.593	0.006
Preoperative lymphocyte				
<1.35	Ref			-
≥1.35	10.623	1.175	96.071	0.035
Preoperative NLR				
<41.825	Ref			-
≥41.825	13.004	1.406	120.226	0.024
SMA calcium volumes core				
<3.2	Ref			
≥3.2	6.810	1.870	24.801	0.004

Note:
OR, odds ratio; CI, confidence interval; NLR, neutrophil-lymphocyte ratio; SMA, superior mesenteric artery

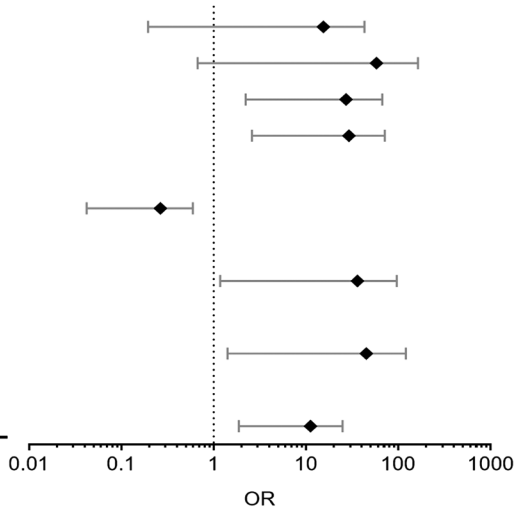

FIGURE 3
Forest plot about multivariate logistic regression analysis of clinicopathologic characteristics in the training cohort for anastomotic leakage.

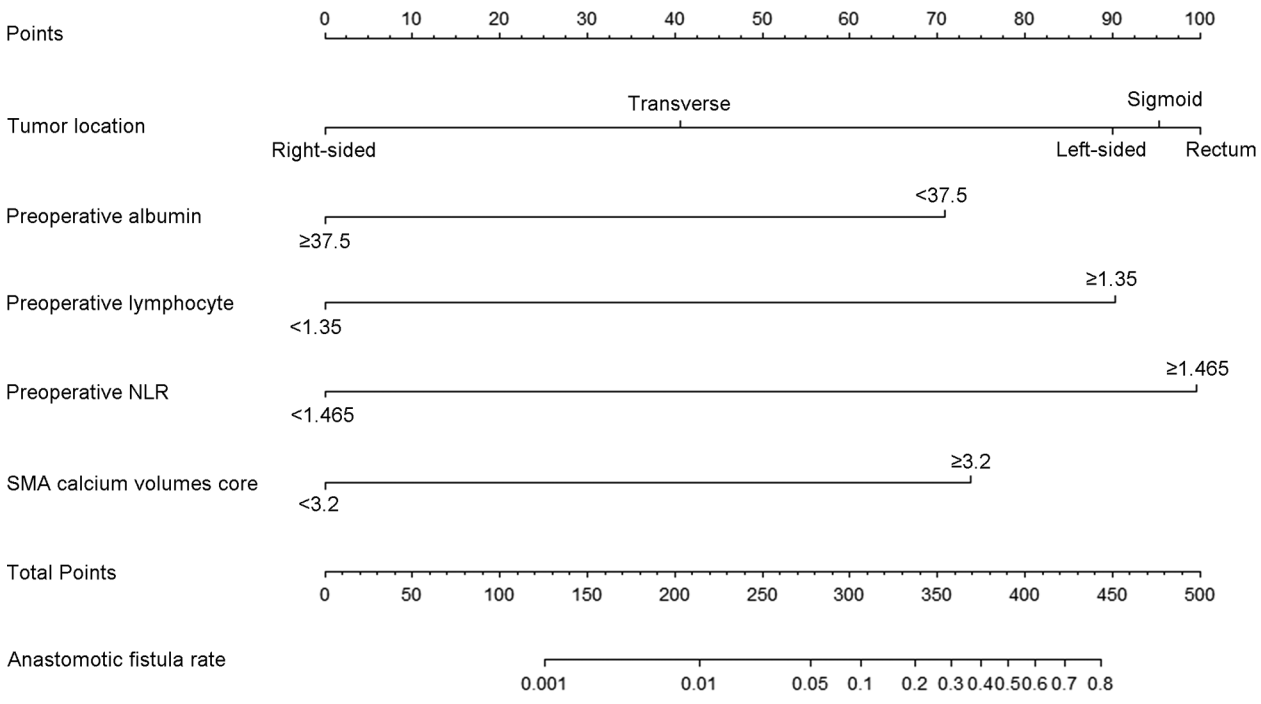

FIGURE 4
The nomogram predicting postoperative AL in patients with colorectal adenocarcinoma. Match the characteristics of patients to the scale of each risk factor in the nomogram to get the corresponding points. All points were added up to obtain the total points, and then total points was matched to the scale of anastomotic fistula rate to obtain the probability of AL. NLR, neutrophil-lymphocyte ratio.

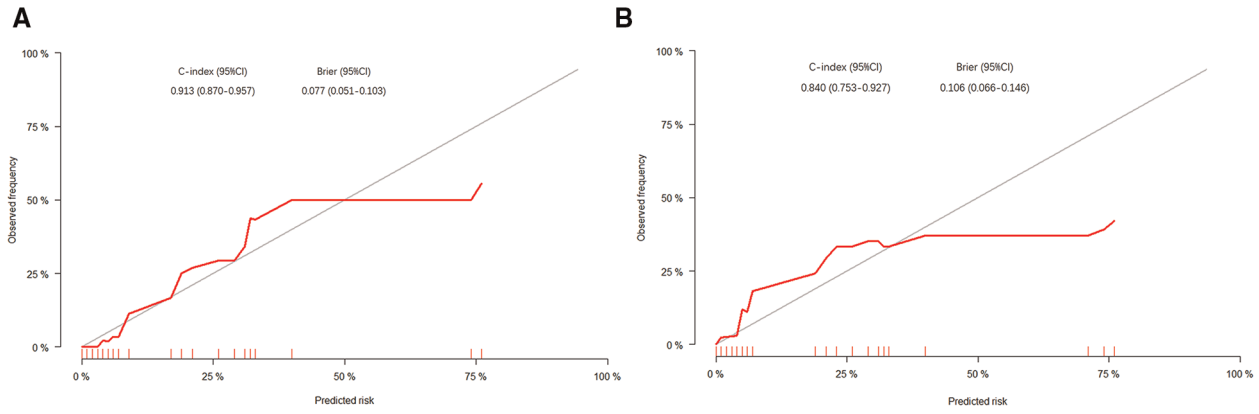

FIGURE 5
The calibration curves of the nomogram in the training cohort (**A**) and validation cohort (**B**). The *X*-axis represented the possibility of AL predicted by the nomogram, and the *Y*-axis represented the possibility of AL observed in patients.

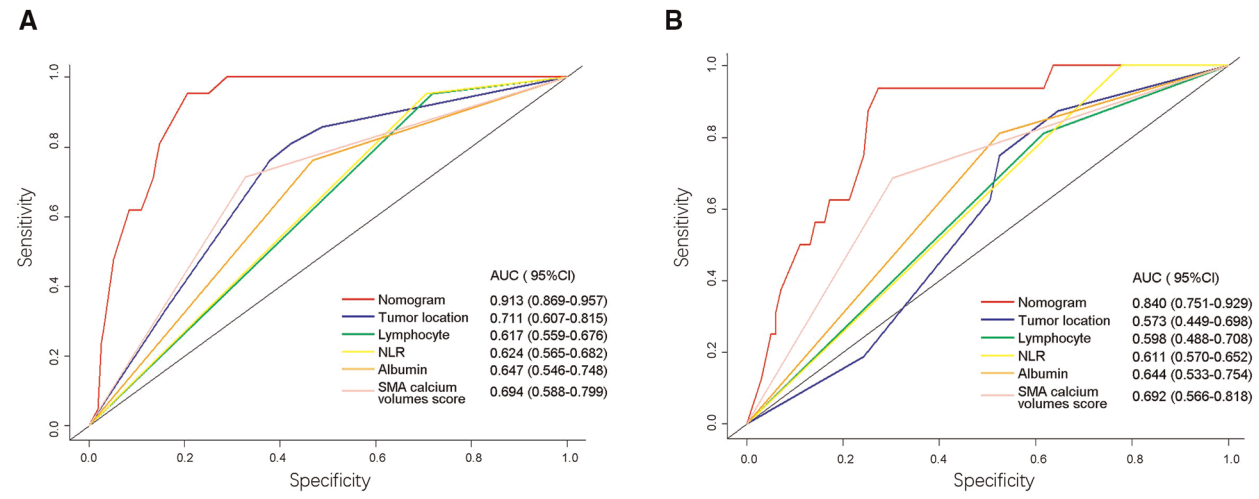

FIGURE 6
Receiver operating characteristic (ROC) curves of the nomogram and five risk factors in training cohort (**A**) and validation cohort (**B**). The values of AUC (95%CI) for the nomogram and five risk factors were listed in the figure. The *X*-axis represented the specificity of the nomogram and five risk factors to predict AL, and the *Y*-axis represented the sensitivity of these items. NLR, neutrophil-lymphocyte ratio; SMA, superior mesenteric artery; AUC, area under the curve.

abnormalities can affect the outcome of gastrointestinal surgery. The calcification of the thoracic aorta, celiac axis and SMA increased the risk of AL after esophageal cancer surgery (30, 31). One meta-analysis showed that calcification of the abdominal aorta might increase the risk of colorectal AL (19). Some prospective studies that explored the correlation between arterial calcification and AL in patients after colorectal cancer surgery were needed. The results of multivariate analysis in this study showed that a high SMA calcification score was an independent risk factor for AL after colorectal cancer surgery. The occurrence of AL was affected by blood perfusion at the anastomotic site. The blood supply of the proximal bowel always comes from direct or compensatory perfusion of SMA after colorectal cancer surgery. SMA with high calcification score has less blood flow, which may reduce the amount of blood circulation in the intestine and prolong the time of compensatory blood supply. Eventually, intestinal healing may be delayed due to insufficient nutrient supply, and the risk of AL will increase.

In this paper, a nomogram based on the multivariate analysis model was constructed to accurately predict the morbidity of AL after colorectal cancer surgery. The nomogram showed that tumor location and preoperative NLR were the two important risk factors for AL. The AL was most

likely to occur in the rectum, sigmoid colon and left-side colon, and surgeons should carefully evaluate these patients' conditions during the perioperative period. The high-level NLR and lymphocyte indicated that the patients had unsuited inflammatory response which might inhibit the tissue growth at the anastomotic site. Many studies showed that some perioperative treatments like NSAIDs did not achieve the purpose of preventing AL (32, 33). Preoperative low albumin and severe SMA calcification could exacerbate nutrient deficiency at the anastomotic site. The severe SMA calcification was also the main risk factor and got approximately 74 points in the nomogram, which suggested that adequate blood supply was necessary for anastomotic healing. Preoperative treatment may be necessary for patients with obvious SMA calcification. The calibration curves in both the training cohort and validation cohort proved the consistency between the predicted value and the actual observation value. The ROC curve of the nomogram had the largest AUC, and the predictive accuracy of the nomogram was better than that of other risk factors. This nomogram can be used clinically to accurately predict the possibility of postoperative AL in patients with colorectal cancer.

Some limitations still existed in this study. This study was a single-center retrospective study, and more samples were needed to be included to obtain high-level evidence. The nomogram in this study showed excellent performance in internal verification, but it still needed to be further tested with more samples.

In conclusion, the occurrence of AL was affected by multiple factors, and a comprehensive evaluation of patients would be necessary. The tumor location closes the anal margin, malnutrition, excessive inflammatory response and severe SMA calcification could increase the risk of AL in patients after colorectal cancer surgery. The nomogram, combining the above risk factors, could effectively predict the probability of postoperative AL in patients with colorectal carcinoma, which can guide surgeons to carry out the appropriate treatment for the prevention of AL.

Data availability statement

The datasets generated during and/or analysed during the current study are available from the corresponding author on reasonable request.

Ethics statement

The study was conducted in accordance with the Declaration of Helsinki (as revised in 2013). The study was approved by the Ethics Committee of Tianjin Medical University General Hospital (NO.: IRB2021-WZ-179) and individual consent for this retrospective analysis was waived.

Author contributions

ZZ, WS, and WF contributed to conception and design of the study. JW, YD, and DL organized the database. ZZ and WS performed the statistical analysis. ZZ wrote the first draft of the manuscript. WS, YY and WF wrote sections of the manuscript. All authors contributed to the article and approved the submitted version.

Funding

This study was funded by Tianjin Key Medical Discipline (Specialty) Construction Project (TJSYXZDXK015) and the Health Science and Technology Project of Tianjin Health Commission [ZC20190].

Acknowledgments

The authors would like to thank Tianjin Medical University General Hospital, Tianjin Key Medical Discipline (Specialty) Construction Project and Health Science and Technology Project of Tianjin Health Commission for support.

Conflict of interest

The authors declare that the research was conducted in the absence of any commercial or financial relationships that could be construed as a potential conflict of interest.

Publisher's note

All claims expressed in this article are solely those of the authors and do not necessarily represent those of their affiliated organizations, or those of the publisher, the editors and the reviewers. Any product that may be evaluated in this article, or claim that may be made by its manufacturer, is not guaranteed or endorsed by the publisher.

References

1. Argilés G, Tabernero J, Labianca R, Hochhauser D, Salazar R, Iveson T, et al. Localised colon cancer: esmo clinical practice guidelines for diagnosis, treatment and follow-up. *Ann Oncol.* (2020) 31(10):1291–305. doi: 10.1016/j.annonc.2020.06.022

2. Glynne-Jones R, Wyrwicz L, Tiret E, Brown G, Rödel C, Cervantes A, et al. Rectal cancer: esmo clinical practice guidelines for diagnosis, treatment and follow-up. *Ann Oncol.* (2017) 28(suppl_4):iv22–40. doi: 10.1093/annonc/mdx224

3. Paun BC, Cassie S, MacLean AR, Dixon E, Buie WD. Postoperative complications following surgery for rectal cancer. *Ann Surg*. (2010) 251 (5):807–18. doi: 10.1097/SLA.0b013e3181dae4ed

4. Mirnezami A, Mirnezami R, Chandrakumaran K, Sasapu K, Sagar P, Finan P. Increased local recurrence and reduced survival from colorectal cancer following anastomotic leak: systematic review and meta-analysis. *Ann Surg*. (2011) 253 (5):890–9. doi: 10.1097/SLA.0b013e3182128929

5. Krarup P-M, Nordholm-Carstensen A, Jorgensen LN, Harling H. Anastomotic leak increases distant recurrence and long-term mortality after curative resection for colonic cancer: a nationwide cohort study. *Ann Surg*. (2014) 259(5):930–8. doi: 10.1097/SLA.0b013e3182a6f2fc

6. Yang J, Chen Q, Jindou L, Cheng Y. The influence of anastomotic leakage for rectal cancer oncologic outcome: a systematic review and meta-analysis. *J Surg Oncol*. (2020) 121(8):1283–97. doi: 10.1002/jso.25921

7. Shen R, Zhang Y, Wang T. Indocyanine green fluorescence angiography and the incidence of anastomotic leak after colorectal resection for colorectal cancer: a meta-analysis. *Dis Colon Rectum*. (2018) 61(10):1228–34. doi: 10.1097/DCR.0000000000001123

8. Matthiessen P, Hallböök O, Rutegård J, Simert G, Sjödahl R. Defunctioning stoma reduces symptomatic anastomotic leakage after low anterior resection of the Rectum for cancer: a randomized multicenter trial. *Ann Surg*. (2007) 246 (2):207–14. doi: 10.1097/SLA.0b013e3180603024

9. Hüser N, Michalski CW, Erkan M, Schuster T, Rosenberg R, Kleeff J, et al. Systematic review and meta-analysis of the role of defunctioning stoma in low rectal cancer surgery. *Ann Surg*. (2008) 248(1):52–60. doi: 10.1097/SLA.0b013e318176bf65

10. Foppa C, Ng SC, Montorsi M, Spinelli A. Anastomotic leak in colorectal cancer patients: new insights and perspectives. *Eur J Surg Oncol*. (2020) 46 (6):943–54. doi: 10.1016/j.ejso.2020.02.027

11. McDermott FD, Heeney A, Kelly ME, Steele RJ, Carlson GL, Winter DC. Systematic review of preoperative, intraoperative and postoperative risk factors for colorectal anastomotic leaks. *Br J Surg*. (2015) 102(5):462–79. doi: 10.1002/bjs.9697

12. Trencheva K, Morrissey KP, Wells M, Mancuso CA, Lee SW, Sonoda T, et al. Identifying important predictors for anastomotic leak after colon and rectal resection: prospective study on 616 patients. *Ann Surg*. (2013) 257(1):108–13. doi: 10.1097/SLA.0b013e318262a6cd

13. Lee SY, Jung MR, Kim CH, Kim YJ, Kim HR. Nutritional risk screening score is an independent predictive factor of anastomotic leakage after rectal cancer surgery. *Eur J Clin Nutr*. (2018) 72(4):489–95. doi: 10.1038/s41430-018-0112-3

14. Xu H, Kong F. Malnutrition-related factors increased the risk of anastomotic leak for rectal cancer patients undergoing surgery. *Biomed Res Int*. (2020) 2020:5059670. doi: 10.1155/2020/5059670

15. Reisinger KW, van Vugt JLA, Tegels JJW, Snijders C, Hulsewé KWE, Hoofwijk AGM, et al. Functional compromise reflected by sarcopenia, frailty, and nutritional depletion predicts adverse postoperative outcome after colorectal cancer surgery. *Ann Surg*. (2015) 261(2):345–52. doi: 10.1097/SLA.0000000000000628

16. Tian W, Xu X, Yao Z, Yang F, Huang M, Zhao R, et al. Early enteral nutrition could reduce risk of recurrent leakage after definitive resection of anastomotic leakage after colorectal cancer surgery. *World J Surg*. (2021) 45 (1):320–30. doi: 10.1007/s00268-020-05787-6

17. Hanahan D, Weinberg RA. Hallmarks of cancer: the next generation. *Cell*. (2011) 144(5):646–74. doi: 10.1016/j.cell.2011.02.013

18. Tuomisto AE, Mäkinen MJ, Väyrynen JP. Systemic inflammation in colorectal cancer: underlying factors, effects, and prognostic significance. *World J Gastroenterol*. (2019) 25(31):4383–404. doi: 10.3748/wjg.v25.i31.4383

19. Tong L, Xie D, Song X, Wu X, Wen S, Liu A. Is abdominal vascular calcification score valuable in predicting the occurrence of colorectal anastomotic leakage? A meta-analysis. *Int J Colorectal Dis*. (2020) 35(4):641–53. doi: 10.1007/s00384-020-03513-1

20. Postaire B, Abet E, Montigny P, Vent PA. Does the degree of calcification of the celiac trunk and superior mesenteric artery on preoperative computerized tomography predict the risk of anastomotic leak after right colectomy? A single center retrospective study. *J Visc Surg*. (2019) 156(3):191–5. doi: 10.1016/j.jviscsurg.2018.10.006

21. Achenbach S, Moselewski F, Ropers D, Ferencik M, Hoffmann U, MacNeill B, et al. Detection of calcified and noncalcified coronary atherosclerotic plaque by contrast-enhanced, submillimeter multidetector spiral computed tomography: a segment-based comparison with intravascular ultrasound. *Circulation*. (2004) 109(1):14–7. doi: 10.1161/01.CIR.0000111517.69230.0F

22. Harrell FE, Califf RM, Pryor DB, Lee KL, Rosati RA. Evaluating the yield of medical tests. *JAMA*. (1982) 247(18):2543–6. doi: 10.1001/jama.1982.03320430047030

23. Montedori A, Cirocchi R, Farinella E, Sciannameo F, Abraha I. Covering ileo- or colostomy in anterior resection for rectal carcinoma. *Cochrane Database Syst Rev*. (2010) 5:CD006878. doi: 10.1002/14651858.CD006878.pub2

24. Park JS, Choi G-S, Kim SH, Kim HR, Kim NK, Lee KY, et al. Multicenter analysis of risk factors for anastomotic leakage after laparoscopic rectal cancer excision: the Korean laparoscopic colorectal surgery study group. *Ann Surg*. (2013) 257(4):665–71. doi: 10.1097/SLA.0b013e31827b8ed9

25. Frasson M, Flor-Lorente B, Rodríguez JLR, Granero-Castro P, Hervás D, Alvarez Rico MA, et al. Risk factors for anastomotic leak after colon resection for cancer: multivariate analysis and nomogram from a multicentric, prospective, national study with 3,193 patients. *Ann Surg*. (2015) 262(2):321–30. doi: 10.1097/SLA.0000000000000973

26. Guthrie GJK, Charles KA, Roxburgh CSD, Horgan PG, McMillan DC, Clarke SJ. The systemic inflammation-based neutrophil-lymphocyte ratio: experience in patients with cancer. *Crit Rev Oncol Hematol*. (2013) 88 (1):218–30. doi: 10.1016/j.critrevonc.2013.03.010

27. Josse JM, Cleghorn MC, Ramji KM, Jiang H, Elnahas A, Jackson TD, et al. The neutrophil-to-lymphocyte ratio predicts Major perioperative complications in patients undergoing colorectal surgery. *Colorectal Dis*. (2016) 18(7):O236–O42. doi: 10.1111/codi.13373

28. Paliogiannis P, Deidda S, Maslyankov S, Paycheva T, Farag A, Mashhour A, et al. Blood cell count indexes as predictors of anastomotic leakage in elective colorectal surgery: a multicenter study on 1,432 patients. *World J Surg Oncol*. (2020) 18(1):89. doi: 10.1186/s12957-020-01856-1

29. Miyakita H, Sadahiro S, Saito G, Okada K, Tanaka A, Suzuki T. Risk scores as useful predictors of perioperative complications in patients with rectal cancer who received radical surgery. *Int J Clin Oncol*. (2017) 22(2):324–31. doi: 10.1007/s10147-016-1054-1

30. Hoek VT, Edomskis PP, Menon AG, Kleinrensink G-J, Lagarde SM, Lange JF, et al. Arterial calcification is a risk factor for anastomotic leakage after esophagectomy: a systematic review and meta-analysis. *Eur J Surg Oncol*. (2020) 46(11):1975–88. doi: 10.1016/j.ejso.2020.06.019

31. Koyanagi K, Ozawa S, Ninomiya Y, Oguma J, Kazuno A, Yatabe K, et al. Association between indocyanine green fluorescence blood flow speed in the gastric conduit wall and superior mesenteric artery calcification: predictive significance for anastomotic leakage after esophagectomy. *Esophagus*. (2021) 18 (2):248–57. doi: 10.1007/s10388-020-00797-8

32. Hakkarainen TW, Steele SR, Bastaworous A, Dellinger EP, Farrokhi E, Farjah F, et al. Nonsteroidal anti-inflammatory drugs and the risk for anastomotic failure: a report from Washington state's surgical care and outcomes assessment program (scoap). *JAMA Surg*. (2015) 150(3):223–8. doi: 10.1001/jamasurg.2014.2239

33. Klein M, Gögenur I, Rosenberg J. Postoperative use of non-steroidal anti-inflammatory drugs in patients with anastomotic leakage requiring reoperation after colorectal resection: cohort study based on prospective data. *Br Med J*. (2012) 345:e6166. doi: 10.1136/bmj.e6166

frontiers | Frontiers in Surgery

TYPE Original Research
PUBLISHED 06 January 2023
DOI 10.3389/fsurg.2022.991624

OPEN ACCESS

EDITED BY
Mengling Feng,
National University of Singapore, Singapore

REVIEWED BY
Jun Cao,
Affiliated Hospital of Yangzhou University, China
Juntao Huang,
Ningbo Medical Center Lihuili Hospital, China

*CORRESPONDENCE
Chao Zhang
zhangchao10767@jlu.edu.cn
Xudong Wang
wangxud@jlu.edu.cn

†These authors have contributed equally to this work

‡This author share first authorship

SPECIALTY SECTION
This article was submitted to Surgical Oncology, a section of the journal Frontiers in Surgery

RECEIVED 11 July 2022
ACCEPTED 24 October 2022
PUBLISHED 06 January 2023

CITATION
Dong H, Zhao S, Zhang C and Wang X (2023) Identification of cuproptosis related subtypes and construction of prognostic signature in gastric cancer.
Front. Surg. 9:991624.
doi: 10.3389/fsurg.2022.991624

Identification of cuproptosis related subtypes and construction of prognostic signature in gastric cancer

Hao Dong[†‡], Shutao Zhao[†], Chao Zhang* and Xudong Wang*

Department of Gastrointestinal Nutrition and Hernia Surgery, The Second Hospital of Jilin University, Changchun, China

Cuprotosis is a novel mechanism of cell death that differs from known mechanisms, which depends on mitochondrial respiration and is closely related to lipoylated components of the tricarboxylic acid (TCA) cycle. However, it is unclear whether cuprotosis-related genes (CRGs) affect the tumor microenvironment (TME) and prognosis of patients with gastric cancer. In this study, the genetic and transcriptional characteristics of CRGs in gastric cancer (GC) were analyzed, and five CRGs that were differentially expressed and correlated with the survival of patients were obtained. Two different molecular subtypes were identified according to the five CRGs. Then, we constructed a CRG_score applied to patients of any age, gender, and stage. Subsequently, we found that cluster B and a high CRG_score had a worse prognosis, fewer immune checkpoints, and higher tumor immune dysfunction and exclusion (TIDE) compared to cluster A and a low CRG_score. In addition, two subtypes and the CRG_score were closely associated with clinicopathological characteristics, human leukocyte antigens (HLAs) and TME cell infiltration. A high CRG_score was featured with decreased microsatellite instability-high (MSI-H) and mutational burden. Meanwhile, the CRG_score was significantly related to the cancer stem cell (CSC) index and chemotherapeutic response. Moreover, we developed a nomogram to predict the survival probability of patients. Our study explained the role of CRGs in GC, and the prognostic signature could potentially provide an approach for personalized tumor therapy.

KEYWORDS
gastric cancer, cuproptosis, molecule subtypes, tumor microenvironment, immunotherapy

Introduction

Gastric cancer (GC), a malignant tumor with high heterogeneity, is one of the global malignant diseases. Although there are regional differences in morbidity and mortality, more than 1 million people suffer from it each year worldwide (1, 2). GC is the fourth primary cause of cancerous tumor death globally (3). The low survival rate of patients with GC is due to the fact that they are primarily in the middle and late stages (1). Common treatments for GC, such as surgery and chemotherapy, are based on traditional diagnostic measures, including clinical symptoms, imaging, and

pathological data (4). However, treatments of inoperable and chemo-resistant GC patients remain many challenges needed to be addressed. Precisely personalized treatments, including immunotherapy and targeted therapy based on biomarkers such as microsatellite instability (MSI), epidermal growth factor receptor (EGFR), and programmed cell death ligand 1 (PD-L1), have been relatively novel and vital treatment strategies in recent years for those challenges (5). The purpose of them is to provide patients with more efficient and healthy drug treatments (6). Therefore, finding prognosis-related biomarkers with efficient treatment is a hot topic and an essential direction.

The self-death of normal cells could prevent cancerization to a certain extent. If damaged cells, such as DNA damage that cannot be repaired, cannot die by themselves, their genes may be mutated, which will promote the transformation to tumor cells of the offspring (7). A variety of cell death mechanisms, such as apoptosis, necroptosis, pyroptosis, autophagy, and ferroptosis, have been verified to be closely related to tumor progression (7, 8). Recently, cuproptosis is a new cell death mechanism that differed from other means. Copper is an indispensable cofactor to keep the body functioning properly. Copper accumulation can promote proteins lipidation in TCA mediated mainly by FDX1 and directly bind them, which induces loss of Fe-S cluster–containing proteins and elevation of HSP70 to activate acute proteotoxic stress leading to cell death (9). Zhang et al. revealed that ferredoxin reductase (FDXR) could regulate the expression of iron-binding protein 2 (IRP2), which affects the tumor suppressor p73, to mediate the development of tumor (10). There is a complex regulatory relationship between the tumor microenvironment (TME) and tumors. The growth of tumor cells depends on various biological factors secreted by TME. In addition to malignant cells, TME also includes adipocytes, fibroblasts, immune cells, extracellular matrix (ECM), and blood vessel-related cells (11). These components interfere with tumor progression through individual or interrelated pathways of action. For example, the vascular system provides tumor nutrition and distant metastasis channels, and tumor-associated macrophages (TAMs) protect tumors from immunosuppression. Fibroblasts can drive tumors away from their primary location (11, 12). However, there are very few studies of cuproptosis in tumors. The relationships between it and tumors, TME, and the prognosis of patients are not clear.

Due to cuprotosis as a newly discovered cell death mode, its role in gastric cancer is little known. We conducted a multifaceted analysis of cuprotosis-related genes (CRGs), hoping to discover the possible mechanism of CRG in the development of gastric cancer. This study explored CRGs' expression profile and associated transcription factors, as well as survival analysis. Then, two subtypes were identified based on CRGs, and TME cell infiltration using CIBERSORT, ssGSEA and ESTIMATE algorithms, survival time, clinical features, TIDE, immune checkpoints, and HLAs between them were analyzed. Subsequently, 567 patients with GC were again divided into two subtypes based on the differentially expressed genes (DEGs) of the two subtypes. In addition, CRG_score was constructed to predict prognosis, clinical characteristics, TME cell infiltration, TIDE, immune checkpoints, HLAs, TMB, CSC, MSI, and drug sensitivity of GC patients.

Materials and method

Data sets source and tissue samples

Gene expression (FPKM value), clinicopathological information, copy number variation, and nucleotide mutation data of GC were obtained from The Cancer Genome Atlas (TCGA) in January 2022. GSE15459 was downed from the Gene Expression Omnibus (GEO). FPKM values are converted to TPM values. The two datasets were merged, quantile normalized, and removed batch effects by the "Combat" algorithm. Comprehensive information of patients in TCGA and GSE15459 was shown in **Supplementary Table S1**. CRGs were identified from the literature (**Supplementary Table S2**) (9). Tumor-associated transcription factors were downloaded from the website (http://www.cistrome.org/). 10 GC cases of fresh frozen tumors and adjacent tissues from the Second Hospital of Jilin University were selected for quantitative real-time PCR (qRT-PCR).

The analysis of subtypes for CRGs

The expression of twelve CRGs was compared between 32 normal and 375 tumor samples in TCGA. Nine CRGs were differentially expressed (P-value <0.05). Then the Kaplan–Meier (KM) survival analysis was performed to screen out five CRGs with survival significance (P-value <0.05). We identified two molecular subtypes with the package "ConsensusClusterPlus" based on the five CRGs (FDX1, DLAT, PDHA1, SLC31A1, ATP7B). Moreover, core transcription factors associated with CRGs were obtained *via* the package dplyr and the Cytoscape software, in which the filter condition was the correlation coefficient >0.45 and false discovery rate (FDR) < 0.001. The biological function differences using Gene Set Variation Analysis (GSVA) and differential expression of CRGs between the two subtypes were analyzed.

Evaluation of clinicopathological data and TME between subtypes

To explore the clinical application, we analyzed differences in age, sex, stage, survival time, and status between the two subtypes.

The survival analysis was performed by survival and survminer packages. The CIBERSORT and ssGSEA algorithms were used to calculate infiltration scores of various immune cells. We assessed the immune score, stromal score, and estimate score in distinct subtypes *via* ESTIMATE algorithm. To further study the differences in immune status between subtypes, TIDE score, dysfunction score, and immune exclusion score were checked, which have a negative correlation with patients' prognosis and immune efficacy (http://tide.dfci.harvard.edu/). To better evaluate the sensitivity of immunotherapy, we compared scores for twenty common therapeutic targets such as CTLA4, CD80, VTCN1, and LAG3 among others, between subtypes. Meanwhile, the expression of HLAs was explored.

Identification and analysis of DEGs

We obtained DEGs between the two subtypes using the limma package (|log Foldchange (FC) | > 0.585 and FDR < 0.05). To better define the cuproptosis subtypes, we retyped all samples based on DEGs by utilizing the ConsensusClusterPlus package and identified two clusters again. Subsequently, the survival analysis, clinical information and the expression of CRGs were performed between two clusters. Furthermore, GO and KEGG were used to explore the functional pathways of DEGs.

Construction and validation of the prognostic CRG_score

Firstly, all samples were equally divided into train and test groups. Then, samples from the train group were used to construct the prognostic CRG_score. Univariate Cox regression analysis was utilized to find prognostic-related DEGs. Next, LASSO regression analysis for prognostic-related DEGs using the glmnet package in R was conducted to prevent overfitting. Subsequently, the seven genes and formula of CRG_score ($e^{(\text{each gene's expression} \times \text{correlative coefficient})}$) were obtained using the multifactorial Cox analysis. According to this formula, each sample obtained a risk score. Samples of the train group were divided into high- and low CRG_score groups based on the median risk score. The test group and all sets were divided into two groups *via* the same method. The survival ROC package was used to construct the ROC curves and obtain the area under the ROC curve (AUC) for 1, 3, 5, and 7 year OS, which can check the accuracy of the model. Moreover, survival time, clinical information, TME cell infiltration, TIDE, immune checkpoints, and HLA were analyzed by the same methods as before between high- and low CRG_score groups. The Gene set enrichment analysis (GSEA) software was conducted to explore the functional pathways in two groups. The filter criterion according to the c2.cp.kegg.v7.5.1symbols.gmt gene set was |normalized enrichment score (NES)| > 1.5, nominal (NOM) p-value <0.05 and FDR q-value <0.05.

Mutation and cancer stem cell (CSC) index analyses

The mutation data was downed from TCGA, which was analyzed to observe the distinction in high- and low CRG_score groups by the maftools package. Meanwhile, we studied the relationships of TMB with survival, the two CRG_score groups and risk score. At the same time, the correlation of TMB with immune cells was explored. We also performed a correlation analysis of CSC and risk score.

Microsatellite instability (MSI) and drug susceptibility analyses

MSI could be used to guide clinical medication. Therefore, the relation of MSI with risk score was studied. To guide the clinical application of drugs, we screened out the common chemotherapeutic drugs based on differential half inhibitory concentration (IC50) values between the two CRG_score groups using pRRophetic and limma packages.

Construction of a nomogram

A nomogram was constructed using the rms package to predict the patients' 1, 3, 5 and 7 -year survival probability, while the calibration curve examined the nomogram's forecasting performance.

Quantitative real-time PCR

Total RNA was extracted from GC patient tissues using Trizol reagent (Invitrogen, Carlsbad, CA, United States). A reverse transcription kit (Takara, Tokyo, Japan) was used to synthesize cDNA. The SYBR Premix Ex Taq™ kit (Takara, Japan) was used to perform the RT-qPCR. The mRNA expression level of SLC25A15, CTSV, RGS4, SYT13, ENTPD2, CA8, and NPTX1 was normalized by GAPDH. The data were determined by the $-\Delta\Delta$Ct means. The primers of the seven genes were listed in **Supplementary Table S3**.

Statistical analyses

All statistical analyses were conducted by R version 4.1.1. $P < 0.05$ was considered statistically significant.

Results

Genetic and transcriptional characteristics of CRGs in GC

The overall experimental design was presented in Figure 1. First, the mutation status in 12 CRGs were explored (Figure 2A). The overall mutation rate is 12% (53/433 samples). ATP7B, DLAT, DLD, ATP7A, and LIPT1 were the top five genes with relatively high levels of mutations. Then, the analyses of the correlation between CRGs expression and mutations were performed. Mutants tended to be accompanied by increased expression of CRGs (DBT, LIAS, DLAT, DLD, PDHB, especially LIAS) compared to wild-type (Supplementary Figure S1). 9 CRGs (75%, 9/12 CRGs) are differentially expressed between normal and tumor tissues (Figure 2B). Almost all 12 CRGs had the changes of somatic copy number variation (CNV). The CNV increases happened in ATP7B, SLC31A1, and LIPT1; nevertheless, DLAT, FDX1, DBT, and PDHB occurred the CNV decreases (Figure 2C). Their chromosomal sites were described in Figure 2D. We performed the survival analyses on 567 samples with GC based on the expression of CRGs. And we observed that 8 CRGs were significant ($P < 0.05$). Among them, seven highly expressed CRGs (87.5%) had a good prognosis, which suggested CRGs may have inhibitory effects on gastric cancer (Figure 2E).

Identification of cuproptosis subtypes in GC

To study the classification of cuproptosis in GC, the 567 samples were classified *via* the consensus clustering analysis according to the expression profiles of 5 CRGs. There were A ($n = 305$) and B ($n = 262$) subtypes in terms of the best k value ($k = 2$) (Figure 3A and Supplementary Figure S2A). The rationality of the clusters was further verified by PCA analysis (Figure 3B). The survival analysis demonstrated that subtype A had a better prognosis than B (Figure 3C). For clinicopathological features, stages of cluster A were lower compared to B (Figure 3D). At the same time, we further analyzed the expression of CRGs of clusters to explore the reasons for differences between clusters. The results indicated that 11 CRGs (91.6%) were more highly expressed in cluster A than B (Figure 3E). Moreover, GSVA proved that cluster A was enriched in N-glycan biosynthesis, citrate and TCA cycles, the metabolisms of sphingolipid, glycerolipid, propanoate, butanoate, pyruvate, fructose and mannose, and cluster B was enriched in neuroactive ligand-receptor interaction (Figure 3F and Supplementary Table S4). At the same time, we evaluated the expression of 20 immune checkpoints between cluster A and B, which showed that 11 checkpoints were differential, of which 9 checkpoints (CD80, HHLA2, ICOSLG, TNFRSF25, CD276, LGALS9, TNFRSF14, VTCN1, TNFSG15) had higher expression of cluster A than B (Figure 3G). Cross-metabolic reprogramming of cancer and immune cells is seen as a determinant of the antitumor immune response. More and more studies have shown that cancer metabolism could regulate antitumor immune response by releasing metabolites. Moreover, immune cells also undergo metabolic reprogramming during proliferation, differentiation, and effector function (13). Results of GSVA and GO analysis mainly focus on cancer metabolism, which is closely related to tumor immune response. In fact, tumor immune response has long been recognized as an important factor in the efficacy of immunotherapy and the prognosis of cancer patients. Therefore, we mainly analyzed the results related to tumor immune infiltration.

Characteristics of TME cell infiltration, TIDE and checkpoints in the cuproptosis subtypes

In order to comprehensively analyze the relationship between CRGs and TME in GC, we observed that stromal, immune, and estimate scores of cluster B were higher than cluster A using the ESTIMATE algorithm (Figure 4A). The scores of dysfunction and TIDE were lower in cluster A than B (Figure 4B). We used CIBERSORT, ssGSEA, and ESTIMATE algorithms to evaluate. The results of CIBERSORT algorithm demonstrated that the differences between cluster A and B were concentrated in T cells, NK cells, Macrophages, and Mast cells (Figure 4C and Supplementary Table S5). The ssGSEA algorithm also verified similar outcomes for these cells (Figures 4D,E and Supplementary Table S6). In addition, For HLA, cluster A had lower expression of DPA1 and DPB1 than B, and the opposite for HLA C and G (Figure 4F). Prognosis-related and differentially expressed 5 CRGs were selected to study their transcription factors, which were demonstrated in Figures 4G,H. Ten hub genes, especially HDAC1 and EZH2 were screened by the Cytoscape software (Figure 4I). Moreover, the expression of core transcription factors in subtype A was higher than that in subtype B (Supplementary Figure S2B).

Identification and analysis of gene subtypes based on DEGs

In order to identify the cuproptosis subtypes clearly, we screened 1,233 DEGs between the two cuproptosis subtypes through the limma package. GO and KEGG for these DEGs were enriched mainly in cell cycle, fat digestion and absorption, PPAR signaling pathway, IL-17 signaling pathway, p53 signaling pathway and DNA replication, which were closely related to cancer (Figures 5A,B and Supplementary

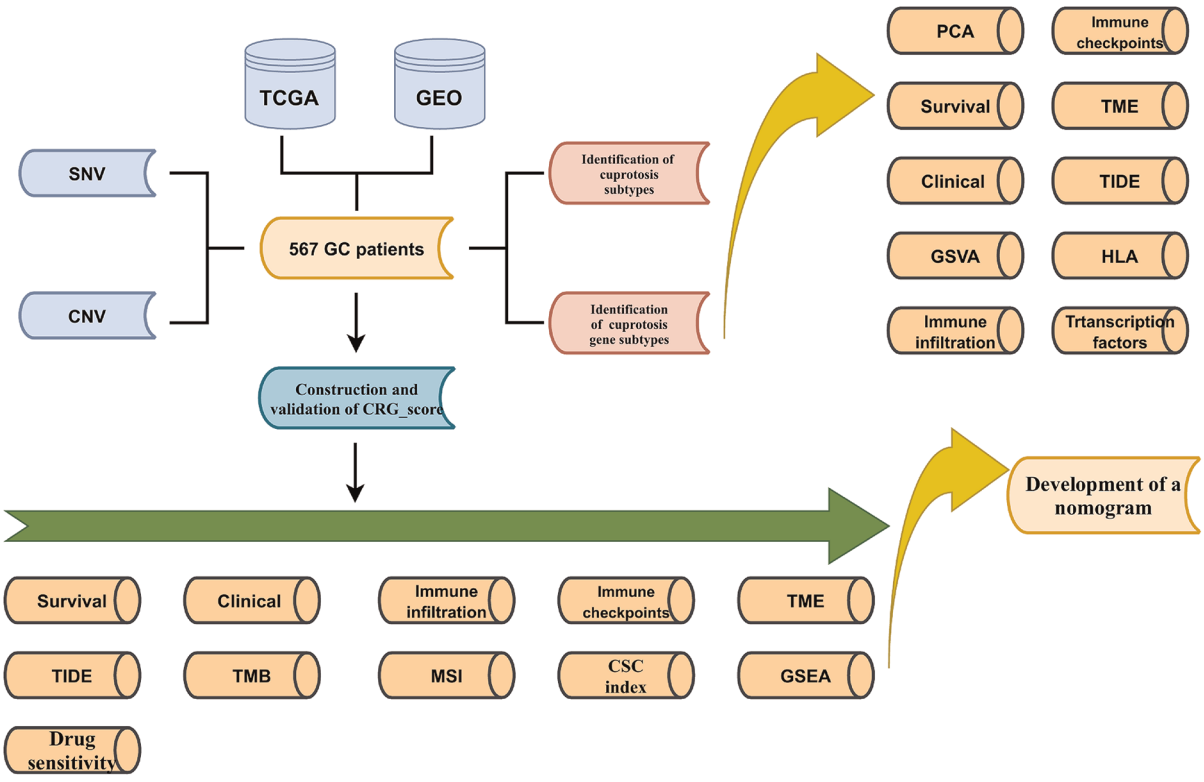

FIGURE 1
Schematic diagram of the flow of the study.

Table S7). Furtherly, we used the univariate COX method to select 304 prognostic-related DEGs and classified all samples according to them (Supplementary Table S8). The results showed that there were still two gene subtypes, which was consistent with the previous typing results (Figure 5C and Supplementary Figure S2C). There were significant differences in expression of CRGs, clinical traits and survival time between A and B gene clusters (Figures 5D, E, F).

Construction of the prognostic CRG_score

LASSO regression analysis was performed for 304 prognostic-related DEGs. We chose the lambda minimum to select the appropriate genes (Supplementary Figure S2D,E). Subsequently, seven genes (SLC25A15, CTSV, RGS4, SYT13, ENTPD2, CA8, NPTX1) were screened to construct the model by the multifactorial Cox analysis. The genes included four high-risk genes (CTSV, RGS4, SYT13, NPTX1) and three low-risk genes (SLC25A15, ENTPD2, CA8). The formula of CRG_score was shown as follows:

Risk score = (−0.27565756734421* expression of SLC25A15) + (−0.235708601387405* expression of ENTPD2) + (−0.124572834187939* expression of CA8) + (0.379774295825035* expression of CTSV) + (0.212171866831215* expression of RGS4) + (0.160140827663568* expression of SYT13) + (0.128438559010339* expression of NPTX1).

Then, both the train group and the test group were divided into high- and low- CRG_score groups. The survival curve demonstrated that the survival of low- CRG_score group was better than high-CRG_score group in the train group ($P < 0.001$). The AUC values of 1-, 3-, 5-, and 7- year were 0.650, 0.810, 0.798, and 0.739, respectively (Figure 6A). For the test group, the result of survival analysis was the same of the train group. The AUC values of 1-, 3-, 5-, and 7- year were 0.596, 0.613, 0.677, and 0.682, respectively (Figure 6B). The relationships between cuproptosis subtypes, gene subtypes, CRG_score groups, and patients' survival status were shown in Figure 6C. Meanwhile, cluster A was associated with a low score, which was consistent with previous survival analyses of both subtypes and CRG_score groups (Figure 6D). Gene cluster A was associated with a high score and low survival time (Figure 6E). For gastric cancer patients of any age, gender, and stage, a high CRG_score was accompanied by low survival time (Figure 6F). There was a significant correlation between the age of the patient and the score (Figure 6G). Stage I patients had a lower score than stage II, III, and IV (Figure 6H).

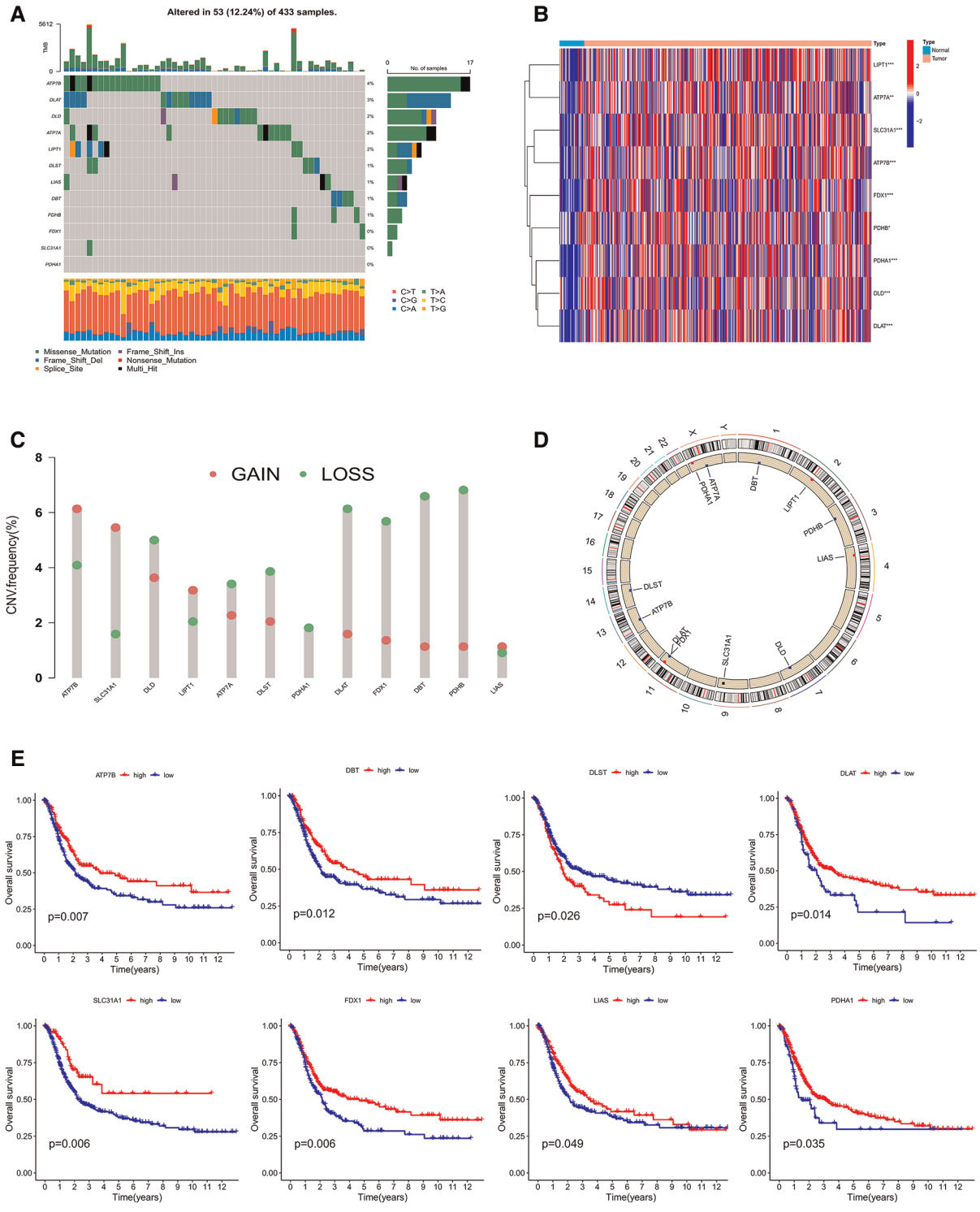

FIGURE 2
(**A**) mutation characteristic of 12 CRGs from TCGA. (**B**) The expression of CRGs between Normal and tumor. (**C**,**D**) The changes of somatic copy number variation in CRGs. (**E**) The survival analysis of CRGs. CRGs, cuprotosis-related genes. (*$P < 0.05$; **$P < 0.01$; ***$P < 0.001$; ns, not significant).

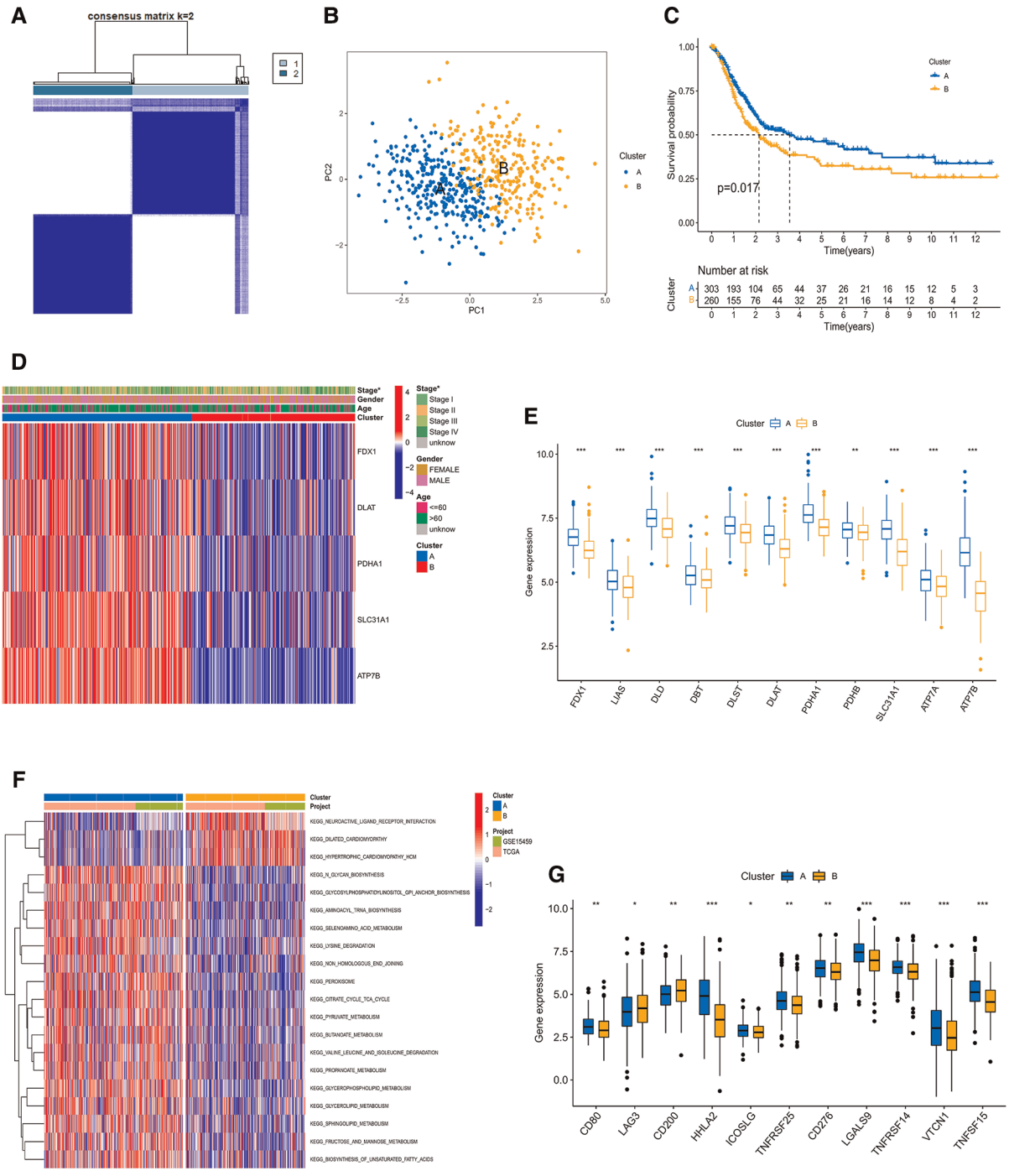

FIGURE 3
(**A**) consensus clustering matrix defining two clusters ($k = 2$). (**B**) The PCA analysis of the two clusters describing an obvious difference. (**C**) The KM curve between A and B subtypes. (**D**) The heatmap showing the correlation of the two subtypes with age, stage, gender, and CRGs. (**E**) The mRNA expression of CRGs between A and B subtypes. PPI, Protein-protein interaction; KM, Kaplan–Meier. (**F**) GSVA of analysis between two distinct subtypes, in which red represents positively correlated pathways and blue negatively correlated pathways. (**G**) Differential expression of immune checkpoints in the two subtypes.

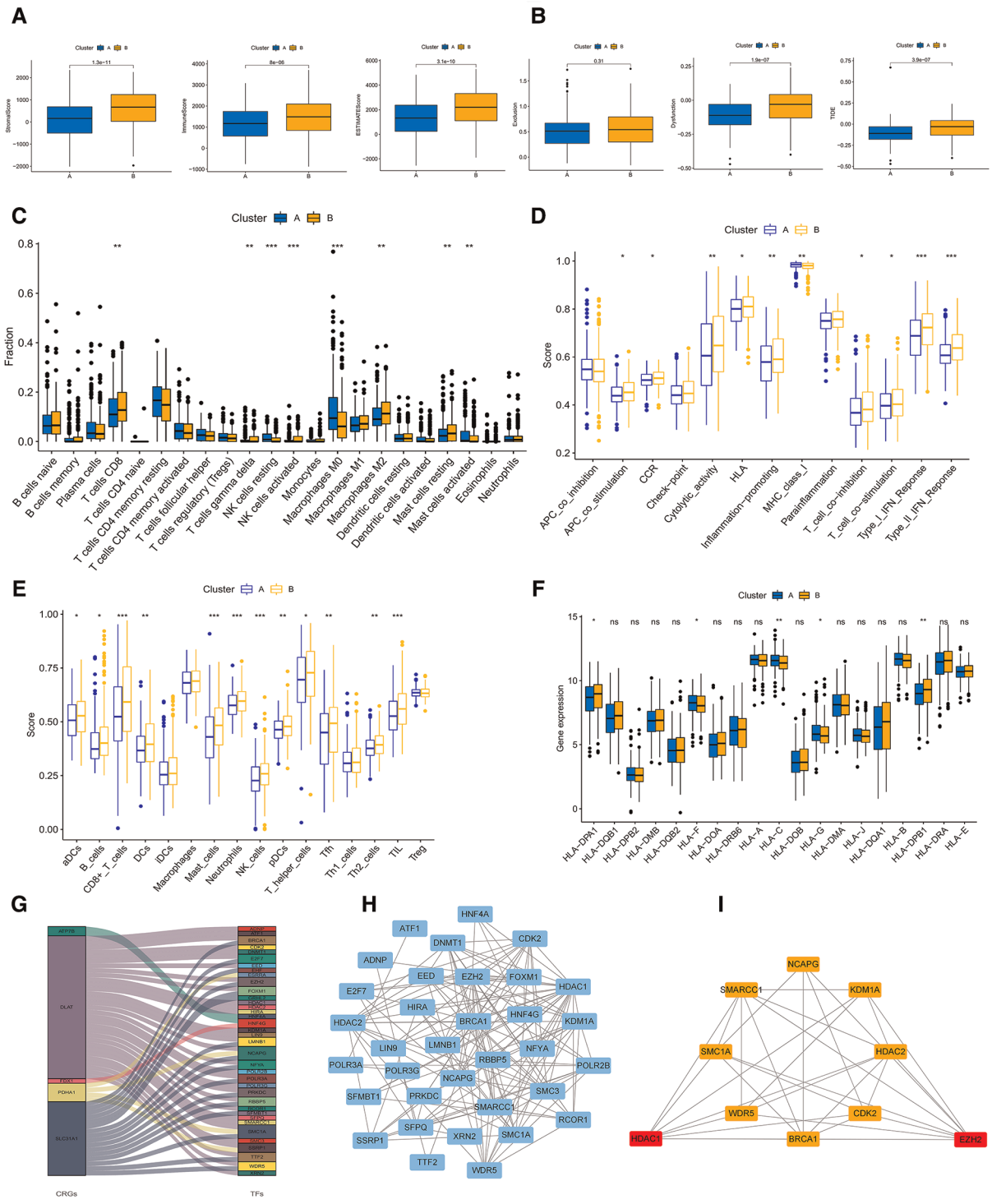

FIGURE 4
(**A**) The stromal, immune, ESTMATE scores of A and B subtypes using ESTMATE algorithm. (**B**) Associations of the TIDE score and the two subtypes. (**C**) TME cells infiltration in A and B subtypes by CIBERSORT algorithm. (**D**,**E**) ssGSEA algorithm calculating the scores of immune cells infiltration in the two clusters. (**F**) The plot showing the expression of HLAs in the two clusters. (**G**) Sankey diagram of CRGs and transcription factors. (**H**) PPI network of the CRGs based on the STRING database. (**I**) The plot of hub transcription factors visualized by Cytoscape. GSVA, gene set variation analysis; TIDE, Tumour Immune Dysfunction and Exclusion; HLAs, human leukocyte antigens; TME, tumor microenvironment. (*$P < 0.05$; **$P < 0.01$; ***$P < 0.001$; ns, not significant).

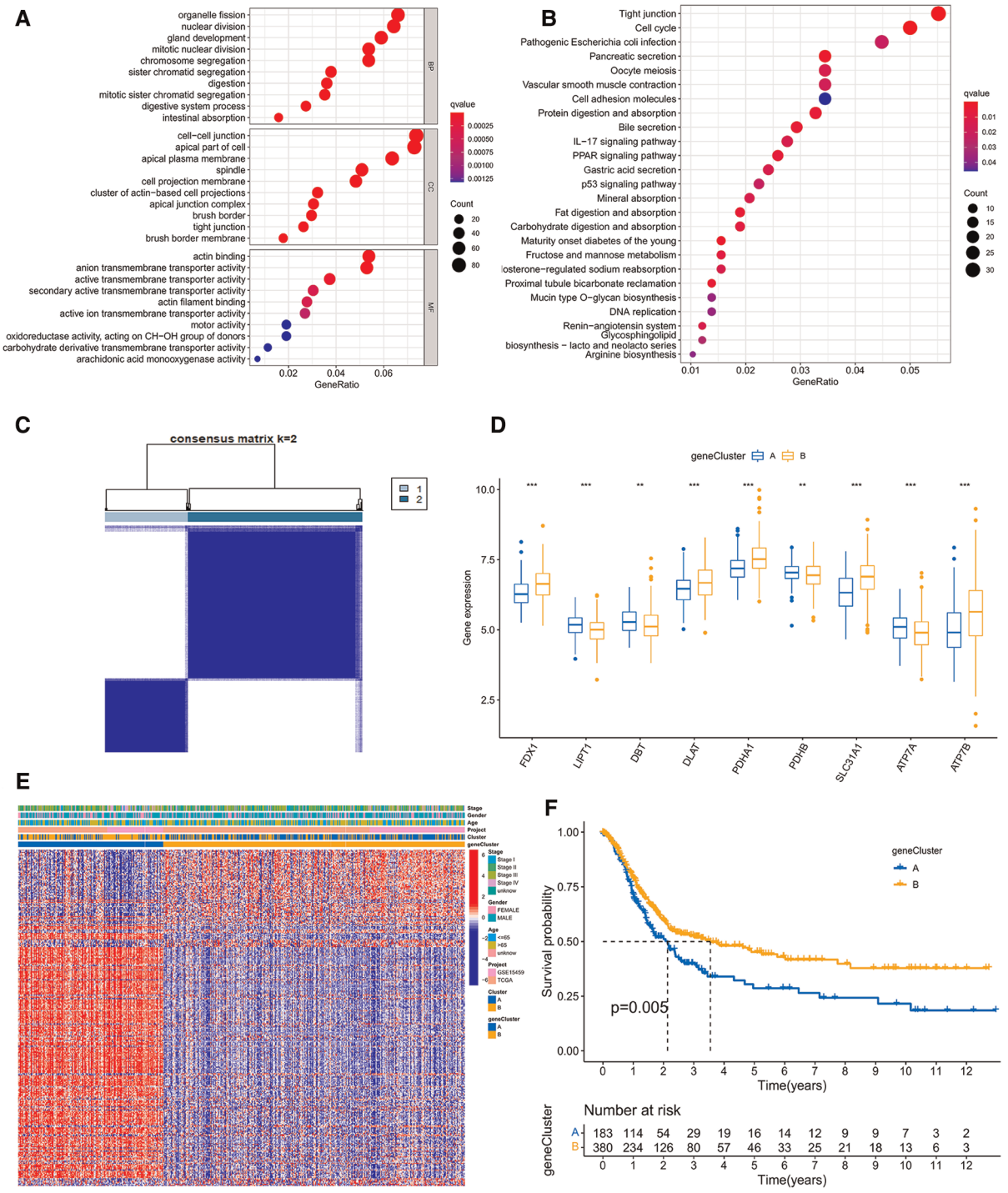

FIGURE 5
(**A**) The GO analysis based on the differentially expressed genes (DEGs). (**B**) The KEGG analysis of DEGs. (**C**) Consensus clustering matrix defining two clusters ($k = 2$) accroding to DEGs. (**D**) The expression of CRGs between A and B geneclusters. (**E**) The heatmap showing the correlation of the subtypes and geneclusters with clinicopathological data and CRGs. (**F**) The survival curve between A and B geneclusters. GO, Gene Ontology; KEGG, Kyoto Encyclopedia of Genes and Genomes.

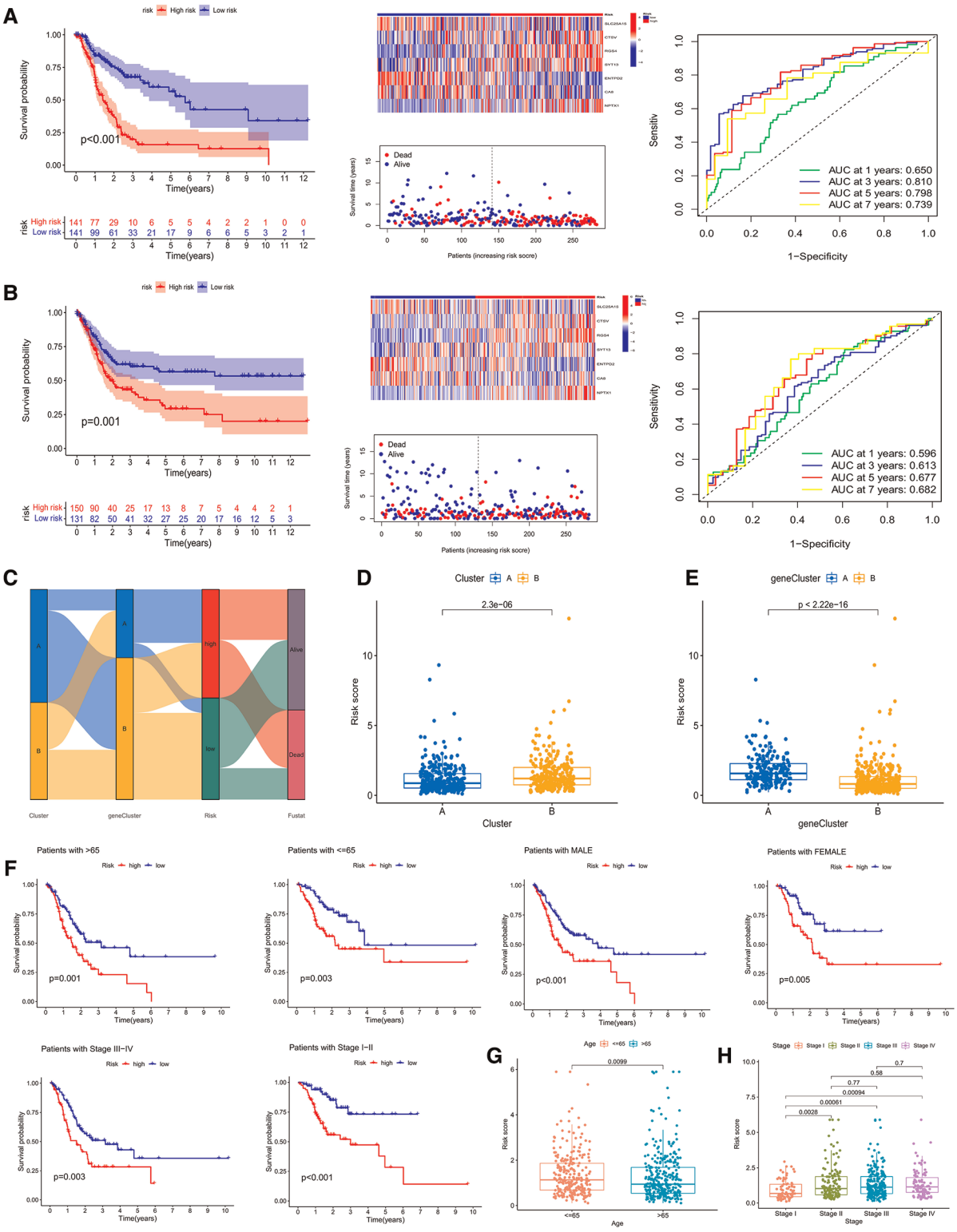

FIGURE 6
survival analysis, heatmap, survival status accompanied with the CRG_score and ROC analysis in the train cohort (**A**) and the test cohort (**B**). (**C**) Sankey picture showing the relationship of subtypes, geneclusters, risk groups and patients survival status. (**D**,**E**) Correlation of two subtypes and genecluster and CRG_score, respectively. (**F**) Applicability of CRG_score to GC patients of any age, gender and stage. (**G**,**H**) Relationship of age and stage with CRG_score, respectively.

Correlation of TME cell infiltration, TIDE and checkpoints with high- and low-CRG_score groups

Similarly, we used three algorithms to assess TME cell infiltration between high- and low-CRG_score groups. By CIBERSORT, we found that low CRG_score was accompanied by high B cells memory, Tregs, T cells CD4 memory activated, plasma cells, NK cells resting, neutrophils, mast cells activated, dendritic cells activated, and Macrophages M0, and low T cells gamma delta, monocytes, mast cells resting, Macrophages M2 (**Figures 7A,B**). Meanwhile, the outcomes of the correlation of TME cell infiltration with risk genes were described in **Figure 7C**. The relationships of TME cell infiltration with survival time were shown in **Supplementary Figures S2F,G**. The analysis of ssGSEA also suggested a significant correlation between TME and two CRG_score groups (**Figures 7D,E**). Expressions of 20 immune checkpoints were assessed between high- and low-CRG_score groups, which showed that 6 checkpoints were differential, of which 4 checkpoints (TNFRSF25, LGALS9, TNFRSF14, VTCN1) had higher expression of low- than high-CRG_score group (**Figure 7F**). For HLA, the low-CRG_score had lower expression of DPA1, DPB2, DMB, DQB2, DOA, DQA1, DPB1 and DRA than the high-CRG_score (**Figure 7G**). At the same time, we found that stromal, immune, and estimate scores of the high-CRG_score group were higher than the low-CRG_score group through the ESTIMATE algorithm (**Figure 7H**). The high CRG_score had the high scores for dysfunction, exclusion and TIDE (**Figure 8A**). The correlation analysis of risk scores and CRGs was described in **Figure 8B**.

Mutation and CSC index analysis

Accumulation of mutations in somatic cells can cause their transformation into cancer cells (14). Meanwhile, a study showed a positive correlation between high TMB and better survival in many cancers (15). Therefore, we downloaded and analyzed the data of mutation from TCGA. The top 10 mutated genes in the low-CRG_score group were TTN (55%), TP53 (43%), MUC16 (38%), ARID1A (27%), LRP1B (28%), SYNE1 (28%), FLG (22%), FAT4 (21%), CSMD3 (22%), PCLO (24%) (**Figure 8C**). The top 10 genes mutated in the high-CRG_score group were the same as those genes, but the rates of mutation were low than low-CRG_score group (38%, 40%, 21%, 19%, 20%, 14%, 16%, 15%, 10%, 12%, correspondingly) (**Figure 8D**). TMB might have associations with endothelial cells, neutrophils, cytotoxic lymphocytes and B lineage (**Figure 8E**). Similarly, the low CRG_score had a high TMB (**Figure 8F**). The relationship between TMB and CRG_score was plotted in **Figure 8G**. Moreover, our results also testified that high TMB had a good prognosis than low TMB (**Figure 8H**). A combined analysis of risk score and TMB demonstrated that H-TMB + low risk had the best prognosis, but L-TMB + high risk had the worst prognosis (**Figure 8I**). There was a negative association between CSC index and risk score (DNAss: $R = -0.19$, $P < 0.001$; RNAss: $R = -0.36$, $P < 0.001$) (**Figures 8J,K**).

MSI, GSEA and drug susceptibility analysis

MSI may predict the efficacy of chemotherapy and immunotherapy and survival of patients (16). Our study suggested that the risk score of MSI-H was higher than MSS and MSI-L (**Figures 8L,M**). The survival analysis of MSI-H and MSS/MSI-L was not meaningful (**Figure 8N**). A combined analysis of risk score and MSI proved that MSI-H + low risk had the best prognosis, but MSS/MSI-L + high risk had the worst prognosis (**Figure 8O**). The GSEA analysis manifested that the high-CRG_score group was fastened on base excision repair, calcium signaling pathway, citrate and TCA cycle, ECM receptor interaction, and focal adhesion. The low-CRG_score group was concentrated on fructose and mannose metabolism, glyoxylate and dicarboxylate metabolism, peroxisome, regulation of actin cytoskeleton, and vascular smooth muscle contraction (**Figure 8P**). To evaluate the difference of drugs between the two risk groups, we screened 67 drugs using the pRRophetic package, of which 13 drugs had higher IC50 values in the high-risk group than in the low-risk group. And the remaining 54 drugs were the opposite (**Figure 9A** and **Supplementary Figures S3, S4**). Furthermore, we screened eight types of drugs which were commonly used in GC according to the results of all drugs, including multitarget tyrosine kinase inhibitor, anti-VEGFR monoclonal antibody, HER-2 tyrosine kinase inhibitor, Hedgehog(Hh) signaling pathway inhibitor, anti-HGFMET monoclonal antibody, anti-mTOR monoclonal antibody, Akt inhibitor, Insulin-like growth factor receptor (IGF-IR) inhibitor. The results showed that sensitivities of sunitinib, AMG.706, GDC.0449, PF.02341066, BMS.754807 for GC patients in the high-risk group were higher than the low-risk group; sorafenib, BIBW2992 and NVP.BEZ235 were opposite (**Figure 9A**). At the same time, we also analyzed a variety of chemotherapeutic drugs that could be sensitive to risk genes (**Figure 9B**).

Construction and validation of a nomogram

Using univariate and multifactor COX regression analysis, we discovered that CRG_score and stage were independent prognostic factors in gastric cancer patients (**Figure 10A** and **Supplementary Figures S2H,I**). Therefore, CRG_score and

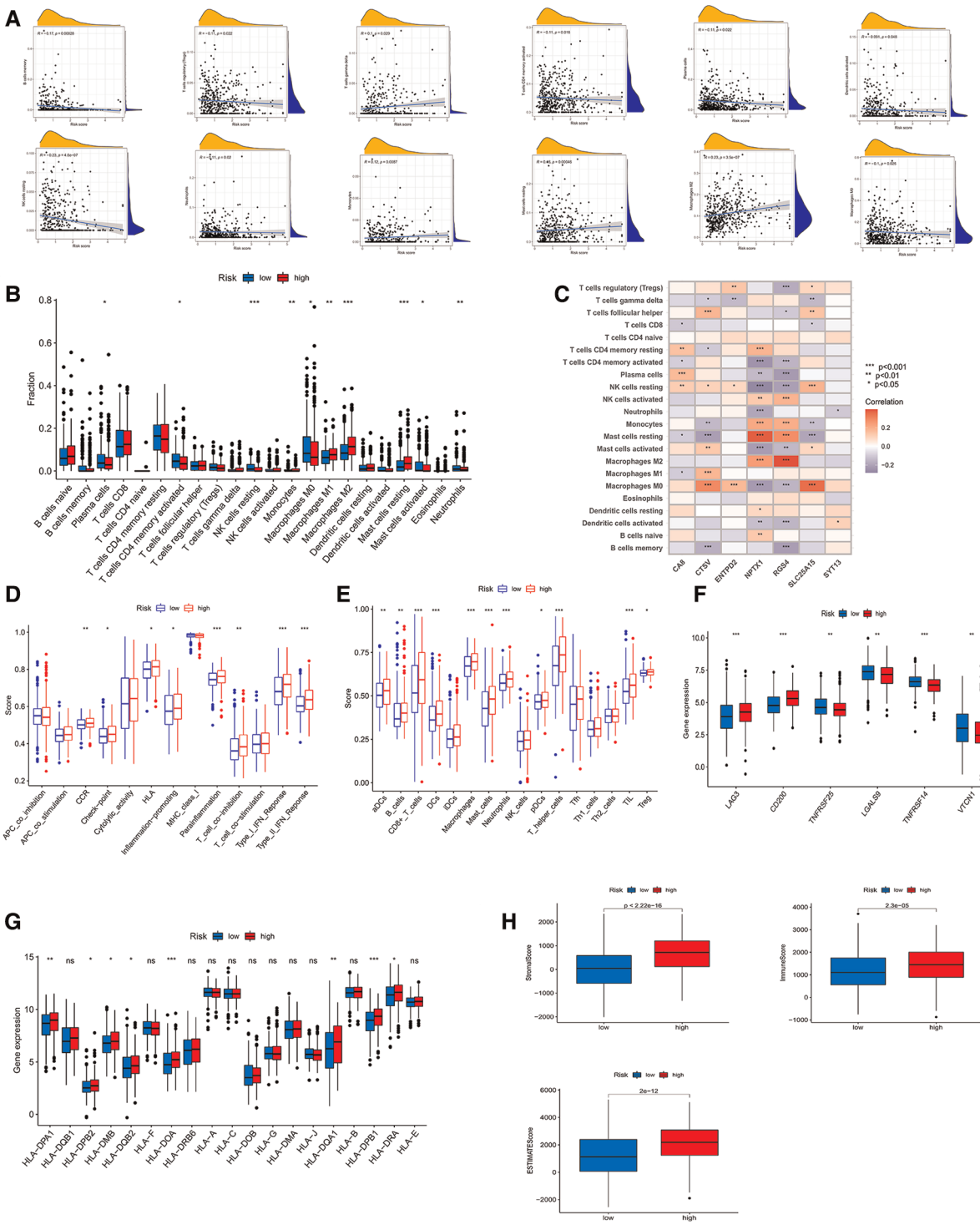

FIGURE 7
(A) correlative analysis between risk score of immune cells. (B) TME cells infiltration in low- and high-CRG_score groups by CIBERSORT algorithm. (C) Associative analysis between 22 immune cells and risk genes. (D,E) ssGSEA algorithm calculating the scores of immune cells infiltration in the risk groups. (F) Differential expression of immune checkpoints in the two CRG_score groups. (G) The diagram showing the expression of HLAs in the two risk groups. (H) The stromal, immune, ESTMATE scores of low- and high-CRG_score groups using ESTMATE algorithm.

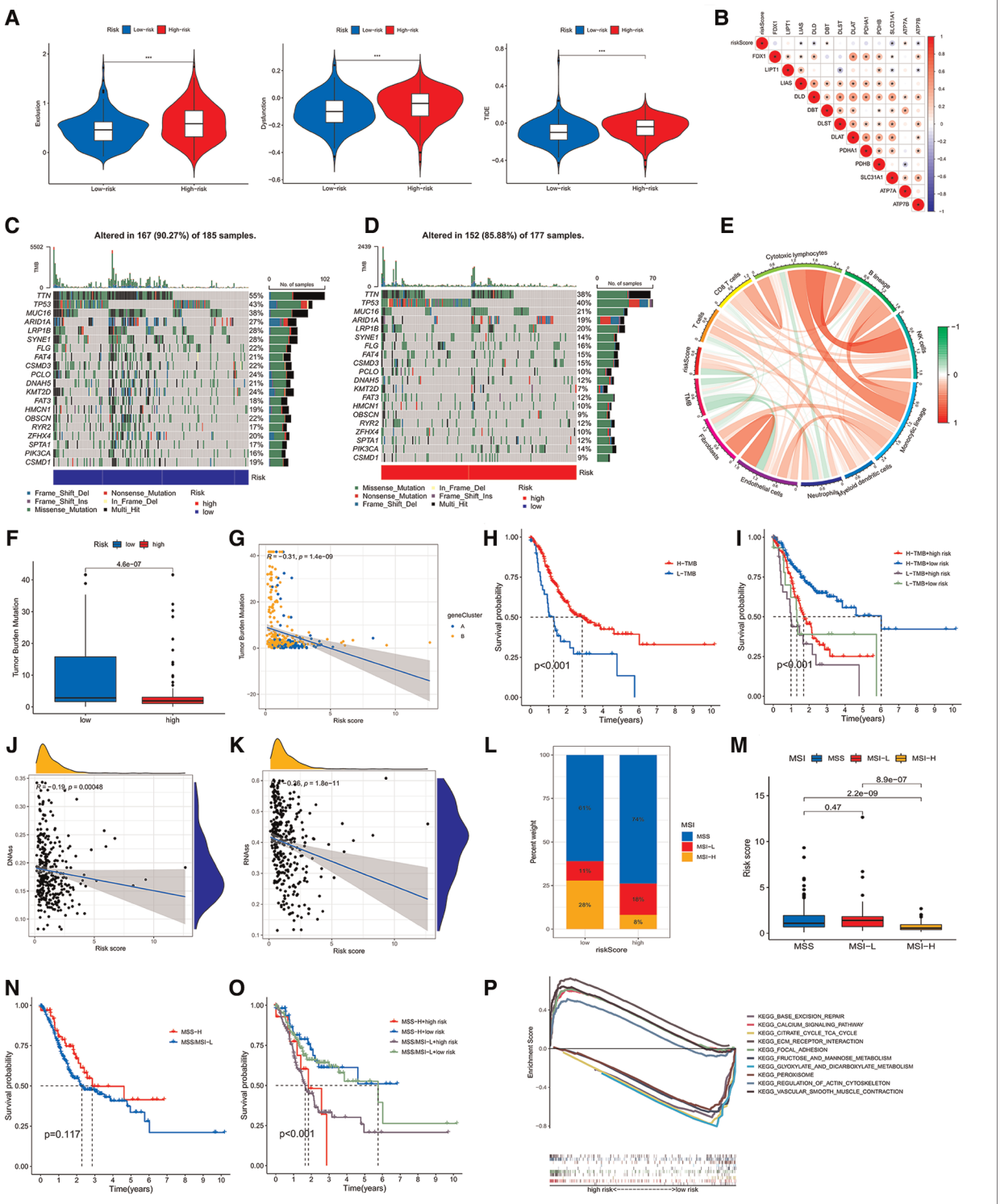

FIGURE 8
(A) associations of the TIDE score and the two risk groups. (B) Correlative analysis between risk score and expression of CRGs. Waterfall chart showing the top 20 mutated genes and their frequencies in the low-risk group (C) and the high-risk group (D). (E) Circle graph showing the relationship between TMB, immune cells and risk score. (F) The diagram showing the levels of TMB in the two risk groups. (G) Correlative analysis between risk score and expression of TMB. (H) The survival analysis of the low- and high-TMB groups. (I) The survival analyses of combined TMB and risk groups. (J,K) Cancer stem cell (CSC) index analyses of riskscore. (L,M) Associative analysis between MSI and riskscore. (H) The survival curve of the MSS/MSI-L and MSI-H groups. (O) The survival analyses of combined MSI and risk groups. (P) The GSEA analysis of low- and high-CRG_score groups.

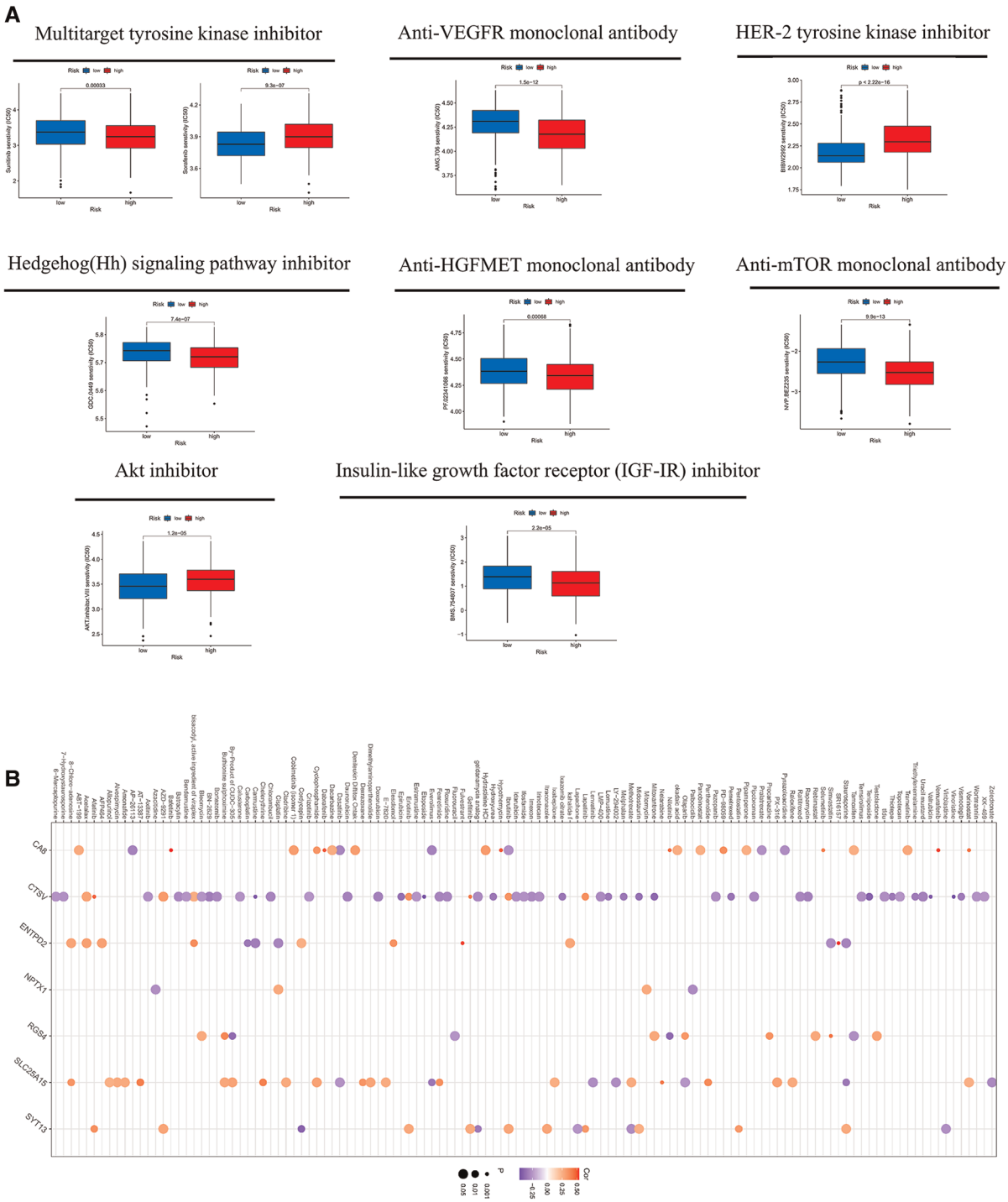

FIGURE 9
(A) the sensitivity of eight types of drugs between high- and low-CRG_score groups. (B) The sensitivity of chemotherapeutic drugs to risk genes.

stage were used to develop a nomogram to predict the survival times of 1, 3, 5, and 7 years (Figure 10B). The calibration graph displayed that the predictive ability of the nomogram was relatively accurate (Figure 10C).

Discussion

Copper, one of the most vitally basic trace metals in the human body, involves in various biological functions,

including the regulation of enzyme function, cofactor for growth and development, redox processes, energy metabolism, iron absorption and cell proliferation (17). Like iron, copper is also closely related to the development of cancers. On the one hand, copper can promote tumorigenesis by activating the MAPK pathway (18). Copper-binding enzymes mediate HIF1-α and Snail to promote the Epithelial to Mesenchymal Transition (EMT) progression of tumors (19). The copper-enzymes LOX (Lysyl Oxidase) promotes adhesion and metastasis of colorectal cancer by affecting the turnover of the Extracellular Matrix (ECM) (20). On the other hand, copper can indirectly suppress tumors by promoting alterations in the recruitment of myeloid precursors or affecting tumor-associated macrophages (TAMs) (17). Accumulation of copper can activate oxidative stress leading to tumor cell death, which may be a potential treatment for cancer (21). Therefore, the role of copper in cancer is complex. In this study, we observed that the expression of CRGs in GC was higher than in normal samples, which was the same as the previous report that copper was elevated in many tumor tissues (22, 23). However, the survival analysis of 567 GC patients indicated that high expression of most CRGs had a better prognosis than low expression. This suggested that the high expression of CRGs may inhibit tumor cells in some way. Recently, Peter Tsvetkov et al. found that the accumulation of copper can induce cell death in a novel mechanism, namely cuproptosis (9). This finding enlightened us that CRGs may induce gastric cancer cell death through cuproptosis, thereby improving the prognosis of patients. Therefore, based on CRGs, we identified two subtypes and developed a CRG_score to explore the role of CRGs in gastric cancer comprehensively.

In our study, we testified that subtype A had a lower CRG_score than B, which suggested subtype A seemly was accossicated with the low-CRG_score group. Meanwhile, we discovered that the survival times and clinical stages of subtype A and the low CRG_score group were lower than subtype B and the high-risk group. Our findings also demonstrated that subtype A and the low CRG_score group had high expression of CRGs. These results again confirmed that high expression of CRGs was related to a better prognosis. Subsequently, ssGSEA and CIBERSORT algorithms showed that the differences of TME in two subtypes and CRG_score groups were Macrophages, NK cells, mast cells and T cells CD4. It is well known that macrophages can be polarized into M1 and M2 types (24). M1 type is mainly involved in the activation of the inflammatory response, while M2 is mainly involved in tissue repair and inhibition of inflammation (25, 26). Initially, macrophages are polarized to the M1 type, and cooperate with other immune cells to eliminate tumor cells. When tumor cells are in low oxygen and low pH, they will release Neuropilin-1 (Nrp-1), TGF-β, IL6, IL4, Tim-3 to promote the transformation of macrophages into M2 type, which can help tumor cells to escape immune and secrete growth factors to enhance tumor growth (27–30). Interestingly, M2 infiltrated highly in the high CRG_score group and subtype B. In the TME, inflammatory and cytotoxic effector functions of NK cells are weakened by a number of cytokines such as IL-23 and IL-1β, where NK cells are called tumor-infiltrating natural killer cells (TINKs). In addition to decreasing the ability of cytotoxicity, TINKs can also inhibit the growth and spread of T cells to reduce their damage to tumors (31, 32). Mast cells are one of the important innate immune cells in the immune system (33). Many studies have shown that low levels of mast cells were associated with poor survival and advanced tumors (34–36). Fortunately, we discovered that the activity of NK cells remained low in subtype A and low CRG_score group; however, the activity of mast cells was high. CD4+ memory T cells are important modulatory elements of the immune system (37). A study has proved that the more CD4+ memory T cells infiltrated in gastric cancer, the longer the patients' survival time (38). Tumor specific antibodies are generated by Plasma cells to damage tumor cells (39). Coincidentally, Plasma cells and CD4 + memory T cells activated were higher in the low-CRG_score than the high- CRG_score group. In summary, TME cell infiltration in subtype A and the low-risk group was more tumor suppression, which may also be one of the reasons for the better prognosis of patients in these two groups.

In this paper, GSEA enrichment analysis showed that high CRG_score was mainly enriched in base excision repair, calcium signaling pathway, citrate, and TCA cycle, ECM receptor interaction, and focal adhesion. Low CRG_score was mainly enriched in pathways related to metabolism. In conclusion, the pathways described above may be the potential mechanism by which CRG_score affects immune infiltration in gastric cancer. Immune checkpoint blockade is considered as a promising approach to immunotherapy of cancer (40). Many immune checkpoints such as CD200, VTCN1, PD-1, CTLA-4 and LAG-3, and so on, were found (41–44). Therefore, we evaluated twenty immune checkpoints and found that subtype A and the low-CRG_score group had higher expression of these checkpoints. TIDE as a computational method is used to predict immune checkpoint blockade (ICB) response. A score based on TIDE is negatively correlated with the effects of immunotherapy (45). The score of TIDE for subtype A and the low-CRG_score group was low. TMB and MSI have emerged as major predictors of immunotherapy efficacy. High TMB and H-MSI often represent favorable immune infiltration and prognosis (46, 47). Interestingly, low CRG_score and subtype A were accompanied by high TMB and H-MSI. In addition, we also assessed the sensitivity of chemotherapeutic drugs between high- and low-CRG_score groups using the pRRophetic package. At the same time, we also analyzed a variety of chemotherapeutic drugs that could be sensitive to risk genes. Moreover, the results of q-RT PCR showed that CTSV, RGS4, SYT13 and NPTX1 were highly expressed in tumor tissues

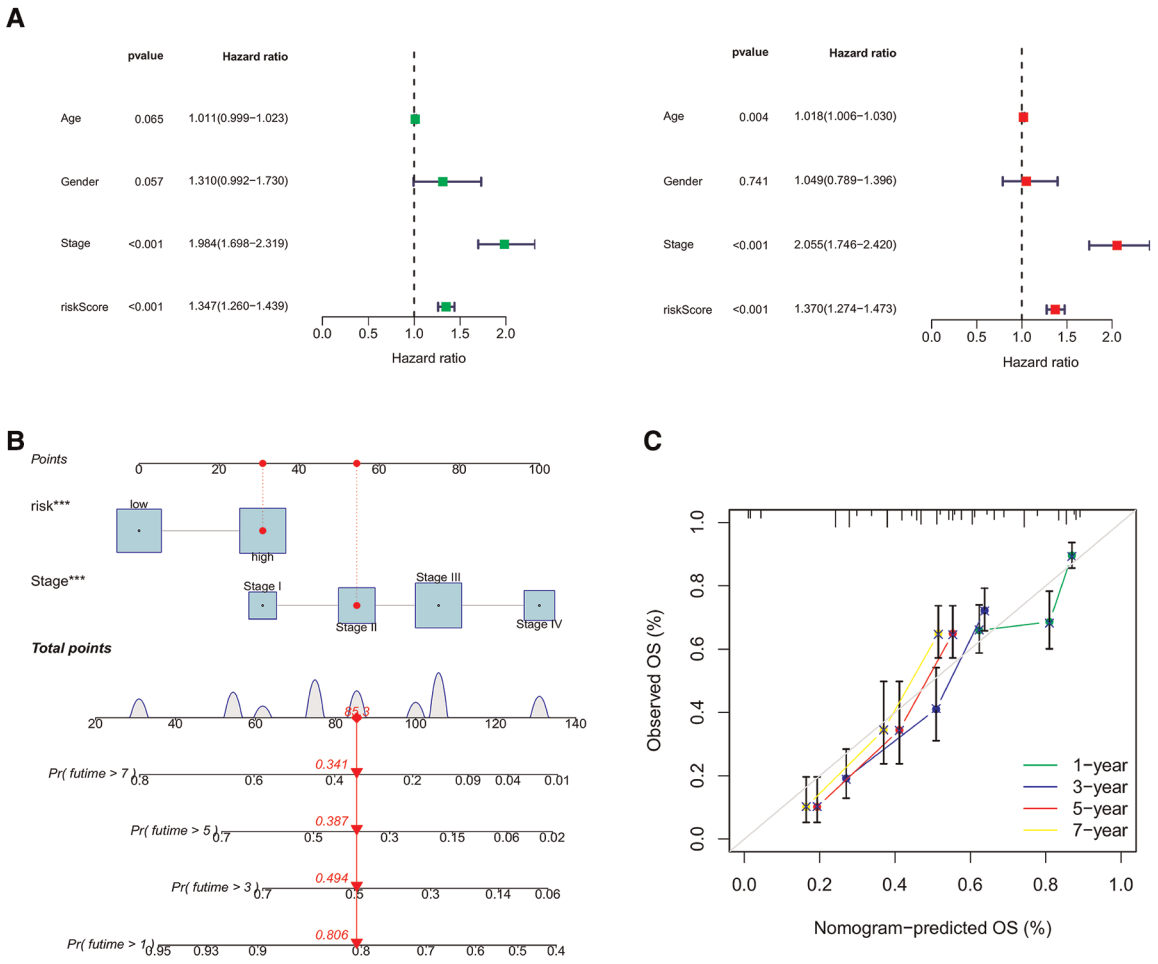

FIGURE 10
(A) the forest illustrations displaying univariate and multifactor COX regression analysis. (B) The nomogram to predict the survival times of 1, 3, 5, and 7 years. (C) The calibration graphs of 1, 3, 5, and 7 years.

compared with adjacent tumor tissues, while SLC25A15, ENTPD2 and CA8 were low expressed. This is consistent with the fact that CTSV, RGS4, SYT13 and NPTX1 were high-risk genes, and SLC25A15, ENTPD2 and CA8 were low-risk genes (**Supplementary Figure S5**).

Transcription factors can recognize specific DNA sequences to control chromatin and transcription for directing gene expression, which constitutes a complex regulatory system (48). Many studies have shown that the changes of biological functions of transcription factors were closely related to the occurrence and development of tumors. In this paper, we found that there were significant differences in the survival time and clinical stage of patients with cuprotosis-related A and B subtypes. Therefore, we assumed whether transcription factors were one of the influencing factors, so we used Cor function to screen out transcription factors that were strongly correlated with the genes of the constructed subtypes, which the screening conditions were: Cor >0.45 and FDR <0.001. Then, six analysis methods (Betweenness, Closeness, Degree, Eigenvector, LAC) were integrated to screen out the core transcription factors using Cytoscape software. Finally, the expression of core transcription factors in subtype A was higher than that in subtype B. This suggests that transcription factors may play a role in the differences between A and B subtypes. This will help us to study the potential mechanism of CRGs in gastric cancer and explore the therapeutic strategies based on targeting transcription factors.

Our study also had several limitations. First, the data of our research was mainly based on the public database. Therefore, more basic experimental validation may be required. Second, our data was derived from TCGA and GEO databases. Thus, we still need to collect more samples to reduce statistical errors. At the same time, the mechanism of action between cuproptosis and immune cells needs to be further explored.

Conclusion

Based on subtypes and prognostic signature of CRGs, the relationships between CRGs and the prognosis of patients, TME cell infiltration, immunotherapy, and drug sensitivities were comprehensively explored. Our study uncovered the roles of cuproptosis in gastric cancer, which could provide a new idea for cancer treatment.

Data availability statement

The datasets presented in this study can be found in online repositories. The names of the repository/repositories and accession number(s) can be found in the article/ **Supplementary Material**.

Ethics statement

The studies involving human participants were reviewed and approved by Ethics Committee of the Second Hospital of Jilin University. The patients/participants provided their written informed consent to participate in this study.

Author contributions

XDW and CZ designed the research. HD took part in designing the research, collected the data, analyzed the date and wrote the manuscript. STZ collected the data, analyzed the date. XDW and CZ solved the disagreements between HD and STZ. All authors contributed to the article and approved the submitted version.

Funding

This work was supported by Department of Finance of Jilin Provincial (No. 2019SCZT023, 2019SCZT051).

Acknowledgments

We thank all the people who contributed to this study.

Conflict of interest

The authors declare that the research was conducted in the absence of any commercial or financial relationships that could be construed as a potential conflict of interest.

Publisher's note

All claims expressed in this article are solely those of the authors and do not necessarily represent those of their affiliated organizations, or those of the publisher, the editors and the reviewers. Any product that may be evaluated in this article, or claim that may be made by its manufacturer, is not guaranteed or endorsed by the publisher.

Supplementary material

The Supplementary Material for this article can be found online at: https://www.frontiersin.org/articles/10.3389/fsurg.2022.991624/full#supplementary-material.

References

1. Wong MCS, Huang J, Chan PSF, Choi P, Lao XQ, Chan SM, et al. Global incidence and mortality of gastric cancer, 1980–2018. *JAMA Netw Open*. (2021) 4(7):e2118457. doi: 10.1001/jamanetworkopen.2021.18457

2. Thrift AP, El-Serag HB. Burden of gastric cancer. *Clin Gastroenterol Hepatol*. (2020) 18(3):534–42. doi: 10.1016/j.cgh.2019.07.045

3. Smyth EC, Nilsson M, Grabsch HI, van Grieken NCT, Lordick F. Gastric cancer. *Lancet*. (2020) 396(10251):635–48. doi: 10.1016/s0140-6736(20)31288-5

4. Joshi SS, Badgwell BD. Current treatment and recent progress in gastric cancer. *CA Cancer J Clin*. (2021) 71(3):264–79. doi: 10.3322/caac.21657

5. Gewandter JS, McDermott MP, Mbowe O, Edwards RR, Katz NP, Turk DC, et al. Navigating trials of personalized pain treatments: we're going to need a bigger boat. *Pain*. (2019) 160(6):1235–9. doi: 10.1097/j.pain.0000000000001504

6. Petrillo A, Smyth EC. Biomarkers for precision treatment in gastric cancer. *Visc Med*. (2020) 36(5):364–72. doi: 10.1159/000510489

7. Strasser A, Vaux DL. Cell death in the origin and treatment of cancer. *Mol Cell*. (2020) 78(6):1045–54. doi: 10.1016/j.molcel.2020.05.014

8. Tang R, Xu J, Zhang B, Liu J, Liang C, Hua J, et al. Ferroptosis, necroptosis, and pyroptosis in anticancer immunity. *J Hematol Oncol*. (2020) 13(1):110. doi: 10.1186/s13045-020-00946-7

9. Tsvetkov P, Coy S, Petrova B, Dreishpoon M, Verma A, Abdusamad M, et al. Copper induces cell death by targeting lipoylated TCA cycle proteins. *Science*. (2022) 375(6586):1254–61. doi: 10.1126/science.abf0529

10. Zhang J, Kong X, Zhang Y, Sun W, Wang J, Chen M, et al. FDXR Regulates TP73 tumor suppressor via IRP2 to modulate aging and tumor suppression. *J Pathol*. (2020) 251(3):284–96. doi: 10.1002/path.5451

11. Arneth B. Tumor microenvironment. *Medicina (Kaunas)*. (2019) 56(1):15. doi: 10.3390/medicina56010015

12. Pan Y, Yu Y, Wang X, Zhang T. Tumor-Associated macrophages in tumor immunity. *Front Immunol*. (2020) 11:583084. doi: 10.3389/fimmu.2020.583084

13. Xia L, Oyang L, Lin J, Tan S, Han Y, Wu N, et al. The cancer metabolic reprogramming and immune response. *Mol Cancer*. (2021) 20(1):28. doi: 10.1186/s12943-021-01316-8

14. Martincorena I, Campbell PJ. Somatic mutation in cancer and Normal cells. *Science*. (2015) 349(6255):1483–9. doi: 10.1126/science.aab4082

15. Samstein RM, Lee CH, Shoushtari AN, Hellmann MD, Shen R, Janjigian YY, et al. Tumor mutational load predicts survival after immunotherapy across multiple cancer types. *Nat Genet*. (2019) 51(2):202–6. doi: 10.1038/s41588-018-0312-8

16. Baretti M, Le DT. DNA Mismatch repair in cancer. *Pharmacol Ther*. (2018) 189:45–62. doi: 10.1016/j.pharmthera.2018.04.004

17. da Silva DA, De Luca A, Squitti R, Rongioletti M, Rossi L, Machado CML, et al. Copper in tumors and the use of copper-based compounds in cancer treatment. *J Inorg Biochem*. (2022) 226:111634. doi: 10.1016/j.jinorgbio.2021.111634

18. Brady DC, Crowe MS, Turski ML, Hobbs GA, Yao X, Chaikuad A, et al. Copper is required for oncogenic BRAF signalling and tumorigenesis. *Nature*. (2014) 509(7501):492–6. doi: 10.1038/nature13180

19. Feng W, Ye F, Xue W, Zhou Z, Kang YJ. Copper regulation of hypoxia-inducible factor-1 activity. *Mol Pharmacol*. (2009) 75(1):174–82. doi: 10.1124/mol.108.051516

20. Baker AM, Bird D, Lang G, Cox TR, Erler JT. Lysyl oxidase enzymatic function increases stiffness to drive colorectal cancer progression through FAK. *Oncogene*. (2013) 32(14):1863–8. doi: 10.1038/onc.2012.202

21. Gupte A, Mumper RJ. Elevated copper and oxidative stress in cancer cells as a target for cancer treatment. *Cancer Treat Rev*. (2009) 35(1):32–46. doi: 10.1016/j.ctrv.2008.07.004

22. Liao Y, Zhao J, Bulek K, Tang F, Chen X, Cai G, et al. Inflammation mobilizes copper metabolism to promote colon tumorigenesis via an IL-17-STEAP4-XIAP axis. *Nat Commun*. (2020) 11(1):900. doi: 10.1038/s41467-020-14698-y

23. Zhu S, Shanbhag V, Wang Y, Lee J, Petris M. A role for the ATP7A copper transporter in tumorigenesis and cisplatin resistance. *J Cancer*. (2017) 8 (11):1952–8. doi: 10.7150/jca.19029

24. Mills CD. Anatomy of a discovery: m1 and m2 macrophages. *Front Immunol*. (2015) 6:212. doi: 10.3389/fimmu.2015.00212

25. Shapouri-Moghaddam A, Mohammadian S, Vazini H, Taghadosi M, Esmaeili SA, Mardani F, et al. Macrophage plasticity, polarization, and function in health and disease. *J Cell Physiol*. (2018) 233(9):6425–40. doi: 10.1002/jcp.26429

26. Funes SC, Rios M, Escobar-Vera J, Kalergis AM. Implications of macrophage polarization in autoimmunity. *Immunology*. (2018) 154(2):186–95. doi: 10.1111/imm.12910

27. Yunna C, Mengru H, Lei W, Weidong C. Macrophage M1/M2 polarization. *Eur J Pharmacol*. (2020) 877:173090. doi: 10.1016/j.ejphar.2020.173090

28. Kawaguchi K, Suzuki E, Nishie M, Kii I, Kataoka TR, Hirata M, et al. Downregulation of neuropilin-1 on macrophages modulates antibody-mediated tumoricidal activity. *Cancer Immunol Immunother*. (2017) 66(9):1131–42. doi: 10.1007/s00262-017-2002-2

29. Yan W, Liu X, Ma H, Zhang H, Song X, Gao L, et al. Tim-3 fosters HCC development by enhancing TGF-beta-mediated alternative activation of macrophages. *Gut*. (2015) 64(10):1593–604. doi: 10.1136/gutjnl-2014-307671

30. Tu D, Dou J, Wang M, Zhuang H, Zhang X. M2 macrophages contribute to cell proliferation and migration of breast cancer. *Cell Biol Int*. (2021) 45(4):831–8. doi: 10.1002/cbin.11528

31. Hinshaw DC, Shevde LA. The tumor microenvironment innately modulates cancer progression. *Cancer Res*. (2019) 79(18):4557–66. doi: 10.1158/0008-5472.CAN-18-3962

32. Maurer S, Kropp KN, Klein G, Steinle A, Haen SP, Walz JS, et al. Platelet-mediated shedding of NKG2D ligands impairs NK cell immune-surveillance of tumor cells. *Oncoimmunology*. (2018) 7(2):e1364827. doi: 10.1080/2162402X.2017.1364827

33. Noto CN, Hoft SG, DiPaolo RJ. Mast cells as important regulators in autoimmunity and cancer development. *Front Cell Dev Biol*. (2021) 9:752350. doi: 10.3389/fcell.2021.752350

34. Hempel Sullivan H, Maynard JP, Heaphy CM, Lu J, De Marzo AM, Lotan TL, et al. Differential mast cell phenotypes in benign versus cancer tissues and prostate cancer oncologic outcomes. *J Pathol*. (2021) 253(4):415–26. doi: 10.1002/path.5606

35. Hempel HA, Cuka NS, Kulac I, Barber JR, Cornish TC, Platz EA, et al. Low intratumoral mast cells are associated with a higher risk of prostate cancer recurrence. *Prostate*. (2017) 77(4):412–24. doi: 10.1002/pros.23280

36. Siiskonen H, Poukka M, Bykachev A, Tyynela-Korhonen K, Sironen R, Pasonen-Seppanen S, et al. Low numbers of tryptase+ and chymase+ mast cells associated with reduced survival and advanced tumor stage in melanoma. *Melanoma Res*. (2015) 25(6):479–85. doi: 10.1097/CMR.0000000000000192

37. Gu-Trantien C, Loi S, Garaud S, Equeter C, Libin M, de Wind A, et al. CD4(+) Follicular helper T cell infiltration predicts breast cancer survival. *J Clin Invest*. (2013) 123(7):2873–92. doi: 10.1172/JCI67428

38. Ning ZK, Hu CG, Huang C, Liu J, Zhou TC, Zong Z. Molecular subtypes and CD4(+) memory T cell-based signature associated with clinical outcomes in gastric cancer. *Front Oncol*. (2020) 10:626912. doi: 10.3389/fonc.2020.626912

39. Wouters MCA, Nelson BH. Prognostic significance of tumor-infiltrating B cells and plasma cells in human cancer. *Clin Cancer Res*. (2018) 24 (24):6125–35. doi: 10.1158/1078-0432.CCR-18-1481

40. Darvin P, Toor SM, Sasidharan Nair V, Elkord E. Immune checkpoint inhibitors: recent progress and potential biomarkers. *Exp Mol Med*. (2018) 50 (12):1–11. doi: 10.1038/s12276-018-0191-1

41. Iizuka A, Nonomura C, Ashizawa T, Kondou R, Ohshima K, Sugino T, et al. A T-cell-engaging B7-H4/CD3-bispecific Fab-scFv antibody targets human breast cancer. *Clin Cancer Res*. (2019) 25(9):2925–34. doi: 10.1158/1078-0432.CCR-17-3123

42. Liu JQ, Hu A, Zhu J, Yu J, Talebian F, Bai XF. CD200-CD200R pathway in the regulation of tumor immune microenvironment and immunotherapy. *Adv Exp Med Biol*. (2020) 1223:155–65. doi: 10.1007/978-3-030-35582-1_8

43. Qin S, Xu L, Yi M, Yu S, Wu K, Luo S. Novel immune checkpoint targets: moving beyond PD-1 and CTLA-4. *Mol Cancer*. (2019) 18(1):155. doi: 10.1186/s12943-019-1091-2

44. Janakiram M, Shah UA, Liu W, Zhao A, Schoenberg MP, Zang X. The third group of the B7-CD28 immune checkpoint family: HHLA2, TMIGD2, B7x, and B7-H3. *Immunol Rev*. (2017) 276(1):26–39. doi: 10.1111/imr.12521

45. Jiang P, Gu S, Pan D, Fu J, Sahu A, Hu X, et al. Signatures of T cell dysfunction and exclusion predict cancer immunotherapy response. *Nat Med*. (2018) 24(10):1550–8. doi: 10.1038/s41591-018-0136-1

46. Liu L, Bai X, Wang J, Tang XR, Wu DH, Du SS, et al. Combination of TMB and CNA stratifies prognostic and predictive responses to immunotherapy across metastatic cancer. *Clin Cancer Res*. (2019) 25(24):7413–23. doi: 10.1158/1078-0432.CCR-19-0558

47. Picard E, Verschoor CP, Ma GW, Pawelec G. Relationships between immune landscapes, genetic subtypes and responses to immunotherapy in colorectal cancer. *Front Immunol*. (2020) 11:369. doi: 10.3389/fimmu.2020.00369

48. Lambert SA, Jolma A, Campitelli LF, Das PK, Yin Y, Albu M, et al. The human transcription factors. *Cell*. (2018) 172(4):650–65. doi: 10.1016/j.cell.2018.01.029

frontiers | Frontiers in Surgery

TYPE Original Research
PUBLISHED 16 January 2023
DOI 10.3389/fsurg.2022.1096387

OPEN ACCESS

EDITED BY
Mengling Feng,
National University of Singapore, Singapore

REVIEWED BY
Albino Eccher,
Integrated University Hospital Verona, Italy
Stefano Marletta,
University of Verona, Italy

*CORRESPONDENCE
Bing Zheng
✉ ntzb2008@163.com

SPECIALTY SECTION
This article was submitted to Surgical Oncology, a section of the journal Frontiers in Surgery

†These authors have contributed equally to this work

RECEIVED 12 November 2022
ACCEPTED 13 December 2022
PUBLISHED 16 January 2023

CITATION
Pan Y, Shen C, Chen X, Cao D, Jiang J, Xu W, Ji C, Pan X and Zheng B (2023) bpMRI and mpMRI for detecting prostate cancer: A retrospective cohort study.
Front. Surg. 9:1096387.
doi: 10.3389/fsurg.2022.1096387

bpMRI and mpMRI for detecting prostate cancer: A retrospective cohort study

Yongsheng Pan[1†], Cheng Shen[1,2†], Xinfeng Chen[1], Dongliang Cao[1], Jie Jiang[1], Wei Xu[1,2], Chen Ji[1], Xiaodong Pan[1] and Bing Zheng[1*]

[1]Department of Urology, The Second Affiliated Hospital of Nantong University, Nantong, China, [2]Medical Research Center, The Second Affiliated Hospital of Nantong University, Nantong, China

Background: We aimed to compare the detection rates of prostate cancer (PCa) and clinically significant prostate cancer(csPCa) by biparametric (bp-) and multiparameter magnetic resonance imaging (mpMRI).

Materials and Methods: A total of 699 patients who underwent transperineal prostate biopsy in the Department of Urology, the Second Affiliated Hospital of Nantong University from January 2018 to December 2021 were retrospectively reviewed. Multivariate analysis was used to explore the influencing factors associated with the detection rates of PCa and csPCa. According to MRI examination before biopsy, the patients were divided into bpMRI group and mpMRI group. The detection rates of PCa and csPCa by bpMRI and mpMRI were compared. Furthermore, stratified analysis was performed for patients in these two groups to compare the detection rates of PCa and csPCa at different tPSA intervals, different prostate volume (PV) intervals and different PI-RADS V2 scores.

Results: A total of 571 patients were finally analyzed in this study after exclusion, and the overall detection rate of PCa was 54.5%. Multivariate analysis showed that patient age, tPSA level, prostate volume and PI-RADS V2 score were independent risk factors affecting the detection rates of PCa and csPCa. The detection rates of PCa and csPCa by bpMRI and mpMRI were comparable (51.3% vs. 57.9%, 44.0% vs. 48.0%, both $P > 0.05$), with no statistical significance. In the tPSA 10–20 ng/ml interval, the detection rates of PCa (59.72% vs. 40.35%, $P = 0.011$) and csPCa (51.39% vs. 28.82%, $P = 0.005$) by mpMRI were significantly higher than those by bpMRI, while in other tPSA interval (tPSA < 4 ng/ml, 4–10 ng/ml, 20–100 ng/ml), different PVs (≤30 ml, 30–60 ml, >60 ml) and different PI-RADS V2 scores (3, 4, and 5), the detection rates of PCa and csPCa were comparable between the two groups.

Conclusion: For detecting PCa and csPCa, bpMRI and mpMRI had similar diagnostic efficacies, whereas mpMRI detected more PCa and csPCa in the tPSA interval of 10–20 ng/ml.

KEYWORDS

biparametric magnetic resonance imaging, multiparameter magnetic resonance imaging, prostate cancer, clinically significant prostate cancer, prostate specific antigen

Introduction

Prostate cancer (PCa) is the second most common male malignant cancer worldwide, and its death rate ranks sixth (1). Nowadays, multiparameter magnetic resonance imaging (mpMRI) plays an important role in the detection of prostate cancer. Due to the application of mpMRI, the detection rates of PCa and clinically significant prostate cancer (csPCa) has significantly improved in the past decade (2–4).

The latest Prostate Image Reporting and Data System (PI-RADS) proposed that the DCE sequence (dynamic contrast enhancement) in mpMRI was with limited efficacy for diagnosing PCa sometimes (2). Only when the suspicious lesion is located in the peripheral zone of the prostate with a PI-RADS score of 3–4 in the T2WI sequence may it help increase the detection rate of csPCa. In clinical practice, some physicians only use the DCE sequence as an "insurance" sequence when the DWI sequence (diffusion weighted imaging) was not enough to make a definitive diagnosis of prostate cancer due to human factors or insufficient signal-to-noise ratio. In recent years, a number of studies have shown the positive effect of biparametric magnetic resonance imaging (bpMRI) on improving the detection rate of csPCa (5, 6). Though suggestions by the European Society of Urogenital Radiology to use complete multiparametric (mp) T2-weighted/diffusion weighted imaging(DWI)/dynamic contrast enhancement (DCE) acquisition for all prostate MRI examinations, the real advantage of functional DCE remains a matter of debate (7). Therefore, the PI-RADS Steering Committee supported the ongoing study of bpMRI in various clinical protocols and recognized the potential advantages of bpMRI, including the avoidance of contrast-related adverse reactions, shorter test times and lower costs (2).

In the present study, we analyzed the clinical data of 699 patients who underwent transperineal prostate biopsy in our center. The detection rates of PCa and csPCa by bpMRI and mpMRI were compared at different tPSA intervals, different prostate volumes and different PI-RADS V2 scores.

Materials and methods

Study design and study population

This is a retrospective study approved by the institutional review board and written informed consent was obtained from all patients. From January 2018 to December 2021, a total of 699 patients suspicious of prostate cancer (PSA $\geq$ 4 ng/ml, or abnormal digital rectal examination results, or abnormal ultrasound or MRI examination results) underwent transperineal prostate biopsy in our hospital. Patients with a previous prostate biopsy history or a prior diagnosis of prostate cancer were excluded.

Surgical method

In this study, all patients underwent transperineal prostate biopsy. They were placed in the lithotomy position, routinely disinfected, and draped with a sterile hole towel. Then 1% lidocaine was used for subcutaneous local infiltration anesthesia of the puncture site in the perineal region. The rectal ultrasound probe was placed in the rectum, and infiltration anesthesia deep to the extraprostatic capsule was done at the puncture site under direct ultrasound guidance. After that, combined cognitive MRI-targeted biopsy and systematic biopsy were performed using 18G puncture needle (model: MC1820, Bard Peripheral Vascular). Cognitive MRI-targeted biopsy was performed with 2 cores per targeted lesion, followed by 12-core systematic biopsy.

The outcomes

The primary outcome was to evaluate the detection rates of PCa and csPCa by bpMRI and mpMRI based on pathological results of prostate biopsies. The secondary outcome was to analyze the detection rates of PCa and csPCa by bpMRI and mpMRI stratified by tPSA level, PV (prostate volume), and PI-RADS score. In different tPSA intervals (<4 ng/ml, 4–10 ng/ml, 10–20 ng/ml, and 20–100 ng/ml), the detection rates of PCa and csPCa by bpMRI and mpMRI were compared. Prostate volume was calculated according to magnetic resonance imaging measurements (V = anteroposterior diameter * transverse diameter * longitudinal diameter * 0.52), and the detection rates of PCa and csPCa by bpMRI and mpMRI were compared in different PV intervals ($\leq$ 30 ml, 30–60 ml, and >60 ml). Also, the detection rates of PCa and csPCa by bpMRI and mpMRI were compared stratified by PI-RADS V2 scores (3, 4, and 5).

Histopathological evaluation and tumor significance

All biopsy samples were reviewed by the same genitourinary pathologist (>15 years of experience). For each prostate cancer-positive biopsy core, the location, Gleason score (GS) based on the International Society of Urological Pathology 2005 consensus (8), and percentage of cancerous tissue per core were determined. In addition, patients were allocated using the International Society of Urological Pathology 2014 consensus Gleason-grade groups (9) based on the GS scoring

criteria (8). In this study, csPCa was defined as ≥ Gleason score of 3 + 4 = 7.

Statistical analysis

In this study, SPSS 23.0 (IBM) software was used for statistical analysis, and patient characteristics were reported using descriptive statistical methods. Continuous variables such as age, PSA level, PSA density, and prostate volume were compared using the t-test. All continuous variables were expressed in the form of mean ± standard deviation, and the chi-square test was applied for categorical variables, $P < 0.05$ was considered statistically significant.

The results

Between January 2018 and December 2021, a total of 699 patients underwent transperineal prostate biopsies in our hospital. Of these 699 patients, 128 were excluded for various reasons (**Figure 1**), such as 53 patients without complete tPSA and fPSA values, 34 patients with tPSA level greater than 100 ng/ml, 31 patients without MRI examination, 5 patients with PI-RADS V2 of 1 or 2, and 5 patients with biopsy pathological results of non-adenocarcinoma type. The remaining 571 patients met the study inclusion criteria and were available for the final analysis. The baseline characteristics of the patients are provided in **Supplementary Table S1**, and statistical tests revealed that the bpMRI group and mpMRI group did not have a significant difference regarding age, tPSA levels, PV, PSA density (PSAD), and PI-RADS V2 score (all $P > 0.05$). The overall detection rates of PCa and csPCa were comparable between the bpMRI group and mpMRI group (51.3% vs. 57.9%, 44.0% vs. 48.0%, both $P > 0.05$), with no statistical significance.

The results of multivariate analysis showed that patients' age, tPSA level, PV, and PI-RADS V2 score were independent risk factors for PCa and csPCa detection (all $P < 0.05$), regardless of MRI patterns ($P > 0.05$) (**Supplementary Tables S2, S3**). Based on the results of multivariate analysis, we chosed three independent risk factors responsible for the detection of PCa and csPCa, tPSA level, PV, and PI-RADS V2 score, for further analysis. According to tPSA levels, patients were divided into four subgroups tPSA < 4 ng/ml, 4 ≤ tPSA ≤ 10 ng/ml, 10 < tPSA ≤ 20 ng/ml, and 20 < tPSA ≤ 100 ng/ml. The results (**Supplementary Table S4**) showed that in the tPSA 10–20 ng/ml interval, the detection rates of PCa (59.72% vs. 40.35%, $P = 0.0109$) and csPCa (51.39% vs. 28.82%, $P = 0.0129$) by mpMRI were significantly higher than those by bpMRI, while in other tPSA intervals (tPSA < 4 ng/ml, 4–10 ng/ml, 20–100 ng/ml), the detection rates of PCa and csPCa by bpMRI and mpMRI were comparable (all $P > 0.05$), with no statistical significance (all $P > 0.05$).

In this study, prostate volumes were calculated based on MRI measurements. In order to compare the detection rates of PCa and csPCa by bpMRI and mpMRI in different prostate volume intervals, patients were divided into three subgroups, PV ≤ 30 ml, 30–60 ml, and >60 ml. However, the results (**Supplementary Table S5**) showed that the detection rates of PCa and csPCa are comparable between the bpMRI and mpMRI group in different prostate volume intervals (all $P > 0.05$), with no statistical significance. In addition, we also found that the detection rates of PCa and csPCa by bpMRI and mpMRI were comparable at different PI-RADS V2 scores (3, 4, and 5) (all $P > 0.05$), with no statistical significance (**Supplementary Table S6**).

Discussion

In recent years, MRI-fusion biopsy has been widely used for diagnosis of prostate cancer in clinical practice, improving the detection rate of clinically significant prostate cancer (10). With the increasing demand for MRI of the prostate, doubts have been raised about whether a comprehensive examination can be obtained while saving time and cost. We all know that the use of dynamic contrast-enhanced imaging (DCE) requires intravenous contrast, which prolongs the time of MRI examination, increases the cost burden for patients, and may even cause contrast-related adverse effects. Alternatively, the examination can be completed in less than 15 min utilizing a bpMRI pattern, making imaging non-traumatic (11, 12). At present, more and more studies have evaluated the diagnostic efficacies of bpMRI and mpMRI methods, and many authors emphasize that the diagnostic efficiency of the two regimens is overlapping (13–15). The results of a multicenter multi-reader trial (PROMIS) showed no significant difference between bpMRI and mpMRI in excluding csPCa (16). As stated in the PIRADS Committee position paper, MRI quality is critical in the bp approach because image quality is sufficient to detect or exclude csPCa (17, 18).

In the present study, we analyzed the detection rates of PCa and csPCa in 571 men who underwent bpMRI or mpMRI, and found that the detection rates of PCa and csPCa by the two MRI modalities were comparable and with no statistical significance. These results suggest that bpMRI can also be used as one of the auxiliary diagnostic modality for prostate cancer, and the diagnostic efficiency of bpMRI for PCa and csPCa is not inferior to that of mpMRI.

As recommended by the PIRADS committee, the current role of DCE is limited to type 3 lesions to determine the nature of equivocal lesions (7). Although the sensitivity of DCE is high, but its specificity may be low. High sensitivity is true positive because it means the proportion of positives

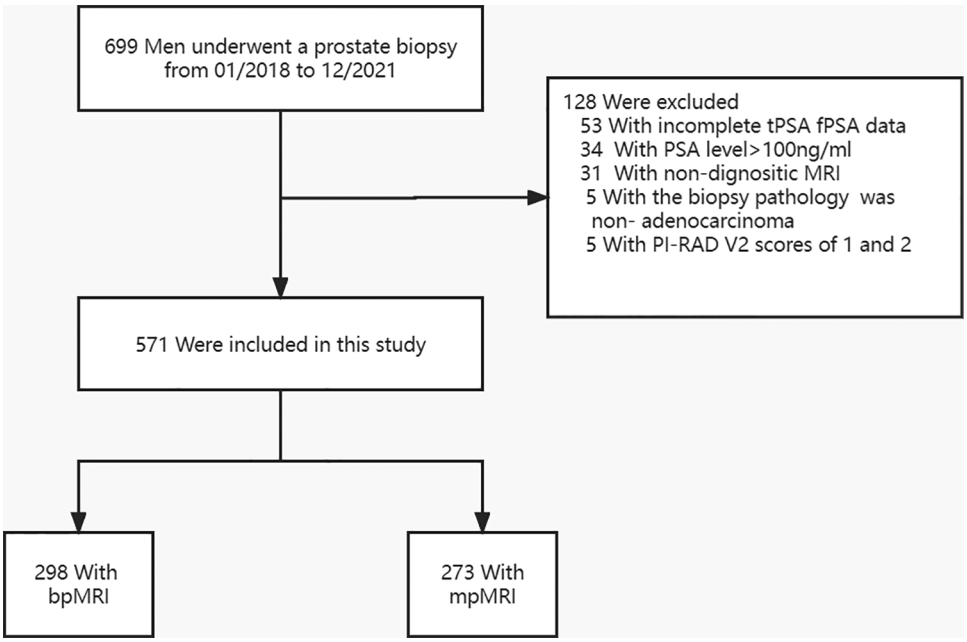

FIGURE 1
Flowchart of the study population. mpMRI, multiparametric magnetic resonance imaging; bpMRI, Biparametric magnetic resonance imaging; tPSA, Total prostate-specific antigen; fPSA, Free prostate-specific antigen; PI-RADS V2, Prostate Imaging Report Data System, version 2.

correctly identified, while specificity is true negative, which means positive results have the possibility of false positives and additional biopsies may be required. Some investigators have found that mpMRI-based diagnostic modality for prostate cancer may lead to more false-positive results (12, 19). In clinical practice, reducing false positive results of MRI means decreasing prostate biopsies in patients, which can reduce the biopsy-related complications such as pain, bleeding, infection, etc. and avoid overdiagnosis and overtreatment. In addition, Kuhl et al. found no significant difference in the diagnostic accuracy of bpMRI and mpMRI in repeated biopsies of 542 men with elevated PSA values (20, 21), which further suggested that the use of bpMRI with diagnostic specificity as an auxiliary modality for prostate cancer may be able to decrease unnecessary prostate biopsies.

Since the diagnostic performance of the bpMRI method is not inferior to that of the mpMRI, the application of the bpMRI method requires high image quality and reader expertise (7). In this study, we retrospectively analyzed the clinical data of 699 patients who underwent prostate biopsy from January 2018 to March 2021. The effect of baseline data of patients on the positive rate of biopsy was analyzed. According to the MRI examination before biopsy, the patients were divided into bpMRI group and mpMRI group, and baseline characteristics between the two groups were comparable. Stratified analysis was performed for patients in the two groups according to tPSA levels, PVs and PI-RADS V2 scores to compare the detection rates of PCa and csPCa by bpMRI and mpMRI. The results of stratified analysis showed that in the tPSA 10–20 ng/ml interval, the detection rate of PCa (58.1% vs. 31.7%, $P = 0.004$) and csPCa (46.8% vs. 20.6%, $P = 0.002$) by mpMRI were significantly higher than those by bpMRI; in the other tPSA intervals, the detection rates of the two MRI modalities were comparable, with no statistical significance. Our study indicates that when patients' tPSA values are in the 10–20 ng/ml interval, they should undergo mpMRI examination which may improve the detection rates of PCa and csPCa. While in other tPSA intervals, they can only undergo bpMRI examinations for detecting PCa and csPCa instead of mpMRI examinations. We speculate that this difference may be due to the fact that prostate cancer lesions do not perform significantly on bpMRI images in the tPSA 10–20 ng/ml interval, while the addition of DCE sequences can improve the sensitivity of interpretation of suspicious lesions. However, it needs to be further studied.

As we all know, the tPSA 4–10 ng/ml is a gray area for prostate cancer determination. When patients' tPSA values is in the gray area, it is often necessary to refer to fPSA and other PSA-related derived indicators such as f/tPSA, PSAD and PSAV (PSA rate) [20]. We supposed mpMRI had higher diagnostic efficiency of PCa and csPCa in the tPSA gray area compared to bpMRI, while further analysis revealed that mpMRI was not superior to bpMRI in this tPSA interval. In

addition, in other tPSA intervals (tPSA < 4 ng/ml, 20–100 ng/ml), different PVs (≤30 ml, 30–60 ml, >60 ml), and different PI-RADS V2 scores (3, 4, and 5), the detection rates of PCa and csPCa were comparable between the two groups, and the difference was not statistically significant.

Limitations

Our study has some limitations (1). This was a single-center retrospective study with a relatively small number of patients, and the current results should be validated in a prospective multicenter clinical trial (2). In this study, patients were divided into the bpMRI group and mpMRI group according to MRI modalities before biopsy. However, the image interpretation of bpMRI and mpMRI was not performed for the same patients undergoing mpMRI examination, respectively. In further studies, the image interpretation of bpMRI and mpMRI could be performed for the same patient to compare the detection rates of PCa and csPCa between the two MRI modalities.

Despite these limitations, our findings validate bpMRI as an alternative to mpMRI for detecting PCa and csPCa in clinical practice. Besides, as a more rapid and simple modality, bpMRI is feasible in our center.

Conclusion

The overall detection rates of PCa and csPCa by bpMRI and mpMRI were comparable, but mpMRI detected more PCa and csPCa in the tPSA interval of 10–20 ng/ml. In other tPSA intervals, bpMRI could be an alternative to mpMRI for detecting PCa and csPCa, regardless of different prostate volumes and PI-RADS scores.

Data availability statement

The original contributions presented in the study are included in the article/**Supplementary Material**, further inquiries can be directed to the corresponding author/s.

Ethics Statement

The Institutional Review Board of the Second Affiliated Hospital of Nantong University approved this study, and all patients who participated signed an informed consent. All patients participating in the study were informed and written informed consent was obtained. The study was approved by The Second Affiliated Hospital of Nantong University Ethics Committee, according to the Declaration of Helsinki.

Author contributions

PYS: Project development, Data collection or management, Data analysis,Manuscript writing. SC: Project development, Data collection or management, Data analysis,Manuscript writing. CXF: Data collection or management, Data analysis. CDL: Data collection or management, Data analysis. JJ: Data collection or management, Data analysis. XW: Data collection or management, Data analysis. JC: Data collection or management, Data analysis. PXD: Data collection or management, Data analysis. ZB: Project development, Data analysis, Manuscript editing. All authors contributed to the article and approved the submitted version.

Funding

This study was supported in part by Jiangsu Provincial Cadre Health Research Project (BJ21010), Nantong Health Committee Research Project (QA2020010), Jiangsu Geriatric Health Research Project (LKM2022059).

Conflict of interest

The authors declare that the research was conducted in the absence of any commercial or financial relationships that could be construed as a potential conflict of interest.

Publisher's note

Supplementary material

The Supplementary Material for this article can be found online at: https://www.frontiersin.org/articles/10.3389/fsurg.2022.1096387/full#supplementary-material.

References

1. Jemal A, Bray F, Center MM, Ferlay J, Ward E, Forman D. Global cancer statistics. *CA Cancer J Clin*. (2011) 61:69–90. doi: 10.3322/caac.20107

2. Turkbey B, Rosenkrantz AB, Haider MA, Padhani AR, Villeirs G, Macura KJ, et al. Prostate imaging reporting and data system version 2.1: 2019 update of prostate imaging reporting and data system version 2. *Eur Urol*. (2019) 76:340–51. doi: 10.1016/j.eururo.2019.02.033

3. Ahmed HU, El-Shater Bosaily A, Brown LC, Gabe R, Kaplan R, Parmar MK, et al. Diagnostic accuracy of multi-parametric MRI and TRUS biopsy in prostate cancer (PROMIS): a paired validating confirmatory study. *Lancet*. (2017) 389:815–22. doi: 10.1016/S0140-6736(16)32401-1

4. Dickinson L, Ahmed HU, Allen C, Barentsz JO, Carey B, Futterer JJ, et al. Magnetic resonance imaging for the detection, localisation, and characterisation of prostate cancer: recommendations from a European consensus meeting. *Eur Urol*. (2011) 59:477–94. doi: 10.1016/j.eururo.2010.12.009

5. Boesen L, Nørgaard N, Løgager V, Balslev I, Bisbjerg R, Thestrup K-C, et al. Assessment of the diagnostic accuracy of biparametric magnetic resonance imaging for prostate cancer in biopsy-naive men: the biparametric MRI for detection of prostate cancer (BIDOC) study. *JAMA Netw Open*. (2018) 1: e180219. doi: 10.1001/jamanetworkopen.2018.0219

6. Jambor I, Boström PJ, Taimen P, Syvänen K, Kähkönen E, Kallajoki M, et al. Novel biparametric MRI and targeted biopsy improves risk stratification in men with a clinical suspicion of prostate cancer (IMPROD trial): biparametric MRI in men with suspicion of PCa. *J Magn Reson Imaging*. (2017) 46:1089–95. doi: 10.1002/jmri.25641

7. Palumbo P, Manetta R, Izzo A, Bruno F, Arrigoni F, De Filippo M, et al. Biparametric (bp) and multiparametric (mp) magnetic resonance imaging (MRI) approach to prostate cancer disease: a narrative review of current debate on dynamic contrast enhancement. *Gland Surg*. (2020) 9:2235–47. doi: 10.21037/gs-20-547

8. Epstein JI, Allsbrook WC, Amin MB, Egevad LL, ISUP Grading Committee. The 2005 international society of urological pathology (ISUP) consensus conference on gleason grading of prostatic carcinoma. *Am J Surg Pathol*. (2005) 29:1228–42. doi: 10.1097/01.pas.0000173646.99337.b1

9. Epstein JI, Egevad L, Amin MB, Delahunt B, Srigley JR, Humphrey PA, et al. The 2014 international society of urological pathology (ISUP) consensus conference on gleason grading of prostatic carcinoma: definition of grading patterns and proposal for a new grading system. *Am J Surg Pathol*. (2016) 40:244–52. doi: 10.1097/PAS.0000000000000530

10. Kasivisvanathan V, Rannikko AS, Borghi M, Panebianco V, Mynderse LA, Vaarala MH, et al. MRI-Targeted or standard biopsy for prostate-cancer diagnosis. *N Engl J Med*. (2018) 378:1767–77. doi: 10.1056/NEJMoa1801993

11. Stanzione A, Imbriaco M, Cocozza S, Fusco F, Rusconi G, Nappi C, et al. Biparametric 3 T magnetic resonance imaging for prostatic cancer detection in a biopsy-naïve patient population: a further improvement of PI-RADS v2? *Eur J Radiol*. (2016) 85:2269–74. doi: 10.1016/j.ejrad.2016.10.009

12. van der Leest M, Israël B, Cornel EB, Zámecnik P, Schoots IG, van der Lelij H, et al. High diagnostic performance of short magnetic resonance imaging protocols for prostate cancer detection in biopsy-naïve men: the next step in magnetic resonance imaging accessibility. *Eur Urol*. (2019) 76:574–81. doi: 10.1016/j.eururo.2019.05.029

13. Scialpi M, Prosperi E, D'Andrea A, Martorana E, Malaspina C, Palumbo B, et al. Biparametric versus multiparametric MRI with non-endorectal coil at 3 T in the detection and localization of prostate cancer. *Anticancer Res*. (2017) 37:1263–71. doi: 10.21873/anticanres.11443

14. Bosaily AE-S, Frangou E, Ahmed HU, Emberton M, Punwani S, Kaplan R, et al. Additional value of dynamic contrast-enhanced sequences in multiparametric prostate magnetic resonance imaging: data from the PROMIS study. *Eur Urol*. (2020) 78:503–11. doi: 10.1016/j.eururo.2020.03.002

15. Rosenkrantz AB, Verma S, Turkbey B. Prostate cancer: top places where tumors hide on multiparametric MRI. *AJR Am J Roentgenol*. (2015) 204: W449–456. doi: 10.2214/AJR.14.13280

16. Woo S, Suh CH, Kim SY, Cho JY, Kim SH, Moon MH. Head-to-Head comparison between biparametric and multiparametric MRI for the diagnosis of prostate cancer: a systematic review and meta-analysis. *AJR Am J Roentgenol*. (2018) 211:W226–41. doi: 10.2214/AJR.18.19880

17. Giganti F, Allen C, Emberton M, Moore CM, Kasivisvanathan V, PRECISION study group. Prostate imaging quality (PI-QUAL): a new quality control scoring system for multiparametric magnetic resonance imaging of the prostate from the PRECISION trial. *Eur Urol Oncol*. (2020) 3:615–9. doi: 10.1016/j.euo.2020.06.007

18. de Rooij M, Israël B, Tummers M, Ahmed HU, Barrett T, Giganti F, et al. ESUR/ESUI consensus statements on multi-parametric MRI for the detection of clinically significant prostate cancer: quality requirements for image acquisition, interpretation and radiologists' training. *Eur Radiol*. (2020) 30:5404–16. doi: 10.1007/s00330-020-06929-z

19. Kang Z, Min X, Weinreb J, Li Q, Feng Z, Wang L. Abbreviated biparametric versus standard multiparametric MRI for diagnosis of prostate cancer: a systematic review and meta-analysis. *AJR Am J Roentgenol*. (2019) 212:357–65. doi: 10.2214/AJR.18.20103

20. Valerio M, Donaldson I, Emberton M, Ehdaie B, Hadaschik BA, Marks LS, et al. Detection of clinically significant prostate cancer using magnetic resonance imaging-ultrasound fusion targeted biopsy: a systematic review. *Eur Urol*. (2015) 68:8–19. doi: 10.1016/j.eururo.2014.10.026

21. Gayet M, van der Aa A, Beerlage HP, Schrier BP, Mulders PFA, Wijkstra H. The value of magnetic resonance imaging and ultrasonography (MRI/US)-fusion biopsy platforms in prostate cancer detection: a systematic review. *BJU Int*. (2016) 117:392–400. doi: 10.1111/bju.13247

frontiers | Frontiers in Surgery

TYPE Original Research
PUBLISHED 18 January 2023
DOI 10.3389/fsurg.2022.975690

OPEN ACCESS

EDITED BY
Kee Yuan Ngiam,
National University Health System (Singapore), Singapore

REVIEWED BY
Agata Janowska,
University of Pisa, Italy
Anurag Srivastava,
National Institute of Cancer Prevention and Research (ICMR), India

*CORRESPONDENCE
Yu Jin
✉ cdyxyjy@126.com

†These authors have contributed equally to this work and share first authorship

SPECIALTY SECTION
This article was submitted to Surgical Oncology, a section of the journal Frontiers in Surgery

RECEIVED 22 June 2022
ACCEPTED 30 December 2022
PUBLISHED 18 January 2023

CITATION
Li Z, Wei J, Zheng H, Zhang Y, Zhang Y, Cao H and Jin Y (2023) Construction, validation and, visualization of a web-based nomogram to identify the best candidates for primary tumor resection in advanced cutaneous melanoma patients.
Front. Surg. 9:975690.
doi: 10.3389/fsurg.2022.975690

Construction, validation and, visualization of a web-based nomogram to identify the best candidates for primary tumor resection in advanced cutaneous melanoma patients

Zhehong Li[1,2†], Junqiang Wei[1†], Honghong Zheng[3], Yafang Zhang[1], Yange Zhang[1], Haiying Cao[1] and Yu Jin[1*]

[1]Traumatology and Orthopaedics, Affiliated Hospital of Chengde Medical University, Chengde, China, [2]Department of General Surgery, Beijing Shijitan Hospital, Capital Medical University, Beijing, China, [3]General Surgery, Affiliated Hospital of Chengde Medical University, Chengde, China

Background: Existing studies have shown whether primary site resection (PSR) in cutaneous melanoma (CM) patients with stage IV is controversial. Our study aimed to identify the clinical characteristics of CM patients with stage IV who benefited from PSR on a population-based study.

Methods: We retrospectively reviewed stage IV CM patients in the Surveillance, Epidemiology, and End Results (SEER) database from 2004 to 2015. Patients were divided into surgical and non-surgical groups according to whether PSR was performed or not. According to the median cancer-specific survival (CSS) time of the non-surgery group, the surgical group was divided into the surgery-benefit group and the non-surgery-benefit group. Multivariate cox regression analysis was used to explore independent CSS prognostic factors in the surgical group. Then, based on the independent prognostic factors of the surgical group, we established a web-based nomogram based on logistics regression.

Results: A total of 574 stage IV CM patients were included in our study, and 491 (85.60%) patients were included in the surgical group. The clinical characteristics (benefit group and non-benefit group) included age, M stage, lesion location, and ulceration status. These independent prognostic factors were includeed to construct a web-based nomogram.

Conclusions: We constructed a web-based nomogram. This model was suitable for identifying the best candidates suitable for PSR in stage IV CM patients.

KEYWORDS

cutaneous melanoma, stage IV, surgery, nomogram, SEER database

Introduction

Cutaneous melanoma (CM) is a highly aggressive malignant tumor that originates from melanocytes (1). Global Cancer Statistics demonstrated that 324,635 new CM individuals were diagnosed and 57,043 deaths for the disease worldwide in 2020 (2). Although the five-year survival rate for CM patients with stage I-III is high [Five-year cancer-specific survival (CSS)

Abbreviations

CM, skin cutaneous melanoma; SEER, Surveillance, Epidemiology, and End Results; CSS, cancer-specific survival; OS, Overall survival; HRs, Hazard Ratios; CIs, confidence intervals; AUC, area under the curve; ROC, receiver operating characteristic; DCA, Decision curve analysis; K-M, Kaplan-Meier; CNS, central nervous system; LDH, lactate dehydrogenase; CTLA-4, cytotoxic T lymphocyte antigen 4; PD-1, programmed death 1; BRAF, B-Raf proto-oncogene; MEK, mitogen-activated protein kinase.

for cutaneous melanoma at stage I, II, and III was 98%, 90%, 77%], the five-year survival rate for stage IV CM patients is less than 20% (3, 4). In the past period, based on further understanding of the molecular pathogenesis of melanoma, significant changes have taken place in the treatment of advanced CM patients. The application of immunotherapy [e.g., checkpoint inhibitors against cytotoxic T lymphocyte antigen 4 (CTLA-4) and/or programmed death 1 (PD-1)], molecular targeted anti-tumor therapy [B-Raf proto-oncogene (BRAF), mitogen-activated protein kinase (MEK)], and neoadjuvant therapy has greatly improved the survival prognosis of CM patients(1, 5–7). However, for stage IV CM patients, the primary site resection (PSR) is controversial because it is a local treatment for a systemic disease (8). Based on the metastatic potential of CM, PSR for stage IV CM is unsatisfactory, and therefore many scholars do not recommend surgery for stage IV CM patients (9, 10). However, another part of the scholars' research showed that the prognosis of stage IV CM patients could be improved by PSR or metastatic lesions surgery(11–13). Therefore, there is still some controversy about whether patients with stage IV melanoma should perform PSR. PSR in stage IV lung cancer patients is also controversial. However, a recent retrospective study has suggested that stage IV lung cancer patients with specific clinicopathological features may benefit from PSR (14). Inspired by these conclusions, we also came up with a new idea that not all stage IV CM patients will benefit from PSR, and patients with specific characteristics can benefit from PSR.

However, large-scale population-based studies are still lacking, and it is clinically significant to screen for the types of patients who would benefit from PSR. Therefore, we aimed to analyze the stage IV CM patients in the Surveillance, Epidemiology, and End Results (SEER) database and establish a web-based nomogram to identify the best candidates for PSR and their characteristics.

Methods

Patients

We obtained permission to access these study data (15708-Nov2020). The inclusion criteria were: patients diagnosed with stage IV CM between 2004 and 2015 with complete follow-up data. Exclusion criteria were as follows: age less than 18 years, Race unknown, TNM stage unknown, treatment unknown, mitotic status unknown, not the first tumor. We obtained

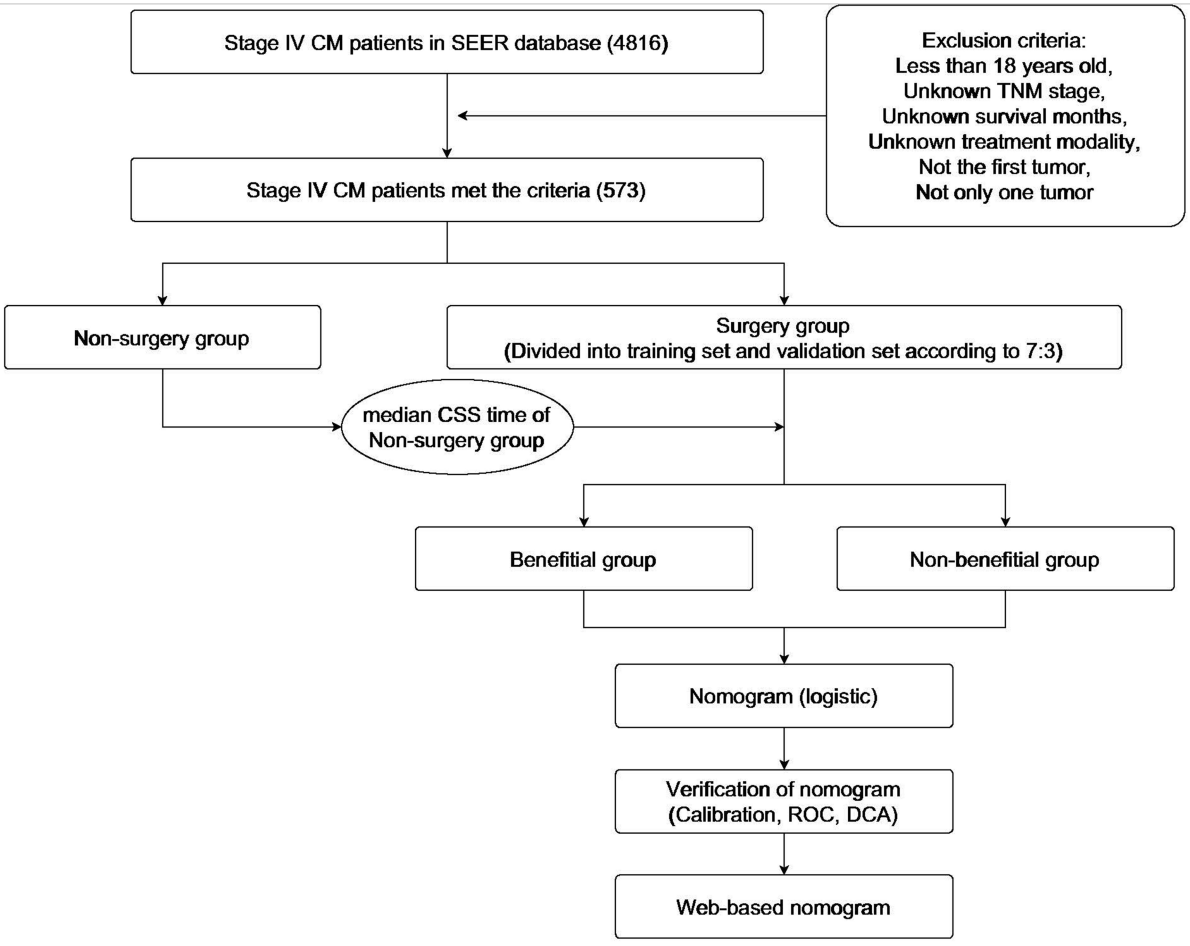

FIGURE 1
The design idea and workflow.

TABLE 1 Demographic information for stage IV melanoma patients.

	All patients	Surgery to primary site (*n*, %)		Non-surgery to primary site (*n*, %)		χ^2/t	*p*-value
Age						0.924	0.356
Mean	63.07	64.52		62.85			
SD	15.17	13.47		15.43			
Race						0.602	0.740
White	549	470	95.72	79	96.34		
Black	13	12	2.44	1	1.22		
Other	11	9	1.83	2	2.44		
Sex						0.304	0.581
Female	167	141	28.72	26	31.71		
Male	406	350	71.28	56	68.29		
Location						1.959	0.743
Head and neck	150	132	26.88	18	21.95		
Trunk	209	179	36.46	30	36.59		
Upper limb and shoulder	87	75	15.27	12	14.63		
Lower limb and hip	111	91	18.53	20	24.39		
Others	16	14	2.85	2	2.44		
Subtype of melanoma						19.128	<0.001
Malignant melanoma	263	208	42.36	55	67.07		
Nodular	185	173	35.23	12	14.63		
Superficial spreading	50	44	8.96	6	7.32		
Others	75	66	13.44	9	10.98		
T stage						1.908	0.592
T1	87	71	14.46	16	19.51		
T2	88	74	15.07	14	17.07		
T3	112	98	19.96	14	17.07		
T4	286	248	50.51	38	46.34		
N stage						0.887	0.829
N0	227	195	39.71	32	39.02		
N1	160	136	27.70	24	29.27		
N2	71	59	12.02	12	14.63		
N3	115	101	20.57	14	17.07		
M stage						6.332	0.042
M1a	125	110	22.40	15	18.29		
M1b	103	95	19.35	8	9.76		
M1c	345	286	58.25	59	71.95		
Ulceration						0.827	0.363
No	178	149	30.35	29	35.37		
Yes	395	342	69.65	53	64.63		
Mitotic rate						4.083	0.130
<1	436	367	74.75	69	84.15		

(*continued*)

TABLE 1 Continued

	All patients	Surgery to primary site (*n*, %)		Non-surgery to primary site (*n*, %)		χ^2/t	*p*-value
=1	100	92	18.74	8	9.76		
≥2	37	32	6.52	5	6.10		
Radiation						3.542	0.060
No	400	350	71.28	50	60.98		
Yes	173	141	28.72	32	39.02		
Chemotherapy						0.446	0.504
No	409	353	71.89	56	68.29		
Yes	164	138	28.11	26	31.71		

baseline data from the SEER database, including patient information (age, sex, and race), melanoma characteristics TNM stage (AJCC 7th Edition Melanoma), location, histological type, mitotic rate, and ulceration), and surgery (primary site resection). CSS was defined as the time from diagnosis to death because of the CM. According to whether the PSR was performed or not, Patients were divided into surgical and non-surgical groups. Based on the median CSS time (8 months) of the non-surgical group, we divided the surgical sets into the surgical beneficial and the surgical non-profitable groups.

Statistical analysis

We used t-tests and chi-square tests for comparing continuous and categorical variables, respectively. Multivariate Cox regression analysis was performed to identify independent prognostic factors associated with CSS. Hazard Ratios (HRs) with 95% confidence intervals (CIs) for each factor were calculated. Statistical analyses were performed by R software (version 4.0.3), all statistical tests were two-sided, and *p*-value <0.05 was considered statistically significant.

Construction, validation, and visualization of a web-based nomogram

Zhang et al. have demonstrated that patients with PSR have a longer median CSS time than those who did not undergo surgery (13). Based on this conclusion, patients who underwent PSR were randomly divided 7:3 into training and validation sets by the "caret" package. We build a logistics-model nomogram based on the independent prognostic factors of CSS. We use the area under the curve (AUC) of the receiver operating characteristic curve (ROC), the calibration curve, and the decision curve analysis (DCA) to evaluate the discriminative ability and accuracy of the nomogram both in training and validation sets. Then, a web-based nomogram was performed using the "Dynnom" package. Finally, based on the results of our prediction model, we divided all patients into three groups, the surgery & beneficial group (probability of benefit >50%), the surgery & non-beneficial group (probability of benefit <50%), and the non-surgical group. The patients in the three groups were analyzed by Kaplan-Meier (K-M), and log-rank tests were calculated. All statistical analyses and image visualizations were performed using R software (version 4.0.3).

Results

Patients clinicopathological characteristics

We identified 573 patients with stage IV CM who met the criteria from the SEER database (see Figure 1). Of these eligible patients, 491 (85.69%) received PSR. Through t-test for age, chi-square test for sex, race, location, histological type, TNM stage, ulceration, and mitosis rate. Patients' clinicopathological data in the surgical and non-surgical groups were relatively balanced ($p > 0.05$). The results showed that the clinicopathological characteristics of the two sets (surgical and non-surgical groups) were comparable (Table 1).

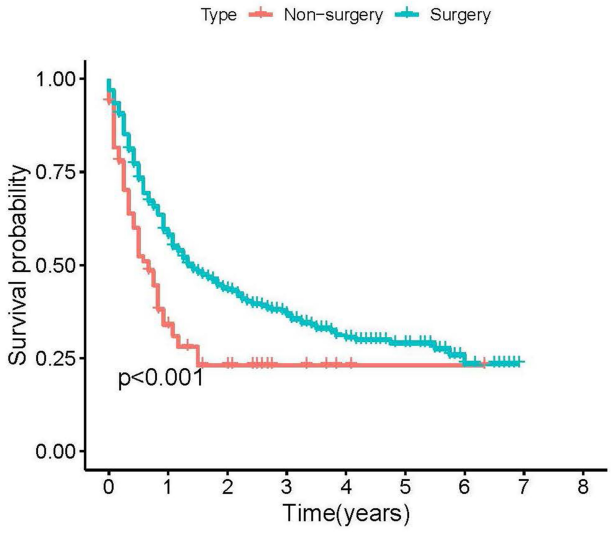

FIGURE 2
Kaplan-Meier plots of stage IV cutaneous melanoma patients according to primary site resection for cancer-specific survival.

TABLE 2 Clinicopathological characteristics of training set and validation set.

	Training set (*n*, %)		Validation set (*n*, %)		χ^2/t	*p*-value
Age					1.315	0.189
Mean	63.44		61.43			
SD	15.21		15.93			
Race					0.986	0.611
White	334	96.25	136	94.44		
Black	7	2.02	5	3.47		
Other	6	1.73	3	2.08		
Sex					0.088	0.767
Female	101	29.11	40	27.78		
Male	246	70.89	104	72.22		
Location					3.490	0.479
Head and neck	93	26.80	39	27.08		
Trunk	126	36.31	53	36.81		
Upper limb and shoulder	52	14.99	23	15.97		
Lower limb and hip	63	18.16	28	19.44		
Others	13	3.75	1	0.69		
Subtype of melanoma					2.384	0.497
Malignant melanoma	145	41.79	63	43.75		
Nodular	118	34.01	55	38.19		
Superficial spreading	33	9.51	11	7.64		
Others	51	14.70	15	10.42		
T stage					2.532	0.47
T1	53	15.27	18	12.50		
T2	50	14.41	24	16.67		
T3	74	21.33	24	16.67		
T4	170	48.99	78	54.17		
N stage					6.366	0.095
N0	149	42.94	46	31.94		
N1	93	26.80	43	29.86		
N2	36	10.37	23	15.97		
N3	69	19.88	32	22.22		
M stage					0.470	0.791
M1a	75	21.61	35	24.31		
M1b	67	19.31	28	19.44		
M1c	205	59.08	81	56.25		
Ulceration					0.023	0.88
No	106	30.55	43	29.86		
Yes	241	69.45	101	70.14		
Mitotic rate					0.449	0.799
<1	260	74.93	107	74.31		
=1	66	19.02	26	18.06		
≥2	21	6.05	11	7.64		

TABLE 3 Multivariate Cox analysis for CSS among population of surgery to primary site.

	Adjust HR	95%CI	*p*-value
Age	1.011	1.001–1.021	0.027
Race			
White	Reference		
Black	1.57	0.703–3.507	0.271
Other	1.761	0.604–5.319	0.300
Sex			
Female	Reference		
Male	1.033	0.751–1.419	0.843
Location			
Head and neck	Reference		
Trunk	1.675	1.144–2.451	0.008
Upper limb and shoulder	1.683	1.064–2.660	0.026
Lower limb and hip	1.535	0.959–2.458	0.074
Others	1.736	0.851–3.540	0.129
Subtype of melanoma			
Malignant melanoma	Reference		
Nodular	1.055	0.755–1.475	0.754
Superficial spreading	1.234	0.729–2.087	0.434
Others	1.074	0.697–1.654	0.746
T stage			
T1	Reference		
T2	0.892	0.521–1.528	0.678
T3	0.787	0.479–1.294	0.345
T4	0.863	0.547–1.362	0.528
N stage			
N0	Reference		
N1	0.875	0.608–1.258	0.47
N2	0.745	0.436–1.274	0.282
N3	1.088	0.736–1.610	0.672
M stage			
M1a	Reference		
M1b	1.671	0.980–2.851	0.059
M1c	3.694	2.361–5.779	<0.001
Ulceration			
No	Reference		
Yes	1.441	1.030–2.014	0.033
Mitotic rate			
<1	Reference		
=1	1.053	0.733–1.513	0.78
≥2	0.829	0.427–1.610	0.58

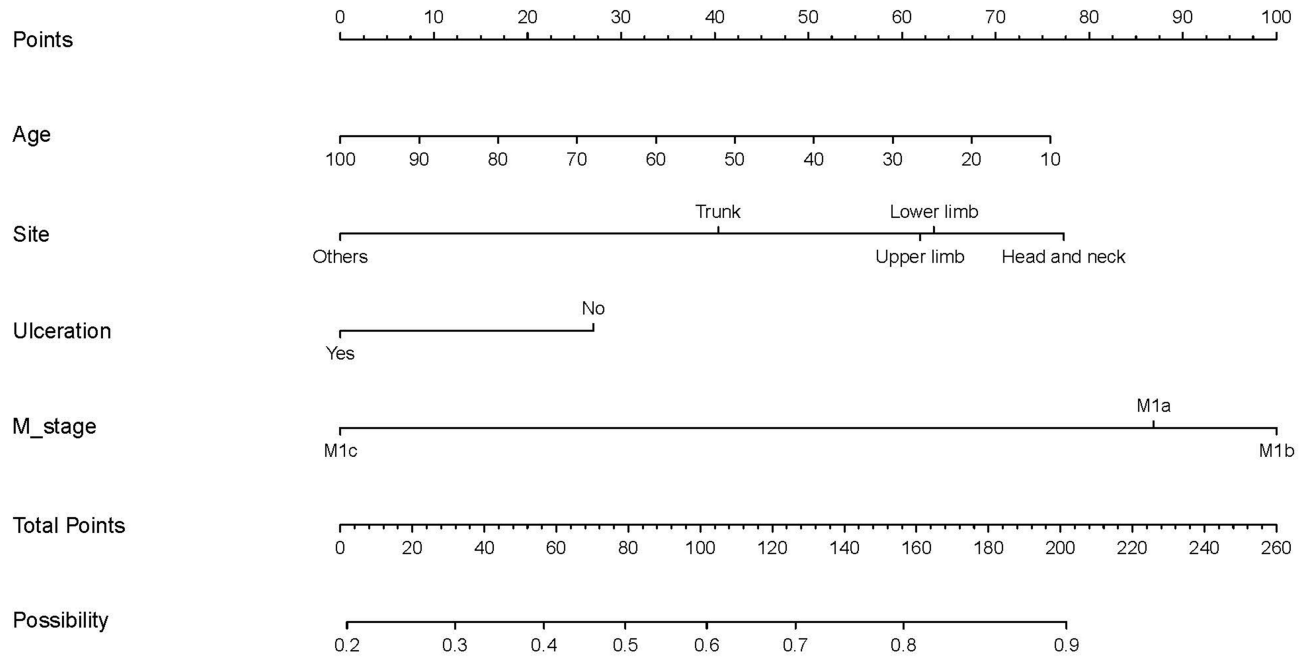

FIGURE 3
A nomogram to predict optimal candidates for primary tumor resection.

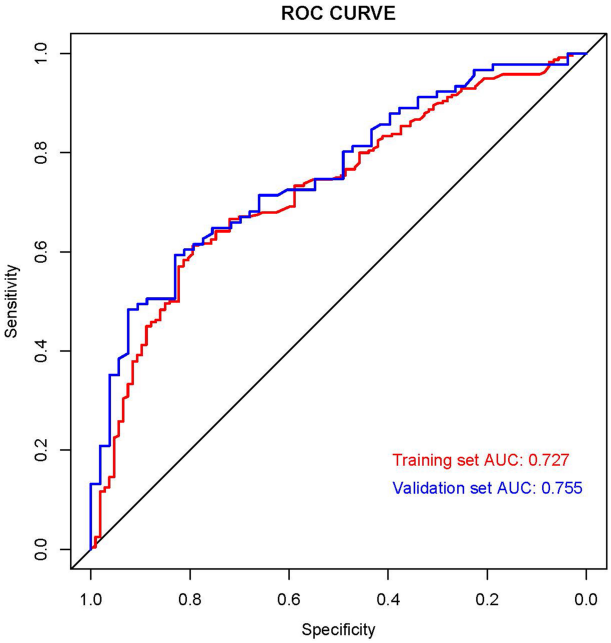

FIGURE 4
ROC curves of the nomogram. ROC curves of the nomogram in the training set (Red) and validation (Blue). ROC, receiver operating characteristic.

analysis and log-rank test of the surgical and the non-surgical groups are shown in Figure 2. The results show that patients with PSR can benefit more than patients without PSR. Then, patients in the surgical group were further divided into the training set ($n = 347$, 70.67%) and the validation set ($n = 144$, 29.33%). Comparability of the training and validation sets was confirmed by the t-test and chi-square test (see Table 2). Multivariate Cox regression analysis on the surgical group, age, M stage, lesion location, and ulceration status were independent prognoses for CSS (see Table 3).

Independent risk factors for CSS in stage Iv Cm patients with primary tumor resection

The median CSS time in the surgical group was 17 months (95% CI = 13.603–20.397 months), and the median CSS in the non-surgical group was 8 months (95%CI = 5.142–10.858 months). The K-M

Establishment and visualization of the nomogram

We defined that a patient who underwent PSR benefited if the survival time exceeded the median CSS time without surgery (8 months). Therefore, patients in the surgery group with survival times longer than 8 months were defined as the surgery benefit group; those with less than or equal to 8 months were defined as the surgery non-benefit group. Independent prognostic factors (age, M stage, lesion location, and ulceration status) were included in the logistics regression model to establish a nomogram in the training set (see Figure 3).

Validation of nomogram and establishment of the web-based nomogram

We established the ROC curves of the training set and the validation set (see Figure 4). The AUC of the nomogram was 0.727 in the training set and 0.755 in the validation set. At the

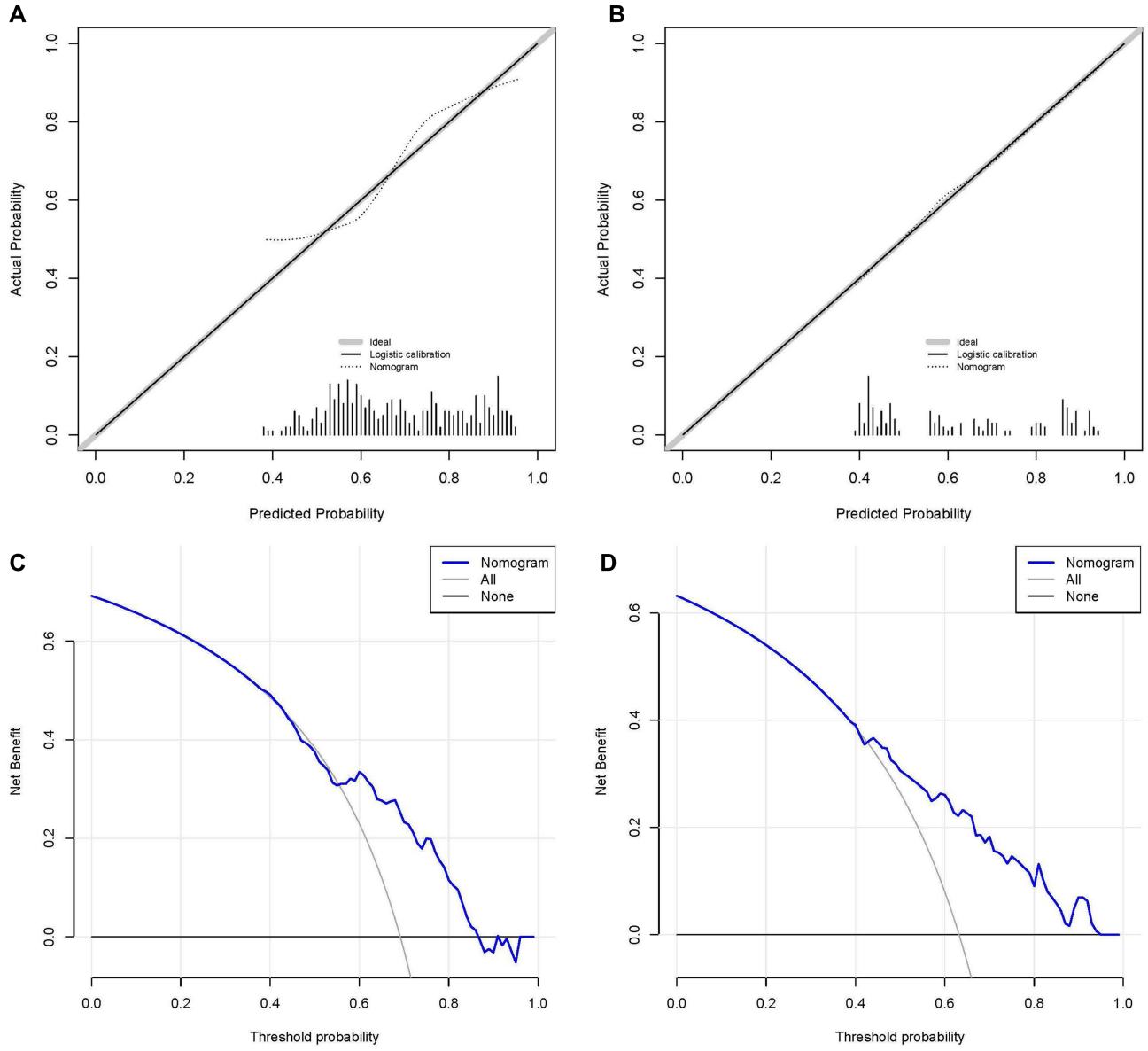

FIGURE 5
Calibration and decision curve analysis. Calibration curves of the nomogram in the training set (A) and the validation set (B), respectively. The nomogram's decision curve analysis in the training set (C) and validation set (D), respectively.

same time, the calibration curves of the training set and the validation set reflected the robust calibration characteristics of the nomogram (Figures 5A,B). DCA indicated that the nomogram could be an excellent predictive model to identify stage IV CM patients suitable for PSR (Figures 5C,D). To further verify the discriminatory ability of the nomogram, we performed K-M analysis and log-rank test (Figure 6). The results showed that the prognosis was more in the beneficial-surgical group than in the non-beneficial-surgical group (p-values < 0.001) or the non-surgical group (p-values < 0.001). However, there was no difference between the non-beneficial & surgical group and the non-surgical group (p-values = 0.489). Based on the validation of the effectiveness of the nomogram, we established a web-based nomogram for further clinical promotion and application (https://zhehongli.shinyapps.io/skcm/).

Clinical use of the web-based nomogram

The operation interface of the web-based nomogram was shown in Figure 7A. We introduced the use of the web-based nomogram by way of an example. For example, a stage IV CM patient had clinicopathological features: 60 years old, stage M of M1a, primary tumor location in the upper limb, and no ulceration at the primary site. Patient characteristics were shown on the left side of the network nomogram (Figure 7A left). The graphical summary (Figure 7A right) and the numerical summary (Figure 7B) showed the probability line and the exact numerical value of the benefit (probability of surgical benefit of primary focus = 0.912, 95% CI = 0.794–0.965), respectively. Therefore, according to the conclusion of the web-based nomogram, this patient could benefit from PSR.

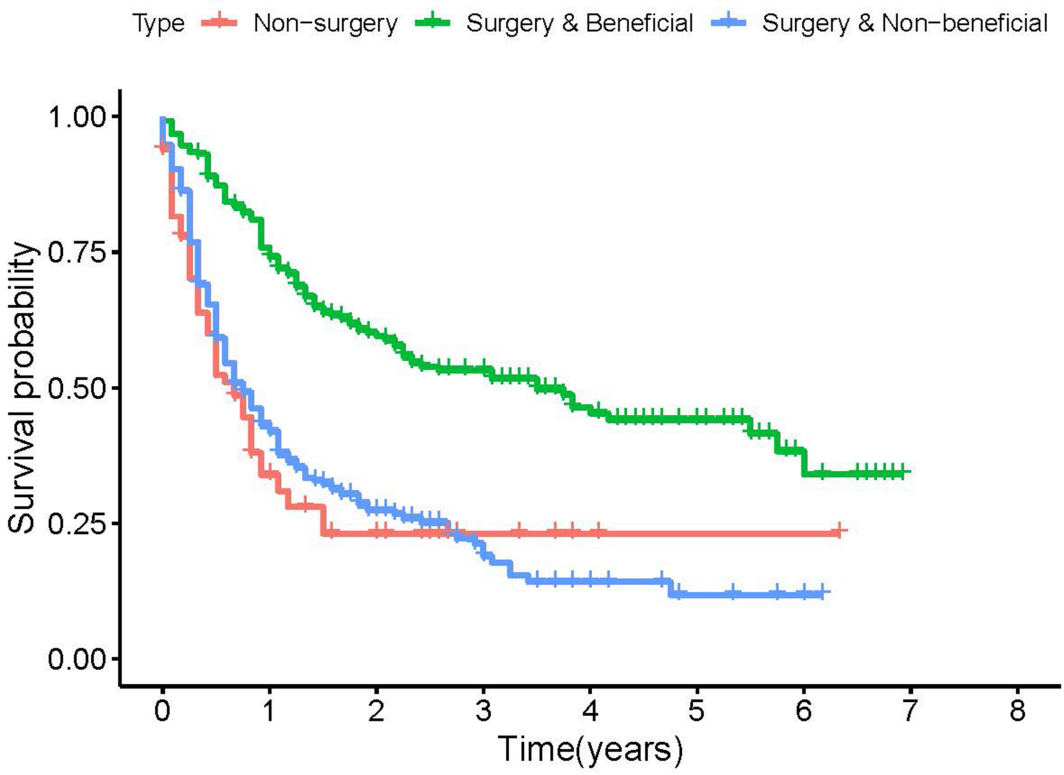

FIGURE 6
Kaplan-Meier plot to differentiate beneficial groups according to our model.

Discussion

CM is a highly malignant tumor originating from melanocytes, which can develop in different tissues and organs such as skin, extremities, mucous membranes, and oculocutaneous membranes, etc (15). The prognosis of CM patients is not good due to its high degree of aggressiveness and metastatic nature (16). With the introduction of targeted therapies and immune checkpoint inhibitors, the survival of patients with advanced melanoma has improved (17, 18). Currently, it is controversial whether PSR should be performed on stage IV CM patients with a primary diagnosis. Many surgeons do not recommend local surgery for stage IV CM patients because the survival time for those is much lower than for patients with stages I-III (9, 10). However, previous retrospective studies have suggested a different perspective: PSR for metastatic CM improves patient prognosis (13, 19). Not all stage IV SCKM patients are suitable for PSR due to individual differences and particularities. In the era of precision therapy, determining the patient's benefit has tremendous significance for the prognosis of stage IV patients. The indications for PSR still need to be clarified due to the lack of relevant studies. Validating the premise that PSR can be beneficial for stage IV CM patients, our study was a pioneering effort to find those patients who are best suited for PSR. To our knowledge, this is the first study to identify the best candidates for PSR in stage IV SCKM patients.

We found that the surgical group's median CSS time was more prolonged (CSS: 17 months vs. 8 months, p-value <0.001). This conclusion further confirmed the necessity of PSR and corroborated Zhang et al. and Tauceri et al. (13, 19). Then, we further divided the patients in the surgical group into surgical benefit and surgical non-benefit groups using the median CSS time (8 months) of the non-surgical group. Finally, we used Cox regression analysis to identify independent prognostic factors and logistic models to construct a nomogram. After such a screening process, stage IV CM patients who were genuinely suitable for PSR were identified. In addition, we built a web-based nomogram to find the best surgical target. Meanwhile, the validation of the nomogram confirmed the excellent predictive performance of our model.

In the nomogram, younger age was one of the essential factors in the benefit from PSR. Older age was associated with worse outcomes for stage IV CM patients who underwent either primary or metastatic surgery (20, 21). This finding suggests that the patient's condition is critical to the traumatic impact of the surgery and the postoperative recovery. In addition, we have also noticed that patients with M1a (skin or subcutaneous metastasis, or distant lymph node metastasis) and M1b (lung metastasis) can benefit from PSR. However, the nomogram concluded that M1c patients were not recommended to undergo surgery, which may be closely related to the occurrence of the central nervous system (CNS) metastasis and/or increased lactate dehydrogenase (LDH) in M1c stage melanoma. LDH is recognized as one of the vital tumor prognostic markers, and its high expression often indicates poor prognosis (22). On the other hand, once melanoma is diagnosed with central nervous system metastasis, its prognosis is abysmal (median OS is only 4 months) (23). The revision of the 8th edition of the AJCC

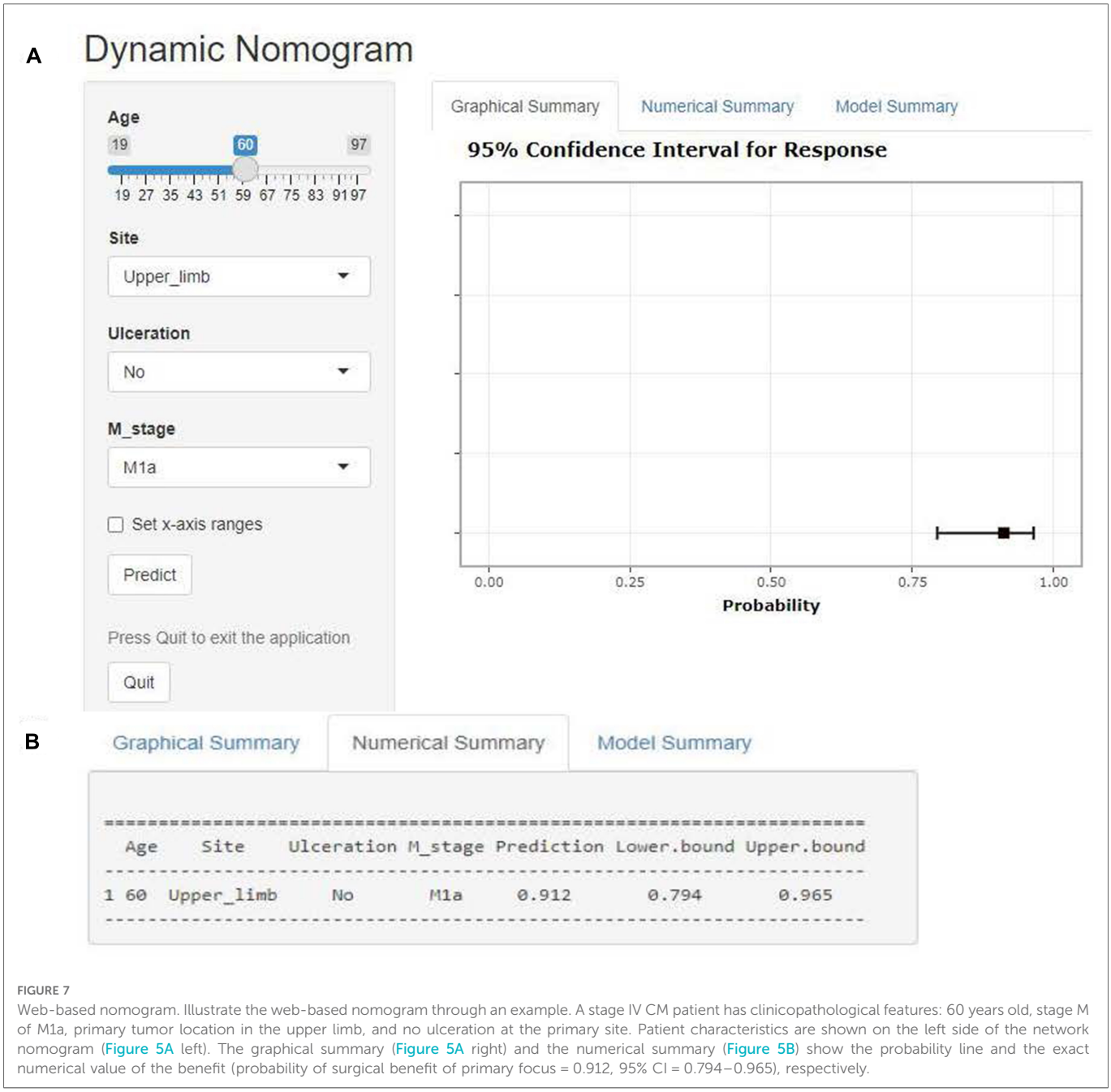

FIGURE 7
Web-based nomogram. Illustrate the web-based nomogram through an example. A stage IV CM patient has clinicopathological features: 60 years old, stage M of M1a, primary tumor location in the upper limb, and no ulceration at the primary site. Patient characteristics are shown on the left side of the network nomogram (Figure 5A left). The graphical summary (Figure 5A right) and the numerical summary (Figure 5B) show the probability line and the exact numerical value of the benefit (probability of surgical benefit of primary focus = 0.912, 95% CI = 0.794–0.965), respectively.

staging guidelines designates CNS metastasis as M1d, further reflecting that the OS of patients with CNS metastases is generally worse (4). Therefore, we have reason to believe that patients with M1c and M1d (8th edition of the AJCC staging guidelines) are not suitable for PSR. A retrospective study by Tas F et al. showed that five-year survival was lower in ulcerated melanoma than in non-ulcerated melanoma (55.3% vs. 81.5%, $p < 0.001$) (24). Ulceration status is defined based on histopathologic examination of the absence of the complete epidermal allodermis over any part of the primary tumor with associated host response, and both the seventh and eighth editions of the AJCC staging guidelines consider ulceration as an additional T-category criterion (4, 25). Previous studies have shown that both breslow tumor thickness and ulceration are independent prognostic factors for OS in CM patients; therefore, we discussed T-staging into two variables: Breslow tumor thickness (T1, T2, T3, and T4) and ulceration (Yes and No) during the study (26, 27). Moreover, our nomogram model suggested that stage IV CM patients without ulceration were better candidates for surgery for the first time. Previous studies have demonstrated that the location of the primary tumor is an important prognostic factor, and whose primary site is the head and neck having a worse prognosis than CM originating from other sites (28, 29). Our study further deduces on this basis that stage IV CM patients whose primary site is the head and neck are more suitable for surgery than other primary sites.

Previous studies have demonstrated that PSR can extend survival time in patients with metastatic cancers that have been screened for, including non-small cell lung cancer (30, 31), breast cancer (32–34),

kidney cancer (35), and colorectal cancer (36, 37). Firstly, symptomatic occupancy consequences are mitigated by surgical resection of primary site tumors. Secondly, tumor excision is helpful for confirming the diagnosis and determining the best course of treatment. Thirdly, PSR in metastatic cancer can prevent tumor-related complications and prolong survival time, but it is also associated with an increased chance of perioperative death (38). By extension, we deduced that before making specific judgments, the advantages and disadvantages of PSR for patients with stage IV CM must be thoroughly evaluated. Our research was carried out to identify the stage IV CM patients who would benefit from PRS. In our study, K-M plots were used to differentiate the beneficiary groups and showed that nomogram-screened patients suitable for surgery had a longer median survival time, with a statistically significant difference. Our study suggested that not all stage IV CM patients were suitable for PSR, that only specific patients will benefit from PSR, and that the potential benefit will vary depending on the characteristics of CM patients.

Some limitations of this study should be noted. Firstly, the lack of unknown information in the SEER database may have produced selection bias during data screening. Secondly, the site of distant metastasis is critical to the prognostic impact of melanoma (e.g., brain, lung, liver, bone, etc.), but there is a lack of relevant data for patients whose melanoma was diagnosed earlier than 2010. Thirdly, this is a retrospective analysis of the SEER database. We do not know the relationship between the quality of survival of CM patients with stage IV and other indicators that may impact prognosis (e.g., targeted therapy, immunotherapy, supportive care).

Conclusions

Based on the confirmation that PSR benefits stage IV CM patients, we propose a new method to screen patients who would truly benefit from PSR. Our study suggested that not all stage IV CM patients were suitable for PSR, that only specific patients will benefit from PSR, and that the potential benefit will vary depending on the characteristics of CM patients. It should be noted that in stage IV CM patients, the younger the age, no ulceration, location in the head and neck, and non-M1c (M1a or M1b) patients will likely benefit from PSR. Meanwhile, we develop a dynamic nomogram (web-based nomogram, https://zhehongli.shinyapps.io/skcm/) based on a static nomogram with good predictive efficacy, achieving good clinical dissemination and application.

Data availability statement

The original contributions presented in the study are included in the article/Supplementary Material, further inquiries can be directed to the corresponding author/s.

Author contributions

All authors contributed to the planning and design of the study. ZHL, JQW and HHZ were involved in review of the raw data and directly involved in the analysis. ZHL, and JQW provided analytical feedback based on aggregated results. ZHL and JQW drafted the manuscript, with input from all authors. ZHL was responsible for the chart making. All authors provided substantive review and commentary on multiple drafts and approved the final version. YJ supervised the study. All authors contributed to the article and approved the submitted version.

Acknowledgments

We are very grateful for the contributions of SEER database that provide information on cancer research, as well as all colleagues involved in the study.

Conflict of interest

The authors declare that the research was conducted in the absence of any commercial or financial relationships that could be construed as a potential conflict of interest.

Publisher's note

References

1. Amaria RN, Menzies AM, Burton EM, Scolyer RA, Tetzlaff MT, Antdbacka R, et al. Neoadjuvant systemic therapy in melanoma: recommendations of the international neoadjuvant melanoma consortium. *Lancet Oncol.* (2019) 20(7): e378–89. doi: 10.1016/S1470-2045(19)30332-8

2. Sung H, Ferlay J, Siegel RL, Laversanne M, Soerjomataram I, Jemal A, et al. Global cancer statistics 2020: gLOBOCAN estimates of incidence and mortality worldwide for 36 cancers in 185 countries. *CA Cancer J Clin.* (2021) 71(3):209–49. doi: 10.3322/caac.21660

3. Balch CM, Buzaid AC, Soong SJ, Atkins MB, Cascinelli N, Coit DG, et al. Final version of the American joint committee on cancer staging system for cutaneous melanoma. *J Clin Oncol.* (2001) 19(16):3635–48. doi: 10.1200/JCO.2001.19.16.3635

4. Gershenwald JE, Scolyer RA, Hess KR, Sondak VK, Long GV, Ross MI, et al. Melanoma staging: evidence-based changes in the American joint committee on cancer eighth edition cancer staging manual. *CA Cancer J Clin.* (2017) 67(6):472–92. doi: 10.3322/caac.21409

5. Long GV, Menzies AM, Nagrial AM, Haydu LE, Hamilton AL, Mann GJ, et al. Prognostic and clinicopathologic associations of oncogenic BRAF in metastatic melanoma. *J Clin Oncol.* (2011) 29(10):1239–46. doi: 10.1200/JCO.2010.32.4327

6. da Silva I P, Ahmed T, Reijers ILM, Weppler AM, Betof Warner A, Patrinely JR, et al. Ipilimumab alone or ipilimumab plus anti-PD-1 therapy in patients with metastatic melanoma resistant to anti-PD-(L)1 monotherapy: a multicentre, retrospective, cohort study. *Lancet Oncol.* (2021) 22(6):836–47. doi: 10.1016/S1470-2045(21)00097-8

7. Eggermont AMM, Kicinski M, Blank CU, et al. Association between immune-related adverse events and recurrence-free survival among patients with stage III melanoma randomized to receive pembrolizumab or placebo: a secondary analysis of a randomized clinical trial. *JAMA Oncol*. (2020) 6(4):519–27. doi: 10.1001/jamaoncol.2019.5570

8. Enomoto LM, Levine EA, Shen P, Votanopoulos KI. Role of surgery for metastatic melanoma. *Surg Clin North Am*. (2020) 100(1):127–39. doi: 10.1016/j.suc.2019.09.011

9. Ghafouri-Fard S, Gholipour M, Taheri M. MicroRNA signature in melanoma: biomarkers and therapeutic targets. *Front Oncol*. (2021) 11:608987. doi: 10.3389/fonc.2021.608987 Published 2021 Apr 22.

10. Erdei E, Torres SM. A new understanding in the epidemiology of melanoma. *Expert Rev Anticancer Ther*. (2010) 10(11):1811–23. doi: 10.1586/era.10.170

11. Howard JH, Thompson JF, Mozzillo N, Nieweg OE, Hoekstra HJ, Roses DF, et al. Metastasectomy for distant metastatic melanoma: analysis of data from the first multicenter selective lymphadenectomy trial (MSLT-I). *Ann Surg Oncol*. (2012) 19(8):2547–55. doi: 10.1245/s10434-012-2398-z

12. Liu JY, Lowe M. Neoadjuvant treatments for advanced resectable melanoma. *J Surg Oncol*. (2019) 119(2):216–21. doi: 10.1002/jso.25352

13. Zhang D, Dong Y, Sun X, Yuan S, Yu J. Surgery of primary tumor improves the survival of newly diagnosed metastatic melanoma: a population-based, propensity-matched study. *Cancer Manag Res*. (2018) 11:339–46. doi: 10.2147/CMAR.S187208

14. Liang H, Liu Z, Huang J, Liu J, Wang W, Li J, et al. Identifying optimal candidates for primary tumor resection among metastatic non-small cell lung cancer patients: a population-based predictive model. *Transl Lung Cancer Res*. (2021) 10(1):279–91. doi: 10.21037/tlcr-20-709

15. MacKie RM, Hauschild A, Eggermont AM. Epidemiology of invasive cutaneous melanoma. *Ann Oncol*. (2009) 20(Suppl 6):vi1–7. doi: 10.1093/annonc/mdp252

16. Guy GP Jr, Thomas CC, Thompson T, Watson M, Massetti GM, Richardson LC, et al. Vital signs: melanoma incidence and mortality trends and projections—united States, 1982–2030. *MMWR Morb Mortal Wkly Rep*. (2015) 64(21):591–6.

17. Verver D, van der Veldt A, van Akkooi A, Verhoef C, Grünhagen DJ, Louwman WJ. Treatment of melanoma of unknown primary in the era of immunotherapy and targeted therapy: a Dutch population-based study. *Int J Cancer*. (2020) 146(1):26–34. doi: 10.1002/ijc.32229

18. Balch CM, Gershenwald JE, Soong SJ, Thompson JF, Atkins MB, Byrd DR, et al. Final version of 2009 AJCC melanoma staging and classification. *J Clin Oncol*. (2009) 27(36):6199–206. doi: 10.1200/JCO.2009.23.4799

19. Tauceri F, Mura G, Roseano M, Framarini M, Ridolfi L, Verdecchia GM. Surgery and adjuvant therapies in the treatment of stage IV melanoma: our experience in 84 patients. *Langenbecks Arch Surg*. (2009) 394(6):1079–84. doi: 10.1007/s00423-008-0312-8

20. Banerjee M, Lao CD, Wancata LM, Muenz DG, Haymart MR, Wong SL. Implications of age and conditional survival estimates for patients with melanoma. *Melanoma Res*. (2016) 26(1):77–82. doi: 10.1097/CMR.0000000000000213

21. Li W, Xiao Y, Xu X, Zhang Y. A novel nomogram and risk classification system predicting the cancer-specific mortality of patients with initially diagnosed metastatic cutaneous melanoma. *Ann Surg Oncol*. (2021) 28(7):3490–500. doi: 10.1245/s10434-020-09341-5

22. Hanahan D, Weinberg RA. Hallmarks of cancer: the next generation. *Cell*. (2011) 144(5):646–74. doi: 10.1016/j.cell.2011.02.013

23. Cohen JV, Tawbi H, Margolin KA, Amravadi R, Bosenberg M, Brastianos PK, et al. Melanoma central nervous system metastases: current approaches, challenges, and opportunities. *Pigment Cell Melanoma Res*. (2016) 29(6):627–42. doi: 10.1111/pcmr.12538

24. Tas F, Erturk K. Primary tumour ulceration in cutaneous melanoma: its role on TNM stages. *Jpn J Clin Oncol*. (2021) 51(2):192–8. doi: 10.1093/jjco/hyaa191

25. Esteva A, Kuprel B, Novoa RA, Ko J, Swetter SM, Blau HM, et al. Corrigendum: dermatologist-level classification of skin cancer with deep neural networks. *Nature*. (2017) 546(7660):686. doi: 10.1038/nature22985

26. Ulmer A, Dietz K, Hodak I, Polzer B, Scheitler S, Yildiz M, et al. Quantitative measurement of melanoma spread in sentinel lymph nodes and survival. *PLoS Med*. (2014) 11(2):e1001604. doi: 10.1371/journal.pmed.1001604 Published 2014 Feb 18.

27. Mo R, Chen C, Mi L, Ma Z, Tan Q. Skin melanoma survival is not superior in females in the new stage IIID of the 8th edition of the staging system: an analysis of data from the surveillance, epidemiology, and end results (SEER) database. *Ann Transl Med*. (2020) 8(21):1381. doi: 10.21037/atm-20-3332

28. Shi K, Camilon PR, Roberts JM, Meier JD. Survival differences between pediatric head and neck versus body melanoma in the surveillance, epidemiology, and end results program. *Laryngoscope*. (2021) 131(2):E635–41. doi: 10.1002/lary.28711

29. Kuruoglu D, Weissler JM, Bustos SS, Moran SL, Davis DMR, Bite U, et al. A 28-year single institution experience with primary skin malignancies in the pediatric population. *J Plast Surg Hand Surg*. (2022) 56(1):53–7. doi: 10.1080/2000656X.2021.1914639

30. Jia J, Guo B, Yang Z, Liu Y, Ga L, Xing G, et al. Outcomes of local thoracic surgery in patients with stage IV non-small-cell lung cancer: a SEER-based analysis. *Eur J Cancer*. (2021) 144:326–40. doi: 10.1016/j.ejca.2020.12.002

31. Wen J, Liu D, Chen D, Chen J, Xu X, Chen C, et al. Treatment of clinical T4 stage superior sulcus non-small cell lung cancer: a propensity-matched analysis of the surveillance, epidemiology, and end results database. *Biosci Rep*. (2019) 39(2):BSR20181545. doi: 10.1042/BSR20181545

32. Blanchard DK, Shetty PB, Hilsenbeck SG, Elledge RM. Association of surgery with improved survival in stage IV breast cancer patients. *Ann Surg*. (2008) 247(5):732–8. doi: 10.1097/SLA.0b013e3181656d32

33. Olson JA Jr, Marcom PK. Benefit or bias? The role of surgery to remove the primary tumor in patients with metastatic breast cancer. *Ann Surg*. (2008) 247(5):739–40. doi: 10.1097/SLA.0b013e3181706140

34. Pérez-Fidalgo JA, Pimentel P, Caballero A, Bermejo B, Barrera JA, Burgues O, et al. Removal of primary tumor improves survival in metastatic breast cancer. Does timing of surgery influence outcomes? *Breast*. (2011) 20(6):548–54. doi: 10.1016/j.breast.2011.06.005

35. Karam JA, Wood CG. The role of surgery in advanced renal cell carcinoma: cytoreductive nephrectomy and metastasectomy. *Hematol Oncol Clin North Am*. (2011) 25(4):753–64. doi: 10.1016/j.hoc.2011.05.002

36. Verhoef C, de Wilt JH, Burger JW, Verheul HM, Koopman M. Surgery of the primary in stage IV colorectal cancer with unresectable metastases. *Eur J Cancer*. (2011) 47(Suppl 3):S61–6. doi: 10.1016/S0959-8049(11)70148-4

37. Faron M, Pignon JP, Malka D, Bermejo B, Barrera JA, Burgues O, et al. Is primary tumour resection associated with survival improvement in patients with colorectal cancer and unresectable synchronous metastases? A pooled analysis of individual data from four randomised trials. *Eur J Cancer*. (2015) 51(2):166–76. doi: 10.1016/j.ejca.2014.10.023

38. Fong Y. Primary tumor resection and patients with asymptomatic colorectal cancer and nonresectable metastases: results of recent randomized trials. *JAMA Surg*. (2021) 156(12):1101–2. doi: 10.1001/jamasurg.2021.5023

frontiers | Frontiers in Oncology

TYPE Original Research
PUBLISHED 25 January 2023
DOI 10.3389/fonc.2023.1034047

OPEN ACCESS

EDITED BY
Mengling Feng,
National University of Singapore, Singapore

REVIEWED BY
Mehmet Uludag,
Şişli Hamidiye Etfal Education and Research Hospital, Türkiye
Gerardo Petruzzi,
Regina Elena National Cancer Institute (IRCCS), Italy

*CORRESPONDENCE
Yousheng Li
guttx@hotmail.com
Chenfang Zhu
sammizz1977@126.com

†These authors have contributed equally to this work and share first authorship

‡These authors have contributed equally to this work and share last authorship

SPECIALTY SECTION
This article was submitted to Surgical Oncology, a section of the journal Frontiers in Oncology

RECEIVED 01 September 2022
ACCEPTED 09 January 2023
PUBLISHED 25 January 2023

CITATION
Zhao F, Wang P, Yu C, Song X, Wang H, Fang J, Zhu C and Li Y (2023) A LASSO-based model to predict central lymph node metastasis in preoperative patients with cN0 papillary thyroid cancer.
Front. Oncol. 13:1034047.
doi: 10.3389/fonc.2023.1034047

A LASSO-based model to predict central lymph node metastasis in preoperative patients with cN0 papillary thyroid cancer

Feng Zhao[1†], Ping Wang[1†], Chaoran Yu[1], Xuefei Song[2], Hui Wang[2], Jun Fang[1], Chenfang Zhu[1*‡] and Yousheng Li[1*‡]

[1]Department of General Surgery, Shanghai Ninth People's Hospital, Shanghai Jiao Tong University School of Medicine, Shanghai, China, [2]Department of Ophthalmology, Shanghai Ninth People's Hospital, Shanghai Jiao Tong University School of Medicine, Shanghai, China

Introduction: Central lymph node metastasis (CLNM) is common in papillary thyroid carcinoma (PTC). Prophylactic central lymph node dissection (PCLND) in clinically negative central compartment lymph node (cN0) PTC patients is still controversial. How to predict CLNM before the operation is very important for surgical decision making.

Methods: In this article, we retrospectively enrolled 243 cN0 PTC patients and gathered data including clinical characteristics, ultrasound (US) characteristics, pathological results of fine-needle aspiration (FNA), thyroid function, eight gene mutations, and immunoenzymatic results. Least absolute shrinkage and selection operator (LASSO) analysis was used for data dimensionality reduction and feature analysis.

Results: According to the results, the important predictors of CLNM were identified. Multivariable logistic regression analysis was used to establish a new nomogram prediction model. The receiver operating characteristic (ROC) curve, calibration curve, and decision curve analysis (DCA) curve were used to evaluate the performance of the new prediction model.

Discussion: The new nomogram prediction model was a reasonable and reliable model for predicting CLNM in cN0 PTC patients, but further validation is warranted.

KEYWORDS

papillary thyroid carcinoma (PTC), central lymph node metastasis (CLNM), least absolute shrinkage and selection operator (LASSO), nomogram prediction model, clinically negative central compartment lymph nodes (cN0), prophylactic central lymph node dissection (PCLND)

Abbreviations: CLNM, central lymph node metastasis; PTC, papillary thyroid carcinoma; PCLND, prophylactic central lymph node dissection; FNA, fine-needle aspiration; LASSO, least absolute shrinkage and selection operator; ROC, receiver operating characteristic; DCA, decision curve analysis; cN0, clinically negative central compartment lymph node; LNM, lymph node metastasis; US, ultrasound; HT, Hashimoto's thyroiditis.

Introduction

Papillary thyroid carcinoma (PTC) is the most common pathological type of thyroid cancer, accounting for more than 80% of thyroid cancers (1, 2). PTC easily metastasizes to cervical lymph nodes. The rate of central lymph node metastasis (CLNM) in PTC ranges from approximately 20% to 80% (3–5). At present, the diagnosis of CLNM mainly depends on preoperative ultrasound (US), but its diagnostic sensitivity is only approximately 20–40% before surgery (6, 7). In PTC patients, positive lymph node metastasis (LNM) is associated with a worse prognosis, more advanced TNM stage, and higher rate of tumor recurrence (8, 9).

Some studies have shown that 30–40% of clinically negative central compartment lymph node (cN0) PTC patients have pathologically confirmed CLNM after prophylactic central lymph node dissection (PCLND) (10–12). However, the use of PCLND in all cN0 PTC patients is still controversial (13, 14). PCLND can improve disease-free survival and decrease the local recurrence rate (15, 16), but it also increases the rate of surgical complications, such as recurrent laryngeal nerve injury and permanent hypothyroidism (17, 18). Thus, it is necessary to predict CLNM in cN0 PTC patients to determine whether PCLND is needed.

Materials and methods

Patients

A total of 243 cN0 PTC patients were retrospectively enrolled in our hospital from January 2019 to July 2021. cN0 PTC patients were referred to as PTC patients without LNM under imaging examination before surgery. After surgery, all patients were divided into pathologically CLNM positive (group A) and pathologically CLNM negative (group B) groups. The clinical characteristics, ultrasound (US) characteristics, pathological fine-needle aspiration (FNA) results, thyroid function, and immunoenzymatic results were retrospectively reviewed and analysed. Paraffin-embedded PTC tissue stored in the Department of Pathology was removed for eight-gene mutation testing. The exclusion criteria were as follows: ① patients had other types of thyroid malignancy; ② patients were confirmed to have CLNM or lateral LNM before the operation; ③ patient had a history of thyroid operations; and ④ patients refused PCLND. The requirement to obtain informed consent from the patients was waived for this retrospective study.

Operation methods

Standard operational procedures have been previously reported according to the "Chinese guidelines for diagnosis and treatment of thyroid diseases". All patients underwent thyroidectomy with PCLND for unilateral PTC and total thyroidectomy with bilateral PCLND for bilateral PTC. All operations were performed by two experienced surgeons of the same surgery quality who had more than 10 years of working experience in our Department of General Surgery.

Clinical and US characteristics, thyroid function, and pathological results

The clinical characteristics collected for analysis included sex (male/female), age (<55 years or ≥55 years), history of thyroid drugs (levothyroxine/thiamazole), history of Hashimoto's thyroiditis (HT), history of nodular goiter, and family history of thyroid cancer. The US characteristics included the location of the tumor (left/right/isthmus), tumor number, tumor size, aspect ratio (≤1/>1), margin, microcalcification, capsule involvement, blood flow signal, HT, hyperthyroidism and TI-RADS classification. Thyroid function included TSH, FT3, FT4, T3, T4, TPOAb, TRAb, and TgAb. Immunohistochemistry factors included *MC, Gal-3, TTF1, TPO, Ki67*, and *CKHi*. Detailed information is provided in Table 1.

Gene mutation testing

A thyroid cancer eight-gene detection kit (Rigen Bio, China) and SLAN-96S Real-Time PCR instrument (Hong Shi, China) were used for thyroid gene mutation testing. The kit included oncogene mutations ($BRAF^{V600E}$, $HRAS^{Q61R}$, $KRAS^{G12C/G12V/Q61R}$ $NRAS^{Q61R}$, and $TERT^{C228T/250T}$) and chromosome rearrangements (*CCDC6-RET*, *PAX8-PPARG*, and *EVT6-NTRK3*). Real-time PCR technology was used to detect point mutations and fusion mutations in eight thyroid cancer-related genes.

Statistical analysis

R (v4.1.2) and SPSS 25 were used for statistical analysis. Continuous variables with a normal distribution, such as age, tumor size and thyroid function, are presented as the mean ± standard deviation and were compared by the t test. Categorical variables, including clinical characteristics, US characteristics, pathological FNA results, thyroid function, immunoenzymatic results, and eight gene mutations, are presented as frequencies or percentages (%) and were compared by the chi-square test or Fisher's test. We converted some continuous variables to categorical variables; for example, patient age was divided into <55 years and ≥55 years (AJCC/UICC TNM staging system version 8), tumor size was divided into ≤10 mm, 10 mm<T ≤ 20 mm, and >20 mm, and thyroid function was divided as well. All variables were analysed by least absolute shrinkage and selection operator (LASSO) analysis. The minimum error of the lambda (λ) value by the cross-validation method was calculated as the standard. The influencing factors of CLNM in cN0 PTC patients were screened out and used to establish a multifactor logistic regression model and then construct a nomogram prediction model. The RS of each patient was calculated by the mathematical formula. $P<0.05$ indicated a significant difference. Receiver operating characteristic (ROC) curves, calibration curves, and decision curve analysis (DCA) curves were used to evaluate the performance of the model.

10.3389/fonc.2023.1034047

TABLE 1 Clinical, US, thyroid function and pathological characteristics of patients undergoing PCLND in different groups.

Variable	Group A (N=92) N (%)	Group B (N=151) N (%)	*P* value
Sex N (%)			**0.048**[a]
Female	41 (44.6)	47 (31.1)	
Male	51 (55.4)	104 (68.9)	
Age (mean ± SD)	43.47 ± 12.37	45.45 ± 12.19	0.225
≥55	13 (14.3)	43 (28.5)	**0.017** [a]
<55	78 (85.7)	108 (71.5)	
Thyroid-related drugs			0.714
No	91 (98.9)	147 (97.4)	
Yes	1 (1.1)	4 (2.6)	
Hashimoto's thyroiditis			1
Positive	8 (8.7)	12 (7.9)	
Negative	84 (91.3)	139 (92.1)	
Nodular goiter			0.118
Positive	14 (15.2)	12 (7.9)	
Negative	78 (84.8)	139 (92.1)	
Family history			0.988
Positive	1 (1.1)	3 (2.0)	
Negative	91 (98.9)	148 (98.0)	
Thyroid function [b]			
TSH			**0.024** [a]
Positive	33 (35.9)	78 (51.7)	
Negative	59 (64.1)	73 (48.3)	
FT3			**0.016** [a]
Positive	28 (30.4)	71 (47.0)	
Negative	64 (69.6)	80 (53.0)	
FT4			0.095
Positive	80 (87.0)	142 (94.0)	
Negative	12 (13.0)	9 (6.0)	
T3			0.417
Positive	43 (46.7)	80 (53.0)	
Negative	49 (53.3)	71 (47.0)	
T4			**0.017** [a]
Positive	82 (89.1)	147 (97.4)	
Negative	10 (10.9)	4 (2.6)	
TgAb			0.232
Positive	27 (29.3)	57 (37.7)	
Negative	65 (70.7)	94 (62.3)	
TPOAb			0.302
Positive	23 (25.0)	63 (41.7)	
Negative	69 (75.0)	88 (58.3)	

(Continued)

10.3389/fonc.2023.1034047

TABLE 1 Continued

Variable	Group A (N=92) N (%)	Group B (N=151) N (%)	*P* value
Characteristics of US			
Bilateral			0.238
No	30 (32.6)	62 (41.1)	
Yes	62 (67.4)	89 (58.9)	
Side N (%)			0.317
Right	39 (42.4)	79 (52.3)	
Left	47 (51.1)	63 (41.7)	
Isthmus	6 (6.5)	9 (6.0)	
Tumor Size N (%)			0.074
≤10 mm	54 (58.7)	108 (72.0)	
>10 mm, ≤20 mm	29 (31.5)	35 (23.3)	
>20 mm	9 (9.8)	8 (4.7)	
Aspect Ratio N (%)			0.331
>1	68 (73.9)	121 (80.1)	
<1	24 (26.1)	30 (19.9))	
Margin			1
Circumscribed	14 (15.2)	23 (15.2)	
Indistinct	78 (84.8)	128 (84.8)	
Microcalcification			0.073
Negative	25 (27.2)	59 (39.1)	
Positive	67 (72.8)	92 (60.9)	
Capsule Involvement			0.186
Negative	73 (79.3)	130 (86.1)	
Positive	19 (20.7)	21 (13.9)	
Internal Vascularity			0.388
Negative	13 (14.1)	29 (19.3)	
Positive	79 (85.9)	121 (80.7)	
TI-RADS			**0.042** [a]
4A/4B	18 (19.6)	49 (32.5)	
4C/5	74 (80.4)	102 (67.5)	
Immunohistochemistry			
MC			0.451
Negative	6 (13.0)	14 (20.3)	
Positive	40 (87.0)	55 (79.7)	
Gal3			0.393
Negative	8 (9.8)	8 (5.7)	
Positive	74 (90.2)	132 (94.3)	
TTF1			0.061
Negative	17 (23.9)	15 (12.4)	
Positive	54 (76.1)	106 (87.6)	

(Continued)

10.3389/fonc.2023.1034047

TABLE 1 Continued

Variable	Group A (N=92) N (%)	Group B (N=151) N (%)	*P* value
TPO			0.245
Negative	75 (96.2)	119 (90.8)	
Positive	3 (3.8)	12 (9.2)	
Ki67 ≥0.02, <0.02			0.101
Negative	24 (33.3)	58 (46.4)	
Positive	48 (66.7)	67 (53.6)	
CKHi			0.965
Negative	11 (19.6)	15 (17.9)	
Positive	45 (80.4)	69 (82.1)	
Gene mutation			
$BRAF^{V600E}$			**<0.001** [a]
Wild-type	8 (8.7)	85 (56.3)	
Mutant	84 (91.3)	66 (43.7)	
$TERT^{C228T/250T}$			0.663
Wild-type	90 (97.8)	150 (99.3)	
Mutant	2 (2.2)	1 (0.7)	
$KRAS^{G12C/G12V/Q61R}$			1
Wild-type	91 (98.9)	149 (99.3)	
Mutant	1 (1.1)	2 (0.7)	
$HRAS^{Q61R}$			1
Wild-type	92 (100)	151 (100)	
Mutant	0	0	
$NRAS^{Q61R}$			1
Wild-type	92 (100%)	151 (100%)	
Mutant	0	0	
CCDC6-RET			1
Wild-type	92 (100%)	151 (100%)	
Mutant	0	0	
PAX8-PPARG			1
Wild-type	92 (100%)	151 (100%)	
Mutant	0	0	
EVT6-NTRK3			1
Wild-type	92 (100%)	151 (100%)	
Mutant	0	0	

(a) Bold values indicate statistical significance ($P<0.05$). (b) The values of thyroid function were divided into positive and negative. Positive means outside the normal reference value range, and negative means within the normal reference value range.

10.3389/fonc.2023.1034047

Result

Clinical characteristics

There were 41 females and 51 males in group A and 47 females and 104 males in group B. The male/female ratios were 1:1.24 and 1:2.21, respectively (P<0.05). The average ages in groups A and B were 43.37 ± 12.37 and 45.45 ± 12.19 years, respectively (P<0.05). The numbers of patients <55 years old in groups A and B were 78 and 108, respectively, and those ≥55 years old were 13 and 43, respectively (P<0.05). A history of taking thyroid drugs, a history of HT, a history of nodular goiter, and a family history of thyroid cancer were not significantly different between groups A and B. Regarding US characteristics, only TI-RADS classification was significantly different (P<0.05) between groups A and B (74 cases and 102 cases, respectively). Other US features were not significantly different between groups A and B (P>0.05). TSH, FT3, and T4 were significantly different between groups A and B (P<0.05). FT4, T3, TPOAb, TRAb, and TgAb levels were not significantly different between groups A and B (P>0.05). Immunohistochemistry factors (*MC, Gal-3, TTF1, TPO, Ki67*, and *CKHi*) were not significantly different between groups A and B (P>0.05). $BRAF^{V600E}$, $KRAS^{G12C/G12V/Q61R}$, and $TERT^{C228T/250T}$ were selected for further analysis because the number of patients with other gene mutations in groups A and B was not sufficient. The number of patients with $BRAF^{V600E}$ was significantly different between groups A and B (84 and 66 cases, 91.3% and 43.7%, P<0.05). $KRAS^{G12C/G12V/Q61R}$ and $TERT^{C228T/250T}$ mutations were not significantly different between the two groups (P>0.05) (Table 1).

Predictive model construction

Five out of forty-nine factors, including age, history of nodular goiter, $BRAF^{V600E}$ mutation, history of HT, and TI-RADS classification, were identified as significant *via* LASSO regression (Figure 1 and Table 2). Among them, $BRAF^{V600E}$ mutation was identified as the top risk factor. The statistical distribution of the five most powerful factors identified by LASSO regression analysis is visualized in Figure 2.

The nomogram prediction model was constructed based on these most powerful factors (Figure 3A). In the nomogram prediction model, each predictive factor was assigned a corresponding score. Among the predictive factors, age ≥55 years had a score of 1, and age <55 years had a score of 0. HT, nodular goiter, and $BRAF^{V600E}$ mutation each had a score of 1 for presence and 0 for absence. The TI-RADS classification T4A~T4B was assigned a score of 1, and T4C~T5 was assigned a score of 2 (AJCC/UICC TNM staging system version 8). According to the corresponding scores from each predictive factor, the total score can be obtained. The diagnostic possibility ranges from 0.1 to 0.8. A diagnostic possibility close to 0.1 was classified as low risk, and a diagnostic possibility close to 0.8 was classified as high risk. The probability of CLNM in cN0 patients could be predicted according to the diagnostic possibility.

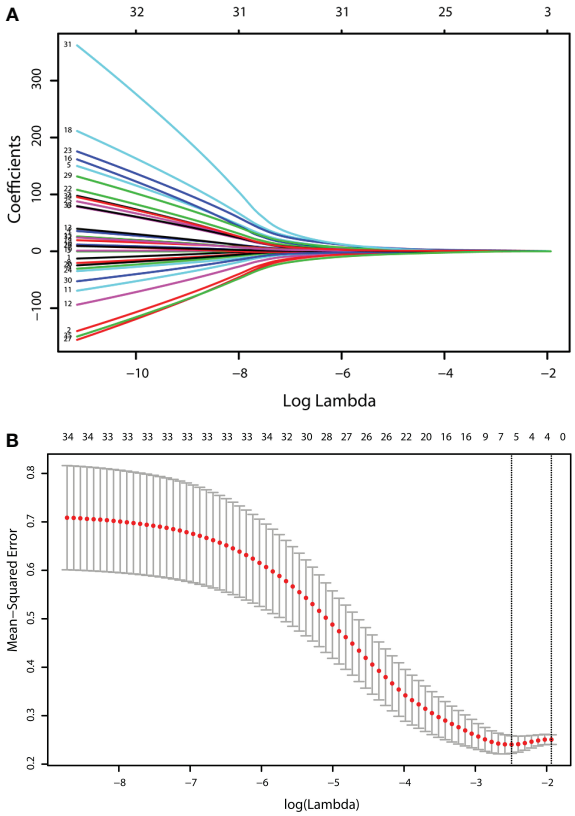

FIGURE 1
Identification of the influencing factors by LASSO regression. LASSO regression identified the following 5 most powerful predictors. **(A)** LASSO coefficient profiles of the 49 characteristics. A coefficient profile plot was produced against the log lambda (λ) sequence. **(B)** The relationship curve between the partial likelihood deviation (binomial deviation) and log(λ) was plotted.

Predictive model performance

The predictive model performance was evaluated by ROC curves, calibration curves, and DCA curves. The area under the ROC curve

TABLE 2 Regression coefficients of the 5 most powerful factors identified by LASSO regression analysis.

Variable	OR	Std. Error	*P* value
Age (≥55)	0.317791	0.6785	0.0911
Nodular goiter	3.935329	1.2365	0.2679
$BRAF^{V600E}$	4.04959	0.6449	**0.0301**[a]
Hashimoto's thyroiditis	1.124409	0.7038	0.8677
TI-RADS (4C/5)	1.752304	0.8284	0.4983

(a) Bold values indicate statistical significance (P<0.05).

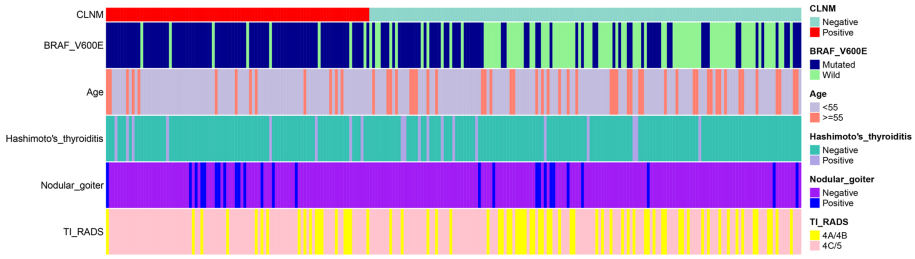

FIGURE 2
Heatmap of the top five significant variables identified based on LASSO regression analysis. Heatmap of the top five significant variables identified *via* LASSO regression, including $BRAF^{V600E}$ mutation, age, history of nodular goiter, history of Hashimoto's thyroiditis and TI-RADS classification.

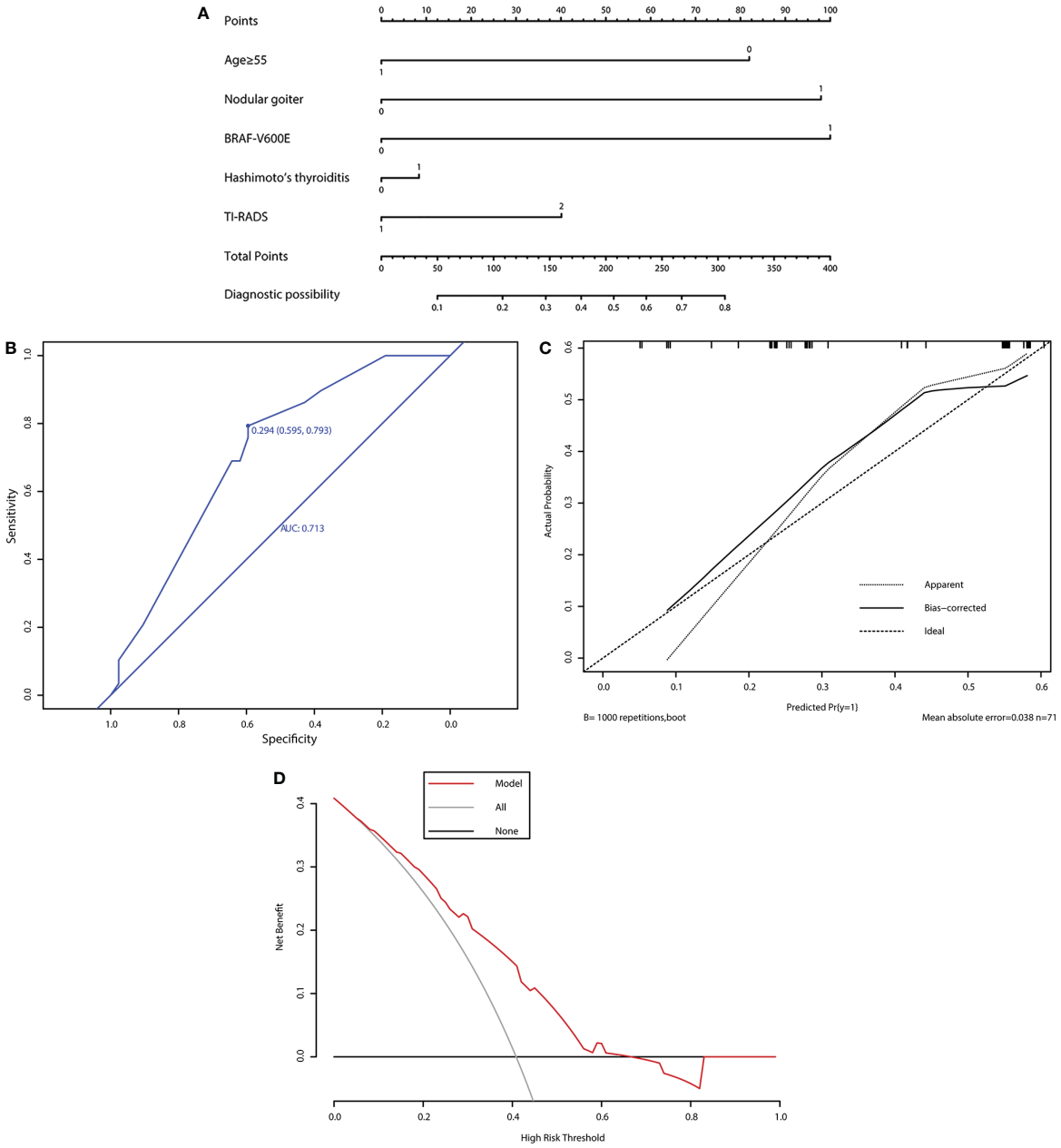

FIGURE 3
Evaluation of the performance of the new prediction model. **(A)** Nomogram for predicting CLNM in PTC patients based on five risk factors. **(B)** The ROC curve and AUC of the nomogram. ROC, receiver operating characteristic. **(C)** Calibration plots of the nomogram for predicting CLNM. **(D)** The DCA method evaluated the performance of the model.

(AUC) of the model was 0.713 (95% CI 0.595–0.793) (Figure 3B). The approximate line and the bias-corrected line represent the performance of our model. After resampling for internal validation, the average absolute error was 3.8%. The threshold probability of CLNM metastasis was between 0.06 and 0.66. The net benefit level of the application of the nomogram prediction model was significantly higher than that of the "non-intervention" and "full intervention" schemes. Meanwhile, the calibration curve displayed a satisfactory consistency (Figure 3C). The DCA curve also suggested good predictive power (Figure 3D).

Discussion

National Comprehensive Cancer Network (NCCN) clinical practice guidelines for thyroid carcinoma and the American Thyroid Association (ATA) guidelines do not recommend PCLND in all cN0 PTC patients (19, 20). The efficacy of PCLND for cN0 PTC is uncertain (15, 21), and the incidence of complications, such as recurrent laryngeal nerve injury, permanent hypoparathyroidism (17, 21), and chyle leakage (18), is high. In contrast, the Chinese Thyroid Association guidelines still recommend PCLND because the rate of CLNM in cN0 PTC is up to 72% (22), which increases the recurrence rate. Reoperation leads to a higher rate of operative complications (23, 24). The 2015 version of the ATA management guideline marks a high rate of CLNM as a pivotal risk factor in the risk stratification evaluation of PTC patients. Therefore, it is necessary to determine the risk of CLNM in cN0 PTC patients and screen out high-risk patients for PCLND.

US, CT, and MRI are usually used for judging the condition of central lymph nodes, but their sensitivity and specificity are not sufficient (25, 26). Zhong et al (27) showed that the incidence of CLNM in cN0 PTC patients was 53.6%. Yasuhiro et al (28) found that the sensitivity of US diagnosis of lateral metastasis was only 27.2%. For this reason, it is unreliable to perform PCLND purely depending on preoperative US. Liu et al (26) showed that there was no significant difference in the diagnosis of lateral neck node metastases between MRI and US. A meta-analysis that included 17 studies showed that the sensitivity and specificity of CT in the detection of CLNM ranged from 23% to 83% and from 64% to 94%, respectively. The pooled sensitivity was 55%, and the pooled specificity was 87% (29). Zhan et al. reported that approximately 40% of cN0 PTC patients actually had CLNM (30). In our study, the rate of CLNM in cN0 patients was 21.40%.

Some previous studies have established diagnostic models for predicting LNM in PTC. Huang et al. (31) used the LASSO method to analyze all US features and some clinical features to establish a CLNM prediction model and web-based calculator, which presented good performance. Xue et al (32) analysed the relationship between US and contrast-enhanced US characteristics and then used univariate and multivariable logistic regression methods to establish a nomogram model. Park et al (33) aimed to develop a radiomics signature using US images of the primary tumor to preoperatively predict LNM in patients with conventional PTC. Zhao et al (34) used independent predictive factors, followed by multivariate logistic regression, to evaluate risk factors by using ROC curve analysis. Most of these articles included the characteristics of US-related factors and some clinical features. Our research included all information we could obtain before surgery, such as family history of thyroid cancer, history of HT, thyroid function and gene mutations.

CLNM is a complex problem, and the use of a single variable to predict CLNM is not reliable. Multivariable regression models are commonly used to identify significant independent risk factors in medical statistical analysis. The threshold of $P<0.05$ is artificially set, and it is easy to lose some important related factors. The LASSO method does not exclude any variables that might impact the outcome, but it did not play an independent role in univariate analysis. This method was properly used to reduce the number of variables. When the weight of low correlation variables is compressed to 0, they were finally eliminated. The LASSO method is a calculation method that is more suitable for datasets that include many variables. The use of the LASSO method before logistic regression follows the "second strike theory" from the combination of generalized genetic factors and environmental factors. We believe that the combination of many factors together brought about the final clinical event of CLNM. The use of LASSO before logistic regression in the calculation process of this study took into consideration the effects of multiple factors and did not arbitrarily rule out any of the possible factors.

In our article, the rate of positive CLNM in younger patients was higher than that in elderly patients, suggesting that age was negatively correlated with CLNM, which was similar to the findings of previous studies (35, 36). Importantly, the rate of positive CLNM in patients with other adverse prognostic factors, including a history of HT, a history of nodular goiter, worse TI-RADS classification and $BRAF^{V600E}$ mutation, was higher, which indicated that these factors were positively related to CLNM. Some studies demonstrated that the $BRAF^{V600E}$ mutation was correlated with CLNM (37, 38), but others obtained the opposite conclusion (39). The relationship between the $BRAF^{V600E}$ mutation and specific clinical pathological features of PTC remains controversial. However, in our research, only the $BRAF^{V600E}$ mutation was confirmed as a significant independent risk factor for CLNM.

All the related variables were subjected to selection by the LASSO method. Using this method, we did not exclude any variables that might definitely impact the outcome, and although these factors did not have not an independent role in univariate analysis, doing this improved the pertinence and accuracy of subsequent logistic regression.

The limitations of our article are as follows. First, this was a single-centre study, which may lead to data bias. Thus, it is necessary to conduct further prospective research and multicenter studies. Finally, the evaluation of some US features is subjective, and interobserver variability may occur. Our retrospective study preliminarily explored the possibility of using certain factors to predict CLNM in cN0 PTC patients.

In conclusion, the nomogram prediction model was able to predict the risk of preoperative CLNM in cN0 PTC patients and has a good predictive performance. Further prospective, multicenter, and larger sample size studies are needed to confirm our findings.

Data availability statement

The processed data required to reproduce these findings cannot be shared at this time as the data also forms part of an ongoing study. Requests to access the datasets should be directed to FZ, phillip_zhao@126.com.

Ethics statement

The studies involving human participants were reviewed and approved by Ethics Committee of Shanghai Ninth People's Hospital, Shanghai Jiao Tong University School of Medicine (SH9H-2020-T346-1). The patients/participants provided their written informed consent to participate in this study.

Author contributions

All authors listed have made a substantial, direct, and intellectual contribution to the work, and approved it for publication.

Funding

This study was supported by funding from the Clinical Research Program of 9th People's Hospital, Shanghai Jiao Tong University School of Medicine (JYLJ202016). This research study was registered in the China clinical trial registry (ChiCTR2200057167).

Conflict of interest

The authors declare that the research was conducted in the absence of any commercial or financial relationships that could be construed as a potential conflict of interest.

Publisher's note

All claims expressed in this article are solely those of the authors and do not necessarily represent those of their affiliated organizations, or those of the publisher, the editors and the reviewers. Any product that may be evaluated in this article, or claim that may be made by its manufacturer, is not guaranteed or endorsed by the publisher.

References

1. Schneider DF, Chen H. New developments in the diagnosis and treatment of thyroid cancer. *CA: Cancer J Clin* (2013) 63(6):374–94. doi: 10.3322/caac.21195

2. Kitahara CM, Sosa JA. The changing incidence of thyroid cancer. *Nat Rev Endocrinol* (2016) 12(11):646–53. doi: 10.1038/nrendo.2016.110

3. Kouvaraki MA, Shapiro SE, Fornage BD, Edeiken-Monro BS, Sherman SI, Vassilopoulou-Sellin R, et al. Role of preoperative ultrasonography in the surgical management of patients with thyroid cancer. *Surgery* (2003) 134(6):946–54. doi: 10.1016/s0039-6060(03)00424-0

4. Teixeira G, Teixeira T, Gubert F, Chikota H, Tufano R. The incidence of central neck micrometastatic disease in patients with papillary thyroid cancer staged preoperatively and intraoperatively as N0. *Surgery* (2011) 150(6):1161–7. doi: 10.1016/j.surg.2011.09.019

5. Kim SY, Kim BW, Pyo JY, Hong SW, Chang HS, Park CS. Macrometastasis in papillary thyroid cancer patients is associated with higher recurrence in lateral neck nodes. *World J Surg* (2018) 42(1):123–9. doi: 10.1007/s00268-017-4158-5

6. Cho SY, Lee TH, Ku YH, Kim HI, Lee GH, Kim MJ. Central lymph node metastasis in papillary thyroid microcarcinoma can be stratified according to the number, the size of metastatic foci, and the presence of desmoplasia. *Surgery* (2015) 157(1):111–8. doi: 10.1016/j.surg.2014.05.023

7. Jianming L, Jibin L, Linxue Q. Suspicious ultrasound characteristics correlate with multiple factors that predict central lymph node metastasis of papillary thyroid carcinoma: Significant role of hbme-1. *Eur J Radiol* (2020) 123:108801. doi: 10.1016/j.ejrad.2019.108801

8. Wang TS, Sosa JA. Thyroid surgery for differentiated thyroid cancer - recent advances and future directions. *Nat Rev Endocrinol* (2018) 14(11):670–83. doi: 10.1038/s41574-018-0080-7

9. Adam MA, Pura J, Goffredo P, Dinan MA, Reed SD, Scheri RP, et al. Presence and number of lymph node metastases are associated with compromised survival for patients younger than age 45 years with papillary thyroid cancer. *J Clin Oncology: Off J Am Soc Clin Oncol* (2015) 33(21):2370–5. doi: 10.1200/JCO.2014.59.8391

10. Enyioha C, Roman SA, Sosa JA. Central lymph node dissection in patients with papillary thyroid cancer: A population level analysis of 14,257 cases. *Am J Surg* (2013) 205(6):655–61. doi: 10.1016/j.amjsurg.2012.06.012

11. Sadowski BM, Snyder SK, Lairmore TC. Routine bilateral central lymph node clearance for papillary thyroid cancer. *Surgery* (2009) 146(4):696–703. doi: 10.1016/j.surg.2009.06.046

12. Alvarado R, Sywak MS, Delbridge L, Sidhu SB. Central lymph node dissection as a secondary procedure for papillary thyroid cancer: Is there added morbidity? *Surgery* (2009) 145(5):514–8. doi: 10.1016/j.surg.2009.01.013

13. Calo PG, Pisano G, Medas F, Marcialis J, Gordini L, Erdas E, et al. Total thyroidectomy without prophylactic central neck dissection in clinically node-negative papillary thyroid cancer: Is it an adequate treatment? *World J Surg Oncol* (2014) 12:152. doi: 10.1186/1477-7819-12-152

14. Conzo G, Mauriello C, Docimo G, Gambardella C, Thomas G, Cavallo F, et al. Clinicopathological pattern of lymph node recurrence of papillary thyroid cancer. *Implications Surgery Int J Surg* (2014) 12 Suppl 1:S194–7. doi: 10.1016/j.ijsu.2014.05.010

15. Nixon IJ, Wang LY, Ganly I, Patel SG, Morris LG, Migliacci JC, et al. Outcomes for patients with papillary thyroid cancer who do not undergo prophylactic central neck dissection. *Br J Surg* (2016) 103(3):218–25. doi: 10.1002/bjs.10036

16. Yazıcı D, Çolakoğlu B, Sağlam B, Sezer H, Kapran Y, Aydın Ö, et al. Effect of prophylactic central neck dissection on the surgical outcomes in papillary thyroid cancer: Experience in a single center. *Eur Arch Oto-Rhino-Laryngology* (2020) 277(5):1491–7. doi: 10.1007/s00405-020-05830-1

17. Ataş H, Akkurt G, Saylam B, Tez M. Central neck dissection is an independent risk factor for incidental parathyroidectomy. *Acta Chirurgica Belgica* (2021) 121(1):36–41. doi: 10.1080/00015458.2020.1828677

18. Park I, Her N, Choe J-H, Kim JS, Kim J-H. Management of chyle leakage after thyroidectomy, cervical lymph node dissection, in patients with thyroid cancer. *Head Neck* (2018) 40(1):7–15. doi: 10.1002/hed.24852

19. Haddad RI, Bischoff L, Ball D, Bernet V, Blomain E, Busaidy NL, et al. Thyroid carcinoma, version 2.2022, nccn clinical practice guidelines in oncology. *J Natl Compr Canc Netw* (2022) 20(8):925–51. doi: 10.6004/jnccn.2022.0040

20. Haugen BR, Alexander EK, Bible KC, Doherty GM, Mandel SJ, Nikiforov YE, et al. 2015 American Thyroid association management guidelines for adult patients with thyroid nodules and differentiated thyroid cancer: The American thyroid association guidelines task force on thyroid nodules and differentiated thyroid cancer. *Thyroid: Off J Am Thyroid Assoc* (2016) 26(1):1–133. doi: 10.1089/thy.2015.0020

21. Medas F, Canu GL, Cappellacci F, Anedda G, Conzo G, Erdas E, et al. Prophylactic central lymph node dissection improves disease-free survival in patients with intermediate and high risk differentiated thyroid carcinoma: A retrospective analysis on 399 patients. *Cancers* (2020) 12(6):E1658. doi: 10.3390/cancers12061658

22. He J, Li J, Cheng Y, Fan J, Jun G, Jiang Z, et al. [Guidelines of Chinese society of clinical oncology (CSCO) differentiated thyroid cancer]. *J Cancer Control Treat* (2021) 34(12):1164–201.

23. Ruggiero FP, Fedok FG. Outcomes in reoperative thyroid cancer. *Otolaryngologic Clinics North America* (2008) 41(6):1261–8. doi: 10.1016/j.otc.2008.06.003

24. Pai SI, Tufano RP. Reoperation for Recurrent/Persistent well-differentiated thyroid cancer. *Otolaryngologic Clinics North America* (2010) 43(2):353–63. doi: 10.1016/j.otc.2010.02.004

25. Ahn JE, Lee JH, Yi JS, Shong YK, Hong SJ, Lee DH, et al. Diagnostic accuracy of ct and ultrasonography for evaluating metastatic cervical lymph nodes in patients with thyroid cancer. *World J Surg* (2008) 32(7):1552–8. doi: 10.1007/s00268-008-9588-7

26. Liu Z, Xun X, Wang Y, Mei L, He L, Zeng W, et al. Mri and ultrasonography detection of cervical lymph node metastases in differentiated thyroid carcinoma before reoperation. *Am J Trans Res* (2014) 6(2):147–54.

27. Zhong X, Lu Y, Yin X, Wang Q, Wang F, He Z. Prophylactic central lymph node dissection performed selectively with Cn0 papillary thyroid carcinoma according to a risk-scoring model. *Gland Surg* (2022) 11(2):378–88. doi: 10.21037/gs-21-906

28. Ito Y, Tomoda C, Uruno T, Takamura Y, Miya A, Kobayashi K, et al. Ultrasonographically and anatomopathologically detectable node metastases in the lateral compartment as indicators of worse relapse-free survival in patients with papillary thyroid carcinoma. *World J Surg* (2005) 29(7):917–20. doi: 10.1007/s00268-005-7789-x

29. Cho SJ, Suh CH, Baek JH, Chung SR, Choi YJ, Lee JH. Diagnostic performance of ct in detection of metastatic cervical lymph nodes in patients with thyroid cancer: A systematic review and meta-analysis. *Eur Radiol* (2019) 29(9):4635–47. doi: 10.1007/s00330-019-06036-8

30. Zhan J, Zhang L-H, Yu Q, Li C-L, Chen Y, Wang W-P, et al. Prediction of cervical lymph node metastasis with contrast-enhanced ultrasound and association between presence of Brafv600e and extrathyroidal extension in papillary thyroid carcinoma. *Ther Adv Med Oncol* (2020) 12:1758835920942367. doi: 10.1177/1758835920942367

31. Huang C, Cong S, Shang S, Wang M, Zheng H, Wu S, et al. Web-based ultrasonic nomogram predicts preoperative central lymph node metastasis of Cn0 papillary thyroid microcarcinoma. *Front Endocrinol (Lausanne)* (2021) 12:734900. doi: 10.3389/fendo.2021.734900

32. Xue T, Liu C, Liu J-J, Hao Y-H, Shi Y-P, Zhang X-X, et al. Analysis of the relevance of the ultrasonographic features of papillary thyroid carcinoma and cervical lymph node metastasis on conventional and contrast-enhanced ultrasonography. *Front Oncol* (2021) 11:794399. doi: 10.3389/fonc.2021.794399

33. Park VY, Han K, Kim HJ, Lee E, Youk JH, Kim EK, et al. Radiomics signature for prediction of lateral lymph node metastasis in conventional papillary thyroid carcinoma. *PloS One* (2020) 15(1):e0227315. doi: 10.1371/journal.pone.0227315

34. Zhao S, Yue W, Wang H, Yao J, Peng C, Liu X, et al. Combined conventional ultrasound and contrast-enhanced computed tomography for cervical lymph node metastasis prediction in papillary thyroid carcinoma. *J Ultrasound Medicine: Off J Am Institute Ultrasound Med* (2022). 9999(1-14):0278-4297 doi: 10.1002/jum.16024

35. Oh HS, Park S, Kim M, Kwon H, Song E, Sung TY, et al. Young age and Male sex are predictors of Large-volume central neck lymph node metastasis in clinical N0 papillary thyroid microcarcinomas. *Thyroid* (2017) 27(10):1285–90. doi: 10.1089/thy.2017.0250

36. Siddiqui S, White MG, Antic T, Grogan RH, Angelos P, Kaplan EL, et al. Clinical and pathologic predictors of lymph node metastasis and recurrence in papillary thyroid microcarcinoma. *Thyroid* (2016) 26(6):807–15. doi: 10.1089/thy.2015.0429

37. So YK, Son Y-I, Park JY, Baek C-H, Jeong H-S, Chung MK. Preoperative braf mutation has different predictive values for lymph node metastasis according to tumor size. *Otolaryngology–Head Neck Surgery: Off J Am Acad Otolaryngology-Head Neck Surg* (2011) 145(3):422–7. doi: 10.1177/0194599811404649

38. Kim SK, Lee JH, Woo J-W, Park I, Choe J-H, Kim J-H, et al. Braf V600e mutation: Differential impact on central lymph node metastasis by tumor size in papillary thyroid carcinoma. *Head Neck* (2016) 38 Suppl 1:E1203–9. doi: 10.1002/hed.24192

39. Guo L, Ma Y-Q, Yao Y, Wu M, Deng Z-H, Zhu F-W, et al. Role of ultrasonographic features and quantified Brafv600e mutation in lymph node metastasis in Chinese patients with papillary thyroid carcinoma. *Sci Rep* (2019) 9(1):75. doi: 10.1038/s41598-018-36171-z

frontiers | Frontiers in Oncology

TYPE Original Research
PUBLISHED 03 February 2023
DOI 10.3389/fonc.2023.1103104

OPEN ACCESS

EDITED BY
Mengling Feng,
National University of Singapore, Singapore

REVIEWED BY
Jochen Weitz,
MKG Augsburg, Germany
Tobias Ettl,
University Medical Center
Regensburg, Germany

*CORRESPONDENCE
Massimo Robiony
massimo.robiony@uniud.it

SPECIALTY SECTION
This article was submitted to
Surgical Oncology,
a section of the journal
Frontiers in Oncology

RECEIVED 19 November 2022
ACCEPTED 23 January 2023
PUBLISHED 03 February 2023

CITATION
Tel A, Bagatto D, Sembronio S, Ferrari S and Robiony M (2023) Double osseous flaps for simultaneous midfacial and mandible reconstruction: Automation in surgical complexity within an entirely computerized workflow.
Front. Oncol. 13:1103104.
doi: 10.3389/fonc.2023.1103104

Double osseous flaps for simultaneous midfacial and mandible reconstruction: Automation in surgical complexity within an entirely computerized workflow

Alessandro Tel[1], Daniele Bagatto[2], Salvatore Sembronio[1], Silvano Ferrari[3] and Massimo Robiony[1]*

[1]Department of Maxillofacial Surgery, University Hospital of Udine, Udine, Italy, [2]Department of Neuroradiology, University Hospital of Udine, Udine, Italy, [3]Department of Maxillofacial Surgery, University Hospital of Parma, Parma, Italy

Introduction: Broad maxillofacial surgical resections involving both the midface and the mandible represent a challenge in terms of reconstruction. Although several papers have explored the possibility of simultaneously using two microsurgical flaps, reports on the implementation of a dual osseous flap strategy are limited, and mainly addressed to static anatomical reconstruction, regardless of functional implications. In particular, there is a lack in the literature of a unifying protocol which illustrates how technology including virtual planning, statistical shape modeling, virtual occlusion, 3D-printing and patient-specific implants can address the functional and accuracy needs required for an optimal reconstruction.

Materials and methods: In this paper, the Authors present their preliminary experience in a two-center study, showing how broad maxillofacial defects, requiring a simultaneous reconstruction in both the mandible and the midface, can be successfully reconstructed using the combination of two osseous flaps in an automated sequence in which all steps are anticipately defined in a virtual plan, accounting for the optimal alignment of temporomandibular joint, predicting the final occlusion and defining a mandibular shape according to a statistical shape model.

Results: Average RMSE for the iliac bone crest flap was of 3.2 $\pm$ 0.36 mm; for the fibula flap, RMSE value was of 2.3 $\pm$ 0.65 mm, for patient-specific implants, for mandibular prostheses the average RMSE was 2.46 mm with 0.76 mm standard deviation. Temporomandibular joint function increased when a TMJ prosthesis was placed.

Conclusions: Double bone free flap is a valuable resource to reconstruct wide defects that simultaneously involve two thirds of the cranio-maxillo-facial skeleton, but a careful virtual planning study should be always performed before approaching this surgical option.

KEYWORDS

virtual surgical planning, double bone flap, computerized automation, 3D printing, point-of-care, statistical shape modeling

1 Introduction

In the last years, the improvement of microsurgery has led to significant advances in reconstructive surgery for skeletal defects. The customization of flap sculpting by virtually simulating precise correspondences between the defect size and the most appropriate flap conformation, and well as the possibility to bring such plans in the surgeon's hands by 3D printing of specific surgical guides, has provided a further impulse to reconstructive microsurgery, fastening flap harvesting and positioning time, while improving outcomes. A variety of studies reported a dual flap strategy, where one osseous flap is generally used for the reconstruction of the bone framework, and another soft tissue flap is used to restore the skin or the mucosal lining, or simply to add volume after conspicuous resections (1). For the most complex defects, several publications report the use of virtual planning workflows to conform a single flap in convoluted spatial arrangements, allowing to optimize the donor flap to the recipient site, which is generally the midface due to its complex geometry including the maxillo-malar buttresses, the alveolar process and the orbit (2–4). However, for defects involving at the same time the midface and the inferior third, one single osseous flap might not be sufficient.

Currently, literature provides scant evidences on the simultaneous use of two osseous flaps: prolonged surgical time, risk of failure and technical complexity represent factors that have limited the adoption of a double bone-flap approach so far. In this respect, virtual surgical planning becomes an indispensable tool to anticipately define with maximum detail all the steps of surgery, from bone shaping, to insetting position and the choice of target vessels for anastomosis; likewise, 3D printing allows to construct surgical guides that assist the surgeon in the correct execution of each planning sequence, creating a fully automated workflow, which optimizes surgical time and increases accuracy and the functional outcomes.

The purpose of this study is to elucidate the technical aspects necessary to plan a simultaneous midfacial and mandible reconstruction with a double osseous free flap strategy, combining a fibula free flap with an iliac crest free flap. We describe an entirely automated sequence of virtual surgical planning and its application, emphasizing the importance of computerized simulation to achieve satisfactory accuracy and functional outcomes.

2 Materials and methods

This is a retrospective observational study performed in two centers with broad oncologic expertise, the University of Udine and the University of Parma. 3 patients were enrolled in this series between January 2021 and June 2022 and fulfilled the following requirements: surgically determined broad skeletal defect with simultaneous involvement of the midface and the mandible; simultaneous use of two osseous flaps for reconstruction; entirely digital workflow. All clinical and demographic features of patients are described in Table 1. We detail the entire workflow of anatomy digitalization, virtual surgical planning and operative sequences to illustrate how computer-guided steps can translate into automated workflows for optimal accuracy and functional restoration. Our institute's local independent Institutional Review Board approved the study protocol (ID: IRB_45_2020).

2.1 Acquisition protocols

According to the concept of multilayer anatomical reconstruction (5), imaging protocols were directed to reproduce virtual anatomy both in the resection area and the two sites for bone flap harvest.

As for the resection area, the following imaging was acquired for the cranio-maxillo-facial region:

- multidetector CT scan with resolution of 768 x 768 voxel and slice thickness of 0.625mm was acquired and reconstructed in bone window density. These parameters were the most suitable to provide a trustful representation of bone anatomy, including thin areas with rarefaction due to pathological processes and partial volume effect.
- MR was acquired using a 3T machine. Contrast-enhanced T1-weighted, T2-weighted, volumetric interpolated breath-hold examination (VIBE), short-T1 inversion recovery (STIR) sequences were acquired as volumetric, with 512 x 512 voxel matrix and 1mm slice thickness. These acquisitions were crucial to characterize soft tissues and spatially define the pathological processes.
- 3D time-of-flight (TOF) sequence with spatial resolution 256x256 and 0.6mm slice thickness was acquired to reconstruct arterial vessels in the face and neck area
- MR venography was performed on a 3T machine to identify venous vasculature using a phased contrast sequence with 256 x 256 voxel matrix and 1mm slice thickness
- Patients furthermore underwent an intraoral scanning procedure to define dental cusps anatomy and use such data to reconstruct a virtual occlusion

As for the flap harvesting sites, for all anatomical regions the protocol was the same, including contrast-enhanced CT scan with 768 x 768 or at least 512 x 512 voxel matrix and a slice thickness of 0.625mm.

2.2 Digitalization of anatomy

In the head and neck region, images were imported into Mimics v25 (Materialise, Leuven, BE) and coregistered within the same coordinate system. First, CT scan was segmented using a thresholding algorithm in the Hounsfield Unit (HU) range of bone, by applying a local selective improvement over thin structures, such as ethmoid and orbital walls. For tumors or pathological processes involving soft tissues, MR sequences were matched and semiautomatic methods based on AI (artificial intelligence)-powered smart brushes were used to accurately segment the tumor mass. A thresholding algorithm in the range of hyperintense values was applied to TOF sequences to yield an accurate representation of arterial vasculature; likewise, 3D phased-contrast venous MR were approached using detection methods based both on voxel contiguity and isointensity to reconstruct well defined 3D networks. Processing of segmentation masks was accurately accomplished especially around

TABLE 1 Demographic, clinical, and digital characteristics of patients enrolled in this study.

ID	Gender	Age	Pathology	Resection	Flap combination	Prosthesis	Components for computer-guided automation			Surgical complications	Accuracy (RMSE)		Follow up (TMJ opening)	
							VSP	guides	Occlusion and TMJ		flap	implant	3-month	6-month
1	Male	27	Fibrous dysplasia of the cranio-maxillo-facial skeleton	Subtotal mandibulectomy with right disarticulation and type 4 maxillary resection	Left fibula + right DCIA	SSM-shaped mandibular implant with right TMJ; 3-segment fibula flap, orbital PMMA implant	Virtual maxillectomy, vascular structures, mandible resection, flap sizing and inset, orbital reconstruction	Maxillary resection, mandible resection, DCIA harvest, fibula harvest, DCIA inset	Virtual wax-up; TMJ reconstruction with fossa and condyle prosthesis	None	3.1mm (DCIA) 2.2mm (fibula)	2.3mm (mandible implant) 2.1 (orbital implant)	28mm	35mm
2	Male	69	Clear-cell odontogenic carcinoma of the mandible with deformation of the midface	Subtotal mandibulectomy with TMJ preservation; type 3 maxillectomy	Right fibula + left DCIA	SSM-shaped mandibular implant, 2-segment fibula flap	Virtual maxillectomy, vascular structures, mandible resection, flap sizing and inset	Maxillary resection, mandible resection, DCIA harvest, fibula harvest, DCIA inset	Virtual wax-up	Intraoral dehiscence	3.6mm (DCIA) 1.7mm (fibula)	3.3mm (mandible implant)	24mm	32mm
3	Female	44	Chondroblastic osteosarcoma of the mandible with maxillary osteoradionecrosis	Segmental mandible resection with type 4 maxillectomy	Left fibula + right DCIA	Mirrored-shape mandibular implant, 1-segment fibula flap	Virtual maxillectomy, vascular structures, mandible resection, flap sizing and inset	Maxillary resection, mandible resection, DCIA harvest, fibula harvest, DCIA inset	Virtual wax-up	Wound dehiscence	2.9mm (DCIA) 3mm (fibula)	1.8mm (mandible implant)	30mm	28mm

10.3389/fonc.2023.1103104

vessels to isolate relevant branches. As for flap donor sites, a baseline pre-contrast scan was used to reconstruct bone surfaces and was then coupled with a contrast-enhanced scan to reconstruct the vasculature and evaluate the position and length of the pedicle. Figure 1 shows the result of anatomical 3D reconstruction.

2.3 Automation and sequencing: virtual planning translated into surgery

• Simulated resection

Objects generated in Mimics were imported in 3-matic v 17 (Materialise, Leuven, BE). As all cases required a composite resection involving both the middle and the inferior third, a resection of the mandible and a maxillectomy were planned. The complex shape of maxillectomies was planned using a freehand brush poly-marking tool to draw complex shapes and define curved resection profiles without being limited to simple planes. A dual-fitting surgical guide was designed, allowing to simultaneously engage dental cusps using a dental splint appendix, and bone as well using patient-fitted surfaces (Figure 2). For subtotal mandibulectomies, the resection was easily defined by positioning a cutting plane.

• Definition of a statistical shape model for mandible reconstruction

For cases needing a total or subtotal mandibulectomy, the Authors searched in their library of mandible STL (standard tessellation language) files the most appropriate geometry to restore the mandible and defined it as "donor". To adapt the donor mandible to the recipient anatomy, a statistical shape model (SSM) was created by computing additional mandibles, selected on the basis of different morphologies, allowing to apply population variance on the target geometry. The resulting mesh, achieved by varying coefficients to selectively modify the SSM, was extracted as an STL file, used to define the shape of the mandible contour of the custom-made prostheses optimized for the current patient (Figure 3).

• Virtual wax-up and definition of the final occlusion

Intraoral scanning was aligned on the dental cusps spared from resection. Data were imported in the software DentalCAD (Exocad GmbH, Darmstadt, Germany) where a virtual occlusion was constructed. For the most complex cases undergoing a complete mandibulectomy and a half maxillectomy, mandibular arch was constructed with a complete digital approach, maximizing intercuspation of mandibular crowns with their superior antagonists. The height of crowns and the identification of an occlusal plane were essential to define the appropriate level to position the fibula free flap for mandible reconstruction.

• Pedicle choice

The 3D reconstruction of the vascular network allowed to visualize in a 3D virtual space the arterial and venous vessels. This enabled to evaluate in a patient-specific approach the relationship between the flap structure and the closest receiving vessels, enabling to identify the neck recipient trunk that requires the shortest path and the minor length of the pedicle (Figure 4).

• Reconstruction of the mandible (fibula surgical planning + custom implant design)

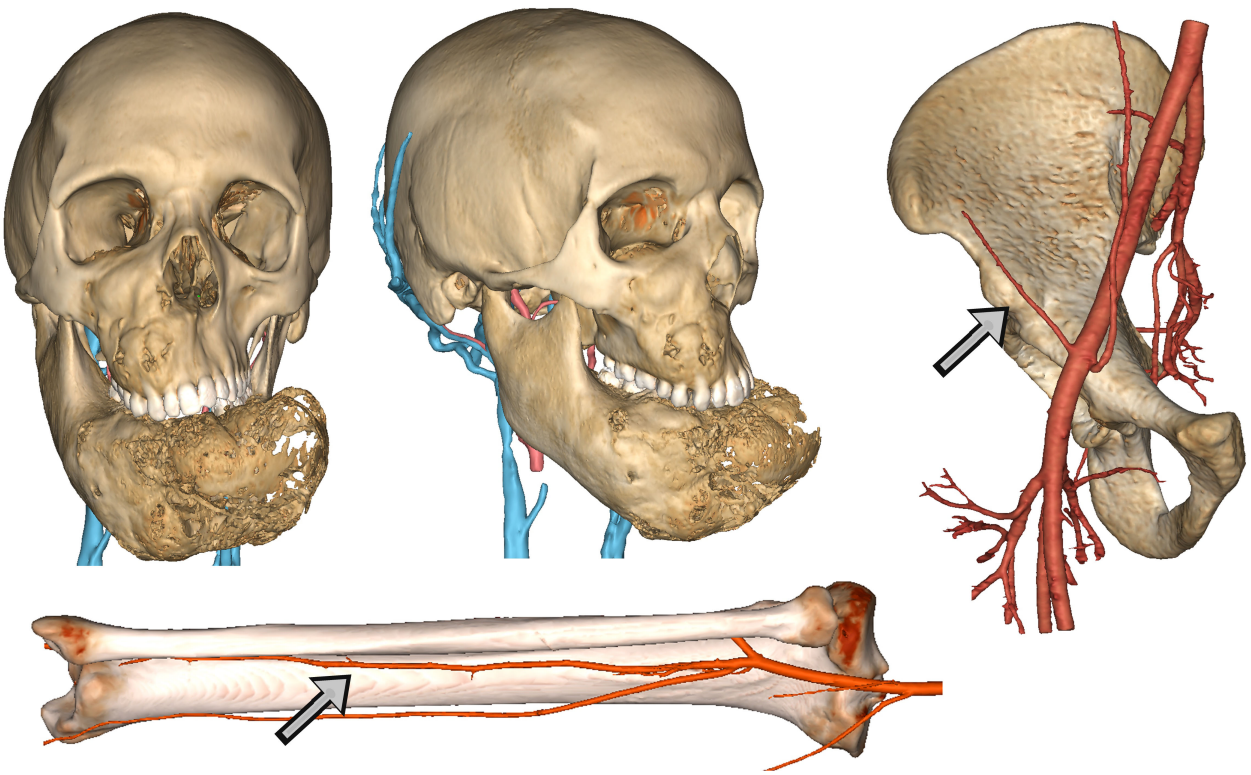

FIGURE 1
Detailed anatomical reconstruction of the craniomaxillofacial model of a fibrous dysplasia involving both the midface and the mandible with massive deformation. Associated, the reconstruction of arterial and venous vasculature is visible. For free flaps, virtual models of donor site were reconstructed with arterial vessels to evaluate the pedicle. Arrows show respectively the deep circumflex iliac artery and the fibular artery.

10.3389/fonc.2023.1103104

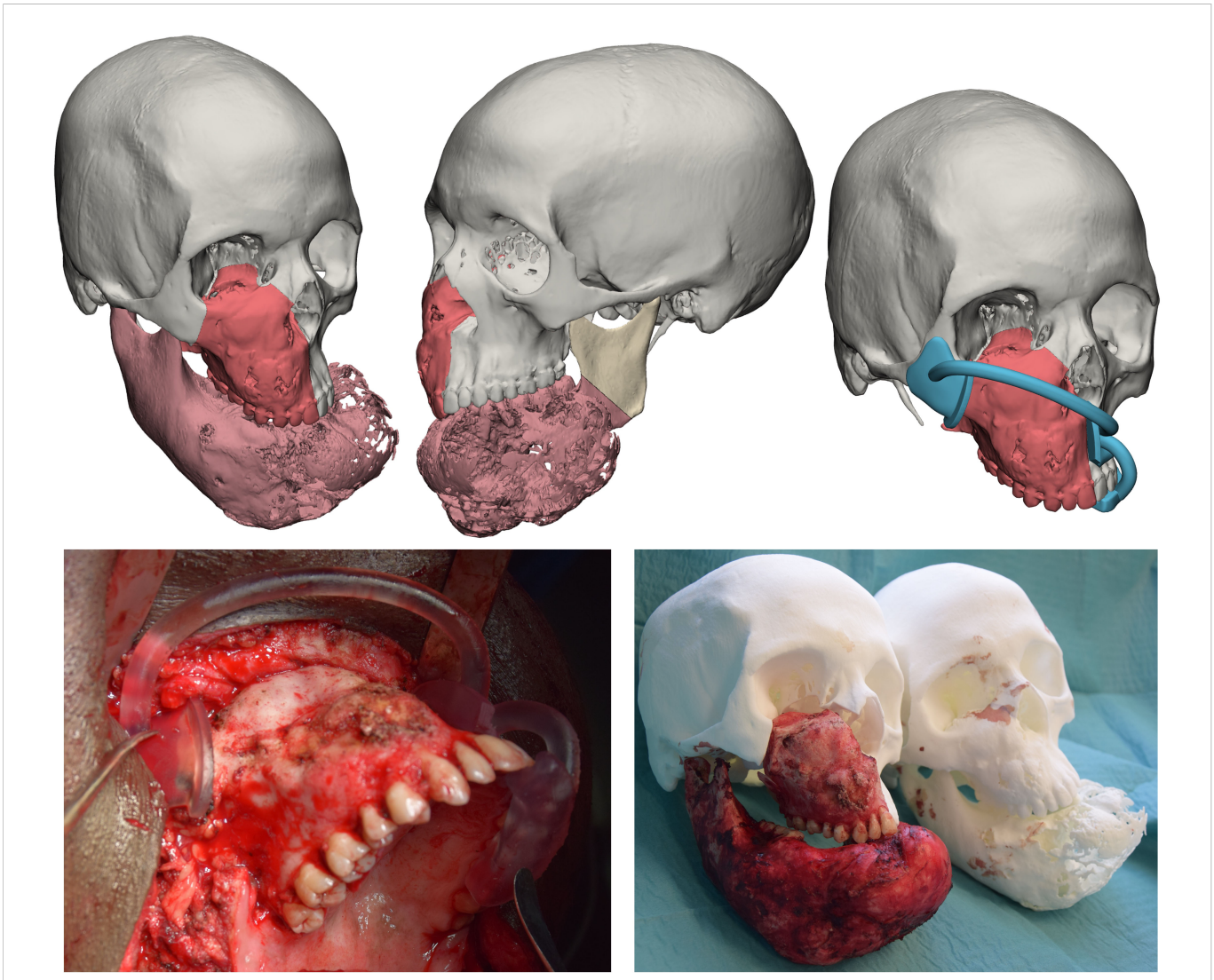

FIGURE 2
Top panel: simulated resection and design of a surgical guide. Bottom panel: intraoperative application of the surgical guide and assessment of resection accuracy by comparison with a 3D printed phantom.

The positioning of fibula flap segments was performed according to two factors: overlying dental crowns and underlying SSM mandibular border. The flap segments were positioned to be compatible with the application of implants and a future dental prosthesis, while at the same time being supported by a customized mandibular implant which included, in disarticulations, reconstruction of the temporomandibular joint (TMJ), coupled with a glenoid fossa. The fibula segments were rotated to keep the pedicle completely lingual. Once satisfied with the position of fibula segments over the mandible, they were individually aligned along the fibula axis and a surgical guide was modelled to assist the exact harvest. Segments were fixed on the customized mandibular prosthesis using the same holes provided by the guide. Microsurgical anastomoses were performed to restore blood flow and a 3D printed model of the dental wax-up was positioned to assess compatibility and define the correct implant site (Figure 5).

- Midface reconstruction

The upper dental arch in occlusal relationship with its inferior antagonist was simulated in a similar way to identify a position of the midface flap compatible with implant placement and a future denture. Although also the scapular tip flap is a viable option, the deep circumflex iliac artery (DCIA) flap was chosen because it did not involve a change in patient positioning. The iliac crest was reoriented in accordance with the resection area to select the most suitable part and size. Subsequently, the simulation included further flap sculpting to trim any bone excess. Finally, an innovative surgical guide was modelled to enable precise DCIA flap insetting, holding the flap secured thanks to a custom-designed socket and at the same time allowing for fixation in the desired position. Similarly, implants were placed in the iliac crest using the 3D printed dental wax-up model (Figure 6).

- Orbital reconstruction

For class IV maxillectomies, the reconstruction of the orbital floor was needed. A mirroring of the contralateral integer orbit was performed to define the optimal shape of the orbital floor and ensure that the reconstruction did not alter the volume symmetry between the orbits. The implant was designed according to such principles and, using a

10.3389/fonc.2023.1103104

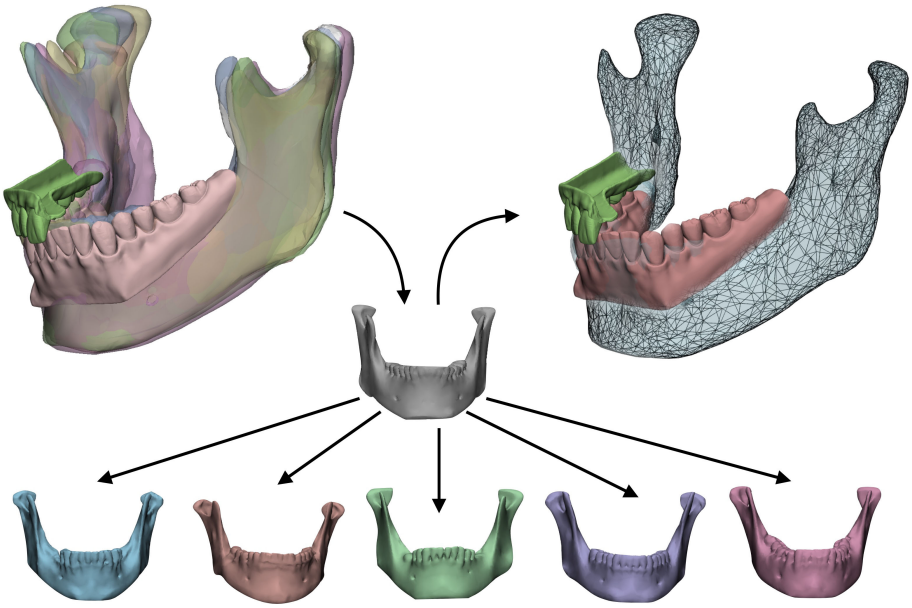

FIGURE 3
Statistical shape model (SSM) associated with digital wax-up. A target model (grey) taken from a library of STL based on anatomical resemblance with the patient is iteratively modified by applying population variance using five modificators. The result is a mesh made suitable for the actual patient which will be used to reconstruct the final shape of the mandibular prosthesis.

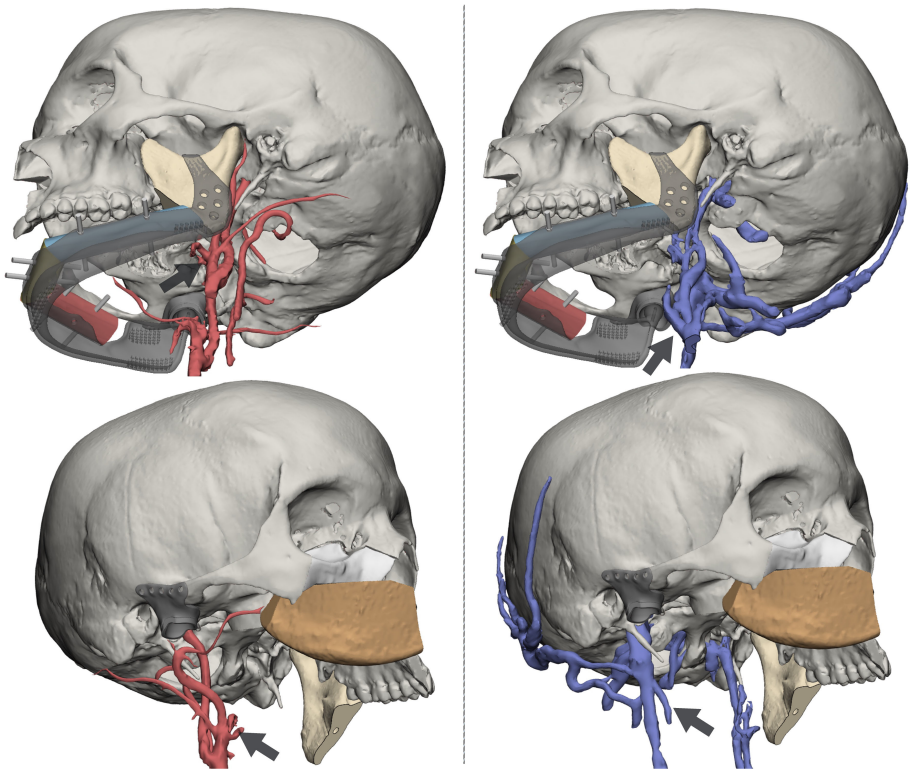

FIGURE 4
Reconstruction of arterial (left panel) and venous (right panel) vasculature from dedicated MR sequences. Black arrows identify vessels targeted for anastomosis: for the DCIA, the facial artery and the facial vein; for the fibula, the superior thyroid artery and the thyrolinguofacial venous trunk.

10.3389/fonc.2023.1103104

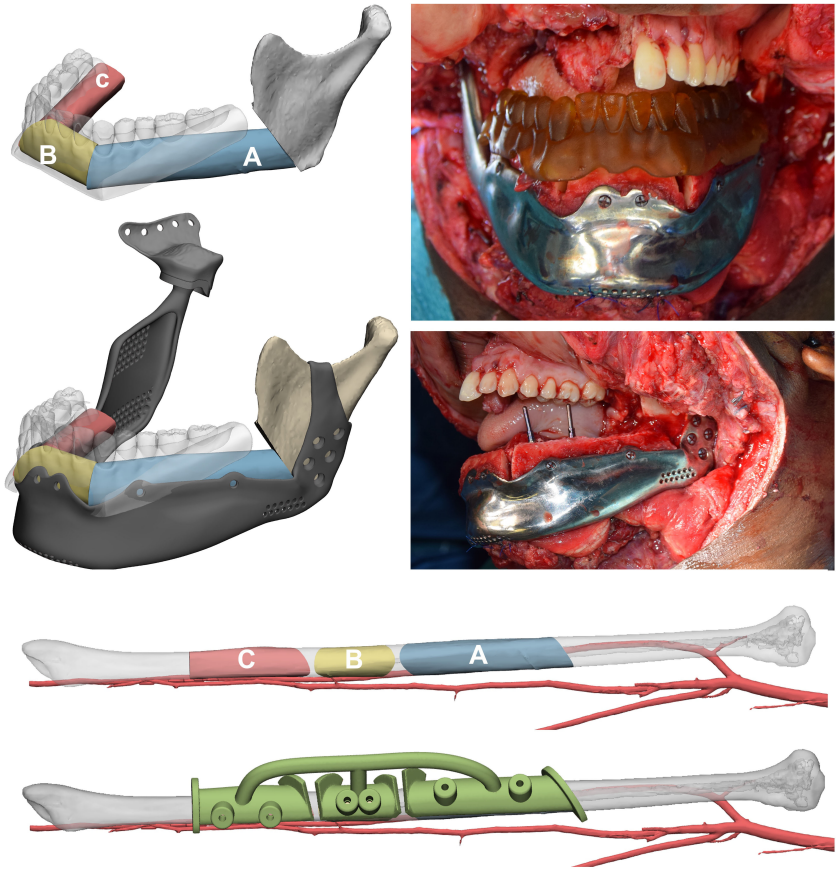

FIGURE 5
Mandibular reconstruction. The order of fibula flap segments is indicated in a proximal to distal sequence both in the mandible and in the native fibula, where a surgical guide to automate harvest was designed. Fibula segments have been positioned according to the virtual occlusion defined using the digital wax-up and their inset on a mandibular patient-specific implant designed on the SSM is simulated. Implants are placed using the 3D-printed wax-up as guide to drill holes.

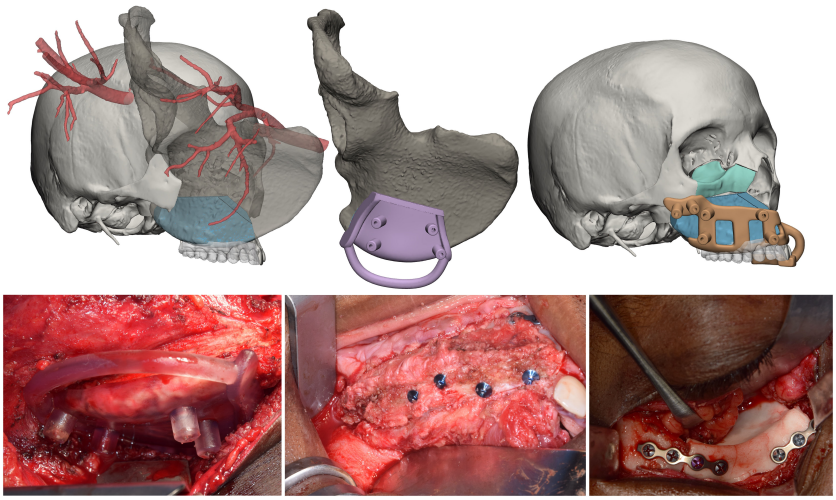

FIGURE 6
Midface reconstruction. The native iliac crest with vascularization is transposed in the defect site, where the flap is sized to ensure optimal geometrical compatibility. A surgical guide to automate the flap harvesting is designed. The flap is positioned in accordance with the digital wax-up, and a surgical guide for repositioning is designed. Finally, the orbital floor is restored by moulding a PMMA orbital implant.

Boolean operator, it was made correspondent with the resection edges. A molding system bearing the negative impression of the implant was designed and 3D printed for the intraoperative creation of an implantable part made of polymethyl methacrylate (6).

2.4 Outcome evaluation

Flap survival was monitored clinically every 3 hours for the first 3 days, and every 6 hours up to the first week. Two weeks after surgery, all patients underwent a postoperative CT scan with the same parameters, which was processed in Mimics to extract flaps and titanium implants from surrounding bone, yielding separate objects. Extracted objects were imported in the same coordinate system as the virtual planning project in order to estimate the deviation of the achieved surgical outcome from its planned equivalent. To quantify this, a part comparison analysis, computing Euclidean distances between pairs of aligned meshes across all their vertices was performed, and results were mapped in a color scale. The overall entity of deviation between the two geometrical entities was expressed as root mean square error (RMSE), allowing to understand the accuracy of flap and implant positioning (Figure 7). Clinical photographs were taken 6-month postoperatively (Figure 8).

3 Results

Clinical and demographic data of patient enrolled in this study are described in Table 1.

For all patients, the reconstruction of the mandible was performed using the fibula free flap, while the midface was reconstructed using the DCIA flap. There were no clinical complications concerning the harvesting sites.

The number of implants inserted in the fibula flap bone ranged between 5 and 6 for total or subtotal resection, while segmental defect, limited to less than one half of the mandible, required from 2 to 3 implants. As for the iliac crest, the implants ranged from 3 to 4 along the superior rim of the flap.

We did not perform a simultaneous dental prosthesis placement in any of the patients, as the customized mandibular prosthesis which supports the flap was not designed to withstand immediate load, nor was the iliac crest flap replacing the maxilla.

For all patients it was possible to identify the arterial trunk for the anastomosis in the virtual plan.

Duration of surgery ranged from a minimum of 13 hours to the maximum of 18 hours and involved two different teams for ablative and reconstructive surgery.

Virtual surgical planning and 3D printed guides were used in all cases according to the sequence detailed in Materials and Methods section. Average RMSE for the iliac bone crest flap was of 3.2 ± 0.36 mm; as for the fibula flap, RMSE value was of 2.3 ± 0.65 mm. As for patient-specific implants, for mandibular prostheses the average RMSE was 2.46 mm with 0.76 mm standard deviation; while there was a single orbital PMMA prosthesis in patient 1 (RMSE=2.1)

After surgery, TMJ functionality was assessed by measuring the average mouth opening, which was of 2.8 ± 0.7 mm at 3-month and 3.4 ± 0.9 mm at 6-month follow-up.

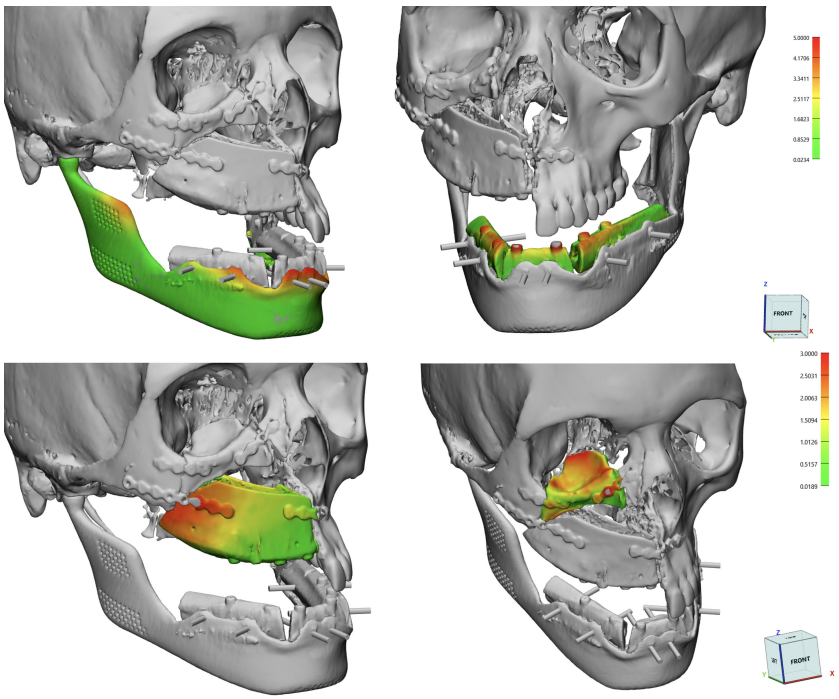

FIGURE 7
Calculations of RMSE using a surface deviation analysis for single subcomponents: DCIA and fibula flaps, mandibular implant, orbital implant.

FIGURE 8
Preoperative vs 6-month postoperative appearance of the patient. Top row: full face photographs; bottom row: intraoral view showing implants placed during surgery.

4 Discussion

Reconstruction of large defects involving different subunits of the facial skeleton represents one of the major challenges in cranio-maxillo-facial surgery. Multiple approaches have been proposed, and can be synthetically ascribed to the following groups:

- single chimeric bone flap
- single bone flap and single soft-tissue flap
- single bone flap and customized prosthesis

Single chimeric bone flaps offer surgeons a versatile solution to perform a composite reconstruction including multiple tissues transposed in different anatomical sites, as each flap territory is based on a vascular supply independent from the interconnection with contiguous parts, with the exception of the "mother" vessel which is anastomized to head and neck vessels. Such flap architecture allows for greater mobilization of tissue subunits, allowing to use a single flap to reconstruct composite defects: in this respect, the scapular tip flap was described a versatile technique allowing to reconstruct midfacial defects, providing at the same time a bicortical bone framework suitable for implant placement, as well as a generous muscular cuff, and eventually the possibility to harvest a myocutaneous paddle using the latissimus dorsi (7, 8). Other flaps, typically the fibula flap, are not harvested as chimeric flaps, but can be arranged in complex spatial conformations which enable the reconstruction of geometrically complex defects (9).

In the last decades, progresses in medical imaging software and additive manufacturing allowed to perform accurate virtual reality simulations to restore the missing parts of the craniofacial skeleton, using digital techniques such as mesh mirroring, polysculpting and CAD-design. The concomitant advancement in metal 3D printing, including technologies such as selective laser sintering (SLS), melting (SLM) and electron-beam melting (EBM) made possible to manufacture complex craniofacial implants that accurately reproduce the native anatomy. Notably, these techniques have been variably combined with microsurgical approaches, leading to the assembly of microsurgical flaps over customized implants, to provide the most trustful restoration of the skeletal framework. Such approaches have been implemented in particular for orbito-maxillary resections, providing an effective method to restore the anatomical integrity of the orbit, while at the same time supplying a soft tissue lining that keeps the implant covered and eventually a native bone component to insert dental implants (10).

Although chimeric flaps represented a significant improvement in microsurgery thanks to the possibility to use a single vascular supply to provide tissue to different anatomical areas, they have a limited indication for very large defects that simultaneously involve the middle and the inferior third of the maxillofacial skeleton. According to Mannelli and colleagues (11), intrinsic chimeric flaps are contraindicated for large soft tissue need (>350 cm^2) and large and complex bone defects (>13-14 cm). Moreover, chimeric flaps require a higher microsurgical training compared with simple flap harvesting, and require the ablative surgical time to be complete prior to harvesting the flap, thus precluding any dual-team surgery, with an increase in surgical time (12). In these cases, several papers have explored the possibility to perform a double microsurgical procedure, which involves the simultaneous harvest and inset of two different microsurgical flaps. Some Authors have collected literature evidence on the use of dual free flap in head and neck reconstruction, concluding that combinations of flaps generally involve a bone and a soft tissue flap, or two soft tissue flaps, in particular, the predominant combination for mandible reconstruction involves the simultaneous use of the fibula free flap with the anterolateral thigh flap (1, 13). However, the simultaneous use of two osseous free flaps is

seldom reported (14), with no previous reports considering the combination of the DCIA and the fibula flap to restore a midfacial and mandibular defect.

In this paper, we report our preliminary experience with a dual osseous flap reconstruction of broad midfacial and mandibular defects using the combination of DCIA and fibula flap, presenting an entirely digital workflow which has several benefits, including: sequencing and strategy; surgical automation, functional restoration, accuracy. First, the precise definition of preoperative anatomy plays a crucial role, and it is of prominent importance to instruct radiologists to acquire images with well-defined protocols for 3D reconstruction to maximize the ease and accuracy of segmentation. In particular, as reported by the same Authors, the use of dedicated MR sequences with maximal spatial resolution parameters allows to perform a differential segmentation which can discriminate between arterial and venous blood flow, leading to trustful models of vasculature that facilitate the visualization of recipient head and neck vessels (5). Similar reconstructions are performed also for the donor region of flaps, enabling to define the length of their pedicle to anticipately establish the most appropriate vascular connection. Another innovative approach is the definition of the ideal shape of the mandible in cases where the preoperative deformation conceals any intelligible shape corresponding to the premorbid condition. This was achieved using a statistical shape model (SSM) applied to a closest-donor template mandible chosen from a library based on similar antropometric features (15) combined with organic mesh modeling to adapt the SSM into optimal articulation with the glenoid fossa. SSM was used as source shape to design the final mandible implant to restore the most accurate shape of the mandibular border, while at the same time supporting the fibula free flap accommodated within a custom-designed socket (16). Likewise, the arrangement of fibula segments was not only guided by the SSM, but also by occlusion: it is important to adopt an occlusion-driven approach to flap positioning, taking into account the final position of dental crowns in their optimal intercuspation with superior antagonists and modifying the height of flap inset according to the desired occlusal plane (17–19). For this purpose, the possibility to recreate all missing dental crowns within a virtual wax-up model was essential to define occlusal relationship and posing, together with the SSM, an additional constraint for optimal flap positioning. As mentioned, given the complexity of such surgeries, simultaneous prosthesis placement with immediate load was not performed in such cases, although it was described for single flap surgeries (17), as it might compromise the stability of flaps. We preferred to delay dental prosthesis placement at 8-12 months after surgery to ensure maximal osteointegration and stability.

For mandibulectomies with condyle disarticulation, TMJ reconstruction was included in the final implant: although for some Authors the condyle is sufficient to restore the function of TMJ (20), we recommend coupling the condyle with a prosthetic glenoid fossa to yield a fully functional TMJ. The same principles were applied to DCIA flap, which was positioned according to an optimal relationship with occlusion. The choice of the iliac crest free flap was based on the possibility of harvesting the flap without a position change for the patient, allowing multiple surgical teams to simultaneously work; moreover, the iliac crest provides a wide, thick-cortical surface for stable implant placement. Virtual surgical planning of iliac crest positioning enabled to perform a detailed osteometric study to establish the most favorable insetting position for implant placement (21). At the same time, a customized orbital implant overlying the DCIA flap was intraoperatively created by PMMA moulding

The fully digital workflow implemented by this study enabled to define a detailed surgical sequence and was performed entirely by the surgical team; likewise, any surgical guide was 3D printed in-house. The advantages of complete clinical management of the virtual planning involve the awareness of surgical accesses, thorough study of the clinical case and virtual interaction with the digital model. The surgical automation allowed by the entirely digital workflow allowed to decrease surgical time for flap shaping and insetting, facilitating all maneuvers related to the geometrical reconstruction of the maxillofacial skeleton using an entirely in-house workflow, with surgical guides for resection, fibula flap and DCIA flap harvest, DCIA flap positioning, as well as a customized mandibular implant shaped on the fibula flap and the SSM (22). In terms of surgical accuracy, the automation of surgical sequence enabled to restrict positional error for flaps and implants within 4 mm for maxillary reconstruction and 2 mm for the neo-mandible, representing a substantial correspondence between the planning and surgical outcome, thus meeting the requirements for functional restoration.

5 Conclusion

This paper reports a preliminary experience in facial reconstructive surgery using the simultaneous combination of two osseous flap in an entirely computer-guided sequence with meticulous study of osteometric and vascular features of flaps and their recipient sites. Virtual planning allowed to match needs in reconstructive properties with functional demands, allowing to tailor flap design and inset on the requirements for an effective occlusion, including temporomandibular joint replacement as well. Virtual surgical planning is an essential part of each reconstructive strategy in a contemporary vision of maxillofacial surgery, especially for complex cases, allowing to precisely define a great number of preoperative variables, to design and manufacture guides that assist the surgeons in accuracy-demanding procedures. Most importantly, the whole sequence of planning was designed by surgeons, that mentalized and reproduced it in the operating room. In conclusion, double bone free flap is a valuable resource to reconstruct wide defects that simultaneously involve two thirds of the cranio-maxillo-facial skeleton, but an extended virtual planning study should be always performed before approaching this surgical option.

Data availability statement

The raw data supporting the conclusions of this article will be made available by the authors, without undue reservation.

Ethics statement

The studies involving human participants were reviewed and approved by IRB_45_2020. The patients/participants provided their written informed consent to participate in this study. Written informed consent was obtained from the individual(s) for the publication of any potentially identifiable images or data included in this article.

Author contributions

AT designed the study, performed virtual surgical planning, created virtual models, 3D printed models, and wrote the full paper. DB acquired radiologic images with required protocols and wrote the imaging part of this paper. SF read and approved the manuscript. MR coordinated the research team and approved the final manuscript before submission. All authors contributed to the article and approved the submitted version.

Conflict of interest

The authors declare that the research was conducted in the absence of any commercial or financial relationships that could be construed as a potential conflict of interest.

Publisher's note

References

1. Wei F-C, Yazar S, Lin C-H, Cheng M-H, Tsao C-K, Chiang Y-C. Double free flaps in head and neck reconstruction. *Clinics Plast Surg* (2005) 32:303–8. doi: 10.1016/j.cps.2005.01.004

2. Khatib B, Patel A, Dierks EJ, Bell RB, Cheng A. The biaxial double-barrel fibula flap–a simplified technique for fibula maxillary reconstruction. *J Oral Maxillofac Surg* (2019) 77:412–25. doi: 10.1016/j.joms.2018.09.019

3. Fu K, Liu Y, Gao N, Cai J, He W, Qiu W. Reconstruction of maxillary and orbital floor defect with free fibula flap and whole individualized titanium mesh assisted by computer techniques. *J Oral Maxillofac Surg* (2017) 75:1791.e1–1791.e9. doi: 10.1016/j.joms.2017.03.054

4. Shipchandler TZ, Waters HH, Knott PD, Fritz MA. Orbitomaxillary reconstruction using the layered fibula osteocutaneous flap. *Arch FACIAL Plast Surg* (2012) 14:6. doi: 10.1001/archfacial.2011.1329

5. Tel A, Bagatto D, Costa F, Sembronio S, Robiony M. Anatomical computerized exploration to excise malignancies in deep facial compartments: An advanced virtual reality protocol for a tailored surgical approach. *Front Oncol* (2022) 12:875990. doi: 10.3389/fonc.2022.875990

6. Tel A, Tuniz F, Sembronio S, Costa F, Bresadola V, Robiony M. Cubik system: maximizing possibilities of in-house computer-guided surgery for complex craniofacial reconstruction. *Int J Oral Maxillofac Surg* (2021) 50:1554–62. doi: 10.1016/j.ijom.2021.07.008

7. Ferri A, Perlangeli G, Bianchi B, Zito F, Sesenna E, Ferrari S. Maxillary reconstruction with scapular tip chimeric free flap. *Microsurgery* (2021) 41:207–15. doi: 10.1002/micr.30700

8. Watanabe K, Takahashi N, Morihisa Y, Ikejiri M, Koga N, Rikimaru H, et al. Maxillary reconstruction using chimeric flaps of the subscapular artery system without vein grafts and the novel usage of chimeric flaps. *J Reconstr Microsurg* (2013) 29:601–6. doi: 10.1055/s-0033-1354736

9. Chen S, Hung K, Lee Y. Maxillary reconstruction with a double-barrel osteocutaneous fibular flap and arteriovenous saphenous loop after a globe-sparing total maxillectomy-a case report: Total maxillary reconstruction using a double-barrel fibular flap. *Microsurgery* (2017) 37:334–8. doi: 10.1002/micr.22441

10. Mertens C, Löwenheim H, Hoffmann J. Image data based reconstruction of the midface using a patient-specific implant in combination with a vascularized osteomyocutaneous scapular flap. *J Cranio-Maxillofacial Surg* (2013) 41:219–25. doi: 10.1016/j.jcms.2012.09.003

11. Mannelli G, Gazzini L, Comini LV, Parrinello G, Nocini R, Marchioni D, et al. Double free flaps in oral cavity and oropharynx reconstruction: Systematic review, indications and limits. *Oral Oncol* (2020) 104:104637. doi: 10.1016/j.oraloncology.2020.104637

12. Sweeny L, Rosenthal EL, Light T, Grayson J, Petrisor D, Troob SH, et al. Outcomes and cost implications of microvascular reconstructions of the head and neck. *Head Neck* (2019) 41:930–9. doi: 10.1002/hed.25424

13. Balasubramanian D, Thankappan K, Kuriakose MA, Duraisamy S, Sharan R, Mathew J, et al. Reconstructive indications of simultaneous double free flaps in the head and neck: A case series and literature review. *Microsurgery* (2012) 32:423–30. doi: 10.1002/micr.21963

14. Barton BM, Blumberg JM, Patel SN. Near-total mandibular reconstruction following osteoradionecrosis with double scapula tip free flap: A case report. *Microsurgery* (2022) 42:80–3. doi: 10.1002/micr.30798

15. Wang E, Tran KL, D'heygere E, Prisman E. Predicting the premorbid shape of a diseased mandible. *Laryngoscope* (2021) 131(3):E781-6. doi: 10.1002/lary.29009

16. Tarsitano A, Battaglia S, Corinaldesi G, Marchetti C, Pellegrino G, Ciocca L. Mandibular reconstruction using a new design for a patient-specific plate to support a fibular free flap and avoid double-barrel technique. *Acta Otorhinolaryngol Ital* (2021) 41:230–5. doi: 10.14639/0392-100X-N0549

17. Williams FC, Hammer DA, Wentland TR, Kim RY. Immediate teeth in fibulas: Planning and digital workflow with point-of-Care 3D printing. *J Oral Maxillofac Surg* (2020) 78:1320–7. doi: 10.1016/j.joms.2020.04.006

18. Chang Y-M, Wei F-C. Fibula jaw-in-a-Day with minimal computer-aided design and manufacturing: Maximizing efficiency, cost-effectiveness, intraoperative flexibility, and quality. *Plast Reconstructive Surg* (2021) 147:476–9. doi: 10.1097/PRS.0000000000007546

19. Cebrian-Carretero Jl, Guinales-Diaz de Cevallos J, Sobrino Ja, Yu T, Burgueno-Garcia M. Predictable dental rehabilitation in maxillomandibular reconstruction with free flaps. the role of implant guided surgery. *Med Oral* (2014), e605–11. doi: 10.4317/medoral.19116

20. Ciocca L, Mazzoni S, Fantini M, Persiani F, Baldissara P, Marchetti C, et al. A CAD/CAM-prototyped anatomical condylar prosthesis connected to a custom-made bone plate to support a fibula free flap. *Med Biol Eng Comput* (2012) 50:743–9. doi: 10.1007/s11517-012-0898-4

21. Zaker Shahrak A, Zor F, Kanatas A, Acikel C, Sapountzis S, Nicoli F, et al. Morphological and morphometric evaluation of the ilium, fibula, and scapula bones for oral and maxillofacial reconstruction: Morphological evaluation of bone donor sites. *Microsurgery* (2014) 34:638–45. doi: 10.1002/micr.22307

22. Lee Z-H, Alfonso AR, Ramly EP, Kantar RS, Yu JW, Daar D, et al. The latest evolution in virtual surgical planning: Customized reconstruction plates in free fibula flap mandibular reconstruction. *Plast Reconstructive Surg* (2020) 146:872–9. doi: 10.1097/PRS.0000000000007161

frontiers | Frontiers in Surgery

TYPE Original Research
PUBLISHED 24 March 2023
DOI 10.3389/fsurg.2023.1125875

OPEN ACCESS

EDITED BY
Francesco Giovinazzo,
Agostino Gemelli University Polyclinic (IRCCS), Italy

REVIEWED BY
Albino Eccher,
Integrated University Hospital Verona, Italy
Elliot Asare,
The University of Utah, United States

*CORRESPONDENCE
Wei Shen
✉ shenweiijs@outlook.com
Chao Cheng
✉ Mr_chengchao@126.com

†These authors have contributed equally to this work

SPECIALTY SECTION
This article was submitted to Surgical Oncology, a section of the journal Frontiers in Surgery

RECEIVED 16 December 2022
ACCEPTED 13 March 2023
PUBLISHED 24 March 2023

CITATION
Liu Y, Zhao S, Du W, Tian Z, Chi H, Chao C and Shen W (2023) Applying interpretable machine learning algorithms to predict risk factors for permanent stoma in patients after TME. Front. Surg. 10:1125875. doi: 10.3389/fsurg.2023.1125875

Applying interpretable machine learning algorithms to predict risk factors for permanent stoma in patients after TME

Yuan Liu[1†], Songyun Zhao[2†], Wenyi Du[1†], Zhiqiang Tian[1], Hao Chi[3], Cheng Chao[2*] and Wei Shen[1*]

[1]Department of General Surgery, Wuxi People's Hospital Affiliated to Nanjing Medical University, Wuxi, China, [2]Department of Neurosurgery, Wuxi People's Hospital Affiliated to Nanjing Medical University, Wuxi, China, [3]Clinical Medical College, Southwest Medical University, Luzhou, China

Objective: The purpose of this study was to develop a machine learning model to identify preoperative and intraoperative high-risk factors and to predict the occurrence of permanent stoma in patients after total mesorectal excision (TME).
Methods: A total of 1,163 patients with rectal cancer were included in the study, including 142 patients with permanent stoma. We collected 24 characteristic variables, including patient demographic characteristics, basic medical history, preoperative examination characteristics, type of surgery, and intraoperative information. Four machine learning algorithms including extreme gradient boosting (XGBoost), random forest (RF), support vector machine (SVM) and k-nearest neighbor algorithm (KNN) were applied to construct the model and evaluate the model using k-fold cross validation method, ROC curve, calibration curve, decision curve analysis (DCA) and external validation.
Results: The XGBoost algorithm showed the best performance among the four prediction models. The ROC curve results showed that XGBoost had a high predictive accuracy with an AUC value of 0.987 in the training set and 0.963 in the validation set. The k-fold cross-validation method was used for internal validation, and the XGBoost model was stable. The calibration curves showed high predictive power of the XGBoost model. DCA curves showed higher benefit rates for patients who received interventional treatment under the XGBoost model. The AUC value for the external validation set was 0.89, indicating that the XGBoost prediction model has good extrapolation.
Conclusion: The prediction model for permanent stoma in patients with rectal cancer derived from the XGBoost machine learning algorithm in this study has high prediction accuracy and clinical utility.

KEYWORDS
rectal cancer, permanent stoma, prognosis, risk factor, machine learning, surgery

1. Introduction

Rectal cancer is a gastrointestinal tumor with an extremely high morbidity and mortality rate. The incidence of colorectal cancer is increasing year by year due to changes in people's lifestyle and dietary habits. A 2019 epidemiological survey (1) showed that the incidence of colorectal cancer ranks third among malignant tumors worldwide, after lung cancer and breast cancer. Total mesorectal excision (TME), a common surgical treatment for rectal cancer, has greatly improved the prognosis of patients with rectal cancer. The principle of surgery is to completely resect the entire mesentery of low and intermediate rectal cancer to

reduce the postoperative recurrence rate of patients while increasing the rate of anal preservation and improving the survival quality of patients (2–4). However, as the level of surgery continues to evolve, clinicians are gradually discovering the limitations of TME, such as patients' vulnerability to serious complications such as anastomotic leakage after surgery (5, 6). The quality of life for patients who develop postoperative complications is poor and there is an increased risk of secondary surgery. Therefore, temporary prophylactic stoma is often used clinically for patients with rectal cancer who have preserved anus, thus reducing the pressure at the anastomosis and reducing the risk of anastomotic leakage (7). Fortunately, some patients can undergo ostomy reversal at the appropriate time to improve quality of life. However, other patients are unable to retract for various reasons and suffer great physical and psychological damage. Some studies (8, 9) have shown that permanent stoma prolongs the life of patients but reduces their quality of life. Therefore, it is crucial to understand high risk factors for permanent stoma so that surgeons can appropriate counsel patients.

Artificial intelligence (AI) is developing rapidly in the medical field (10). Machine learning, as a major branch of AI, has the advantages of more stable model building and more accurate prediction, is favored by clinicians and is used in clinical prediction and other aspects (11, 12). In this study, we analyzed the clinical information of rectal cancer patients and applied machine learning algorithms to establish a prediction model for permanent stoma in rectal cancer patients to aid clinicians in making timely and accurate individualized treatment plans.

2. Materials and methods

2.1. Study subjects

In the study, we used data from the clinical databases of Wuxi People's Hospital affiliated to Nanjing Medical University and Wuxi Second People's Hospital. Inclusion criteria: (1) patients were diagnosed with rectal cancer by pathological examination; (2) patients were treated with TME surgery; and (3) the surgical team consisted of senior doctors who had the ability to independently perform TME and enterostomy. Exclusion criteria were as follows: (1) patients with other malignant tumors; (2) patients who had been diagnosed with distant metastasis of rectal cancer; (3) patients with other diseases of the rectum; (4) patients diagnosed with life-threatening cardiovascular diseases such as cerebral infarction; (5) patients diagnosed with important organ diseases such as liver failure or kidney failure; and (6) missing case records or missed visits. Patients were followed up for at least three years after surgery. Two surgeons performed medical history, physical examination and abdominal ultrasound, computed tomography (CT) and other imaging examinations on patients every three months. The study was approved by the Ethics Review Committee of Wuxi People's Hospital, with approval number KY22086.

2.2. Study design and data collection

Clinical data were retrospectively collected from January 2010 to January 2018 from patients with rectal cancer at Wuxi People's Hospital and Wuxi Second People's Hospital, including 25 preoperative variables (within 24 h of the day of surgery) and intraoperative variables. Preoperative variables collected included patient demographic characteristics (gender, age, smoking history, alcohol history, and body mass index), basic clinical characteristics (American Society of Anesthesiologists score, nutrition risk screening 2002 score, history of surgery, chemotherapy, and radiotherapy), basic medical history (anemia, rectal stenosis, diabetes, hypertension, hyperlipidemia, and coronary artery disease), laboratory tests (carcinoembryonic antigen, carbohydrate antigen 19-9, and albumin), and tumor characteristics (T-category, N-category, tumor recurrence, tumor size, and tumor distance from the dentate line). Intraoperative variables collected included whether a permanent stoma was performed.

2.3. Definition of permanent stoma

A permanent stoma is defined as a permanent stoma created during the patient's initial surgery or a permanent stoma created during the progression of the patient's disease. With the patient's consent, the decision to create a permanent stoma is made by the surgeon, taking into account the patient's physical condition and disease progression.

2.4. Development and evaluation of predictive models for machine learning algorithms

SPSS software and R software were applied for the construction and evaluation of clinical prediction models. (1) Univariate and multivariate regression analyses were performed. The chi-square test was applied to categorical variables to compare the differences between the two groups; a *t*-test was performed for continuous variables that conformed to a normal distribution; and the rank sum test was selected for continuous variables that did not conform to a normal distribution. $P < 0.05$ indicated that the difference was statistically significant. Logistic regression analysis of variables with significance in the univariate analysis was performed to obtain independent influences on permanent stoma in patients with rectal cancer. (2) Evaluate and build prediction models. Rectal cancer patients from Wuxi People's Hospital from January 2010 to December 2016 were selected as the internal validation set, and rectal cancer patients from Wuxi Second People's Hospital from January 2017 to January 2018 were selected as the external validation set. The internal validation set was randomly divided into training set (70%) and test set (30%). The independent impact factors derived from the regression analysis were incorporated into four machine learning algorithm prediction models: support vector machine (SVM), random forest (RF), extreme gradient boosting (XGBoost), and

k-nearest neighbor algorithm (KNN). The four models were evaluated by three aspects, i.e., discrimination, calibration, and clinical usefulness, and the best model was selected for prediction analysis. The ROC curve was plotted to obtain the AUC value and determine the predictive efficiency of the model; the calibration curve was plotted to assess whether there was good agreement between the predicted and actual results of the model; and decision curve analysis (DCA) was plotted to assess the benefit to the patient after interventional treatment. Internal validation was completed using the k-fold cross-validation method. (4) External validation of the best model using an external test set, plotting ROC curves and calibration curves, and determining the generalizability and predictive efficiency of the model. (5) Model interpretation. The contribution of each feature in the sample to the prediction is obtained by SHAP analysis, i.e., the Shapley value. The SHAP summary plot, which ranks the importance of risk factors, and the SHAP force plot, which analyzes and interprets the prediction results of individual samples, are constructed based on the Shapley values.

3. Results

3.1. Basic clinical information of the patient

A total of 1,163 patients were included in the study (Figure 1), including 142 (12.21%) patients with permanent stomas.

3.2. Analysis of risk factors for permanent stoma in patients with rectal cancer

The results of univariate analysis showed that there was a significant difference between the permanent stoma group and the nonpermanent stoma group in terms of age, history of hypertension, history of diabetes mellitus, tumor recurrence, history of adjuvant radiotherapy, history of adjuvant chemotherapy, distance of the tumor from the dentate line, and whether there was rectal stenosis ($P < 0.05$). The results of multivariate analysis showed that age ≥65 years, history of hypertension, history of diabetes mellitus, history of adjuvant radiotherapy, history of adjuvant chemotherapy, tumor distance ≥5 cm from the dentate line, and rectal stenosis were independent influencing factors for permanent stoma in patients with rectal cancer ($P < 0.05$) (Table 1).

3.3. Model building and evaluation

The ROC curve results show that XGBoost has an AUC value as high as 0.987 in the training set; the AUC value in the validation set is 0.963, which is the best performance among the four models (Figures 2A,B, Table 2). The calibration curve results show that the calibration curves of the four models are similar to the ideal curves, and the models have high consistency between the predicted and actual results (Figure 2C). The DCA curves showed

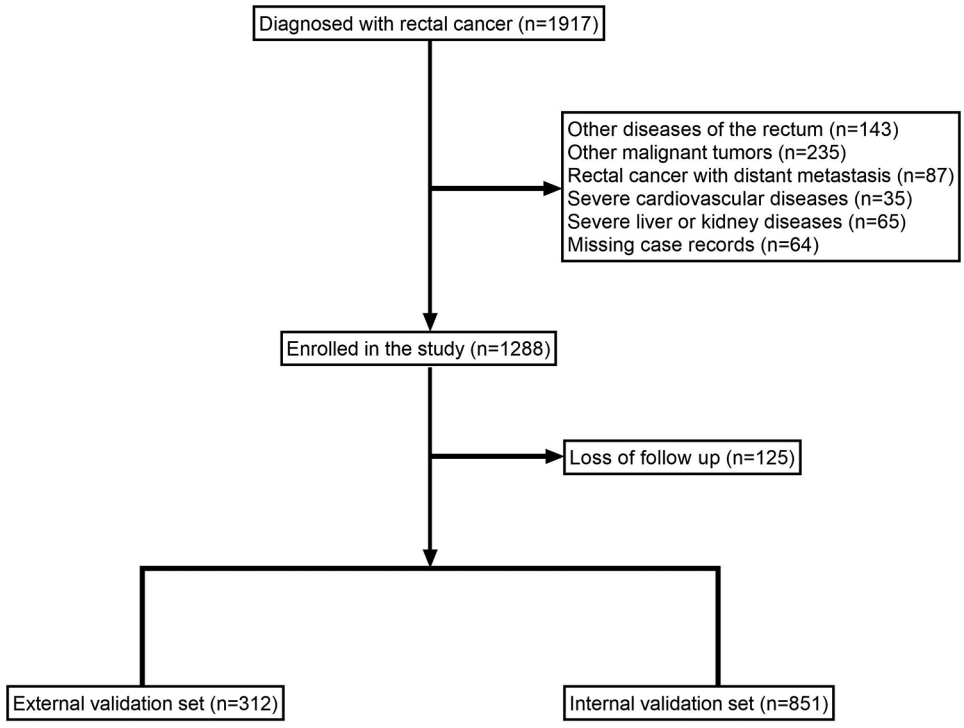

FIGURE 1
Flow diagram of patients included in the study.

TABLE 1 Univariate and multivariate analysis of variables related to permanent stoma.

Variants		Univariate analysis			Multivariate analysis		
		OR	95%CI	*P*-value	OR	95%CI	*P*-value
Sex	Female	Reference					
	Male	1.033	[0.693, 1.541]	0.873			
Age	<65	Reference			Reference		
	≥65	4.16	[2.290, 7.555]	<0.001	3.665	[1.44,10.434]	0.010
BMI	<25 kg/m^2	Reference					
	≥25 kg/m^2	1.24	[0.834, 1.843]	0.288			
ASA	<3	Reference					
	≥3	1.049	[0.707, 1.556]	0.811			
Drinking history	No	Reference					
	Yes	1.15	[0.773, 1.711]	0.490			
Smoking history	No	Reference					
	Yes	1.029	[0.694, 1.524]	0.888			
Surgical history	No	Reference					
	Yes	1.051	[0.704, 1.568]	0.808			
Anemia	No	Reference					
	Yes	1.044	[0.705, 1.548]	0.828			
Rectal stenosis	No	Reference			Reference		
	Yes	23.101	[14.240, 37.477]	<0.001	17.296	[8.201,39.173]	<0.001
Hyperlipidemia	No	Reference					
	Yes	1.347	[0.906, 2.003]	0.141			
Hypertensive	No	Reference			Reference		
	Yes	4.757	[3.121, 7.251]	<0.001	4.541	[2.188,9.783]	<0.001
Diabetes	No	Reference			Reference		
	Yes	3.858	[2.435, 6.114]	<0.001	4.316	[2.004,9.885]	<0.001
Coronary heart disease	No	Reference					
	Yes	0.954	[0.644, 1.414]	0.816			
T-category	T1~T2	Reference					
	T3~T4	1.069	[0.717, 1.595]	0.744			
N-category	N0	Reference					
	N1~N2	0.921	[0.613, 1.384]	0.692			
Tumor size	<5 cm	Reference					
	≥5 cm	0.725	[0.479, 1.099]	0.130			
Tumour recurrence	No	Reference			Reference		
	Yes	3.05	[1.573, 5.911]	0.001	1.302	[0.412,3.997]	0.647
Distance from dentate line	≥5 cm	Reference			Reference		
	<5 cm	52.999	[31.188, 90.063]	<0.001	34.79	[16.223,80.558]	<0.001
Adjuvant Radiotherapy	No	Reference			Reference		
	Yes	2.817	[1.797, 4.417]	<0.001	2.652	[1.251,5.865]	0.013
Adjuvant Chemotherapy	No	Reference			Reference		
	Yes	12.084	[7.206, 20.266]	<0.001	8.816	[4.073,20.545]	<0.001
Albumin	<30 g/L	Reference					
	≥30 g/L	0.73	[0.490, 1.088]	0.122			
CEA level	<5 ng/ml	Reference					
	≥5 ng/ml	0.93	[0.627, 1.378]	0.716			
CA19-9 level	<37 U/ml	Reference					
	≥37 U/ml	0.843	[0.569, 1.250]	0.395			
NRS2002 score	<3	Reference					
	≥3	0.714	[0.456, 1.119]	0.142			

OR, odds ratio; CI, confidence interval; BMI, body mass index; ASA, The American Society of Anesthesiologists; ALB, albumin; CEA, carcinoembryonic antigen; CA19-9, carbohydrate antigen 19-9; NRS2002, nutrition risk screening 2002.

that all four models achieved a net clinical benefit relative to either the full treatment or no treatment plan (Figure 2D). The k-fold cross-validation method was used to compare the generalization ability of the four models. Taking the test set $N = 256$ cases (30.08%) and the remaining samples as the training set for 10-fold cross-validation, AUC = 0.9456 ± 0.0367 in the validation set of XGBoost, AUC = 0.9088 in the test set, accuracy = 0.9102 (Figures 3A–C); AUC = 0.9025 ± 0.0627 in the validation set of RF, AUC = 0.8789 in the test set, accuracy = 0.8750; AUC = 0.9274 ± 0.0440 in the validation set of SVM, AUC = 0.9006 in the test set, accuracy = 0.9414; AUC = 0.8720 ± 0.0713 in the validation set of KNN, AUC = 0.8743 in the test set, accuracy = 0.9336. After

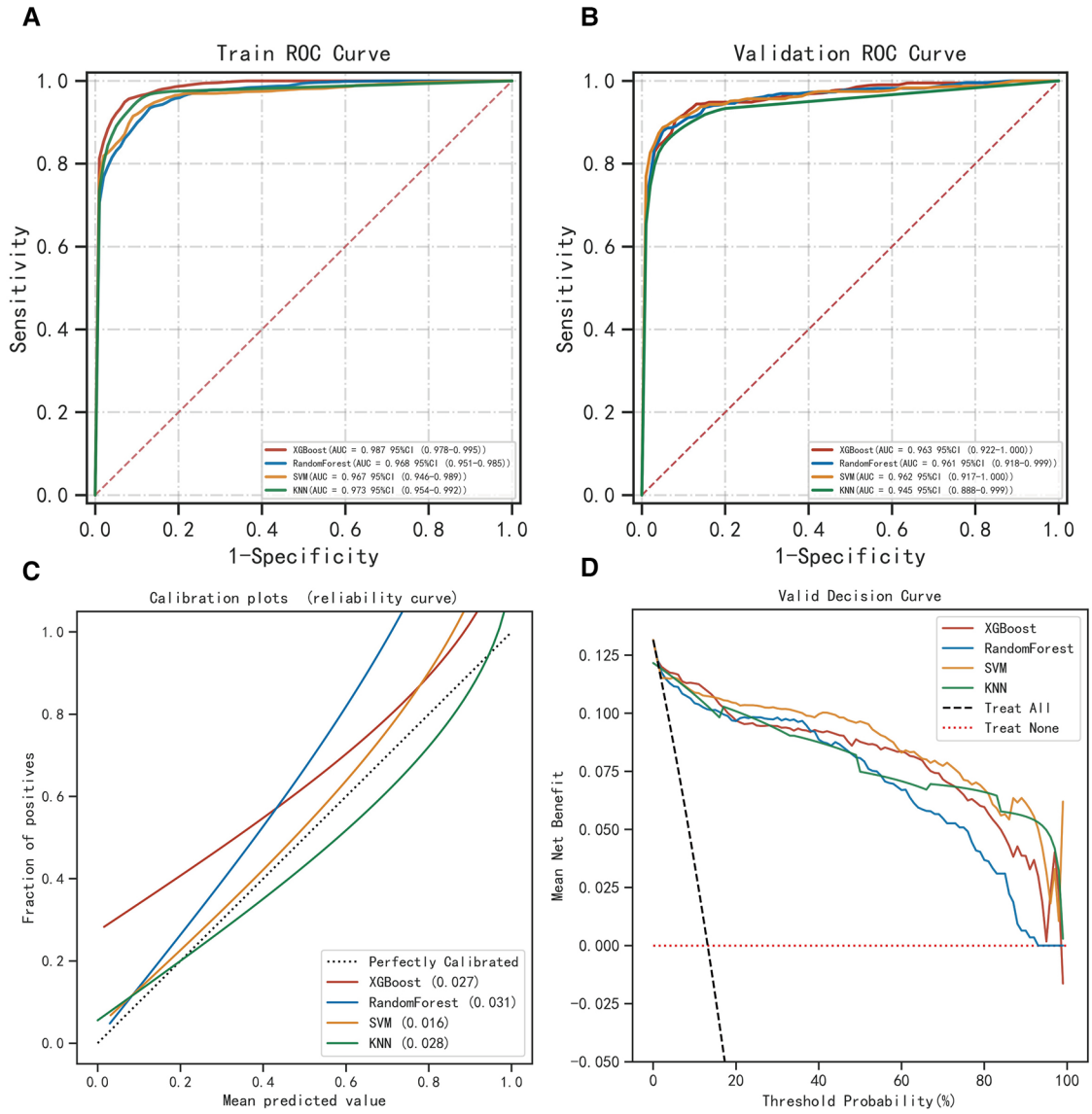

FIGURE 2
Evaluation of the four models for predicting permanent stoma. (A) ROC curves for the training set of the four models. (B) ROC curves for the validation set of the four models. (C) Calibration plots of the four models. The 45° dotted line on each graph represents the perfect match between the observed (*y*-axis) and predicted (*x*-axis) complication probabilitys. A closer distance between two curves indicates greater accuracy. (D) DCA curves of the four models. The intersection of the red curve and the All curve is the starting point, and the intersection of the red curve and the None curve is the node within which the corresponding patients can benefit.

TABLE 2 Evaluation of the performance of the four models.

		AUC(95%CI)	Accuracy(95%CI)	Sensitivity(95%CI)	Specificity(95%CI)	F1 Score(95%CI)
KNN	Training set	0.973 (0.954–0.992)	0.954 (0.950-0.958)	0.946 (0.922-0.969)	0.910 (0.889-0.931)	0.883 (0.865-0.900)
	Validation set	0.945 (0.888–0.999)	0.949 (0.938–0.959)	0.879 (0.833–0.925)	0.931 (0.900–0.963)	0.838 (0.795–0.881)
XGBoost	Training set	0.987 (0.978–0.995)	0.934 (0.928–0.939)	0.957 (0.948–0.965)	0.927 (0.920–0.933)	0.799 (0.786–0.813)
	Validation set	0.963 (0.922–1.000)	0.916 (0.902–0.929)	0.926 (0.888–0.964)	0.923 (0.903–0.943)	0.743 (0.699–0.787)
RandomForest	Training set	0.968 (0.951–0.985)	0.897 (0.885–0.909)	0.925 (0.902–0.948)	0.890 (0.872–0.908)	0.714 (0.692–0.735)
	Validation set	0.961 (0.918–0.999)	0.889 (0.868–0.910)	0.890 (0.852–0.927)	0.961 (0.945–0.976)	0.678 (0.622–0.735)
SVM	Training set	0.967 (0.946–0.989)	0.911 (0.905–0.916)	0.923 (0.910–0.935)	0.906 (0.898–0.914)	0.740 (0.731–0.749)
	Validation set	0.962 (0.917–1.000)	0.897 (0.880–0.914)	0.909 (0.869–0.950)	0.951 (0.932–0.970)	0.697(0.644–0.750)

CI, confidence interval.

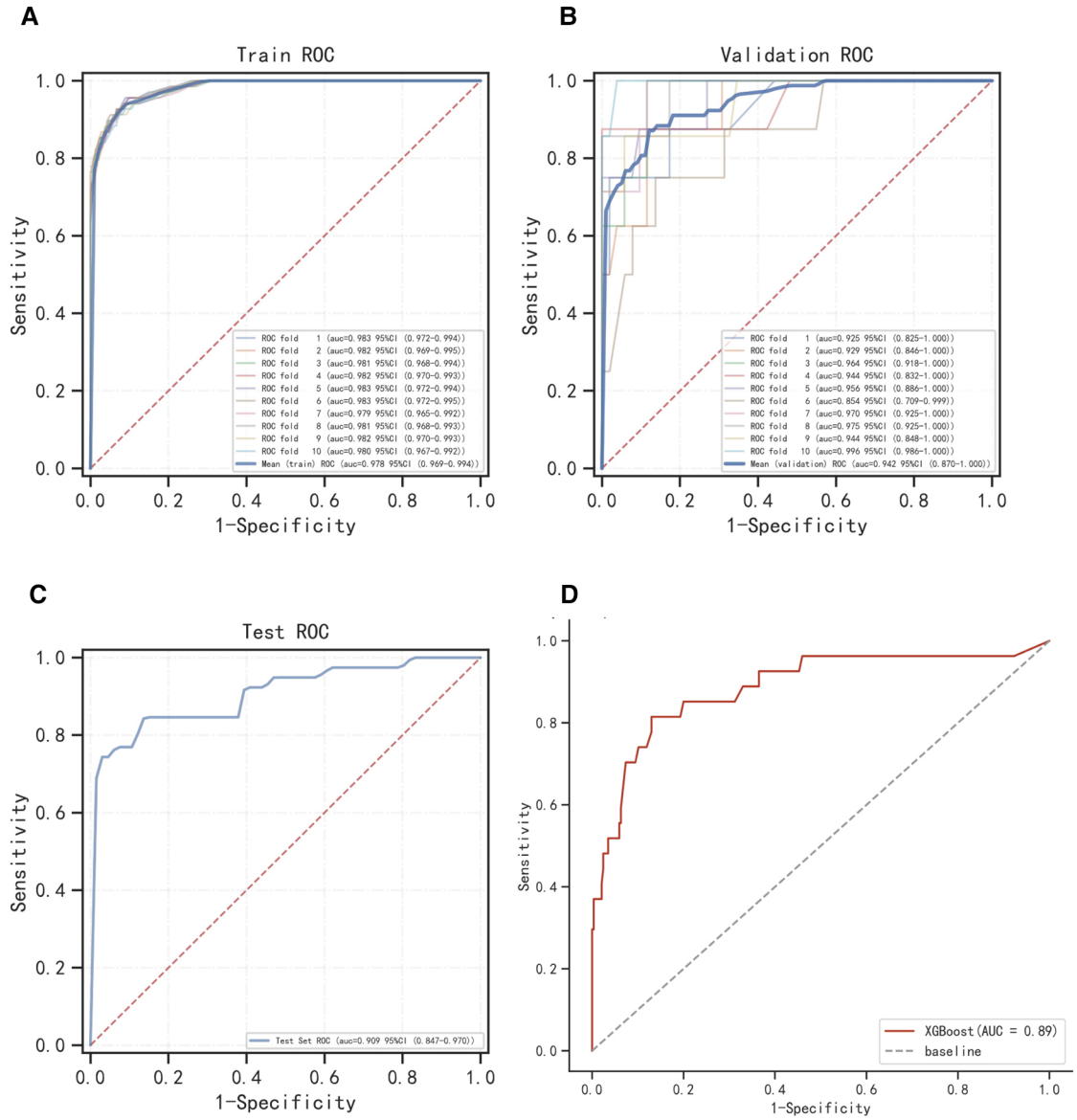

FIGURE 3
Internal validation of XGBoost model. (A) ROC curve of XGBoost model for the training set. (B) ROC curve of XGBoost model for the validation set. (C) ROC curve of XGBoost model for the test set. (D) External validation of XGBoost model.

a comprehensive comparison, the XGBoost algorithm was chosen to construct the model in this study.

3.4. Model external validation

The results of the ROC curve showed that the AUC value of the external validation set was 0.89, indicating that the prediction model was highly accurate in determining the disease (Figure 3D).

3.5. Model explanation

The SHAP summary plot results showed that the risk factors for permanent stoma in patients with rectal cancer were ranked as tumor distance from the dentate line ≥5 cm, history of adjuvant chemotherapy, rectal stricture, history of diabetes mellitus, history of hypertension, history of adjuvant radiotherapy, and age ≥65 years (Figure 4). The SHAP force plot shows the predictive analysis of the study model for four patients with rectal cancer with permanent stoma. The model predicts a 0.052 probability of permanent stoma in patient I, with an increased probability of chemotherapy and rectal stenosis and a decreased probability of age <65 years; the model predicts a 0.291 probability of permanent stoma in patient II, with an increased probability of history of hypertension, chemotherapy, and rectal stenosis and a decreased probability of no history of diabetes; the model predicts a 0.964 probability of permanent stoma in patient III, and the probability was increased by history of chemotherapy, history of hypertension, rectal stenosis, and tumor <5 cm from the dentate

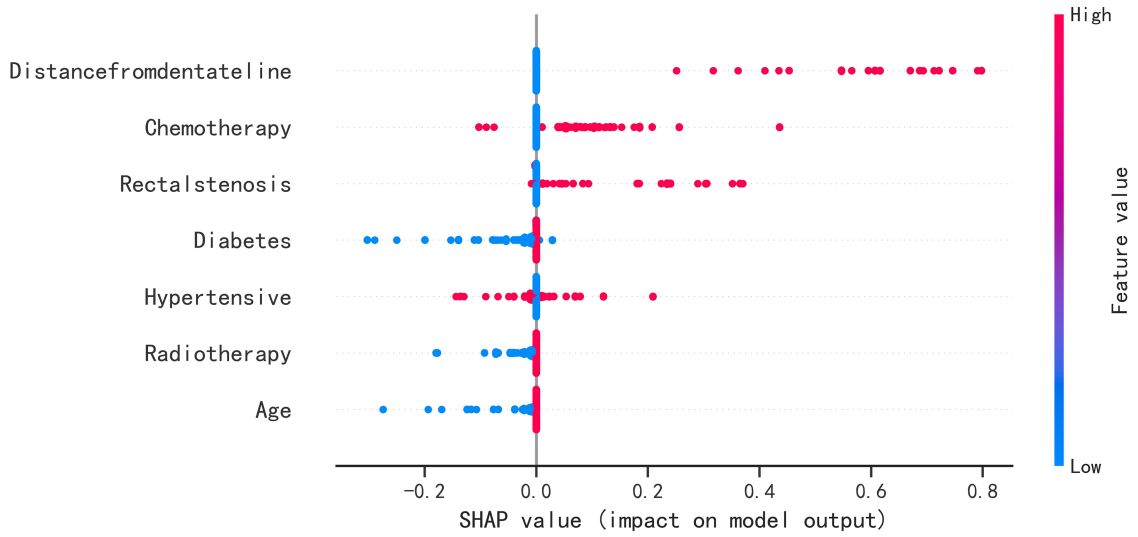

FIGURE 4
SHAP summary plot. Risk factors are arranged along the y-axis based on their importance, which is given by the mean of their absolute Shapley values. The higher the risk factor is positioned in the plot, the more important it is for the model.

line, and decreased by the patient's lack of diabetes; the model predicted a 0.002 probability of permanent stoma in patient IV, and decreased by the patient's lack of diabetes (Figures 5A–D).

4. Discussion

The current study evaluated risk prediction models constructed by four machine learning algorithms. Among them, the XGBoost algorithm exhibited the highest accuracy and was efficient, flexible, and universally adaptable (13). Compared with the RF algorithm, the XGBoost algorithm takes full account of the regularization problem and can effectively avoid model overfitting. The SVM algorithm and KNN algorithm have higher accuracy and can avoid the problem of overfitting well, but the stability of the two algorithms is poor when solving problems with multiple features and large samples (14). The XGBoost algorithm is more suitable for multidimensional studies and reduces the computation and training time. Compared with the SVM algorithm and KNN algorithm, the XGBoost algorithm is more advantageous. Therefore, with a comprehensive comparison of four machine learning algorithms, this study chose to use the XGBoost algorithm to construct a model to predict permanent stoma in patients with rectal cancer. Some studies (15, 16) have validated the effectiveness of machine learning algorithm applications in clinical diagnosis as well as prognosis. Moreover, machine learning techniques can also accurately predict adverse outcomes in disease progression compared to traditional diagnostic methods. Machine learning algorithms also played a great role in building the prediction model in this study. The model in this study can help clinical decision makers accurately identify high-risk patients, provide timely interventional treatment and improve patient prognosis. On the other hand, the model can help medical institutions allocate medical resources rationally, focus on the vital signs of high-risk patients, and effectively improve the survival rate of rectal cancer patients. Moreover, this study also used SHAP analysis to explain the model, and the results showed that advanced age, distance of the tumor from the dentate line, rectal stenosis, history of diabetes, history of hypertension, history of adjuvant chemotherapy, and history of adjuvant radiotherapy were risk factors for permanent stoma in patients with rectal cancer.

Patients of advanced age and those with a history of underlying medical conditions such as hypertension and diabetes mellitus are in poor physical condition. Patients have sclerotic and poorly dilated vascular walls that are friable (17–19). Additionally, their coagulation function is altered to some extent (20), which prevents rapid physiological hemostasis. All these factors lead to a weakened blood supply to the patient's gastrointestinal tract and a greater risk of postoperative anastomotic leakage. Some elderly patients do not have high quality of life requirements and have their own concerns about secondary surgery, so clinicians may prefer to consider permanent stoma for such patients. In addition, four samples were used in this study to explain how the model predicted permanent ostomy. For example, in the disease prediction analysis of samples I, II and III, a history of chemotherapy was one of the significant risk factors. Chemotherapy is often used as a treatment option for malignant tumors such as rectal cancer and liver cancer, and is highly selective to maximize inhibition of tumor growth and spread (21, 22). However, some of the chemotherapy modalities are more irritating to the abdominal cavity and aggravate the degree of abdominal adhesions. It also inhibits the normal physiological function of the bone marrow, and patients experience postoperative anemia and immune dysfunction, which affects the near and long-term outcome. On the other hand, patients can have severe abdominal inflammatory reactions as well as gastrointestinal reactions, which do not prevent the occurrence of intestinal obstruction (23). Studies by Makrin et al. (24, 25) also

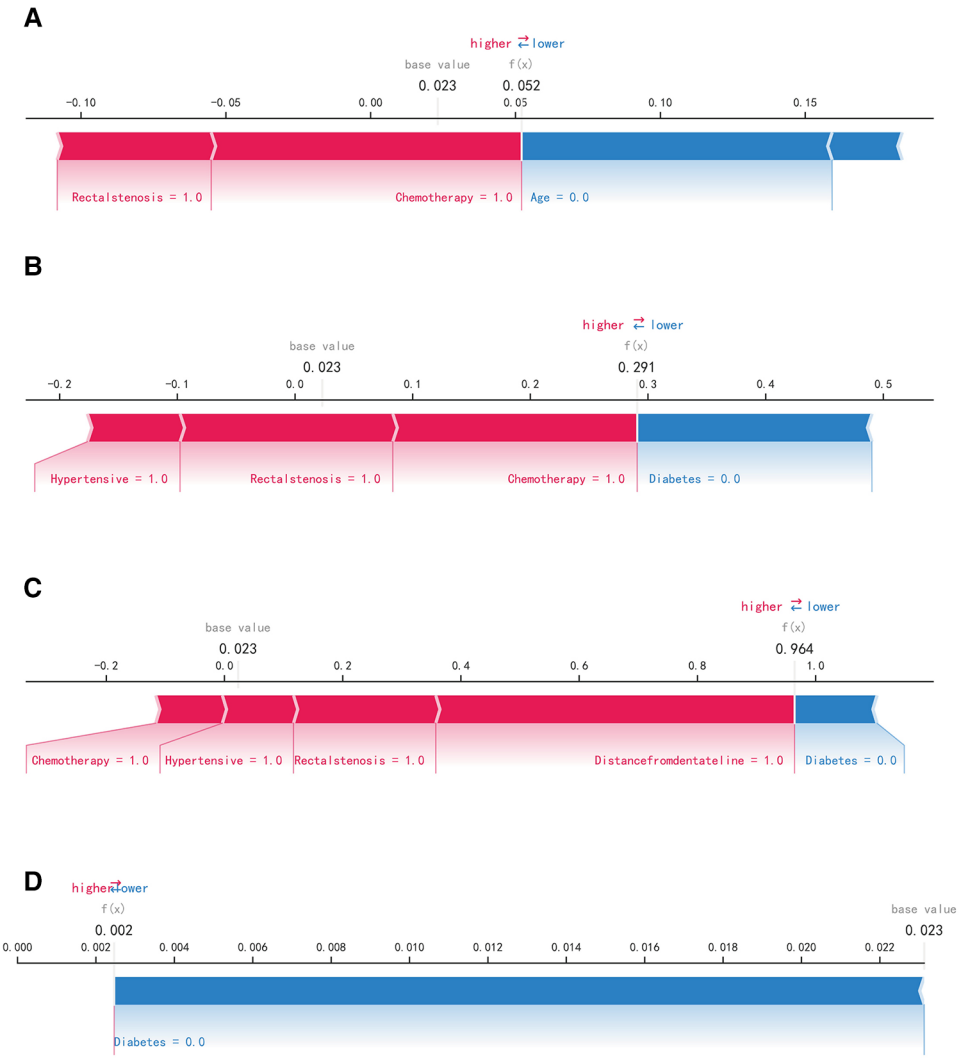

FIGURE 5
SHAP force plot. The contributing variables are arranged in the horizontal line, sorted by the absolute value of their impact. Blue represents features that have a negative effect on disease prediction, with a decrease in SHAP values; red represents features that have a positive effect on disease prediction, with an increase in SHAP values. (A) Predictive Analysis of Patient I. (B) Predictive Analysis of Patient II. (C) Predictive Analysis of Patient III. (D) Predictive Analysis of Patient IV.

demonstrated that intraperitoneal chemotherapy has a detrimental effect on the recovery of the gastrointestinal tract and is most likely one of the risk factors for postoperative intestinal obstruction, further confirming the higher risk of permanent stoma in patients treated with chemotherapy. The current study also found that radiotherapy is one of the risk factors for the permanence of stoma in patients. Patients with rectal cancer choose radiotherapy to reduce the postoperative recurrence rate of the tumor and to improve survival. Zhu et al. (26, 27) discussed the effectiveness of postoperative radiotherapy for rectal cancer and demonstrated that this treatment modality can significantly reduce the local recurrence rate of rectal cancer and improve the quality of survival of patients. However, as with intraperitoneal chemotherapy, radiation therapy is more damaging to the gastrointestinal tract. On the one hand, it restricts its peristaltic function and causes stiffness of the intestinal wall, which in the long run decreases the compliance of the intestine; on the other hand, radiotherapy directly damages intestinal epithelial cells and vascular endothelial cells, and the intestinal wall gradually fibroses. Some studies (28) performed pathological biopsies of tumors in most patients treated with adjuvant radiotherapy and found reduced microvascular counts at the tumor cut edges, an increased percentage of stenotic vessels, and significant fibrosis of the surrounding intestinal wall. Additionally, a study by Kumagai et al. (29) showed that radiotherapy is highly susceptible to complications of intestinal perforation and intestinal obstruction, and these complications increase the risk of permanent stoma to some extent. The results of the current study also revealed a greater risk of perpetuation of the diseased artificial orifice in rectal stenosis. TME carries out a radical tumor resection with complete removal of the mesentery around the rectal cancer, which requires the operator to ligate at the beginning of the inferior mesenteric artery, which is highly likely to cause the intestinal canal at the anastomosis to be in a hypoxic and

hypoperfused state. If patients with rectal stenosis remain in this state for a long time, the fibrous tissue of the intestinal canal will further proliferate, leading to severe postoperative bowel obstruction (27). Such patients not only feel severe pain at the anus during defecation but are also unable to undergo ostomy reversal, which further aggravates physical and psychological trauma. This suggests that clinicians should closely monitor the patient's vital status before surgery, prepare the intestine and prevent the occurrence of stenosis; select a reasonable surgical approach during surgery, fully free the colon to the splenic area to reduce anastomotic tension and ensure a good blood supply to the anastomosis; and perform regular postoperative rectal finger examination to dilate the anus and loosen the stenotic ring. Doctors can use balloon dilation to reduce the degree of stenosis when dealing with patients with mild stenosis symptoms; when dealing with patients with more severe stenosis symptoms, they should promptly inform patients of their condition, communicate well with doctors and patients, and reduce the psychological burden of patients. In addition, Mak (21) considered local recurrence of tumors as a risk factor for stoma permanence. His study showed that recurrent tumors occupy the intestinal space, making it more difficult for food to pass normally through the intestinal lumen, which can easily cause intestinal obstruction. Moreover, tumor infiltration of the intestinal canal causes stiffness of the intestinal wall, which weakens peristalsis and aggravates the degree of obstruction, so patients are highly susceptible to permanent stoma (21, 30, 31). However, in the present study, tumor recurrence was not a risk factor for permanent stoma in patients with rectal cancer. Our analysis suggests that this may be related to the small number of cases of rectal cancer recurrence in this study, and more relevant cases will be added in the future to improve the study. It also suggests that clinicians should strengthen the postoperative follow-up of rectal cancer patients, promptly review them after discovering discomfort, and intervene early to relieve symptoms.

The current study comprehensively evaluated the model in terms of discrimination, calibration, and clinical utility, but the study has some limitations. The study included multiple aspects of risk factors but did not consider aspects such as imaging. Although the machine learning algorithms were more accurate, their models were more complex and less interpretable. The entire computational and decision-making process of the model runs in a black box, which is not as intuitive and clear as the logistic regression model (32–34). On the other hand, the current study was a single-center retrospective study, which has the disadvantages of selection bias, distribution bias, and retrospective bias. It is necessary to add multicenter prospective studies to future studies to further increase the reliability of the results.

5. Conclusion

This study developed a model based on the XGBoost machine learning algorithm to predict the risk of permanent stoma in rectal cancer. The model has good prediction accuracy and clinical utility, which facilitates surgeons in diagnosing patients in a timely manner. The model predicted patients at high risk for permanent stoma and identified advanced age, distance of the tumor from the dentate line, rectal stenosis, history of diabetes, history of hypertension, history of chemotherapy, and history of radiotherapy as high risk factors.

Data availability statement

The original contributions presented in the study are included in the article/Supplementary Material, further inquiries can be directed to the corresponding author/s.

Ethics statement

The studies involving human participants were reviewed and approved by Ethics Review Committee of Wuxi People's Hospital. The patients/participants provided their written informed consent to participate in this study.

Author contributions

YL and SZ conceived the study and participated in the study design, performance, coordination and manuscript writing. WD, ZT, and HC performed the literature review and graphics production. WS helped with the final revision of this manuscript. All authors reviewed and approved the final manuscript.

Funding

This work was supported by the Top Talent Support Program for young and middle-aged people of Wuxi Health Committee (Grant No. HB2020007).

Conflict of interest

The authors declare that the research was conducted in the absence of any commercial or financial relationships that could be construed as a potential conflict of interest.

Publisher's note

References

1. Mattiuzzi C, Sanchis-Gomar F, Lippi G. Concise update on colorectal cancer epidemiology. *Ann Transl Med*. (2019) 7(21):609. doi: 10.21037/atm.2019.07.91

2. São Julião GP, Habr-Gama A, Vailati BB, Araujo SEA, Fernandez LM, Perez RO. New strategies in rectal cancer. *Surg Clin North Am*. (2017) 97(3):587–604. doi: 10.1016/j.suc.2017.01.008

3. Heald RJ, Ryall RD. Recurrence and survival after total mesorectal excision for rectal cancer. *Lancet*. (1986) 1(8496):1479–82. doi: 10.1016/S0140-6736(86)91510-2

4. Khalfallah M, Dougaz W, Jerraya H, Nouira R, Bouasker I, Dziri C. Prognostic factors in rectal cancer: where is the evidence? *Tunis Med*. (2017) 95(2):79–86.

5. Allaix ME, Giraudo G, Ferrarese A, Arezzo A, Rebecchi F, Morino M. 10-Year oncologic outcomes after laparoscopic or open total mesorectal excision for rectal cancer. *World J Surg*. (2016) 40(12):3052–62. doi: 10.1007/s00268-016-3631-x

6. Bedrikovetski S, Dudi-Venkata NN, Kroon HM, Moore JW, Hunter RA, Sammour T. Outcomes of minimally invasive versus open proctectomy for rectal cancer: a propensity-matched analysis of bi-national colorectal cancer audit data. *Dis Colon Rectum*. (2020) 63(6):778–87. doi: 10.1097/DCR.0000000000001654

7. Foppa C, Ng SC, Montorsi M, Spinelli A. Anastomotic leak in colorectal cancer patients: new insights and perspectives. *Eur J Surg Oncol*. (2020) 46(6):943–54. doi: 10.1016/j.ejso.2020.02.027

8. Näsvall P, Dahlstrand U, Löwenmark T, Rutegård J, Gunnarsson U, Strigård K. Quality of life in patients with a permanent stoma after rectal cancer surgery. *Qual Life Res*. (2017) 26(1):55–64. doi: 10.1007/s11136-016-1367-6

9. Bianchi R, Mamadou-Pathé B, von Känel R, Roth R, Schreiner P, Rossel JB, et al. Effect of closed and permanent stoma on disease course, psychological well-being and working capacity in Swiss IBD cohort study patients. *PLoS ONE*. (2022) 17(9):e0274665. doi: 10.1371/journal.pone.0274665

10. Deo RC. Machine learning in medicine. *Circulation*. (2015) 132(20):1920–30. doi: 10.1161/CIRCULATIONAHA.115.001593

11. Katiyar A, Mohanty A, Hua J, Chao S, Lopes R, Datta A, et al. A Bayesian approach to determine the composition of heterogeneous cancer tissue. *BMC Bioinformatics*. (2018) 19(Suppl 3):90. doi: 10.1186/s12859-018-2062-0

12. Cypko MA, Stoehr M, Oeltze-Jafra S, Dietz A, Lemke HU. A guide for constructing Bayesian network graphs of cancer treatment decisions. *Stud Health Technol Inform*. (2017) 245:1355.

13. Wang L, Wang X, Chen A, Jin X, Che H. Prediction of type 2 diabetes risk and its effect evaluation based on the XGBoost model. *Healthcare (Basel)*. (2020) 8(3). doi: 10.3390/healthcare8030247

14. Hao PY, Chiang JH, Chen YD. Possibilistic classification by support vector networks. *Neural Netw*. (2022) 149:40–56. doi: 10.1016/j.neunet.2022.02.007

15. Karadaghy OA, Shew M, New J, Bur AM. Development and assessment of a machine learning model to help predict survival among patients with oral squamous cell carcinoma. *JAMA Otolaryngol Head Neck Surg*. (2019) 145(12):1115–20. doi: 10.1001/jamaoto.2019.0981

16. Tseng YJ, Wang HY, Lin TW, Lu JJ, Hsieh CH, Liao CT. Development of a machine learning model for survival risk stratification of patients with advanced oral cancer. *JAMA Netw Open*. (2020) 3(8):e2011768. doi: 10.1001/jamanetworkopen.2020.11768

17. Kuryba AJ, Scott NA, Hill J, van der Meulen JH, Walker K. Determinants of stoma reversal in rectal cancer patients who had an anterior resection between 2009 and 2012 in the English national health service. *Colorectal Dis*. (2016) 18(6):O199–205. doi: 10.1111/codi.13339

18. den Dulk M, Smit M, Peeters KC, Kranenbarg EM, Rutten HJ, Wiggers T, et al. A multivariate analysis of limiting factors for stoma reversal in patients with rectal cancer entered into the total mesorectal excision (TME) trial: a retrospective study. *Lancet Oncol*. (2007) 8(4):297–303. doi: 10.1016/S1470-2045(07)70047-5

19. Kairaluoma M, Rissanen H, Kultti V, Mecklin JP, Kellokumpu I. Outcome of temporary stomas. A prospective study of temporary intestinal stomas constructed between 1989 and 1996. *Dig Surg*. (2002) 19(1):45–51. doi: 10.1159/000052005

20. Afshin A, Forouzanfar MH, Reitsma MB, Sur P, Estep K, Lee A, et al. Health effects of overweight and obesity in 195 countries over 25 years. *N Engl J Med*. (2017) 377(1):13–27. doi: 10.1056/NEJMoa1614362

21. Mak JCK, Foo DCC, Wei R, Law WL. Sphincter-preserving surgery for low rectal cancers: incidence and risk factors for permanent stoma. *World J Surg*. (2017) 41(11):2912–22. doi: 10.1007/s00268-017-4090-8

22. Kim MJ, Kim YS, Park SC, Sohn DK, Kim DY, Chang HJ, et al. Risk factors for permanent stoma after rectal cancer surgery with temporary ileostomy. *Surgery*. (2016) 159(3):721–7. doi: 10.1016/j.surg.2015.09.011

23. Song O, Kim KH, Lee SY, Kim CH, Kim YJ, Kim HR. Risk factors of stoma re-creation after closure of diverting ileostomy in patients with rectal cancer who underwent low anterior resection or intersphincteric resection with loop ileostomy. *Ann Surg Treat Res*. (2018) 94(4):203–8. doi: 10.4174/astr.2018.94.4.203

24. Makrin V, Lev-Chelouche D, Even Sapir E, Paran H, Rabau M, Gutman M. Intraperitoneal heated chemotherapy affects healing of experimental colonic anastomosis: an animal study. *J Surg Oncol*. (2005) 89(1):18–22. doi: 10.1002/jso.20161

25. Mehta PP, Griffin J, Ganta S, Rangraj M, Steichen F. Laparoscopic-assisted colon resections: long-term results and survival. *Jsls*. (2005) 9(2):184–8.

26. Li CC, Liang JA, Chung CY, Chen WT, Chien CR. Effectiveness of intensity-modulated radiotherapy for rectal cancer patients treated with neoadjuvant concurrent chemoradiotherapy: a population-based propensity score-matched analysis. *Anticancer Res*. (2019) 39(3):1479–84. doi: 10.21873/anticanres.13265

27. Zhu H, Bai B, Shan L, Wang X, Chen M, Mao W, et al. Preoperative radiotherapy for patients with rectal cancer: a risk factor for non-reversal of ileostomy caused by stenosis or stiffness proximal to colorectal anastomosis. *Oncotarget*. (2017) 8(59):100746–53. doi: 10.18632/oncotarget.20602

28. Zhong QH, Wu PH, Qin QY, Kuang YY, Ma TH, Wang HM, et al. Pathological insights of radiotherapy-related damage to surgical margin after preoperative radiotherapy in patients with rectal cancer. *Zhonghua Wai Ke Za Zhi*. (2017) 55(7):507–14. doi: 10.3760/cma.j.issn.0529-5815.2017.07.007

29. Kumagai T, Rahman F, Smith AM. The microbiome and radiation induced-bowel injury: evidence for potential mechanistic role in disease pathogenesis. *Nutrients*. (2018) 10(10). doi: 10.3390/nu10101405

30. Lim SW, Kim HJ, Kim CH, Huh JW, Kim YJ, Kim HR. Risk factors for permanent stoma after low anterior resection for rectal cancer. *Langenbecks Arch Surg*. (2013) 398(2):259–64. doi: 10.1007/s00423-012-1038-1

31. Junginger T, Gönner U, Trinh TT, Lollert A, Oberholzer K, Berres M. Permanent stoma after low anterior resection for rectal cancer. *Dis Colon Rectum*. (2010) 53(q):1632–9. doi: 10.1007/DCR.0b013e3181ed0aae

32. Rudin C. Stop explaining black box machine learning models for high stakes decisions and use interpretable models instead. *Nat Mach Intell*. (2019) 1(5):206–15. doi: 10.1038/s42256-019-0048-x

33. Nohara Y, Iihara K, Nakashima N. Interpretable machine learning techniques for causal inference using balancing scores as meta-features. *Annu Int Conf IEEE Eng Med Biol Soc*. (2018) 2018:4042–5. doi: 10.1109/embc.2018.8513026

34. Figueroa Barraza J, López Droguett E, Martins MR. Towards interpretable deep learning: a feature selection framework for prognostics and health management using deep neural networks. *Sensors (Basel)*. (2021) 21(17). doi: 10.3390/s21175888

frontiers | Frontiers in Oncology

TYPE Original Research
PUBLISHED 10 May 2023
DOI 10.3389/fonc.2023.1171837

OPEN ACCESS

EDITED BY
Mengling Feng,
National University of Singapore, Singapore

REVIEWED BY
Vincent Kam Wai Wong,
Macau University of Science and Technology, Macao SAR, China
Zhimin Geng,
Xi'an Jiaotong University, China
Xiaoming Xing,
The Affiliated Hospital of Qingdao University, China

*CORRESPONDENCE
Songxiao Xu
xusx@zjcc.org.cn
Yongyi Chen
yongyichen13@fudan.edu.cn

RECEIVED 01 March 2023
ACCEPTED 24 April 2023
PUBLISHED 10 May 2023

CITATION
Zhou Y, Chen S, Wu Y, Li L, Lou Q, Chen Y and Xu S (2023) Multi-clinical index classifier combined with AI algorithm model to predict the prognosis of gallbladder cancer.
Front. Oncol. 13:1171837.
doi: 10.3389/fonc.2023.1171837

Multi-clinical index classifier combined with AI algorithm model to predict the prognosis of gallbladder cancer

Yun Zhou[1,2], Siyu Chen[2], Yuchen Wu[2], Lanqing Li[3], Qinqin Lou[3], Yongyi Chen[2*] and Songxiao Xu[2*]

[1]Physical Examination Center, The Cancer Hospital of the University of Chinese Academy of Sciences (Zhejiang Cancer Hospital), The Key Laboratory of Zhejiang Province for Aptamers and Theranostics, Institute of Basic Medicine and Cancer (IBMC), Chinese Academy of Sciences, Hangzhou, Zhejiang, China, [2]The Clinical Laboratory Department, The Cancer Hospital of the University of Chinese Academy of Sciences (Zhejiang Cancer Hospital), The Key Laboratory of Zhejiang Province for Aptamers and Theranostics, Institute of Basic Medicine and Cancer (IBMC), Chinese Academy of Sciences, Hangzhou, Zhejiang, China, [3]Key Laboratory of Precision Medicine in Diagnosis and Monitoring Research of Zhejiang Province, Hangzhou, Zhejiang, China

Objectives: It is significant to develop effective prognostic strategies and techniques for improving the survival rate of gallbladder carcinoma (GBC). We aim to develop the prediction model from multi-clinical indicators combined artificial intelligence (AI) algorithm for the prognosis of GBC.

Methods: A total of 122 patients with GBC from January 2015 to December 2019 were collected in this study. Based on the analysis of correlation, relative risk, receiver operator characteristic curve, and importance by AI algorithm analysis between clinical factors and recurrence and survival, the two multi-index classifiers (MIC1 and MIC2) were obtained. The two classifiers combined eight AI algorithms to model the recurrence and survival. The two models with the highest area under the curve (AUC) were selected to test the performance of prognosis prediction in the testing dataset.

Results: The MIC1 has ten indicators, and the MIC2 has nine indicators. The combination of the MIC1 classifier and the "avNNet" model can predict recurrence with an AUC of 0.944. The MIC2 classifier and "glmet" model combination can predict survival with an AUC of 0.882. The Kaplan-Meier analysis shows that MIC1 and MIC2 indicators can effectively predict the median survival of DFS and OS, and there is no statistically significant difference in the prediction results of the indicators (MIC1: χ^2 = 6.849, P = 0.653; MIC2: χ^2 = 9.14, P = 0.519).

Conclusions: The MIC1 and MIC2 combined with avNNet and mda models have high sensitivity and specificity in predicting the prognosis of GBC.

KEYWORDS

gallbladder cancer (GBC), recurrence, survival, prediction models, prognosis

1 Introduction

Gallbladder cancer (GBC) is the most invasive gastrointestinal malignant tumor in the world, with a median survival time of about six months and a five-year survival rate of less than 5% (1). It has vast geographical differences and is more common in some developing countries (2). As one of the most common biliary malignant tumors, it is a subtype with the worst prognosis and low survival time (3). The poor prognosis of GBC patients is related to tumor invasiveness, delayed diagnosis, lack of reliable biomarkers, and effective treatment. Radical surgery is the only way for patients with primary GBC to be cured (4). Surgical treatment of GBC should be performed in the medical center of experienced biliary surgeons and pathologists. The choice of operation should be based on the TNM stage of GBC (5). Patients with GBC still have a high recurrence rate after surgery (about 25%-65%) (6). Postoperative recurrence of GBC can be treated by reoperation and palliative treatment (7). Due to the originally extended resection, it is hard to extend the resection again, which leads to a poor prognosis. Therefore, the reasonable and practical assessment of recurrence and survival is the key to postoperative management.

Presently, the postoperative evaluation of GBC is mainly based on clinicopathological factors, such as TNM stage, histological type, and degree of differentiation (8). However, the clinicopathological criteria of GBC in official organizations have yet to be wholly unified (9). Pathological factors cannot fully reflect the recurrence and mortality of patients undergoing radical cholecystectomy. Finding new methods to predict recurrence and survival may help improve the prognosis management of GBC. Deepening research on dynamic monitoring of blood biomarkers can effectively evaluate the onset and progression of GBC after the operation. In analyzing targeted prediction and prognostic markers of GBC, the higher expression proportion of predictive targeting markers such as vascular endothelial growth factor and epidermal growth factor receptor in GBC come to light. Negi et al. reported that the percentage of positive lymph nodes is more capable of independently predicting the prognosis of patients undergoing radical cholecystectomy than the location or number of lymph nodes invaded (10). Masashi et al. evaluated the relationship between preoperative C-reactive protein/albumin ratio and overall survival (OS) and disease-free survival (DFS) (11). They found that the C-reactive protein/albumin ratio ≥ 0.07 was a significant independent predictor of OS, and high levels of carbohydrate antigen were significant independent predictors of DFS.

There have been studies to explore suitable biomarkers for early diagnosis, identify the molecular pathway of changes, and develop relevant biomarkers for early diagnosis, treatment, and prognosis. Despite these advances, the survival rate of patients with GBC has not improved. Since single-factor monitoring may not be able to predict recurrence and survival accurately, joint detection of multiple indicators is of great significance for the accurate assessment of the onset and progression of the disease. Our group has done previous research based on the prognosis of GBC (12). Through retrospective analysis of 260 patients with GBC who underwent radical resection, it was found that patients with high preoperative fibrinogen levels had poor DFS and OS after the operation, especially those with poor differentiation. These results suggested that fibrinogen may be a prognostic biomarker for GBC. In addition, developing various potential indicators (such as hematological markers) to form a classifier and combined with an artificial intelligence (AI) algorithm to construct a prediction model will effectively supplement the pathological factors to predict the prognosis of patients with GBC.

To further explore the significance of various clinical indicators in the prognosis of GBC, we optimized and matched the data of 260 previous patients and finally enrolled 122 patients for this study. A comprehensive evaluation of the routine tumor markers, clinicopathological features, and blood indicators may effectively improve the prediction of the prognosis of GBC. Here, we report two models with high sensitivity and specificity for predicting GBC recurrence and survival formed by combining two multi-index classifiers (MIC1 and MIC2) with two AI algorithms (avNNet and glmnet). We aim to explore the clinical value of two models for predicting the recurrence and survival of GBC (Figure 1).

2 Materials and methods

2.1 Subject

A total of 122 patients with GBC from January 2015 to December 2019 were collected in this study. The admission criteria were as follows: 1) GBC diagnosed by histopathology; 2) radical cholecystectomy and postoperative pathology showed R0 margin; 3) no preoperative anticancer treatment; 4) no other malignant tumor and hematological diseases; 5) complete clinical data. This study was approved by the Ethics Committee of the Zhejiang Cancer Hospital (IRB-2022-780).

2.2 Data collection

In this study, the hospital information management system was used to collect original clinical data such as gender, age, height, weight, smoking history, and drinking history. Hematological parameters and pathological data were also collected. Follow-up data, including specific dates of recurrence and death, were collected through the hospital system or by telephone. Fasting blood samples were collected from all patients within one week before surgery, and the tests were performed strictly according to the instructions of the instrument and reagent.

2.3 Surgical strategy

All patients underwent radical resection of GBC and underwent strict imaging evaluation, which was in line with the Chinese consensus on diagnosing and treating GBC. All cases were confirmed to be R0 resection by pathology.

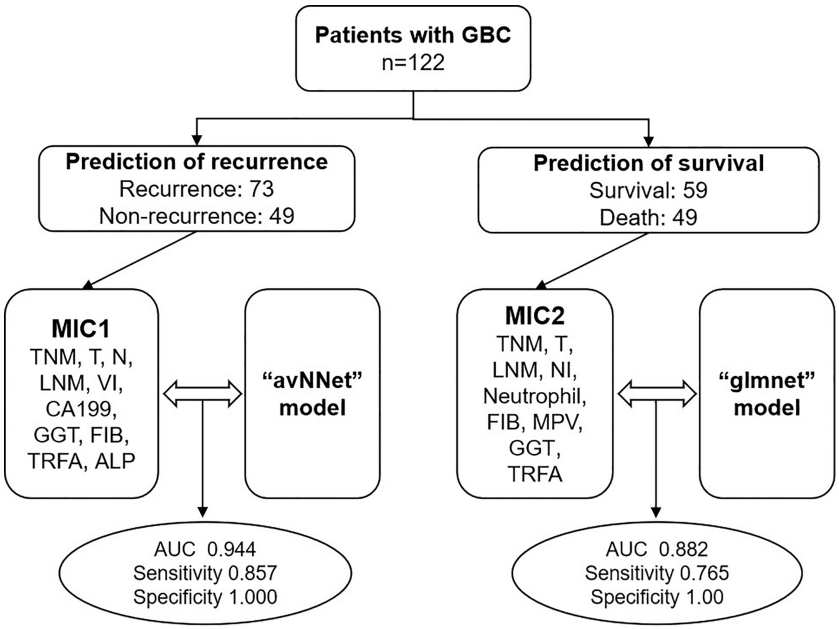

FIGURE 1
Flowchart of multi-clinical index classifier combined with AI algorithm model to predict the prognosis of GBC. TNM, TNM-stage; T, T-stage; N, N-stage; LNM, lymph node metastasis; VI, vascular invasion; NI, nerve invasion; CA199, carbohydrate antigen 199, GGT, gamma-glutamyl transpeptidase; FIB, fibrinogen; MPV, mean platelet volume; TRFA, fibrinogen/albumin; ALP, alkaline phosphatase.

2.4 Histopathological examination

After surgical resection, the tissues were subjected to histopathological examination to collect tumor-related histopathological information. A professional pathologist performed a pathological study. According to the AJCC Cancer staging Manual, 8th edition, all cases were produced by TNM based on pathological data.

2.5 Follow-up data

The time between surgery and cancer recurrence was defined as DFS, and the time from surgery to death was defined as OS. The follow-up deadline was March 30, 2023. The maximum follow-up period was 80 months, and the median follow-up period was 27 months.

2.6 AI algorithm analysis

To enhance the usability and stability of the model, a critical evaluation is required to screen for pathological factors significantly associated with recurrence. The feature screening method uses the Boruta algorithm to estimate the contribution score of each feature in the model through the random forest strategy. The significance test can divide the features into three categories: Confirmed, Tentative, and Rejected, in which "Confirmed" is determined as an essential feature for subsequent model construction. The data is divided into a testing set and a training set. A variety of supervised classification algorithms are used to construct the prediction model. The classification algorithm includes eight algorithms: "avNNet", "gbm", "glmnet", "mda", "plr", "svmRadial", "naive_bayes" and "ranger". The prediction models are constructed respectively, and the optimal model of each algorithm is obtained by using a 5-fold cross-validation method. According to the optimal model created by each algorithm, the ROC analysis method is used to evaluate the performance of the model in the testing set, and the algorithm model with the most significant AUC is selected as the final model.

2.7 Statistical analysis

The correlation of continuous and regular distribution variables was analyzed by independent sample t-test, and the correlation of two classification variables was analyzed by Pearson χ^2 test. Then, the statistically significant data were assessed for relative risk and were divided into a high-risk group and a low-risk group according to the average of each index. Their p-value, risk ratio (RR), and 95% confidence interval (CI) of RR were calculated. The subjects' working characteristic (ROC) curve was drawn by Medcalc, and the cut-off value of each index was obtained based on the Youden index. Kaplan-Meier method was used to estimate the difference between OS and DFS, and the Log Rank method and Breslow method were used to test the difference in survival analysis. SPSS was used to draw the Kaplan-Meier survival curve. The above statistics were completed by SPSS25.0 statistical software. The statistical results of bilateral $P < 0.05$ were considered statistically significant.

3 Results

3.1 Correlation between recurrence, survival, and clinical characteristics

A total of 122 patients and clinical characteristics in this work were detailed in Table 1; Table S1. In 122 cases with GBC, 73

10.3389/fonc.2023.1171837

TABLE 1 Clinical characteristics of enrolled patients with GBC.

Characteristics	N(%)	P(95%(CI))
Gender		
Male	40 (0.3278)	0.599 (−0.234 - 0.135)
Female	82 (0.6721)	
Age		
≥ 64	67 (0.5492)	0.567 (−0.124 - 0.225)
< 64	55 (0.4508)	
Scope of surgery		
Normal	111 (0.9008)	0.000 (0.345 - 0.527)
Expansion	8 (0.0655)	
Postoperative chemotherapy		
Routine chemotherapy	35 (0.2869)	0.399 (−0.406 - 0.088)
post-recurrence chemotherapy	87 (0.7131)	
Tumor location		
Neck	31 (0.2541)	0.009 (−0.423 - −0.063)
Body	91 (0.7459)	
Tumor size		
≥ 3	70 (0.5738)	0.022 (−0.375 - −0.03)
< 3	52 (0.4262)	
Differentiation		
Low	27 (0.2213)	0.388 (−0.296 - 0.117)
High	95 (0.7787)	
PVI, HAI		
Yes	6 (0.0492)	0.000 (−0.528 - −0.348)
No	116 (0.9508)	
T		
T3+T4	45 (0.3689)	0.000 (−0.61 - −0.324)
T1+T2	77 (0.6311)	
N		
N1+N2	49 (0.4016)	0.000 (−0.562 - −0.252)
N0	73 (0.5984)	
M		
M1	7 (0.0574)	0.096 (−0.639 - 0.065)
M0	115 (0.9426)	
TNM		
III+IV	71 (0.5820)	0.000 (−0.699 - −0.402)
I+II	51 (0.4180)	
LNM		
Metastasis	54 (0.4426)	0.000 (−0.562 - −0.252)
Normal	68 (0.5574)	
RLN count		
≥ 5	73 (0.5984)	0.108 (−0.322 - 0.032)
< 5	49 (0.4016)	
Vascular invasion		
Yes	23 (0.1885)	0.002 (−0.49 - −0.119)
No	99 (0.8115)	
Nerve invasion		
Yes	25 (0.2049)	0.002 (−0.473 - −0.107)
No	97 (0.7951)	

PVI, portal vein invasion; HAI, hepatic artery invasion; T, T-stage; N, N-stage; M, M-stage; TNM, TNM-stage; LNM, lymph node metastasis; RLN, regional lymph node.

(59.84%) had a postoperative recurrence, and 49 (40.16%) had no recurrence. There were 40 males (32.79%) and 82 females (67.21%). The median age was 64 years (40-92 years). The tumors in the neck and body of the gallbladder were 31 cases (25.41%) and 91 cases (74.59%), respectively. Postoperative pathological results showed that 27 patients (22.13%) were poorly differentiated and 95 (77.87%) highly differentiated. The tumor size was expressed as the maximum diameter of the tumor, with a median of 3 cm (0.6-13 cm). The vascular invasion occurred in 23 cases (18.85%), nerve invasion in 25 patients (20.49%), and lymph node metastasis in 54 cases (44.26%). The median number of regional lymph nodes was 5 (0–23). According to the pathological features, TNM staging was performed in 51 cases (41.80%) of stage I and II and 71 (58.20%) of stage III and IV.

Table S2 shows 26 clinical indicators related to patients' recurrence. The results also show that recurrence is unrelated to sex, age, and degree of differentiation. However, it relates to the TNM stage, operation scope, tumor site, lymph node metastasis, and nerve and vascular invasion. In short, patients with late TNM stage ($P < 0.001$), lymph node metastasis ($P < 0.001$), and high levels of alkaline phosphatase (ALP) ($P < 0.001$) were significantly correlated with recurrence. Table S3 shows 22 clinical indicators related to patients' survival. The results show that patients with late TNM stage ($P < 0.001$), lymph node metastasis ($P < 0.001$), and high levels of fibrinogen (FIB) ($P = 0.001$) and ferritin (FER) ($P = 0.001$) were significantly correlated with recurrence.

3.2 The filtering of candidate indicators of MIC1 and MIC2 in clinical characteristics

The relative risk analysis of recurrence and death was carried out for the factors related to the recurrence outcome. The results of TNM staging, T staging, N staging, lymph node metastasis (LNM), tumor in the gallbladder neck, non-extended surgical range, vascular and nerve invasion, high level of FIB, fibrinogen/albumin

(TRFA), carbohydrate antigen 125 (CA125), carbohydrate antigen 199 (CA199), glutamic oxalacetic transaminase (AST), FER, direct bilirubin (DBIL), total bile acid (TBA), ALP, gamma-glutamyl transpeptidase (GGT), total bilirubin (TBIL), neutrophil, and thrombocytocrit (PCT), a total of 22 clinical factors are risk factors for recurrence of GBC (Table S4). Based on the ROC analysis of the 23 risk factors for recurrence prediction, 14 risk factors with AUC > 0.5 and P < 0.05 were selected as the MIC1 candidate indicators for predicting recurrence (Table 2).

The same method was used to screen risk factors for predicting death from data from 108 patients. The results showed that advanced TNM staging, late T staging, late N staging, lymph node metastasis, high regional lymph node count, nerve invasion, high level of FIB, TRFA, CA125, FER, ALP, GGT, neutrophil count, white blood cell count (WBC) and PHOS, a total of 16 clinical detection factors are risk factors for predicting survival in patients with GBC within five years (Table S5). Based on the ROC analysis of the 16 risk factors, 15 risk factors with AUC > 0.5 and P < 0.05 were selected as the MIC2 candidate indicators to predict survival (Table 3).

TABLE 2 ROC analysis of MIC1 candidate indicators for recurrence in patients with GBC.

Factor	AUC	P	95%CI	
			Low	High
TNM	0.780	0.000	0.696	0.865
CA199	0.759	0.000	0.674	0.844
GGT	0.734	0.000	0.645	0.823
LNM	0.722	0.000	0.634	0.809
T	0.719	0.000	0.631	0.808
FIB	0.710	0.000	0.616	0.804
TRFA	0.706	0.000	0.612	0.800
N	0.706	0.000	0.614	0.797
FER	0.685	0.000	0.592	0.777
ALP	0.658	0.001	0.565	0.751
CA125	0.650	0.002	0.556	0.745
PCT	0.636	0.006	0.539	0.733
Neutrophil	0.629	0.009	0.532	0.727
NI	0.599	0.046	0.502	0.697
Site	0.598	0.051	0.500	0.696
VI	0.596	0.055	0.498	0.693
Size	0.594	0.067	0.493	0.694
AST	0.586	0.087	0.488	0.684
Scope of surgery	0.564	0.211	0.464	0.663
DBIL	0.559	0.244	0.460	0.658
TBA	0.555	0.284	0.455	0.655
TBIL	0.553	0.295	0.454	0.652
PVI, HAI	0.547	0.360	0.447	0.647

TNM, TNM-stage; CA199, carbohydrate antigen 199; GGT, gamma-glutamyl transpeptidase; LNM, lymph node metastasis; T, T-stage; FIB, fibrinogen; TRFA, fibrinogen/albumin; N, N-stage; FER, ferritin; ALP, alkaline phosphatase; CA125, carbohydrate antigen 125; PCT, thrombocytocrit; NI, nerve invasion; VI, vascular invasion; AST, glutamic oxalacetic transaminase; DBIL, direct bilirubin; TBA, total bile acid; TBIL, total bilirubin; PVI, portal vein invasion; HAI, hepatic artery invasion.

3.3 Evaluation of the recurrence prediction power of MIC1 combined AI algorithm in GBC

Fourteen MIC1 candidate indicators of 122 patients were used to construct a predictive model to evaluate the risk of recurrence. "Confirmed" are selected by the Boruta algorithm, and these ten "Confirmed" features are set as MIC1 for modeling and analysis (Figure 2A). The patients were divided into a training dataset and a testing dataset for the proportion of 8:2. According to the optimal model constructed by each algorithm, the ROC analysis method is used to evaluate the performance of the model in the testing set, and the algorithm model with most significant AUC is selected as the final model. The ROC curves of the optimal model constructed by the nine algorithms in the training and testing dataset are shown in Figures 2B, C. The results show that the MIC1-based model constructed by the avNNet algorithm has the highest AUC of 0.944 in the testing set, and the model is selected as the final recurrence risk prediction model (Figure 2D). The ROC curve was drawn with the predicted value in the testing set, and the best diagnostic cut-off value

TABLE 3 ROC analysis of MIC2 candidate indicators for survival in patients with GBC.

Factor	AUC	P	95%CI	
			Low	High
TNM	0.812	0.000	0.705	0.919
T	0.761	0.000	0.646	0.877
FIB	0.747	0.000	0.625	0.869
TRFA	0.737	0.000	0.614	0.860
GGT	0.705	0.001	0.583	0.827
FER	0.705	0.001	0.583	0.827
PHOS	0.693	0.003	0.567	0.819
Neutrophil	0.689	0.003	0.565	0.814
CA125	0.683	0.005	0.556	0.809
LNM	0.679	0.005	0.553	0.806
N	0.659	0.016	0.530	0.789
WBC	0.652	0.022	0.522	0.782
RLN	0.646	0.029	0.515	0.777
NI	0.636	0.042	0.505	0.767
MPV	0.633	0.054	0.498	0.767

TNM, TNM-stage; T, T-stage; FIB, fibrinogen; TRFA, fibrinogen/albumin; GGT, gamma-glutamyl transpeptidase; FER, ferritin; CA125, carbohydrate antigen 125; LNM, lymph node metastasis; N, N-stage; WBC, white blood cell count; RLN, regional lymph node; NI, nerve invasion; MPV, mean platelet volume; ALP, alkaline phosphatase.

10.3389/fonc.2023.1171837

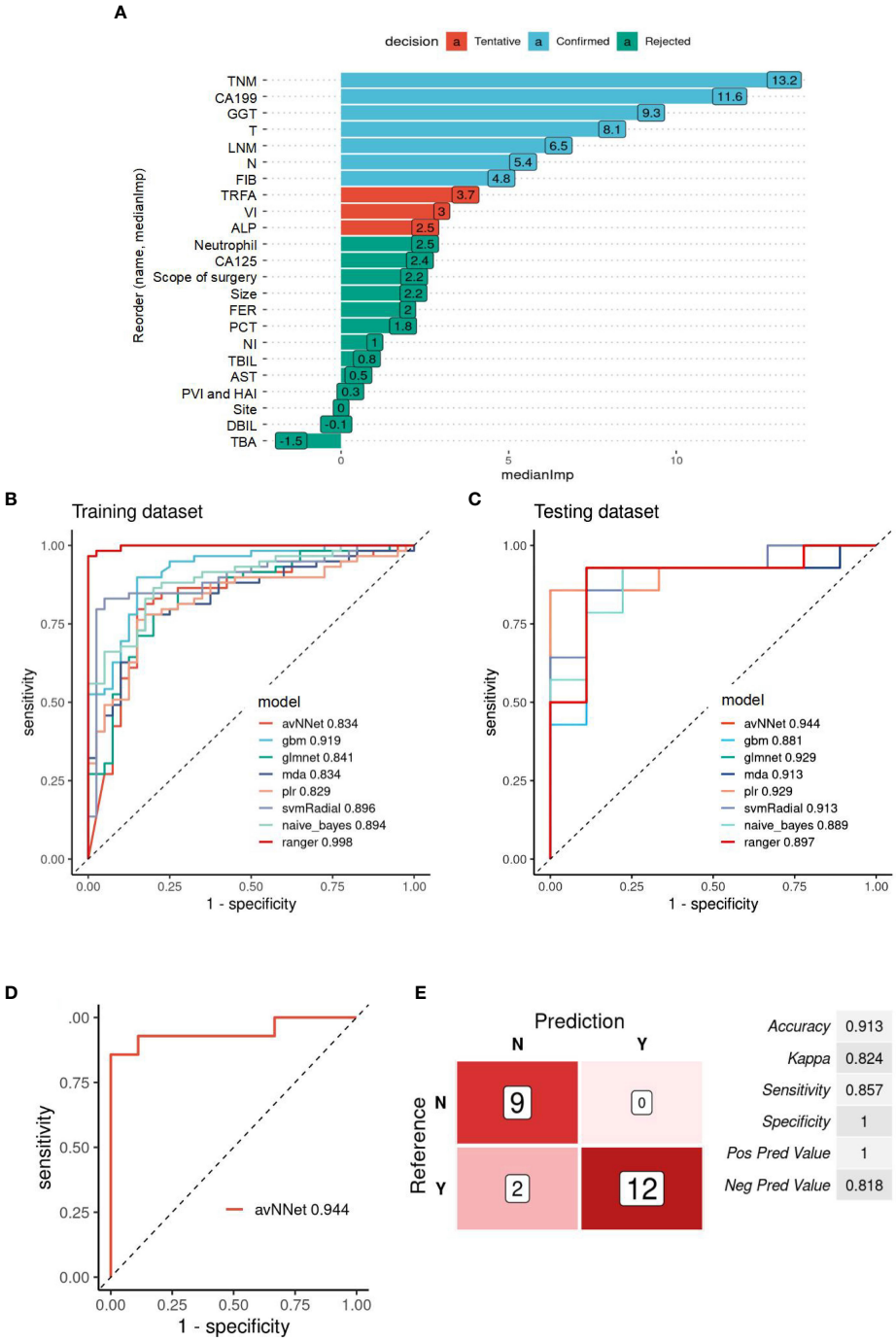

FIGURE 2
Evaluation of the recurrence prediction power of MIC1 combined AI Algorithm in GBC. **(A)** Statistical plot of the contribution of each feature in the model estimated by the random forest strategy. By testing the significance obtained, the features can be classified into three categories: Confirmed, Tentative, and Rejected. "Confirmed" is selected as an important feature for MIC1 modeling analysis. **(B)** ROC curves of the MIC1-based optimal models constructed by the nine algorithms in the training and **(C)** testing datasets. **(D)** ROC curves of the MIC1-based "avNNet" model in testing datasets, AUC=0.944. **(E)** The evaluation indicators of MIC1-based "avNNet" model prediction efficacy. TNM, TNM-stage; CA199, carbohydrate antigen 199; GGT, gamma-glutamyl transpeptidase; T, T-stage; LNM, lymph node metastasis; N, N-stage; FIB, fibrinogen; TRFA, fibrinogen/albumin; VI, vascular invasion; ALP, alkaline phosphatase; CA125, carbohydrate antigen 125; FER, ferritin; PCT, thrombocytocrit; NI, nerve invasion; TBIL, total bilirubin; AS, glutamic oxalacetic transaminase; DBIL, direct bilirubin; TBA, total bile acid.

was set to 0.255 according to the Youden-index. When the predictive value of the diagnostic model is less than 0.255, it is considered low risk (no recurrence) within four years. When the model's predictive value is more than 0.255, it is regarded as high risk (recurrence), and the evaluation indicators to obtain the predictive efficiency of the model are shown in Figure 2E. The results show that the accuracy, sensitivity, and specificity of predicting recurrence in GBC by the MIC1-based model are 0.913, 0.824, and 0.857, respectively.

3.4 Evaluation of the survival prediction power of MIC2 combined AI algorithm in GBC

The same method was used to construct a prediction model based on the information of 15 MIC2 candidate indicators to evaluate the survival risk of patients. Nine "Confirmed" features are selected as MIC2 for modeling and analysis (Figure 3A). According to the proportion of 7:3, the patients were divided into training and testing datasets. The ROC curves of the optimal model constructed by the nine algorithms in the training set and testing set are shown in Figures 3B, C. The MIC2-based model constructed by the "glmnet" algorithm has the highest AUC of 0.882 in the testing dataset, and the model is selected as the final survival risk prediction model (Figure 3D). Set the optimal diagnostic cut-off value to 0.331 according to the Youden-index value. When the predicted value of the diagnostic model is less than 0.331, the patient to be tested is considered low risk (survival) within four years. When the model's predicted value is more than 0.331, the patient to be tested is regarded as high risk. The model's prediction efficiency evaluation indicators are obtained, as shown in Figure 3E. The results show that the accuracy, sensitivity, and specificity of predicting recurrence in GBC by the MIC2-based model are 0.871, 0.765, and 1, respectively.

3.5 Kaplan-Meier analysis of MIC1 and MIC2 estimation power of DFS and OS in GBC

The MIC1 and MIC2 estimation power of DFS and OS were analyzed by Kaplan-Meier. Kaplan-Meier analysis of MIC1 indicators predicted DFS in 122 patients (Table S6). The DFS of patients with late TNM stage, late T stage, late N stage, vascular invasion, lymph node metastasis, and high levels of CA199, FIB, and TRFA were worse than patients with a low level of them (Figure S1). However, there was no significant difference in DFS predicted by high levels of GGT and ALP. Kaplan-Meier analysis of MIC2 indicators predicted OS in 108 patients similarly (Table S7). The results show that the OS of patients with advanced TNM stage, late T stage, lymph node metastasis, nerve invasion, high FIB, MPV, and TRFA are worse than patients with a low level of them (Figure S2). The results suggest that when evaluating the OS and DFS of GBC patients, personalized management can be done by comprehensively analyzing the MIC1 and MIC2 indicators.

4 Discussion

Although many new chemotherapeutic drugs are produced and used to treat GBC, surgical resection is still the most effective. However, the recurrence and low survival rate after resection of GBC is still a complex problem that modern medicine cannot overcome. Usually, early diagnosis of GBC and timely and effective treatment can improve the five-year survival rate to 75% (1). Currently, the clinic can only manage the postoperative prognosis according to the basic pathological information, such as a clinical stage. However, the repeated adjustment of AJCC staging criteria still does not effectively affect the prognosis judgment (13). The lack of pragmatic markers to identify patients with poor prognoses may be challenging to manage forecasts effectively. Many meaningful research results have been reported to solve the problem of predicting the prognosis of GBC.

Although conventional tumor markers such as CA199, CA125, and CEA are prognostic indicators of GBC, they are still not ideal as a single index to predict the prognosis of GBC due to the lack of specificity of GBC (14). Cui et al. analyzed the clinical information such as neutrophil-lymphocyte ratio (NLR), monocyte-lymphocyte ratio (MLR), and ALP. It was only confirmed that NLR before treatment was an independent prognostic factor and biomarker of poor OS in GBC patients with different treatments (15). But what is interesting is that the predictive value of MLR in patients with GBC after the operation is related to age. There is a significant difference in the cut-off value of MLR between ≤ 60 years old and > 60 years old in patients with GBC (16). In our study, ALP (RR=1.495, 95% CI: 1.145-1.952) and GGT (RR=1.472, 95%CI:1.126-1.925) were risk factors for the recurrence of GBC. Pancreatic biliary reflux is a risk factor for GBC and cholangiocarcinoma, so the early diagnosis and treatment of pancreatic juice reflux plays a vital role in preventing GBC and cholangiocarcinoma (17). Studies have shown that GGT and ALP significantly increase in pancreatic and biliary reflux patients (18). Our results also showed that ferritin was a risk predictor of recurrence (RR=1.698, 95% CI: 1.302-2.215 ($P < 0.001$)). Because cancer cells can produce synthesis and secrete ferritin, cancer cells affect the uptake and clearance of ferritin. When cells are damaged and necrotic, the ferritin stored in the cytoplasm will flow into the blood, increasing ferritin. Nerve infiltration and lymphatic vascular invasion of GBC are independent risk factors for early recurrence of T-staged advanced GBC after radical resection (19, 20). Wang et al. reported that lymph node metastasis and platelet count were predictors of OS (21). Yang et al. found that tumors in the neck of the gallbladder significantly increased the difficulty of the operation and reduced the chance of radical resection. Gallbladder neck tumors can independently predict poor prognosis (22). In addition, the increase of preoperative fibrinogen-specific albumin was significantly correlated with the negative OS rate of GBC patients. The growth of preoperative albumin level was a prognostic factor for GBC patients. The best critical value of the preoperative fibrinogen-specific albumin ROC curve was 0.08 (23). FIB plays a key role in the coagulation pathway and in the coagulation cascade (24). Elevated plasma fibrinogen levels reflect the hypercoagulable state and thrombophilia induced by tumor cells (25). In addition, FIB has been shown to be associated with adverse clinical outcomes in various types of cancers such as gastric, cervical, colorectal, ovarian, and urothelial cancers (26–29). Serum ALB levels can reflect systemic inflammatory response and nutritional status, and reduced ALB levels have been shown to be associated with poor prognosis in a variety of cancers (30). The predictive effect of TRFA is more sensitive in predicting the prognosis of patients with malignant tumors (31). Many of these research results are also reflected synchronously in the risk factor analysis part of this study.

Although there are many studies on prognostic risk factors, few studies combined with multi-index classifiers predict postoperative recurrence and survival of GBC (32). In this study, the combination of the MIC1 classifier and the "avNNet" model can predict recurrence with an AUC of 0.944, and a sensitivity and specificity

10.3389/fonc.2023.1171837

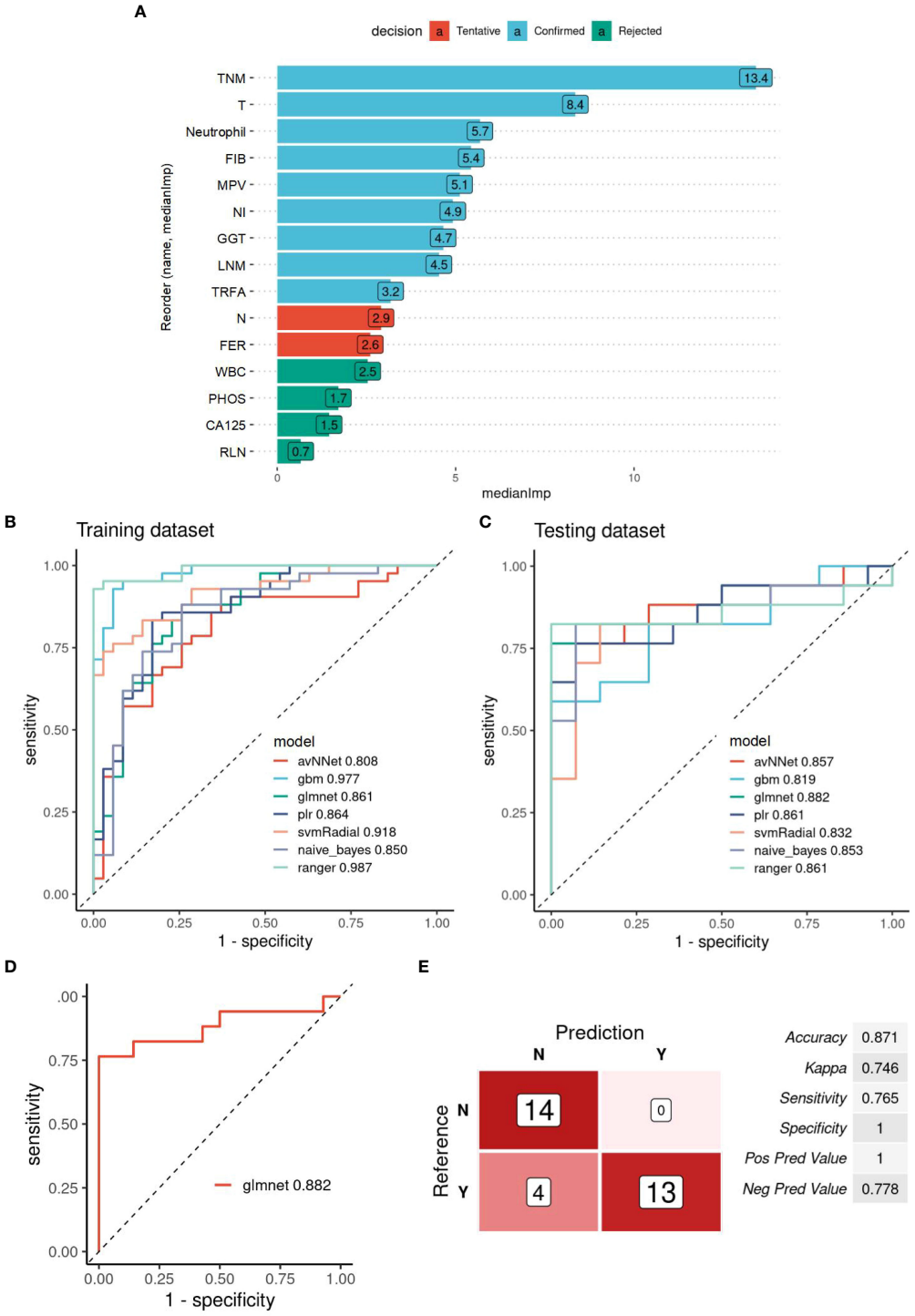

FIGURE 3
Evaluation of the survival prediction power of MIC2 combined AI Algorithm in GBC. **(A)** Statistical plot of the contribution of each feature in the model estimated by the random forest strategy. By testing the significance obtained, the features can be classified into three categories: Confirmed, Tentative, and Rejected. "Confirmed" is selected as an important feature for MIC2 modeling analysis. **(B)** ROC curves of the MIC2-based optimal models constructed by the nine algorithms in the training and (C.) testing datasets. **(D)** ROC curves of the MIC2-based "glmnet" model in testing datasets, AUC=0.882. **(E)** The evaluation indicators of MIC2-based "glmnet" model prediction efficacy. TNM, TNM-stage; T, T-stage; FIB, fibrinogen; MPV, mean platelet volume; NI, nerve invasion; GGT, gamma-glutamyl transpeptidase; LNM, lymph node metastasis; TRFA, fibrinogen/albumin; N, N-stage; FER, ferritin; WBC, white blood cell count; CA125, carbohydrate antigen 125; RLN, regional lymph node.

of 0.857 and 1.000, respectively. The MIC2 classifier and "glmnet" model combination can predict survival with an AUC of 0.882, and a sensitivity and specificity of 0.765 and 1, respectively. These two models showed excellent performance in predicting the prognosis of GBC. Furthermore, Kaplan-Meier analysis of MIC1 and MIC2 indicators shows their performance in predicting DFS and OS of GBC. Eight of the ten MIC1 indicators can effectively predict the median survival of DFS, and there is no statistically significant difference in the prediction results of the eight indicators (χ^2 = 6.849, P = 0.653). In addition, seven of the nine MIC2 indicators can effectively predict the median survival of OS, and there is no statistically significant difference in the prediction results of the seven indicators (χ^2 = 9.14, P = 0.519).

The study of GBC is often limited by the difficulty of collecting clinical samples due to the low incidence. In addition, because of some unavoidable confounding factors, we did not contain sufficient information on participants in the sample, such as more long-term survival and outcome. In the future, further validation is needed to build up the fundamental basis for clinical application. We will expand alignment to validate the two models. Moreover, systematic prospective studies should be designed in sizeable multi-center sample cohorts, and the performance of these two prediction models should be studied more deeply and systematically.

5 Conclusion

Based on the clinical data of 122 patients, two multi-index classifiers, MIC1 and MIC2, were produced for predicting postoperative recurrence and survival of GBC by correlation analysis, relative risk analysis, ROC analysis, and AI algorithm Modeling. The MIC1 and MIC2 combined with avNNet and glmnet models to predict recurrence and survival were evaluated with high sensitivity and specificity. The prediction ability of indicators in the two classifiers to DFS and OS is assessed by Kaplan-Meier analysis. As a cheap, simple, reliable, and repeatable method, clinical multi-index analysis can be used to predict the prognosis of GBC in clinical practice. We aim to improve the postoperative prognosis management of GBC through these two classifier models and provide personalized treatment monitoring to improve the survival rate of GBC. Our findings may offer an attractive strategy for the prognostic management of GBC.

Data availability statement

The original contributions presented in the study are included in the article/Supplementary Material. Further inquiries can be directed to the corresponding authors.

Ethics statement

The studies involving human participants were reviewed and approved by the Ethics Committee of the Zhejiang Cancer Hospital. Written informed consent for participation was not required for this study in accordance with the national legislation and the institutional requirements.

Author contributions

(I) Conception and design: YZ. (II) Administrative support: SC, YC, and SX. (III) Provision of study materials or patients and collection and assembly of data: YW. (IV) Data analysis and interpretation and manuscript writing: LL and QL. (V) Final approval of manuscript: All authors. All authors approved the final version of the manuscript. All authors contributed to the article.

Funding

This work was supported by grants from Zhejiang Nature Science Foundation (No. LY21H200001), Zhejiang Provincial Science and Technology Department Foundation (No. 2022500399), Pioneer and lead goose of R&D program of Zhejiang (No. 2022C03002) and Scientific research start-up fund for talents of Zhejiang Cancer Hospital at the fifth level.

Conflict of interest

The authors declare that the research was conducted in the absence of any commercial or financial relationships that could be construed as a potential conflict of interest.

Publisher's note

Supplementary material

The Supplementary Material for this article can be found online at: https://www.frontiersin.org/articles/10.3389/fonc.2023.1171837/full#supplementary-material

References

1. Goetze TO. Gallbladder carcinoma: Prognostic factors and therapeutic options. *World J Gastroenterol* (2015) 21(43):12211–7. doi: 10.3748/wjg.v21.i43.12211

2. Ramalhosa F, Amaral MJ, Serôdio M, Oliveira RC, Teixeira P, Cipriano MA, et al. Clinicopathological prognostic factors for gallbladder carcinoma: a retrospective study. *J Gastrointestinal Oncol* (2022) 13(4):1997–2006. doi: 10.21037/jgo-22-61

3. Chen H, Wu X, Duan Y, Zhi D, Zou M, Zhao Z, et al. Ursolic acid isolated from isodon excisoides induces apoptosis and inhibits invasion of GBC-SD gallbladder carcinoma cells. *Oncol Lett* (2019) 18(2):1467–74. doi: 10.3892/ol.2019.10397

4. Kim WJ, Lim TW, Park PJ, Choi SB, Kim WB. Clinicopathological differences in T2 gallbladder cancer according to tumor location. *Cancer control: J Moffitt Cancer Center* (2020) 27(1):1073274820915514–1073274820915514. doi: 10.1177/1073274820915514

5. Xu L, Tan H, Liu X, Huang J, Liu L, Si S, et al. Survival benefits of simple versus extended cholecystectomy and lymphadenectomy for patients with T1b gallbladder cancer: An analysis of the surveillance, epidemiology, and end results database (2004 to 2013). *Cancer Med* (2020) 9(11):3668–79. doi: 10.1002/cam4.2989

6. Zheng H, Wang JJ, Zhao LJ, Yang XR, Yu YL. Exosomal miR-182 regulates the effect of RECK on gallbladder cancer. *World J Gastroenterol* (2020) 26(9):933–46. doi: 10.3748/wjg.v26.i9.933

7. Xue C, He Y, Hu Q, Yu Y, Chen X, Chen J, et al. Downregulation of PIM1 regulates glycolysis and suppresses tumor progression in gallbladder cancer. *Cancer Manage Res* (2018) 10:5101–12. doi: 10.2147/CMAR.S184381

8. Sun L, Ke X, Wang D, Yin H, Jin B, Xu H, et al. Prognostic value of the albumin-to-γ-glutamyltransferase ratio for gallbladder cancer patients and establishing a nomogram for overall survival. *J Cancer* (2021) 12(14):4172–82. doi: 10.7150/jca.49242

9. Wang J, Bo X, Wang C, Xin Y, Nan L, Luo R, et al. Low immune index correlates with favorable prognosis but with reduced benefit from chemotherapy in gallbladder cancer. *Cancer Sci* (2020) 111(1):219–28. doi: 10.1111/cas.14239

10. Negi SS, Singh A, Chaudhary A. Lymph nodal involvement as prognostic factor in gallbladder cancer: Location, count or ratio? *J Gastrointestinal Surg* (2011) 15 (6):1017–25. doi: 10.1007/s11605-011-1528-4

11. Inoue M, Hakoda K, Sawada H, Hotta R, Ohmori I, Miyamoto K, et al. Locally advanced gallbladder cancer treated with effective chemotherapy and subsequent curative resection: a case report. *J Med Case Rep* (2022) 16(1):30–0. doi: 10.1186/s13256-021-03248-9

12. Wu Y, Zhang S, Qian X, Zhu J, Zheng S, Wu J, et al. The prognostic value of preoperative fibrinogen in patients with radical cholecystectomy. *Advanced Gut Microbiome Res* (2022) 24(29):5370539. doi: 10.1155/2022/5370539

13. Giannis D, Cerullo M, Moris D, Shah KN, Herbert G, Zani S, et al. Validation of the 8th edition american joint commission on cancer (AJCC) gallbladder cancer staging system: Prognostic discrimination and identification of key predictive factors. *Cancers* (2021) 13(3):547. doi: 10.3390/cancers13030547

14. Sachan A, Saluja SS, Nekarakanti PK, Nimisha, Mahajan B, Nag HH, et al. Raised CA19-9 and CEA have prognostic relevance in gallbladder carcinoma. *BMC Cancer* (2020) 20(1):826. doi: 10.1186/s12885-020-07334-x

15. Cui X, Zhu S, Tao Z, Deng X, Wang Y, Gao Y, et al. Long-term outcomes and prognostic markers in gallbladder cancer. *Medicine* (2018) 97(28):e11396. doi: 10.1097/MD.0000000000011396

16. Xu W, Wu X, Wang X, Yu S, Xu G, Xiong J, et al. Prognostic significance of the preoperative lymphocyte to monocyte ratio in patients with gallbladder carcinoma. *Cancer Manage Res* (2020) 12:3271–83. doi: 10.2147/CMAR.S243326

17. Kamisawa T, Kuruma S, Tabata T, Chiba K, Iwasaki S, Koizumi S, et al. Pancreaticobiliary maljunction and biliary cancer. *J Gastroenterol* (2015) 50(3):273–9. doi: 10.1007/s00535-014-1015-2

18. Xiang YK, Zhang C, Yang YL, Tian XT, Kong C, Qiu BN, et al. Diagnostic value of gamma-glutamyl transferase and alkaline phosphatase for cholecystolithiasis complicated with occult pancreaticobiliary reflux. *Zhonghua Yi Xue Za Zhi* (2022) 102(18):1359–63. doi: 10.3760/cma.j.cn112137-20220112-00083

19. Peng DZ, Nie GL, Li B, Cai YL, Lu J, Xiong XZ, et al. Prediction of early recurrence after R0 resection for gallbladder carcinoma of stage T1b-T3. *Cancer Manage Res* (2022) 14:37–47. doi: 10.2147/CMAR.S342674

20. Lei JJ, Zhang J, Chen C, Li Q, Su JB, Zhang D, et al. Analysis of perineural invasion with clinicopathological factors and prognosis for curatively resected gallbladder carcinoma. *Zhonghua Wai Ke Za Zhi* (2022) 60(7):695–702. doi: 10.3760/cma.j.cn112139-20220108-00016

21. Wang RT, Zhang LQ, Mu YP, Li JB, Xu XS, Pang Q, et al. Prognostic significance of preoperative platelet count in patients with gallbladder cancer. *World J Gastroenterol* (2015) 21(17):5303–10. doi: 10.3748/wjg.v21.i17.5303

22. Yang XW, Yuan JM, Chen JY, Yang J, Gao QG, Yan XZ, et al. The prognostic importance of jaundice in surgical resection with curative intent for gallbladder cancer. *BMC Cancer* (2014) 14:652. doi: 10.1186/1471-2407-14-652

23. Xu WY, Zhang HH, Xiong JP, Yang XB, Bai Y, Lin JZ, et al. Prognostic significance of the fibrinogen-to-Albumin ratio in gallbladder cancer patients. *World J Gastroenterol* (2018) 24(29):3281–92. doi: 10.3748/wjg.v24.i29.3281

24. Lee SE, Lee JH, Ryu KW, Nam B-H, Cho SJ, Lee JY, et al. Preoperative plasma fibrinogen level is a useful predictor of adjacent organ involvement in patients with advanced gastric cancer. *J Gastric Cancer* (2012) 12(2):81–7. doi: 10.5230/jgc.2012.12.2.81

25. Demir O, Demirag G, Aslan G. Prospective evaluation of hematological parameters in preoperative renal cell cancer patients. *BMC Urol* (2022) 22(1):201–1. doi: 10.1186/s12894-022-01118-0

26. Cao Y, Ni X, Wang Y, Wang L, Yuan K, Gan G, et al. Clinical and prognostic significance of combined plasma fibrinogen concentrations and the monocyte-to-lymphocyte ratio in patients with ovarian cancer. *Ann Trans Med* (2019) 7(11):242–2. doi: 10.21037/atm.2019.04.78

27. Li M, Wu Y, Zhang J, Huang L, Wu X, Yuan Y. Prognostic value of pretreatment plasma fibrinogen in patients with colorectal cancer: A systematic review and meta-analysis. *Medicine* (2019) 98(37):e16974–4. doi: 10.1097/MD.0000000000016974

28. Repetto O, Maiero S, Magris R, Miolo G, Cozzi MR, Steffan A, et al. Quantitative proteomic approach targeted to fibrinogen β chain in tissue gastric carcinoma. *Int J Mol Sci* (2018) 19(3):759. doi: 10.3390/ijms19030759

29. Sun Y, Han W, Song Y, Gao P, Yang Y, Yu D, et al. Prognostic value of preoperative fibrinogen for predicting clinical outcome in patients with nonmetastatic colorectal cancer. *Cancer Manage Res* (2020) 12:13301–9. doi: 10.2147/CMAR.S275498

30. Son HJ, Park Jw Fau - Chang HJ, Chang Hj Fau - Kim DY, Kim Dy Fau - Kim BC, Kim Bc Fau - Kim SY, Kim Sy Fau - Park SC, et al. Preoperative plasma hyperfibrinogenemia is predictive of poor prognosis in patients with nonmetastatic colon cancer. *Ann Surg Oncol* (2013) 20(9):2908–13. doi: 10.1245/s10434-013-2968-8

31. Tan Z, Zhang M, Han Q, Wen J, Luo K, Lin P, et al. A novel blood tool of cancer prognosis in esophageal squamous cell carcinoma: the Fibrinogen/Albumin ratio. *J Cancer* (2017) 8(6):1025–9. doi: 10.7150/jca.16491

32. Xu WY, Zhang HH, Yang XB, Bai Y, Lin JZ, Long JY, et al. Prognostic significance of combined preoperative fibrinogen and CA199 in gallbladder cancer patients. *World J Gastroenterol* (2018) 24(13):1451–63. doi: 10.3748/wjg.v24.i13.1451

frontiers | Frontiers in Oncology

TYPE Original Research
PUBLISHED 05 July 2023
DOI 10.3389/fonc.2023.1164739

OPEN ACCESS

EDITED BY
Po-Hsiang Tsui,
Chang Gung University, Taiwan

REVIEWED BY
Hirotaka Tashiro,
National Hospital Organization Kure Medical Center, Japan
Hao Wang,
Peking Union Medical College Graduate School, China

*CORRESPONDENCE
Qiang Wang
qiang.wang@ki.se
Kuansheng Ma
kuanshengma@outlook.com

‡These authors have contributed equally as co-corresponding authors to this work

RECEIVED 13 February 2023
ACCEPTED 19 June 2023
PUBLISHED 05 July 2023

CITATION
Li C, Wang Q, Zou M, Cai P, Li X, Feng K, Zhang L, Sparrelid E, Brismar TB and Ma K (2023) A radiomics model based on preoperative gadoxetic acid–enhanced magnetic resonance imaging for predicting post-hepatectomy liver failure in patients with hepatocellular carcinoma.
Front. Oncol. 13:1164739.
doi: 10.3389/fonc.2023.1164739

A radiomics model based on preoperative gadoxetic acid–enhanced magnetic resonance imaging for predicting post-hepatectomy liver failure in patients with hepatocellular carcinoma

Changfeng Li[1], Qiang Wang[2,3*‡], Mengda Zou[1], Ping Cai[4], Xuesong Li[1], Kai Feng[1], Leida Zhang[1], Ernesto Sparrelid[5], Torkel B. Brismar[2,3] and Kuansheng Ma[1*‡]

[1]Institute of Hepatobiliary Surgery, Southwest Hospital, Army Medical University, Chongqing, China, [2]Division of Medical Imaging and Technology, Department of Clinical Science, Intervention and Technology (CLINTEC), Karolinska Institutet, Stockholm, Sweden, [3]Division of Radiology, Department of Clinical Science, Intervention and Technology (CLINTEC), Karolinska Institutet, Karolinska University Hospital, Stockholm, Sweden, [4]Department of Radiology, Southwest Hospital, Army Medical University, Chongqing, China, [5]Division of Surgery, Department of Clinical Science, Intervention and Technology (CLINTEC), Karolinska Institutet, Karolinska University Hospital, Stockholm, Sweden

Background: Post-hepatectomy liver failure (PHLF) is a fatal complication after liver resection in patients with hepatocellular carcinoma (HCC). It is of clinical importance to estimate the risk of PHLF preoperatively.

Aims: This study aimed to develop and validate a prediction model based on preoperative gadoxetic acid–enhanced magnetic resonance imaging to estimate the risk of PHLF in patients with HCC.

Methods: A total of 276 patients were retrospectively included and randomly divided into training and test cohorts (194:82). Clinicopathological variables were assessed to identify significant indicators for PHLF prediction. Radiomics features were extracted from the normal liver parenchyma at the hepatobiliary phase and the reproducible, robust and non-redundant ones were filtered for modeling. Prediction models were developed using clinicopathological variables (Clin-model), radiomics features (Rad-model), and their combination.

Results: The PHLF incidence rate was 24% in the whole cohort. The combined model, consisting of albumin–bilirubin (ALBI) score, indocyanine green retention test at 15 min (ICG-R15), and Rad-score (derived from 16 radiomics features) outperformed the Clin-model and the Rad-model. It yielded an area under the receiver operating characteristic curve (AUC) of 0.84 (95% confidence interval (CI): 0.77–0.90) in the training cohort and 0.82 (95% CI: 0.72–0.91) in the test cohort. The model demonstrated a good consistency by the Hosmer–

Lemeshow test and the calibration curve. The combined model was visualized as a nomogram for estimating individual risk of PHLF.

Conclusion: A model combining clinicopathological risk factors and radiomics signature can be applied to identify patients with high risk of PHLF and serve as a decision aid when planning surgery treatment in patients with HCC.

KEYWORDS

radiomics, magnetic resonance imaging, liver failure, hepatectomy, hepatocellular carcinoma

Introduction

Liver resection remains the mainstay modality in the treatment of hepatocellular carcinoma (HCC) with a curative intent. With the advances of surgical techniques and perioperative management in recent years, cases of extended or complex liver resection are increasing (1), which makes it increasingly important to make individual evaluations to avoid insufficient remnant liver volumes and impaired liver function after the surgery, the so-called post-hepatectomy liver failure (PHLF). At present, PHLF poses a fatal threat after liver resection and is the prominent cause of perioperative mortality (2), with a reported incidence as high as 40% (3).

Precise evaluation of liver function makes it possible to predict PHLF preoperatively. Previous studies have explored blood biochemistry tests, indocyanine green (ICG) test (4), and clinical scoring systems such as Child–Pugh score (5) and the Model for End-Stage Liver Disease (MELD) score (6) and computed tomography (CT)-based remnant liver volume (7) in the prediction of PHLF. However, the overall performance of these factors has been suboptimal. A more accurate, non-invasive approach for comprehensive liver function evaluation is urgently needed.

Gadoxetic acid (Primovist®) is a T1 magnetic resonance imaging (MRI) contrast medium widely used in clinical practice for liver lesion detection and characterization. Compared with the extracellular contrast media, it is actively taken up by hepatocyte at 10–40 min after administration (the so-called hepatobiliary phase) (8). Recent studies have shown that gadoxetic acid–enhanced MRI is promising in quantitative evaluation of liver function (9, 10). Classically, the methods used are based on the measurement of signal intensity (for instance relative liver enhancement or liver-to-muscle ratio or liver-to-spleen ratio), T1 relaxometry (e.g., T1 reduction rate), or dynamic contrast–enhanced MRI parameters (including hepatic extraction fraction) (11). These gadoxetic acid–enhanced MRI-derived parameters have shown a good correlation with ICG test and clinical scoring systems (Child–Pugh grades and MELD score), indicating a potential value in prediction of PHLF (10, 12, 13). However, when measuring signal intensity or T1 relaxation time, regions of interest (ROIs) with a limited diameter are most often placed in a single selected slice, which may not fully represent the whole liver function. Furthermore, the placement of the ROI is subjective, potentially reducing the reproducibility. In addition, the measurement of T1 relaxation time or dynamic contrast–enhanced MRI often requires additional scanning sequences (14).

Radiomics is a burgeoning technique, which can extract a great number of features from clinical routine medical imaging and transform them into mineable data for quantitative analysis (15). The basic assumption of radiomics is that the delicate pathophysiological alterations at cellular or molecular levels can be reflected by signal changes on images. The quantification of these imaging features and analyzing them through advanced algorithms or deep learning techniques can aid the clinician to solve clinical issues, such as disease diagnosis, prognosis, or prediction of treatment response. In the field of hepatobiliary imaging, previous studies have demonstrated that radiomics can significantly improve diagnostic and prognostic accuracy in HCC, such as the prediction of microvascular invasion (15), tumor differentiation (16), and early recurrence after hepatectomy (17).

In this study, it was tested whether radiomics analysis of gadoxetic-enhanced MR images can be used to predict PHLF in patients undergoing surgery due to HCC. The hypothesis was that radiomics analysis can detect delicate imaging features reflecting varying levels of liver function.

Materials and methods

Study design and patient selection

The research protocol of this single-center, retrospective study was reviewed and approved by the Institutional Review Board of Southwest Hospital, Army Medical University (No. (B) KY2021068). Written informed consent was waived due to the retrospective property of this study.

Consecutive patients undergoing hepatectomy during the period between January 2017 and March 2019 were retrieved according to the following inclusion and exclusion criteria. The inclusion criteria were 1) histopathologically confirmed HCC by resected specimen and 2) preoperative gadoxetic acid–enhanced MRI within 4 weeks before hepatectomy. The exclusion criteria were 1) anti-cancer treatment before hepatectomy, including radiofrequency ablation, hepatectomy, transarterial chemoembolization, portal vein embolization, targeted therapy, and immunotherapy, and 2)

insufficient imaging quality (such as motion artifacts). In final, 276 patients were included in this study, and they were randomly divided into training and test cohorts at a ratio of 7:3, in which the training cohort was exclusively used for model development, while test cohort was used for to validate the performance of the model. Figure 1 gives more details about this process.

The reporting of this study followed the Checklist for Artificial Intelligence in Medical Imaging (CLAIM) guidance (18). The CLAIM checklist is provided at Supplementary Table S1. The process of model development is illustrated in Figure 2.

Clinicopathological characteristics

Clinicopathological variables comprised of age, gender, body mass index, hepatitis B infection status, cirrhosis, tumor size, Child–Pugh grade, the albumin–bilirubin (ALBI) score (Grade 1 or Grade 2/3) (19), alanine aminotransferase (ALT), aspartate transaminase (AST), platelet, ICG-R15 test, liver resection extent (minor, if resected segments < 3 or major ≥ 3 segments) (20), laparoscopic-assisted operation, intraoperative blood loss, and liver resection duration. The scattered missing values were replaced by imputation of the median value.

Definition of PHLF

PHLF was defined according to the International Study Group of Liver Surgery (ISGLS) standard: an increased international normalized ratio (INR) and hyperbilirubinemia (above the normal range of the local laboratory) on postoperative day 5 or afterwards (21). According to this definition, the patients were grouped into PHLF group and non-PHLF group.

MR imaging acquisition

All patients underwent preoperative gadoxetic acid–enhanced MRI on a scanner (3.0 T, Magnetom Trio, Siemens Healthcare) with a six-channel body coil. Dynamic contrast–enhanced images were acquired using T1-weighted 3D volume interpolated breath hold sequence before, at the time of aorta enhancement, and 60 s, 180 s, 5 min, and 15 min after administration of contrast media. Gadoxetic acid (Primovist, Bayer Pharma, Berlin, Germany, 0.1 ml/kg body weight) was injected through an antecubital vein at a rate of 1.0 ml/s followed by a flush of saline at the same rate. Hepatobiliary phase was obtained at 15 min after injection. Detailed scanning parameters are provided in Supplementary Table S2.

Delineation of normal liver tissue and inter-observer agreement evaluation

Delineation of normal liver tissue (exclusion of blood vessels, bile ducts, and cyst areas) was performed on images obtained in the hepatobiliary phase using the open-source software ITK-SNAP (http://www.itksnap.org/). Initially, 30 MR images were randomly selected for volume of interest (VOI) delineation by two researchers (with 2 years and 20 years of liver MRI experience, respectively) independently to evaluate reproducibility and stability of the extracted radiomics features. The inter-observer agreement was measured by interclass coefficient (ICC) on the VOI-based feature

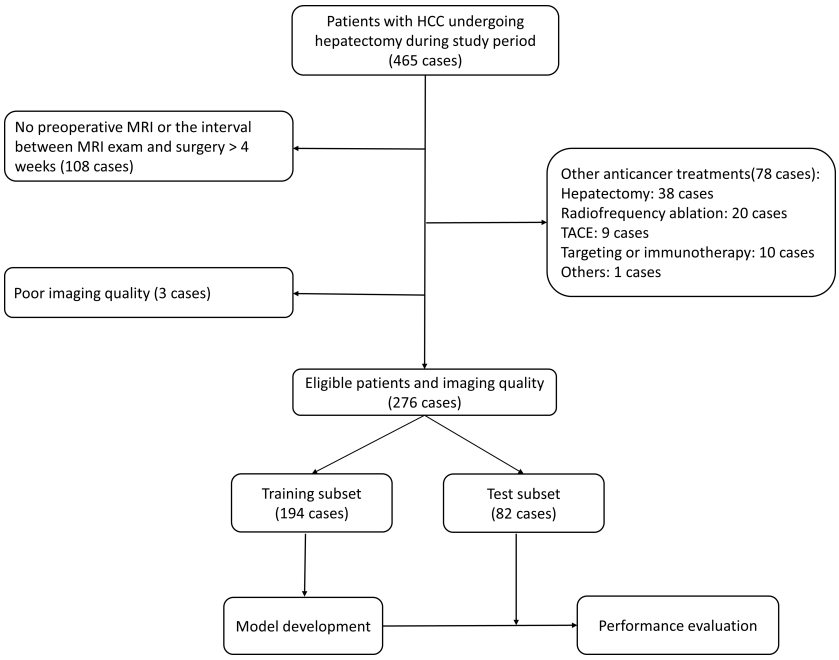

FIGURE 1
Flowchart of patient selection.

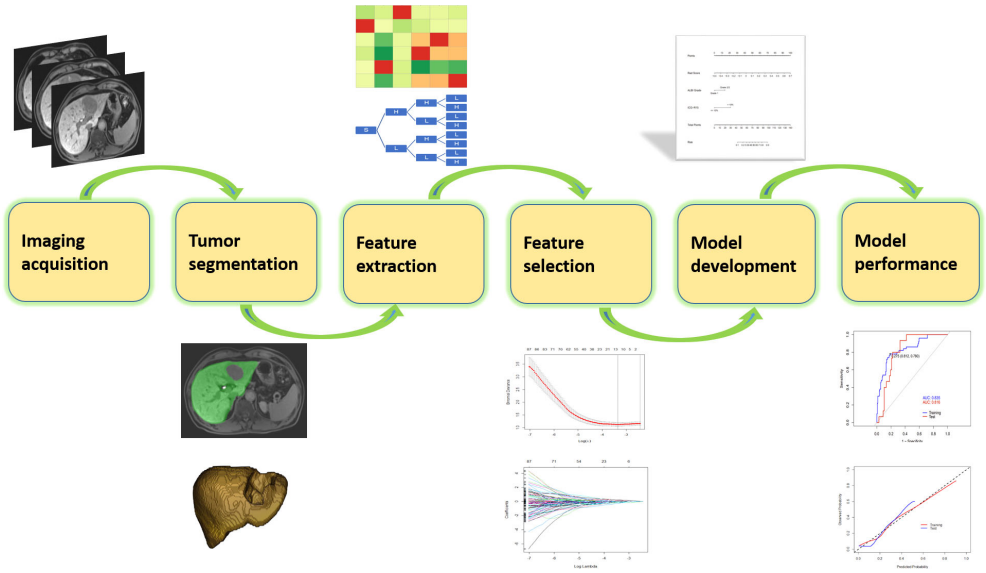

FIGURE 2
Workflow of the development of a radiomics-based model.

extraction. Features with ICC >0.75 were regarded as agreeable reproducibility and included for further analysis (22, 23). The liver delineation was then performed on the remaining patients by one researcher. The results were saved as a VOI file for further analysis. When contouring the liver, the researchers were blinded to the patients' clinical information.

Imaging preprocessing and radiomics feature extraction

Before feature extraction, all images were interpolated to a voxel size of $1 \times 1 \times 1$ mm^3, and the intensity histogram was discretized into a bin width of 25. A Python package, pyradiomics (https://github.com/AIM-Harvard/pyradiomics), was exploited to extract radiomics features from the manually delineated VOI. The terminology of the radiomics features extracted by pyradiomics is in accordance with the Image Biomarker Standardisation Initiative (24). The following categories of features were extracted: (1) shape, including 2D and 3D (n = 14); (2) first-order statistics (n = 18); (3) gray level co-occurrence matrix-derived feature (n = 24); (4) gray level run length matrix-derived feature (n = 16); (5) gray level size zone-derived feature (n = 16); (6) gray level dependence matrix-derived feature (n = 14); and (7) neighboring gray tone difference matrix feature (n = 5), (8) above features extracted from the wavelet transformed images (n = 744). In total, 851 features were exacted.

Radiomics feature selection and radiomics model construction

In the training cohort, radiomics feature selection for the model construction involved two steps. First, after normalization of the radiomics features by z-score method, Spearman correlation analysis was performed among the features and only one of the pairs with a correlation coefficient >0.99 was kept in order to reduce redundancy. Second, the filtered features were fed into the least absolute shrinkage and selection operator (LASSO) regression analysis to detect the most informative features to avoid potential overfitting. The superparameter lambda (λ) in LASSO was determined by the fivefold cross-validation. Features with non-zero coefficient were selected for model development (termed as "Rad-model").

Clinical model construction

To detect independent risk factors for PHLF incidence, univariable regression analysis on clinicopathological variables were performed in the training cohort. The variables where the correlation to PHLF had a p-value <0.05 were used in a multivariable logistic regression analysis. A clinical model (coined as "Clin-model") was then constructed using clinicopathological variables with $p < 0.05$ after the multivariable regression analysis.

Combined model construction

Radiomics risk score (Rad-score) was then calculated for each patient through linear combination of included features in the Rad-model weighted by the corresponding coefficient. Clinicopathological variables in the Clin-model and the Rad-score were then collected to construct a combined model through logistic regression analysis. The ideal one was determined by the backward stepwise selection strategy using likelihood ratio test with Akaike information criteria (AIC) at the minimum value.

Statistical analysis

Continuous variables with normal distribution were expressed as mean ± standard deviation and compared using Mann–Whitney U test between non-PHLF and PHLF groups. Categorical variables were presented as number (percentage) and were compared by Chi-square test or Fisher's exact test. The performance of the models was evaluated based on their abilities of discrimination, calibration, and clinical usefulness in both training and test cohorts. The discrimination capability was assessed by the area under the receiver operating characteristic curve (AUC). Calibration capacity of the model was intuitively assessed by calibration curve. The goodness of fit of the model was measured by Hosmer–Lemeshow test, with p-value > 0.05 indicating a good result. Clinical usefulness of the model was evaluated by decision curve analysis (DCA). All statistical analyses were performed on R software (R Foundation for Statistical Computing, Vienna, Austria). A two-sided $p < 0.05$ was regarded as statistically significant.

Results

Patient basic characteristics

There were 238 men and 38 women among the 276 included patients, with a majority of patients <55 years (71.4%). According to the ISGLS criteria, 65 patients were diagnosed with PHLF, and the incidence rate of PHLF was 24% in the entire cohort. The training cohort contained 194 patients, and the test cohort contained 82 patients. The baseline characteristics between the two cohorts was balanced, with $p > 0.05$ for all variables, including the PHLF incidence. Table 1 provides detailed information about the entire, training, and test cohorts.

Clinical model construction

Based on univariable and multivariable logistic regression analyses, three significant clinicopathological variables were

TABLE 1 Patient clinicopathological characteristics.

Variables	Total (n=276)	Training cohort, No. (%)			Test cohort, No. (%)			p-value[a]
		PHLF (–) (n=144)	PHLF (+) (n=50)	p-value	PHLF (–) (n=67)	PHLF (+) (n=15)	p-value	
Gender				0.489			0.202	1.000
Female	38 (13.8)	22 (15.3)	5 (10.0)		11 (16.4)	0 (0.0)		
Male	238 (86.2)	122 (84.7)	45 (90.0)		56 (83.6)	15 (100.0)		
Age (years)				0.578			0.194	0.566
≤ 55	197 (71.4)	103 (71.5)	33 (66.0)		52 (77.6)	9 (60.0)		
> 55	79 (28.6)	41 (28.5)	17 (34.0)		15 (22.4)	6 (40.0)		
BMI (kg/m^2)				0.274			0.334	1.000
≤ 18.5	6 (2.17)	2 (1.39)	2 (4.0)		1 (1.5)	1 (6.67)		
> 18.8	270 (97.8)	142 (98.6)	48 (96.0)		66 (98.5)	14 (93.3)		
Etiology of hepatitis				0.891			0.503	0.872
HBV	212 (76.8)	109 (75.7)	39 (78.0)		51 (76.1)	13 (86.7)		
None/others	64 (23.2)	35 (24.3)	11 (22.0)		16 (23.9)	2 (13.3)		
Cirrhosis status				1.000			0.641	0.817
Present	146 (52.9)	77 (53.5)	27 (54.0)		33 (49.3)	9 (60.0)		
Absent	130 (47.1)	67 (46.5)	23 (46.0)		34 (50.7)	6 (40.0)		
ALT (IU/L)				0.220			0.087	0.147
≤ 42	158 (57.2)	91 (63.2)	26 (52.0)		37 (55.2)	4 (26.7)		
> 42	118 (42.8)	53 (36.8)	24 (48.0)		30 (44.8)	11 (73.3)		
AST (IU/L)				0.018			0.955	1.000
≤ 42	158 (57.2)	90 (62.5)	21 (42.0)		39 (58.2)	8 (53.3)		
> 42	118 (42.8)	54 (37.5)	29 (58.0)		28 (41.8)	7 (46.7)		
Platelet (×10^9/L)				0.013			0.475	1.000

(Continued)

TABLE 1 Continued

Variables	Total (n=276)	Training cohort, No. (%)			Test cohort, No. (%)			*p*-value[a]
		PHLF (–) (n=144)	PHLF (+) (n=50)	*p*-value	PHLF (–) (n=67)	PHLF (+) (n=15)	*p*-value	
≤ 125	96 (34.8)	42 (29.2)	25 (50.0)		22 (32.8)	7 (46.7)		
> 125	180 (65.2)	102 (70.8)	25 (50.0)		45 (67.2)	8 (53.3)		
Child–Pugh grade				1.000			0.183	1.000
A	272 (98.6)	142 (98.6)	49 (98.0)		67 (100.0)	14 (93.3)		
B	4 (1.45)	2 (1.39)	1 (2.0)		0 (0.0)	1 (6.7)		
ALBI score				0.001			0.003	0.282
Grade 1	126 (45.7)	73 (50.7)	11 (22.0)		40 (59.7)	2 (13.3)		
Grade 2/3	150 (54.3)	71 (49.3)	39 (78.0)		27 (40.3)	13 (86.7)		
ICG-R15 test				<0.001			1.000	0.986
≤ 10%	254 (92.0)	139 (96.5)	39 (78.0)		62 (92.5)	14 (93.3)		
> 10%	22 (7.97)	5 (3.47)	11 (22.0)		5 (7.46)	1 (6.67)		
Tumor size (cm)				0.739			0.602	0.410
≤ 5	130 (47.1)	69 (47.9)	26 (52.0)		30 (44.8)	5 (33.3)		
> 5	146 (52.9)	75 (52.1)	24 (48.0)		37 (55.2)	10 (66.7)		
Resection extent				0.629			1.000	0.832
Minor	196 (71.0)	105 (72.9)	34 (68.0)		46 (68.7)	11 (73.3)		
Major	80 (29.0)	39 (27.1)	16 (32.0)		21 (31.3)	4 (26.7)		
Laparoscopic operation				1.000			0.218	1.000
Yes	42 (15.2)	22 (15.3)	8 (16.0)		8 (11.9)	4 (26.7)		
No	234 (84.8)	122 (84.7)	42 (84.0)		59 (88.1)	11 (73.3)		
Intraoperative blood loss (ml)				0.553			0.459	0.857
≤ 400	222 (80.4)	117 (81.2)	38 (76.0)		56 (83.6)	11 (73.3)		
> 400	54 (19.6)	27 (18.8)	12 (24.0)		11 (16.4)	4 (26.7)		
Liver resection time (min)				0.549			1.000	0.071
≤ 60	227 (82.3)	125 (86.8)	41 (82.0)		50 (75.8)	12 (75.0)		
> 60	49 (17.7)	19 (13.2)	9 (18.0)		16 (24.2)	4 (25.0)		
MELD score				0.744			0.151	0.763
≤ 9	259 (93.8)	135 (93.8)	46 (92.0)		65 (97.0)	13 (86.7)		
> 9	17 (6.16)	9 (6.25)	4 (8.0)		2 (3.0)	2 (13.3)		

ALBI score, albumin–bilirubin score; ALT, alanine transaminase; AST, aspartate transaminase; BMI, body mass index; HBV, hepatitis B virus; ICG-R15, indocyanine green retention rate at 15 min; MELD score, Model for End-Stage Liver Disease score; PHLF, post-hepatectomy liver failure.
[a]Between training and test cohorts. Data are expressed as n (%).

detected, including platelet, ALBI score, and ICG-R15 ($p < 0.05$) (Table 2). The Clin-model was based on these three variables. The AUC of the Clin-model in the training and the test cohort was 0.74 (95% confidence interval, CI: 0.65–0.83) and 0.71 (95% CI: 0.57–0.84) respectively (Table 3). The formula of the Clin-model is provided in Supplementary Material S1.

Radiomics feature selection and model construction

Among the 851 extracted radiomics features, 494 features (58%) showed an ICC ≥ 0.75, and these features were subjected to the two-step feature selection strategy. In the first step, 315 features

10.3389/fonc.2023.1164739

TABLE 2 Clinicopathological risk factors for post-hepatectomy liver failure in patients with hepatocellular carcinoma.

Variables	Univariable analysis		Multivariable analysis	
	OR (95% CI)	*p*-value	OR (95% CI)	*p*-value
Gender				
Male vs. female	1.62 (0.58–4.54)	0.357		
Age (years)				
> 55 vs. ≤ 55	1.29 (0.65–2.58)	0.463		
BMI (kg/m^2)				
≤ 18.5 vs. > 18.5	2.96 (0.35–25.21)	0.285		
Etiology of hepatitis				
HBV vs. none/others	1.14 (0.53–2.46)	0.741		
Cirrhosis status				
Present vs. absent	1.02 (0.54–1.95)	0.949		
ALT (IU/L)				
> 42 vs. ≤ 42	1.59 (0.83–3.04)	0.165		
AST (IU/L)				
> 42 vs. ≤ 42	2.30 (1.20–4.43)	0.013	1.69 (0.82–3.48)	0.153
Platelet (×109/L)				
≤ 125 vs. > 125	2.43 (1.26–4.73)	0.008	2.50 (1.22–5.17)	0.013
Child–Pugh grade				
B vs. A	1.45 (0.13–16.33)	0.764		
ALBI score				
Grade 2/3 vs. Grade 1	3.65 (1.73–7.68)	0.001	3.20 (1.46–7.00)	0.004
ICG-R15 test				
> 10% vs. ≤ 10%	7.84 (2.57–23.92)	<0.001	4.87 (1.5–16.02)	0.009
Tumor size (cm)				
≤ 5 vs. > 5	1.18 (0.62–2.25)	0.619		
Resection extent				
Major vs. minor	1.27 (0.63–2.55)	0.507		
Laparoscopic operation				
Yes vs. no	1.06 (0.42–2.47)	0.903		
Intraoperative blood loss (ml)				
> 400 vs. ≤ 400	1.37 (0.63–2.96)	0.421		
Liver resection time (min)				
> 60 vs. ≤ 60	1.44 (0.61–3.44)	0.407		
MELD score				
> 9 vs. ≤ 9	1.30 (0.38–4.44)	0.671		

ALBI score, albumin–bilirubin score; ALT, alanine transaminase; AST, aspartate transaminase; BMI, body mass index; CI, confidence interval; HBV, hepatitis B virus; ICG-R15, indocyanine green retention rate at 15 min; MELD score, Model for End-Stage Liver Disease score; OR, odds ratio.

TABLE 3 Performance of the models for post-hepatectomy liver failure prediction in training and test cohorts.

		Clin-model	Rad-model	Combined model
Training cohort	Cut-off value	0.27	0.29	0.28
	AUC (95% CI)	0.74 (0.65–0.83)	0.79 (0.72–0.86)	0.84 (0.77–0.90)
	Sensitivity	0.70	0.70	0.78
	Specificity	0.74	0.76	0.81
	PPV	0.49	0.51	0.59
	NPV	0.88	0.88	0.91
	Accuracy	0.73	0.75	0.80
Test cohort	AUC (95% CI)	0.71 (0.57–0.84)	0.79 (0.69–0.89)	0.82 (0.72–0.91)
	Sensitivity	0.87	0.87	0.93
	Specificity	0.55	0.70	0.67
	PPV	0.30	0.39	0.39
	NPV	0.95	0.96	0.98
	Accuracy	0.61	0.73	0.72

AUC, area under the receiver operating characteristics curve; CI, confidence interval; PPV, positive predictive value; NPV, negative predictive value.

remained after excluding one of paired features with a correlation coefficient > 0.99. In the second step, 16 non-zero coefficient features were selected by LASSO-logistic regression analysis (Figure 3) and were subsequently used for constructing the Rad-model. The Rad-model had an AUC of 0.79 (95% CI: 0.72–0.86) in the training cohort and 0.79 (95% CI: 0.69–0.89) in the test cohort (Table 3). The difference in the Clin-model and the Rad-model in performance was not significant (Delong test, $p = 0.24$).

Combined model construction

The individual Rad-score was calculated through a linear combination of the included variables in the Rad-model weighted by the corresponding coefficients (Supplementary Figure S1 and Supplementary Material S2). A third model, the combined model, was then constructed according to the AIC minimum value, which includes ALBI score, ICG-R15, and rad-score.

Performance evaluation of the combined model

The combined model yielded an AUC of 0.84 (95% CI: 0.77–0.90) in the training cohort, with sensitivity of 0.78 and specificity of 0.81 (Figure 4A). It exhibited an AUC of 0.82 (95% CI: 0.72–0.91) and sensitivity of 0.93 and 0.67 in the test cohort (Table 3). The AUC difference was significant between the combined model and the Clin-model ($p < 0.05$), but not between the combined model and the Rad-model ($p = 0.08$, Table 3). The combined model has been visualized as a nomogram (Figure 5) for clinical utility. An online tool to facilitate its calculation is available at https://onlinetools.shinyapps.io/onlineTool/.

The optimal cutoff value of the model was set at 0.28. The calibration curve showed a good agreement between the combined model predicted values and observed PHLF rate (Hosmer–Lemeshow test $p > 0.05$) (Figures 4B, C). The DCA plot illustrated that compared with the "treat-all" and "treat-none" strategies, the net benefit was higher for the combined model than the Clin-model and the Rad-model, implying that the combined model was beneficial for clinical utility (Figure 4D).

Discussion

To predict PHLF in patients with HCC, we developed and validated a nomogram model combining two clinicopathological variables (ALBI score and ICG-R15) and one radiomics variable (Rad-score) derived from radiomics analysis of preoperative T1-weighted gadoxetic acid–enhanced MRI. This prediction model yielded an AUC of 0.82 in the test cohort, indicating a promising tool for clinical utility.

Until now, only few studies have explored radiomics for prediction of PHLF. Zhu et al. proposed a nomogram model including ICG-R15 and radiomics signature based on hepatobiliary phase of gadoxetic acid–enhanced MRI from 101 patients (25). The model yielded an AUC of 0.89 in prediction PHLF in patients undergoing major liver resection. However, the study did not further validate the model in an independent test cohort. Chen et al. developed a combined model incorporating platelet, tumor size, and radiomics score deriving from preoperative gadoxetic acid–enhanced MRI for predicting PHLF (26). They validated the model at another medical center, obtaining an AUC of 0.84. However, in that study, they did not present their model with a formula or nomogram, which made it hard to reproduce or translate their model into clinical utility. In addition, their radiomics analysis was based on a single MRI slice per patient, which may not fully reflect the liver function. There are also two radiomics models based on CT modality for PHLF prediction (27, 28). Those studies had a rather limited sample size (112 and 186 cases), which may explain the unusual

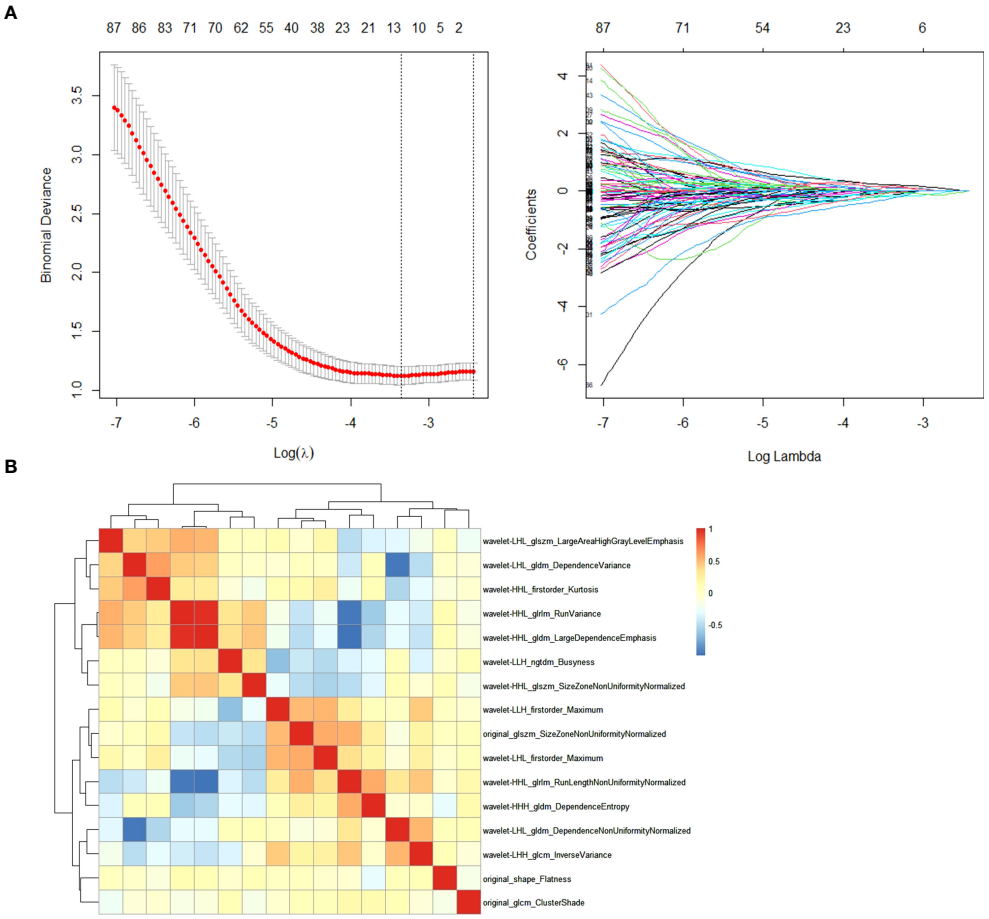

FIGURE 3
(A) Feature selection through the least absolute shrinkage and selection operator (LASSO) algorithm. **(B)** Heatmap of the correlation coefficient matrix of the selected 16 features through LASSO.

outcome with AUCs in their respective test cohorts higher than that in their training cohorts (27, 28).

The Rad-model alone showed an effective prediction efficacy, almost comparable to our combined model. A majority of the radiomics features in the Rad-model (13/16) belonged to wavelet-derived features. Those described low and high frequency signals, representing homogeneity and heterogeneity of the liver tissue (29). Unfortunately, the two previously published studies on radiomics of hepatobiliary phase of gadoxetic acid–enhanced MRI, by Zhu and Chen as mentioned above, did not adopt wavelet filter, so it is not possible to make comparisons regarding the specific radiomics features. However, wavelet-derived features do frequently appear in other gadoxetic acid–enhanced MRI radiomics models, for instance, in the prediction of microvascular invasion (30) or tumor grading for HCC (31), indicating that they capture important structural features of hepatic tumor or parenchyma (14).

Another variable in our prediction model is ICG-R15. This was consistent with Zhu's PHLF prediction model, in which ICG-R15 was the only clinical predictor (25). Currently, ICG-R15 still serves as a reference standard in the quantitative evaluation of liver function before liver resection and plays an essential role in treatment management of HCC patients (32, 33). Nevertheless, the role of ICG test as an independent risk factor for PHLF prediction remains controversial, as it can be influenced by many factors, such as blood flow or hyperbilirubinemia (32, 34). This might explain why only approximately half of currently available studies (5/11) could successfully use ICG to predict PHLF as shown in a systematnic review (3).

Our model also consists of a predictor of ALBI grade, which is a simple and objective scoring system adopting just two common biochemistry tests (serum albumin and bilirubin) for quantitative evaluation of liver function in HCC patients (19). It was proposed to overcome the limitation of the conventional Child–Pugh scoring system and has proven to be a reliable, effective tool for liver function evaluation, applicable in several different geographic regions (19). Xiang et al. have shown that ALBI could predict PHLF with an AUC of 0.64 in the test cohort (28). In the multivariable regression analysis for Clin-model, ALBI grade demonstrated an independent risk factor for PHLF incidence (odds ratio: 3.2, Grade 2/3 vs. Grade 1). However, neither Child–Pugh nor MELD score was a significant risk factor for PHLF prediction in our cohort.

This research has some limitations to be acknowledged. First, the retrospective nature of this study bore incoherent selection biases that could have had an impact on the results. However, this issue was partially compensated *via* inclusion of consecutive patients. Second, our model was not validated in an external cohort. Additional

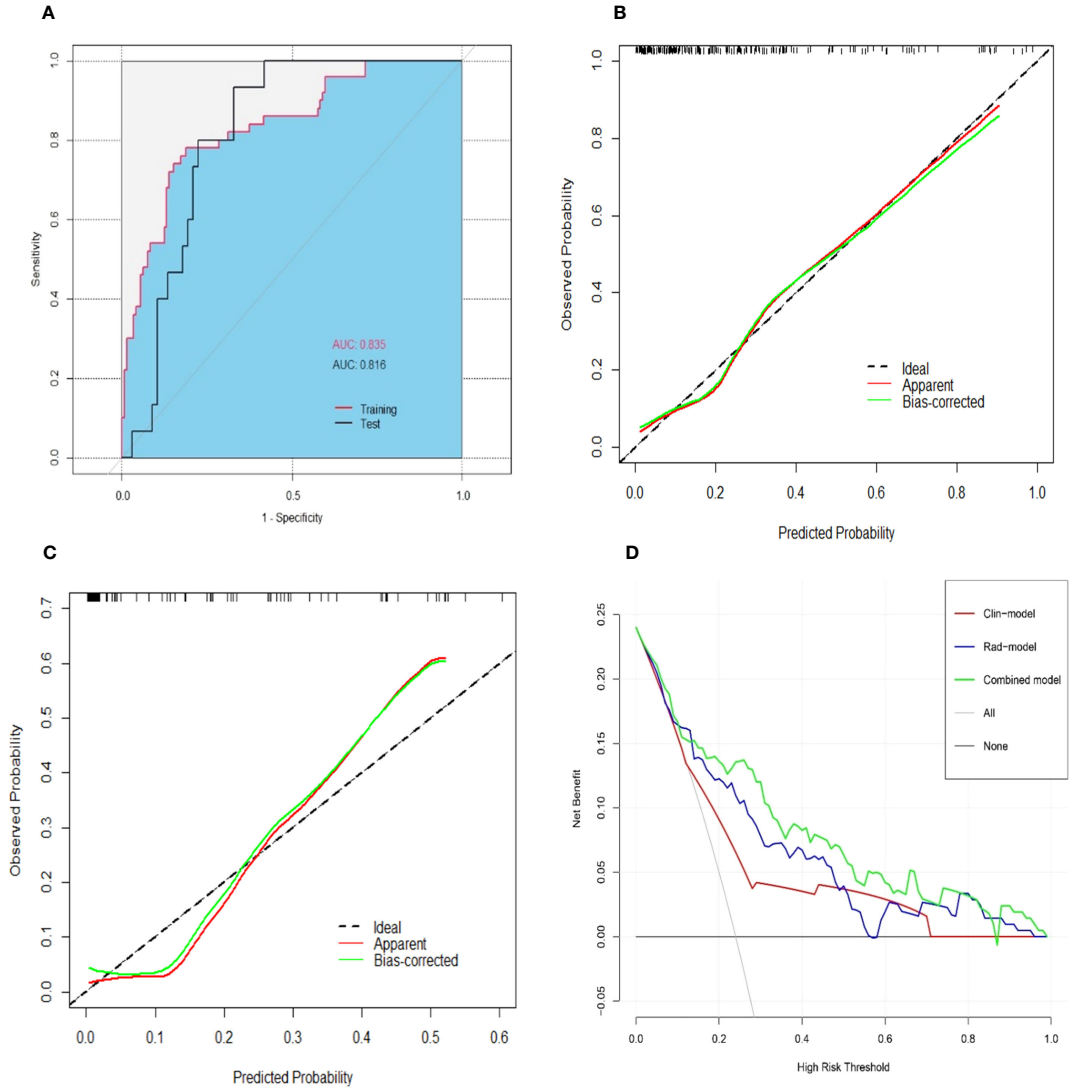

FIGURE 4
Performance of the combined model for predicting post-hepatectomy liver failure. An area under the receiver operating characteristic curve in the training and test cohorts **(A)**. Calibration curves in the training **(B)** and test cohorts **(C)** illustrated a good consistency between the model-predicted probability and the actual probability of PHLF. The red line stands for the combined model, while the green line describes the combined model calibrated by 1,000 bootstrap resampling strategy. The dash line indicates an ideal situation that the model-predicted probability perfectly matches the actual probability of PHLF. The decision curve analysis **(D)** showed that the combined model (green line) yielded a highest net benefit at different risk threshold of PHLF, compared with the clinical model (red line) and the radiomics model (blue line). Note: AUC, area under the receiver operating characteristic curve; PHLF, post-hepatectomy liver failure.

validation in larger prospective multicenter cohorts is warranted to generalize our prediction model. Third, the radiomics analysis was performed based on the whole normal liver parenchyma, rather than the future liver remnant (FLR) only. A study based on FLR only might show better AUC than presented here. The large AUC observed in our study might be explained by a strong relationship in radiomics between FLR and resected part. Lastly, the resection extent was not included in our prediction model, as it was not significant during univariable logistic regression analysis. Traditionally, the hepatic resection extent is regarded as an important indicator for PHLF. However, its role may be impaired with the development of surgical concepts and skills, equipment, perioperative management, and anesthesia techniques. Currently, the occurrence of PHLF is assumed as a consequence of multiple clinicopathological factors during the perioperative period, including baseline liver/patient characteristics and intraoperative and postoperative factors (35). Interestingly, among the four existing studies that developed the radiomics models for PHLF prediction using preoperative imaging (25–28), only one study detected the resection extent significant and included it in their model (28). Furthermore, we compared the difference in the prediction performance between our proposed models with and without the variable of the resection extent, and the test showed an insignificant result (Supplementary Table S3). Due to the simplicity principle, this variable was not included in our final models. Future studies can further investigate the effect of this variable on the incidence of PHLF.

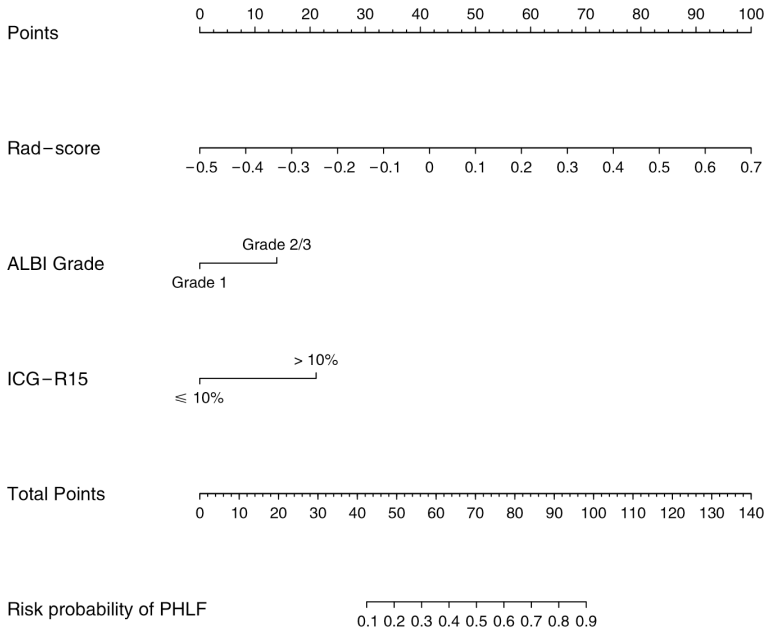

FIGURE 5
Nomogram for predicting post-hepatectomy liver failure in patients with hepatocellular carcinoma. ALBI, the albumin–bilirubin score; ICG-R15, indocyanine green retention rate at 15 min; PHLF, post-hepatectomy liver failure.

In conclusion, a prediction nomogram combining clinical risk factors and radiomics signature based on preoperative gadoxetic acid–enhanced MRI was constructed, and it can potentially be an effective tool for predicting liver failure after liver resection in patients with hepatocellular carcinoma.

Data availability statement

The original contributions presented in the study are included in the article/Supplementary Material. Further inquiries can be directed to the corresponding authors.

Ethics statement

The studies involving human participants were reviewed and approved by The Institutional Review Board of Southwest Hospital, Army Medical University. The ethics committee waived the requirement of written informed consent for participation.

Author contributions

Conceptualization: KM and QW. Data curation: CL, QW, PC, MZ, XL, KF, and LZ. Formal analysis: CL, QW, and KM. Funding acquisition: KM and QW. Investigation: CL, MZ, XL, and KF. Methodology: KM, QW, and TB. Project administration: KM and LZ. Software: PC and XL. Supervision: KM, TB, LZ, and ES. Writing—original draft: CL and QW. Writing—review and editing: all authors. All authors contributed to the article and approved the submitted version.

Funding

This work was funded by the National Natural Science Foundation of China (No. 82073346), and Famous Teachers section of the Chongqing Talents Program (4246ZP112). QW receives a scholarship from the China Scholarship Council (CSC) (No. 201907930009) and the Analytic Imaging Diagnostic Arena (AIDA) Clinical Fellowship (No. 2232 Wang).

Conflict of interest

The authors declare that the research was conducted in the absence of any commercial or financial relationships that could be construed as a potential conflict of interest.

Publisher's note

Supplementary material

The Supplementary Material for this article can be found online at: https://www.frontiersin.org/articles/10.3389/fonc.2023.1164739/full#supplementary-material

References

1. Jarnagin WR, Gonen M, Fong Y, DeMatteo RP, Ben-Porat L, Little S, et al. Improvement in perioperative outcome after hepatic resection: analysis of 1,803 consecutive cases over the past decade. *Ann Surg* (2002) 236:397–407. doi: 10.1097/01.SLA.0000029003.66466.B3

2. Rassam F, Zhang T, Cieslak KP, Lavini C, Stoker J, Bennink RJ, et al. Comparison between dynamic gadoxetate-enhanced MRI and ^{99m}Tc-mebrofenin hepatobiliary scintigraphy with SPECT for quantitative assessment of liver function. *Eur Radiol* (2019) 29:5063–72. doi: 10.1007/s00330-019-06029-7

3. Wang Q, Wang A, Sparrelid E, Zhang J, Zhao Y, Ma K, et al. Predictive value of gadoxetic acid-enhanced MRI for posthepatectomy liver failure: a systematic review. *Eur Radiol* (2022) 32:1792–803. doi: 10.1007/s00330-021-08297-8

4. Sunagawa Y, Yamada S, Kato Y, Sonohara F, Takami H, Inokawa Y, et al. Perioperative assessment of indocyanine green elimination rate accurately predicts postoperative liver failure in patients undergoing hepatectomy. *J Hepatobiliary Pancreat Sci* (2021) 28:86–94. doi: 10.1002/jhbp.833

5. Zou H, Yang X, Li QL, Zhou QX, Xiong L, Wen Y. A comparative study of albumin-bilirubin score with child-pugh score, model for end-stage liver disease score and indocyanine green R15 in predicting posthepatectomy liver failure for hepatocellular carcinoma patients. *Dig Dis* (2018) 36:236–43. doi: 10.1159/000486590

6. Chin KM, Allen JC, Teo JY, Kam JH, Tan EK, Koh Y, et al. Predictors of post-hepatectomy liver failure in patients undergoing extensive liver resections for hepatocellular carcinoma. *Ann Hepatobiliary Pancreat Surg* (2018) 22:185–96. doi: 10.14701/ahbps.2018.22.3.185

7. Yamamoto R, Sugiura T, Okamura Y, Ito T, Yamamoto Y, Ashida R, et al. Utility of remnant liver volume for predicting posthepatectomy liver failure after hepatectomy with extrahepatic bile duct resection. *BJS Open* (2021) 5:zraa049. doi: 10.1093/bjsopen/zraa049

8. Brismar TB, Dahlstrom N, Edsborg N, Persson A, Smedby O, Albiin N. Liver vessel enhancement by gd-BOPTA and gd-EOB-DTPA: a comparison in healthy volunteers. *Acta Radiol Sep* (2009) 50:709–15. doi: 10.1080/02841850903055603

9. Bastati N, Beer L, Mandorfer M, Poetter-Lang S, Tamandl D, Bican Y, et al. Does the functional liver imaging score derived from gadoxetic acid-enhanced MRI predict outcomes in chronic liver disease? *Radiology*. (2020) 294:98–107. doi: 10.1148/radiol.2019190734

10. Yoon JH, Lee JM, Kang HJ, Ahn SJ, Yang H, Kim E, et al. Quantitative assessment of liver function by using gadoxetic acid-enhanced MRI: hepatocyte uptake ratio. *Radiology*. (2019) 290:125–33. doi: 10.1148/radiol.2018180753

11. Bae KE, Kim SY, Lee SS, Kim KW, Won HJ, Shin YM, et al. Assessment of hepatic function with gd-EOB-DTPA-enhanced hepatic MRI. *Dig Dis* (2012) 30:617–22. doi: 10.1159/000343092

12. Nilsson H, Blomqvist L, Douglas L, Nordell A, Janczewska I, Näslund E, et al. Gd-EOB-DTPA-enhanced MRI for the assessment of liver function and volume in liver cirrhosis. *Br J Radiol* (2013) 86:20120653. doi: 10.1259/bjr.20120653

13. Kim YC, Kim MJ, Park YN, Kim KS, Ahn SH, Jung SE, et al. Relationship between severity of liver dysfunction and the relative ratio of liver to aortic enhancement (RE) on MRI using hepatocyte-specific contrast. *J Magn Reson Imaging* (2014) 39:24–30. doi: 10.1002/jmri.24100

14. Lambin P, Leijenaar RTH, Deist TM, Peerlings J, de Jong EEC, van Timmeren J, et al. Radiomics: the bridge between medical imaging and personalized medicine. *Nat Rev Clin Oncol* (2017) 14:749–62. doi: 10.1038/nrclinonc.2017.141

15. Wang Q, Li C, Zhang J, Hu X, Fan Y, Ma K, et al. Radiomics models for predicting microvascular invasion in hepatocellular carcinoma: a systematic review and radiomics quality score assessment. *Cancers (Basel)* (2021) 13:5864. doi: 10.3390/cancers13225864

16. Ding Y, Ruan S, Wang Y, Shao J, Sun R, Tian W, et al. Novel deep learning radiomics model for preoperative evaluation of hepatocellular carcinoma differentiation based on computed tomography data. *Clin Transl Med* (2021) 11:e570. doi: 10.1002/ctm2.570

17. Zhao Y, Wu J, Zhang Q, Hua Z, Qi W, Wang N, et al. Radiomics analysis based on multiparametric MRI for predicting early recurrence in hepatocellular carcinoma after partial hepatectomy. *J Magn Reson Imaging* (2021) 53:1066–79. doi: 10.1002/jmri.27424

18. Mongan J, Moy L, Kahn CEJr. Checklist for artificial intelligence in medical imaging (CLAIM): a guide for authors and reviewers. *Radiol Artif Intell* (2020) 2:e200029. doi: 10.1148/ryai.2020200029

19. Johnson PJ, Berhane S, Kagebayashi C, Satomura S, Teng M, Reeves HL, et al. Assessment of liver function in patients with hepatocellular carcinoma: a new evidence-based approach-the ALBI grade. *J Clin Oncol* (2015) 33:550–8. doi: 10.1200/JCO.2014.57.9151

20. Dahiya D, Wu TJ, Lee CF, Chan KM, Lee WC, Chen MF. Minor versus major hepatic resection for small hepatocellular carcinoma (HCC) in cirrhotic patients: a 20-year experience. *Surgery*. (2010) 147:676–85. doi: 10.1016/j.surg.2009.10.043

21. Rahbari NN, Garden OJ, Padbury R, Brooke-Smith M, Crawford M, Adam R, et al. Posthepatectomy liver failure: a definition and grading by the international study group of liver surgery (ISGLS). *Surgery*. (2011) 149:713–24. doi: 10.1016/j.surg.2010.10.001

22. Koo TK, Li MY. A guideline of selecting and reporting intraclass correlation coefficients for reliability research. *J Chiropr Med* (2016) 15:155–63. doi: 10.1016/j.jcm.2016.02.012

23. Gu D, Xie Y, Wei J, Li W, Ye Z, Zhu Z, et al. MRI-Based radiomics signature: a potential biomarker for identifying glypican 3-positive hepatocellular carcinoma. *J Magn Reson Imaging* (2020) 52:1679–87. doi: 10.1002/jmri.27199

24. Zwanenburg A, Vallières M, Abdalah MA, Aerts HJWL, Andrearczyk V, Apte A, et al. The image biomarker standardization initiative: standardized quantitative radiomics for high-throughput image-based phenotyping. *Radiology*. (2020) 295:328–38. doi: 10.1148/radiol.2020191145

25. Zhu WS, Shi SY, Yang ZH, Song C, Shen J. Radiomics model based on preoperative gadoxetic acid-enhanced MRI for predicting liver failure. *World J Gastroenterol* (2020) 26:1208–20. doi: 10.3748/wjg.v26.i11.1208

26. Chen Y, Liu Z, Mo Y, Li B, Zhou Q, Peng S, et al. Prediction of post-hepatectomy liver failure in patients with hepatocellular carcinoma based on radiomics using gd-EOB-DTPA-Enhanced MRI: the liver failure model. *Front Oncol* (2021) 11:605296. doi: 10.3389/fonc.2021.605296

27. Cai W, He B, Hu M, Zhang W, Xiao D, Yu H, et al. A radiomics-based nomogram for the preoperative prediction of posthepatectomy liver failure in patients with hepatocellular carcinoma. *Surg Oncol* (2019) 28:78–85. doi: 10.1016/j.suronc.2018.11.013

28. Xiang F, Liang X, Yang L, Liu X, Yan S. CT radiomics nomogram for the preoperative prediction of severe post-hepatectomy liver failure in patients with huge (≥ 10 cm) hepatocellular carcinoma. *World J Surg Oncol* (2021) 19:344. doi: 10.1186/s12957-021-02459-0

29. Zhou J, Lu J, Gao C, Zeng J, Zhou C, Lai X, et al. Predicting the response to neoadjuvant chemotherapy for breast cancer: wavelet transforming radiomics in MRI. *BMC Canc* (2020) 20:100. doi: 10.1186/s12885-020-6523-2

30. Xu X, Zhang HL, Liu QP, Sun SW, Zhang J, Zhu FP, et al. Radiomic analysis of contrast-enhanced CT predicts microvascular invasion and outcome in hepatocellular carcinoma. *J Hepatol* (2019) 70:1133–44. doi: 10.1016/j.jhep.2019.02.023

31. Wu M, Tan H, Gao F, Hai J, Ning P, Chen J, et al. Predicting the grade of hepatocellular carcinoma based on non-contrast-enhanced MRI radiomics signature. *Eur Radiol* (2019) 29:2802–11. doi: 10.1007/s00330-018-5787-2

32. Vos JJ, Wietasch JK, Absalom AR, Hendriks HG, Scheeren TW. Green light for liver function monitoring using indocyanine green? an overview of current clinical applications. *Anaesthesia*. (2014) 69:1364–76. doi: 10.1111/anae.12755

33. Clavien PA, Petrowsky H, DeOliveira ML, Graf R. Strategies for safer liver surgery and partial liver transplantation. *N Engl J Med* (2007) 356:1545–59. doi: 10.1056/NEJMra065156

34. Iimuro Y. ICG clearance test and 99mTc-GSA SPECT/CT fusion images. *Visc Med* (2017) 33:449–54. doi: 10.1159/000479046

35. Shen YN, Zheng ML, Guo CX, Bai XL, Pan Y, Yao WY, et al. The role of imaging in prediction of post-hepatectomy liver failure. *Clin Imag* (2018) 52:137–45. doi: 10.1016/j.clinimag.2018.07.019

frontiers | Frontiers in Oncology

TYPE Original Research
PUBLISHED 06 September 2023
DOI 10.3389/fonc.2023.960502

OPEN ACCESS

EDITED BY
Mengling Feng,
National University of Singapore, Singapore

REVIEWED BY
Yong Zhou,
Sichuan University, China
Nasser Khaled Yaghi,
Barrow Neurological Institute (BNI),
United States

*CORRESPONDENCE
Dongxu Zhao
dxzhao@jlu.edu.cn

RECEIVED 03 June 2022
ACCEPTED 14 August 2023
PUBLISHED 06 September 2023

CITATION
Tong Y, Jiang L, Cui Y, Pi Y, Gong Y and Zhao D (2023) Clinical characteristic–assisted surgical benefit stratification for resection of primary tumor in patients with advanced primary malignant bone neoplasms: a population-based propensity score–matched analysis. *Front. Oncol.* 13:960502. doi: 10.3389/fonc.2023.960502

Clinical characteristic–assisted surgical benefit stratification for resection of primary tumor in patients with advanced primary malignant bone neoplasms: a population-based propensity score–matched analysis

Yuexin Tong[1], Liming Jiang[1], Yuekai Cui[2], Yangwei Pi[1], Yan Gong[1] and Dongxu Zhao[1*]

[1]Department of Orthopedics, The China-Japan Union Hospital of Jilin University, Changchun, Jilin, China, [2]The Second Clinical Medical School of The Wenzhou Medical University, Wenzhou, Zhejiang, China

Background: Primary tumor resection (PTR) is the standard treatment for patients with primary malignant bone neoplasms (PMBNs). However, it remains unclear whether patients with advanced PMBNs still benefit from PTR. This study aimed to develop a prediction model to estimate the beneficial probability of PTR for this population.

Methods: This study extracted data from patients diagnosed with advanced PMBNs, as recorded in the Surveillance, Epidemiology, and End Results (SEER) database, with the period from 2004 to 2015. The patient cohort was then bifurcated into two groups: those who underwent surgical procedures and the non-surgery group. Propensity score matching (PSM) was utilized to mitigate any confounding factors in the study. The survival rates of patients from both the surgical and non-surgery groups were evaluated using Kaplan–Meier (K-M) curves analysis. Moreover, the study used this method to assess the capacity of the nomogram to distinguish patients likely to derive benefits from surgical intervention. The study was grounded in the hypothesis that patients who underwent PTR and survived beyond the median overall survival (OS) time would potentially benefit from the surgery. Subsequently, logistic regression analysis was performed to ascertain significant predictors, facilitating the development of a nomogram. This nomogram was subjected to both internal and external validation using receiver operating characteristic curves, area under the curve analysis, calibration plots, and decision curve analysis.

Results: The SEER database provided a total of 839 eligible patients for the study, among which 536 (63.9%) underwent PTR. Following a 2:1 PSM analysis, patients were classified into two groups: 364 patients in the surgery group and 182 patients in the non-surgery group. Both K-M curves and multivariate Cox regression analysis revealed that patients who received PTR had a longer

survival duration, observed both before and after PSM. Crucial factors such as age, M stage, and tumor size were identified to be significantly correlated with surgical benefits in patients with advanced PMBNs. Subsequently, a nomogram was developed that uses these independent predictors. The validation of this predictive model confirmed its high accuracy and excellent discrimination ability of the nomogram to distinguish patients who would most likely benefit from surgical intervention.

Conclusion: In this study, we devised a user-friendly nomogram to forecast the likehood of surgical benefits for patients diagnosed with advanced PMBNs. This tool facilitates the identification of the most suitable candidates for PTR, thus promoting more discerning and effective use of surgical intervention in this patient population.

KEYWORDS

primary malignant bone neoplasms, primary tumor resection, nomogram, survival benefit, SEER database

Introduction

Primary malignant bone neoplasms (PMBNs) diverge from other forms of cancer, representing a rare category of mesenchymal-derived tumors that makes up only 0.2%–1% of all malignant tumors (1, 2). The most prevalent type of PMBNs is osteosarcoma, followed by chondrosarcoma, Ewing sarcoma, and chordoma, respectively (3). Typically, the first symptoms that patients present with at the initial diagnosis of PMBNs are pain and localized mass. Radiographic findings generally show mixed osteolytic and osteogenic aggressive bone destruction, substantial unmineralized soft tissue mass, and even pathological fractures (4, 5). In recent years, advancements in surgical techniques and adjuvant therapy have improved survival rates; the 5-year survival rate for patients with early-stage PMBNs can reach as high as 70% (6, 7). However, the prognosis remains grim for those with advanced PMBNs, particularly for patients with distant metastases (DMs). The reported 5-year survival rates for patients with metastatic osteosarcoma, Ewing's sarcoma, and chondrosarcoma were significantly low at 25%, <30%, and 28.4%, respectively (8, 9).

Surgical intervention is generally recognized as a fundamental treatment approach for patients with PMBNs. However, for those diagnosed with advanced and metastatic disease, systemic chemotherapy, targeted molecular therapy, and palliative treatment serve as principal strategies (10–12). Emerging evidence suggests that primary tumor resection (PTR) also offers significant survival benefits for patients with advanced PMBNs (13–15). This is presumably due to the ability of PTR to counteract the immunosuppressive effects, even in the advanced stage of the disease (16). Moreover, by reducing the tumor burden *in vivo*, PTR may enhance the efficacy of postoperative chemotherapy, thus improving patient survival results (17). Notwithstanding, there are conflicting findings in the literature. For instance, a study by Song et al. reached seemingly contradictory conclusions in a study in which found that PTR was not associated with extended survival in patients with metastatic chondrosarcoma characterized by a dedifferentiated subtype and histological grade III (18). Similarly, Matsuoka and colleagues found that performing PTR did not have a positive impact on survival rates for patients with advanced vertebral column bone sarcomas (19). These findings suggest that not all patients with advanced PMBNs benefit from surgical intervention at the primary site. In addition, considerable surgical resection of the tumor or extremity can cause significant physical alternations, including disabilities and noticeable changes in appearance (20). Such changes can result in various psychiatric conditions, such as depression and anxiety, and may even contribute to an increased suicide rate (21).

Given these considerations, it is of substantial interest to explore the factors associated with surgical benefits in patients with advanced PMBNs and to create a validated instrument to assess the probability of benefit from PTR in this population. This tool could facilitate the selection of valuable PTR treatment for suitable patients and allow appropriate treatment options for frail patients. To meet this need, our study aims to construct a predictive model by analyzing data from a population-based database. This model will quantify the surgical benefit for patients with advanced PMBNs and help to identify optimal candidates for PTR.

Abbreviations: PMBNs, primary malignant bone neoplasms; DM, distant metastasis; PTR, primary tumor resection; SEER, Surveillance, Epidemiology, and End Results; ROC, receiver operating characteristic curve; AUC, area under the curve; DCA, decision curve analyses; OS, overall survival; CSS, cancer-specific survival; PSM, propensity score matching; CI, confidence interval; HR, hazard ratio; NACT, chemotherapy; NACTRT, neoadjuvant chemoradiotherapy; VEGF, vascular endothelial growth factor; EGF, epidermal growth factor; CTCs, circulating tumor cells.

Methods

Study population

The Surveillance, Epidemiology, and End Results (SEER) database is the most extensive population-based cancer database, covering approximately 30% of the population in the United states (22). We have applied for access to the data released from the SEER database (SEER ID: 15685-Nov2020) and downloaded the data for patients with the field of "Site recode ICD-O-3/WHO 2008" with bone and joint during the period from 2004 to 2015 through the SEER*Stat 8.4.0 software. Furthermore, the data for the external validation set were obtained from the China–Japan Union Hospital of Jilin University. Two orthopedic surgeons were assigned to record clinical, pathological, and therapeutic information on the patient using a blinded method. In this study, patients with PMBNs were staged by the American Joint Committee on Cancer (AJCC) tumor node metastasis (TNM) classification system. Patients who met the following criteria were included in the study: (1) diagnosis was histologically confirmed, (2) AJCC stage of III–IV, and (3) with adequate follow-up. Patients who met the following criteria were excluded: (1) PMBNs were not the first tumor; (2) unknown whether surgery or not; and (3) unknown TNM stage, race, histological type, marital status, and tumor size. The demographic information, clinicopathological variables, and survival data of eligible patients were included (race, age, gender, histological type, histological grade, primary site, tumor size, TNM stage, marital status, radiotherapy, chemotherapy, surgery at primary site, surgery at DM, and follow-up information). The information contained within both the SEER database and our medical institution's records lacks personally identifiable data, thus negating the requirement for patient-informed consent. Consequently, our local ethics committee waived the need for ethics approval. The term "overall survival" (OS) is defined as the time interval from the date of diagnosis to the date of death from any cause, whereas "cancer-specific survival" (CSS) refers to the duration from the initial diagnosis of PMBNs to death specifically attributable to cancer. The selection process for the study population and the overall study design workflow are depicted in Figure 1.

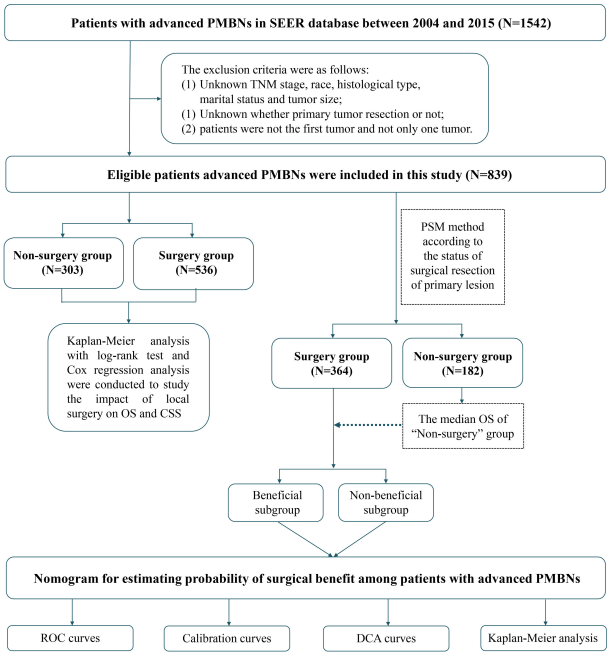

FIGURE 1
Overall flowchart of this study. SEER, Surveillance, Epidemiology, and End Results; ROC, receiver operating characteristic curve; DCA, decision curve analyses.

Statistical analysis

According to the status of surgical treatment, the patients with advanced PMBNs were divided into two groups: the surgery group and the non-surgery group. The propensity score matching (PSM) method was employed to balance significant patient characteristics between these two groups to mitigate potential bias in the baseline data. Patients were matched on the logit scale using the nearest propensity score (PS) in a 2:1 ratio (with a caliper value of 0.03). Chi-square tests were conducted to assess all study variables, both before and after PSM. A Kaplan–Meier survival curve and a log-rank test were plotted to compare OS and CSS between the two groups. A multivariate Cox proportional hazard regression analysis was further executed to determine the relationship between PTR and survival outcomes. Furthermore, the hazard ratio (HR) and its 95% confidence intervals (CIs) were computed. All statistical methods in this study were performed with the SPSS 25.0 (IBM Corporation, Armonk, NY, USA) and R version 4.0.2 software (http://www.r-project.org/).

Construction and verification of nomogram

Our study hypothesized that patients diagnosed with advanced PMBNs who underwent PTR and survived beyond the median OS of patients who did not receive PTR would benefit from this surgical procedure. Patients from the surgery group were arbitrarily split into a training set and a validation set at a ratio of 1:1. The training set was utilized for constructing a nomogram, whereas the validation set and the external validation set were deployed for the nomogram's validation. Afterward, the univariate and multivariate logistic regression analyses were carried out to identify the predictors independently associated with surgical benefits. On the basis of these identified factors related to surgical benefits, we established a visually appealing nomogram utilizing the "rms" package in R software. Furthermore, we developed a web-based probability calculator using the "Dynnom" package. The nomogram's discrimination power was assessed by the receiver operating characteristic (ROC) curves and their corresponding area

FIGURE 2
The epidemiological analysis of 839 patients with advanced PMBNs. **(A)** The integrated bar plot and heatmap of demographics information, tumor characteristics, and clinical outcomes of patients with advanced PMBNs. **(B)** The pie chart of variables in the patients with advanced PMBNs. PMBNs, primary malignant bone neoplasms.

TABLE 1 Clinical and pathological characteristics for patients with advanced PMBNs before PSM.

Variables	Overall (n = 546, %)	Non-surgery (n = 182, %)	Surgery (n = 364, %)	p-value
Age				**0.012**
<50 years	612 (72.94)	205 (67.66)	407 (75.93)	
≥50 years	227 (27.06)	98 (32.34)	129 (24.07)	
Race				**0.843**
Black	94 (11.20)	36 (11.88)	58 (10.82)	
Other	65 (7.75)	22 (7.26)	43 (8.02)	
White	680 (81.05)	245 (80.86)	435 (81.16)	
Gender				**0.950**
Female	321 (38.26)	115 (37.95)	206 (38.43)	
Male	518 (61.74)	188 (62.05)	330 (61.57)	
Marital status				**0.240**
Married	225 (26.82)	89 (29.37)	136 (25.37)	
Unmarried	614 (73.18)	214 (70.63)	400 (74.63)	
Histological type				**<0.001**
Osteosarcoma	375 (44.70)	84 (27.72)	291 (54.29)	
Chondrosarcoma	126 (15.02)	43 (14.19)	83 (15.49)	
Ewing tumor	217 (25.86)	120 (39.60)	97 (18.10)	
Other	121 (14.42)	56 (18.48)	65 (12.13)	

(Continued)

TABLE 1 Continued

Variables	Overall (n = 546, %)	Non-surgery (n = 182, %)	Surgery (n = 364, %)	p-value
Primary site				<0.001
Extremity	500 (59.59)	116 (38.28)	384 (71.64)	
Axial	339 (40.41)	187 (61.72)	152 (28.36)	
Grade				<0.001
Grade I–II	63 (7.51)	22 (7.26)	41 (7.65)	
Grade III–IV	451 (53.75)	106 (34.98)	345 (64.37)	
Unknown	325 (38.74)	175 (57.76)	150 (27.99)	
T stage				0.648
T1	210 (25.03)	78 (25.74)	132 (24.63)	
T2	497 (59.24)	182 (60.07)	315 (58.77)	
T3	132 (15.73)	43 (14.19)	89 (16.60)	
N stage				0.044
N0	690 (82.24)	238 (78.55)	452 (84.33)	
N1	149 (17.76)	65 (21.45)	84 (15.67)	
M stage				0.0003
M0	146 (17.40)	33 (10.89)	113 (21.08)	
M1	693 (82.60)	270 (89.11)	423 (78.92)	
Tumor size				0.586
<8 cm	240 (28.61)	88 (29.04)	152 (28.36)	
8–12 cm	276 (32.90)	105 (34.65)	171 (31.90)	
>12 cm	323 (38.50)	110 (36.30)	213 (39.74)	
Surgery to DM				<0.001
No	729 (86.89)	285 (94.06)	444 (82.84)	
Yes	110 (13.11)	18 (5.94)	92 (17.16)	
Radiotherapy				<0.001
No	546 (65.08)	138 (45.54)	408 (76.12)	
Yes	293 (34.92)	165 (54.46)	128 (23.88)	
Chemotherapy				1.000
No	166 (19.79)	60 (19.80)	106 (19.78)	
Yes	673 (80.21)	243 (80.20)	430 (80.22)	

under the curve (AUC). Calibration plots were generated to evaluate the concordance between the predicted and actual outcomes of the patients.

Clinical utility of the nomogram

We employed decision curve analysis (DCA) curves to appraise the net clinical benefit of the predictive model. In an additional effort to authenticate the clinical utility of the nomogram, the total points of each patient in both the training set and the validation set were computed. Subsequently, different benefit states were established. Patients whose beneficial probability exceeded 0.5 were classified into the Sur-Benefit subset, and those with a beneficial probability of 0.5 or less were categorized into the Sur-Nonbenefit subset. Kaplan–Meier survival curves were utilized to compare OS across these three groups and to test whether the nomogram could successfully discern patients who would reap the benefits of surgery.

10.3389/fonc.2023.960502

TABLE 2 Clinical and pathological characteristics for patients with advanced PMBNs after PSM.

Variables	Overall (n = 546, %)	Non-surgery (n = 182, %)	Surgery (n = 364, %)	p-value
Age				0.722
<50 years	370 (67.77)	121 (66.48)	249 (68.41)	
≥50 years	176 (32.23)	61 (33.52)	115 (31.59)	
Race				0.984
Black	74 (13.55)	24 (13.19)	50 (13.74)	
Other	33 (6.04)	11 (6.04)	22 (6.04)	
White	439 (80.40)	147 (80.77)	292 (80.22)	
Gender				0.562
Female	235 (43.04)	82 (45.05)	153 (42.03)	
Male	311 (56.96)	100 (54.95)	211 (57.97)	
Marital status				1.000
Married	168 (30.77)	56 (30.77)	112 (30.77)	
Unmarried	378 (69.23)	126 (69.23)	252 (69.23)	
Histological type				0.058
Osteosarcoma	216 (39.56)	62 (34.07)	154 (42.31)	
Chondrosarcoma	100 (18.32)	28 (15.38)	72 (19.78)	
Ewing tumor	141 (25.82)	54 (29.67)	87 (23.90)	
Other	89 (16.30)	38 (20.88)	51 (14.01)	
Primary site				0.054
Extremity	315 (57.69)	94 (51.65)	221 (60.71)	
Axial	231 (42.31)	88 (48.35)	143 (39.29)	
Grade				0.409
Grade I–II	51 (9.34)	15 (8.24)	36 (9.89)	
Grade III–IV	282 (51.65)	89 (48.90)	193 (53.02)	
Unknown	213 (39.01)	78 (42.86)	135 (37.09)	
T stage				0.832
T1	160 (29.30)	53 (29.12)	107 (29.40)	
T2	306 (56.04)	100 (54.95)	206 (56.59)	
T3	80 (14.65)	29 (15.93)	51 (14.01)	
N stage				0.846
N0	445 (81.50)	147 (80.77)	298 (81.87)	
N1	101 (18.50)	35 (19.23)	66 (18.13)	
M stage				0.350
M0	91 (16.67)	26 (14.29)	65 (17.86)	
M1	455 (83.33)	156 (85.71)	299 (82.14)	
Tumor size				0.876
<8 cm	175 (32.05)	60 (32.97)	115 (31.59)	
8–12 cm	180 (32.97)	61 (33.52)	119 (32.69)	

(Continued)

TABLE 2 Continued

Variables	Overall (n = 546, %)	Non-surgery (n = 182, %)	Surgery (n = 364, %)	p-value
>12 cm	191 (34.98)	61 (33.52)	130 (35.71)	
Surgery to DM				0.131
No	487 (89.19)	168 (92.31)	319 (87.64)	
Yes	59 (10.81)	14 (7.69)	45 (12.36)	
Radiotherapy				0.008
No	347 (63.55)	101 (55.49)	246 (67.58)	
Yes	199 (36.45)	81 (44.51)	118 (32.42)	
Chemotherapy				0.858
No/Unknown	128 (23.44)	44 (24.18)	84 (23.08)	
Yes	418 (76.56)	138 (75.82)	280 (76.92)	

Result

Clinicopathologic characteristics before and after PSM

Between 2004 and 2015, a total of 839 patients diagnosed with advanced PMBNs were identified in the SEER database. Among these, 536 patients (or 63.9%) underwent PTR, whereas the remaining 303 patients (or 36.1%) did not receive surgical treatment. Comprehensive demographic information, tumor characteristics, and patient outcomes were encapsulated in an integrated bar plot and heatmap (Figure 2). In addition, 43 eligible patients from our medical institution were incorporated into the study to validate the discriminative power of the newly developed nomogram externally. Significant discrepancies were observed in variables such as age, histology type, primary site, grade, N stage, M stage, surgery to DM, and radiotherapy between the surgery group and the non-surgery group. This indicates that the baseline characteristics between the two groups were not harmonized ($P < 0.05$) (Table 1). Following a 2:1 PSM analysis, 364 patients were matched to the surgery group and 182 to the non-surgery group. After PSM, all clinicopathologic variables, except for radiotherapy, were balanced after PSM ($P > 0.05$) (Table 2).

The correlation between PTR, radiotherapy, chemotherapy, and survival outcomes in patients with advanced PMBNs

Kaplan–Meier curves with log-rank test showed that patients who received PTR had longer OS and CSS than patients without surgery before and after PSM (Figures 3A–D). In addition, the median OS and CSS of the surgery group were 34 months (95% CI, 29.09–38.91) and 34 months (95% CI, 27.51–40.50), whereas the median OS and CSS of the non-surgery group were 15 months (95% CI, 12.61–17.39) and 15 months (95% CI, 12.30–17.71). After PSM, the survival benefit of PTR remained in patients with advanced PMBNs, the median OS and CSS of the surgery group were 32 months (95% CI, 26.46–37.54) and 34 months (95% CI, 28.01–39.99), whereas the median OS and CSS of the non-surgery group were 13 months (95% CI, 9.98–16.02) and 14 months (95% CI, 10.52–17.48). According their surgical status, all patients were classified as follows: without surgery (patients who did not receive PTR), partial excision 1 [patients who received local tumor destruction or partial resection/internal hemipelvectomy (pelvis)], partial excision 2 (patients who received radical excision or resection of lesion with limb salvage), and amputation; subsequently, a survival analysis of the different surgical procedures was conducted, with the results showing that, while surgery can improve survival in patients with advanced PMBNs, amputation does not appear to provide a survival benefit for OS and CSS in this patient group, and there was no statistical difference between local tumor destruction and limb salvage (all the p-value > 0.05), but the survival benefits for OS and CSS of local tumor resections (both limb salvage and local tumor destruction) were significantly better than amputation and no surgery (all the p-value < 0.05) (Figures 3E–H).

The multivariate Cox proportional hazard regression analysis indicated that surgery was an independent protective factor for both OS and CSS, both before and after PSM (Figure 4). Furthermore, considering the variability in the effectiveness of radiotherapy and chemotherapy depending on the histological type of PMBNs, we analyzed the relationship between these treatment modalities and survival outcomes among patients with different histological types of advanced PMBNs. The findings suggest that neither radiotherapy nor chemotherapy impacted the prognosis of patients with advanced chondrosarcoma or advanced Ewing sarcoma (Figures 5E–L). However, for patients with advanced osteosarcoma, adjuvant chemotherapy still demonstrated significant survival benefits ($p < 0.05$; Figures 5C, D), whereas radiotherapy appeared to adversely affect the survival outcomes in this patient group ($p < 0.05$; Figures 5A, B).

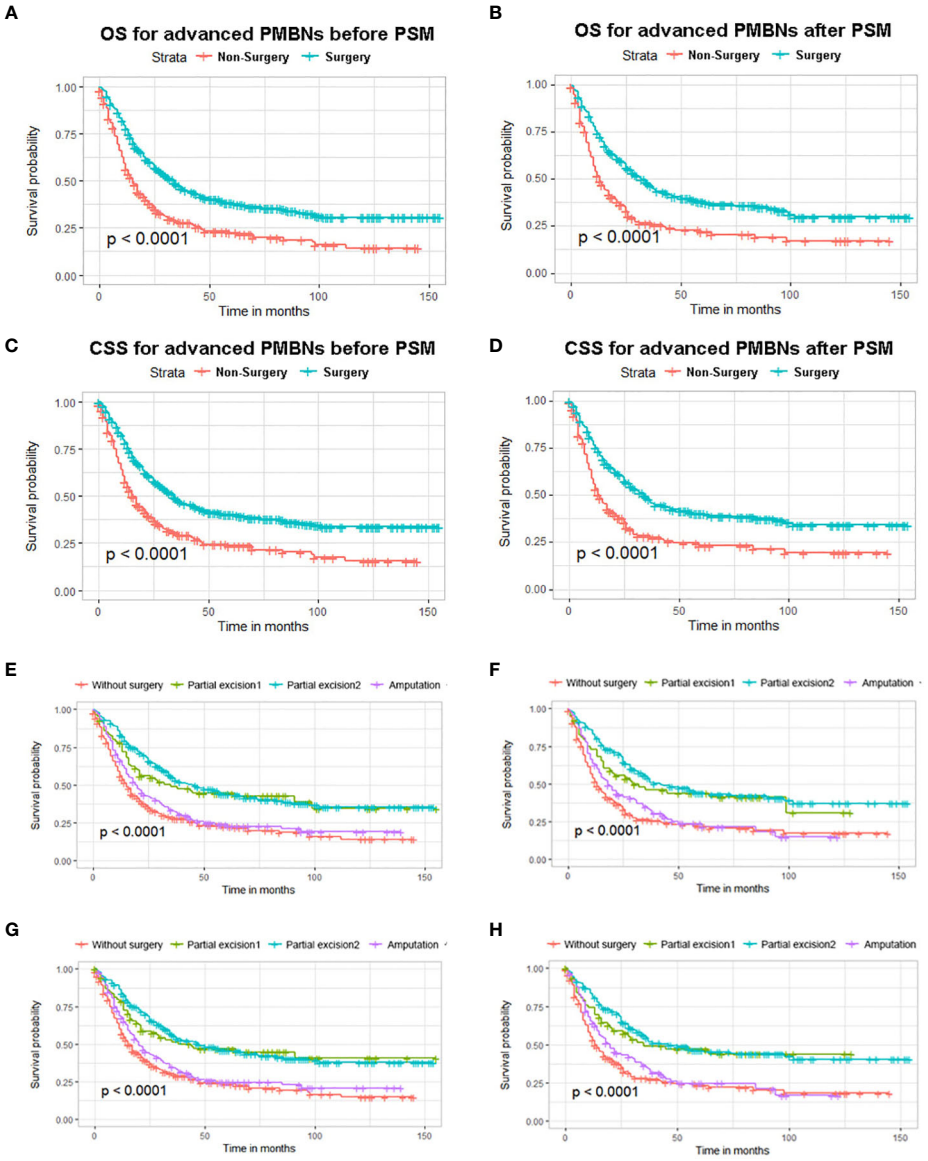

FIGURE 3
The impact of primary tumor resection on the survival outcomes of patients with advanced PMBNs. Kaplan–Meier survival curves of OS before PSM **(A)** and after PSM **(B)** and of CSS before PSM **(C)** and after PSM **(D)** in the surgery and non-surgery groups. OS analysis of different surgical approaches before PSM **(E)** and after PSM **(F)**, and CSS analysis of different surgical approaches before PSM **(G)** and after PSM **(H)**. PMBNs, primary malignant bone neoplasms; OS, overall survival; CSS, cancer-specific survival; PSM, propensity score matching.

Nomogram to identify optimal patients for surgery

On the basis of our assumption, patients with advanced PMBNs who received PTR were divided into a Sur-Benefit subset (survival time greater than 13 months) and a Sur-Nonbenefit subset (survival time less than or equal to 13 months). The univariate and multivariate logistic regression analyses determined three independent surgery benefit–related factors: age, M stage, and tumor size (Table 3). Then, a nomogram model was constructed to quantify the probability of surgical benefit and thus screen optimal candidates for surgical resection of primary tumors among patients with advanced PMBNs (Figure 6), which can be accessed via https://yxyx.shinyapps.io/sugicalbenefitofadvancedPMBNs/ (Figure 7). Moreover, the ROC curves were drawn for both the training and validation sets to assess the predictive capacity of this model. The AUC of the nomogram was 0.763 (95% CI, 0.691–0.835) in the training set (Figure 8A), 0.766 (95% CI, 0.685–0.848) in the validation set (Figure 8B), and 0.722 (95% CI, 0.640–0.878) in the external validation set (Figure 9A). Moreover, the AUC value of the comprehensive model exceeded the AUCs of age, size, and M stage individually in all three sets, indicating the robust discriminatory power of the nomogram (Figures 8C, D, 9B). The calibration plots demonstrated an excellent alignment between the nomogram's prediction and the actual outcomes in the training set (Figure 10A), the validation set (Figure 10B), and the external validation set (Figure 9C). The DCA curves demonstrated a positive

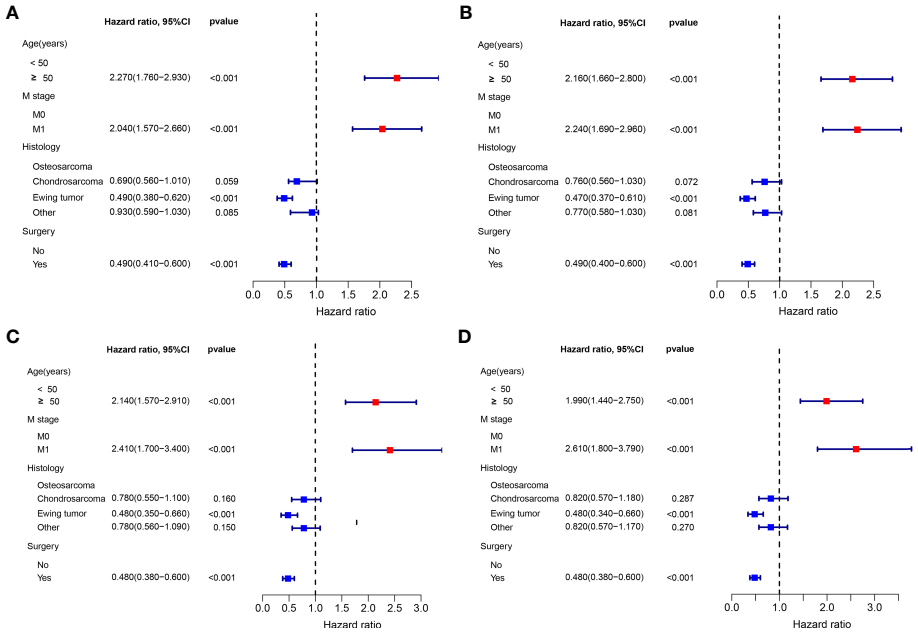

FIGURE 4
The forest plot for illustration of results of multivariate Cox regression analysis in patients with advanced PMBNs for OS before PSM **(A)** and after PSM **(C)** and for CSS before PSM **(B)** and after PSM **(D)**. PMBNs, primary malignant bone neoplasms; OS, overall survival; CSS, cancer-specific survival; PSM, propensity score matching.

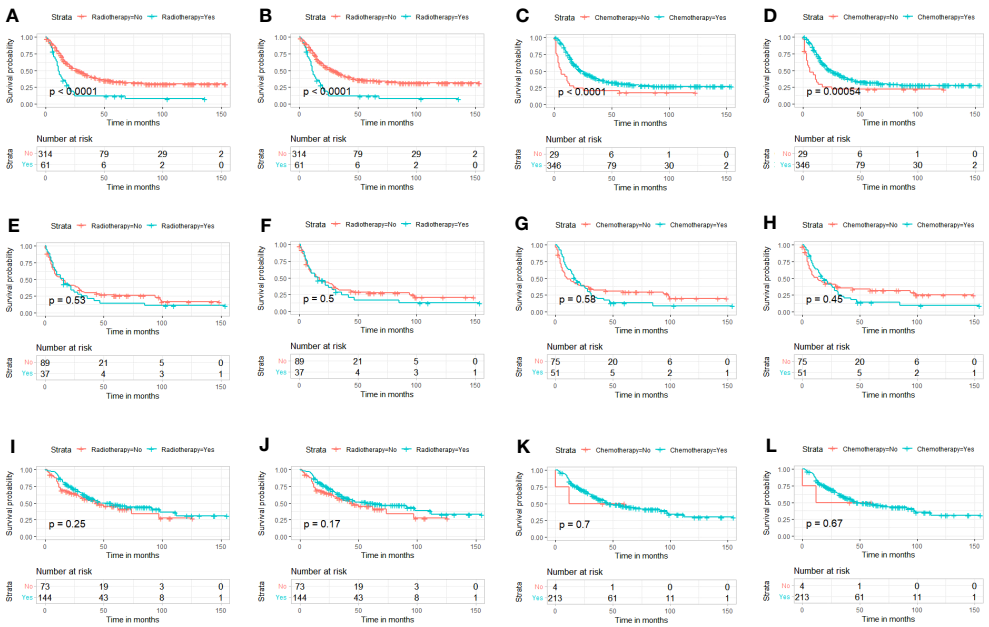

FIGURE 5
K-M survival analysis to study the correlation between radiotherapy and survival in advanced osteosarcoma [**(A)** OS; **(B)** CSS], the correlation between chemotherapy and survival in advanced osteosarcoma [**(C)**, OS; **(D)**, CSS]. The correlation between radiotherapy and survival in advanced chondrosarcoma [**(E)** OS; **(F)** CSS], and the correlation between chemotherapy and survival in advanced chondrosarcoma [**(G)** OS; **(H)** CSS]. The correlation between radiotherapy and survival in advanced Ewing sarcoma [**(I)** OS; **(J)** CSS)], and the correlation between chemotherapy and survival in advanced Ewing sarcoma [**(K)** OS; **(L)** CSS]. K-M, Kaplan–Meier; OS, overall survival; CSS, cancer-specific survival.

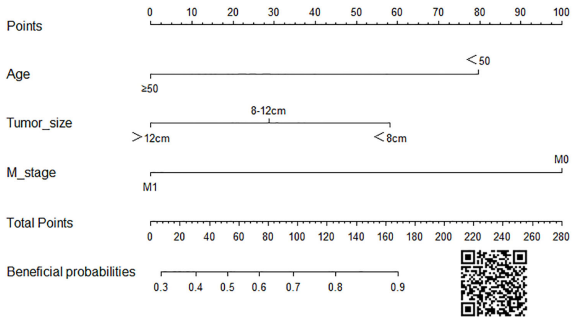

FIGURE 6
The visualized nomogram to predict the probability of surgical benefit in patients with advanced PMBNs. PMBNs, primary malignant bone neoplasms.

net benefit in all three sets, reinforcing the strong clinical utility of the nomogram (Figures 10C, D, 9D).

Kaplan–Meier survival analysis was used to validate the discriminative capacity of the nomogram by comparing the survival disparities between the Sur-Benefit subset, Non-Benefit subset, and the Non-Surgery group. The Sur-Benefit subset displayed a higher survival rate in the training set than the Non-Benefit and Non-Surgery groups ($P < 0.001$). Notably, patients not anticipated to benefit from PTR demonstrated even poorer prognoses than those who did not undergo surgery ($P = 0.0096$), suggesting the nomogram's excellent potential in identifying the most suitable candidates for PTR (Figure 11A). In the validation set, the Sur-Benefit subset survived longer than the Non-Benefit subset and the Non-Surgery group ($P < 0.001$), whereas no difference was observed between the Non-Benefit subset and the Non-Surgery group (Figure 11B).

Discussion

The rare nature of advanced PMBNs inevitably contributes to a paucity of research focused on clinical management strategies, leading to differing viewpoints in medical decision-making when treating these patients (23). Recent literature has underscored the survival benefits associated with PTR in patients with PMBNs (24, 25), significantly attributed to the reversal of immune suppression triggered by the tumor. Tumor-bearing patients often exhibit an "ignorance" or inadequate response to tumor antigens due to shortfalls in T cells, B cells, and antigen-presenting cells, consequently inducing tumor-mediated immunosuppression (26, 27). Surgical resection of the solid tumor partially revives immune competency, with both CD4+ T cells and CD8+ T cells implicated in re-establishing tumor immunity (27). Therefore, even in advanced tumors, excision of the primary lesion can impart a degree of survival benefit to patients. However, a study by Song et al. suggested limited survival benefit of PTR in patients with DM and spinal chondrosarcoma patients for over 70 years (28). Furthermore, another study proposed that surgery did not significantly influence survival rates in patients with metastatic axial (pelvic/spinal) osteosarcoma (29). These collective findings

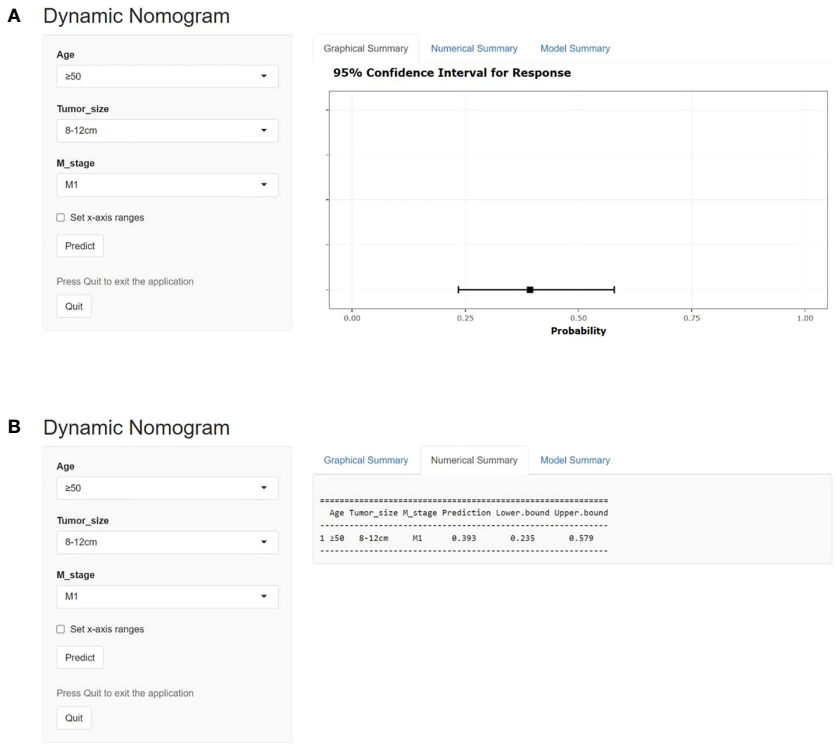

FIGURE 7
The operator interface of the web-based probability calculator. **(A)** Graphically demonstrates representation of the expected benefit rate for this patient, and **(B)** is specific value for the expected benefit rate for this patient.

10.3389/fonc.2023.960502

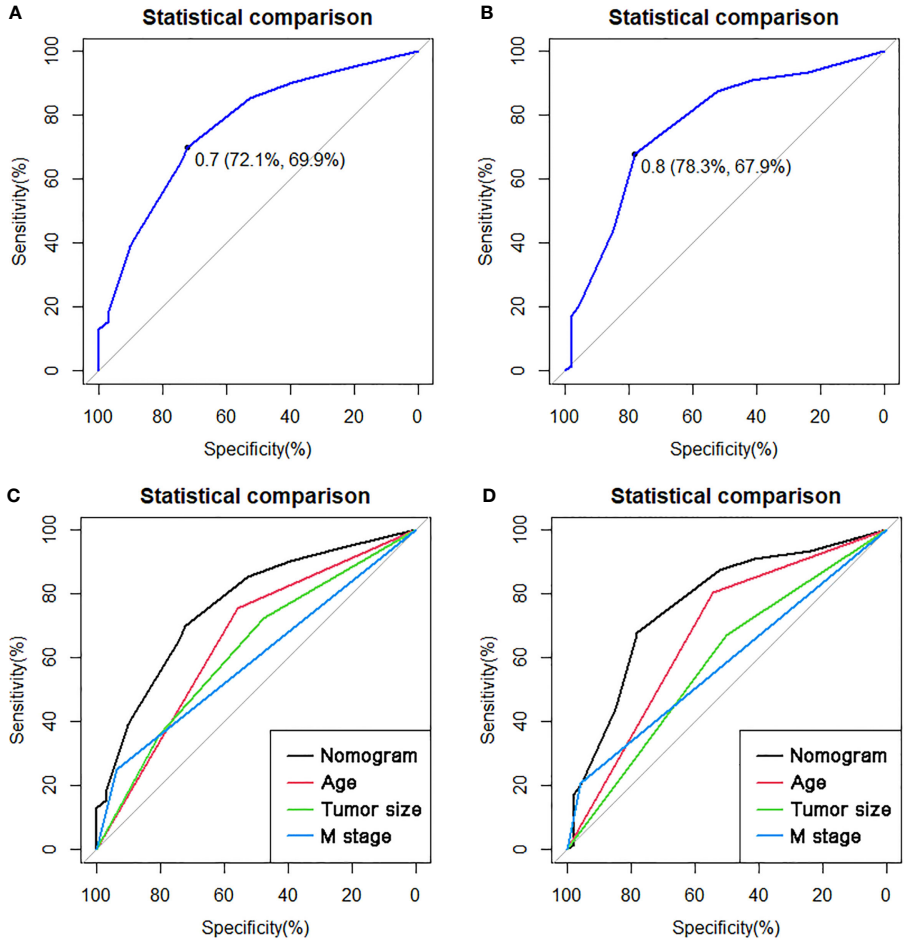

FIGURE 8
The ROC curves in the training set **(A)** and the validation set **(B)**. Comparison of the value of AUC between comprehensive nomogram and each independent predictors in the training set **(C)** and the validation set **(D)**. ROC, receiver operating characteristic curve; AUC, area under the curve.

hint at the notion that, due to inherent patient heterogeneity, not all patients with advanced PMBNs may benefit from the procedure. Current studies still lack a reliable and user-friendly tool that can inform orthopedic surgeons about the individual-specific probability of obtaining a benefit from PTR.

In this study, we not only reinforced the beneficial impact of PTR in the treatment of patients with advanced PMBNs, but, crucially, we also developed a visualized nomogram designed to precisely categorize these patients based on their anticipated probability of benefiting from localized surgery. The validation to this model exhibited exceptional discriminatory capacity and clinical utility. Moreover, the validation of an externally sourced dataset from another geographical area showcased the wide-ranging applicability of the model. As illustrated in Figure 11, our comprehensive model significantly outperforms assessments based on individual clinicopathological attributes when evaluating the potential for surgical benefit. We have also developed a web-based probability calculator to enhance its clinical utility. In simple terms, users can visit the provided website or scan the QR code and input the patient's age, tumor size, and metastasis status on the left-hand side of the web interface. Upon clicking the "Predict" button, the calculated probability of surgical benefit for the patient appears on the right-hand side of the web interface (as shown graphically in Figure 7A) and the specific data (presented in Figure 7B). Importantly, our data indicate that, for patients projected by our model to not benefit from surgery, PTR does not appear to improve their prognosis, with their survival even appearing to be worse than those who did not undergo PTR, possibly due to surgical complications (30). These findings echo previous studies and further validate the necessity of a comprehensive assessment of surgical benefit probability for the clinical management of patients with advanced PMBNs. Patient selection is critical to achieving significant improvements in survival after PTR.

Our study suggests that M stage, age at diagnosis, and tumor size are independently related to the potential benefits patients can derive from PTR. Of these variables, the status of DM exhibited the strongest correlation with the probability of surgical benefit. Previous studies have demonstrated improved survival in in patients with PMBNs with metastatic disease who underwent PTR (31, 32). This could be attributed to the reduction of the overall tumor load and the eradication of the primary source of cells capable of metastasizing (33). Nevertheless, the "self-seeding" theory suggests that circulating tumor cells (CTCs) originating from metastatic sites could return to the primary site, thus

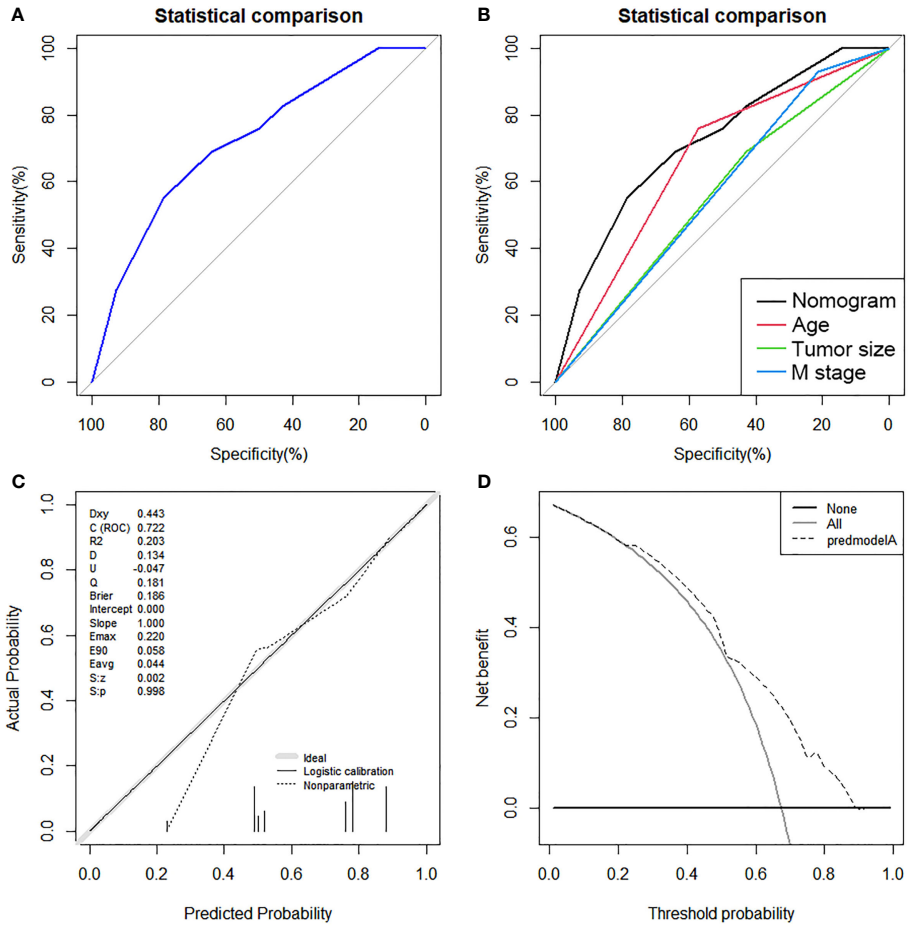

FIGURE 9
The ROC curve **(A)**, comparison of the value of AUC **(B)**, calibration curve **(C)** and DCA curve **(D)** of the external validation set.

promoting local tumor progression (33). Despite the majority of CTCs perishing in the hostile environment of the circulatory system, the surviving cells that return to the primary site could create a favorable tumor microenvironment by inhibiting immune surveillance, enhancing angiogenesis, supporting tumor growth, and fostering further metastases (34, 35). As noted earlier, even some animal models have shown the reversal of immunosuppression following the resection of the primary tumor in the presence of persistent metastases (16). The topic of surgical intervention in patients with metastatic PMBNs remains somewhat contentious, with conflicting results reported in several studies (36, 37). The "dormancy hypothesis" proposes that the growth of the metastatic site typically comprises temporary dormancy of the single-cell stage and the avascular micrometastasis stage. Patients who underwent PTR exhibited significantly elevated levels of vascular endothelial growth factor (VEGF), epidermal growth factor (EGF)–like growth factors, and other yet unidentified proliferative inducers, compared with their respective serum levels (38, 39). This theory also indicates that the release of these mediators, caused by the surgical procedure, could lead to a surgery-driven escape from dormancy and the subsequent acceleration of relapses (40). These observations imply that metastatic disease must be fully considered when evaluating the probability of surgical benefit in patients with advanced PMBNs. Furthermore, our results show that older patients might derive fewer benefits from PTR, potentially due to poorer nutritional status, decreased physiological reserve, more complex underlying conditions, and reduced tolerance to surgical treatment. Previous studies also show that axial bone involvement is higher in older patients with PMBNs compared with their younger counterparts (41, 42). The complicated anatomy of the axial bone site leads to more significant surgical risks and technical difficulties potentially resulting in more severe complications. Given the frail physical condition of the elderly, the likelihood of surgical benefit in this population is significantly reduced (43). The primary tumor size was also identified as an independent factor associated with the potential benefit of surgery. A larger tumor size increases the possibility of positive surgical margins, and larger tumors are often characterized by more aggressive biological behavior, indicating a higher risk of local recurrence. Therefore, the newly developed nomogram, which includes the predictors mentioned above, could be valuable for estimating the probability of surgical benefit and subsequently identifying the most suitable candidates for PTR among patients with advanced PMBNs. It should be acknowledged that this study also has some limitations. First, the general condition information of patients was not recorded in the

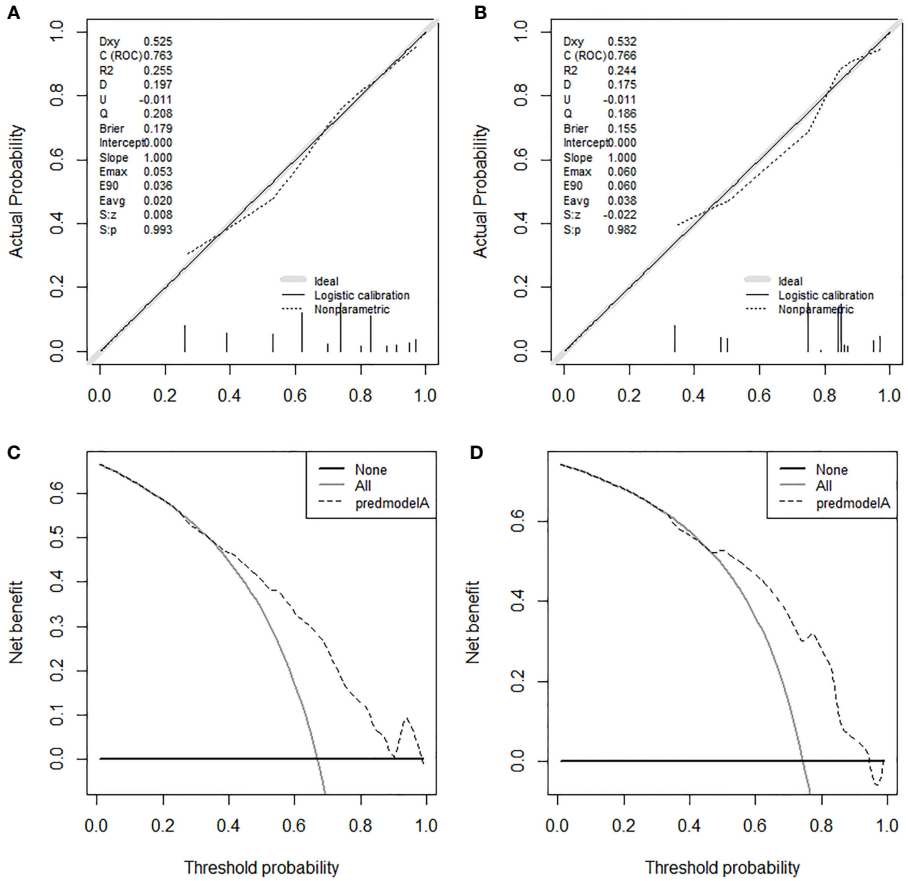

FIGURE 10
The calibration curves in the training set **(A)** and the validation set **(B)**. The DCA curves in the training set **(C)** and the validation set **(D)**. DCA, decision curve analyses.

SEER database, which might have a biased effect on the choice of surgical treatment in patients with advanced PMBNs. Second, increasing evidence indicates that neoadjuvant chemotherapy (NACT) and neoadjuvant chemoradiotherapy (NACTRT) can provide survival benefits for patients with PMBNs. In contrast, detailed protocols and doses of radiotherapy and chemotherapy were not available from this database. Finally, the metastatic site was a crucial factor in the prognosis of patients with PMBNs, especially the lung metastasis. However, because of the limitation of the SEER database in finding the year of record, we could not obtain a sufficient sample size of patients with known metastatic conditions for analysis.

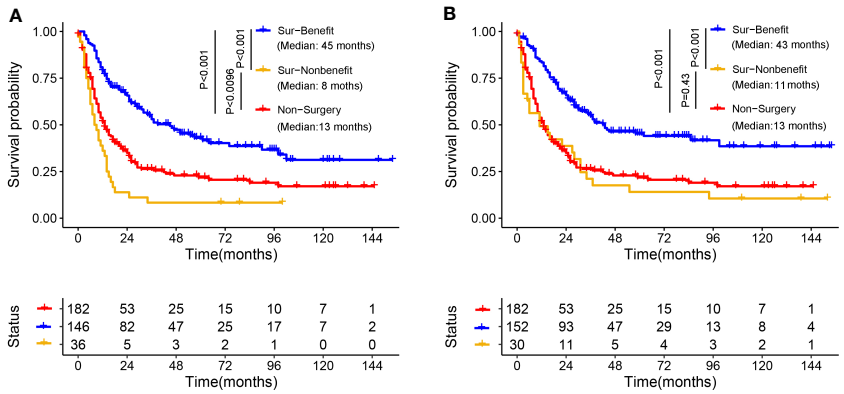

FIGURE 11
Validation of the distinguishing ability of nomogram in the matched cohort. K-M survival analysis to compare survival difference of the patients among the Sur-Benefit, Sur-Nonbenefit, and Non-Surgery groups in the training set **(A)** and the validation set **(B)**. K-M, Kaplan–Meier.

10.3389/fonc.2023.960502

TABLE 3 Univariate and multivariate logistic analyses of factors related to surgical benefit in patients with advanced PMBNs.

Variables	Univariate analysis			Multivariate analysis		
	OR	95% CI	p-value	OR	95% CI	p-value
Age						
<50 years	Reference			Reference		
≥50 years	0.26	0.13–0.49	<0.001	0.22	0.11–0.44	<0.001
Race						
Black	Reference					
Other	0.72	0.16–3.27	0.671			
White	0.82	0.32–2.09	0.671			
Gender						
Female	Reference					
Male	0.92	0.49–1.71	0.783			
Marital status						
Married	Reference					
Unmarried	1.48	0.77–2.84	0.244			
Histological type						
Osteosarcoma	Reference					
Chondrosarcoma	0.56	0.25–1.28	0.171			
Ewing sarcoma	1.65	0.68–4.01	0.266			
Other	0.66	0.28–1.56	0.342			
Primary site						
Extremity	Reference					
Axial	1.06	0.56–2	0.86			
Grade						
Grade I–II	Reference					
Grade III–IV	0.59	0.21–1.68	0.324			
Unknown	2.62	0.79–8.68	0.116			
T stage						
T1	Reference					
T2	0.5	0.24–1.04	0.064			
T3	0.89	0.32–2.49	0.83			
N stage						
N0	Reference					
N1	2.17	0.77–6.11	0.14			
M stage						
M0	Reference			Reference		
M1	0.21	0.07–0.62	0.005	0.15	0.05–0.49	0.002
Tumor size						
<8 cm	Reference			Reference		

(Continued)

TABLE 3 Continued

Variables	Univariate analysis			Multivariate analysis		
	OR	95% CI	p-value	OR	95% CI	p-value
8–12 cm	0.61	0.27–1.4	0.247	0.57	0.23–1.41	0.227
>12 cm	0.32	0.14–0.72	0.006	0.33	0.14–0.79	0.013
Surgery to DM						
No	Reference					
Yes	1.83	0.58–5.82	0.306			
Radiotherapy						
No	Reference					
Yes	1.31	0.66–2.59	0.445			
Chemotherapy						
No	Reference					
Yes	1.97	0.97–3.99	0.061			

Conclusion

Our study shows that PTR can improve survival in advanced PMBNs, except for amputation. Using a well-validated prediction model, we quantified the probability of benefiting from PTR in these patients, thus helping to allocate surgical treatment more appropriately.

Data availability statement

The raw data supporting the conclusions of this article will be made available by the authors, without undue reservation.

Ethics statement

We received permission to access the research data file in the SEER program from the National Cancer Institute, USA (reference number 15685-Nov2020). Approval was waived by the ethics committee of China–Japan Union Hospital of Jilin University, as research data is publicly available and de-identified.

Author contributions

YT and DZ conceived of and designed the study. YT and YC collected the clinical data and literature review. YT conducted the statistical analysis. YT, LJ, YP, and YG generated the figures and tables. YT wrote the manuscript. YT and DZ revised the manuscript. DZ supervised the research. All authors critically read the manuscript to improve intellectual content. All authors contributed to the article and approved the submitted version.

Acknowledgments

We are thankful for the contribution of the SEER database and the 18 registries supplying cancer research information and thank all colleagues and staff involved in the study for their contributions.

Conflict of interest

The authors declare that the research was conducted in the absence of any commercial or financial relationships that could be construed as a potential conflict of interest.

Publisher's note

References

1. Strauss S, Frezza A, Abecassis N, Bajpai J, Bauer S, Biagini R, et al. Bone sarcomas: ESMO-EURACAN-GENTURIS-ERN PaedCan Clinical Practice Guideline for diagnosis, treatment and follow-up. *Ann Oncol* (2021) 32(12):1520–36. doi: 10.1016/j.annonc.2021.08.1995

2. Bashaireh K, Alorjani M, Jahmani R, Al Khateeb A, Nimri F, Al-Ebbini M, et al. Primary bone tumors in north of Jordan. *J Epidemiol Global Health* (2021) 11(1):132–6. doi: 10.2991/jegh.k.201102.001

3. Valery P, Laversanne M, Bray F. Bone cancer incidence by morphological subtype: a global assessment. *Cancer causes control CCC* (2015) 26(8):1127–39. doi: 10.1007/s10552-015-0607-3

4. Liu C, Xi Y, Li M, Jiao Q, Zhang H, Yang Q, et al. Dedifferentiated chondrosarcoma: Radiological features, prognostic factors and survival statistics in 23 patients. *PLoS One* (2017) 12(3):e0173665. doi: 10.1371/journal.pone.0173665

5. Siclari V, Qin L. Targeting the osteosarcoma cancer stem cell. *J orthopaedic Surg Res* (2010) 5:78. doi: 10.1186/1749-799X-5-78

6. Alexander J, Binitie O, Letson G, Joyce D. Osteosarcoma: an evolving understanding of a complex disease. *J Am Acad Orthopaedic Surgeons* (2021) 29(20):e993–e1004. doi: 10.5435/JAAOS-D-20-00838

7. Damron T, Ward W, Stewart A. Osteosarcoma, chondrosarcoma, and Ewing's sarcoma: National Cancer Data Base Report. *Clin orthopaedics related Res* (2007) 459:40–7. doi: 10.1097/BLO.0b013e318059b8c9

8. Gaspar N, Hawkins D, Dirksen U, Lewis I, Ferrari S, Le Deley M, et al. Ewing sarcoma: current management and future approaches through collaboration. *J Clin Oncol* (2015) 33(27):3036–46. doi: 10.1200/JCO.2014.59.5256

9. Teo H, Peh W. Primary bone tumors of adulthood. *Cancer Imaging* (2004) 4(2):74–83. doi: 10.1102/1470-7330.2004.0004

10. Mavrogenis A, Rossi G, Palmerini E, Errani C, Rimondi E, Ruggieri P, et al. Palliative treatments for advanced osteosarcoma. *J BUON* (2012) 17(3):436–45.

11. Zheng C, Tang F, Min L, Hornicek F, Duan Z, Tu C. PTEN in osteosarcoma: Recent advances and the therapeutic potential. *Biochim Biophys Acta Rev Cancer* (2020) 1874(2):188405. doi: 10.1016/j.bbcan.2020.188405

12. Speetjens F, de Jong Y, Gelderblom H, Bovée J. Molecular oncogenesis of chondrosarcoma: impact for targeted treatment. *Curr Opin Oncol* (2016) 28(4):314–22. doi: 10.1097/CCO.0000000000000300

13. Wang W, Ding H, Sun Z, Jin C, Zhu Y, Wang X. A population-based propensity-matched study of regional dissections in patients with metastatic osteosarcoma. *J orthopaedic Surg Res* (2020) 15(1):107. doi: 10.1186/s13018-020-01592-y

14. Raciborska A, Bilska K, Rogowska E, Godziński J, Woźniak W. Surgical treatment of patients with disseminated Ewing sarcoma in our clinical experience. *Ortopedia traumatologia rehabilitacja* (2011) 13(3):271–7.

15. Malik A, Alexander J, Mayerson J, Khan S, Scharschmidt T. Is surgical resection of the primary site associated with an improved overall survival for patients with primary Malignant bone tumors who have metastatic disease at presentation? *Clin orthopaedics related Res* (2020) 478(10):2284–95. doi: 10.1097/CORR.0000000000001361

16. Danna E, Sinha P, Gilbert M, Clements V, Pulaski B, Ostrand-Rosenberg S. Surgical removal of primary tumor reverses tumor-induced immunosuppression despite the presence of metastatic disease. *Cancer Res* (2004) 64(6):2205–11. doi: 10.1158/0008-5472.CAN-03-2646

17. Tsukamoto S, Errani C, Angelini A, Mavrogenis A. Current treatment considerations for osteosarcoma metastatic at presentation. *Orthopedics* (2020) 43(5):e345–58. doi: 10.3928/01477447-20200721-05

18. Song K, Song J, Chen F, Lin K, Ma X, Jiang J. Does resection of the primary tumor improve survival in patients with metastatic chondrosarcoma? *Clin orthopaedics related Res* (2019) 477(3):573–83. doi: 10.1097/CORR.0000000000000632

19. Matsuoka M, Onodera T, Yokota I, Iwasaki K, Hishimura R, Suzuki Y, et al. Does primary tumor resection in patients with metastatic primary mobile vertebral column sarcoma improve survival? *World Neurosurg* (2022) 163:e647–e654. doi: 10.1016/j.wneu.2022.06.056

20. Fauske L, Lorem G, Grov E, Bondevik H. Changes in the body image of bone sarcoma survivors following surgical treatment–A qualitative study. *J Surg Oncol* (2016) 113(2):229–34. doi: 10.1002/jso.24138

21. Yu K, Wu B, Chen Y, Kang H, Song K, Dong Y, et al. Suicide and accidental deaths among patients with primary Malignant bone tumors. *J Bone Oncol* (2021) 27:100353. doi: 10.1016/j.jbo.2021.100353

22. Chen X, Pang Z, Wang Y, Bie F, Zeng Y, Wang G, et al. The role of surgery for atypical bronchopulmonary carcinoid tumor: Development and validation of a model based on Surveillance, Epidemiology, and End Results (SEER) database. *Lung Cancer* (2020) 139:94–102. doi: 10.1016/j.lungcan.2019.11.006

23. Gatta G, Capocaccia R, Botta L, Mallone S, De Angelis R, Ardanaz E, et al. Burden and centralised treatment in Europe of rare tumours: results of RARECAREnet-a population-based study. *Lancet Oncol* (2017) 18(8):1022–39. doi: 10.1016/S1470-2045(17)30445-X

24. Wang Z, Chen G, Chen X, Huang X, Liu M, Pan W, et al. Predictors of the survival of patients with chondrosarcoma of bone and metastatic disease at diagnosis. *J Cancer* (2019) 10(11):2457–63. doi: 10.7150/jca.30388

25. Zhang L, Akiyama T, Fukushima T, Iwata S, Takeshita K, Kawai A, et al. Surgical resection of the primary lesion for osteosarcoma patients with metastasis at initial diagnosis. *Japanese J Clin Oncol* (2021) 51(3):416–23. doi: 10.1093/jjco/hyaa204

26. Hu X, Zhang J, Wang J, Fu J, Li T, Zheng X, et al. Landscape of B cell immunity and related immune evasion in human cancers. *Nat Genet* (2019) 51(3):560–7. doi: 10.1038/s41588-018-0339-x

27. Thommen D, Schumacher T. T cell dysfunction in cancer. *Cancer Cell* (2018) 33(4):547–62. doi: 10.1016/j.ccell.2018.03.012

28. Song K, Lin K, Kang H, Dong Y, Guan H, Li F. Primary tumor resection prolongs survival in spinal chondrosarcoma patients with distant metastasis. *Spine* (2020) 45(24):E1661–8. doi: 10.1097/BRS.0000000000003694

29. Song K, Song J, Lin K, Chen F, Ma X, Jiang J, et al. Survival analysis of patients with metastatic osteosarcoma: a Surveillance, Epidemiology, and End Results population-based study. *Int orthopaedics* (2019) 43(8):1983–91. doi: 10.1007/s00264-019-04348-4

30. Yu K, Chen Y, Tian Y, Kang H, Song K, Dong Y, et al. Characteristics, incidence, and risk factors for death from fatal pneumonia among patients with primary Malignant bone tumors: a SEER-based observational study. *Trans Cancer Res* (2021) 10(8):3659–70. doi: 10.21037/tcr-21-306

31. Xu G, Wu H, Zhang Y, Xu Y, Guo X, Baklaushev V, et al. Risk and prognostic factors for different organ metastasis in primary osteosarcoma: A large population-Based analysis. *Orthopaedic Surg* (2022) 14(4):714–9. doi: 10.1111/os.13243

32. Tsuchie H, Emori M, Nagasawa H, Murahashi Y, Mizushima E, Shimizu J, et al. Impact of primary tumor resection on metastasis to the lung in patients with bone and soft-tissue sarcoma. *In Vivo (Athens Greece)* (2021) 35(6):3467–73. doi: 10.21873/invivo.12647

33. Criscitiello C, Giuliano M, Curigliano G, De Laurentiis M, Arpino G, Carlomagno N, et al. Surgery of the primary tumor in *de novo* metastatic breast cancer: To do or not to do? *Eur J Surg Oncol* (2015) 41(10):1288–92. doi: 10.1016/j.ejso.2015.07.013

34. Kim M, Oskarsson T, Acharyya S, Nguyen D, Zhang X, Norton L, et al. Tumor self-seeding by circulating cancer cells. *Cell* (2009) 139(7):1315–26. doi: 10.1016/j.cell.2009.11.025

35. Massagué J, Obenauf A. Metastatic colonization by circulating tumour cells. *Nature* (2016) 529(7586):298–306. doi: 10.1038/nature17038

36. Tohme S, Simmons R, Tsung A. Surgery for cancer: A trigger for metastases. *Cancer Res* (2017) 77(7):1548–52. doi: 10.1158/0008-5472.CAN-16-1536

37. van der Bij G, Oosterling S, Beelen R, Meijer S, Coffey J, van Egmond M. The perioperative period is an underutilized window of therapeutic opportunity in patients with colorectal cancer. *Ann Surg* (2009) 249(5):727–34. doi: 10.1097/SLA.0b013e3181a3ddbd

38. Hormbrey E, Han C, Roberts A, McGrouther D, Harris A. The relationship of human wound vascular endothelial growth factor (VEGF) after breast cancer surgery to circulating VEGF and angiogenesis. *Clin Cancer Res* (2003) 9(12):4332–9.

39. Ikeda M, Furukawa H, Imamura H, Shimizu J, Ishida H, Masutani S, et al. Surgery for gastric cancer increases plasma levels of vascular endothelial growth factor and von Willebrand factor. *Gastric Cancer* (2002) 5(3):137–41. doi: 10.1007/s101200200024

40. Demicheli R, Retsky M, Hrushesky W, Baum M. Tumor dormancy and surgery-driven interruption of dormancy in breast cancer: learning from failures. *Nat Clin Pract Oncol* (2007) 4(12):699–710. doi: 10.1038/ncponc0999

41. Kumar R, Kumar M, Malhotra K, Patel S. Primary osteosarcoma in the elderly revisited: current concepts in diagnosis and treatment. *Curr Oncol Rep* (2018) 20(2):13. doi: 10.1007/s11912-018-0658-1

42. Tsuchie H, Emori M, Nagasawa H, Miyakoshi N, Murahashi Y, Shimizu J, et al. Prognosis of primary osteosarcoma in elderly patients: A comparison between young and elderly patients. *Med principles Pract* (2019) 28(5):425–31. doi: 10.1159/000500404

43. Pan Y, Chen D, Hu T, Lv G, Dai Z. Characteristics and prognostic factors of patients with osteosarcoma older than 60 years from the SEER database. *Cancer control* (2019) 26(1):1073274819888893. doi: 10.1177/1073274819888893

Frontiers in Surgery

Explores and improves surgical practice and clinical patient management

A multidisciplinary journal which explores surgical practices - from fundamental principles to advances in microsurgery and minimally invasive techniques. It fosters innovation and improves the clinical management of patients.

Discover the latest Research Topics

See more →

Frontiers

Avenue du Tribunal-Fédéral 34
1005 Lausanne, Switzerland
frontiersin.org

Contact us

+41 (0)21 510 17 00
frontiersin.org/about/contact